Research Topics

Novel approaches in cardiac imaging

Edited by
Giuseppe Pannarale, Artur Dziewierz, Francesco Pelliccia and
Carlo Gaudio

Published in
Frontiers in Cardiovascular Medicine

ISSN 1664-8714
ISBN 978-2-8325-2779-5
DOI 10.3389/978-2-8325-2779-5

About Frontiers

Frontiers is more than just an open access publisher of scholarly articles: it is a pioneering approach to the world of academia, radically improving the way scholarly research is managed. The grand vision of Frontiers is a world where all people have an equal opportunity to seek, share and generate knowledge. Frontiers provides immediate and permanent online open access to all its publications, but this alone is not enough to realize our grand goals.

Frontiers journal series

The Frontiers journal series is a multi-tier and interdisciplinary set of open-access, online journals, promising a paradigm shift from the current review, selection and dissemination processes in academic publishing. All Frontiers journals are driven by researchers for researchers; therefore, they constitute a service to the scholarly community. At the same time, the *Frontiers journal series* operates on a revolutionary invention, the tiered publishing system, initially addressing specific communities of scholars, and gradually climbing up to broader public understanding, thus serving the interests of the lay society, too.

Dedication to quality

Each Frontiers article is a landmark of the highest quality, thanks to genuinely collaborative interactions between authors and review editors, who include some of the world's best academicians. Research must be certified by peers before entering a stream of knowledge that may eventually reach the public - and shape society; therefore, Frontiers only applies the most rigorous and unbiased reviews. Frontiers revolutionizes research publishing by freely delivering the most outstanding research, evaluated with no bias from both the academic and social point of view. By applying the most advanced information technologies, Frontiers is catapulting scholarly publishing into a new generation.

What are Frontiers Research Topics?

Frontiers Research Topics are very popular trademarks of the *Frontiers journals series*: they are collections of at least ten articles, all centered on a particular subject. With their unique mix of varied contributions from Original Research to Review Articles, Frontiers Research Topics unify the most influential researchers, the latest key findings and historical advances in a hot research area.

Find out more on how to host your own Frontiers Research Topic or contribute to one as an author by contacting the Frontiers editorial office: frontiersin.org/about/contact

Novel approaches in cardiac imaging

Topic editors
Giuseppe Pannarale — Sapienza University of Rome, Italy
Artur Dziewierz — Jagiellonian University Medical College, Poland
Francesco Pelliccia — Sapienza University of Rome, Italy
Carlo Gaudio — Sapienza University of Rome, Italy

Citation
Pannarale, G., Dziewierz, A., Pelliccia, F., Gaudio, C., eds. (2023). *Novel approaches in cardiac imaging*. Lausanne: Frontiers Media SA. doi: 10.3389/978-2-8325-2779-5

Table of contents

frontiers | Frontiers in Cardiovascular Medicine

TYPE Editorial
PUBLISHED 07 June 2023
DOI 10.3389/fcvm.2023.1221927

OPEN ACCESS

EDITED AND REVIEWED BY
Ruud B. van Heeswijk,
Centre Hospitalier Universitaire Vaudois (CHUV), Switzerland

*CORRESPONDENCE
Francesco Pelliccia
✉ f.pelliccia@mclink.it

RECEIVED 13 May 2023
ACCEPTED 30 May 2023
PUBLISHED 07 June 2023

CITATION
Pelliccia F, Dziewierz A, Pannarale G and Gaudio C (2023) Editorial: Novel approaches in cardiac imaging.
Front. Cardiovasc. Med. 10:1221927.
doi: 10.3389/fcvm.2023.1221927

Editorial: Novel approaches in cardiac imaging

Francesco Pelliccia[1]*, Artur Dziewierz[2], Giuseppe Pannarale[1] and Carlo Gaudio[1]

[1]Department of Cardiovascular Sciences, University Sapienza, Rome, Italy, [2]2nd Department of Cardiology, Institute of Cardiology, Jagiellonian University Medical College, Krakow, Poland

KEYWORDS

cardiac imaging, echocardiography, computed tomography, magnetic resonance, artificial inteligence-AI

Editorial on the Research Topic
Novel approaches in cardiac imaging

Over the past decade, advancements in cardiovascular imaging (1–3) have coincided with significant progress in diagnosing and treating various cardiac conditions (4–8). The implementation of speckle-tracking echocardiography now enables early detection of cardiac pathology while simultaneously reducing assessment variability between operators. Cardiac magnetic resonance has emerged as the gold-standard technique for non-invasively assessing biventricular dimensions, function, and myocardial tissue characteristics. Moreover, coronary computed tomography provides crucial information on plaque characteristics through non-invasive assessment of coronary arteries. Hybrid cardiac imaging combines various techniques and offers supplementary diagnostic and prognostic information. Last but not least, integrating artificial intelligence into modern cardiac imaging analysis promises a new frontier in diagnostic potential. Future technological advancements are expected to further emphasize the role of cardiovascular imaging in evaluating underlying pathophysiologic processes, thereby integrating pathophysiology, molecular medicine, and cardiovascular imaging.

This Special Issue delves into these significant aspects through 16 original research articles, an updated literature review, a systematic review and meta-analysis, and a case report. Here is a brief overview of these articles.

Chen et al. suggested a novel pipeline for labeling and imaging myocardial and vascular structures, which could be implemented in cardiac studies for examining heart structures at the single-cell level.

Guo et al. introduced a pioneering technology that combines diagnostic ultrasound with cyclic Arg-Gly-Asp-modified microbubbles targeting GP IIb/IIIa receptors. This approach can rapidly identify advanced atherosclerotic plaques and concurrently provide targeted therapy by dissolving activated and aggregated platelets.

El-Saadi et al. conducted a head-to-head comparison of myocardial strain using fast-strain encoding and feature tracking imaging in acute myocardial infarction. Both techniques exhibit acceptable agreement with two-dimensional echocardiography for longitudinal strain, with fast-strain encoding demonstrating higher sensitivity and specificity for detecting infarcted segments.

Zhang et al. evaluated left ventricular function in hypertrophic cardiomyopathy patients with preserved ejection fraction using left ventricular strain patterns derived by cardiac magnetic resonance feature tracking. The results suggest that left ventricular strain patterns are more sensitive than conventional ejection fraction for detecting subclinical cardiac dysfunction in hypertrophic cardiomyopathy. Also, strain patterns correlate with cardiac biomarkers, such as cardiac troponin and N-terminal prohormone of the brain natriuretic peptide.

Vattay et al. investigated the relationship between quantitative plaque metrics from coronary computed tomography angiography and segmental myocardial ischemia assessed using dynamic perfusion. Their findings suggest that total plaque volume is independently associated with myocardial blood flow but not with the severity of coronary stenosis.

Tang et al. explored the additional effects of mitral regurgitation on left ventricular strain impairment in patients with essential hypertension. Results showed that global peak strain was significantly more impaired in hypertensives with mitral regurgitation than in those without valvular insufficiency. Interestingly, the degree of mitral regurgitation was independently correlated with left ventricular global radial peak strain, circumferential peak strain, and global longitudinal peak strain.

Yu et al. assessed the diagnostic capability of real-time four-dimensional transesophageal echocardiography in detecting implant-related thrombus in patients who have undergone transcatheter left atrial appendage closure or have a cardiac implantable electronic device. The novel technique demonstrated a superior thrombus detection rate compared to conventional two-dimensional echocardiography. Furthermore, this real-time four-dimensional transesophageal echocardiography approach revealed distinct imaging features between a thrombus on an occluder and an electronic device.

Wang et al. investigated the utility of myocardial work parameters derived from pressure-strain loops in assessing cardiac function and predicting clinical prognosis in patients with pulmonary hypertension. The technique yielded two novel indices: right ventricular global constructive work and pulmonary arterial systolic pressure estimate. Both were predictive of clinical outcomes in patients with pulmonary hypertension.

Dejea et al. described the customization of an isolated, perfused heart system compatible with synchrotron-based x-ray phase contrast imaging. This innovative setup enables high-spatial resolution studies of heart architecture throughout the cardiac cycle, offering insights into the structural dynamics of the heart, including the effects of pharmaceuticals and other agents on the cardiac cycle.

Wang et al. compared longitudinal changes in color Tissue Doppler Imaging curves between normal controls and individuals at risk of future cardiac events. Noteworthy, they demonstrated that this technique could reveal an accelerated aging process in the hearts of individuals with cardiac risk factors. Consequently, they proposed Tissue Doppler Imaging as a valuable tool for identifying high-risk patients in a clinical setting.

Zhu et al. assessed fetal cardiovascular parameters using a two-dimensional speckle tracking technique to distinguish the size and systolic function differences in the left and right ventricles during pregnancy. They discovered that fetal cardiovascular physiology is characterized by a larger right ventricular volume (especially after 32 weeks) and greater left ventricular outputs, as indicated by higher ejection fraction, cardiac output, and stroke volume values.

Muraru et al. evaluated whether left ventricular volumes and ejection fraction measurements obtained by three-dimensional echocardiography offer any additional prognostic value over those acquired by two-dimensional echocardiography. Notably, in a total of 725 consecutive patients, left ventricular ejection fraction and end-systolic volume derived from three-dimensional echocardiography showed a stronger association with outcomes than the corresponding two-dimensional parameters.

Chen et al. proposed a novel method for labeling and imaging myocardial and vascular structures by using fluorescent dyes and transgenic markers. This innovative technique elucidates the three-dimensional morphology and spatial arrangement of cardiomyocytes and highlights structural differences in endothelial cells and capillaries. Overall, this new pipeline can define the structures of the entire heart at the single-cell level.

Beyls et al. investigated whether right ventricular longitudinal shortening fraction, a two-dimensional speckle tracking parameter used to assess right ventricular systolic function, yields consistent results regardless of whether it is assessed with conventional transthoracic echocardiography or transesophageal echocardiography. Crucially, the authors demonstrated that the values of the right ventricular longitudinal shortening fraction obtained with the two techniques are interchangeable.

Kusunose et al. applied a previously developed artificial intelligence model to predict heart failure and calculate the probability of elevated pulmonary artery wedge pressure. The findings showed the potential for using an artificial intelligence model on chest x-ray to predict pulmonary artery wedge pressure and its capacity to supplement prognostic information from other conventional clinical prognostic factors in heart failure. According to the authors of the study, these findings could enhance the accuracy of prediction models in heart failure, potentially leading to more informed clinical decision-making.

Erevik et al. aimed to determine the left ventricular response to increased exercise duration and intensity using novel echocardiographic tools to evaluate myocardial work and fatigue. They found that increased exercise intensity and duration during a cardiopulmonary exercise test and a 91-km mountain bike leisure race were associated with increased myocardial wasted work post-exercise, without changes in left ventricular ejection fraction and global longitudinal strain compared to baseline. These findings suggest that markers of myocardial inefficiency may precede a reduction in global left ventricular function, thus serving as early indicators of myocardial fatigue.

Yao et al. critically reviewed the benefits and limitations of four current ultrasound imaging modalities for assessing plaque vulnerability, considering the biological characteristics of the vulnerable plaque, and their value in clinical diagnosis, prognosis, and treatment efficacy assessment.

Sharma et al. conducted a systematic review and meta-analysis of the clinical application of longitudinal layer-specific strain as a diagnostic and prognostic instrument in ischemic heart disease. Their findings demonstrated that epicardial longitudinal layer-specific strain was the most significant diagnostic marker in patients with stable angina pectoris, whereas endocardial longitudinal layer-specific strain was the strongest diagnostic marker in patients with acute coronary syndrome. Furthermore, endocardial circumferential strain was a significant predictor of adverse outcomes in stable patients, while epicardial longitudinal layer-specific strain was the best predictor of outcomes in unstable patients.

Lin et al. presented a case of multiple biventricular aneurysms in arrhythmogenic cardiomyopathy, emphasizing that the pathological characteristics of arrhythmogenic cardiomyopathy can be better visualized using high-frequency linear ultrasound, with provides superior resolution.

In conclusion, future technological advancements, as discussed in this Special Issue, are expected to underscore the role of cardiovascular imaging in evaluating underlying pathophysiologic processes, thereby bridging the gap between pathophysiology, molecular medicine, and cardiovascular imaging (9, 10). Accordingly, multimodality imaging holds the promise of providing an unprecedented volume of diagnostic information, including an accurate depiction of coronary anatomy, atherosclerosis, myocardial ischemia, and tissue characterization. Such comprehensive data could enhance the diagnostic work-up and therapeutic options in real-world clinical practice.

Author contributions

All authors listed have made a substantial, direct, and intellectual contribution to the work and approved it for publication.

Conflict of interest

The authors declare that the research was conducted in the absence of any commercial or financial relationships that could be construed as a potential conflict of interest.

Publisher's note

References

1. López L, Rossello X, Romaguera D, Alonso-Gómez ÁM, Toledo E, Fortuny E, et al. The Palma echo platform: rationale and design of an echocardiography core lab. *Front Cardiovasc Med.* (2022) 9:909347. doi: 10.3389/fcvm.2022.909347

2. Ismail TF, Strugnell W, Coletti C, Božić-Iven M, Weingärtner S, Hammernik K, et al. Cardiac MR: from theory to practice. *Front Cardiovasc Med.* (2022) 9:826283. doi: 10.3389/fcvm.2022.826283

3. Del Torto A, Guaricci AI, Pomarico F, Guglielmo M, Fusini L, Monitillo F, et al. Advances in multimodality cardiovascular imaging in the diagnosis of heart failure with preserved ejection fraction. *Front Cardiovasc Med.* (2022) 9:758975. doi: 10.3389/fcvm.2022.758975

4. Marazzi G, Wajngarten M, Vitale C, Patrizi R, Pelliccia F, Gebara O, et al. Effect of free fatty acid inhibition on silent and symptomatic myocardial ischemia in diabetic patients with coronary artery disease. *Int J Cardiol.* (2007) 120(1):79–84. doi: 10.1016/j.ijcard.2006.08.082

5. Marazzi G, Pelliccia F, Campolongo G, Quattrino S, Cacciotti L, Volterrani M, et al. Usefulness of nutraceuticals (armolipid plus) versus ezetimibe and combination in statin-intolerant patients with dyslipidemia with coronary heart disease. *Am J Cardiol.* (2015) 116(12):1798–801. doi: 10.1016/j.amjcard.2015.09.023

6. Pelliccia F, Pasceri V, Marazzi G, Rosano G, Greco C, Gaudio C. A pilot randomized study of ranolazine for reduction of myocardial damage during elective percutaneous coronary intervention. *Am Heart J.* (2012) 163(6):1019–23. doi: 10.1016/j.ahj.2012.03.018

7. Pelliccia F, Patti G, Rosano G, Greco C, Gaudio C. Efficacy and safety of eplerenone in the management of mild to moderate arterial hypertension: systematic review and meta-analysis. *Int J Cardiol.* (2014) 177(1):219–28. doi: 10.1016/j.ijcard.2014.09.091

8. Vitale C, Marazzi G, Pelliccia F, Volterrani M, Cerquetani E, Spoletini I, et al. Trimetazidine improves exercise performance in patients with peripheral arterial disease. *Pharmacol Res.* (2011) 63(4):278–83. doi: 10.1016/j.phrs.2011.01.003

9. Chen C, Qin C, Qiu H, Tarroni G, Duan J, Bai W, et al. Deep learning for cardiac image segmentation: a review. *Front Cardiovasc Med.* (2020) 7:25. doi: 10.3389/fcvm.2020.00025

10. Kolossváry M, Dey D. Editorial: radiomics in cardiovascular imaging. *Front Cardiovasc Med.* (2022) 9:876713. doi: 10.3389/fcvm.2022.876713

frontiers | Frontiers in Cardiovascular Medicine

TYPE Original Research
PUBLISHED 22 July 2022
DOI 10.3389/fcvm.2022.946557

Effects of diagnostic ultrasound with cRGD-microbubbles on simultaneous detection and treatment of atherosclerotic plaque in ApoE$^{-/-}$ mice

Shengcun Guo, Shengye Zhang, Kui Chen, Xi Chen and Fudong Hu*

Department of Cardiology, The First Affiliated Hospital of Zhengzhou University, Zhengzhou, China

Background: Atherosclerotic vulnerable plaque is the leading cause of acute fatal cardiovascular events. Thus, early rapid identification and appropriate treatment of atherosclerotic plaque maybe can prevent fatal cardiovascular events. However, few non–invasive molecular imaging techniques are currently available for the simultaneous detection and targeted treatment of atherosclerotic plaques. We hypothesized that diagnostic ultrasound (DU) combined with cyclic Arg-Gly-Asp-modified microbubbles (MB_R) could provide targeted imaging and dissolution of activated platelets to identify advanced atherosclerotic plaques and improve plaque instability.

Methods: Three mouse models, apolipoprotein E-deficient mice on a hypercholesterolemic diet (HCD) or normal chow diet and wild-type mice on an HCD were used. The most appropriate ultrasonic mechanical index (MI) was determined based on the expression of GP IIb/IIIa in sham, DU alone and $DUMB_R$-treated groups at MI values of 0.5, 1.5, and 1.9. The video intensity (VI) values, activated platelets and plaque instability were analyzed by ultrasound molecular imaging, scanning electron microscopy and histopathological methods.

Results: We found that the VI values of ultrasound molecular imaging of MB_R were positively correlated with plaque GP IIb/IIIa expression, vulnerability index and necrotic center / fiber cap ratio. 24 h after treatment at different MIs, compared with those of the other groups, both the VI values and GP IIb/IIIa expression were significantly reduced in MI 1.5 and MI 1.9 $DUMB_R$-treated groups. The plaque vulnerability index and necrotic center / fiber cap ratio were significantly decreased in MI 1.5-treated group, which may be due to targeted dissolution of activated platelets, with a reduction in von Willebrand factor expression.

OPEN ACCESS

EDITED BY
Carlo Gaudio,
Sapienza University of Rome, Italy

REVIEWED BY
Gustav Strijkers,
Amsterdam University Medical Center, Netherlands
Francesco Pelliccia,
Sapienza University of Rome, Italy

*CORRESPONDENCE
Fudong Hu
hufudong2005@126.com

SPECIALTY SECTION
This article was submitted to Cardiovascular Imaging, a section of the journal Frontiers in Cardiovascular Medicine

RECEIVED 17 May 2022
ACCEPTED 01 July 2022
PUBLISHED 22 July 2022

CITATION
Guo S, Zhang S, Chen K, Chen X and Hu F (2022) Effects of diagnostic ultrasound with cRGD-microbubbles on simultaneous detection and treatment of atherosclerotic plaque in ApoE$^{-/-}$ mice.
Front. Cardiovasc. Med. 9:946557.
doi: 10.3389/fcvm.2022.946557

Conclusion: DUMB$_R$ targeting GP IIb/IIIa receptors could rapidly detect advanced atherosclerotic plaques and simultaneously give targeted therapy by dissolving activated and aggregated platelets. This technology may represent a novel approach for the simultaneous identification and treatment of atherosclerotic plaques.

KEYWORDS

atherosclerotic plaque, diagnostic ultrasound, microbubbles, activated platelets, GP IIb/IIIa receptor

Introduction

Cardiovascular disease is the leading cause of morbidity and mortality worldwide (1). The typical underlying pathology is the sudden rupture or erosion of an atherosclerotic vulnerable plaque, followed by platelet activation, aggregation and subsequent thrombus formation (2). Accumulating evidence suggests that activated platelets within plaques are significantly correlated with plaque vulnerability (3, 4). Therefore, the rapid identification and immediate therapy of activated and aggregated platelets may be critical for the diagnosis and treatment of atherosclerotic plaques. Currently, activated platelets can be detected by imaging methods, but approaches applied to stabilize vulnerable plaques are limited to the application of antiplatelet drugs, such as aspirin, clopidogrel, ticagrelor, GP IIb/IIIa receptor inhibitors and plasminogen activators, in the clinic. These agents cannot reduce adverse cardiovascular events and may have drug-associated adverse effects after either systemic or oral administration, leading to drug resistance in the long term (5–7). Therefore, it is vital to develop a non–invasive imaging approach that allows the simultaneous diagnosis and treatment of activated platelets, as well as tracking of the therapeutic effect.

To date, a non–invasive molecular imaging method that is capable of synchronous detection and targeted therapy of high-risk plaques is not available. Among all imaging modalities, ultrasound molecular imaging, also known as diagnostic ultrasound (DU) combined with microbubbles (MB), has the advantages of being non–invasive, free of radiation-associated risk, available, inexpensive, and inherently real-time, prompting us to use it for the development of a specific theranostic approach (8). Recently, our previous study successfully used DU + MB to target activated platelets to identify high-risk plaques (4); however, whether the DU + MB technology could be able to simultaneously detect and treat atherosclerotic plaques by targeting activated and aggregated platelets in chronic atherosclerotic plaques remains unknown. Multiple studies demonstrated that DU + MB treatment can significantly dissolve acute intravascular thrombi in large vessels and microthrombi (platelet-rich) in microvasculature in models of acute myocardial infarction (9–12), and whether DU in combination with MB treatment could be applied in the chronic atherosclerosis remains unclear.

The glycoprotein (GP) IIb/IIIa complex, known as αIIbβ3 integrin, is the major receptor expressed on the surface of activated platelets, and mediates platelet bridging, subsequent aggregation and thrombus formation *via* a high-affinity state (13, 14). Our previous studies demonstrated that the GP IIb/IIIa receptor of activated platelets is significantly correlated with plaque vulnerability (4). These features render the GP IIb/IIIa receptor an ideal target for both molecular imaging of aggregated platelets and targeted therapy of atherosclerotic plaques. We developed a cyclic Arg-Gly-Asp (RGD)-modified MB (MB$_R$) with 30-fold higher affinity and stability in binding the GP IIb/IIIa complex than linear MB and used MB$_R$ for the targeted detection of activated platelets and thrombi in large arteries (4, 15), without facilitating platelet activation and crosslinking, which might cause thrombosis (16). These targeted MB$_R$ bind GP IIb/IIIa on activated platelets, allowing real-time imaging and safe dissolution of aggregated platelets, thereby stabilizing atherosclerotic plaques.

The current study examined whether DU combined with MB$_R$ (DUMB$_R$) is capable of simultaneous targeted imaging and dissolution of aggregated platelets to detect advanced atherosclerotic plaques and improve plaque instability.

Methods

Animal groups

The animal study protocols were approved by the Institutional Animal Care and Use Committee of Zhengzhou University. The present study conformed to the rules of the Guide for the Care and Use of Laboratory Animals published by

---

Abbreviations: MB$_R$, cyclic Arg-Gly-Asp (RGD)-modified microbubble; ApoE$^{-/-}$, apolipoprotein E-deficient; HCD, hypercholesterolemic diet; DUMB$_R$, diagnostic ultrasound combined with MB$_R$; MI, mechanical index; MB$_C$, negative control MB; α-SMA, α-smooth muscle actin; SMCs, smooth muscle cells; vWF, von Willebrand factor; TF, tissue factor; MCP-1, monocyte chemotactic protein; VCAM-1, vascular cell adhesion molecule-1; NC/FC, necrotic center/fiber cap.

the U.S. National Institutes of Health (NIH 8th edition, 2011) and the guidelines for experimental atherosclerosis studies described in the American Heart Association (AHA) Statement.

Male wild-type C57BL/6 and apolipoprotein E-deficient (ApoE$^{-/-}$) mice were purchased from Vital River Laboratory Animal Technology Co. Ltd. (Beijing, China). The following groups were used: ApoE$^{-/-}$ mice fed a hypercholesterolemic diet (ApoE$^{-/-}$ + HCD, $n = 180$), ApoE$^{-/-}$ mice fed a normal laboratory diet (ApoE$^{-/-}$ + NLD, $n = 12$), and wild-type C57BL/6 mice fed an HCD (C57BL/6 + HCD; $n = 12$). For experiments, 6-week-old mice were had free access to their respective diets (purchased from Medicience Biomedical Co. Ltd.) and tap water for up to 30 weeks.

Experimental protocol

To observe the correlation between GP IIb/IIIa and plaque instability, 6 mice per group were randomly selected for the contrast enhanced ultrasound tested experiments and another 6 mice for blockade experiments. The abdominal aorta was collected, and hematoxylin and eosin (H & E) and immunohistochemical staining were performed.

To establish an appropriate DU mechanical index (MI), 36 HCD-fed ApoE$^{-/-}$ mice were randomly divided into a sham group and five treatment groups ($n = 6$ per group). The sham group was subjected to the DU transducer in the "off" setting and injected with MB$_R$. The five treated groups were divided into three DUMB$_R$-treated groups, a DU-only-treated group and a DU+negative control microbubble (DUMB$_C$) treatment group. The DUMB$_R$-treated groups were insonated with different MI values (0.5, 1.5, and 1.9) and injected with MB$_R$, while the DU-only-treated group was insonated with an MI of 1.9 in the absence of any microbubbles, and DUMB$_C$-treated group was insonated with an MI of 1.9 and received an injection of MB$_C$. The mice were subjected to targeted ultrasound molecular imaging before and 24 h after the treatment. Then, the mice were sacrificed 24 h after treatment and the abdominal aortas were collected for immunohistochemistry. In addition, another 12 HCD-fed ApoE$^{-/-}$ mice were randomly divided into DUMB$_R$-treated groups with an MI of 1.5 or 1.9. At 24 h after treatment, the abdominal aortas were collected for scanning electron microscopy.

To evaluate the influence of DUMB$_R$ treatment on surrounding normal tissue surrounding the abdominal aorta, samples of the abdominal skin and mesentery from the different groups were obtained for H & E staining. In addition, to assess the bleeding time of DUMB$_R$, 5 mm of the mouse tail was cut off from the tip and immersed in saline at 37°C. The bleeding time was determined by the time required to stop visible blood flow for at least 1 min.

To explore the mechanism by which plaque instability was reversed, 72 HCD-fed ApoE$^{-/-}$ mice were randomly selected to receive the DUMB$_R$ treatment with an appropriate MI that was previously determined. The abdominal aortas were collected before and 0 h, 24 h and 8 weeks after DUMB$_R$ treatment for H&E, immunohistochemistry, histoimmunofluorescence and scanning electron microscopy.

To evaluate the therapeutic effect of DUMB$_R$ treatment on plaques, 48 HCD-fed ApoE$^{-/-}$ mice were randomly divided into DUMB$_R$ treatment ($n = 12$), DUMB$_C$ treatment ($n = 12$), DU only ($n = 12$) and control ($n = 12$) groups; the mice were continued to be fed a laboratory diet for 12 weeks after receiving the respective interventions. Plaque instability was assessed by H & E/Masson's trichrome staining and IHC at 12 weeks after treatment. The number of activated platelets aggregated on abdominal aortic plaque was counted by scanning electron microscopy. The animal grouping and experimental protocol are illustrated in Figure 1.

Microbubble preparation and characterization

The generation of GP IIb/IIIa-targeted and negative control MBs (MB$_R$ and MB$_C$, respectively) and validation of the binding characteristics were performed as previously described (15). The concentration, and particle size distribution of the two types of MBs were characterized with a Coulter counter (Beckman Coulter Inc., Brea, CA, United States).

Ultrasound molecular imaging of atherosclerotic plaques

The mice underwent ultrasound molecular imaging performed with a Sequoia ultrasound system using a linear-array probe (15L7; MI: 0–1.9; frequency: 7–15 MHz; Siemens Medical Systems) with Cadence contrast pulse sequencing as previously described (4). Briefly, imaging was performed at a centerline frequency of 7.0 MHz and MI of 0.18 in the longitudinal axis view. Real-time images were obtained for 6 min after an intravenous injection with a bolus of microbubbles. Then, the MI was transiently increased to 1.0 for 3 s to destroy adhered MBs, and subsequent post-destruction images were acquired at an index of 0.18 to obtain the background images of residual bubbles present in the bloodstream. The averaged post-destruction contrast frames were digitally subtracted from the averaged pre-destruction frames at 6 min to identify the signal attributable to retained microbubbles using Yabko MCE2.7 image analysis software (University of Virginia, Charlottesville, VA, United States) and then color-coded; the background-subtracted video intensity was measured from the abdominal aorta (4, 17). To confirm the correlation of video intensity value of UMI with plaque GP IIb/IIIa or vulnerability,

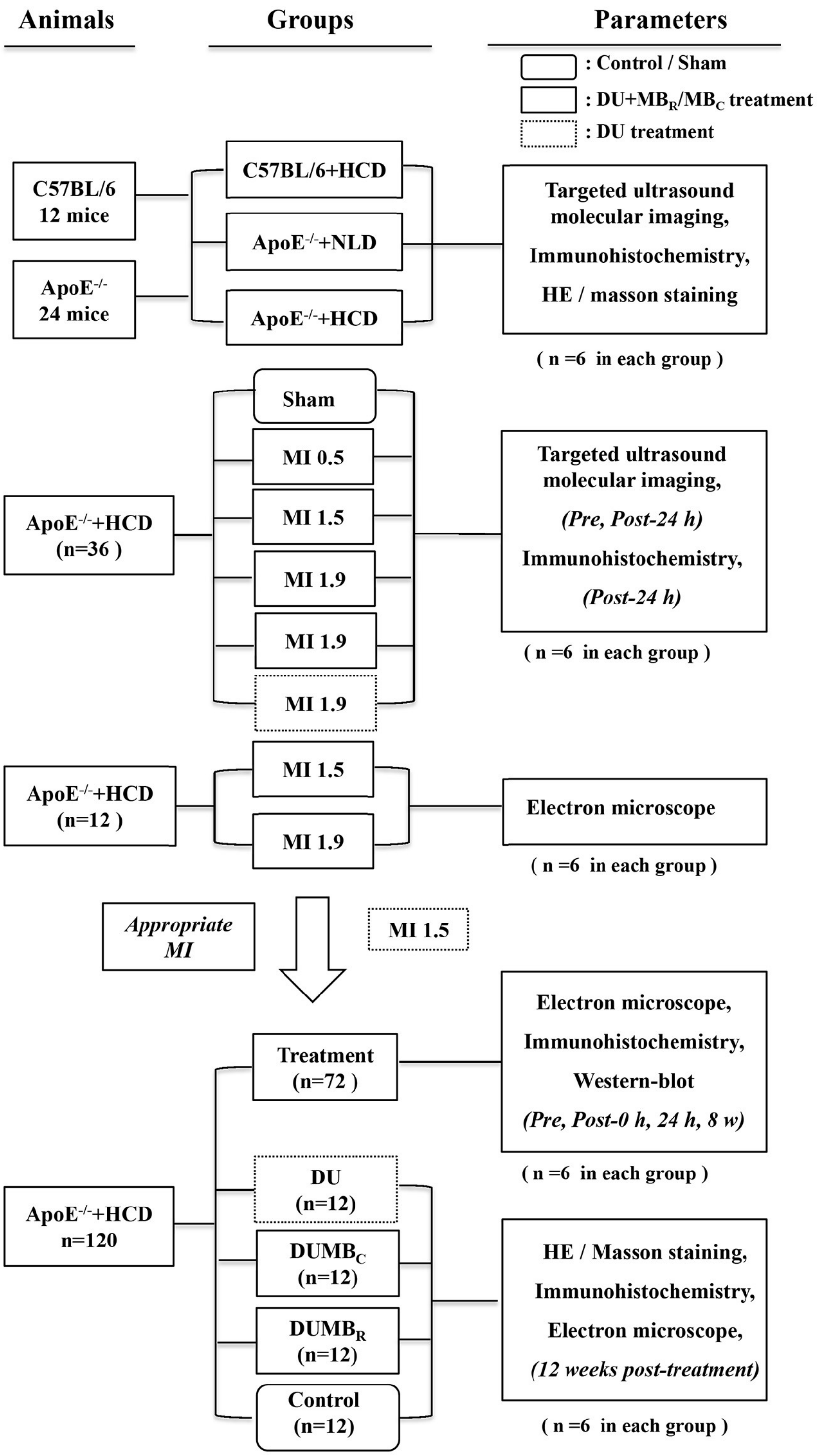

FIGURE 1
Illustration of the experimental protocol.

contrast enhanced ultrasound was performed in C57BL/6 + HCD, ApoE$^{-/-}$ + NLD and ApoE$^{-/-}$ + HCD mice ($n = 6$ each), with an intravenous injection of 1×10^6 MB$_R$ or negative control MB (MB$_C$) in a total volume of 0.1 ml in a random order. To demonstrate the high affinity of MB$_R$ for the GP IIb/IIIa receptor *in vivo*, a competitive GP IIb/IIIa antagonist, Eptifibatide (integrilin), was injected at a dose of 1.8 µg/g to saturate integrins, followed by an injection of MB_R or MB_C and contrast enhanced ultrasound. To determine the appropriate MI, mice from the sham or DUMB/DU groups were observed by contrast enhanced ultrasound before treatment and continued feeding until 24 h after treatment; contrast enhanced ultrasound was performed again with an injection of a bolus of 1×10^6 MB_R as described above (4, 18).

$DUMB_R$ treatment of atherosclerotic plaques

A Siemens Acuson Sequoia with a 15L7 linear-array transducer (frequency range, 7–15 MHz; elevation plane, 5 mm) and contrast pulse sequencing (Siemens Medical Systems) was employed as the ultrasonic therapy device. The mice in the sham group were not subjected to the DU treatment, while the mice in the $DUMB_R$, DU only and $DUMB_C$ groups were treated with DU. The transducer was fixed on a steel stand with a scale and held 0.5 cm over the abdominal skin with ultrasound gel. In the $DUMB_R$/$DUMB_C$-treated groups, during the infusion of microbubbles (0.008 mL/min) *via* a tail vein catheter, contrast pulse sequencing was utilized to visualize the abdominal aortic longitudinal axis at an MI of 0.18 until evidence of contrast filling with the whole abdominal aorta was observed. The MI was increased to high MIs (0.5, 1.5, and 1.9) for 30 s while scanning the whole abdominal aorta. Then, the MI was decreased to 0.18, and real-time imaging was repeated until the evidence as above was observed again. High-MI impulses were repeated for 30 s. This sequence of high- and low-MI imaging was repeated for 30 min (10, 19). The sound beam was aimed to expose the whole abdominal aorta by manually swinging the probe.

Detection of activated platelets by scanning electron microscopy

Abdominal aorta tissue samples were fixed with 2.5% glutaraldehyde and prepared for scanning electron microscopy following a standard procedure. Activated platelets adhered and aggregated on the surface of the vessel lumen were observed by SEM (S-3000N; Hitachi, Tokyo, Japan) at 20 kV. The number of platelets was counted per field (25.2 × 25.2 mm) in 10 optical fields.

Fluorescence staining

Histoimmunofluorescence was performed as described previously (20). Briefly, 3 µm sections were permeabilized, blocked and then incubated with rabbit polyclonal antibody against mouse CD31 (Abcam, Cambridge, MA, United States) to detect endotheliocytes. An Alexa Fluor 488-conjugated secondary antibody (Invitrogen) was used. Cell nuclei were counterstained with DAPI. Sections were imaged using a fluorescence microscope (Olympus, Tokyo, Japan). The number of angiogenesis was calculated in 10 randomly selected 400 × high-power fields from 6 separate sections per sample.

Histology and immunohistochemistry

The samples of the abdominal aorta used for the histopathologic examination were fixed in 4% paraformaldehyde, dehydrated, paraffin-embedded, and sectioned at 3 µm. Five representative serial sections were selected in each site in the proximal, intermediate, and distal ends of the abdominal aortas of each animal. H&E staining, Masson's trichrome staining and immunostaining were performed as previously described (4). Images were observed under an optical microscope.

The fiber lipid deposition and collagen fiber were assessed by H&E and Masson's trichrome staining (MST-8003; Matxin Labs Pvt., Ltd., Bangalore, India). For immunohistochemistry staining, the primary antibodies included rabbit anti-mouse polyclonal antibodies specific for α-smooth muscle actin (α-SMA) (ab5694), CD68 (ab125212), GP IIb integrin (ab63983), von Willebrand factor (vWF) (ab9378), tissue factor (TF) (ab104513), monocyte chemotactic protein (MCP-1) (ab25124) and vascular cell adhesion molecule-1 (VCAM-1) (monoclonal antibody; ab134047, all from Abcam), and a rat anti-mouse monoclonal antibody specific for TER-119 (550565, BD Biosciences). The secondary antibodies were peroxidase-conjugated anti-rabbit or rat IgG. Incubation without primary antibodies and/or with isotype-matched immunoglobulins was used as a negative control for all immunostaining. To determine the specificity of platelet staining, the primary antibody was substituted with the GP IIb/IIIa antigen-antibody complex as a pre–absorption negative control.

Plaque quantification of histopathologic indicators

The necrotic center/fiber cap (NC/FC) ratio was calculated by the area of lipid deposition and collagen fiber which were measured by planimetry. The areas of positive staining for SMCs and macrophages were quantified as percentages of positive staining within the total plaque area using Image-Pro Plus (IPP, Media Cybernetics, Rockville, MD, United States). The plaque vulnerability index was calculated using the following formula: vulnerability index = (macrophages % + lipids %) / (SMCs % + collagen %) (4, 21). The content of GP IIb/IIIa was measured by the following two methods as previously described: the percentage of GP IIb/IIIa expression in the plaque and the percentage of GP IIb/IIIa coverage in the endothelium (4). The extravasation of erythrocytes in plaques was quantified by counting the average number of erythrocytes in 10 randomly selected 400 × high-power fields from 6 separate sections per sample. The vWF content in plaques was measured by counting the average number of vWF-positive endothelial cells. In addition, the areas of positive immunoreactivity for other factors, such as TF, VCAM-1 and MCP-1, in plaques were quantified as described above for SMCs.

The histopathologic indicators were quantified at the three selected sites and averaged per section per site. All measurements and analyses of the ultrasound molecular imaging, scanning electron microscopy, histology, and immunolabeling data were performed by two individuals who were blinded to the experimental design.

Western blot analysis

Proteins were obtained from whole abdominal aorta homogenates. Immunoblotting was performed to assess the expression of TF, VCAM-1 and MCP-1. The immunoreactive bands were visualized by Odyssey Software (version 1.2; LI-COR, Lincoln, NE, United States), and quantified using Image J (NIH, Bethesda, MD, United States) as previously described (22).

Statistical analysis

Data were analyzed using SPSS v.13.0 (SPSS, Inc., Chicago, IL, United States) and are presented as the mean ± standard deviation. The normal distributions of continuous variables were confirmed by the Kolmogorov-Smirnov test. For the variables with normal distributions, 2-tailed Student's *t*-test (for comparisons between two groups) or one-way analysis of variance (for comparisons among three or more groups or time points), followed by Bonferroni (for comparisons with equal variance) or Dunnett's T3 (for comparisons without equal variance) *post-hoc* tests were used for the statistical analysis. For the variables with non–normal distributions, the Mann-Whitney rank sum test was used. Spearman's rank correlation was used to assess the linear correlation between selected variables. A P value$<$0.05 was considered statistically significant.

Results

MB characterization

The two types of MBs used in this study had a mean diameter of approximately 2.55 µm, and the mean concentrations were approximately 1.15×10^9 MB per ml. Supplementary Table 1 summarizes the parameters of MB_C and MB_R. There were no significant differences in the mean diameter or concentration between the two types of MB ($P > 0.05$). The particle size distribution of MB_C and MB_R was shown by Supplementary Figures 3A,B.

The correlation among GP IIb/IIIa expression, plaque vulnerability and video intensity of ultrasound molecular imaging

To explore the relationship between GP IIb/IIIa expression and plaque vulnerability, GP IIb/IIIa expression in abdominal aortic plaques was detected in three experimental mouse groups (Figure 2A); H & E and Masson's trichrome staining, as well as CD68 and α-SMA immunolabeling were used to assess the plaque vulnerability index and the NC/FC ratio (Figure 2A); the quantitative results showed that both GP IIb/IIIa expression in plaques and coverage of the endothelium were highest in the $ApoE^{-/-}$ + HCD group, followed by $ApoE^{-/-}$ + NLD and C57BL/6 + HCD groups ($P < 0.05$; Figure 2B). Interestingly, GP IIb/IIIa expression in plaques were correlated with GP IIb/IIIa coverage of the endothelium (Figure 2C); GP IIb/IIIa expression in whole plaques and the coverage of the endothelium was also correlated with plaque vulnerability index and NC/FC ratio (Figures 2D–G).

In addition, the background-subtracted video intensity (Figure 3A) of MB_R and MB_C were comparable in both the tested and blocked groups of C57BL/6 + HCD mice, but the video intensity of MB_R were significantly higher than those of MB_C in the other two tested groups. The video intensity of MB_R in the tested group was highest in the $ApoE^{-/-}$ + HCD group, followed by $ApoE^{-/-}$ + NLD and C57BL/6 + HCD groups ($P < 0.05$; Figure 3B), with the similar trend as GP IIb/IIIa expression. The treatment with the GP IIb/IIIa antagonist decreased the video intensity to the level of MB_C in these groups ($P < 0.05$; Figure 3B), indicating that the binding between MB_R and GP IIb/IIIa receptor was mostly inhibited by Eptifibatide. Notably, the video intensity of MB_R in the tested group was correlated with GP IIb/IIIa coverage of the endothelium and expression in plaques (Figures 3C,D), and the plaque vulnerability index and NC/FC ratio (Figures 3E,F).

The effects of $DUMB_R$ treatment on plaques, skin and mesentery: Results of various ultrasonic MI values

Ultrasound molecular imaging was used to reveal the video intensity of MB_R or MB_C in the abdominal aorta in different treatment mouse groups before and 24 h after $DUMB_R$

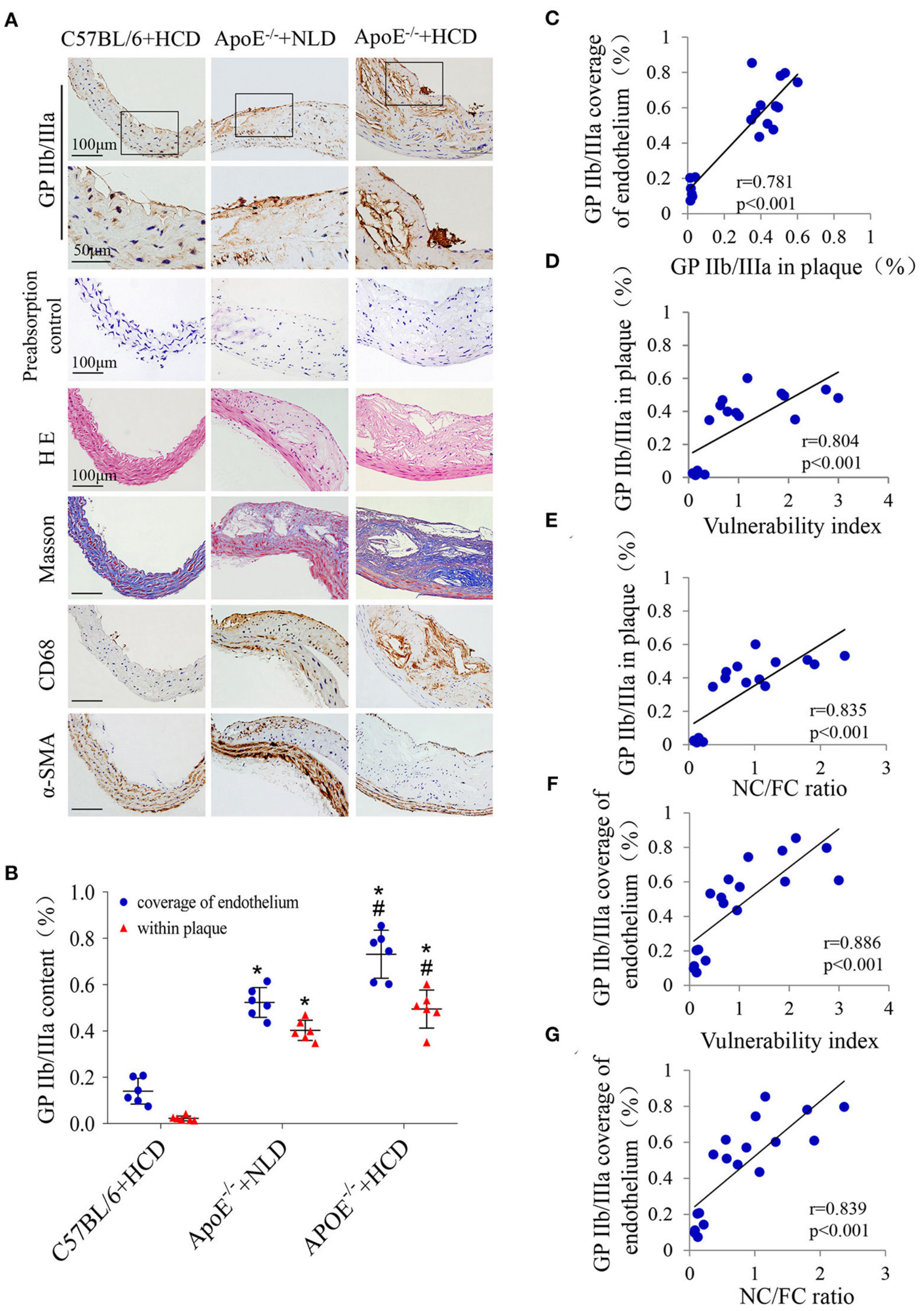

FIGURE 2
Correlations between GP IIb/IIIa expression and the plaque vulnerability indicators. **(A)** Representative images of aortic tissue visualized by H & E and Masson's trichrome staining or labeling with antibodies against GP IIb/IIIa, α-SMA and CD68 are shown. The primary antibody was substituted with the GP IIb/IIIa antigen-antibody complex as a preabsorption negative control. **(B)** The GP IIb/IIIa content in total plaque and coverage of the endothelium were quantified. Correlations between GP IIb/IIIa expression in plaques and **(C)** GP IIb/IIIa coverage of the endothelium, **(D)** plaque vulnerability index and **(E)** NC/FC ratio; and between GP IIb/IIIa coverage of the endothelium and **(F)** plaque vulnerability index and **(G)** NC/FC ratio were determined. $n = 6$ per group. Data represent the mean ± standard deviation. $^*P < 0.05$ vs. C57BL/6 + HCD, $^\#P < 0.05$ vs. ApoE $^{-/-}$ + NLD. α-SMA: α-smooth muscle actin; NC/FC: necrotic center/fiber cap.

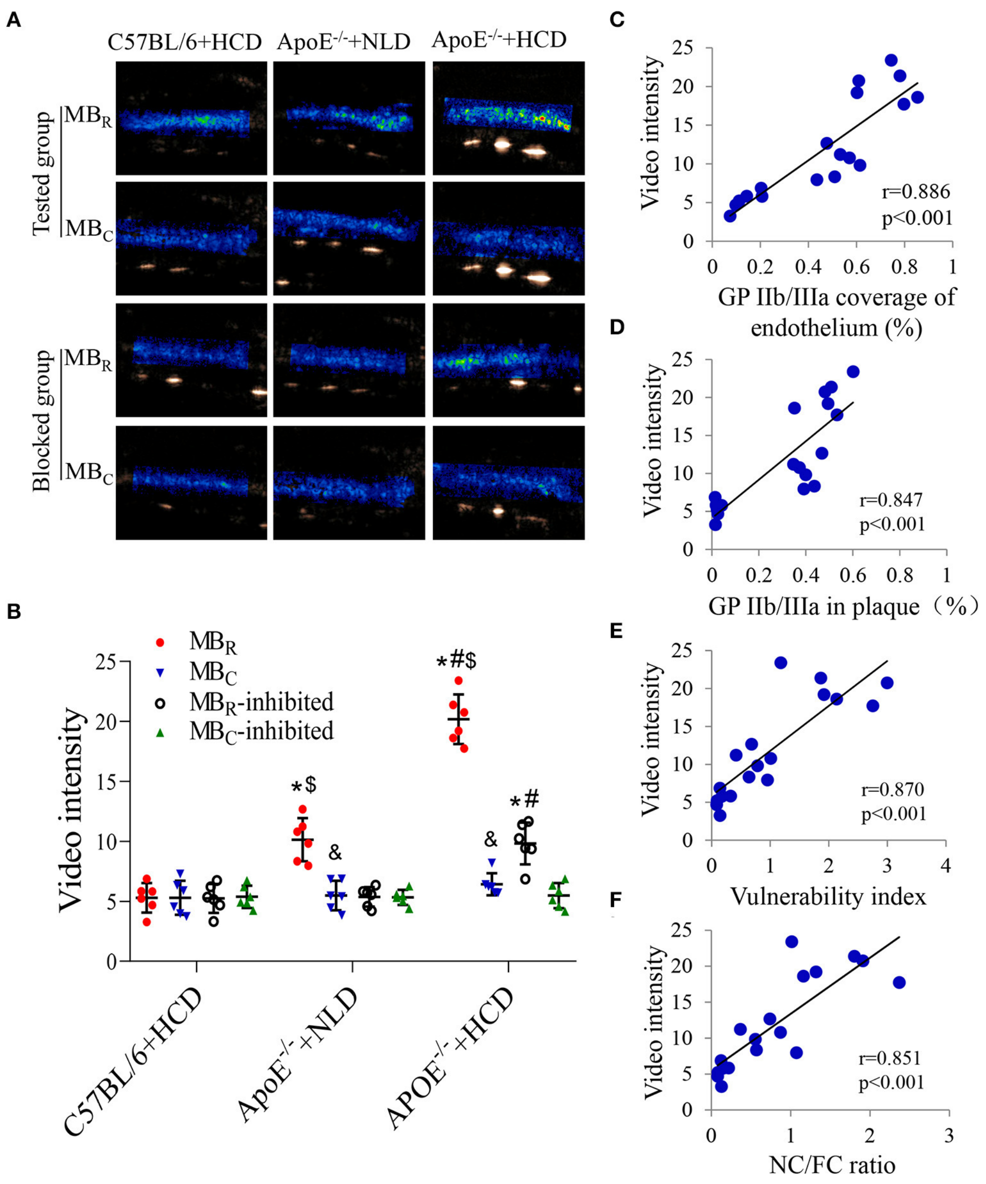

FIGURE 3

Correlations between video intensity of ultrasound molecular imaging and GP IIb/IIIa expression, and the plaque vulnerability indicators. **(A)** Background-subtracted, color-coded images were obtained after injection of MB_R or negative control (MB_C). **(B)** Video intensity of MB_R and MB_C in the tested mice and their inhibited groups were quantified ($n = 6$ per group). Correlations between the video intensity of MB_R in tested group and **(C)** GP IIb/IIIa coverage of the endothelium, **(D)** GP IIb/IIIa expression in plaques, **(E)** the plaque vulnerability index, and **(F)** the NC/FC ratio are shown. $n = 6$ per group. Data represent the mean ± standard deviation. $^{*}P < 0.05$ vs. C57BL/6 + HCD, $^{\#}P<0.05$ vs. ApoE $^{-/-}$ + NLD, $^{\&}P < 0.05$, MB_C vs. MB_R, $^{\$}P < 0.05$, MB_R vs. MB_R-inhibited. MB_R: cyclic Arg-Gly-Asp (RGD)-modified microbubble; NC/FC: necrotic center/fiber cap.

treatment (Figure 4A). Before treatment, the video intensity were comparable among the six different treatment mouse groups, indicating equivalent plaque vulnerability in these mice ($P > 0.05$; Figure 4D). 24 h after treatment, the video intensity were comparable in the sham group, MI 0.5 $DUMB_R$-treated group and DU-only group and were slightly higher than those in the $DUMB_C$-treated group, while the video intensity in the MI 1.5 and MI 1.9 $DUMB_R$ treatment groups were significantly decreased compared with those in the other four groups ($P < 0.05$; Figure 4D).

GP IIb/IIIa immunostaining was used to assess the activated and aggregated platelets in abdominal aortic plaques in different treatment groups 24h after treatment (Figure 4B), the ratio of GP IIb/IIIa coverage of the endothelium did not significantly differ among the sham, MI 0.5 $DUMB_R$-treated and DU-only groups, but was slightly decreased in $DUMB_C$-treated group, and further decreases were observed in the MI 1.5 and MI 1.9 DUMB$_R$-treated groups compared with the sham, MI 0.5-treated and DU-only groups ($P < 0.05$; Figure 4E). A similar expression pattern was observed in plaques in these groups ($P < 0.05$; Figure 4F). Notably, the plaque endothelium was destroyed in the MI 1.9 DUMB$_R$-treated group compared with that in the other groups. in addition, we further used scanning electron microscopy to observe the activated platelets adhered

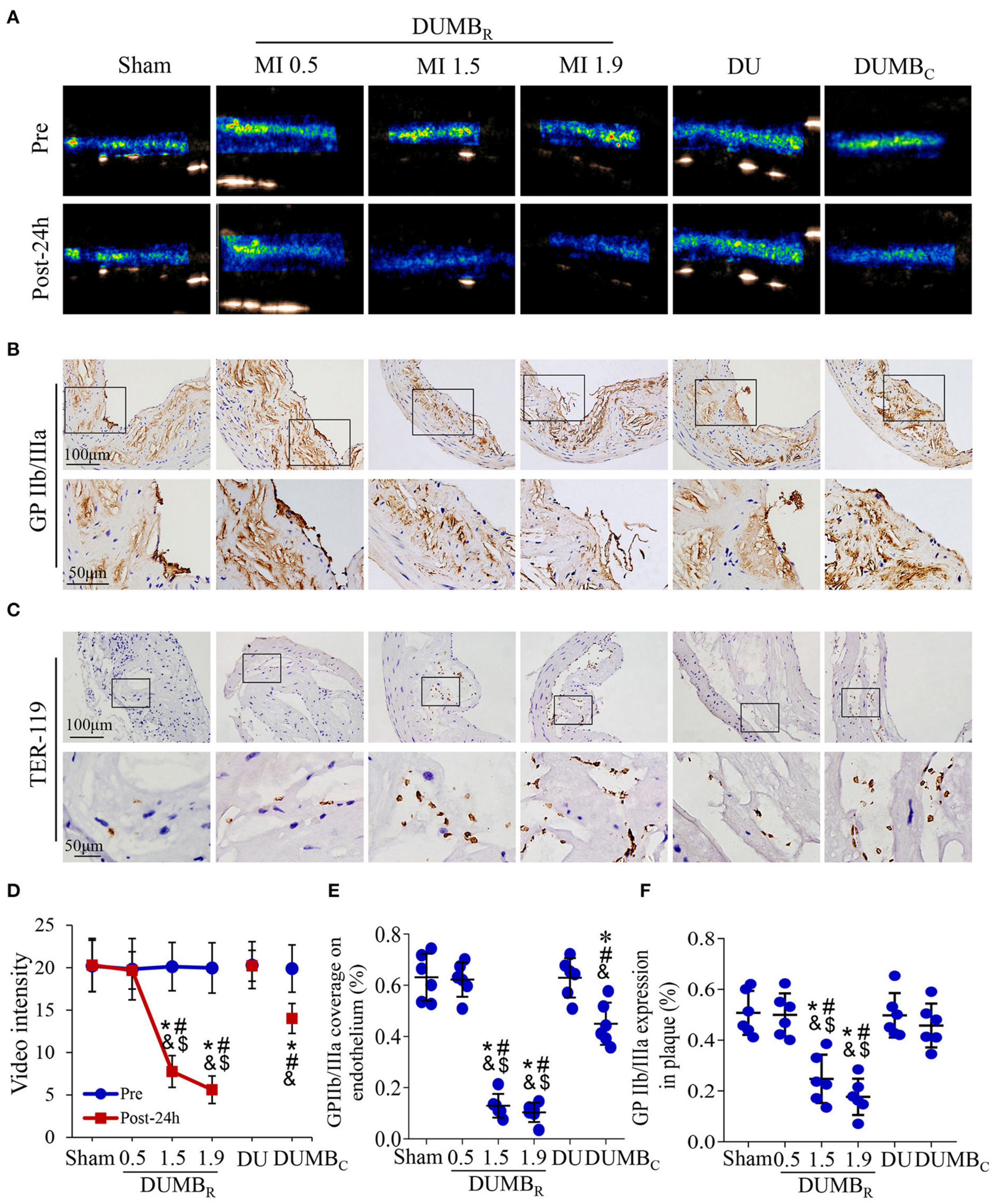

FIGURE 4
Continued

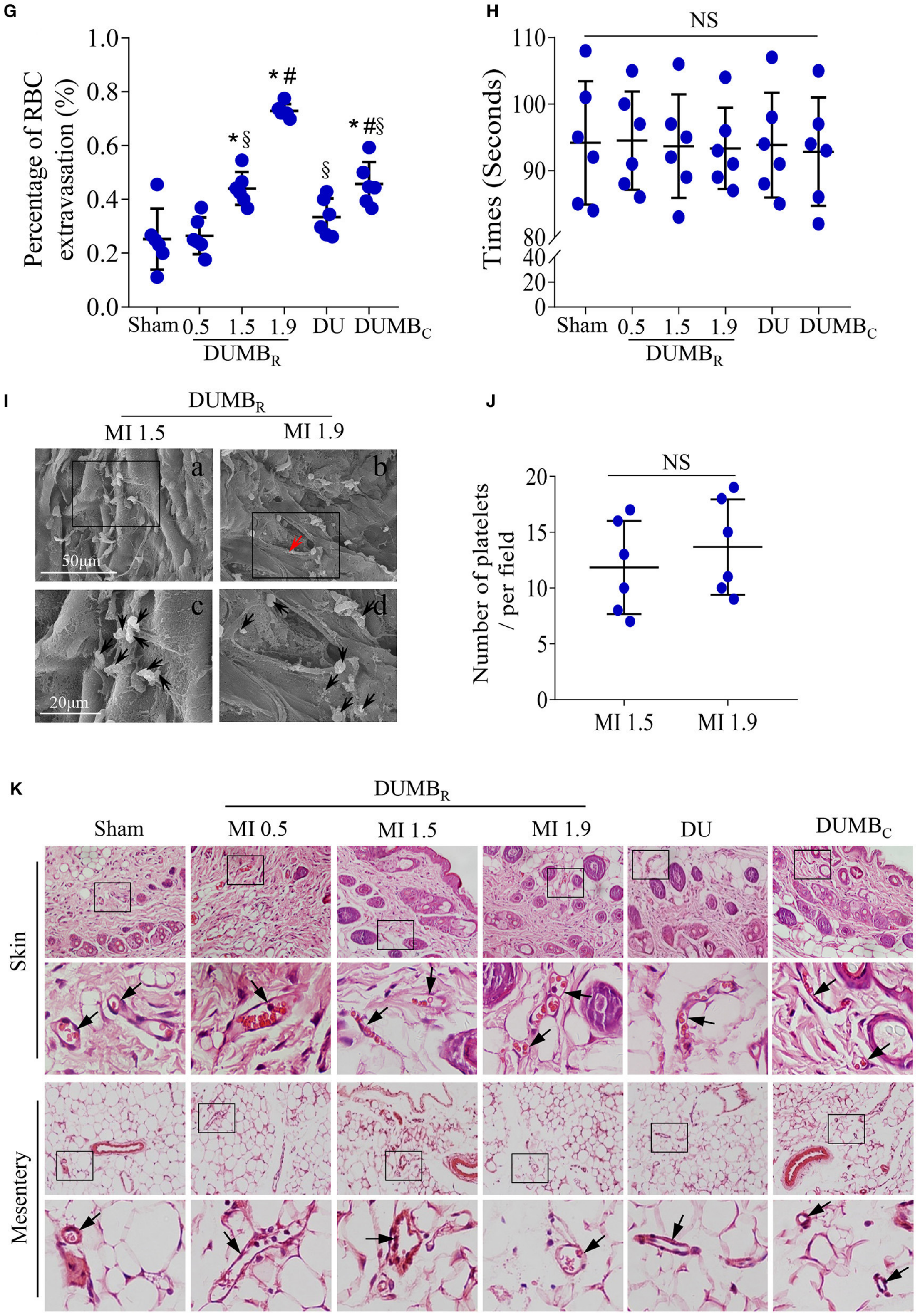

FIGURE 4

Effects of DUMB$_R$ treatment on plaques: Results of various ultrasonic mechanical index (MI) values. **(A)** Background-subtracted, color-coded images of ultrasound molecular imaging for MB$_R$ or MB$_C$ before and 24 h after treatment. Representative images of immunohistochemical

(Continued)

FIGURE 4
staining for **(B)** GP IIb/IIIa and **(C)** TER-119 in plaques are shown. **(D)** The video intensity of MB_R or MB_C in mice was quantified. Quantitative analysis of the **(E)** GP IIb/IIIa coverage on the endothelium, **(F)** GP IIb/IIIa expression in plaques, and **(G)** the average number of red blood cells at 24 h after treatment. **(H)** Bleeding times were assessed by surgical tail transection in the six treated mouse groups ($P > 0.05$). **(I)** Platelets (black arrowheads) adhering to the site of atherosclerotic lesions were observed by scanning electron microscopy after the $DUMB_R$ treatment at an MI of 1.5 or 1.9 groups. Panel b and its magnified images in panel d show that the endothelium was incomplete (red arrowheads). **(J)** Average number of activated platelets was quantified. **(K)** Representative images of abdominal skin and mesentery stained with H & E. Red blood cells were observed in complete vessels (black arrowheads). $n = 6$ per group. $^*P < 0.05$ vs. sham, $^\#P < 0.05$ vs. MI 0.9, $^\&P < 0.05$ vs. DU only, $^\$P < 0.05$ vs. $DUMB_C$, $^\S P < 0.05$ vs. MI 1.9 $DUMB_R$; $DUMB_R$: diagnostic ultrasound combined with MB_R. $DUMB_C$, diagnostic ultrasound combined with MB_C.

to the surface of the vessel lumen in the MI 1.5 and MI 1.9 $DUMB_R$ treatment groups. there was no significant difference in the number of activated platelets between the two groups ($P > 0.05$; Figures 4I,J), but the structures of plaque endothelium were indeed incomplete in the MI 1.9 $DUMB_R$ Group compared with those in the MI 1.5 $DUMB_R$ group (Figure 4I). In addition, TER-119 immunostaining was used to reveal the extravasation of erythrocytes within plaques in different treatment groups 24 h after treatment (Figure 4C). The number of exosmotic erythrocytes was most significantly increased in the MI 1.9 $DUMB_R$ Group, followed by the $DUMB_C$ Group, MI 1.5 and 0.5 $DUMB_R$ Groups, the DU only group and sham group ($P < 0.05$; Figure 4G). Moreover, Supplementary Figure 1 demonstrated that expression of TER-119 was slightly increased at 24 h after treatment, but significantly decreased at 8 Weeks and 12 Weeks after $DUMB_R$ treatment at an MI of 1.5 compared with pretreatment ($P < 0.05$). These indicate that $DUMB_R$ treatment did not further increase erythrocyte extravasation within plaques and MI 1.5 may be a safer ultrasonic condition for $DUMB_R$ treatment of atherosclerotic plaque.

H & E staining of abdominal skin and the mesentery was used to evaluate the influence of $DUMB_R$ treatment on surrounding normal tissue. No significant extravasated erythrocytes or, degeneration or necrosis of cells was found in the skin and mesentery after $DUMB_R$ treatment at different MI values or after DU only treatment or $DUMB_C$ treatment groups (Figure 4K). Furthermore, the bleeding time were assessed by surgical tail transection, there were no differences in bleeding times among the six treatment mouse groups ($P > 0.05$, Figure 4H). Thus, $DUMB_R$ treatment at different MI values does not compromise normal tissue surrounding the abdominal aorta and prolonging the bleeding time.

Targeted dissolution of activated platelets aggregated on plaque

Immunohistochemistry of GP IIb/IIIa was performed at the four time points to assess the activated platelets aggregated on plaque (Figure 5A). Compared with pretreatment, GP IIb/IIIa coverage of the endothelium was significantly decreased at 0 h, 24 h, and 8 weeks after $DUMB_R$ treatment ($P < 0.05$; Figure 5B), and a similar expression trend was observed in plaques ($P < 0.05$; Figure 5C). In addition, we further used scanning electron microscopy to detect the activated platelets adhered on the surface of plaques in the groups at four time points (Figure 5D). The number of activated platelets aggregated on the endothelium showed a trend similar to that of GP IIb/IIIa expression (Figure 5E).

$DUMB_R$ treatment reduces the expression of platelet adhesion promoters, thrombogenic factors, adhesion molecules, chemokines and microvasculature in plaques

To explore the possible mechanism of plaque instability improvement, the expression of vWF, TF, VCAM-1 and MCP-1 in the plaques is shown by immunohistochemistry in Figure 6A. No significant difference in the expression of the platelet adhesion promoter (represented by vWF) was observed immediately after $DUMB_R$ treatment compared with pretreatment; however, at 24 h and 8 weeks after treatment, the expression of vWF was significantly decreased ($P < 0.05$; Figures 6A,B). Similar patterns were observed in the expression of thrombogenic factors, endothelial adhesion molecules and macrophage chemokines ($P < 0.05$; Figures 6A,C); consistently, the expression of TF, VCAM-1 and MCP-1 by western-blotting also presented similar expression trends ($P < 0.05$; Figures 6D,E). In addition, plaque microvasculature (marked by CD31) were dramatically decreased at 24 h, and 8 weeks after treatment ($P < 0.05$; Supplementary Figures 2A,B).

$DUMB_R$ treatment improves plaque instability

Twelve weeks after $DUMB_R$ treatment, H & E and Masson's trichrome staining, as well as CD68, α-SMA and GP IIb/IIIa immunolabeling of abdominal aortic plaques (Figure 7A), revealed that both GP IIb/IIIa expression in plaques and coverage of the endothelium were markedly reduced in the $DUMB_R$ treatment group, followed by $DUMB_C$ treatment, DU only and control groups. Similar trends were observed in the abundance of macrophages,

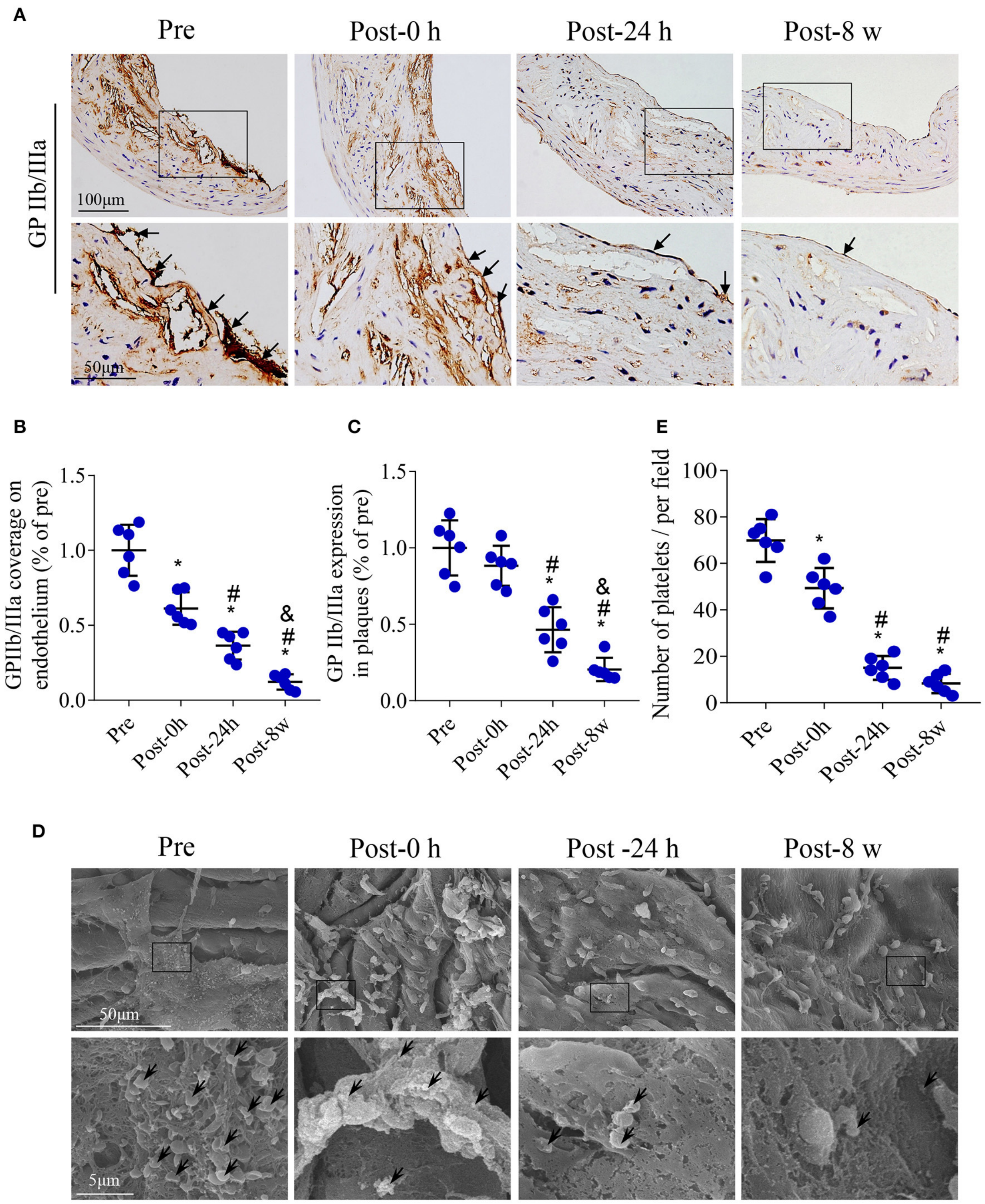

FIGURE 5

Effects of DUMB$_R$ treatment at an MI of 1.5 on activated platelets in plaques. **(A)** Representative images of GP IIb/IIIa labeling in plaques and the endothelium (arrows) of the aorta are shown. Quantifications of **(B)** GP IIb/IIIa coverage of the endothelium and **(C)** total plaque GP IIb/IIIa content are shown. **(D)** Platelets (black arrowheads) adhering to the endothelium of atherosclerotic lesions were observed by scanning electron microscopy. **(E)** Quantitative analysis of the average number of activated platelets. $n = 6$ per group. $^{*}P < 0.05$ vs. pretreatment, $^{\#}P < 0.05$ vs. Post-0 h, $^{\&}P < 0.05$ vs. Post-24 h.

the vulnerability index and NC/FC ratio ($P < 0.05$; Figures 7B–D,F,G). In contrast, the expression of SMCs showed the opposite trend (Figure 7E). Additionally, the results of scanning electron microscopy also indicated that at 12 weeks after DUMB$_R$ treatment, compared to the DUMB$_C$ treatment and other two groups, fewer activated platelets

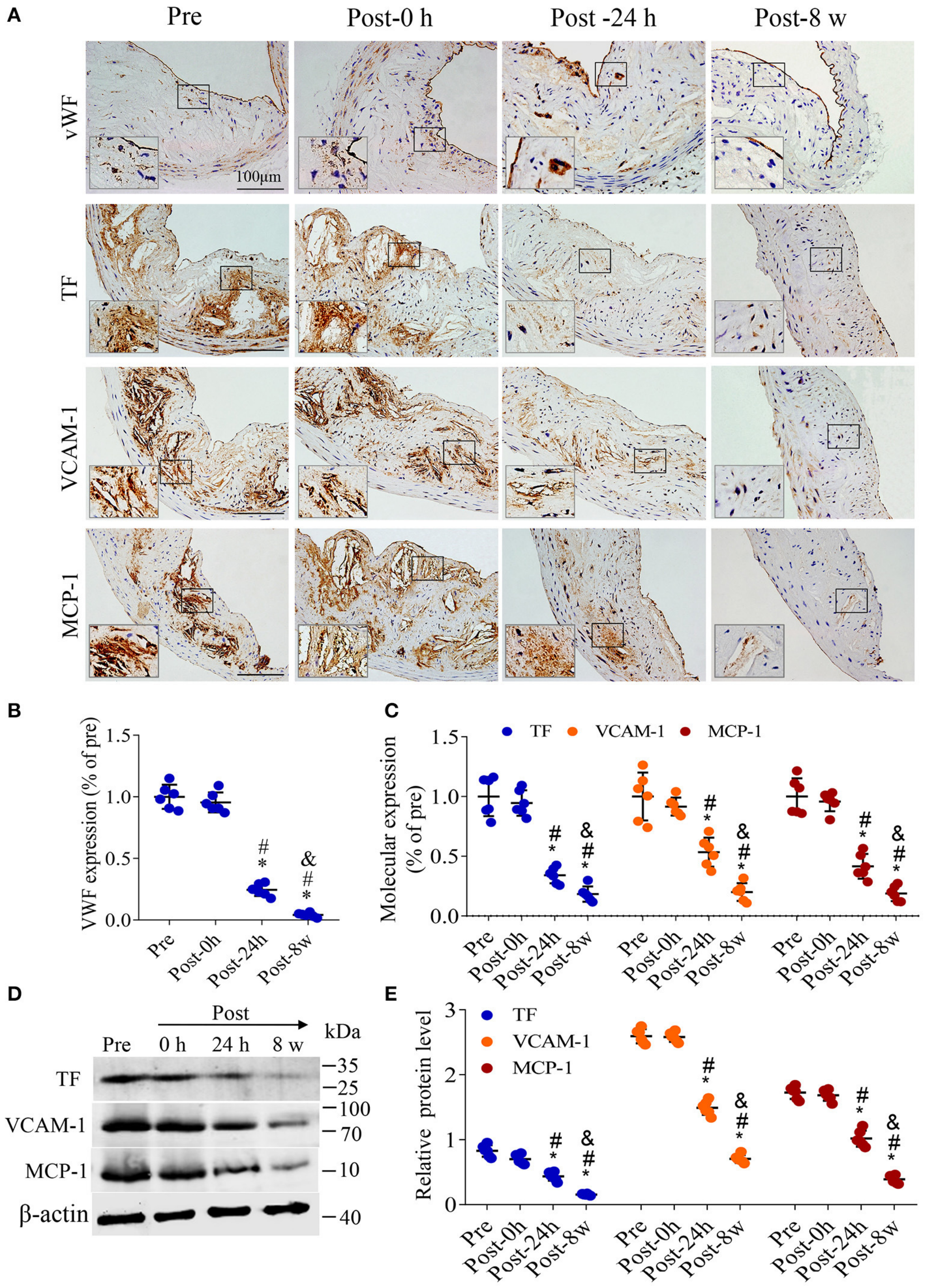

FIGURE 6
$\mathrm{DUMB_R}$ treatment reduces the expression of platelet adhesion promoters, thrombogenic factors, adhesion molecules and chemokines. **(A)** Representative images of Immunohistochemistry for von Willebrand factor (vWF), tissue factor (TF), vascular cell adhesion molecule-1 (VCAM-1) and monocyte chemotactic protein (MCP-1) before treatment and at 0 h, 24 h and 8 weeks after treatment with $\mathrm{DUMB_R}$ at an MI of 1.5. Quantification of **(B)** vWF, **(C)** TF, VCAM-1 and MCP-1 at different time points is shown. **(D)** Representative immunoprecipitation images of TF, VCAM-1 and MCP-1 in plaques before treatment and at 0 h, 24 h, and 8 w after treatment with $\mathrm{DUMB_R}$ at an MI of 1.5. **(E)** Quantification of the immunoblot strip. $n = 6$ per group. $^{*}P < 0.05$ vs. pretreatment. $^{\#}P < 0.05$ vs. Post-0 h, $^{\&}P < 0.05$ vs. Post-24 h, $n = 6$ per group.

adhered and aggregated on the endothelium (Figures 7H,I), which is consistent with the expression of GP IIb/IIIa described above. In summary, DUMBR could identify unstable plaques and simultaneously improve their stability by specifically dissolving activated platelets as illustrated in Figure 7J.

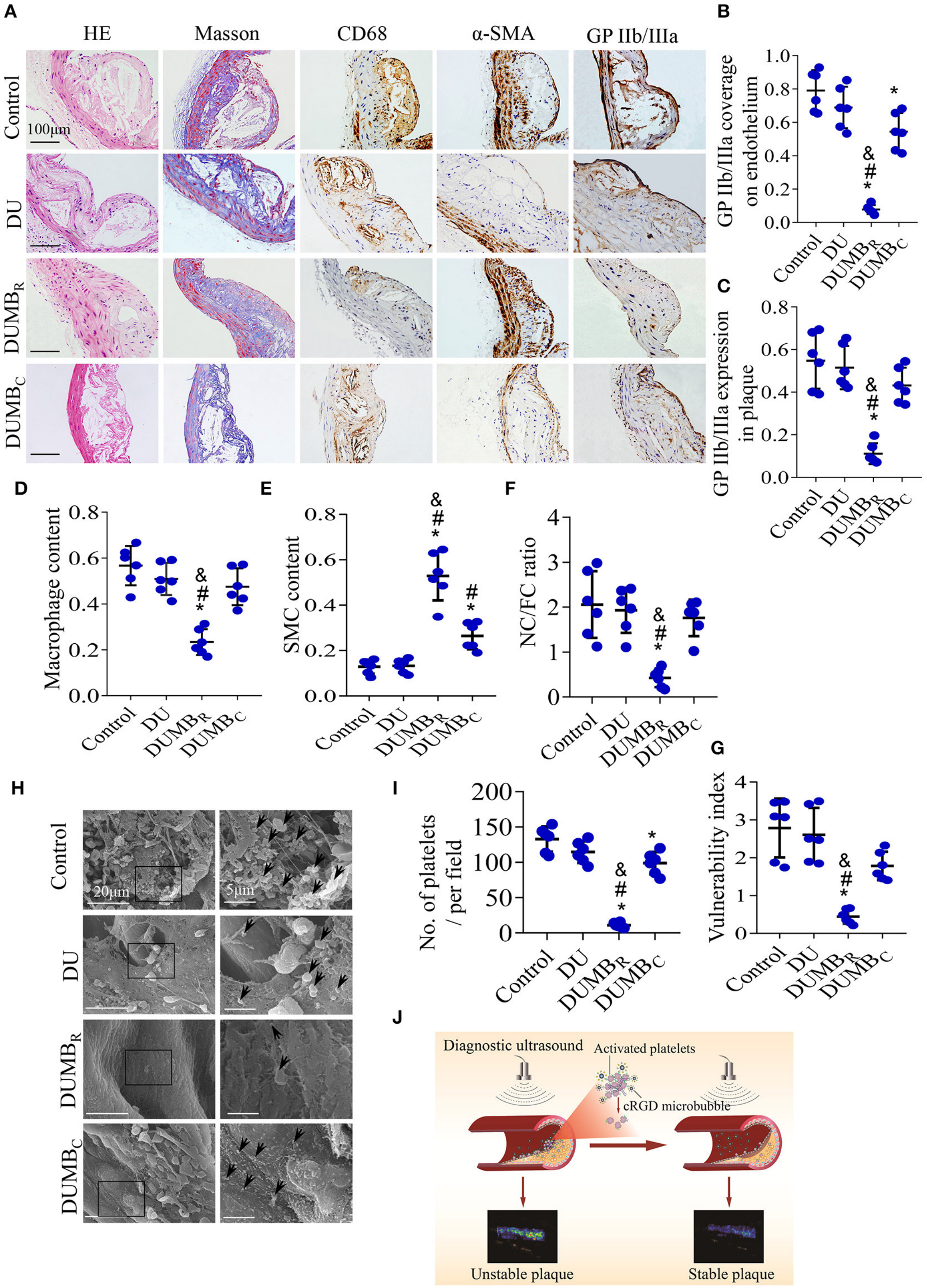

FIGURE 7
Effect of DUMB$_R$ treatment on plaque instability. **(A)** Representative images of H & E and Masson's trichrome staining and immunolabeling with antibodies against α-SMA, CD68 and GP IIb/IIIa. Quantitative analyses of **(B)** GP IIb/IIIa coverage of the endothelium, **(C)** total plaque GP IIb/IIIa content, **(D)** plaque macrophage and **(E)** SMC content were shown. **(F)** The plaque NC/FC ratio and **(G)** vulnerability index were calculated. **(H)** Representative scanning electron microscopy images of activated platelets (black arrowheads). **(I)** Average number of activated platelets was quantified. **(J)** Illustration of DUMB$_R$ identifying unstable plaques and simultaneously improving their stability by specifically dissolving activated platelets. n = 6 per group. $^*P < 0.05$ vs. control, $^\#P < 0.05$ vs. DU, $^\&P < 0.05$ vs. DUMB$_C$. DUMB$_R$, diagnostic ultrasound combined with MB$_R$; DUMB$_C$, diagnostic ultrasound combined with MB$_C$.

Discussion

The present study demonstrated that DUMB$_R$ targeting GP IIb/IIIa receptors could simultaneously and specifically diagnose and treat atherosclerotic plaques and evaluate the treatment effect. The underlying mechanism of stabilizing atherosclerotic plaques may be due to the targeted dissolution of activated and aggregated platelets, with a reduction in vWF expression, which further reduces the thrombogenic risk, vascular inflammation, and macrophage recruitment, and ultimately enhances plaque stability. This theranostic approach combining diagnostic and therapeutic capabilities in a single type of targeted MB with high specificity and affinity may represent a novel application for the detection and stabilization of atherosclerotic plaques while avoiding systemic adverse effects.

A key contributor to thrombosis, activated platelets could be considered a critical factor leading to plaque instability and rupture, and the GP IIb/IIIa receptor of activated platelets has been regarded as a target for the diagnosis of high-risk plaques (3, 4). This was supported by our finding that GP IIb/IIIa coverage of the endothelium or expression in plaques was correlated with both plaque vulnerability index, the ratio of NC/FC and video intensity of ultrasound molecular imaging for MB$_R$ on plaques. Moreover, our results also revealed that the video intensity of MB$_R$ in plaques was comparable at baseline, while a significant reduction was observed in the MI 1.5 and 1.9 DUMB$_R$-treated groups, which was mainly due to the platelet aggregated clot disruption caused by ultrasound-MB$_R$ cavitation effect. This indicates that DUMB$_R$ could detect the consistency of the plaque features before treatment and reliably evaluating the therapeutic efficacy after treatment, which is consistent with previous reports (4, 11).

As a critical biomarker of plaque instability, GP IIb/IIIa receptor on activated platelets in plaques has also been proposed as a key target for the treatment of advanced atherosclerotic plaques (14). Accumulating evidence suggests that effective antiplatelet drug therapy, affecting the process of platelet activation, adhesion or aggregation can stabilize atherosclerotic plaques but yields a limited reduction in fatal acute events and an increased risk of bleeding complications after systemic administration (6, 17, 23). Additionally, pioneering groups have demonstrated that DU+MB can dissolve acute intravascular thrombi in large vessels and platelet-rich microthrombi in small vessels or microvessels both *in vitro* and *in vivo* (9, 10). However, the application of such modalities to atherosclerotic plaques is still limited, and to date, the effect of DUMB$_R$ treatment on plaque instability and the underlying mechanism have not been explored. In the present study, the particle size distribution of MBs results show that the MBs contain not only micron-sized MBs but also a large number of nano-sized MBs, which could penetrate into the neovascular wall through the microvascular space (24), allowing more MBs to enter the atherosclerotic plaque and reach the activated platelets in the plaque. Hence, DUMB$_R$ can effectively dissolve activated and aggregated platelets in atherosclerotic plaques. The results of immunohistochemistry and scanning electron microscopy illustrate that DUMB$_R$ at an ultrasound MI of 1.5 significantly reduced GP IIb/IIIa expression coverage on endothelia and within plaques and the number of activated platelets on endothelia. This phenomenon could be explained by the dissolution of aggregated platelets by ultrasound-medicated destruction of MB$_R$. More importantly, our results also indicate that dissolving aggregated platelets by DUMB$_R$ significantly improved plaque instability. After treatment with DUMB$_R$ at an MI of 1.5, the SMC content in the plaques was obviously increased, while the macrophage content, the corresponding vulnerability index and the NC/FC ratio were significantly decreased, thereby improving plaque instability. Therefore, DUMB$_R$ targeting GP IIb/IIIa receptors can effectively dissolve activated and aggregated platelets in plaques and improve the instability of atherosclerotic plaques.

It is widely believed that DUMB$_R$ at an appropriate MI can confer excellent antiplatelet efficacy and has minor side effects. Ultrasonic MI is one of the most important parameters that determine the conditions of ultrasound molecular imaging or targeted therapy (25). To determine the most suitable MI parameters, a series of factors, such as the video intensity of ultrasound molecular imaging of MB$_R$, activated platelets and erythrocyte extravasation in plaque, were observed at four different levels of ultrasonic MI with or without MB$_R$. Our results indicate that the video intensity of the abdominal aorta gradually decreased as the ultrasonic MI increased, reaching a plateau at 1.5 and did not further decrease even when the MI was increased to 1.9 with MB$_R$ or MB$_C$. This finding was further supported by the GP IIb/IIIa immunostaining and scanning electron microscopy results. Nonetheless, the endothelium of the plaque was destroyed in the group treated with DUMB$_R$ at an MI of 1.9 compared with that in the other treatment groups as observed by GP IIb/IIIa immunostaining. Additionally, the scanning electron microscopy results also showed that the structure of the plaque endothelium was incomplete in the MI 1.9 DUMB$_R$ group compared with that in the MI 1.5 DUMB$_R$ group. This finding indicates that the DUMB$_R$ treatment at an MI of 1.5 did not increase the risk of endothelial damage but had a therapeutic effect similar to that of the MI 1.9 group, which is consistent with the observation of a positive relationship between MB-mediated ultrasound cavitation intensity and vascular endothelial damage (26). In addition, our TER-119 immunostaining results revealed that the extravasation of erythrocytes within plaques was more significantly increased in the MI 1.9 DUMB$_R$ group compared to that in the DUMB$_C$ and MI 1.5 DUMB$_R$ groups and the other groups. This finding indirectly indicated that DU at higher MI values with MB$_R$ may induce the fibrous cap rupture or intraplaque hemorrhage resulting from capillary damage in high-risk atherosclerotic plaques (20), which requires careful attention. Previous studies demonstrated that both MB destruction and the number of microvascular ruptures were proportional to the applied MI, which just confirmed our findings (20, 26, 27). Notably, our supplementary results show that immunostaining for TER-119 did not further increase after DUMB$_R$ treatment at an MI of 1.5 and continued to decrease over time. In this study, we also found that the DUMB$_R$ at an MI of 1.5 did not prolong the bleeding time. Therefore, these above indicate that DUMB$_R$ treatment at an MI of 1.5 is more appropriate and safer for targeted dissolution of activated and aggregated platelets and has fewer adverse effects on normal tissues.

Once an atherosclerotic vulnerable plaque suddenly disrupts or erodes, the subendothelial matter is exposed to circulating blood components, leading to platelet activation and subsequent thrombus formation; endotheliogenic vWF first initiates platelet adhesion onto the endothelium *via* an interaction its A1 domain and the GP Ib-V-IX receptor in the initial phase; then induces the activation of platelet GP IIb/IIIa receptor through an "inside-out" conformational change that switches to a high-affinity state and finally permits the activation of TF in the subsequent enlarged stage (14, 28, 29). Thereafter, TF binds activated coagulation factor VII and recruits the circulating platelets and inflammatory cells, resulting in a vicious cycle of "platelet activation-thrombogenesis" (29, 30). Hence, dissolution of aggregated platelets by DUMB$_R$, which reduces the number of activated platelets and the levels of related mediators, may interrupt this cycle and reduce platelet activation and thrombus formation. Our current immunohistochemical results show that the expression of vWF at 24 h and 8 weeks after DUMB$_R$ treatment was significantly reduced compared with that in the pretreatment group. Moreover, the levels of TF were markedly decreased, indicating that DUMB$_R$ could decrease the risk of thrombus formation. In addition, the content of adhesion molecules and macrophage infiltration, which could aggravate the inflammatory response, causing plaque instability or rupture, was also significantly decreased. The same phenomenon was reflected in the western blotting data. In addition, in our study, both plaque vulnerability and atherosclerotic lesion areas were markedly decreased after the treatment with DUMB$_R$.These finding indicate that DUMB$_R$ treatment could reduce vWF expression, which further reduces the thrombogenic risk, vascular inflammation, and macrophage recruitment, and ultimately improve plaque instability. Furthermore, our supplementary results show that plaque microvasculature declined over time after the DUMB$_R$ treatment which may further enhances plaque stability. In summary, the DUMB$_R$ strategy in current study could specifically identify, target, and dissolve aggregated platelets and then evaluate the therapeutic efficacy in real time after treatment. It is exciting that a strategy combining DU with MB has been applied to the dissolution of acute platelet-rich thrombi in mouse, rat and canine models (10, 11, 31), highlighting the potential for future application in atherosclerotic plaques in humans but needed to be investigated by further clinical trials. Therefore, the DUMB$_R$ approaches used in the current study, which could provide targeted identification and dissolution of aggregated platelets in plaques to avoid systemic side effects, may provide a novel strategy for detecting and stabilizing atherosclerotic plaques.

There are several limitations of our study. First, the amount of GP IIb/IIIa on activated platelets is much greater than that of other integrins, such as αvβ3, αvβ1, and αvβ6. However, these integrins can also bind MB$_R$ similar to GP IIb/IIIa, contributing to an enhanced ultrasound signal for MB$_R$, which is weaker in the presence of a GP IIb/IIIa inhibitor; thus, we can assume that the signal of MB$_R$ was mainly derived from GP IIb/IIIa of activated platelets on plaques. An alternative approach could make apply MB with a GP IIb/IIIa-specific antibody, but immunogenicity may limit its clinical applications (4, 15, 32). Second, we did not observe in real-time whether the platelet aggregates returned at other time points within 12 weeks or longer after a single DUMB$_R$ treatment. However, GP IIb/IIIa expression and the number of platelets aggregates were indeed significantly decreased at 24 h, 8 weeks and 12 weeks after treatment, and the DUMB$_R$ treatment group was more stable than the other groups at 12 weeks, which was consistent with previous studies (20). Third, similar to previous studies (33), only a small fraction of the atherosclerotic plaques that were generated could be defined as vulnerable plaques, which could cause severe cardiovascular events; however, plaque vulnerability was observed in many mice, especially those fed an HCD, as evidenced by the atherosclerotic vulnerable indicators. Moreover, the technology has never been applied for the intracranial plaques, but multiple studies have proved that certain intensity of ultrasound could achieve the penetration of the skull and application on intracranial microthrombi (10, 34), which would provide a potential adjunct to therapy of intracranial plaques. Furthermore, our study was performed in a mouse model, which may not completely reflect all aspects of atherosclerotic plaques in humans, although the ultrasonic parameters used in the present study have potential value for clinical applications, further studies verifying the results in larger animals or humans could rapidly promote the translation of this novel theranostic method to clinical application, which is the goal of our future research.

Conclusion

In conclusion, the data in this study indicate that DU combined with MB$_R$ targeting GP IIb/IIIa receptors could simultaneously and selectively identify and stabilize atherosclerotic plaques by imaging and dissolving aggregated platelets. Therefore, DUMB$_R$ technology combining diagnostic and therapeutic capabilities using a single type of targeted MB may represent a novel application for the simultaneous detection and therapy of atherosclerotic plaque.

Data availability statement

The raw data supporting the conclusions of this article will be made available by the authors, without undue reservation.

Ethics statement

The animal study was reviewed and approved by Institutional Animal Care and Use Committee of Zhengzhou University.

Author contributions

FH and SG conceived and designed the experiments. SG, SZ, and XC performed the experiments. SG, KC, and FH analyzed and interpreted the data. FH, SG, SZ, and KC drafted the manuscript and critically assessed its contents. All authors have read and approved the final version of the manuscript, have made important contributions to the study, and are familiar with the data.

Funding

This study was supported by the National Natural Science Foundation of China (No. 81701695) and Youth Foundation of the First Affiliated Hospital of Zhengzhou University (No. YNQN2017118). This study was also supported by the Medical Science and Technology Research Project of Henan Province (Grant No. SBGJ202102153) and Henan Provincial Science and Technology Research Projects (Grant Nos. 212102310799 and 222102310577).

Conflict of interest

The authors declare that the research was conducted in the absence of any commercial or financial relationships that could be construed as a potential conflict of interest.

Publisher's note

Supplementary material

The Supplementary Material for this article can be found online at: https://www.frontiersin.org/articles/10.3389/fcvm.2022.946557/full#supplementary-material

References

1. Collaborators GBDCoD. Global R. and national age-sex-specific mortality for 282 causes of death in 195 countries and territories, 1980-2017: a systematic analysis for the global burden of disease study 2017. *Lancet.* (2018) 392:1736–88. doi: 10.1016/S0140-6736(18)32203-7

2. Arbab-Zadeh A, Fuster V. From detecting the vulnerable plaque to managing the vulnerable patient: jacc state-of-the-art review. *J Am Coll Cardiol.* (2019) 74:1582–93. doi: 10.1016/j.jacc.2019.07.062

3. Jackson SP. Arterial thrombosis–insidious, unpredictable and deadly. *Nat Med.* (2011) 17:1423–36. doi: 10.1038/nm.2515

4. Guo S, Shen S, Wang J, Wang H, Li M, Liu Y, et al. Detection of high-risk atherosclerotic plaques with ultrasound molecular imaging of glycoprotein iib/iiia receptor on activated platelets. *Theranostics.* (2015) 5:418–30. doi: 10.7150/thno.10020

5. Berny-Lang MA, Jakubowski JA, Sugidachi A, Barnard MR, Michelson AD, Frelinger AL. 3rd. P2y12 receptor blockade augments glycoprotein iib-iiia antagonist inhibition of platelet activation, aggregation, and procoagulant activity. *J Am Heart Assoc.* (2013) 2:e000026. doi: 10.1161/JAHA.113.000026

6. Becker RC, Bassand JP, Budaj A, Wojdyla DM, James SK, Cornel JH, et al. Bleeding complications with the P2y12 receptor antagonists clopidogrel and ticagrelor in the platelet inhibition and patient outcomes (Plato) trial. *Eur Heart J.* (2011) 32:2933–44. doi: 10.1093/eurheartj/ehr422

7. Baqi Y, Muller CE. Antithrombotic P2y12 receptor antagonists: recent developments in drug discovery. *Drug Discov Today.* (2019) 24:325–33. doi: 10.1016/j.drudis.2018.09.021

8. Rix A, Curaj A, Liehn E, Kiessling F. Ultrasound microbubbles for diagnosis and treatment of cardiovascular diseases. *Semin Thromb Hemost.* (2019) 46:545-52. doi: 10.1055/s-0039-1688492

9. Xie F, Lof J, Everbach C, He A, Bennett RM, Matsunaga T, et al. Treatment of acute intravascular thrombi with diagnostic ultrasound and intravenous microbubbles. *JACC Cardiovasc Imaging.* (2009) 2:511–8. doi: 10.1016/j.jcmg.2009.02.002

10. Lu Y, Wang J, Huang R, Chen G, Zhong L, Shen S, et al. Microbubble-mediated sonothrombolysis improves outcome after thrombotic microembolism-induced acute ischemic stroke. *Stroke.* (2016) 47:1344–53. doi: 10.1161/STROKEAHA.115.012056

11. Wang X, Gkanatsas Y, Palasubramaniam J, Hohmann JD, Chen YC, Lim B, et al. Thrombus-targeted theranostic microbubbles: a new technology towards concurrent rapid ultrasound diagnosis and bleeding-free fibrinolytic treatment of thrombosis. *Theranostics.* (2016) 6:726–38. doi: 10.7150/thno.14514

12. Lux J, Vezeridis AM, Hoyt K, Adams SR, Armstrong AM, Sirsi SR, et al. Thrombin-activatable microbubbles as potential ultrasound contrast agents for

the detection of acute thrombosis. *ACS Appl Mater Interfaces.* (2017) 9:37587–96. doi: 10.1021/acsami.7b10592

13. Durrant TN, van den Bosch MT, Hers I. Integrin Alphaiibbeta3 outside-in signaling. *Blood.* (2017) 130:1607–19. doi: 10.1182/blood-2017-03-773614

14. Huang J, Li X, Shi X, Zhu M, Wang J, Huang S, et al. Platelet integrin Alphaiibbeta3: signal transduction, regulation, and its therapeutic targeting. *J Hematol Oncol.* (2019) 12:26. doi: 10.1186/s13045-019-0709-6

15. Hu G, Liu C, Liao Y, Yang L, Huang R, Wu J, et al. Ultrasound molecular imaging of arterial thrombi with novel microbubbles modified by cyclic rgd in vitro and in vivo. *Thromb Haemost.* (2012) 107:172–83. doi: 10.1160/TH10-11-0701

16. Gupta AS, Huang G, Lestini BJ, Sagnella S, Kottke-Marchant K, Marchant RE. Rgd-modified liposomes targeted to activated platelets as a potential vascular drug delivery system. *Thromb Haemost.* (2005) 93:106–14. doi: 10.1160/TH04-06-0340

17. Guo CG, Chen L, Chan EW, Cheung KS, Isshiki T, Wong ICK, et al. Systematic review with meta-analysis: the risk of gastrointestinal bleeding in patients taking third-generation P2y12 inhibitors compared with clopidogrel. *Aliment Pharmacol Ther.* (2019) 49:7–19. doi: 10.1111/apt.15059

18. Kaufmann BA, Sanders JM, Davis C, Xie A, Aldred P, Sarembock IJ, et al. Molecular imaging of inflammation in atherosclerosis with targeted ultrasound detection of vascular cell adhesion molecule-1. *Circulation.* (2007) 116:276–84. doi: 10.1161/CIRCULATIONAHA.106.684738

19. Xie F, Lof J, Matsunaga T, Zutshi R, Porter TR. Diagnostic ultrasound combined with glycoprotein Iib/Iiia-targeted microbubbles improves microvascular recovery after acute coronary thrombotic occlusions. *Circulation.* (2009) 119:1378–85. doi: 10.1161/CIRCULATIONAHA.108.825067

20. Li X, Guo S, Xu T, He X, Sun Y, Chen X, et al. Therapeutic ultrasound combined with microbubbles improves atherosclerotic plaque stability by selectively destroying the intraplaque neovasculature. *Theranostics.* (2020) 10:2522–37. doi: 10.7150/thno.39553

21. Mao Y, Liu XQ, Song Y, Zhai CG, Xu XL, Zhang L, et al. Fibroblast growth factor-2/Platelet-derived growth factor enhances atherosclerotic plaque stability. *J Cell Mol Med.* (2020) 24:1128–40. doi: 10.1111/jcmm.14850

22. Zhu J, Liu B, Wang Z, Wang D, Ni H, Zhang L, et al. Exosomes from nicotine-stimulated macrophages accelerate atherosclerosis through Mir-21-3p/Pten-mediated Vsmc migration and proliferation. *Theranostics.* (2019) 9:6901–19. doi: 10.7150/thno.37357

23. Maschino F, Hurault-Delarue C, Chebbane L, Fabry V, Montastruc JL, Bagheri H, et al. Bleeding adverse drug reactions (Adrs) in patients exposed to antiplatelet plus serotonin reuptake inhibitor drugs: analysis of the french spontaneous reporting database for a controversial Adr. *Eur J Clin Pharmacol.* (2012) 68:1557–60. doi: 10.1007/s00228-012-1268-8

24. Exner AA, Kolios MC. Bursting microbubbles: how nanobubble contrast agents can enable the future of medical ultrasound molecular imaging and image-guided therapy. *Curr Opin Colloid Interface Sci.* (2021) 54:101463. doi: 10.1016/j.cocis.2021.101463

25. Ay T, Havaux X, Van Camp G, Campanelli B, Gisellu G, Pasquet A, et al. Destruction of contrast microbubbles by ultrasound: effects on myocardial function, coronary perfusion pressure, and microvascular integrity. *Circulation.* (2001) 104:461–6. doi: 10.1161/hc3001.092038

26. Skyba DM, Price RJ, Linka AZ, Skalak TC, Kaul S. Direct in vivo visualization of intravascular destruction of microbubbles by ultrasound and its local effects on tissue. *Circulation.* (1998) 98:290–3. doi: 10.1161/01.cir.98.4.290

27. Wang J, Zhao Z, Shen S, Zhang C, Guo S, Lu Y, et al. Selective depletion of tumor neovasculature by microbubble destruction with appropriate ultrasound pressure. *Int J Cancer.* (2015) 137:2478–91. doi: 10.1002/ijc.29597

28. Chen Y, Ju LA, Zhou F, Liao J, Xue L, Su QP, et al. An integrin alphaiibbeta3 intermediate affinity state mediates biomechanical platelet aggregation. *Nat Mater.* (2019) 18:760–69. doi: 10.1038/s41563-019-0323-6

29. Parahuleva MS, Worsch M, Euler G, Choukeir M, Mardini A, Parviz B, et al. Factor Vii activating protease expression in human platelets and accumulation in symptomatic carotid plaque. *J Am Heart Assoc.* (2020) 9:e016445. doi: 10.1161/JAHA.120.016445

30. Asada Y, Yamashita A, Sato Y, Hatakeyama K. Pathophysiology of Atherothrombosis: Mechanisms of Thrombus Formation on Disrupted Atherosclerotic Plaques. *Pathol Int.* (2020). doi: 10.1111/pin.12921

31. Li H, Lu Y, Sun Y, Chen G, Wang J, Wang S, et al. Diagnostic ultrasound and microbubbles treatment improves outcomes of coronary no-reflow in canine models by sonothrombolysis. *Crit Care Med.* (2018) 46:e912–20. doi: 10.1097/CCM.0000000000003255

32. Kasirer-Friede A, Kahn ML, Shattil SJ. Platelet integrins and immunoreceptors. *Immunol Rev.* (2007) 218:247–64. doi: 10.1111/j.1600-065X.2007.00532.x

33. Shiomi M, Ito T, Hirouchi Y, Enomoto M. Fibromuscular cap composition is important for the stability of established atherosclerotic plaques in mature Whhl rabbits treated with statins. *Atherosclerosis.* (2001) 157:75–84. doi: 10.1016/s0021-9150(00)00708-5

34. Gao S, Zhang Y, Wu J, Shi WT, Lof J, Vignon F, et al. Improvements in cerebral blood flow and recanalization rates with transcranial diagnostic ultrasound and intravenous microbubbles after acute cerebral emboli. *Invest Radiol.* (2014) 49:593–600. doi: 10.1097/RLI.0000000000000059

frontiers | Frontiers in Cardiovascular Medicine

TYPE Original Research
PUBLISHED 28 July 2022
DOI 10.3389/fcvm.2022.949440

OPEN ACCESS

EDITED BY
Giuseppe Pannarale,
Sapienza University of Rome, Italy

REVIEWED BY
Sebastian Kelle,
Deutsches Herzzentrum
Berlin, Germany
Francesco Pelliccia,
Sapienza University of Rome, Italy

*CORRESPONDENCE
Walid El-Saadi
walid.el-saadi@liu.se

SPECIALTY SECTION
This article was submitted to
Cardiovascular Imaging,
a section of the journal
Frontiers in Cardiovascular Medicine

RECEIVED 20 May 2022
ACCEPTED 04 July 2022
PUBLISHED 28 July 2022

CITATION
El-Saadi W, Engvall JE, Alfredsson J, Karlsson J-E, Martins M, Sederholm S, Faisal Zaman S, Ebbers T and Kihlberg J (2022) A head-to-head comparison of myocardial strain by fast-strain encoding and feature tracking imaging in acute myocardial infarction. *Front. Cardiovasc. Med.* 9:949440. doi: 10.3389/fcvm.2022.949440

A head-to-head comparison of myocardial strain by fast-strain encoding and feature tracking imaging in acute myocardial infarction

Walid El-Saadi[1,2]*, Jan Edvin Engvall[3,4], Joakim Alfredsson[5], Jan-Erik Karlsson[1,2], Marcelo Martins[6], Sofia Sederholm[5], Shaikh Faisal Zaman[2,4], Tino Ebbers[2,4] and Johan Kihlberg[4,6]

[1]Department of Internal Medicine, Ryhov County Hospital, Region Jönköping County, Jönköping, Sweden, [2]Department of Health, Medicine and Caring Sciences, Linköping University, Linköping, Sweden, [3]Department of Clinical Physiology in Linköping and Department of Health, Medicine and Caring Sciences, Linköping University, Linköping, Sweden, [4]Center for Medical Imaging Science and Visualization, Linköping University, Linköping, Sweden, [5]Department of Cardiology in Linköping and Department of Health Medicine and Caring Sciences, Linköping University, Linköping, Sweden, [6]Department of Radiology in Linköping and Department of Health Medicine and Caring Sciences, Linköping University, Linköping, Sweden

Background: Myocardial infarction (MI) is a major cause of heart failure. Left ventricular adverse remodeling is common post-MI. Several studies have demonstrated a correlation between reduced myocardial strain and the development of adverse remodeling. Cardiac magnetic resonance (CMR) with fast-strain encoding (fast-SENC) or feature tracking (FT) enables rapid assessment of myocardial deformation. The aim of this study was to establish a head-to-head comparison of fast-SENC and FT in post-ST-elevated myocardial infarction (STEMI) patients, with clinical 2D speckle tracking echocardiography (2DEcho) as a reference.

Methods: Thirty patients treated with primary percutaneous coronary intervention for STEMI were investigated. All participants underwent CMR examination with late gadolinium enhancement, cine-loop steady-state free precession, and fast-SENC imaging using a 1.5T scanner as well as a 2DEcho. Global longitudinal strain (GLS), segmental longitudinal strain (SLS), global circumferential strain (GCS), and segmental circumferential strain (SCS) were assessed along with the MI scar extent.

Results: The GCS measurements from fast-SENC and FT were nearly identical: the mean difference was 0.01 (2.5)% (95% CI – 0.92 to 0.95). For GLS, fast-SENC values were higher than FT, with a mean difference of 1.8 (1.4)% (95% CI 1.31–2.35). Tests of significance for GLS did not show any differences between the MR methods and 2DEcho. Average strain in the infarct-related artery (IRA) segments compared to the remote myocardium was significantly lower for the left anterior descending artery and right coronary artery culprits but not for the left circumflex artery culprits. Fast-SENC displayed a higher area under the curve for detecting infarcted segments than FT for both SCS and SLS.

Conclusion: GLS and GCS did not significantly differ between fast-SENC and FT. Both showed acceptable agreement with 2DEcho for longitudinal strain. Segments perfused by the IRA showed significantly reduced strain values compared to the remote myocardium. Fast-SENC presented a higher sensitivity and specificity for detecting infarcted segments than FT.

KEYWORDS

cine magnetic resonance imaging, myocardial ischemia, ST elevation myocardial infarction, myocardial stunning, left ventricular dysfunction, left ventricular remodeling

Introduction

Coronary artery disease is a major cause of heart failure worldwide, as more patients now survive myocardial infarction (MI) due to improvements in prevention as well as in the availability of primary percutaneous coronary intervention (pPCI) in the case of ST-elevation MI (STEMI) (1–4). Left ventricular (LV) adverse remodeling, which may develop post-MI, is a complex process, initiated by scarring, which results in myocardial functional and anatomical deterioration (1, 2, 4). A myocardial scar is characterized by wall thinning and abnormal wall motion. On a global level, increased LV volumes,

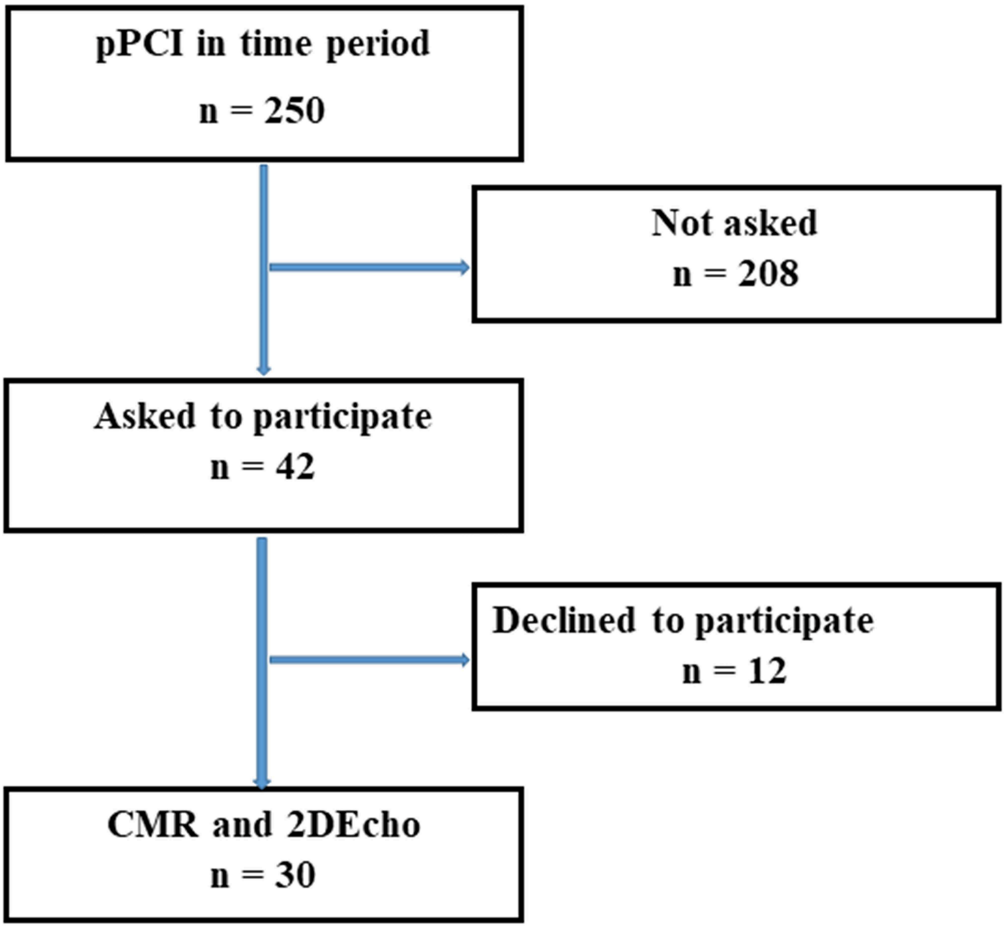

FIGURE 1
Flowchart of study design.

partial bulging of the LV wall, and reduced left ventricular ejection fraction (LVEF) are typical characteristics of remodeling (4, 5). Beyond LV volumes and LVEF, measurements of myocardial deformation, frequently denominated "strain," can add information on the reduction in myocardial performance not yet visible in the gold standard LVEF (6). Two-dimensional echocardiography (2DEcho) studies have demonstrated that strain may predict adverse remodeling (4, 7). 2DEcho is a time and cost-effective standard procedure in post-MI care but is limited by the skills of the operator and problems evaluating segments due to artifacts and pulmonary shadowing (8). Cardiac magnetic resonance (CMR) is considered the reference method for the assessment of LV anatomy and function but has some drawbacks, such as being time-consuming, unsuitable for claustrophobic patients, and often requiring the use of gadolinium contrast, which is contraindicated in renal failure (9–12). Late gadolinium enhancement (LGE) is the method of choice for detecting myocardial necrosis and scarring (2, 9, 13, 14). LGE imaging is commonly performed about 10–20 min after contrast injection to detect injured myocytes, infarct scar area, and its transmural extent, features that are not available with other imaging methods (2, 9, 13). Strain assessment by feature tracking (FT) or fast-strain encoding (fast-SENC) CMR may add to the evaluation of patients with acute MI by identifying individuals who could be at risk of developing adverse remodeling (10, 15, 16). Both techniques can assess strain in the longitudinal and circumferential directions, which has been shown to predict adverse remodeling of the LV (16–19). The techniques used in FT and fast-SENC are discussed in Amzulescu et al. (6). FT is computed on cine-loops which are part of the standard balanced steady-state free precession (bSSFP) CMR examination (8, 16). These segmented 2D cine-loops are acquired over the entire heart cycle, usually "averaged" from 5 to 10 heartbeats, which makes deformation measurement possible for each time step (6, 16, 20). Feature tracking (FT) uses either optical flow technology or non-rigid elastic registration (21). Fast-SENC utilizes parallel tags and needs only a single heartbeat for image acquisition, and post-processing can be completed in <2 min. This may eliminate the need for breath-holding, which is especially valuable in patients with respiratory diseases. In patients with cardiac arrhythmia, a single heartbeat image acquisition will also result in fewer artifacts (22).

The aim of this study was to establish a head-to-head comparison of myocardial strain assessment, in both longitudinal and circumferential directions between fast-SENC and FT in STEMI patients immediately post-pPCI using echocardiographic speckle-tracking strain as the reference.

TABLE 1 Patient characteristic.

Patient demographics ($n = 30$)	**Mean (*SD*)**
Men/women	22/8
Age (years)	69 (10)
Height (cm)	173 (11)
Weight (kg)	81 (16)
BMI (kg/m^2)	27 (5)
eGFR (ml/min)	79 (24)
Cardiovascular risk profile	
Family history of cardiovascular disease	4
Diabetes	9
Hyperlipidemia	17
Hypertension	21
History of MI	10
Previously treated PCI	8
Culprit artery	
LAD	13
LCX	6
RCA	11
Cardiac magnetic resonance imaging characteristics	
Left ventricular morphology	
LVEDV (ml)	159 (43)
LVESV (ml)	84 (36)
LVSV (ml)	75 (19)
LV Mass (g)	124 (27)
LVEF %	48 (9)
MI scar %	15 (9)

Means with standard deviation (*SD*) in parentheses. For abbreviations, please see text.

Materials and methods

Study population

Patients with STEMI, treated with pPCI were offered CMR and 2DEcho within 2 days, while still in the hospital, between 4 November 2019 and 16 November 2020. In this time span, a total

TABLE 2 Global circumferential and longitudinal strain.

Myocardial strain direction	**Mean % (*SD*)**	**95% CI for mean**
GCS		
Fast-SENC	−13.6 (3.7)	−14.9 to −12.2
FT	−13.6 (3.7)	−15.0 to −12.2
GLS		
Fast-SENC	−14.8 (2.9)	−15.9 to −13.7
FT	−13.0 (2.8)	−14.0 to −11.9
2DEcho	−13.3 (3.7)	−14.7 to −11.9

Global circumferential strain (GCS) and global longitudinal strain (GLS) derived from fast-SENC, FT and 2DEcho. Means and standard deviation (SD) in parenthesis with 95% confidence intervals are presented.

of 250 patients were treated with pPCI for STEMI at our hospital. Forty-two patients were asked to participate, 12 declined, and 30 were finally enrolled in the study after giving written and oral consent, see Figure 1. The study complied with the Declaration of Helsinki and with agreements on Good Clinical Practice. The study protocol was approved by the Swedish Ethical Review Authority in Uppsala, registration number 2019-00480.

CMR acquisition and post-processing

CMR including cine bSSFP, LGE, and fast-SENC was acquired on a 1.5T scanner (Achieva d-Stream, Philips Healthcare, Best, the Netherlands). The fast-SENC acquisition had a voxel size of 4.0 × 4.0 × 10 mm^3, which was reconstructed to 1.0 × 1.0 × 10 mm^3. The acquisition length was one

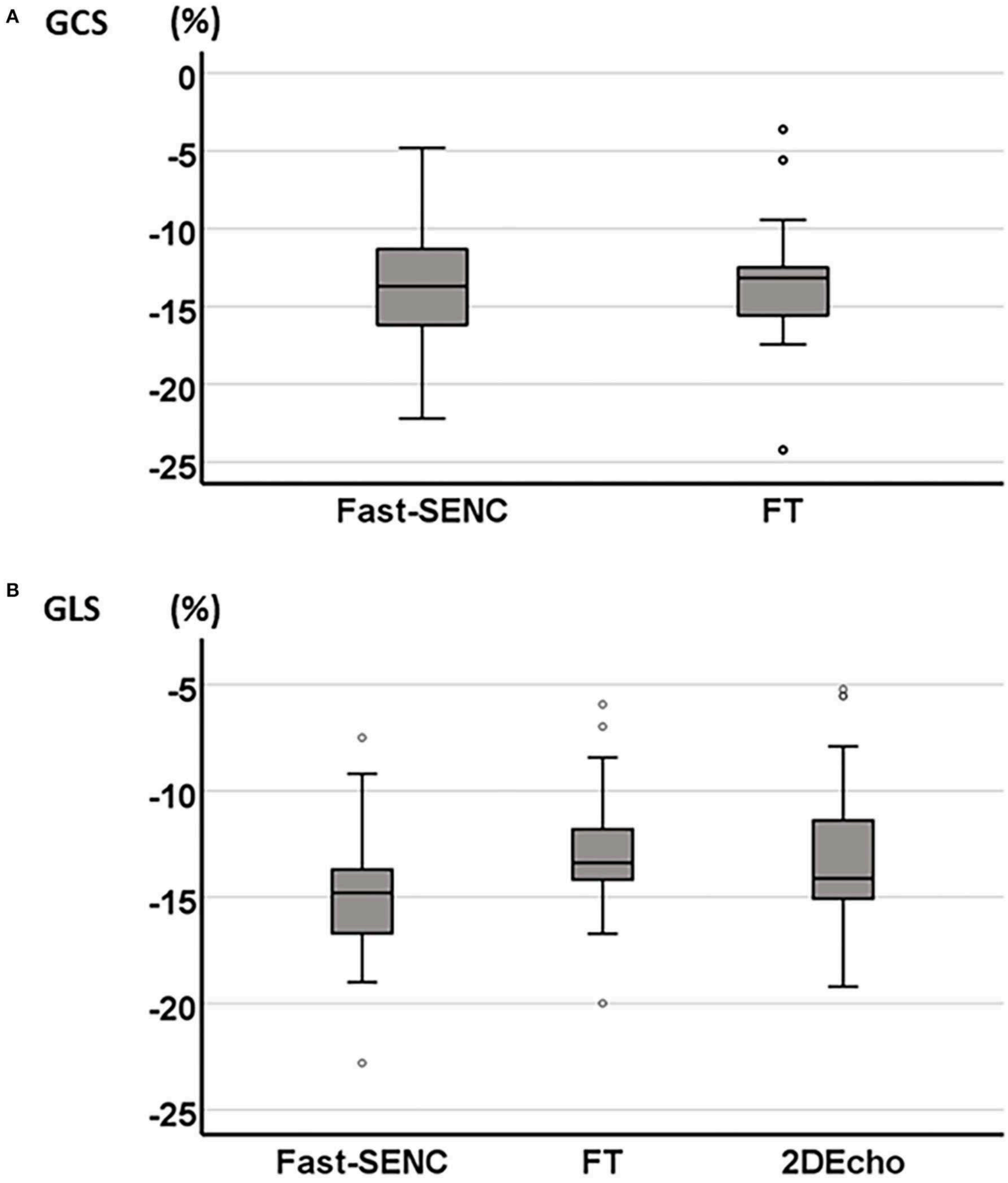

FIGURE 2
Boxplot of mean GCS derived from fast-SENC and FT **(A)** and mean GLS derived from fast-SENC, FT, and 2DEcho **(B)**.

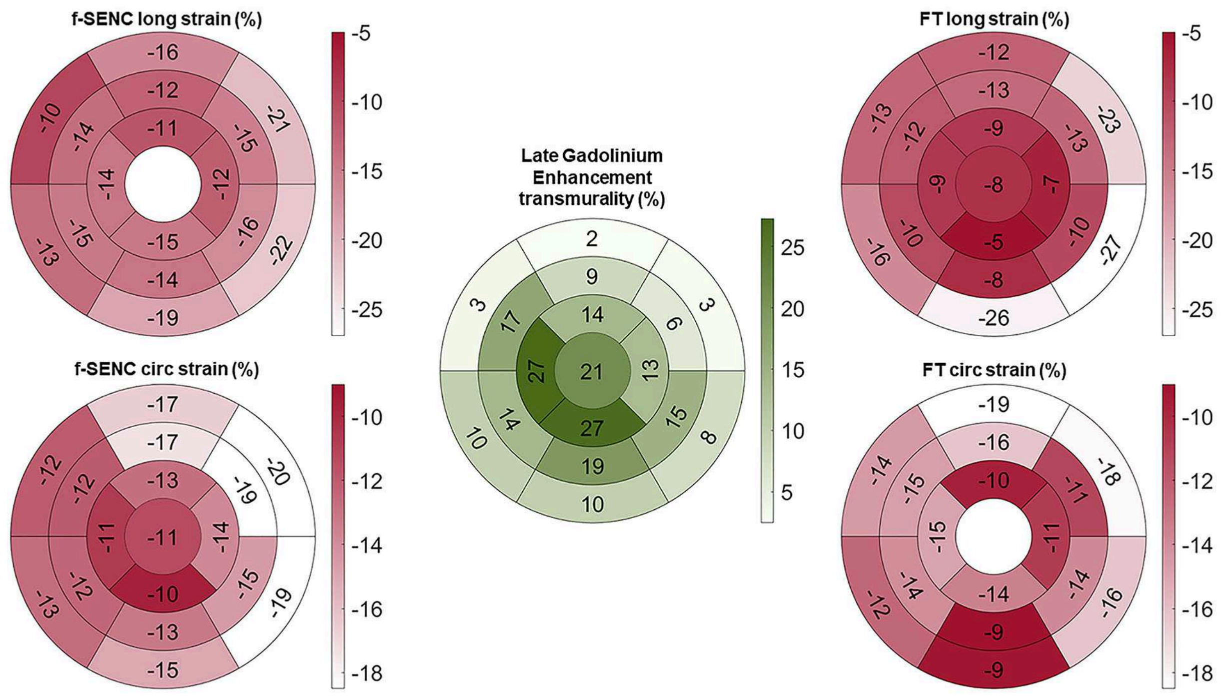

FIGURE 3
Bull's eye of mean longitudinal strain (long) and global circumferential strain (circ) of fast-SENC and FT with myocardial injury detected with late gadolinium enhancement (LGE).

cardiac cycle for each cardiac view, requiring a 1-s breath hold at a heart rate of 60 beats per minute, enabling the images to be reconstructed into 22 phases. The following acquisition parameters were used for fast-SENC: repetition time (TR) = 11 ms, echo time (TE) = 0.7 ms, flip angle = 30°. Fast-SENC strain analysis was performed in the MyoStrain software (Myocardial Solutions Inc. v 5.1.4, Morrisville, NC, USA), the technique utilizes tags parallel to the acquired image and is an adaptation of SENC, enabling the acquisition of cardiac deformation in a single heartbeat. Longitudinal strain (LS) was derived from three different short-axis (SA) views, covering the left ventricle at the basal, midventricular, and apical level. Circumferential strain (CS) was derived from two-, three- and four-chamber long axis (LA) views. The LV 17-segment model of the American Heart Association (AHA) was used, excluding the SA apical segment (23). The time required for performing post-processing was recorded, and the time span of the acquisitions was obtained from the DICOM header of the stored images. For FT, bSSFP images were acquired with a spatial resolution of 1.2 × 1.2 × 8 mm^3 and reconstructed into 30 cardiac phases. The FT algorithm is based on non-elastic registration of segmented endo- and epicardial surfaces with the deformation field being tracked over time. The following FT acquisition parameters were used: TR = 3.3 ms, TE = 1.6 ms, and flip angle = 60°. The typical breath-hold duration was 9 s for each view, at a heart rate of 60 beats per minute. Three different LA (two-, three-, and four-chamber) and SA (at basal, midventricular, and apical levels) images were obtained, excluding the SA apical segment. CS was derived from the SA segments and LS from the LA image segments according to the AHA model (23). The images were segmented for volume, left ventricular mass (LVM), and MI scar in the Segment software (v 2.2 R7056, Medviso AB, Lund, Sweden), which also included a module that was used for FT strain analysis (non-rigid elastic registration). LGE was acquired in the same views as the cine images, using the PSIR-technique with a resolution of 1.5 × 1.5 × 10 mm^3 with a typical breath-hold duration of 12 s for each image. All strain values were evaluated at end-systole, which was determined from aortic valve closure. One observer performed segmentation for FT strain, LV volume, and MI scar analysis. A "scar" segment was defined if the LGE-positive area was >1%. The processing time for FT and fast-SENC was recorded for 10 randomly selected patients. For analysis of intraobserver and interobserver reproducibility, patients were re-analyzed twice by one CMR operator and once by another CMR operator, both experienced in the field. Operators were certified for the acquisition and analysis of fast-SENC by the vendor.

Echocardiography

Standard transthoracic 2DEcho was recorded for clinical routine evaluation by clinically experienced technicians with the patient in the left lateral decubitus position. Speckle tracking 2DEcho allows for the evaluation of myocardial deformation by assessing the movements of small natural acoustic markers during a heart cycle. A Vivid E-95 Ultrasound System (GE Vingmed Ultrasound; Horten, Norway) equipped with a 4Vc-probe was used for assessment of myocardial function and structure via the parasternal long axis, the apical two-, three-, and four-chamber views and when necessary also the subcostal views. End-systolic global longitudinal strain (GLS) was analyzed offline using the 2DS tool in EchoPAC PC Integrated version 203.74 (GE Ultrasound, Horten, Norway), by an echocardiographic specialist experienced in speckle tracking.

TABLE 3 Correlation chart of global strain.

Correlation variables	*r* (df)	*p*
GCS		
Fast-SENC vs. FT	0.77 (28)	<0.01
GLS		
Fast-SENC vs. FT	0.88 (28)	<0.01
2DEcho vs. fast-SENC	0.65 (27)	<0.01
2DEcho vs. FT	0.75 (27)	<0.01
GCS vs. MI scar		
Fast-SENC	0.65 (28)	<0.01
FT	0.54 (28)	<0.01
GLS vs. MI scar		
Fast-SENC	0.41 (28)	0.02
FT	0.47 (28)	<0.01
2DEcho	0.53 (27)	<0.01
GCS vs. LVEF		
Fast-SENC	−0.32 (28)	0.09
FT	−0.22 (28)	0.25
GLS vs. LVEF		
Fast-SENC	−0.19 (28)	0.31
FT	−0.30 (28)	0.11
2DEcho	−0.35 (27)	0.06
GCS vs. LVEDV		
Fast-SENC	0.33 (28)	0.08
FT	0.31 (28)	0.09
GLS vs. LVEDV		
Fast-SENC	0.09 (28)	0.63
FT	0.18 (28)	0.34
2DEcho	0.09 (27)	0.64

Pearson correlation coefficients (r) with degrees of freedom (df = n-2), for global circumferential strain (GCS) and global longitudinal strain (GLS) correlated to myocardial infarction (MI) scar, left ventricular ejection fraction (LVEF), and left ventricular end-diastolic volume (LVEDV).

Comparison methodology

Global circumferential strain (GCS) and global longitudinal strain (GLS) derived from FT and fast-SENC were compared head-to-head. Speckle tracking end-systolic GLS from the 2DEcho gray scale was calculated for reference. All strains were correlated to $\mathrm{LVEF}_{\mathrm{CMR}}$, MI scar, and its segmental extent ("transmurality"). The diagnostic performance of segmental circumferential strain (SCS) and segmental longitudinal strain (SLS) was based on individual segments and the regional strain was calculated by assigning myocardial segments to the three major coronary artery perfusion territories according to Cerqueira et al. (23). Strain in segments belonging to the infarct-related artery (IRA) was compared to remote myocardial segments. The detection of scar segments based on strain results was presented as the area under the curve (AUC) from receiver operating characteristics curve (ROC) analysis. Sensitivity was calculated at a specificity of 80% for the detection of any infarcted segment as well as for segments with transmurality >50%.

Statistical analysis

Analysis was performed using SPSS 27 (IBM Inc, Armonk, New York, USA). Continuous variables were presented as mean with SD (in parenthesis). Differences in continuous variables were tested with the analysis of variance non-parametric Friedman's Chi square test, where the level of significance was set to $p < 0.01$. Pearson correlation coefficients (ρ, df) where df $= N-2$, were calculated to express the degree of linear association between the variables. The correlation hypothesis tested was that $\rho = 0$ vs. $\rho \neq 0$ with a significance level set to $p < 0.01$. The intraclass correlation coefficient (ICC) was calculated, scatterplot graphs were drawn to depict the linear relationship between the variables and boxplots were created to illustrate the distribution of myocardial strain. Bland–Altman difference plots were presented to evaluate the agreement between the CMR methods.

Results

Scar and ejection fraction

The subjects were enrolled and treated with pPCI after identification of the culprit artery in each case. The cohort displayed a median door-to-balloon time of 67 min. Average scar size was 15 (9) % of LVM with a median Troponin-T of 1,640 ng/l, equivalent to 164 × upper level of normal. LGE revealed scar in 240 out of 510 segments (47%) with 122 segments having scar transmurality < 25%, 78 segments between 25 and 49%, and only 40 segments had a transmurality

≥ 50%. In 13 patients the LVEF_{CMR} was little affected, $\text{LVEF}_{\text{CMR}} \geq 50\%$. Patients with maintained LVEF_{CMR} had smaller scar size 10 (5) % than those with depressed LVEFCMR < 50% whose scar size was 19 (10) %, ($p < 0.01$). Patient demographics and CMR imaging characteristics are presented in Table 1.

Myocardial strain

Strain comparisons are given in terms of "higher" when more negative, and "lower" when less negative, according to Voigt et al. (24). The GCS measurements from fast-SENC and FT were nearly identical, with a mean difference of 0.01

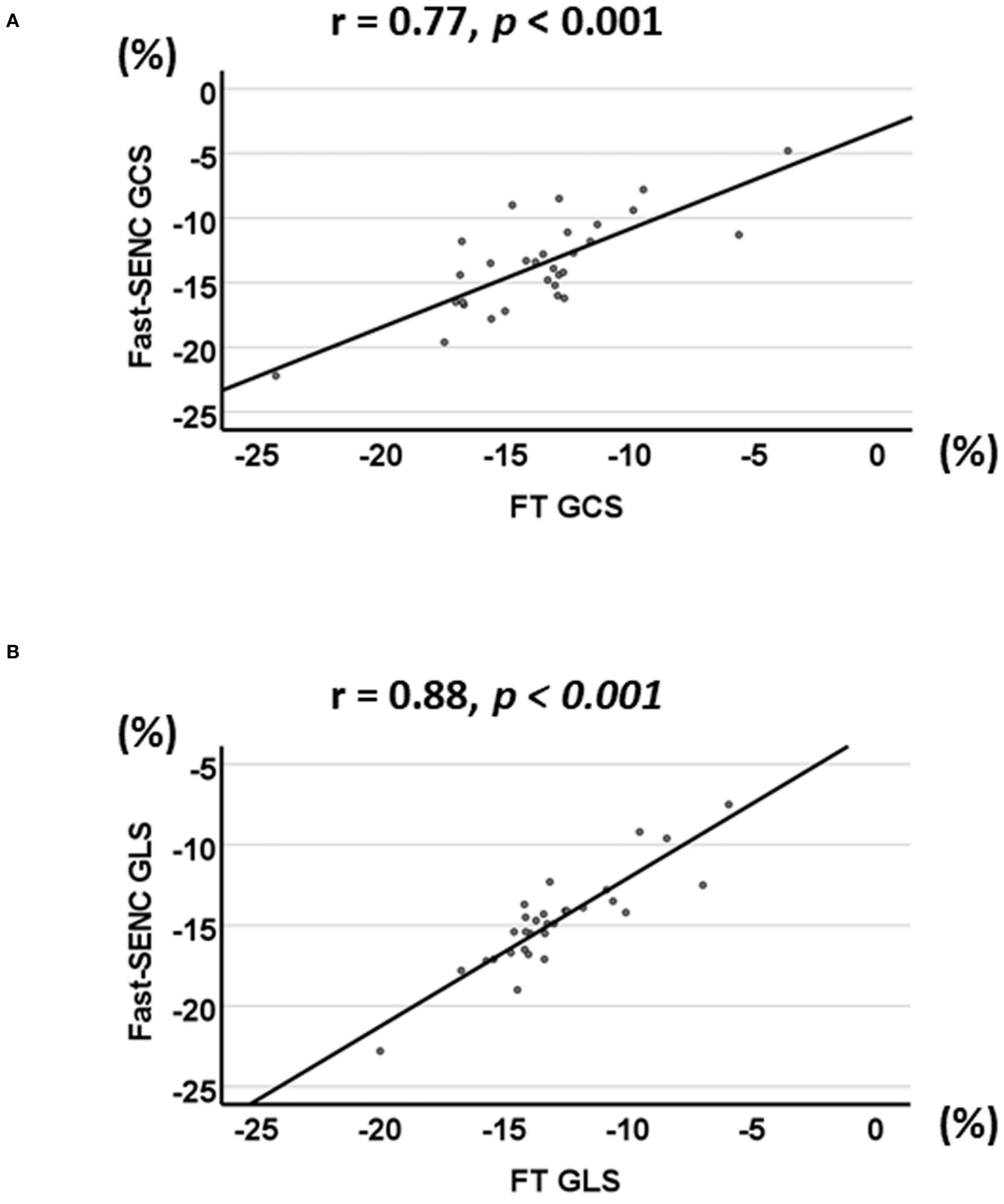

FIGURE 4
Linear correlation (*r*) between fast-SENC and FT for GCS **(A)** and GLS **(B)**.

(2.5)% (95% CI—0.92 to 0.95). For GLS, fast-SENC values were higher than FT with a mean difference of 1.8 (1.4)% (95% CI 1.31–2.35), Table 2 and Figures 2, 3. Statistical testing for GLS did not show significant differences between fast-SENC or FT and 2DEcho ($p > 0.01$). The correlations between GCS or GLS from the two myocardial deformation techniques and MI scar, $LVEDV_{CMR}$ and $LVEF_{CMR}$ are shown together with Bland–Altman graphs in Table 3 and partly in Figures 4, 5. Average strain in the IRA segments compared to the remote myocardium was significantly ($p < 0.001$) lower for left anterior descending artery (LAD) and right coronary artery culprits but not for left circumflex artery culprits, Table 4 and Figure 6. The average SCS from fast-SENC showed a higher correlation to MI scar than the average SCS for FT for each IRA segment distribution ($p < 0.001$). The highest correlation factor was computed for the average SCS and scar in the LAD region ($\rho = 0.65$, $p < 0.001$). In general, correlations were higher for fast-SENC in both strain directions compared to FT and 2DEcho, except for SLS vs. scar in LAD segments, Table 5. Figure 7 shows a two-chamber view example of an extensive anterior

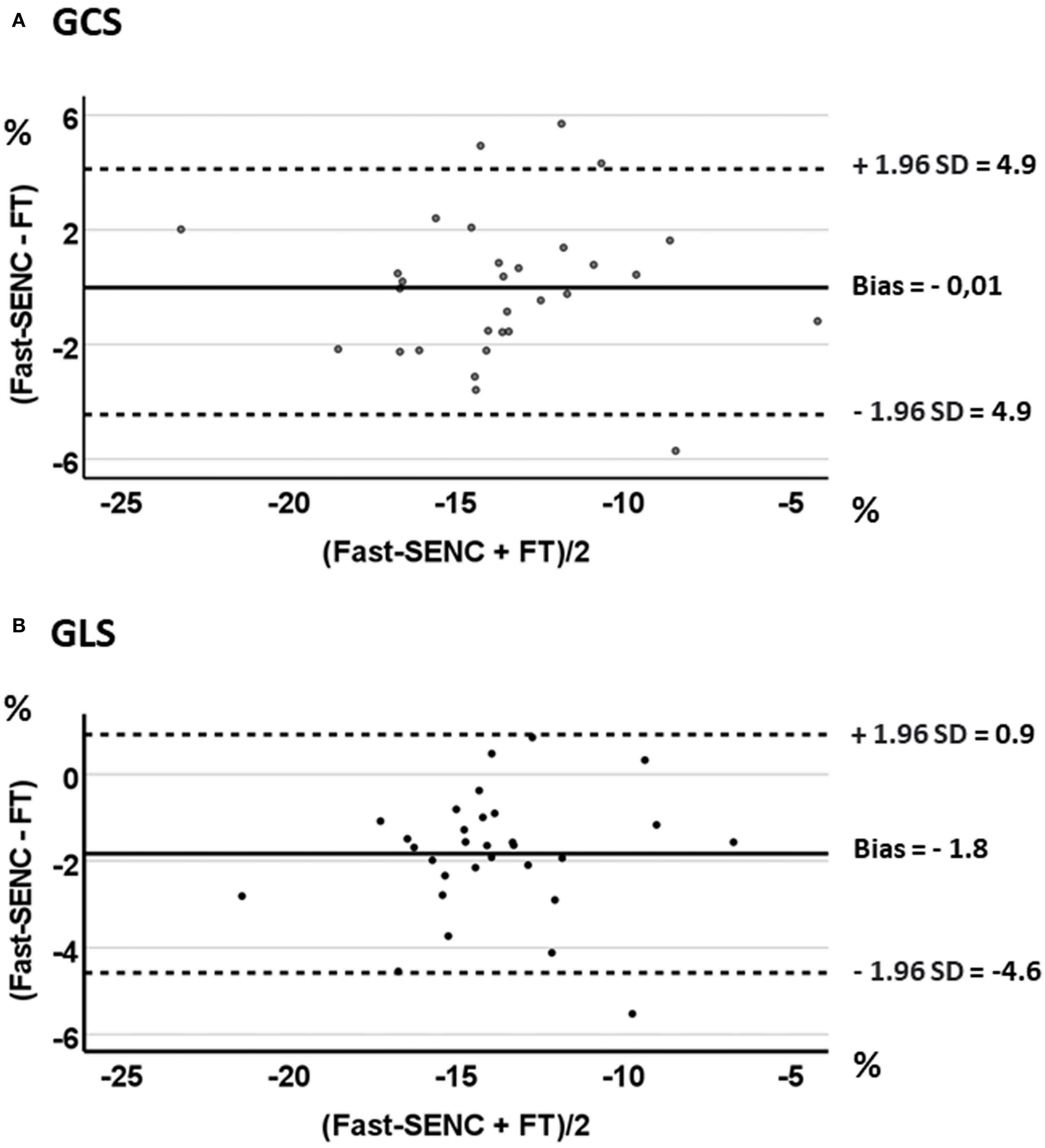

FIGURE 5
Bland-Altman plots with limits of agreement (1.96 SD) for fast-SENC and FT for GCS **(A)** and GLS **(B)**.

TABLE 4 Strain in culprit versus remote segments.

IRA (segments)	Strain direction %	Remote segments	Culprit segments	*p*
LAD (1, 2, 7, 8, 13, 14)		***n* = 130**	***n* = 78**	
	SCS			
	Fast-SENC	−15 (7)	−8 (6)	<0.01
	FT	−13 (8)	−9 (9)	<0.01
	SLS			
	Fast-SENC	−17 (7)	−9 (6)	<0.01
	FT SLS	−14 (11)	−9 (6)	<0.01
LCX (5, 6, 11, 12, 16)		***n* = 66**	***n* = 30**	
	SCS			
	Fast-SENC	−16 (5)	−15 (6)	0.41
	FT	−16 (8)	−13 (7)	0.04
	SLS			
	Fast-SENC	−15 (6)	−15 (5)	0.23
	FT	−13 (8)	−16 (9)	0.37
RCA (3, 4, 9, 10, 15)		***n* = 121**	***n* = 55**	
	SCS			
	Fast-SENC	−18 (6)	−11 (6)	<0.01
	FT	−17 (7)	−11 (9)	<0.01
	SLS			
	Fast-SENC	−17 (5)	−14 (6)	0.01
	FT	−15 (7)	−13 (8)	<0.01

Segmental strains for infarcted related artery (IRA) and remote segments with means, standard deviation (SD) in parenthesis with p-values are presented. The 17-segment model of the American Heart Association, excluding the apical cap (segment 17) was used for left anterior descending artery (LAD), left circumflex artery (LCX) and right coronary artery (RCA).

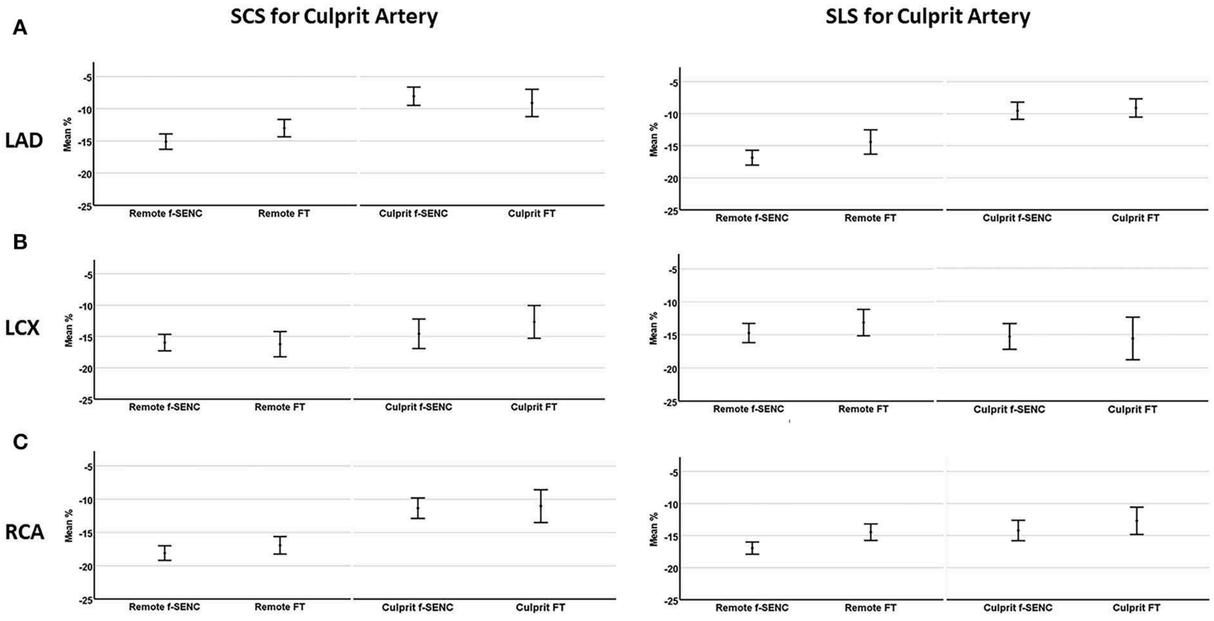

FIGURE 6
Mean strain of culprit artery segments and remote myocardium for left anterior descending artery **(A)**, left circumflex artery **(B)**, and right coronary artery **(C)**. Segmental circumferential strain (SCS) and segmental longitudinal strain (SLS) are presented for each infarcted related artery.

TABLE 5 Correlations of segmental strain.

IRA	Correlation variables	r (df)	*p*
LAD segments ($n = 180$)			
Segments: 1, 2, 7, 8, 13, 14	**SCS vs. MI scar**		
	Fast-SENC	0.65 (178)	<0.01
	FT	0.59 (178)	<0.01
	SLS vs. MI scar		
	Fast-SENC	0.48 (178)	<0.01
	FT SLS	0.40 (178)	<0.01
	2DEcho	0.54 (178)	<0.01
LCX segments ($n = 150$)			
Segments: 5, 6, 11, 12, 16	**SCS vs. MI scar**		
	Fast-SENC	0.44 (148)	<0.01
	FT	0.24 (148)	<0.01
	SLS vs. MI scar		
	Fast-SENC	0.33 (148)	<0.01
	FT	0.20 (148)	0.01
	2DEcho	0.29 (148)	<0.01
RCA segments ($n = 150$)			
Segments: 3, 4, 9, 10, 15	**SCS vs. MI scar**		
	Fast-SENC	0.50 (148)	<0.01
	FT	0.25 (148)	<0.01
	SLS vs. MI scar		
	Fast-SENC	0.40 (148)	<0.01
	FT	0.25 (148)	<0.01
	2Decho	0.32 (148)	<0.01

Segmental strain for infarcted related artery (IRA) with Pearson correlation coefficient r (df = N-2) to myocardial infarction transmurality (MI scar) with p-values are presented. The 17-segment model of the American Heart Association was used, excluding the apical cap (segment 17), for each coronary artery.

infarction with LGE, fast-SENC$_{CMR}$, and speckle tracking strain from 2DEcho.

Receiver operating characteristics analysis

Fast-SENC had a higher AUC for detecting infarcted segments than FT for both SCS and SLS. SCS derived from fast-SENC detected segments with scar transmurality >50%, with the highest sensitivity (73%) at a specificity of 80% and AUC (0.88). SLS derived from 2DEcho detected scar transmurality >50%, with the sensitivity of 73% at specificity of 80%, and AUC of 0.83, Figure 8.

Acquisition and reproducibility

All patients had good image quality for fast-SENC, cine bSSFP, LGE, and 2DEcho. The end-systolic phase was captured at 304 (SD 33 ms) ms after the R-wave for cine images, and at 303 (SD 34 ms) ms for the fast-SENC mages. The fast-SENC acquisition took 120 (SD 30 s) s and its post-processing 213 (SD 17 s) s, Table 6. The acquisition of the FT took 180 (60 s) s, and the post-processing took 150 (30 s). The fast-SENC interobserver reproducibility for GCS and GLS had an ICC of 0.98 (CI 0.97–0.99) and 1.00 (CI 0.99–1.00), and intraobserver reproducibility of ICC 0.98 (CI 0.95–0.99) and 1.00 (CI 0.99–1.00) for GCS and GLS respectively, Table 6. The interobserver reproducibility for FT GCS and GLS was ICC 0.96 (CI 0.89–0.99) and 0.98 (CI 0.94–1.0), Table 6.

Discussion

We performed a head-to-head comparison of myocardial strain assessment between fast-SENC and FT in post-STEMI patients. We were able to demonstrate good interobserver reproducibility and high correlations between the MR techniques with minor differences comparing GLS$_{CMR}$ to GLS of 2DEcho. This is in line with Bucius et al. who found high global strain correlations between fast-SENC, FT and myocardial tagging but who also presented a considerably greater bias between the methods than shown in our study. Furthermore, Obokata et al. also demonstrated high correlation and fairly wide limits of agreement between FT and speckle tracking echocardiography (25, 26).

The assessment of LV contractile dysfunction after a STEMI has important prognostic relevance (11). Although LVEF is an important parameter post-MI, it may not be sufficiently sensitive for detecting subtle changes (6). The myocardial strain has been found to decline earlier than LVEF, which makes it an important complementing method for the evaluation of the LV (25). Many of the segments in our study had a scar transmurality <25%, so only subtle wall motion abnormalities should be expected. Still, we were able to detect significant differences in strain between IRA segments compared to the remote myocardium. This illustrates that strain measurement after myocardial infarction (MI) could possibly be useful for risk stratification of patients.

We were also able to demonstrate high correlations, with slightly higher absolute values for fast-SENC compared to FT and 2DEcho, in the detection of scar segments in the three perfusion territories. Few gadolinium-free alternatives exist for the detection of infarcted myocardial regions, but GCS has been proposed for this task (14). In our study, we could confirm this correlation between GCS and infarcted segments at a level similar to that in previous studies (14).

Both MR deformation methods provide a rapid and objective assessment of myocardial function, which makes them viable alternatives to other time-consuming MR procedures. Additional larger studies with patient follow-up could further

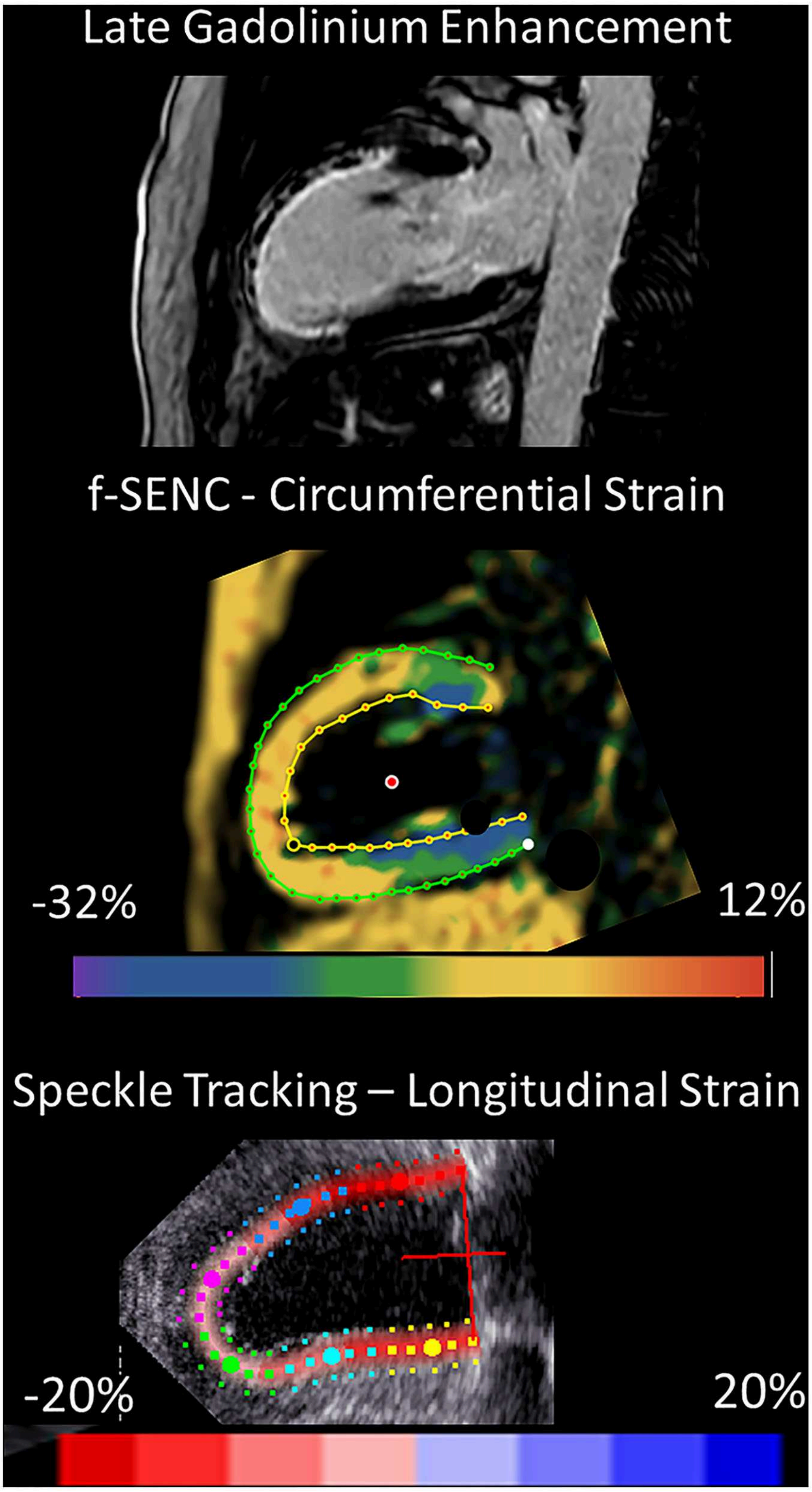

FIGURE 7
2-chamber view of an extensive anterior infarction with the transmural extent of late gadolinium enhancement and zones of no-reflow in the superior viewport, distinctly positive circumferential strain by fast-SENC in the scar area (yellow, middle viewport) and the corresponding speckle tracking longitudinal strain from 2DEcho (pale pink, lower viewport).

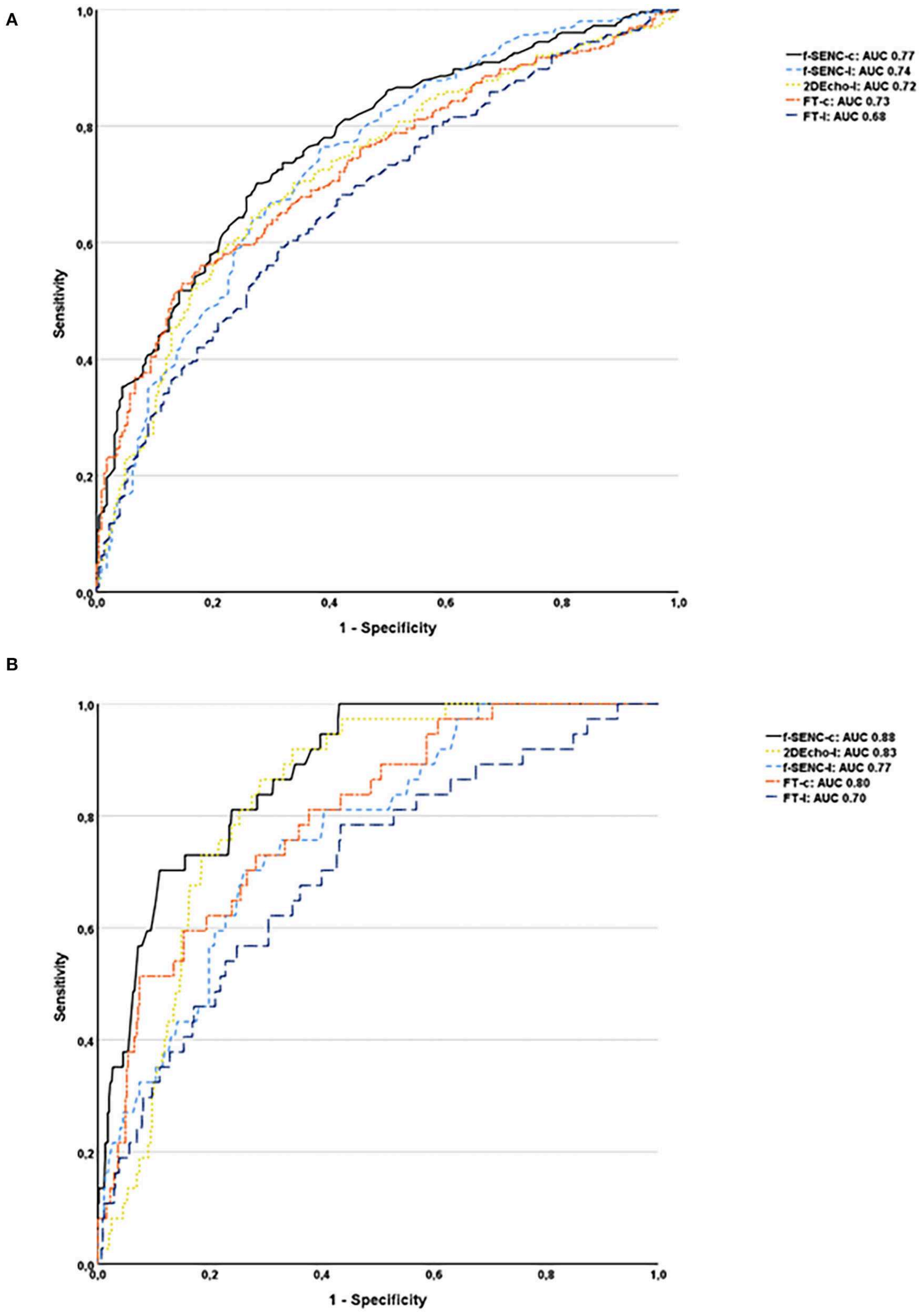

FIGURE 8
Receiver operator characteristics analysis of all infarcted segments **(A)** and segments with the transmurality >50% for fast-SENC, FT, and 2DEcho are presented with circumferential strain (-c), segmental longitudinal strain (-l), and area under the curve (AUC) **(B)**.

TABLE 6 Time spent in data collection and post-processing.

	Acquisition time (s)	Post processing time (s)	Interobserver reproducibility GCS GLS
Fast-SENC	120 (30)	213 (17)	0.98 (CI 0.97–0.99) 1.00 (CI 0.99–1.00)
FT	180 (60)	150 (30)	0.96 (CI 0.89–0.99) 0.98 (CI 0.94–1.00)

Acquisition and post processing time with means and standard deviation (SD) in parenthesis. Interobserver reproducibility for global circumferential strain (GCS) and global longitudinal strain (GLS) with 95% confidence intervals are shown.

identify conditions related to the development of adverse remodeling in subjects with reduced strain values.

Conclusion

Fast-strain encoding showed higher sensitivity and specificity for detecting infarcted segments than FT. Segmental strain calculated for the perfusion territory of the infarct-related artery showed significantly lower strain values compared to the remote myocardium and this correlated with infarct transmurality. This study was not designed to explore the reproducibility of segmental strain values, but for global strain measurement, excellent reproducibility was detected. The GLS and GCS did not differ significantly between the two methods. Both MR methods showed acceptable clinical agreement with speckle tracking GLS obtained from echocardiography. The acquisition time of fast-SENC was very short, facilitating the investigation of patients with respiratory compromise.

Limitations

This was a study of STEMI patients early after the pPCI and the results may not be applicable in all situations of reduced systolic LV function. Most infarcted segments had MI transmurality $<25\%$ which may result in a very subtle lowering of strain. The relatively low number of participants also limits the conclusions. The participating patients were somewhat younger and the male proportion was larger than average for STEMI patients in our catchment area. The presence of risk factors was typical, but the reporting of a family history of cardiac disease in first-degree relatives was probably underrepresented or forgotten by the patients. Adding tagging or displacement encoding with stimulated echoes would have complemented the assessment of deformation measurements using CMR. The present study was limited to the acute phase of STEMI treatment and did not include patient follow-up. We have used the standard AHA definition of perfusion territories, but variation between left- and right-dominated coronary vessel anatomies may especially affect the partition of segments between the LCX and RCA territories, which could have weakened the associations in our evaluation.

Data availability statement

The datasets presented in this article are not readily available because of privacy concerns of the patients. However, data can be made available through the corresponding author, upon reasonable request. Requests to access the datasets should be directed to walid.el-saadi@liu.se.

Ethics statement

The studies involving human participants were reviewed and approved by the Swedish Ethical Review Authority in Uppsala, registration number 2019-00480. The patients/participants provided their written informed consent to participate in this study.

Author contributions

JE, JK, TE, MM, and SF participated in the design method and CMR acquisition, to ensure high-quality images. JE included patients, reviewed the manuscript, coordinated, and supported the study with research funding. WE-S, J-EK, and JK analyzed and interpreted the data, performed the statistical analysis, and wrote the manuscript with the assistance of all the other co-authors. JA and SS revised the manuscript for important related content and helped with the interpretation of the data and results. All authors made relevant contributions to the study. Before publication, the manuscript was reviewed and approved by all authors.

Funding

Financial support for WE-S was obtained from Futurum—the unit for research and education, the academy for health and care in County Hospital Jönköping, and the Research Council of Southeastern Sweden. The study was supported by the Faculty of Medicine and Health Sciences, Linköping University, Sweden. This study was not supported by any specific funding that could have influenced the results.

Acknowledgments

We thank Mats Nilsson, Ph.D. Statistician/Epidemiologist, Futurum—Academy for Health and Care, Region Jönköping

County, for statistical supervision, and the Medical Library County Hospital Jönköping for their support.

Conflict of interest

The authors declare that the research was conducted in the absence of any commercial or financial relationships that could be construed as a potential conflict of interest.

Publisher's note

References

1. Bhatt AS, Ambrosy AP, Velazquez EJ. Adverse remodeling and reverse remodeling after myocardial infarction. *Curr Cardiol Rep.* (2017) 19:71. doi: 10.1007/s11886-017-0876-4

2. Bulluck H, Dharmakumar R, Arai AE, Berry C, Hausenloy DJ. Cardiovascular magnetic resonance in acute ST-Segment-Elevation myocardial infarction: recent advances, controversies, and future directions. *Circulation.* (2018) 137:1949–64. doi: 10.1161/CIRCULATIONAHA.117.030693

3. Galli A, Lombardi F. Postinfarct left ventricular remodelling: a prevailing cause of heart failure. *Cardiol Res Pract.* (2016) 2016:2579832. doi: 10.1155/2016/2579832

4. Bochenek T, Wita K, Tabor Z, Grabka M, Krzych L, Wrobel W, et al. Value of speckle-tracking echocardiography for prediction of left ventricular remodeling in patients with ST-Elevation myocardial infarction treated by primary percutaneous intervention. *J Am Soc Echocardiogr.* (2011) 24:1342–8. doi: 10.1016/j.echo.2011.09.003

5. Curley D, Lavin Plaza B, Shah AM, Botnar RM. Molecular imaging of cardiac remodelling after myocardial infarction. *Basic Res Cardiol.* (2018) 113:10. doi: 10.1007/s00395-018-0668-z

6. Amzulescu MS, De Craene M, Langet H, Pasquet A, Vancraeynest D, Pouleur AC, et al. Myocardial strain imaging: review of general principles, validation, and sources of discrepancies. *Eur Heart J Cardiovasc Imaging.* (2019) 20:605–19. doi: 10.1093/ehjci/jez041

7. Joyce E, Hoogslag GE, Leong DP, Debonnaire P, Katsanos S, Boden H, et al. Association between left ventricular global longitudinal strain and adverse left ventricular dilatation after ST-Segment-Elevation myocardial infarction. *Circ Cardiovasc Imaging.* (2014) 7:74–81. doi: 10.1161/CIRCIMAGING.113.000982

8. Yang L, Cao S, Liu W, Wang T, Xu H, Gao C, et al. Cardiac magnetic resonance feature tracking: a novel method to assess left ventricular three-dimensional strain mechanics after chronic myocardial infarction. *Acad Radiol.* (2021) 28:619–27. doi: 10.1016/j.acra.2020.03.013

9. Arnold JR, McCann GP. Cardiovascular magnetic resonance: applications and practical considerations for the general cardiologist. *Heart.* (2020) 106:174–81. doi: 10.1136/heartjnl-2019-314856

10. Rahman ZU, Sethi P, Murtaza G, Virk HUH, Rai A, Mahmod M, et al. Feature tracking cardiac magnetic resonance imaging: a review of a novel non-invasive cardiac imaging technique. *World J Cardiol.* (2017) 9:312–9. doi: 10.4330/wjc.v9.i4.312

11. Neizel M, Lossnitzer D, Korosoglou G, Schaufele T, Peykarjou H, Steen H, et al. Strain-encoded MRI for evaluation of left ventricular function and transmurality in acute myocardial infarction. *Circ Cardiovasc Imaging.* (2009) 2:116–22. doi: 10.1161/CIRCIMAGING.108.789032

12. Kihlberg J, Gupta V, Haraldsson H, Sigfridsson A, Sarvari SI, Ebbers T, et al. Clinical validation of three cardiovascular magnetic resonance techniques to measure strain and torsion in patients with suspected coronary artery disease. *J Cardiovasc Magn Reson.* (2020) 22:83. doi: 10.1186/s12968-020-00684-2

13. Jimenez Juan L, Crean AM, Wintersperger BJ. Late gadolinium enhancement imaging in assessment of myocardial viability: techniques and clinical applications. *Radiol Clin North Am.* (2015) 53:397–411. doi: 10.1016/j.rcl.2014.11.004

14. Polacin M, Karolyi M, Eberhard M, Gotschy A, Baessler B, Alkadhi H, et al. Segmental strain analysis for the detection of chronic ischemic scars in non-contrast cardiac MRI cine images. *Sci Rep.* (2021) 11:12376. doi: 10.1038/s41598-021-90283-7

15. Giusca S, Korosoglou G, Zieschang V, Stoiber L, Schnackenburg B, Stehning C, et al. Reproducibility study on myocardial strain assessment using fast-SENC cardiac magnetic resonance imaging. *Sci Rep.* (2018) 8:14100. doi: 10.1038/s41598-018-32226-3

16. Reindl M, Tiller C, Holzknecht M, Lechner I, Eisner D, Riepl L, et al. Global longitudinal strain by feature tracking for optimized prediction of adverse remodeling after St-elevation myocardial infarction. *Clin Res Cardiol.* (2021) 110:61–71. doi: 10.1007/s00392-020-01649-2

17. Cha MJ, Lee JH, Jung HN, Kim Y, Choe YH, Kim SM. Cardiac magnetic resonance-tissue tracking for the early prediction of adverse left ventricular remodeling after St-segment elevation myocardial infarction. *Int J Cardiovasc Imaging.* (2019) 35:2095–102. doi: 10.1007/s10554-019-01659-w

18. Reindl M, Reinstadler SJ, Tiller C, Feistritzer HJ, Kofler M, Brix A, et al. Prognosis-based definition of left ventricular remodeling after St-elevation myocardial infarction. *Eur Radiol.* (2019) 29:2330–9. doi: 10.1007/s00330-018-5875-3

19. Holmes AA, Romero J, Levsky JM, Haramati LB, Phuong N, Rezai-Gharai L, et al. Circumferential strain acquired by CMR early after acute myocardial infarction adds incremental predictive value to late gadolinium enhancement imaging to predict late myocardial remodeling and subsequent risk of sudden cardiac death. *J Interv Card Electrophysiol.* (2017) 50:211–8. doi: 10.1007/s10840-017-0296-9

20. Lange T, Stiermaier T, Backhaus SJ, Boom PC, Kowallick JT, de Waha-Thiele S, et al. Functional and prognostic implications of cardiac magnetic resonance feature tracking-derived remote myocardial strain analyses in patients following acute myocardial infarction. *Clin Res Cardiol.* (2021) 110:270–80. doi: 10.1007/s00392-020-01747-1

21. Morais P, Marchi A, Bogaert JA, Dresselaers T, Heyde B, D'Hooge J, et al. Cardiovascular magnetic resonance myocardial feature tracking using a non-rigid, elastic image registration algorithm: assessment of variability in a real-life clinical setting. *J Cardiovasc Magn Reson.* (2017) 19:24. doi: 10.1186/s12968-017-0333-y

22. Korosoglou G, Giusca S, Hofmann NP, Patel AR, Lapinskas T, Pieske B, et al. Strain-encoded magnetic resonance: a method for the assessment of myocardial deformation. *ESC Heart Fail.* (2019) 6:584–602. doi: 10.1002/ehf2.12442

23. Cerqueira MD, Weissman NJ, Dilsizian V, Jacobs AK, Kaul S, Laskey WK, et al. Standardized myocardial segmentation and nomenclature for tomographic imaging of the heart. *Circulation.* (2002) 105:539–42. doi: 10.1161/hc0402.102975

24. Voigt JU, Pedrizzetti G, Lysyansky P, Marwick TH, Houle H, Baumann R, et al. Definitions for a common standard for 2D speckle tracking echocardiography: consensus document of the EACVI/ASE/Industry task force to standardize deformation imaging. *Eur Heart J Cardiovasc Imaging.* (2015) 16:1–11. doi: 10.1093/ehjci/jeu184

25. Bucius P, Erley J, Tanacli R, Zieschang V, Giusca S, Korosoglou G, et al. Comparison of feature tracking, fast-senc, and myocardial tagging for global and segmental left ventricular strain. *ESC Heart Fail.* (2020) 7:523–32. doi: 10.1002/ehf2.12576

26. Obokata M, Nagata Y, Wu VC, Kado Y, Kurabayashi M, Otsuji Y, et al. Direct comparison of cardiac magnetic resonance feature tracking and 2D/3D echocardiography speckle tracking for evaluation of global left ventricular strain. *Eur Heart J Cardiovasc Imaging.* (2016) 17:525–32. doi: 10.1093/ehjci/jev227

frontiers | Frontiers in Cardiovascular Medicine

TYPE Original Research
PUBLISHED 04 August 2022
DOI 10.3389/fcvm.2022.945198

Three-dimensional visualization of heart-wide myocardial architecture and vascular network simultaneously at single-cell resolution

Jianwei Chen[1,2], Guangcai Liu[1], Wen Sun[1], Yuanfang Zheng[1], Jing Jin[1], Siqi Chen[1], Jing Yuan[1,2], Hui Gong[1,2,3], Qingming Luo[4] and Xiaoquan Yang[1,2]*

[1]Britton Chance Center for Biomedical Photonics, Wuhan National Laboratory for Optoelectronics, MoE Key Laboratory for Biomedical Photonics, Huazhong University of Science and Technology, Wuhan, China, [2]HUST-Suzhou Institute for Brainsmatics, Jiangsu Industrial Technology Research Institute (JITRI), Suzhou, China, [3]CAS Center for Excellence in Brain Science and Intelligence Technology, Chinese Academy of Science, Shanghai, China, [4]School of Biomedical Engineering, Hainan University, Haikou, China

OPEN ACCESS

EDITED BY
Tzung Hsiai,
University of California, Los Angeles,
United States

REVIEWED BY
Raul Catena,
IBM, Switzerland
Yiqiang Zhang,
University of Hawaii at Manoa,
United States
Carlo Gaudio,
Sapienza University of Rome, Italy

*CORRESPONDENCE
Xiaoquan Yang
xqyang@hust.edu.cn

SPECIALTY SECTION
This article was submitted to Cardiovascular Imaging, a section of the journal Frontiers in Cardiovascular Medicine

RECEIVED 16 May 2022
ACCEPTED 18 July 2022
PUBLISHED 04 August 2022

CITATION
Chen J, Liu G, Sun W, Zheng Y, Jin J, Chen S, Yuan J, Gong H, Luo Q and Yang X (2022) Three-dimensional visualization of heart-wide myocardial architecture and vascular network simultaneously at single-cell resolution.
Front. Cardiovasc. Med. 9:945198.
doi: 10.3389/fcvm.2022.945198

Obtaining various structures of the entire mature heart at single-cell resolution is highly desired in cardiac studies; however, effective methodologies are still lacking. Here, we propose a pipeline for labeling and imaging myocardial and vascular structures. In this pipeline, the myocardium is counterstained using fluorescent dyes and the cardiovasculature is labeled using transgenic markers. High-definition dual-color fluorescence micro-optical sectioning tomography is used to perform heart-wide tissue imaging, enabling the acquisition of whole-heart data at a voxel resolution of $0.32 \times 0.32 \times 1\ \mu m^3$. Obtained structural data demonstrated the superiority of the pipeline. In particular, the three-dimensional morphology and spatial arrangement of reconstructed cardiomyocytes were revealed, and high-resolution vascular data helped determine differences in the features of endothelial cells and complex coiled capillaries. Our pipeline can be used in cardiac studies for examining the structures of the entire heart at the single-cell level.

KEYWORDS

whole heart, 3D imaging, single-cell resolution, vasculature, cardiomyocytes

Introduction

The heart is the key organ in the circulatory system responsible for pumping blood throughout the body. Myocardial and cardiovascular tissues are the main components of the heart and assist the heart in functioning properly. In particular, the cardiac vasculature is the main venue for the exchange of oxygen and carbon dioxide in the blood as well as nutrients and waste. Moreover, through the contraction, cardiomyocytes provide pressure for blood pumping. Thus, abnormalities in myocardial and vascular structures may affect the functions of the heart, causing cardiomyopathies and cardiovascular diseases (1). Atherosclerosis is a cardiovascular disease with high incidence and is characterized by thickening of the arterial wall (2). Previous studies have mainly focused on arterial abnormalities. However, less attention has been paid to capillaries that are involved in microcirculation and are critical in the cardiovascular system (3). Hence, the complete vasculature network should be visualized at the capillary level in cardiovascular disease studies. Hypertrophic cardiomyopathy has a typical pathology of myocyte disarray; however, the heart-wide distribution of such structural abnormalities is not completely clear (4). Therefore, imaging of the entire myocardium at the single-cell resolution can help locate lesions. Moreover, because both myocardial and vascular abnormalities are involved in some microcirculatory diseases, the interaction between the myocardium and intramyocardial vessels affects blood flow (5, 6). Thus, the simultaneous acquisition of myocardial and vascular images can reveal their spatial correlation (7). Heart-wide fine structures, especially the myocardium at the single-cell scale and the cardiac vasculature at the capillary level, must be examined in research on cardiac mechanisms and diseases.

Substantial efforts have been made to visualize the heart-wide structure. Microcomputed tomography and magnetic resonance imaging have been mostly used in traditional cardiac imaging and provide a basis for gross structural studies and clinical disease diagnoses (8, 9). However, because these technologies are limited by an intrinsic resolution of approximately 10 μm, they fail to reveal the fine structure of cardiomyocytes and capillaries. An optical microscope with submicron spatial resolution is a suitable tool for measurement. However, an optical microscope fails to cover the entire heart because of high optical scattering caused by the complex refractive index of biological tissues. Therefore, optical scattering is the main obstacle that must be overcome. Various optical clearing technologies have been used to make heart tissue transparent (10, 11). After optical clearing, a light-sheet microscope can be used for imaging the entire heart at micron-scale spatial resolution. However, optical clearing cannot fundamentally solve the problem of compositional differences among heart tissues, resulting in poorer images at greater imaging depths (12). To date, methods for the three-dimensional (3D) imaging of cardiomyocytes and cardiovasculature in the intact mature heart at submicron resolution are not available.

Mechanical sectioning of tissues, which is widely used in histological studies, is another strategy for overcoming optical scattering (13, 14). The tissue is embedded and cut using a microtome into slices with a thickness of several microns. Subsequently, an optical microscope can be used for the imaging of sectioned tissues without interference from optical scattering. However, this method provides only two-dimensional (2D) information on the tissue. In the last decade, several strategies combining a microtome and block-face imaging have been proposed for obtaining 3D structural information on the entire organ (15–18), including fluorescence micro-optical sectioning tomography (fMOST). Scholars have successfully used fMOST to examine the comprehensive anatomy of the brain, including the cell architecture, neural circuits, and vascular networks (19–21). Although this promising technology can be applied in cardiac imaging, some challenges still need to be addressed. First, the heart should be properly labeled and embedded to ensure optical contrast and adequate hardness, respectively. Second, the optical microscope and microtome should be well aligned to ensure high imaging quality. Third, the acquired images of cardiomyocytes and cardiovasculature should be processed for further analysis.

In this study, we established a technical pipeline for labeling and imaging cardiac architecture and networks within a given mouse heart. We labeled cardiomyocytes and cardiovasculature by using a fluorescent dye and transgenic marker, respectively. Subsequently, we acquired the images of these two structures at a voxel resolution of $0.32 \times 0.32 \times 1\ \mu m^3$ through the latest fMOST approach, namely high-definition dual-color fMOST (HD-dfMOST). We present these two structures individually to reveal the myocardial configuration and vascular network. In addition, we show these two structures simultaneously to display their spatial correlation. Furthermore, we visualized curvature changes in the vascular wall by using 3D traced and reconstructed vascular data. The results demonstrated the feasibility of our pipeline and the superiority of the single-cell resolved 3D cardiac data set.

Materials and methods

Overview of the pipeline for 3D imaging of the whole heart at single-cell resolution

We developed a three-step pipeline for tissue preparation, heart-wide imaging, and data processing, respectively (Figure 1). Briefly, in Step 1, the heart tissue was labeled with fluorescent proteins and embedded in resin to prepare it for imaging and cutting. In Step 2, the heart tissue was sequentially imaged and cut under the guidance of HD-dfMOST until data for the whole heart had been acquired. In Step 3, the myocardial and vascular data were processed and observed at single-cell resolution.

In Step 1, we prepared the heart tissue for subsequent fluorescence imaging and tissue cutting (Figure 1A). To genetically label blood vessels, we crossed Tek-Cre mice with Ai47 mice (Tek-Cre:Ai47 mice), wherein we labeled endothelial cells present on the microvascular wall with green fluorescent protein [GFP; (22)]. We used the fluorescent dye propidium iodide (PI) for the real-time staining of myocardial architecture during imaging (17). Furthermore, we embedded the heart tissue into HM20, a stiff resin, for thin tissue sectioning and fluorescent protein expression imaging (23).

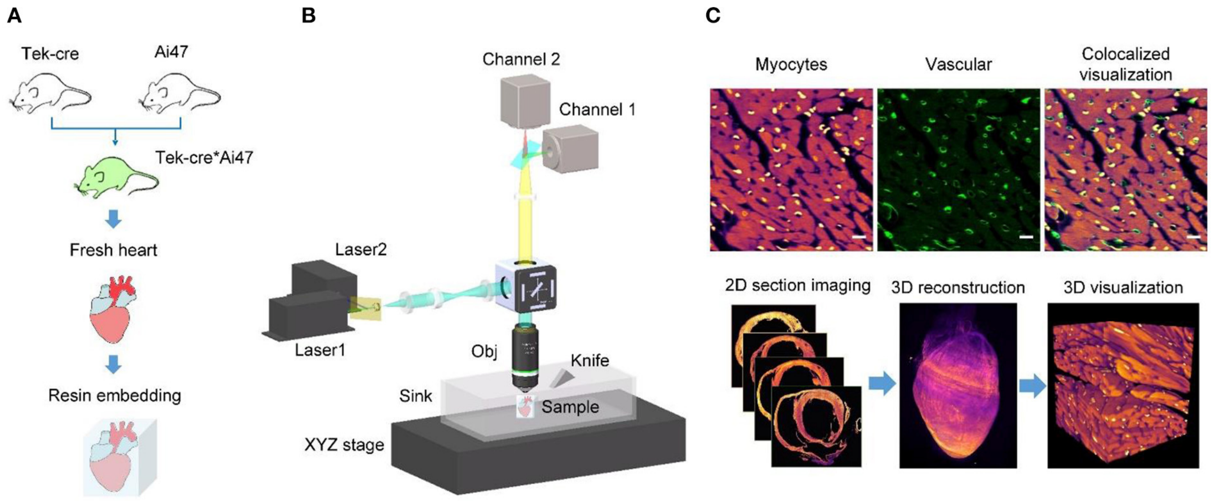

FIGURE 1
Single-cell-level heart-wide data acquisition pipeline. **(A)** Whole-heart sample preparation. We produced vascular fluorescent-labeled transgenic mice (Tek-cre*Ai47) by crossing two transgenic mice (Tek-cre and Ai47), obtained their fresh heart tissues, and embedded them into HM20, a stiff resin. **(B)** System setup of HD-dfMOST. The system is composed of a line-illumination modulation (LiMo) microscope and a microtome. (Obj, objective lens; sCMOS, scientific complementary metal oxide semiconductors). **(C)** Cardiac fMOST data were processed and are shown in 2D and 3D.

In Step 2, we performed heart-wide *in-situ* imaging through HD-dfMOST (Figure 1B). Details of the HD-dfMOST system were reported in our previous study (18). The system comprised a line-illumination modulation (LiMo) microscope and a custom-built microtome. In the LiMo microscope, two lasers with wavelengths of 488 and 561 nm, respectively, were coupled and modulated as a line beam through a cylindrical lens and then focused on the sample surface through an objective lens to excite the GFP and PI. Fluorescence signals were collected by the objective lens and a tube lens and subsequently detected by two scientific complementary metal oxide semiconductor (sCMOS) cameras (i.e., channels 1 and 2). The microtome consisted of a fixed diamond knife and a three-axis linear motorized stage to cut the stiff resin into thin sections with a high degree of flatness. Specifically, every time, a shallow layer of a 2-μm-thick tissue was imaged using the LiMo microscope, in which a 660-μm-wide and 1-μm-thick strip stack was imaged through line scanning back and forth. Subsequently, the tissue was aligned with and moved toward the microtome at a feed speed of 5 mm/s to remove the imaged surface, exposing the new block face for myocardial architecture staining. The sample was then lifted for the next round of tissue imaging and cutting. These steps were repeated until the whole heart had been imaged. We obtained the 3D data set of the entire heart at a consistent voxel resolution of $0.32 \times 0.32 \times 1\ \mu m^3$.

In Step 3, we processed the acquired data and obtained 2D and 3D high-resolution heart-wide myocardial and vascular images (Figure 1C). The data acquired using the LiMo microscope were in the form of strip images. We stitched these strips and removed their neighboring overlap to obtain complete section images. The original imaging data had a voxel size of $0.32 \times 0.32 \times 1\ \mu m^3$. To facilitate the subsequent processing and analysis of terabyte-scale whole-heart volumetric images, the original data sets were reformatted from TIFF to TDat at multilevel resolution (24). For 2D images, myocardial and vascular structures were colored in fuchsia and green, respectively, in ImageJ software (version 1.51, National Institutes of Health, Bethesda, MD, USA). Typically, the myocardial image is displayed with a thickness of 1 μm to present the details of cardiomyocytes, whereas the vascular image is displayed with a thickness of hundreds of microns to demonstrate the connectivity of the network. Morphological parameters, such as nucleus size and vessel diameter, were quantitatively analyzed using ImageJ software. In the detailed operation, we defined the distance of each pixel in the set scale and the start and end points of specific features and measured the feature size. The depth coding of a partial capillary network (Figure 3D) was generated using a depth coding algorithm and processed using Matlab software (version R2017a, The MathWorks Inc., Natick, MA, USA). Two structures were simultaneously displayed using ImageJ software by merging two-channel images. For 3D images, the whole heart was reconstructed three dimensionally by stacking sequential 2D images in Amira software (version 6.11, FEI, Mérignac Cedex, France). The data were down-sampled to a voxel size of $10 \times 10 \times 10\ \mu m^3$ for displaying the whole heart because the original whole-heart data set had a size of approximately 7 TB. Thus, the existing computer memory and image software were unable to process such a large amount of data directly. Partial raw data from the regions of interest were rebuilt using Amira software with a voxel size of 0.32 × 0.32 × 1 μm^3. Furthermore, a partial vascular network was traced using the down-sampled vascular data with a voxel size of 10 × 10 × 10 μm^3 in Amira software (Figures 4F, 5). First, we located the aorta on the basis of the original axial image (Figure 3A). The aorta could be easily identified because it had an obvious hollow shape and was located in the middle of the axial image. Next, we continuously traced the vascular branch by using consecutive sequential images. We segmented the outline of blood vessels in 2D mode by using the segmentation editor in Amira software. In particular, we set the segmentation threshold to automatically obtain the foreground of blood vessels and then examined automatically segmented images one by one and manually labeled inaccurate segmentation. After the completion of segmentation, we used the SurfaceGen module of Amira software to automatically extract the surface model of the vessel contour and perform smoothing of the 3D model in Amira. Furthermore, we used the GetCurvature function in Amira to visualize the curvature of blood vessels (Figure 5).

Animals

Tek-Cre mice were obtained from Jackson Laboratory (Stock No. 008863, Bar Harbor, ME, USA). Ai47 mice were kindly donated by Dr. Hongkui Zeng. Ai47 mice were crossed with Tek-Cre mice, and a double-positive mouse (8 weeks old) was used in the present study. Because the Ai47 mouse expresses only GFP and the Tek mouse expresses no fluorescent reporter, the crossed mouse expresses only GFP (19). All mice were kept under a 12-h light/dark cycle with food and water provided *ad libitum*.

Tissue preparation

Mice were deeply anesthetized with 1% sodium pentobarbital solution (1% wt/vol) and subsequently perfused with 0.01 M phosphate-buffered saline (PBS, Sigma-Aldrich Inc., St Louis, MO, USA) to flush blood vessels, followed by perfusion with 4% (1% wt/vol) paraformaldehyde (Sigma-Aldrich Inc.) and 2.5% sucrose in 0.01 M PBS for fixation. The hearts were excised and fixed in 4% paraformaldehyde at 4°C for 24 h. After fixation, the intact hearts were rinsed overnight at 4°C in 0.01 M PBS solution.

Embedding method

To embed a whole mouse heart, the intact heart was dehydrated in graded ethanol series (50, 75, and 95% ethanol, changing from one concentration to the next in 1, 2, and 2 h, respectively; then, the samples were incubated in 100% ethanol for 1, 2, and 2 h each time, respectively, and the ethanol solution was changed three times). Subsequently, the sample was infiltrated in a Lowicryl HM20 resin kit (Electron Microscopy Sciences, Hatfield, PA): 50% and 75% for 2 h each and 100% for 2, 24, and 24 h, respectively. Finally, the whole heart was embedded in a gelatin capsule filled with HM20 and polymerized at 38°C for 24 h, at 45°C for 8 h, and at 52°C for 6 h.

Mouse heart imaging

To obtain vascular and myocardial information on the mouse heart, the sample was placed on the HD-dfMOST system for sectioning and imaging. The whole sample was immersed in a water sink containing PI solution for real-time staining of the myocardial architecture. Whole-heart imaging was performed in a water bath. In our experiment, the sample was imaged at a voxel resolution of 0.32 × 0.32 × 1.0 μm^3. The heart sample colabeled with myocardial architecture and blood vessels was imaged through two channels (GFP and PI, respectively).

The following devices were used in the HD-dfMOST system (Figure 1B): lasers (488 and 561 nm, Cobolt, Sweden), lenses (L1, AC050-008-A-ML, f 7.5 mm; L2, AC254-250-A, f 250 mm; L3, TL, AC254-125-A-ML, f 125 mm, Thorlabs, USA), a cylindrical lens (ACY254-100-A, f 100 mm, Thorlabs, USA), an objective lens (XLUMPLFLN 20XW, 1.0 NA, Olympus, Japan), dichroic mirrors (ZT488/561rpc Chroma USA), excitation filters (ZET488/561 m, Chroma, USA), sCOMS cameras (ORCA-flash4.0 V3, Hamamatsu, Japan), and an XYZ linear stage (x-axis XML210, y-axis XMS100, z-axis GTS30V, Newport, USA).

Depth-coding algorithm

The algorithm for capillaries depth-coding is as follows:

```
Input: Image numbers k, Binarization threshold
Output: Depth-coded images
for n = 1 to k do
repeat
Image binarization
Linearize the color bar according to the number of images
Assign a single color to each image according to the order of the color bar and the order of images correspondingly
Stack these colored images sequentially
until all the images have been proceed
end for
```

Results

Display of heart-wide myocardial structures at single-cell resolution

Figure 2 presents myocardial data collected through HD-dfMOST. The myocardial fluorescent signal was excited by a 561-nm laser, and 9,972 sagittal sections were collected

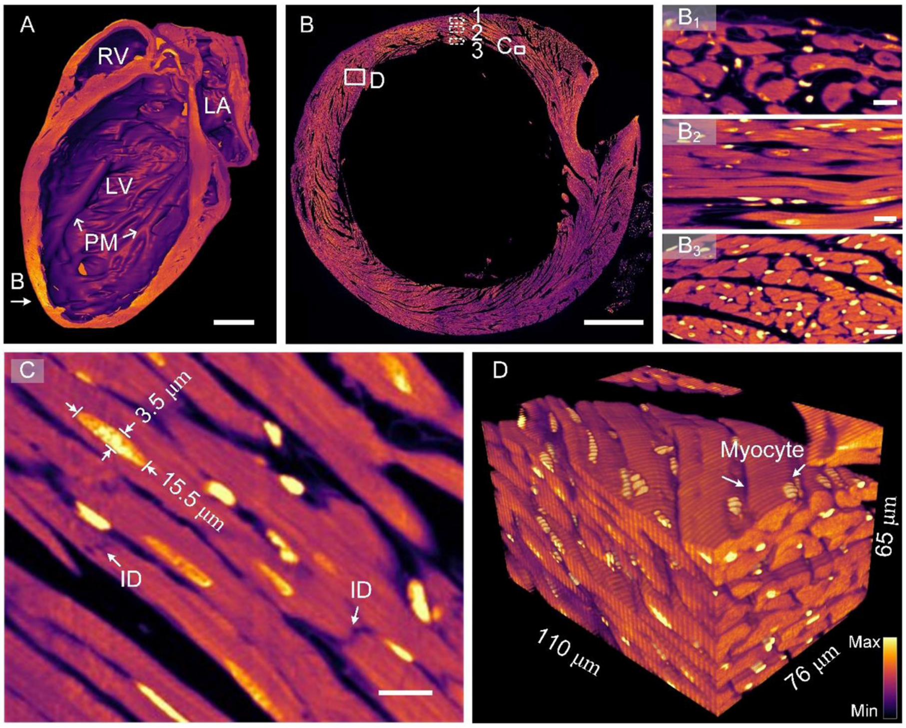

FIGURE 2
Images of heart-wide myocardial architecture at single-cell resolution. **(A)** Sagittal section view of reconstructed whole-heart myocardial data. LA, left atrium; LV, left ventricle; RV, right ventricle; PM, papillary muscle. Scale bar: 1 μm. **(B)** Original image of an axial section of the heart. **(B$_1$–B$_3$)** display the cardiac muscle cells of the ventricular wall from the outside layer (epicardium), middle layer (myocardium), and inside layer (endocardium). Scale bars: 500 and 10 μm, respectively. **(C)** Enlarged view of the corresponding rectangle in **(B)**. ID, intercalated disc. Scale bar: 10 μm. **(D)** A reconstructed myocardial data block with a single resolvable myocyte.

with a data size of 6.09 TB and colored in fuchsia. Figure 2A presents the 3D rendering of the half heart in a coronal view. The chambers of the heart are displayed, including the left ventricle (LV), right ventricle (RV), and left atrium (LA). The ventricular wall of the LV was thicker than that of the RV, which is consistent with the gross anatomy (25). In particular, papillary muscle was observed in the LV, indicating that resin embedding provides adequate physical support to the hollow organ. Even the dangling PM tissue was well preserved after ultrathin tissue cutting. Figure 2B presents the raw data of an axial image with a voxel resolution of $0.32 \times 0.32 \times 1.0\,\mu m^3$, and Figure 2A indicates the position of the section. Figures 2B$_1$–B$_3$ show regions located on the epicardium, myocardium, and endocardium of the ventricular wall, respectively (Figure 2B). The cardiomyocytes were differently oriented in these images. The subepicardial muscle fibers were oriented vertically downward, the medial muscle fibers were horizontally arranged in a ring, and the subendocardial muscle fibers were vertically oriented. These findings indicated that the arrangement of ventricular myocardial fibers was divided into three layers, which is consistent with the results of a previous study (26). Fine structures of cardiomyocytes are presented in the enlarged Figure 2C, corresponding to the white rectangle in Figure 2B. The nuclei were located in the middle of cardiomyocytes. The measured nucleus had an elliptical shape with a major axis of 15.5 μm and a minor axis of 3.5 μm. Moreover, intercalated discs (IDs) connecting cardiomyocytes were identified; they are indicated by white arrows. The IDs appear dark because PI mainly binds to genetic molecules such as DNA and RNA and the IDs contain no genetic molecules. These cell junctions normally have a jagged shape and own a feature size at the submicron level (27); the high resolution enabled us to identify them. Figure 2D presents a 3D reconstruction of cardiomyocytes from 65 raw images corresponding to the selected area in Figure 2B. This image allows us to three-dimensionally visualize the morphology and orientation of cardiomyocytes. Each cardiomyocyte appeared cylindrical in the 3D image. In addition, the spatial arrangement of cardiomyocytes was displayed; the local group of cardiac muscle cells had a similar trend, which is consistent with the traditional anatomical model diagram (28). Supplementary Video 1 presents rendered myocardial data, more intuitively showing the morphology and orientation of myocardial assemble. The results indicate that the proposed pipeline can be used to microscopically identify

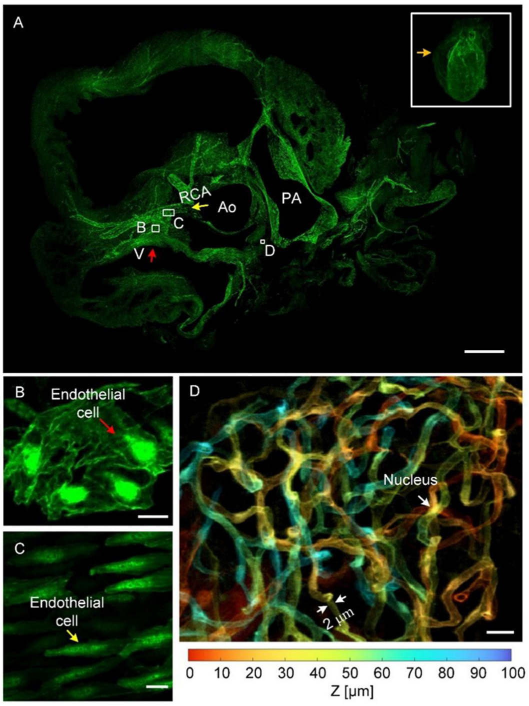

FIGURE 3
Images of the whole-heart vascular network at the capillary level. **(A)** The 3D rendering of whole-heart vascular data (top right) and the MIP generated from raw axial vascular images with a thickness of 300 μm. V, vein; RCA, right coronary artery; Ao, aorta; PA, pulmonary artery. Scale bar: 500 μm. **(B,C)** Scaled images corresponding to the white rectangles in **(A)**, with an MIP of 100-μm-thick raw images, displaying endothelial cells in the vein and RCA, respectively. Scale bars: 10 μm. **(D)** An enlarged view of the area indicating a depth-coded 100-μm-thick MIP image **(A)**, showing a partial capillary network with depth information. Scale bar: 10 μm.

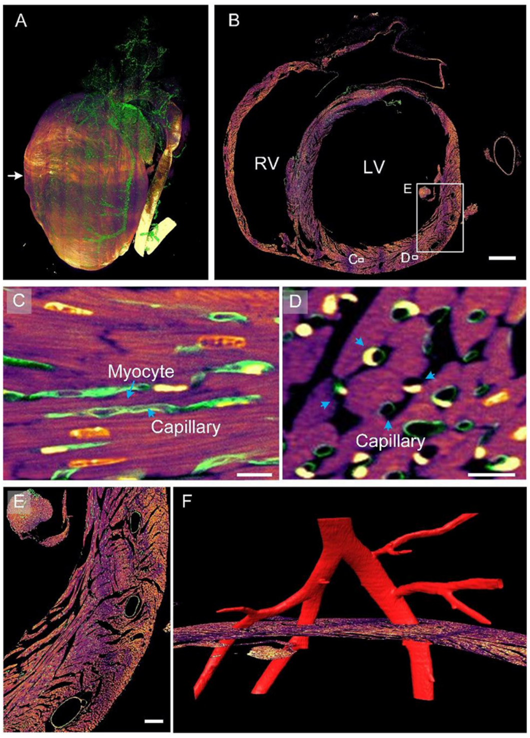

FIGURE 4
Myocardial and vascular data of the entire heart within a given mouse. **(A)** The 3D rendering of heart-wide myocardial and vascular data. The myocardial structure is in fuchsia and the vascular structure in green. **(B)** A selected axial section in the middle of the heart. LV, left ventricle; RV, right ventricle. Scale bar: 500 μm. **(C,D)** Enlarged views of corresponding white boxes in **(B)** revealing the spatial correlation between cardiomyocytes and capillaries. Scale bars: 10 μm. **(E,F)** Enlarged image of the white square in **(B)**. Scale bar: 100 μm.

cardiomyocytes at the single-cell level and visualize them three dimensionally in combination with PI counterstaining and HD-dfMOST imaging.

Exhibition of the whole-heart comprehensive vascular network at the capillary level

Figure 3 presents cardiovascular data imaged through HD-dfMOST. The vascular signal was excited using a 488-nm laser, and the data had a size of 0.96 TB. The 3D rendering of the whole-heart vascular network is shown in the top right rectangular area of Figure 3A. The 3D contour of the heart was observed as a cone shape through the background signal. The maximum intensity projection (MIP) of 300 selected raw axial images is shown in Figure 3A, and the location of the images is indicated by an orange arrow. The right coronary artery (RCA) extending from the aorta (Ao) and crossing the vein (V) was observed in the MIP image. The endothelial cells of the vein and the RCA are shown in the enlarged Figures 3B,C through the stacking of 10 and 100 raw images, respectively. Every endothelial cell, even their nuclei, could be observed due to the submicron imaging resolution of HD-dfMOST. The endothelial cells of the vein appeared in polygons with spherical nuclei located in the middle (Figure 3B). The cells of the RCA appeared in fusiform with nuclei of similar shape (Figure 3C). The morphological heterogeneity of endothelial cells was reported in a previous study (29) but has rarely been studied through *in-situ* 3D optical imaging. Partially complicated capillaries closed to the pulmonary artery are shown in the enlarged Figure 3D, which was obtained by stacking 100 raw images and corresponds to the white rectangle in Figure 3A. Multiple winding branches in this 100-μm-thick section were noted. Here, we coded the depth information of capillaries into different colors, which helped us visualize their connectivity and spatial relationship. In addition, by using HD-dfMOST, we could resolve capillaries with a diameter of at least 2 μm. In particular, the nuclei of the capillaries appeared as long bright stripes, demonstrating the high resolution of the imaging system. Supplementary Video 2 further presents rendered cardiovascular data, intuitively showing the cardiovascular network and the complex three-dimensional spatial winding of capillaries. These results confirm that the proposed pipeline is capable of labeling and imaging whole-heart vessels at the capillary level.

Simultaneous presentation of myocardial and vascular structures in a given heart

On the basis of the dual-structural labeling and dual-color imaging achieved using the proposed pipeline, we present myocardial and vascular data of a heart colocalized in one coordinate. The 3D rendering of the myocardial and vascular structures of the whole heart is shown in Figure 4A, where the myocardial structures are colored fuchsia and the vascular structures green. The heart is a muscular organ that mainly consists of myocardial tissues, as indicated by the image mainly appearing fuchsia in color. The blood vessels were continuously labeled and completely observed in the image. An original axial image located in the middle of the heart at a resolution of 0.32 $\times$ 0.32 $\times$ 1.0 μm^3 is displayed in Figure 4B. Capillaries were distributed between cardiomyocytes, as shown in the enlarged Figure 4C, corresponding to the white rectangle in Figure 4B. Small vessels were located right in the gaps in the myocardium, indicating that the two-channel data were co-located. The capillaries and cardiomyocytes had the same orientation. The observations are consistent with the cardiac mechanism indicating that capillaries supply nutrients and oxygen to cardiomyocytes (30). Both cardiomyocytes and capillaries appeared as quasi-circular cross-sections with a staggered arrangement (Figure 4D), indicating that these two structures were spatially close. This means that cardiomyocytes can provide pressure for pumping blood through muscle contraction (30). Supplementary Video 3 further presents rendered co-localized myocardial and vascular data stereo showing the spatial distribution of myocardial and vascular structures. Three hollow elliptical structures were distributed on the outer edge of the ventricular wall (Figure 4E), indicating that three blood vessels may travel through the ventricular wall. We reconstructed the vascular data three dimensionally and observed that an artery was divided into three branches passing through the three cavities (Figure 4F), confirming our assumption. This example indicates that the pipeline can be used to examine the spatial correlation between cardiomyocytes and vessels in 2D or 3D.

3D display of the continuous blood vessel network

We reconstructed a partial cardiovascular network in 3D, starting from the aorta (Figure 5A). The aorta divided into two branches, namely the left coronary artery (LCA) and RCA, as shown in the reconstructed result (Figure 5A). The RCA divided into two equal dominated branches, whereas the LCA diverged after some distance, which is consistent with the findings of a previous study (25). Here, we mainly traced the branches of the LCA. At least five branches were identified along the trunk from the aorta to the apex of the heart (as indicated by blue arrows). In addition, we obtained the curvature of vessels in accordance with labeled contours. The difference in curvature of the vessels is qualitatively represented using colors in Figure 5A. As indicated by the color bar, the maximum curvature is presented in red, whereas the minimum curvature is presented in blue. The overall trend of the curvature of the outer contour was a gradual decrease with increasing distance of the branch from the aorta. In addition, we visualized these vessels in an endoscopic view, observing detailed curvature changes from the inner wall of the blood vessel. The inner walls of branches 1–4 are presented in Figures 5B–E, respectively. The inner wall of the LCA had larger curvature because the wall mostly appeared in red (Figure 5B). However, the junction of the aorta and LCA appeared in blue, as indicated by the white arrow, indicating smaller curvature. The smaller curvature may be due to such a shape providing a smooth transition between vascular branches, avoiding sudden and considerable blood flow pressure at these locations. Similar morphological characteristics are presented in Figures 5C–E. We observed that the small curvature area became larger with a decrease in the vessel diameter, as indicated by white arrows in Figures 5C,E. This trend was possibly caused by a decrease in blood pressure with a decrease in the vessel size (31). In summary, the proposed pipeline provided multiple views of 3D cardiac microstructures and thus can be used for comprehensively studying these structures and functions.

Discussion

Whole-heart 3D data set at the single-cell scale

Previous studies have performed 3D imaging of the whole mouse heart at single-cell resolution. However, because of the limited imaging range, most of these studies have performed imaging of the embryonic heart to study its development process because the heart is the first-derived functional embryonic organ (32). To the best of our knowledge, only a few complete mature mouse heart data sets have been presented—those imaged through optical imaging techniques, as summarized in Table 1. Knife-edge scanning microscopy (KESM) applied light microscopy to image microtome sectioned tissue on the surface of the knife, achieving a voxel resolution of 0.5 $\times$ 0.5 $\times$ 5 μm^3 (33). KESM could locate the spatial distribution of intrinsic cardiac neurons because neurons were stained with cresyl violet and imaged based on structural contrast. However,

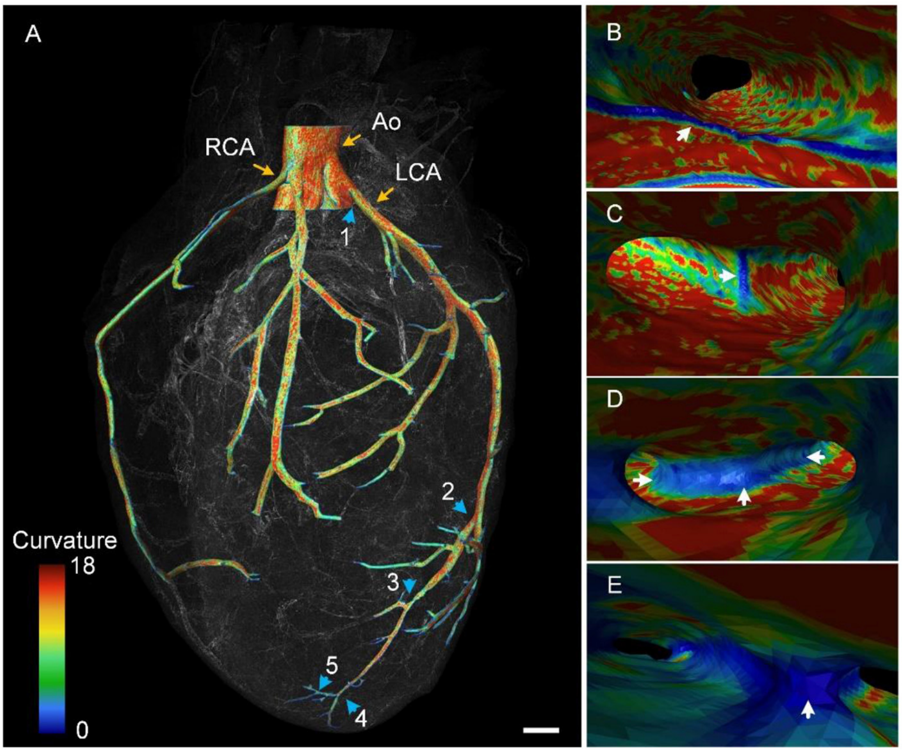

FIGURE 5
Color-coded vascular network based on the curvature of the vascular wall. **(A)** The 3D rendering of the reconstructed vascular network. Blue arrows point out five branches along the LCA. Ao, aorta; LCA, left coronary artery; RCA, right coronary artery. **(B–E)** Endoscopic perspective of corresponding branches 1–4 in **(A)** with colors representing the curvature difference. **(B)** is the division of the Ao and LCA.

TABLE 1 Comparison of whole heart optical imaging techniques.

Imaging techniques	KESM	TPTC	c-LSFM	HD-dfMOST
Imaging resolution (μm^3)	0.5 × 0.5 × 5	0.78 × 0.78 × 2.0	4.5 × 4.5 × 18.0	0.32 × 0.32 × 1.0
Fluorescence compatibility	N	Y	Y	Y
Observing structures	Cardiac neurons	Cell nuclei and vasculature	Myocardial fiber	Cardiomyocytes and vasculature
Reference	(33)	(34)	(35)	This study

KESM obtains nonfluorescent labeled structural data, failing to reveal multi-structural spatial relationships. Two-photon tissue cytometry (TPTC) combines two-photon microscopy to perform deep tissue imaging and a milling machine to perform sequential tissue cutting, achieving a voxel resolution of 0.78 × 0.78 × 2.0 μm^3 (34). TPTC was capable of simultaneously imaging fluorescently labeled cell nuclei and vasculature. However, the point scanning scheme slows down the speed of data acquisition, and the paraffin embedding of the samples prevents labeling with fluorescence proteins. Cardiac light sheet fluorescence microscopy (c-LSFM) owned the advantage of high-speed whole heart imaging through tissue clearing and light-sheet microscope (35). But to cover the whole organ, a long working distance objective with low numerical aperture (0.13) was used, resulting in a low resolution of 4.5 × 4.5 × 18.0 μm^3.

This is the first study to present a set of fluorescently labeled myocardial and vascular heart-wide 3D data for a given mature mouse. We presented individual fine cardiac structures at a single myocyte and capillary level at a submicron voxel imaging resolution of 0.32 × 0.32 × 1.0 μm^3 (Figures 2, 3). Moreover, we visualized these structures simultaneously to reveal their spatial correlation or locate one structure through the other (Figure 4). Moreover, we analyzed detailed geometric features in both outer and inner views through subsequent 3D data reconstruction (Figure 5).

Biomedical perspectives

The pipeline established in this study can be used for examining heart-wide 3D fine structures. A global heart-specific coordinate system is required to define the location and orientation of specific structures (29). Here, for the system to be specific to the heart, the coordinate system should be built on the basis of the cardiac anatomy, and the characteristic anatomy of the whole heart should be considered for global imaging. Our pipeline can build such a coordinate system. By using a proper structural labeling method, we can set one channel to image architectural data, such as cardiomyocytes, and build a coordinate system based on three non-coplanar feature points, namely the apex of the heart, centroids of the aorta, and centroids of the descending aorta. In addition, we can set other channels to image target structures such as vessels and neurons. Similar methods have been developed to depict brain-wide connections, including the vascular network and neural connection, through a brain-wide positioning system (19, 21). Thus, a similar approach can be used in heart studies.

The single-cell-resolution heart-wide data set obtained using this pipeline can serve as the basis for heart disease research. For instance, by comparing the structural difference between the normal and diseased heart at the single-cell level, lesions in the whole heart can be precisely located (36). Furthermore, examining the data sets of diseased hearts in different stages of a disease may help understand lesion development in the disease (37). A combination of knowledge derived from these data sets and clinical imaging findings may guide the selection of medication and surgical treatment (38).

Limitations

We aimed to demonstrate the feasibility and effectiveness of the proposed pipeline; thus, only two cardiac structures, namely the cardiovascular and myocardium, are presented. However, multicolor imaging is not technically difficult. By using proper specific labeling techniques, additional types of cardiac structures, such as collagen and cardiac neurons, can be imaged within a given mouse heart, enabling the study of the whole cardiac structure and heart-wide multistructural linkages. Here we imaged a cardiac slice stained by PI and DAPI solutions under a commercial microscope (Zeiss Axio Observer A1; Zeiss, Germany), and the result is shown in Supplementary Figure 1. This result help demonstrates that multi-color options are feasible. Moreover, only a mature mouse model was used in this study. However, this pipeline can be used for imaging the primate and human heart after appropriate modifications (39).

In this study, we did not perform a large-scale quantitative analysis of cardiac data because cardiac structures are considerably different from brain structures in terms of geometrical dimensions and structural features. For example, neural cells are approximately spherical, whereas cardiomyocytes are approximately cylindrical. Because of this difference, the previously established automated analysis methods, such as 3D BrainCV and NeuroGPS-Tree, could not be fully used in this work (40, 41). Most of the 3D reconstruction results obtained in this study were based on semiautomatic image segmentation, resulting in a considerable workload. To demonstrate the potential of the single-cell-resolution heart-wide data for cell measurement, we segmented a myocardial fiber and five nuclei from Figure 2D, and the result is shown in Supplementary Figure 2. The quantitative statistics of the five nuclei volume is 87.2 ± 6.1 μm. In the future, we will be focusing on developing automated cardiac quantitative analysis tools.

Data availability statement

The original contributions presented in the study are included in the article/Supplementary materials, further inquiries can be directed to the corresponding author/s.

Ethics statement

The animal study was reviewed and approved by Institutional Animal Ethics Committee of Huazhong University of Science and Technology.

Author contributions

QL, HG, JY, JC, and XY conceived and designed the study. WS, YZ, JJ, and JC performed the experiments and data analysis. GL and SC performed the whole-heart data acquisition. HG, JC, and XY prepared the figures and wrote the manuscript. All authors contributed to the article and approved the submitted version.

Funding

This work was financially supported by the National Natural Science Foundation of China projects (Nos. 81827901, 82102235, and 81871082), Hubei Provincial Natural Science Foundation of China (No. 2020CFB129), and the Director Fund of the Wuhan National Laboratory for Optoelectronics (WNLO).

Acknowledgments

We thank the colleagues of the MOST group from Britton Chance Center for Biomedical Photonics for their assistance.

Conflict of interest

The authors declare that the research was conducted in the absence of any commercial or financial relationships that could be construed as a potential conflict of interest.

Publisher's note

Supplementary material

The Supplementary Material for this article can be found online at: https://www.frontiersin.org/articles/10.3389/fcvm.2022.945198/full#supplementary-material

SUPPLEMENTARY FIGURE 1
Image of a cardiac slice stained by PI and DAPI fluorescent dyes. Scale bars: 50 μm.

SUPPLEMENTARY FIGURE 2
Segment a myocardial fiber and five nuclei from Figure 2D and quantify the volume of these cardiomyocyte nuclei.

SUPPLEMENTARY VIDEO 1
Rendered myocardial data shows the morphology and orientation of myocardial assembly.

SUPPLEMENTARY VIDEO 2
Rendered cardiovascular data shows the complex three-dimensional spatial winding of capillaries.

SUPPLEMENTARY VIDEO 3
Rendered co-localized myocardial and vascular data shows spatial distribution of myocardial and vascular structures.

References

1. McKenna WJ, Maron BJ, Thiene G. Classification, epidemiology, and global burden of cardiomyopathies. *Circ Res.* (2017) 121:722–30. doi: 10.1161/CIRCRESAHA.117.309711

2. Sanz J, Fayad ZA. Imaging of atherosclerotic cardiovascular disease. *Nature.* (2008) 451:953–7. doi: 10.1038/nature06803

3. Ziegler T, Abdel Rahman F, Jurisch V, Kupatt C. Atherosclerosis and the capillary network; pathophysiology and potential therapeutic strategies. *Cells.* (2020) 9:50. doi: 10.3390/cells9010050

4. Marian AJ, Braunwald E. Hypertrophic cardiomyopathy: genetics, pathogenesis, clinical manifestations, diagnosis, and therapy. *Circ Res.* (2017) 121:749–70. doi: 10.1161/CIRCRESAHA.117.311059

5. Algranati D, Kassab GS, Lanir Y. Mechanisms of myocardium-coronary vessel interaction. *Am J Physiol Heart Circul Physiol.* (2010) 298:H861–73. doi: 10.1152/ajpheart.00925.2009

6. Chilian WM, Eastham CL, Layne SM, Marcus ML. Small vessel phenomena in the coronary microcirculation: phasic intramyocardial perfusion and coronary microvascular dynamics. *Prog Cardiovasc Dis.* (1988) 31:17–38. doi: 10.1016/0033-0620(88)90009-6

7. Chien KR, Domian IJ, Parker KK. Cardiogenesis and the complex biology of regenerative cardiovascular medicine. *Science.* (2008) 322:1494–7. doi: 10.1126/science.1163267

8. Ambale-Venkatesh B, Lima JA. Cardiac MRI: a central prognostic tool in myocardial fibrosis. *Nat Rev Cardiol.* (2015) 12:18–29. doi: 10.1038/nrcardio.2014.159

9. Sangaralingham SJ, Ritman EL, McKie PM, Ichiki T, Lerman A, Scott CG, et al. Cardiac micro–computed tomography imaging of the aging coronary vasculature. *Circ Cardiovasc Imaging.* (2012) 5:518–24. doi: 10.1161/CIRCIMAGING.112.973057

10. Susaki EA, Tainaka K, Perrin D, Yukinaga H, Kuno A, Ueda HR. Advanced CUBIC protocols for whole-brain and whole-body clearing and imaging. *Nat Protoc.* (2015) 10:1709–27. doi: 10.1038/nprot.2015.085

11. Glaser AK, Reder NP, Chen Y, Yin C, Wei L, Kang S, et al. Multi-immersion open-top light-sheet microscope for high-throughput imaging of cleared tissues. *Nat Commun.* (2019) 10:1–8. doi: 10.1038/s41467-019-10534-0

12. Weiss KR, Voigt FF, Shepherd DP, Huisken J. Tutorial: practical considerations for tissue clearing and imaging. *Nat Protoc.* (2021) 16:2732–48. doi: 10.1038/s41596-021-00502-8

13. Bensley JG, De Matteo R, Harding R, Black MJ. Three-dimensional direct measurement of cardiomyocyte volume, nuclearity, and ploidy in thick histological sections. *Sci Rep.* (2016) 6:1–10. doi: 10.1038/srep23756

14. Kuett L, Catena R, Özcan A, Plüss A, Schraml P, Moch H, et al. Three-dimensional imaging mass cytometry for highly multiplexed molecular and cellular mapping of tissues and the tumor microenvironment. *Nat Cancer.* (2022) 3:122–33. doi: 10.1038/s43018-021-00301-w

15. Li A, Gong H, Zhang B, Wang Q, Yan C, Wu J, et al. Micro-optical sectioning tomography to obtain a high-resolution atlas of the mouse brain. *Science.* (2010) 330:1404–8. doi: 10.1126/science.1191776

16. Ragan T, Kadiri LR, Venkataraju KU, Bahlmann K, Sutin J, Taranda J, et al. Serial two-photon tomography for automated ex vivo mouse brain imaging. *Nat Methods.* (2012) 9:255–8. doi: 10.1038/nmeth.1854

17. Gong H, Xu D, Yuan J, Li X, Guo C, Peng J, et al. High-throughput dual-colour precision imaging for brain-wide connectome with cytoarchitectonic landmarks at the cellular level. *Nat Commun.* (2016) 7:1–12. doi: 10.1038/ncomms12142

18. Zhong Q, Li A, Jin R, Zhang D, Li X, Jia X, et al. High-definition imaging using line-illumination modulation microscopy. *Nat Methods.* (2021) 18:309–15. doi: 10.1038/s41592-021-01074-x

19. Li X, Yu B, Sun Q, Zhang Y, Ren M, Zhang X, et al. Generation of a whole-brain atlas for the cholinergic system and mesoscopic projectome analysis of basal forebrain cholinergic neurons. *Proc Natl Acad Sci.* (2018) 115:415–20. doi: 10.1073/pnas.1703601115

20. Sun Q, Li X, Ren M, Zhao M, Zhong Q, Ren Y, et al. A whole-brain map of long-range inputs to GABAergic interneurons in the mouse medial prefrontal cortex. *Nat Neurosci.* (2019) 22:1357–70. doi: 10.1038/s41593-019-0429-9

21. Xiong B, Li A, Lou Y, Chen S, Long B, Peng J, et al. Precise cerebral vascular atlas in stereotaxic coordinates of whole mouse brain. *Front Neuroanat.* (2017) 11:128. doi: 10.3389/fnana.2017.00128

22. Dumont D, Yamaguchi T, Conlon R, Rossant J, Breitman M. tek, a novel tyrosine kinase gene located on mouse chromosome 4, is expressed in endothelial cells and their presumptive precursors. *Oncogene.* (1992) 7:1471–80.

23. Yang Z, Hu B, Zhang Y, Luo Q, Gong H. Development of a plastic embedding method for large-volume and fluorescent-protein-expressing tissues. *PLoS ONE.* (2013) 8:e60877. doi: 10.1371/journal.pone.0060877

24. Li Y, Gong H, Yang X, Yuan J, Jiang T, Li X, et al. TDat: an efficient platform for processing petabyte-scale whole-brain volumetric images. *Front Neural Circuits.* (2017) 11:51. doi: 10.3389/fncir.2017.00051

25. Ruberte J, Carretero A, Navarro M, editors. *Morphological Mouse Phenotyping: Anatomy, Histology And Imaging.* Amsterdam: Elsevier (2017). doi: 10.1016/B978-0-12-812972-2.50002-7

26. Sengupta PP, Korinek J, Belohlavek M, Narula J, Vannan MA, Jahangir A, et al. Left ventricular structure and function: basic science for cardiac imaging. *J Am Coll Cardiol.* (2006) 48:1988–2001. doi: 10.1016/j.jacc.2006.08.030

27. Pinali C, Bennett HJ, Davenport JB, Caldwell JL, Starborg T, Trafford AW, et al. Three-dimensional structure of the intercalated disc reveals plicate domain and gap junction remodeling in heart failure. *Biophys J.* (2015) 108:498–507. doi: 10.1016/j.bpj.2014.12.001

28. Hill AJ, Iaizzo PA. In: comparative cardiac anatomy. In: Iaizzo PA, editor. *Handbook of Cardiac Anatomy, Physiology, and Devices*. Cham: Springer (2015). p. 89–114. doi: 10.1007/978-3-319-19464-6_6

29. Aird WC. Phenotypic heterogeneity of the endothelium: I. structure, function, and mechanisms. *Circ Res.* (2007) 100:158–73. doi: 10.1161/01.RES.0000255691.76142.4a

30. Laflamme MA, Sebastian MM, Buetow BS. Cardiovascular. In: Treuting PM, Dintzis S, Montine KS, editors. *Comparative Anatomy and Histology.* Amsterdam: Academic Press (2012). p. 135–53. doi: 10.1016/B978-0-12-381361-9.00010-X

31. Li JK, editor. *Dynamics of the Vascular System*. World Scientific (2004).

32. Lapierre-Landry M, Kolesová H, Liu Y, Watanabe M, Jenkins MW. Three-dimensional alignment of microvasculature and cardiomyocytes in the developing ventricle. *Sci Rep.* (2020) 10:1–15. doi: 10.1038/s41598-020-71816-y

33. Achanta S, Gorky J, Leung C, Moss A, Robbins S, Eisenman L, et al. A comprehensive integrated anatomical and molecular atlas of rat intrinsic cardiac nervous system. *iScience.* (2020) 23:101140. doi: 10.1016/j.isci.2020.101140

34. Ragan T, Sylvan JD, Kim KH, Huang H, Bahlmann K, Lee RT, et al. High-resolution whole organ imaging using two-photon tissue cytometry. *J Biomed Opt.* (2007) 12:014015. doi: 10.1117/1.2435626

35. Fei P, Lee J. Packard, RRS, Sereti KI, Xu H, Ma J, et al. Cardiac light-sheet fluorescent microscopy for multi-scale and rapid imaging of architecture and function. *Sci Rep.* (2016) 6:1–12. doi: 10.1038/srep22489

36. Niwa K, Perloff JK, Bhuta SM, Laks H, Drinkwater DC, Child JS, et al. Structural abnormalities of great arterial walls in congenital heart disease: light and electron microscopic analyses. *Circulation.* (2001) 103:393–400. doi: 10.1161/01.CIR.103.3.393

37. Khalique Z, Ferreira PF, Scott AD, Nielles-Vallespin S, Firmin DN, Pennell DJ. Diffusion tensor cardiovascular magnetic resonance imaging: a clinical perspective. *JACC-Cardiovasc Imag.* (2020) 13:1235–55. doi: 10.1016/j.jcmg.2019.07.016

38. Voros S, Rinehart S, Qian Z, Joshi P, Vazquez G, Fischer C, et al. Coronary atherosclerosis imaging by coronary CT angiography: current status, correlation with intravascular interrogation and meta-analysis. *JACC-Cardiovasc Imag.* (2011) 4:537–48. doi: 10.1016/j.jcmg.2011.03.006

39. Zhou C, Yang X, Wu S, Zhong Q, Luo T, Li A, et al. Continuous subcellular resolution three-dimensional imaging on intact macaque brain. *Sci Bull.* (2021) 67:85–96. doi: 10.1016/j.scib.2021.08.003

40. Quan T, Zhou H, Li J, Li S, Li A, Li Y, et al. NeuroGPS-Tree: automatic reconstruction of large-scale neuronal populations with dense neurites. *Nat Methods.* (2016) 13:51–4. doi: 10.1038/nmeth.3662

41. Wu J, He Y, Yang Z, Guo C, Luo Q, Zhou W, et al. 3D BrainCV: simultaneous visualization and analysis of cells and capillaries in a whole mouse brain with one-micron voxel resolution. *Neuroimage.* (2014) 87:199–208. doi: 10.1016/j.neuroimage.2013.10.036

frontiers | Frontiers in Cardiovascular Medicine

TYPE Original Research
PUBLISHED 08 September 2022
DOI 10.3389/fcvm.2022.974805

OPEN ACCESS

EDITED BY
Carlo Gaudio,
Sapienza University of Rome, Italy

REVIEWED BY
Alexander Van Rosendael,
Leiden University Medical Center
(LUMC), Netherlands
Yoshiki Matsuo,
Kishiwada Tokushukai Hospital, Japan

*CORRESPONDENCE
Bálint Szilveszter
szilveszter.balint@gmail.com

SPECIALTY SECTION
This article was submitted to
Cardiovascular Imaging,
a section of the journal
Frontiers in Cardiovascular Medicine

RECEIVED 21 June 2022
ACCEPTED 11 August 2022
PUBLISHED 08 September 2022

CITATION
Vattay B, Borzsák S, Boussoussou M, Vecsey-Nagy M, Jermendy ÁL, Suhai FI, Maurovich-Horvat P, Merkely B, Kolossváry M and Szilveszter B (2022) Association between coronary plaque volume and myocardial ischemia detected by dynamic perfusion CT imaging. *Front. Cardiovasc. Med.* 9:974805.
doi: 10.3389/fcvm.2022.974805

Association between coronary plaque volume and myocardial ischemia detected by dynamic perfusion CT imaging

Borbála Vattay[1], Sarolta Borzsák[1], Melinda Boussoussou[1], Milán Vecsey-Nagy[1], Ádám L. Jermendy[1], Ferenc I. Suhai[1], Pál Maurovich-Horvat[1,2], Béla Merkely[1], Márton Kolossváry[1] and Bálint Szilveszter[1]*

[1]Cardiovascular Imaging Research Group, Heart and Vascular Center, Semmelweis University, Budapest, Hungary, [2]Medical Imaging Center, Semmelweis University, Budapest, Hungary

Introduction: We aimed to evaluate the relationship between quantitative plaque metrics derived from coronary CT angiography (CTA) and segmental myocardial ischemia using dynamic perfusion CT (DPCT).

Methods: In a prospective single-center study, patients with $>$ 30% stenosis on rest CTA underwent regadenoson stress DPCT. 480 myocardium segments of 30 patients were analyzed. Quantitative plaque assessment included total plaque volume (PV), area stenosis, and remodeling index (RI). High-risk plaque (HRP) was defined as low-attenuation plaque burden $>$ 4% or RI $>$ 1.1. Absolute myocardial blood flow (MBF) and relative MBF (MBFi: MBF/75th percentile of all MBF values) were quantified. Linear and logistic mixed models correcting for intra-patient clustering and clinical factors were used to evaluate the association between total PV, area stenosis, HRP and MBF or myocardial ischemia (MBF $<$ 101 ml/100 g/min).

Results: Median MBF and MBFi were 111 ml/100 g/min and 0.94, respectively. The number of ischemic segments were 164/480 (34.2%). Total PV of all feeding vessels of a given myocardial territory differed significantly between ischemic and non-ischemic myocardial segments ($p = 0.001$). Area stenosis and HRP features were not linked to MBF or MBFi (all $p > 0.05$). Increase in PV led to reduced MBF and MBFi after adjusting for risk factors including hypertension, diabetes, and statin use (per 10 mm^3; $\beta = -0.035$, $p < 0.01$ for MBF; $\beta = -0.0002$, $p < 0.01$ for MBFi). Similarly, using multivariate logistic regression total PV was associated with ischemia (OR = 1.01, $p = 0.033$; per 10 mm^3) after adjustments for clinical risk factors, area stenosis and HRP.

Conclusion: Total PV was independently associated with myocardial ischemia based on MBF, while area stenosis and HRP were not.

KEYWORDS

dynamic perfusion CT, myocardial blood flow, coronary computed tomography, coronary plaque volume, quantitative plaque analysis

Introduction

Currently luminal stenosis is the most dominant factor in the management of coronary artery disease (CAD) (1). Quantitative plaque assessment and adverse plaque characteristics may further improve cardiovascular risk prediction and patient management (2). Furthermore, anatomical and functional assessment of CAD could also improve clinical outcomes (3), however, the link between stenosis severity and myocardial ischemia is controversial (4).

CT angiography (CTA) is a uniquely suited imaging modality that can simultaneously evaluate plaque morphology and ischemia (5). Also, CTA allows accurate characterization and quantification of coronary plaques over stenosis assessment. Moreover, myocardial dynamic perfusion CT (DPCT) provides functional data and can quantitatively assess myocardial perfusion during pharmacological stress (6).

Former observational studies evaluated the link between coronary plaque burden and global myocardial ischemia using qualitative/visual assessment by either static CT perfusion (CTP) (7), stress echocardiography (8) or SPECT (9). Based on these studies, whether stenosis severity, adverse plaque features or coronary plaque burden is predictive for ischemia remains uncertain. Also, it is unknown whether quantitative plaque characterization can predict segmental ischemia as assessed by quantitative DPCT imaging. Previous studies exclusively reported vessel-based data, however, we applied a novel segment-based analysis considering only coronary lesions corresponding to myocardial territories.

Our aim was to elucidate the association between quantitative atherosclerotic plaque metrics derived from coronary CTA and segmental myocardial ischemia based on myocardial blood flow (MBF) as detected by DPCT imaging.

Materials and methods

Study population and protocol

Patients with stable chest pain and $>$ 30% coronary stenosis detected on rest CTA were screened for our prospective, single-center study. Inclusion criteria were at least 30% stenosis in one of the main coronary arteries and excellent image quality for the quantitative analysis of the whole coronary tree. Exclusion criteria were prior myocardial infarction or revascularization, heart transplantation, contraindication to regadenoson or low image quality for quantitative assessment of coronary lesions. Regadenoson stress DPCT was performed at a separate appointment after written informed consent was obtained from all patients. Subjects with low image quality for the assessment of myocardial ischemia were excluded ($n = 1$). Patients were enrolled in the analysis if found eligible based on inclusion and exclusion criteria. Flow chart of the study is shown in **Figure 1**.

The study was approved by the national ethical committee (National Institute of Pharmacy and Nutrition—OGYÉI/719/2017) and was performed in accordance with the Helsinki declaration.

Demographic data and comorbidities were collected by reviewing patients' medical records. Hypertension was determined as systolic blood pressure $>$ 140 mmHg and/or diastolic blood pressure $>$ 90 mmHg based on office measurements or the use of antihypertensive therapy. Diagnosis of hyperlipidemia was based on total cholesterol level $>$ 200 mg/dL or the administration of lipid-lowering medication. Diabetes mellitus was defined as elevated plasma glucose levels (fasting plasma glucose $\geq$ 126 mg/dL; HbA1C $\geq$ 6.5%) or the use of antidiabetic medication or insulin therapy.

Coronary CT angiography protocol

Prospectively triggered CTA scan of the heart was performed according to the guidelines of the Society of Cardiovascular Computed Tomography (SCCT) with a 256-slice multidetector row CT (Brilliance iCT, Philips Healthcare, Cleveland, OH, United States) (10). *Per os* beta blocker was administered 1 h prior examination if the heart rate (HR) was above 65 beats/min. All patients received 0.8 mg of sublingual nitroglycerine before CTA scanning if systolic blood pressure was $>$ 100 mmHg, and in case of HR $>$ 60 beats per minute intravenous beta blocker was additionally administered. Image acquisition was performed at diastole (75–81% of the R–R interval) or at systole (37–43% of the R–R interval) in case of HR $>$ 70 beats per minute despite premedication. The following scan parameters were applied: 270 ms gantry rotation time, 128 × 0.625 mm collimation, tube voltage 100–120 kVp, and tube current 200–300 mAs based on patient's body mass index (BMI). A four-phasic contrast injection protocol was used with 85–95 ml contrast agent at a flow rate of 4.5–5.5 ml/s. Axial images were reconstructed with 0.6 mm slice thickness using iterative reconstruction (iDose4 Level 5, Philips Healthcare, Cleveland, OH, United States).

Dynamic perfusion CT protocol

Stress DPCT scan was performed after rest CTA at a separate appointment with the same scanner. Hyperemia was induced using single dose of 400 µg intravenous regadenoson (Rapiscan®, GE Healthcare) (11). Stress acquisition was performed during a single breath-hold in inspiration, 1 min after bolus regadenoson was administered during peak stress covering 25–30 cardiac cycles (12). Patients' HR, oxygen saturation and blood pressure were monitored to confirm

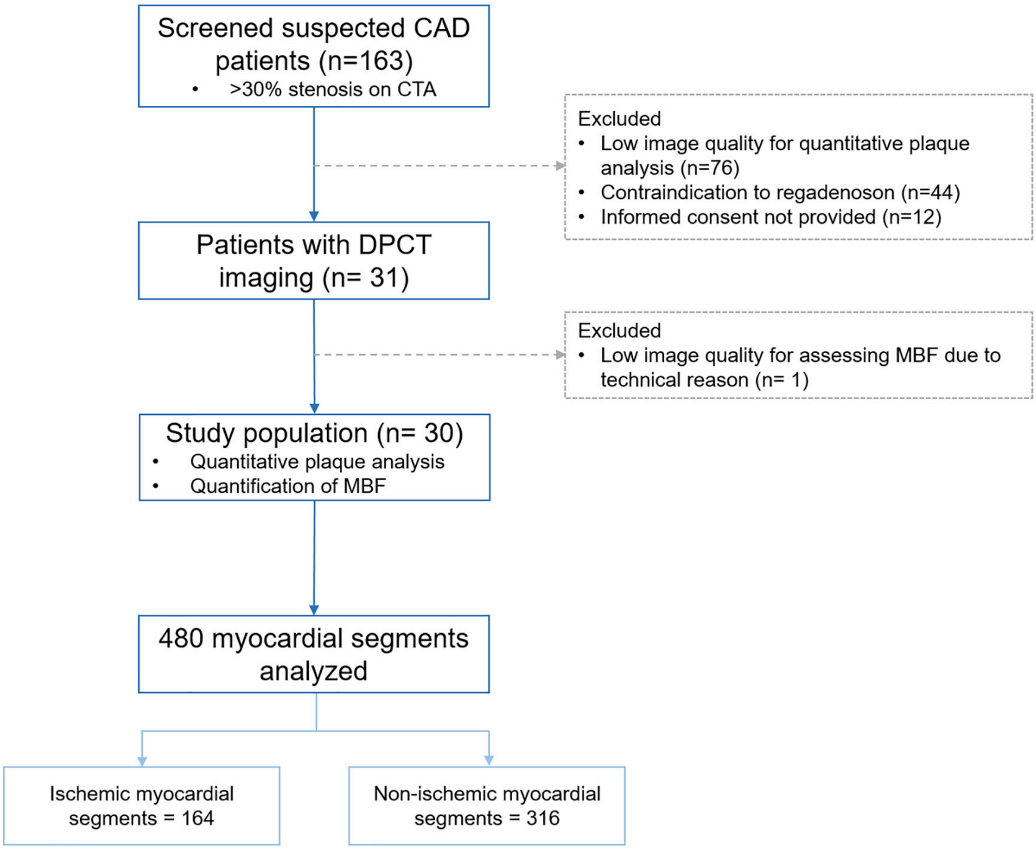

FIGURE 1
Flow-chart of the study. CAD, Coronary artery disease; CTA, CT angiography; DPCT, Dynamic perfusion CT; MBF, Myocardial blood flow.

appropriate levels of stress for CTP imaging. Contrast injection protocol included 50–60 ml contrast bolus at an infusion rate of 5 ml/s, followed by 30 ml saline chaser. Prospective electrocardiogram (ECG)-gated dynamic mode (with 64 × 1.25 mm collimation, 360° reconstruction, 8 cm coverage) was acquired in systolic phase (35% of the RR interval), with tube voltage of 80–120 kVp and tube current of 100–250 mAs based on patient's BMI. Images were reconstructed using hybrid iterative reconstruction (iDOSE4 level 5, Philips Healthcare, Cleveland, OH, United States) with 2.0 mm slice thickness and 2.0 mm increment.

Quantitative plaque analysis

Coronary artery segments were defined using an 18-segment model as recommended by the SCCT guidelines (10). CTA images were transferred into a dedicated software tool (QAngioCT Research Edition v3.1; Medis Medical Imaging Systems, Leiden, The Netherlands) for quantitative plaque analysis. Images were analyzed by a single reader (BV, 3 years of experience with cardiac CT) blinded to patient's data and perfusion parameters. The software automatically extracted the coronary tree. All coronary vessels with a diameter $>$ 1.5 mm were evaluated. After automatic contouring of the lumen and vessel wall, manual correction was performed—if needed—in both longitudinal and cross-sectional views at 0.5 mm increments. The proximal and distal borders of coronary plaques were defined for quantification. Coronary plaque was defined on the CTA based on former publications (13). Chronic total occlusions were not present in current patient population. Plaque composition was determined using fixed thresholds: low-attenuation plaque (LAP): −100–30 HU; non-calcified plaque (NCP): 31–350 HU; calcified plaque (CP): $\geq$ 351 HU. Volumes of total plaque, LAP, NCP and CP were calculated. LAP burden defined as the ratio of LAP volume and vessel volume (LAP volume × 100%/vessel volume) was also determined. Lumen area stenosis was defined at the site of the maximal luminal stenosis of the coronary plaque. Remodeling index (RI) was calculated as the ratio of the vessel wall area at the site of the maximal luminal narrowing and the reference vessel wall area. High-risk plaque (HRP) was defined based on quantitative LAP burden $>$ 4% or a RI $>$ 1.1 (2, 14).

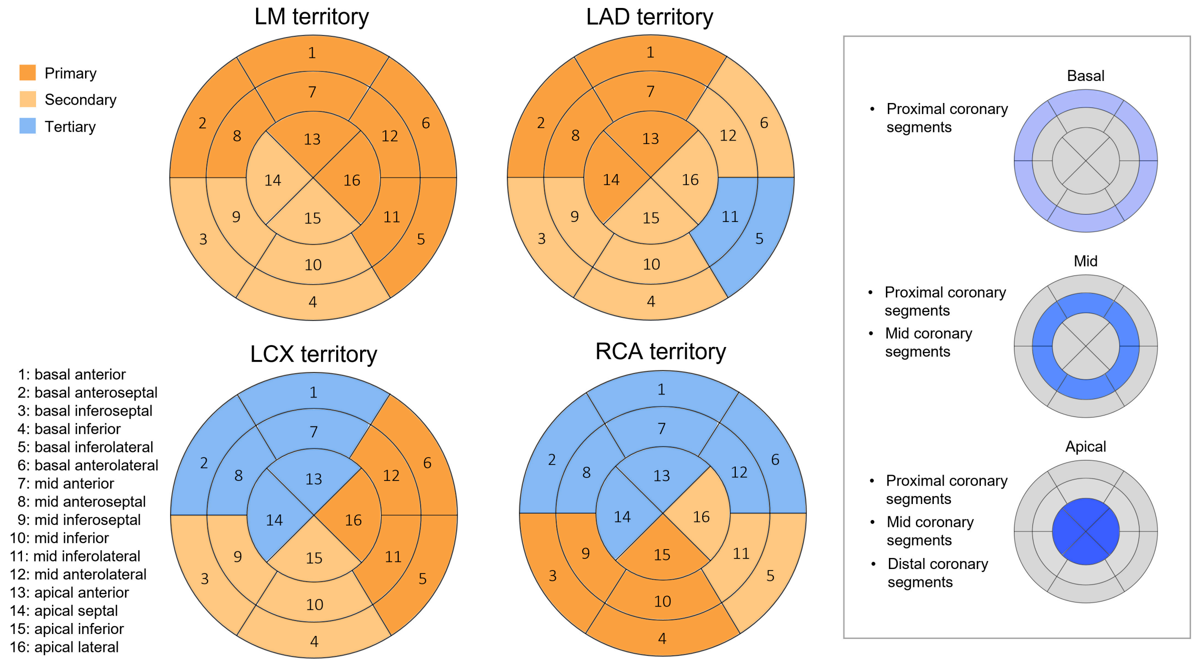

FIGURE 2
Integration of coronary anatomy and myocardial territories. Vessel territories were defined based on the modified method after Cerci et al. for LM, LAD, LCX, and RCA. The following categories were determined for myocardial segments: primary—most commonly supplied territories in case of right dominance; secondary—might be supplied territories in case of normal variations; tertiary—usually not supplied territories. In addition, coronary segment-based analysis was also used, taking lesion location into account. For that, basal segments were aligned with proximal, mid segments with proximal and mid, and apical segments with proximal, mid and distal coronary segments. LAD, Left anterior descending; LCX, Left circumflex; LM, Left main; RCA, Right coronary artery.

Myocardial perfusion analysis

DPCT images were analyzed using a dedicated software (Intellispace Portal; Philips Healthcare, Cleveland, OH, United States). Elastic registration and temporal filtering were applied for motion artifact reduction. Time-attenuation curves (TAC) created in the left ventricular outflow tract were used as arterial input function for perfusion analysis. Short-axis views were created for the assessment of the left ventricular myocardial tissue. MBF was computed applying a hybrid deconvolution method (12). The assessment of MBF was obtained by two readers (B.V and S.B, 3 and 4 years of experience with cardiac CT) in random order blinded to plaque data and patient characteristics. A ROI > 0.5 cm2 was set in each myocardial segment (intramural) using a 16-segment model excluding the apex carefully avoiding any artifacts on short-axial images (15). Segmental myocardial ischemia was defined as MBF < 101 ml/100 g/min based on Pontone et al. (16). In addition, relative MBF (MBFi) for each segment was also calculated as the ratio of absolute MBF to reference MBF, latter defined as the 75th percentile of all MBF values of a given patient (17).

Integration of coronary anatomy and myocardial territories

Coronary lesions were assigned to the corresponding myocardial segment based on the modified method after Cerci et al. for the CORE320 (Coronary Artery Evaluation Using 320-Row Multidetector CTA) trial (18). Former studies performed vessel-based analysis for the alignment of myocardial territories and supplying vessels. For our segment-based approach, we defined all coronary artery segments that supply a given myocardial segment of the 16 analyzed segments based on dominance, segment location in relation to basal, mid-ventricular or apical regions (**Figure 2**).

After the adjudication was performed by B.S.,—with 8 years of experience in cardiac imaging—volumes for total, NCP and CP of all relevant supplying coronary segments were summed for each myocardial segment. LAP burden was also calculated from the summed LAP and vessel volume. If LAP burden exceeded 4% of all plaque supplying a given segment, or the highest RI of the corresponding lesions was > 1.1, we marked as HRP. Summed plaque volumes (PVs), the highest degree of lumen area stenosis and HRP

(LAP burden > 4% or a RI > 1.1) of the supplying coronary segments were analyzed for the corresponding myocardial segment.

Statistical analysis

Continuous variables are presented as mean and standard deviation, whereas categorical parameters are presented as frequency with percentages. Independent *t*-test was used to compare parameters describing coronary plaque burden between ischemic and non-ischemic segments. Pearson correlation was used to define the association between total, NCP and CP volumes. Linear and logistic mixed models correcting for intra-patient clustering and clinical factors were used to assess the association between total PV, maximal area stenosis, quantitative HRP features and absolute MBF, MBFi or myocardial ischemia using 101 ml/100 g/min as cut-off value for MBF. Models were adjusted for predefined clinical risk factors of CAD and possible modifiers of ischemia including hypertension, diabetes mellitus and statin therapy.

Intraclass correlation coefficient (ICC) of MBF was calculated for 160 segments of 10 randomly selected patients between two readers with 3 or more years of experience in cardiac CT imaging (BV and SB). ICC values greater than 0.80 were considered good, values above 0.90 were considered to have excellent reproducibility. Also, reproducibility of quantitative plaque assessment was evaluated between two independent readers based on 10 plaques of randomly selected patients. All statistical analyses were performed using SPSS (version 24.0) and R software (version 3.6.1). $P < 0.05$ was defined as statistically significant.

Results

Patient characteristics

The baseline characteristics of the 30 analyzed patients (mean age 60.9 ± 8.3 years, 26.7% female, mean BMI 28.9 ± 3.8 kg/m^2) are summarized in Table 1. Common comorbidities were hypertension (76.7%) and dyslipidemia (76.7%).

On average, 13.0 ± 8.6 days have passed between the two examinations. Mean effective radiation dose was 4.4 ± 1.1 mSv for rest CTA and 8.9 ± 4.0 mSv for DPCT. A total of 496 coronary artery segments and 480 myocardial segments were evaluated quantitatively. ICC between readers was 0.96 and 0.93 for MBF and total PV, respectively.

TABLE 1 Patient characteristics.

	Patient population $N = 30$
Age, years	60.9 ± 8.3
Male gender, *n* (%)	22 (73.3)
BMI, kg/m^2	28.9 ± 3.8
Hypertension, *n* (%)	23 (76.7)
Diabetes mellitus, *n* (%)	2 (6.7)
Dyslipidemia, *n* (%)	23 (76.7)
Smoking, *n* (%)	16 (53.3)
Cerebrovascular disease, *n* (%)	1 (3.3)
Peripheral artery disease, *n* (%)	3 (10.0)
Family history of premature CAD, *n* (%)	9 (30.0)
Oral anticoagulant therapy, *n* (%)	6 (20.0)
Statin therapy, *n* (%)	16 (53.3)
ACE-I/ARB therapy, *n* (%)	18 (60.0)
Beta-blocker therapy, *n* (%)	15 (50.0)

Continuous variables are described as mean ± SD, whereas categorical variables are represented as frequencies and percentage.
ACE-I, Angiotensin-converting-enzyme inhibitor; ARB, Angiotensin receptor blocker; BMI, Body mass index; CAD, Coronary artery disease.

Plaque characteristics and segmental myocardial ischemia

Total PV, NCP volume, and CP volume differed significantly between ischemic and non-ischemic myocardial segments, 120.5 ± 119.5 mm^3 vs. 84.6 ± 82.2 mm^3, $p = 0.001$; 62.3 ± 59.5 mm^3 vs. 51.4 ± 54.9 mm^3, $p = 0.045$; 58.3 ± 91.8 mm^3 vs. 33.3 ± 50.6 mm^3, $p = 0.001$; respectively (**Table 2**). Median and interquartile range (IQR) of PVs for ischemic and non-ischemic myocardial segments were: total PV: 82.9 (31.1–179.6) vs. 68.7 (25.8–114.7) mm^3; NCP volume: 46.1 (24.3–93.7) vs. 31.6 (12.4–73.8) mm^3; CP volume: 15.9 (0.1–78.2) vs. 17.3 (2.2–46.1) mm^3. **Figure 3** demonstrates box plots of quantitative PVs in coronary segments supplying ischemic and non-ischemic myocardial segments. On a patient level, the average of maximal lumen area stenosis of the worst lesion was 54.7 ± 15.9%. On a segmental level, the average of the maximal lumen area stenosis was 37.2 ± 22.7% for ischemic and 33.5 ± 20.7% for non-ischemic myocardial segments ($p = 0.072$). HRP was present in 21.3% in ischemic and 19.0% in non-ischemic territories ($p = 0.539$).

Number of ischemic segments were 164/480 (34.2%). Median MBF was 111 ml/100 g/min, while median MBFi was 0.94.

Total PV strongly correlated with NCP volume ($r = 0.73$, $p < 0.001$) and CP volume ($r = 0.83$, $p < 0.001$), we therefore included total PV in the multivariate prediction models to avoid multicollinearity.

TABLE 2 Coronary plaque characteristics in ischemic and non-ischemic myocardial segments.

	Ischemic myocardial segments $N = 164$	Non-ischemic myocardial segments $N = 316$	*P*
Total plaque volume, mm^3	120.5 ± 119.5	84.6 ± 82.2	**0.001**
NCP volume, mm^3	62.3 ± 59.5	51.4 ± 54.9	**0.045**
CP volume, mm^3	58.3 ± 91.8	33.3 ± 50.6	**0.001**
High-risk plaque, *n* (%)	35 (21.3)	60 (19.0)	0.539
Lumen area stenosis,%	37.2 ± 22.7	33.5 ± 20.7	0.072

Myocardial ischemia was defined as MBF < 101 ml/100 g/min. Continuous variables are described as mean ± SD, whereas categorical variables are represented as frequencies and percentage.
Bold values indicate significant differences based on the p-values.
CP, Calcified plaque; MBF, Myocardial blood flow; NCP, Non-calcified plaque.

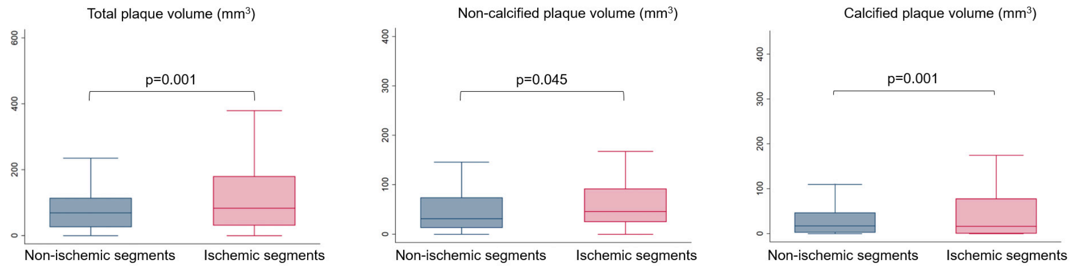

FIGURE 3
Box plots showing the distribution of total, non-calcified and calcified plaque volumes related to ischemic and non-ischemic myocardial segments based on DPCT (MBF < 101 ml/100 g/min vs. ≥ 101 ml/100 g/min). DPCT, Dynamic perfusion CT; MBF, Myocardial blood flow.

Predictors of absolute and relative myocardial blood flow

Using linear mixed models, univariate analysis revealed that total PV predicted both absolute and relative MBF values (Table 3). Clinical risk factors (including hypertension, diabetes mellitus, and statin use), HRP and stenosis severity were not associated with impaired myocardial perfusion based on MBF and MBFi.

On multivariate analysis, total PV increase led to reduced absolute and relative MBF values even after adjusting for clinical risk factors, lumen area stenosis and HRP features: per 10 mm^3; $\beta = -0.035$, $p < 0.01$ for MBF and $\beta = -0.0002$, $p < 0.01$ for MBFi. Notably, lumen area stenosis and quantitative HRP features were not linked to absolute or relative MBF values (all $p > 0.05$).

Predictors of myocardial ischemia based on myocardial blood flow threshold

On univariate logistic regression total PV and lumen area stenosis were significant predictors of myocardial ischemia based on MBF < 101 ml/100 g/min (Table 4). After adjusting for predefined clinical risk factors, stenosis severity and HRP, increase in total PV was independently associated with myocardial ischemia: OR: 1.01, $p = 0.033$ (per 10 mm^3). However, on multivariate analysis HRP feature and lumen area stenosis were not linked to ischemia (both $p > 0.05$).

Discussion

We used a novel approach to define the contribution of coronary PV to limited flow (ischemia) of all feeding coronary segments considering only coronary lesions prior to a given myocardial territory. We established that total PV influenced myocardial perfusion on a segmental level, independent from stenosis severity, HRP and risk factors. Moreover, maximal luminal area stenosis and the presence of HRP were not linked to myocardial ischemia based on MBF. Reproducibility was excellent for the evaluation of MBF or total PV.

While there are several alternative imaging modalities to analyze the hemodynamic consequence of coronary plaques, CT is the only non-invasive modality for the combined assessment of morphology and function of CAD. CT can provide several additional anatomical parameters that could be incremental as compared with traditional evaluation focusing on luminal stenosis or lesion length. In agreement with our findings, total PV was linked to visual perfusion defects as assessed by SPECT (9, 19). Liu et al. also reported that low-density PV

TABLE 3 Univariate analysis of the predictors of absolute and relative myocardial blood flow (MBFi) detected by DPCT using linear mixed models.

Predictors	**Absolute MBF detected by DPCT**			**Relative MBF detected by DPCT**		
	Univariate model			**Univariate model**		
	β	**95% CI**	***P***	**β**	**95% CI**	***P***
Total plaque volume, per 10 mm^3	**-0.025**	**-0.043—0.007**	**0.006**	**-0.0002**	**-0.0003—0.0001**	**0.004**
NCP volume, per 10 mm^3	−0.025	−0.053–0.003	0.079	−0.0002	−0.0004–0.0000	0.077
CP volume, per 10 mm^3	**-0.046**	**-0.078—0.014**	**0.005**	**-0.0002**	**-0.0004—0.00006**	**0.008**
Remodeling index	1.934	−2.427–6.295	0.384	0.003	−0.029–0.036	0.838
High-risk plaque	1.952	−1.767–5.672	0.303	0.018	−0.009–0.045	0.191
Lumen area stenosis	−4.479	−12.008–3.050	0.243	−0.042	−0.093–0.009	0.108
Age, years	−0.172	−1.208–0.864	0.736	0.0006	−0.001–0.002	0.463
BMI, kg/m^2	−0.791	−3.037–1.455	0.477	**0.004**	**0.0007–0.007**	**0.017**
Hypertension	−1.482	−21.491–18.527	0.881	0.010	−0.019–0.039	0.491
Diabetes mellitus	1.542	−32.393–35.478	0.926	0.018	−0.031–0.068	0.456
Smoking	1.536	−15.424–18.496	0.854	0.013	−0.011–0.038	0.274
Statin therapy	−3.201	−20.127–13.724	0.701	−0.005	−0.030–0.020	0.658

Bold values indicate significant differences based on the p-values.
CP, Calcified plaque; BMI, Body mass index; DPCT, Dynamic perfusion CT; MBF, Myocardial blood flow; MBFi, Myocardial blood flow index; NCP, Non-calcified plaque.

TABLE 4 Univariate logistic regression analysis of the predictors of myocardial ischemia detected by DPCT.

Predictors	**Myocardial ischemia detected by DPCT**		
	Univariate model		
	OR	**95% CI**	***P***
Total plaque volume, per 10 mm^3	**1.01**	**1.002–1.012**	**0.003**
NCP volume, per 10 mm^3	**1.01**	**1.004–1.018**	**0.002**
CP volume, per 10 mm^3	1.01	0.997–1.015	0.172
Remodeling index	1.14	0.422–3.059	0.801
High-risk plaque	0.79	0.333–1.890	0.601
Lumen area stenosis	**8.05**	**1.340–48.333**	**0.023**
Age, years	1.03	0.839–1.268	0.770
BMI, kg/m^2	1.26	0.787–2.019	0.335
Hypertension	2.86	0.046–177.116	0.617
Diabetes mellitus	1.74	0.003–883.279	0.861
Smoking	0.96	0.031–29.434	0.982
Statin therapy	4.06	0.108–152.174	0.448

Myocardial ischemia was defined as MBF $<$ 101 ml/100 g/min.
Bold values indicate significant differences based on the p-values.
CP, Calcified plaque; BMI, Body mass index; DPCT, Dynamic perfusion CT; MBF, Myocardial blood flow; NCP, Non-calcified plaque.

and diameter stenosis were also independently associated with myocardial ischemia. Driessen et al. evaluated 208 patients who underwent (15O) H_2O PET-MPI and coronary CTA and found that plaque length and volume were inversely associated with MBF in a sub-study of the PACIFIC trial (20). Moreover, this study suggested a link between decreased flow and NCP volume or positive remodeling in a vessel-based analysis. The multicenter CORE 320 study demonstrated that combined CTA and CTP has excellent diagnostic performance to detect flow-limiting lesions (more than 50%) by invasive angiography and perfusion defects by SPECT. van Rosendael et al. utilized static stress CTP in a total of 84 patients to evaluate the relationship between morphological plaque features and visual perfusion deficits (7). Interestingly, increasing stenosis severity and lesion length were predictors of ischemia, however PVs were not. Previous studies examining the association between PV and ischemia in stable angina patients reported highly variable mean values for total PV: 69.0 ± 16.8 mm^3 vs. 49.6 ± 17.2 mm^3 by van Rosendael et al. (7), 114 ± 118 mm^3 vs. 62 ± 89 mm^3 by Diaz-Zamudio et al. (9), and 694.6 ± 485.1 mm^3 vs. 422.3 ± 387.9 mm^3 by Min et al. (21), for ischemic and non-ischemic myocardial territories, respectively. In our current study, total PV for ischemic segments were 120.5 ± 119.5 mm^3 while for non-ischemic segments it was 84.6 ± 82.2 mm^3.

As highlighted above, there are conflicting results on whether luminal narrowing, plaque composition and vulnerability or plaque burden precipitate ischemia. This could originate from the high inter-vendor, inter-scanner, inter-protocol variability of coronary plaque assessment and from the methodology used for the characterization of ischemia. To our knowledge, there are currently no studies evaluating both myocardial ischemia and CAD quantitatively, on a segment level using CT imaging. Also, most of the former studies used visual assessment for detecting perfusion defects. However, quantitative methods are more reproducible and might provide

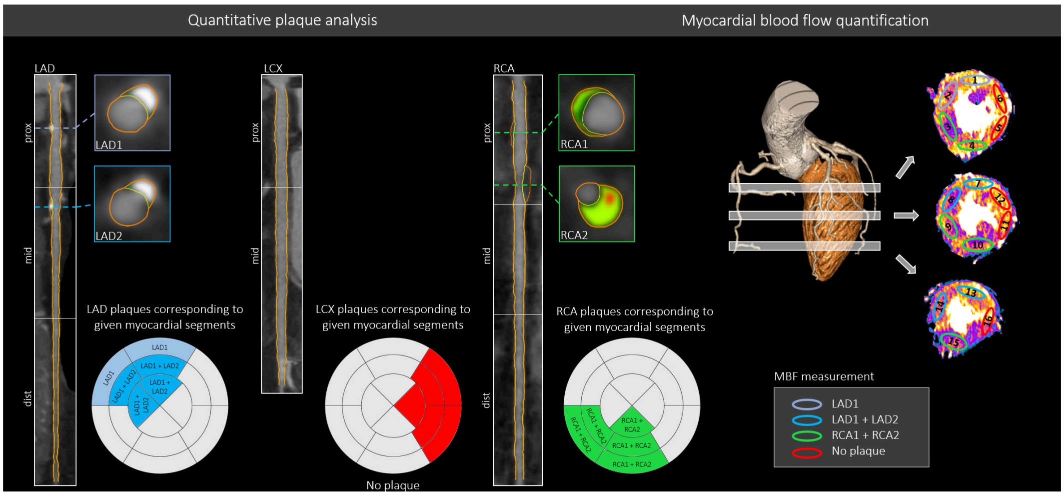

FIGURE 4
Comprehensive plaque assessment and the evaluation of myocardial ischemia based on CT images. A representative case of our study depicts the images of a 62-year-old male patient who underwent coronary CTA and DPCT imaging for the evaluation of CAD and corresponding myocardial ischemia. In this case, plaques were detected and quantified in the proximal LAD (LAD1), mid-LAD (LAD2) and proximal RCA (RCA1 + RCA2) coronary segments. All coronary plaques based on their location were matched for a given myocardial territory. MBF was quantified for all 16 myocardial segments using DPCT images. By creating a myocardial vessel territory map for each coronary segment, we could derive the total plaque volume that possibly influences the blood flow quantified as MBF on DPCT to any of the 16 analyzed LV territories (see **Figure 2** for segmental classification). In this case, basal anterior (1) and basal anteroseptal (2) myocardial segments were influenced by the proximal LAD (LAD1) lesion, while the mid anterior (7), mid anteroseptal (8), apical anterior (13), and apical septal (14) myocardial segments were affected by two lesions: LAD1 and LAD2 (mid LAD segment) as they are located more distally. No plaques were present in the LCX. Regarding the RCA, two plaques were detected in the proximal RCA segment (RCA1 and RCA2), therefore all myocardial segments corresponding to the RCA were influenced by two plaques (RCA1 and RCA2). Plaque volumes of the lesions aligned for a given myocardial segment were summed and accounted for in the analysis, while the highest degree of lumen area stenosis of the corresponding lesions was included in the analysis. Light blue color indicates LV segments related to proximal LAD lesion, dark blue color indicates LV territories related to both proximal and mid-LAD lesions, whereas green color shows myocardial territories corresponding to the RCA lesions. LCX demonstrated no coronary lesions. ROI-s were placed in each myocardial segment on short-axial images. CAD, Coronary artery disease; CTA, CT angiography; DPCT, Dynamic perfusion CT; LAD, Left anterior descending; LCX, Left circumflex; LV, Left ventricle; MBF, Myocardial blood flow; RCA, Right coronary artery.

a more detailed analysis of LV blood flow based on different perfusion markers. One of the largest challenges is the precise alignment of a myocardial territory to its feeding vessels. The most common approach is to calculate an accumulated PV for a given vessel, however this could not tailor unique variations in coronary anatomy and lesions on the distal coronary segments should not be taken into consideration when assessing perfusion in the basal myocardium. Authors of the CORE320 trial sought to assign coronary lesions to the corresponding myocardial segment taking anatomical variations and coronary dominance into account (18). For our segment-based approach, we defined all coronary artery segments that supply a given myocardial segment (16-segment model) based on dominance, segment location in relation to basal, mid-ventricular or apical regions (**Figure 2**). A representative case and the detailed description of our methodology are demonstrated on **Figure 4**. Using this approach, we aimed to overcome a main limitation of former studies which performed vessel-based analysis when evaluating ischemia. However, a distally localized lesion in the coronary vessel does not limit the flow of the most basal segments and this could substantially influence the results. Also, apical region of the heart can be supplied by several contributing vessel segments and therefore all of the lesions should be taken into consideration.

The discordance between stenosis severity and ischemia has been reported using both non-invasive and invasive methods. As previously described by Schuijf et al. in patients with obstructive CAD detected on coronary CTA, only 50% had ischemia using SPECT, while ischemia was detected in 15% of patients without obstructive CAD (4). Similarly, in the FAME study discrepancy was identified between anatomic and functional stenosis severity assessed by invasive angiography and FFR (22). Despite these findings, our current clinical management heavily relies on treating coronary lesions based on ischemic burden. However, total coronary plaque burden might step forward as the target of early interventions to stabilize HRPs, reduce the progression of coronary PV and luminal stenosis and thus ultimately to prevent adverse events.

Conflicting results regarding the relationship of plaques and ischemia may originate from the different capabilities of the modality utilized in the trials. CT has several advantages as compared with other techniques such as better spatial resolution, robust plaque assessment and reproducible quantitative measures of perfusion. CT imaging can define the hemodynamic significance of CAD by defining either lesion-specific ischemia using CT derived fractional flow reserve (FFR) or global ischemia on DPCT imaging. Radiation dose however still limits its use—especially using dynamic CT protocols—for a large subset of patients. Growing body of evidence suggests that anatomical information derived from CTA outperforms traditional ischemia testing for defining lesion-specific ischemia as obtained from invasive FFR. The CREDENCE trial demonstrated a strong association between atherosclerotic PVs, lumen size and invasive FFR (23). Our study provides unique insight in the interplay of coronary plaque burden, stenosis severity, HRP anatomy and corresponding myocardial ischemia on CTA. While HRP was linked to lesion-specific ischemia based on several trials (24), we did not see an association with reduced MBF on a segmental level. We found that considering all possible plaque on the feeding vessels of a given myocardial territory, total PV aggravates MBF or MBFi (per 10 mm^3; $\beta = -0.035$, $p < 0.01$ for MBF and $\beta = -0.0002$, $p < 0.01$ for MBFi). This observation seems valid across different stages of stenosis severity and thus detailed plaque quantification could effectively guide secondary prevention therapy in a large spectrum of contemporary chest pain patients. Integrating plaque burden in the clinical CTA reports and thus in personalized patient management should be in the focus rather than luminal narrowing *per se*.

We acknowledge the limitations of our study. First, the sample size is limited after excluding patients with non-diagnostic image quality for quantitative plaque analysis or patients without intermediate stenosis. Excellent image quality is a prerequisite for quantitative plaque analysis. This could result in selection bias for our analysis. Quantitative plaque analysis is time-consuming and currently only a research tool, not used in routine clinical practice. However, experts of the field underline its role in risk prediction and tools are being developed for automated quantification in the near future. Also, our study is underpowered for the assessment of gender differences in CAD and corresponding ischemia or for outcome analysis.

Conclusion

Total coronary PV was independently associated with myocardial ischemia based on MBF derived from DPCT imaging, while area stenosis and HRP were not. Incorporating these quantitative plaque characteristics in a comprehensive coronary CTA evaluation could improve the prediction of ischemic CAD, independently of lesion severity.

Data availability statement

The data that support the findings of this study are available from the corresponding author, upon reasonable request.

Ethics statement

The studies involving human participants were reviewed and approved by National Institute of Pharmacy and Nutrition—OGYÉI/719/2017. The patients/participants provided their written informed consent to participate in this study.

Author contributions

BS, MK, PM-H, and BM contributed to conception and design of the study. BV, SB, and BS performed the measurements. BV, SB, MB, MV-N, FS, ÁJ, and BS contributed to patient enrollment. BV, SB, and MB organized the database. BS and MK performed the statistical analysis. BV and BS wrote the first draft of the manuscript. MK, MV-N, FS, SB, and MB wrote sections of the manuscript. All authors contributed to manuscript revision, read, and approved the submitted version.

Funding

This project was supported by the KH-17 Program of the National Research, Development and Innovation Office of the Ministry of Innovation and Technology in Hungary (NKFIH). This study was supported by the National Research, Development and Innovation Office of Hungary (NKFIA; NVKP_16-1-2016-0017 National Heart Program). This research was supported by the Thematic Excellence Program (Tématerületi Kiválósági Program, 2020-4.1.1.-TKP2020) of the Ministry for Innovation and Technology in Hungary, within the framework of the Therapeutic Development and Bioimaging programs of the Semmelweis University. MB was supported by the ÚNKP-21-3-II-SE New National Excellence Program of the Ministry for Innovation and Technology from the source of the National Research, Development and Innovation fund.

Conflict of interest

The authors declare that the research was conducted in the absence of any commercial or financial relationships that could be construed as a potential conflict of interest.

Publisher's note

References

1. Knuuti J, Wijns W, Saraste A, Capodanno D, Barbato E, Funck-Brentano C, et al. 2019 ESC Guidelines for the diagnosis and management of chronic coronary syndromes. *Eur Heart J.* (2020) 41:407–77.

2. Williams MC, Kwiecinski J, Doris M, McElhinney P, D'Souza MS, Cadet S, et al. Low-Attenuation noncalcified plaque on coronary computed tomography angiography predicts myocardial infarction: results from the multicenter SCOT-HEART trial (Scottish Computed Tomography of the HEART). *Circulation.* (2020) 141:1452–62. doi: 10.1161/CIRCULATIONAHA.120.049840

3. Xaplanteris P, Fournier S, Pijls NHJ, Fearon WF, Barbato E, Tonino PAL, et al. Five-year outcomes with PCI guided by fractional flow reserve. *N Engl J Med.* (2018) 379:250–9. doi: 10.1056/NEJMoa1803538

4. Schuijf JD, Wijns W, Jukema JW, Atsma DE, de Roos A, Lamb HJ, et al. Relationship between noninvasive coronary angiography with multi-slice computed tomography and myocardial perfusion imaging. *J Am Coll Cardiol.* (2006) 48:2508–14. doi: 10.1016/j.jacc.2006.05.080

5. Pontone G, Rossi A, Guglielmo M, Dweck MR, Gaemperli O, Nieman K, et al. Clinical applications of cardiac computed tomography: a consensus paper of the european association of cardiovascular imaging-part I. *Eur Heart J Cardiovasc Imaging.* (2022) 23:299–314. doi: 10.1093/ehjci/jeab293

6. Nieman K, Balla S. Dynamic CT myocardial perfusion imaging. *J Cardiovasc Comput Tomogr.* (2020) 14:303–6. doi: 10.1016/j.jcct.2019.09.003

7. van Rosendael AR, Kroft LJ, Broersen A, Dijkstra J, van den Hoogen IJ, van Zwet EW, et al. Relation between quantitative coronary CTA and myocardial ischemia by adenosine stress myocardial CT perfusion. *J Nucl Cardiol.* (2017) 24:1253–62. doi: 10.1007/s12350-016-0393-7

8. Eskerud I, Gerdts E, Larsen TH, Simon J, Maurovich-Horvat P, Lonnebakken MT. Total coronary atherosclerotic plaque burden is associated with myocardial ischemia in non-obstructive coronary artery disease. *Int J Cardiol Heart Vasc.* (2021) 35:100831. doi: 10.1016/j.ijcha.2021.100831

9. Diaz-Zamudio M, Fuchs TA, Slomka P, Otaki Y, Arsanjani R, Gransar H, et al. Quantitative plaque features from coronary computed tomography angiography to identify regional ischemia by myocardial perfusion imaging. *Eur Heart J Cardiovasc Imaging.* (2017) 18:499–507. doi: 10.1093/ehjci/jew274

10. Abbara S, Blanke P, Maroules CD, Cheezum M, Choi AD, Han BK, et al. SCCT guidelines for the performance and acquisition of coronary computed tomographic angiography: a report of the society of cardiovascular computed tomography guidelines committee: endorsed by the north american society for cardiovascular imaging (NASCI). *J Cardiovasc Comput Tomogr.* (2016) 10:435–49. doi: 10.1016/j.jcct.2016.10.002

11. Iskandrian AE, Bateman TM, Belardinelli L, Blackburn B, Cerqueira MD, Hendel RC, et al. Adenosine versus regadenoson comparative evaluation in myocardial perfusion imaging: results of the ADVANCE phase 3 multicenter international trial. *J Nucl Cardiol.* (2007) 14:645–58. doi: 10.1016/j.nuclcard.2007.06.114

12. Tanabe Y, Kido T, Uetani T, Kurata A, Kono T, Ogimoto A, et al. Differentiation of myocardial ischemia and infarction assessed by dynamic computed tomography perfusion imaging and comparison with cardiac magnetic resonance and single-photon emission computed tomography. *Eur Radiol.* (2016) 26:3790–801. doi: 10.1007/s00330-016-4238-1

13. Achenbach S, Moselewski F, Ropers D, Ferencik M, Hoffmann U, MacNeill B, et al. Detection of calcified and noncalcified coronary atherosclerotic plaque by contrast-enhanced, submillimeter multidetector spiral computed tomography: a segment-based comparison with intravascular ultrasound. *Circulation.* (2004) 109:14–7. doi: 10.1161/01.CIR.0000111517.69230.0F

14. Motoyama S, Sarai M, Harigaya H, Anno H, Inoue K, Hara T, et al. Computed tomographic angiography characteristics of atherosclerotic plaques subsequently resulting in acute coronary syndrome. *J Am Coll Cardiol.* (2009) 54:49–57. doi: 10.1016/j.jacc.2009.02.068

15. Cerqueira MD, Weissman NJ, Dilsizian V, Jacobs AK, Kaul S, Laskey WK, et al. Standardized myocardial segmentation and nomenclature for tomographic imaging of the heart. a statement for healthcare professionals from the cardiac imaging committee of the council on clinical cardiology of the american heart association. *Circulation.* (2002) 105:539–42. doi: 10.1161/hc0402.102975

16. Pontone G, Baggiano A, Andreini D, Guaricci AI, Guglielmo M, Muscogiuri G, et al. Dynamic stress computed tomography perfusion with a whole-heart coverage scanner in addition to coronary computed tomography angiography and fractional flow reserve computed tomography derived. *JACC Cardiovasc Imaging.* (2019) 12:2460–71. doi: 10.1016/j.jcmg.2019.02.015

17. Nous FMA, Geisler T, Kruk MBP, Alkadhi H, Kitagawa K, Vliegenthart R, et al. Dynamic myocardial perfusion CT for the detection of hemodynamically significant coronary artery disease. *JACC Cardiovasc Imaging.* (2022) 15:75–87. doi: 10.1016/j.jcmg.2021.07.021

18. Cerci RJ, Arbab-Zadeh A, George RT, Miller JM, Vavere AL, Mehra V, et al. Aligning coronary anatomy and myocardial perfusion territories: an algorithm for the CORE320 multicenter study. *Circ Cardiovasc Imaging.* (2012) 5:587–95. doi: 10.1161/CIRCIMAGING.111.970608

19. Liu T, Yuan X, Wang C, Sun M, Jin S, Dai X. Quantification of plaque characteristics detected by dual source computed tomography angiography to predict myocardial ischemia as assessed by single photon emission computed tomography myocardial perfusion imaging. *Quant Imaging Med Surg.* (2019) 9:711–21. doi: 10.21037/qims.2019.04.07

20. Driessen RS, Stuijfzand WJ, Raijmakers PG, Danad I, Min JK, Leipsic JA, et al. Effect of plaque burden and morphology on myocardial blood flow and fractional flow reserve. *J Am Coll Cardiol.* (2018) 71:499–509. doi: 10.1016/j.jacc.2017.11.054

21. Min JK, Chang HJ, Andreini D, Pontone G, Guglielmo M, Bax JJ. Coronary CTA plaque volume severity stages according to invasive coronary angiography and FFR. *J Cardiovasc Comput Tomogr.* (2022). doi: 10.1016/j.jcct.2022.03.001 [Epub ahead of print].

22. Tonino PA, Fearon WF, De Bruyne B, Oldroyd KG, Leesar MA, Ver Lee PN, et al. Angiographic versus functional severity of coronary artery stenoses in the FAME study fractional flow reserve versus angiography in multivessel evaluation. *J Am Coll Cardiol.* (2010) 55:2816–21. doi: 10.1016/j.jacc.2009.11.096

23. Stuijfzand WJ, van Rosendael AR, Lin FY, Chang HJ, van den Hoogen IJ, Gianni U, et al. Stress myocardial perfusion imaging vs coronary computed tomographic angiography for diagnosis of invasive vessel-specific coronary physiology: predictive modeling results from the computed tomographic evaluation of atherosclerotic determinants of myocardial ischemia (CREDENCE) Trial. *JAMA Cardiol.* (2020) 5:1338–48. doi: 10.1001/jamacardio.2020.3409

24. Danad I, Raijmakers PG, Driessen RS, Leipsic J, Raju R, Naoum C, et al. Comparison of Coronary CT Angiography, SPECT, PET, and Hybrid Imaging for Diagnosis of Ischemic Heart Disease Determined by Fractional Flow Reserve. *JAMA Cardiol.* (2017) 2:1100–7. doi: 10.1001/jamacardio.2017.2471

frontiers | Frontiers in Cardiovascular Medicine

TYPE Original Research
PUBLISHED 04 October 2022
DOI 10.3389/fcvm.2022.963110

OPEN ACCESS

EDITED BY
Carlo Gaudio,
Sapienza University of Rome, Italy

REVIEWED BY
Liwei Hu,
Shanghai Children's Medical Center, China
Bruno Pinamonti,
University Health Organization Giuliano Isontina (ASU GI), Italy

*CORRESPONDENCE
Fabao Gao
gaofabao@wchscu.cn

SPECIALTY SECTION
This article was submitted to Cardiovascular Imaging, a section of the journal Frontiers in Cardiovascular Medicine

RECEIVED 07 June 2022
ACCEPTED 15 September 2022
PUBLISHED 04 October 2022

CITATION
Zhang L, Wan Y, He B, Wang L, Zhu D and Gao F (2022) Left ventricular strain patterns and their relationships with cardiac biomarkers in hypertrophic cardiomyopathy patients with preserved left ventricular ejection fraction.
Front. Cardiovasc. Med. 9:963110.
doi: 10.3389/fcvm.2022.963110

Left ventricular strain patterns and their relationships with cardiac biomarkers in hypertrophic cardiomyopathy patients with preserved left ventricular ejection fraction

Lisha Zhang[1], Yixuan Wan[1], Bo He[1], Lei Wang[2], Dongyong Zhu[1] and Fabao Gao[1,2]*

[1]Department of Radiology, West China Hospital, Sichuan University, Chengdu, China, [2]Molecular Imaging Center, West China Hospital, Sichuan University, Chengdu, China

Aims: This study aims to assess left ventricular (LV) function in hypertrophic cardiomyopathy (HCM) patients with preserved left ventricular ejection fraction (LVEF) by LV strain patterns based on cardiac magnetic resonance feature tracking (CMR-FT) and to explore the relationships between LV strain patterns and cardiac biomarkers in these patients, such as cardiac troponin (cTnT) and N-terminal prohormone of the brain natriuretic peptide (NT-proBNP).

Methods: A total of 64 HCM patients with preserved LVEF and 33 healthy people were included in this study. All subjects underwent contrast-enhanced CMR, and all patients took blood tests for cTnT and NT-proBNP during hospitalization.

Results: Despite the absence of a significant difference in LVEF between HCM patients and healthy controls, almost all global and segmental strains in radial, circumferential, and longitudinal directions in the HCM group deteriorated significantly as compared to controls ($p < 0.05$). Moreover, some global and segmental strains correlated significantly with NT-proBNP and cTnT in HCM patients, and the best correlations were global radial strain (GRS) ($r = -0.553$, $p < 0.001$) and mid-ventricular radial strain (MRS) ($r = -0.582$, $p < 0.001$), respectively, with a moderate correlation. The receiver operating characteristic (ROC) results showed that among the LV deformation parameters, GRS [area under the curve (AUC), 0.76; sensitivity, 0.49; specificity, 1.00], MRS (AUC, 0.81; sensitivity, 0.77; specificity, 0.79) demonstrated greater diagnostic accuracy to predict elevated NT-proBNP, and abnormal cTnT, respectively. Their cut-off values were 21.17 and 20.94%, respectively. Finally, all global strains demonstrated moderate, good, and excellent intra- and inter-observer reproducibility.

Conclusion: LV strain patterns can be used to assess the subclinical cardiac function of HCM patients on the merit of being more sensitive than LVEF. In addition, LV strain patterns can detect serious HCM patients and may be helpful to non-invasively predict elevated NT-proBNP and cTnT.

KEYWORDS

hypertrophic cardiomyopathy, cardiac magnetic resonance feature tracking, cardiac troponin T, N-terminal prohormone of the brain natriuretic peptide, strain

Introduction

As a commonly inherited cardiomyopathy with an incidence of 1:500, hypertrophic cardiomyopathy (HCM) is the most common cause of sudden death among young people (1). Its clinical diagnosis depends on LV hypertrophy, which cannot be accounted for by other reasons and is identified by cardiac magnetic resonance (CMR) or echocardiography (2). Left ventricular ejection fraction (LVEF) is usually regarded as the most frequently used index in assessing cardiac function and predicting the prognosis of HCM patients (3). However, as we know, LVEF in many HCM patients is normal (LVEF $\geq$ 50%). Given this condition, it seems unsuitable to depend only on LVEF to assess the cardiac function of HCM patients. Cardiac magnetic resonance feature tracking (CMR-FT), a post-processing technology with high sensitivity and good repeatability, can detect functional impairment of the heart before LVEF decreases and has thus been studied in many heart diseases (4, 5). Studies of HCM patients have shown that CMR-FT-based global strains in the radial, circumferential, and longitudinal directions decreased significantly compared to healthy controls, which can also be used to predict the prognosis of HCM patients (6–8). As two biomarkers of cardiac injuries exist in the blood circulation system, cardiac troponin (cTnT) and N-terminal prohormone of the brain natriuretic peptide (NT-proBNP) are used for many cardiac diseases (9–11). However, there are few studies reporting the relationships between left ventricular (LV) strain patterns and cardiac biomarkers in HCM patients with preserved LVEF. Given this gap, this present study is intended to use LV strain patterns to assess HCM patients with preserved LVEF and to explore the relationships between LV strain patterns and NT-proBNP (or cTnT) in HCM patients with preserved LVEF.

Methods

Patients and controls

A total of 64 HCM patients with preserved LVEF and 33 healthy people were included in this retrospective study at West China Hospital, Sichuan University, Chengdu, China. They all underwent contrast-enhanced CMR exams during their hospitalization from February 2018 to February 2022. HCM patients also took the biochemical tests on NT-proBNP and cTnT not exceeding ± 3 days before or after the CMR exams. During the same period, healthy subjects received contrast-enhanced CMR exams at West China Hospital, Sichuan University, Chengdu. According to the guidelines of the European Society of Cardiology (ESC) (12), HCM is defined as the maximum diastolic wall above 15 mm in thickness. The exclusion criteria for HCM patients are as follows: (1) age $<$ 18; (2) LVEF $\leq$ 50%; (3) blood pressure $\geq$ 160/100 mmHg, complete bundle branch block, coronary stenosis higher than 20%, permanent mechanical device implant, myocardial resection, alcohol septal ablation or heart transplant, related valvular dysfunction, glomerular filtration rate (GFR) $<$ 60 mL/min/1.73m^2, malignant tumor, severe infection, connective tissue disease, and other systemic diseases. (4) suffering from diseases that cause elevated levels of adrenaline, glucocorticoids, and thyroxine—such as pheochromocytoma, Cushing's syndrome, primary thyroid hyperthyroidism, and sub-acute thyroiditis. (5) poor CMR image quality for post-processing. The threshold value of cTnT is 14 pg/mL (13). According to the 2017 American Heart Association (AHA) criteria, the cut-off value of NT-proBNP is 800 pg/mL (14). The criteria for excluding the

---

Abbreviations: HCM, Hypertrophic cardiomyopathy; CMR, Cardiac magnetic resonance; LVEF, Left ventricular ejection fraction; CMR-FT, Cardiac magnetic resonance feature tracking; NT-proBNP N,-terminal prohormone of the brain natriuretic peptide; cTnT, Cardiac troponin T; LV, Left ventricular; LGE, Late gadolinium enhancement; MLVWT, Maximum LV wall thickness; GRS, Global radial strain; GCS, Global circumferential strain; GLS, Global longitudinal strain; ARS, Apical radial strain; ACS, Apical circumferential strain; ALS, Apical longitudinal strain; MRS, Mid-ventricular radial strain; MCS, Mid-ventricular circumferential strain; MLS, Mid-ventricular longitudinal strain; BRS, Basal radial strain; BCS, Basal circumferential strain; BLS, Basal longitudinal strain; ICC, Intraclass correlation coefficient; SD, Standard deviation; IQR, Interquartile range; NYHA, New York Heart Association; ROC, Receiver operating characteristic; CI, Confidence interval; LVOTO, Left ventricular outflow tract obstruction; AUC, Area under the curve.

controls included chronic disease, cardiovascular disease, family history, hypertension (blood pressure ≥ 140/90 mmHg), or severe arrhythmia. The Ethics Committee approved all data in this study of West China Hospital, Sichuan University, Chengdu, China, in agreement with the Helsinki Declaration.

CMR protocol

CMR images were obtained using Siemens 3.0 T CMR scanners (Skyra; Siemens Medical Solutions, Erlangen, Germany) in a supine position with the head first. Electrocardiographic gating and respiratory gating were adopted during the scanning. Cine-CMR views, including 2- and 4-chamber long-axis views and a set of short-axis views covering the entire LV, were required using the sequence of balanced steady-state free-precession. Scan parameters included the field of view = 350–400 mm, repetition time/echo time = 3.0–3.6/1.5–1.8 ms, flip angle = 60°, and slice thickness = 8 mm. Late gadolinium enhancement (LGE) images were obtained 10 to 15 min after intravenous administration of gadodiamide (Magnevist; Bayer Schering Pharma, Berlin, Germany) at a speed of 0.2 mmol/kg scanned by the inversion recovery echo sequence. Its parameters included field of view = 350–400 mm, repetition time/echo time = 4.5–4.6/1.3–1.5 ms, flip angle =15°, inversion time = 200–300 ms, and slice thickness = 8 mm.

CMR data analysis

Two radiologists conducted CMR data analysis with over 5 years of experience in imaging analysis. When they differed in opinion, they would negotiate with each other to achieve a consensus. The CMR image data acquired from the scanning workstation were loaded in software named "CVI.42" (Circle Cardiovascular Imaging, version 5.11, Calgary, AB, Canada) for analyzing LV function and characterization. First, a short-axis stock was dragged into the SHORT 3D module by drawing up the optimal endocardium and epicardium to acquire the basic cardiac function parameters, including LVEF, end-diastolic volume, end-systolic volume, and stroke volume. Meanwhile, a cardiac cycle measured maximum left ventricle wall thickness (MLVWT) during the end of diastole. Second, 2- and 4-chamber long-axis views and a set of short-axis views were transmitted into the Feature Tracking module. The optimal endocardium and epicardium were drawn up, excluding papillary muscles (Figure 1). Then CVI.42 would automatically calculate the cardiac strain parameters such as global and segmental strains (Figure 1). LV contractility was evaluated by global radial strain (GRS), global circumferential strain (GCS), global longitudinal strain (GLS), apical radial strain (ARS), apical circumferential strain (ACS), apical longitudinal strain (ALS), mid-ventricular radial strain (MRS), mid-ventricular circumferential strain (MCS), mid-ventricular longitudinal strain (MLS), basal radial strain (BRS), basal circumferential strain (BCS), and basal longitudinal strain (BLS).

Repeatability

Scans of 20 randomly selected subjects in patients and controls were repeatedly examined by the same observer with an interval of 2 weeks to represent the intra-observer repeatability by calculating the intra-class correlation coefficient (ICC). ICC also represented inter-observer repeatability, which was generated by measuring the same subject by two independent, experienced, and double-blinded observers.

Statistical analysis

Statistical analysis was performed by IBM SPSS (V. 26.0, ARMONK, NY, USA). The mean ± standard deviation (SD) or median with interquartile range (IQR) [25%, 75%] was used to represent continuous variables. The Chi-square test or Fisher's exact test was performed to assess the difference in classified data such as sex, clinical symptoms, etc. The Mann–Whitney U-test or Student's *t*-test was used to compare the continuous variables, including MLVWT, LVEF, strain, etc. The difference in New York Heart Association (NYHA) classification was presented by the Kruskal–Wallis rank test. The receiver operating characteristic (ROC) curve was analyzed to assess the predictive value of LV strain parameters for elevated NT-proBNP and abnormal cTnT in HCM patients. ICC was used to assess the intra- and inter-observer consistency, whose values were defined as the 95% confidence interval (CI) lower limit exhibited poor (< 0.5), moderate (0.5–0.75), good (0.75–0.9), or excellent (> 0.9) reliability (15). The Spearman's rank correlation coefficient was calculated to assess the correlations between continuous parameters when a two-tailed $p < 0.05$, and the difference in the corresponding data was considered statistically significant.

Results

Patient characteristics

There were 64 patients and 33 healthy controls included in the study. There was no significant difference in age (mean age, 48 ± 10 years vs. 50 ± 14 years; $p = 0.365$), LVEF (61.02 ± 5.40 % vs. 62.92 ± 8.00 %; $p = 0.170$) and sex (39

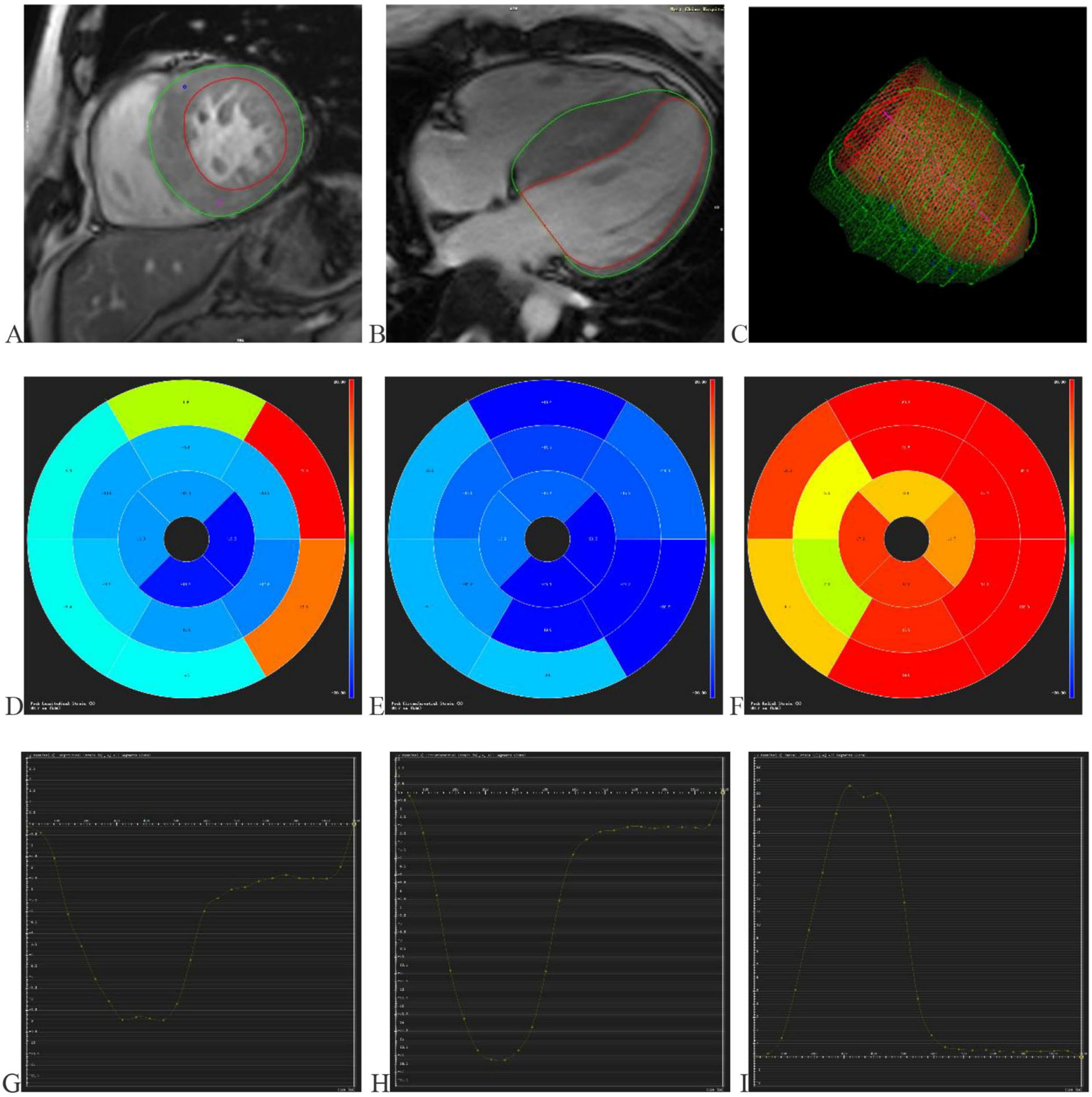

FIGURE 1
Displays the progress and outcomes of LV strains. **(A)** Delineating the LV endocardium and epicardium in the short-axis view. **(B)** Delineating the LV endocardium and epicardium in the 4-chamber long axis view. **(C)** The optimal endocardium and epicardium are shown in 3D space. The segmental strain round cake is mapped into 16 sections in the circumferential **(D)**, longitudinal **(E)**, and radial **(F)** directions. The global circumferential **(G)**, longitudinal **(H)**, and radial **(I)** strain curves in one cardiac cycle. LV (left ventricular).

men and 25 women vs. 20 men and 13 women; $p = 0.975$) between the two groups. It can be seen that, compared to controls, the MLVWT in HCM patients significantly thickened. In the HCM group, there were 53 (82.81%) patients showing positive LGE, 7 (10.94%) showing atrial fibrillation, 42 (65.63%) showing left ventricular outflow tract obstruction (LVOTO), and 27 (42.19%) showing mitral regurgitation. According to NYHA classification, 13 (20.31%) individuals were NYHA class I, 40 (62.50%) were NYHA class II, 8 (12.50%) were NYHA class III, and 3 (4.69%) were NYHA class IV in this group. Interestingly, almost all LGE positive parts overlapped with the regions of myocardial hypertrophy and were mainly in the mid-wall. Other basic information is supplemented in Table 1.

TABLE 1 Basic information about HCM patients and healthy controls.

Parameter, unit	**Controls ($n = 33$)**	**HCM ($n = 64$)**	***p*-value**
Age, years, (SD)	48 (10)	50 (14)	0.365
Male, *n (%)*	20 (73.33)	39 (60.94)	0.975
Heart rate, bpm, (SD)	N/A	72 (11)	
Respiration, rpm, (SD)	N/A	20 (1)	
Height, cm, (SD)	N/A	162 (9)[a]	
Weight, kg, (SD)	N/A	62.6 (10.5)	
Dizzy, *n (%)*	N/A	10 (15.63)	-
Bosom frowsty, *n (%)*	N/A	30 (46.88)	-
Bosom painful, *n (%)*	N/A	29 (45.31)	-
Palpitation, *n (%)*	N/A	15 (23.44)	-
Amaurosis, *n (%)*	N/A	11 (17.19)	-
Syncope, *n (%)*	N/A	15 (23.44)	-
Family histories, *n (%)*	N/A	3 (4.69)	-
Personal histories			
Smoking, *n (%)*	N/A	21 (32.81)	-
Drinking, *n (%)*	N/A	9 (14.06)	-
Atrial fibrillation, *n (%)*	0	7 (10.94)	0.144
NYHA classification (I/II/III/IV)	N/A	13/40/8/4	-
Volumes and functions			
LVEF, % (SD)	61.02 (5.40)	62.92 (8.00)	0.170
LVEDV, mL (SD)	127.54 (27.81)	133.57 (29.59)	0.334
LVESV, mL (SD)	50.00 (14.26)	50.64 (17.41)	0.856
LVSV, mL (SD)	77.53 (16.59)	82.77 (17.69)	0.161
MLVWT, mm, (SD)	8.61 (1.69)	22.00 (5.53)	<0.001*
RVEF, % (SD)	56.60 (7.35)	58.53 (9.33)	0.268
RVEDV, mL (SD)	119.12 (29.37)	95.15 (25.74)	<0.001*
RVESV, mL (IQR)	49.40 (40.10, 63.90)	39.00 (31.40, 49.58)	0.004*
RVSV, mL (SD)	66.31 (14.11)	55.48 (16.60)	0.002*
LGE presence, *n (%)*	0	53 (82.81)	<0.001*
Mitral regurgitation, *n (%)*	0	27 (42.19)	<0.001*
LVOTO, *n (%)*	0	42 (65.62)	<0.001*
Biomarkers, pg/mL			
NT-proBNP (IQR)	N/A	989.00(356.50, 1869.75)[b]	-
cTnT (IQR)	N/A	14.25(9.98, 22.83)	-

Statistical significance was defined as $p < 0.05$. Data were expressed as mean (SD), absolute numbers (percentages), or median (IQR 25%, 75%).

*$p < 0.05$ vs. controls. HCM, hypertrophic cardiomyopathy; SD, standard deviation; IQR, interquartile range; NYHA, New York Heart Association; LVEF, left ventricular ejection fraction; LVEDV, left ventricular end-diastolic volume; LVESV, left ventricular end-systolic volume; LVSV, left ventricular stroke volume; RVEF, right ventricular ejection fraction; RVEDV, right ventricular end-diastolic volume; RVESV, right ventricular end-systolic volume; RVSV, right ventricular stroke volume; LGE, late gadolinium enhancement; LVOTO, left ventricular outflow tract obstruction; NT-proBNP, N-terminal prohormone of the brain natriuretic peptide; and cTnT, cardiac troponin T.

[a] Height was available in n = 61. b NT-proBNP was available in n = 62.

LV myocardial deformation in HCM patients and healthy controls

Even though no significant difference was observed in LVEF (61.02 ± 5.40 % vs. 62.92 ± 8.00 %; $p = 0.170$) between HCM patients and controls, compared controls, all LV global and segmental strains in HCM patients showed a trend of impairment with statistical significance except for ARS and BCS. Those above specific values can be seen in Table 2.

NT-ProBNP

There were 35 (56.45%) HCM patients in the elevated NT-proBNP group ($\geq$ 800 pg/mL) and 27 (43.55%) HCM patients in the non-elevated NT-proBNP group ($<$ 800 pg/mL). However, the indicators of two patients were unfortunately lost. Between the two groups, there was no significant difference in age (mean age, 49 ± 13 years vs. 50 ± 16 years; $p = 0.765$) and LVEF (63.97 ± 7.23% vs. 62.06 ± 8.43 %; $p = 0.351$). However, compared to the non-elevated NT-proBNP group, GRS, GCS, ARS, ACS, MRS, MCS, BRS, and BCS decreased significantly in the elevated NT-proBNP group ($p < 0.05$). Although the differences in GLS, ALS, MLS, and BLS between the two groups were not statistically significant ($p > 0.05$), they still exhibited a declining trend. The accurate values of all the above strains across the two groups are presented in Table 3. Among the LV deformation parameters in HCM patients, GRS ($r = -0.553$, $p < 0.001$) showed the best correlation with NT-proBNP level in the global strains, while MRS ($r = -0.475$, $p < 0.001$) showed the best correlation with NT-proBNP level in the segmental strains (Table 4). In addition, GRS showed the highest predictive value for elevated NT-proBNP [area under the curve (AUC), 0.76; sensitivity, 0.49; specificity, 1.00] in the global strains, while BRS showed the highest predictive value for elevated NT-proBNP (AUC, 0.72; sensitivity, 0.69; specificity, 0.82) in the segmental strains (Figure 2). Their cut-off values were 21.17 and 33.57%, respectively.

cTnT

There were 29 (45.31%) patients in the normal cTnT group ($<$ 14 pg/mL) and 35 (54.69%) patients in the abnormal cTnT group ($\geq$ 14 pg/mL). There was no significant difference between the two groups in age (mean age, 53 ± 12 years vs. 48 ± 16 years; $p = 0.243$) and sex (16 men and 13 women vs. 23 men and 12 women; $p = 0.390$). Compared to that in the normal cTnT group, GRS, GCS, GLS, ARS, ACS, ALS, MRS, MCS, and BRS in the abnormal cTnT group decreased significantly ($p < 0.05$), and MLS, BCS, and BLS also tended to decline, regardless of hardly any statistical difference ($p >$ 0.05). These detailed data are presented in Table 5. Among the

TABLE 2 LV strains in HCM patients and healthy controls.

Strain, %	**Controls ($n = 33$)**	**HCM ($n = 64$)**	***p*–value**
GRS (IQR)	36.84 (27.94, 41.29)	24.60 (20.69, 35.09)	0.001*
GCS (IQR)	−21.01 (−22.84, −17.94)	−17.79 (−20.92, −12.14)	0.007*
GLS (SD)	−14.67 (3.14)	−9.44 (3.41)	<0.001*
ARS (IQR)	29.53 (23.83, 43.73)	26.36 (19.96, 38.09)	0.201
ACS (IQR)	−23.91 (−26.82, −18.63)	−19.68 (−24.16, −16.11)	0.016*
ALS (SD)	−17.85 (2.69)	−14.00 (3.73)	<0.001*
MRS (IQR)	28.62 (24.09, 38.51)	20.73 (15.01, 29.73)	<0.001*
MCS (SD)	−20.50 (3.95)	−17.18 (4.35)	<0.001*
MLS (SD)	−14.57 (3.51)	−8.64 (4.59)	<0.001*
BRS (IQR)	46.35 (36.87, 59.07)	34.31 (27.71, 41.73)	<0.001*
BCS (IQR)	−18.29 (−21.19, −16.11)	−16.88 (−19.28, −14.66)	0.114
BLS (IQR)	−10.99 (−14.46, −7.61)	−5.32 (−9.95, 5.07)	<0.001*

Statistical significance was defined as $p < 0.05$. Data were expressed as mean (SD) or median (IQR 25%, 75%).

[*] $p < 0.05$ vs. controls. LV left ventricular; HCM, hypertrophic cardiomyopathy; SD, standard deviation; IQR, interquartile range; GRS, global radial strain; GCS, global circumferential strain; GLS, global longitudinal strain; ARS, apical radial strain; ACS, apical circumferential strain; ALS, apical longitudinal strain; MRS, mid–ventricular radial strain; MCS, mid–ventricular circumferential strain; MLS, mid–ventricular longitudinal strain; BRS, basal radial strain; BCS, basal circumferential strain; and BLS, basal longitudinal strain.

TABLE 3 LV strains in HCM patients with and without elevated NT–proBNP.

Strain, %	**NT–proBNP < 800 pg/mL ($n = 27$)**	**NT–proBNP≥ 800 pg/mL ($n = 35$)**	***p*–value**
GRS (IQR)	30.00 (23.96, 41.42)	21.87 (18.68, 28.61)	0.001*
GCS (SD)	−19.63 (4.02)	−16.41 (3.62)	0.002*
GLS (IQR)	−11.35 (−12.90, −8.29)	−9.37 (−10.57, −6.11)	0.058
ARS (IQR)	31.08 (25.89, 40.98)	22.54 (17.26, 32.33)	0.011*
ACS (SD)	−21.62 (3.45)	−18.45 (5.41)	0.030*
ALS (SD)	−14.79 (3.44)	−13.35 (3.17)	0.093
MRS (SD)	28.12 (12.93)	19.16 (7.90)	0.003*
MCS (SD)	−18.90 (4.51)	−15.71 (3.66)	0.003*
MLS (IQR)	−9.38 (−13.54, −4.68)	−9.40 (−11.20, 6.47)	0.230
BRS (IQR)	38.34 (34.13, 53.56)	30.17 (24.59, 38.40)	0.003*
BCS (IQR)	−18.45 (−19.55, −16.20)	−16.61 (−18.46, −14.08)	0.005*
BLS (IQR)	−5.63 (−10.75, −2.27)	−3.90 (−8.45, 6.66)	0.109

Statistical significance was defined as $p < 0.05$. Data were expressed as mean (SD) or median (IQR 25%, 75%).

[*] $p < 0.05$ vs. controls. LV left ventricular; HCM, hypertrophic cardiomyopathy; SD, standard deviation; IQR, interquartile range; GRS, global radial strain; GCS, global circumferential strain; GLS, global longitudinal strain; ARS, apical radial strain; ACS, apical circumferential strain; ALS, apical longitudinal strain; MRS, mid–ventricular radial strain; MCS, mid–ventricular circumferential strain; MLS, mid–ventricular longitudinal strain; BRS, basal radial strain; BCS, basal circumferential strain; BLS, basal longitudinal strain; and NT–proBNP, N–terminal prohormone of the brain natriuretic peptide.

LV deformation parameters in HCM patients, GRS ($r = -0.535$, $p < 0.001$) showed the best correlation with cTnT level in the global strains, while MRS ($r = -0.582$, $p < 0.001$) showed the best correlation with cTnT level in the segmental strains (Table 6). Furthermore, GRS showed the highest predictive value for abnormal cTnT (AUC, 0.75; sensitivity, 1.00; specificity, 0.45) in the global strains, while MRS showed the highest predictive value for abnormal cTnT (AUC, 0.81; sensitivity, 0.77; specificity, 0.79) in the segmental strains (Figure 2). Their cut-off values were 37.91 and 20.94%, respectively.

Reproducibility

GLS exhibited a good intra- (ICC = 0.94; 95% CI, 0.86–0.97) and an excellent inter-observer (ICC = 0.97; 95% CI, 0.92–0.99) reproducibility. GRS also exhibited a good intra- (ICC = 0.93; 95% CI, 0.83–0.97) and a moderate inter-observer (ICC = 0.85; 95% CI, 0.65–0.94) reproducibility, whereas GCS exhibited a moderate intra- (ICC = 0.85; 95% CI, 0.66–0.94) and an excellent inter-observer (ICC = 0.98; 95% CI, 0.94–0.99) reproducibility.

Discussion

This study has made the following findings. First, despite the insignificant difference in LVEF between controls and HCM patients, all LV global and segmental strains in HCM patients exhibited a declining trend with statistical significance except for ARS and BCS. Second, NT-proBNP levels in most HCM patients increased. Compared to the non-elevated NT-proBNP group (< 800 pg/mL), some global and segmental strains, including GRS, GCS, ARS, ACS, MRS, MCS, BRS, and BCS in the elevated NT-proBNP group, decreased significantly. Third, the cTnT level in some HCM patients increased. In addition, LV global and segmental strains in the abnormal cTnT group, except for MLS, BCS, and BLS, had decreased significantly compared to the normal cTnT group in HCM patients. Fourth, some strains were correlated considerably with NT-proBNP and cTnT in HCM patients, with the optimal correlations falling on GRS in the global strains and MRS in the segmental strains.

TABLE 4 Correlations of LV strains with NT–proBNP in HCM patients.

Strain (%)	**NT–proBNP (pg/mL)**	
	Rho	***p***
GRS	−0.553	<0.001
GCS	0.428	0.001
GLS	0.281	0.027
ARS	−0.381	0.002
ACS	0.281	0.027
ALS	0.315	0.013
MRS	−0.475	<0.001
MCS	0.434	<0.001
MLS	0.225	0.079
BRS	−0.430	<0.001
BCS	0.335	0.008
BLS	0.126	0.327

Statistical significance was defined as $p < 0.05$. LV left ventricular; HCM, hypertrophic cardiomyopathy; GRS, global radial strain; GCS, global circumferential strain; GLS, global longitudinal strain; ARS, apical radial strain; ACS, apical circumferential strain; ALS, apical longitudinal strain; MRS, mid–ventricular radial strain; MCS, mid–ventricular circumferential strain; MLS, mid–ventricular longitudinal strain; BRS, basal radial strain; BCS, basal circumferential strain; BLS, basal longitudinal strain; and NT–proBNP, N–terminal prohormone of the brain natriuretic peptide.

Furthermore, BRS and MRS showed the highest predictive value for elevated NT-proBNP and abnormal cTnT in the segmental strains, respectively. Among the global strains, GRS showed the highest predictive value for elevated NT-proBNP and abnormal cTnT. Lastly, global strains in the three directions presented moderate to slightly high intra- and inter-observer reproducibility. The best intra- and inter-observer reproducibility was exhibited by GLS and GCS, respectively.

LV myocardial deformation

First, this study focused on HCM with preserved LVEF in hospitalized patients. Therefore, the percentage of HCM patients with LGE (82.81%) and LVOTO (65.63%) was high compared with a prior study that focused on all HCM patients with preserved LVEF (16). Such an approach helped us learn more accurately about more serious HCM patients of this subtype, thus promoting their clinical management.

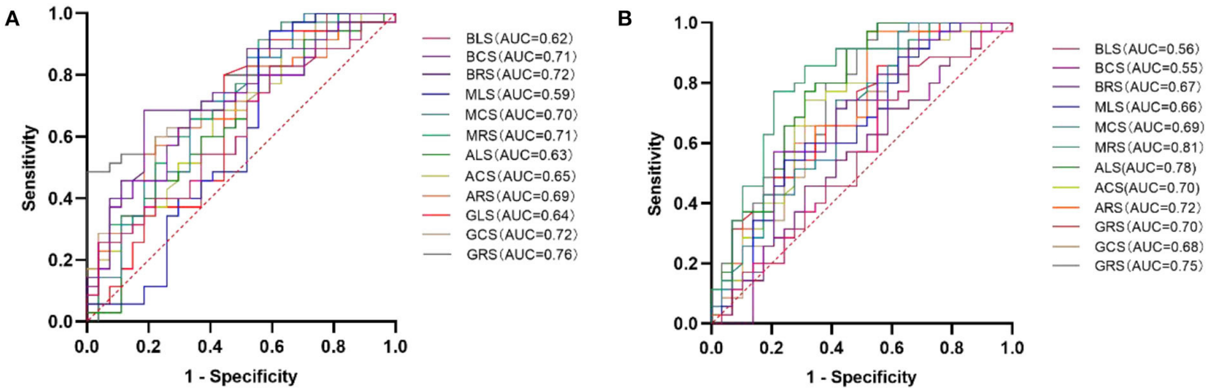

FIGURE 2
ROC curve analysis of LV deformation parameters for predicting elevated NT-proBNP **(A)** and cTnT **(B)** in HCM patients. HCM, hypertrophic cardiomyopathy; LV, left ventricular; ROC, receiver operating characteristic; AUC, area under the curve; GRS, global radial strain; GCS, global circumferential strain; GLS, global longitudinal strain; ARS, apical radial strain; ACS, apical circumferential strain; ALS, apical longitudinal strain; MRS, mid-ventricular radial strain; MCS, mid-ventricular circumferential strain; MLS, mid-ventricular longitudinal strain; BRS, basal radial strain; BCS, basal circumferential strain; BLS, basal longitudinal strain; NT-proBNP, N-terminal prohormone of the brain natriuretic peptide; and cTnT, cardiac troponin T.

TABLE 5 LV strains in HCM patients with and without elevated cTnT.

Strain, %	cTnT < 14 pg/mL ($n = 29$)	cTnT ≥ 14 pg/mL ($n = 35$)	p–value
GRS (SD)	35.00 (14.18)	23.50 (6.26)	<0.001*
GCS (SD)	−19.24 (4.54)	−16.73 (3.35)	0.014*
GLS (SD)	−10.75 (3.33)	−8.36 (3.12)	0.004*
ARS (IQR)	30.17 (24.22, 53.42)	24.45 (17.60, 32.33)	0.003*
ACS (SD)	−22.11 (5.81)	−18.17 (5.15)	0.006*
ALS (SD)	−15.76 (3.26)	−12.54 (2.74)	<0.001*
MRS (SD)	29.59 (12.06)	18.06 (7.34)	<0.001*
MCS (SD)	−18.85 (4.63)	−15.80 (3.62)	0.004*
MLS (SD)	−9.80 (4.77)	−7.67 (4.27)	0.065
BRS (IQR)	38.34 (32.88, 55.44)	30.17 (26.56, 38.78)	0.022*
BCS (SD)	−17.23 (4.41)	−17.23 (2.63)	0.963
BLS (IQR)	−5.56 (−10.71, 4.59)	−5.31 (−8.88, 5.58)	0.434

Statistical significance was defined as $p < 0.05$. Data were expressed as mean (SD) or median (IQR 25%, 75%).

*$p < 0.05$ vs. controls. LV left ventricular; HCM, hypertrophic cardiomyopathy; SD, standard deviation; IQR, interquartile range; GRS, global radial strain; GCS, global circumferential strain; GLS, global longitudinal strain; ARS, apical radial strain; ACS, apical circumferential strain; ALS, apical longitudinal strain; MRS, mid–ventricular radial strain; MCS, mid–ventricular circumferential strain; MLS, mid–ventricular longitudinal strain; BRS, basal radial strain; BCS, basal circumferential strain; BLS, basal longitudinal strain; and cTnT, cardiac troponin.

TABLE 6 Correlations of LV strains with cTnT in HCM patients.

Strain (%)	cTnT (pg/mL)	
	Rho	P
GRS	−0.535	<0.001
GCS	0.401	0.001
GLS	0.408	0.001
ARS	−0.455	<0.001
ACS	0.398	0.001
ALS	0.537	<0.001
MRS	−0.582	<0.001
MCS	0.411	0.001
MLS	0.330	0.008
BRS	−0.343	0.005
BCS	0.088	0.488
BLS	0.126	0.321

Statistical significance was defined as $p < 0.05$. LV left ventricular; HCM, hypertrophic cardiomyopathy; GRS, global radial strain; GCS, global circumferential strain; GLS, global longitudinal strain; ARS, apical radial strain; ACS, apical circumferential strain; ALS, apical longitudinal strain; MRS, mid–ventricular radial strain; MCS, mid–ventricular circumferential strain; MLS, mid–ventricular longitudinal strain; BRS, basal radial strain; BCS, basal circumferential strain; BLS, basal longitudinal strain; and cTnT, cardiac troponin T.

Second, consistent with a previous study (6), we also found that even though the difference in LVEF between the two groups was not significant, LV strains of HCM patients were impaired significantly compared with healthy people, which may be related to the fact that, in the progress of HCM, cardiac hypertrophy and coronary microvascular dysfunction result in ischemia and fibrosis, which lead to a decrease in myocardial contraction ability (17–19). Therefore, CMR-FT can indicate changes in subclinical myocardial contractility in HCM patients independent of LVEF and heart failure (HF) classification. Besides, compared with using LVEF for assessing global cardiac function, CMR-FT can more clearly and accurately demonstrate the impaired local cardiac function by means of changes in segmental strains.

Furthermore, we found that global strains from the three directions showed moderate to better intra- and inter-observer reproducibility. GLS showed the best intra-observer reproducibility, and GLS showed the best inter-observer reproducibility. Some authors proposed that the poor reproducibility for GRS might be due to the geometry of the heart with analysis in a plane of movement with the smallest potential diameter for tracking (20), while other people speculated that the lower reproducibility of GRS might be correlated with the measurement of the interaction of the epicardium and endocardium during the tracking, which is not necessary for the derivation of GLS and GCS (21).

NT-ProBNP and cTnT

NT-proBNP, a neurohormone, is synthesized and released by atrial cells in normal organs. Nonetheless, with the development of HF, ventricular cells can also generate it in response to wall stress (22). NT-proBNP has emerged as a useful and reliable biomarker in diagnosing and predicting HF (23). Furthermore, it may also be conducive to the risk stratification of some cardiac diseases (24, 25). Compared with BNP, NT-proBNP is more stable on the merit of its longer half-life (23). Some studies reported that NT-proBNP was associated with cardiac fibrosis, deterioration of cardiac function, and prognosis in HCM patients (26–29). According to the 2016 ESC guideline (30), the NT-proBNP cutoff value is 125 pg/mL, whereas the 2017 AHA criteria suggested using a threshold of 800 pg/mL (14). A study indicated that compared to the cut-off value of NT-proBNP of the ESC guideline, the AHA criteria are more conducive to risk stratification in HCM patients (31). Accordingly, in this study, we chose 800 pg/mL as the threshold criterion for the group. c-TnT was considered a preferred biomarker in detecting cardiac injury owing to its high sensitivity and specificity (32). Some studies found that as cTnT could be elevated in many HCM patients, it could predict the prognosis and help with risk stratification in HCM patients (32–35). In this study, we found that there were 35 patients (56.45%) with elevated NT-proBNP and 35 (54.69%) patients in the abnormal cTnT group, which is consistent with the previous studies (28, 29, 34, 36). Furthermore, we also found that some global and segmental strains decreased significantly in the elevated NT-proBNP group compared to the non-elevated NT-proBNP group. The performance of the groups with and without elevated cTnT was similar to that of the NT-proBNP group. Additionally, some strains were significantly correlated with NT-proBNP and cTnT in HCM patients. The best strains were GRS (NT-proBNP: $r = -0.553$, $p < 0.001$; cTnT: $r = -0.535$, $p < 0.001$) in the global strains and MRS (NT-proBNP: $r = -0.475$, $p < 0.001$; cTnT: $r = -0.582$, $p < 0.001$) in the segmental strains with moderate correlations. According to ROC analysis, we found that BRS (AUC, 0.72; sensitivity, 0.69; specificity, 0.82) and MRS (AUC, 0.81; sensitivity, 0.77; specificity, 0.79) showed the highest predictive value for elevated NT-proBNP and abnormal cTnT in the segmental strains, respectively. Their cut-off values were 33.57 and 20.94%, respectively. Among the global strains, GRS showed the highest predictive value for elevated NT-proBNP (AUC, 0.76; sensitivity, 0.49; specificity, 1.00) and abnormal cTnT (AUC, 0.75; sensitivity, 1.00; specificity, 0.45). Their cut-off values were 21.17 and 37.91%, respectively. Therefore, LV strain patterns can be used to monitor changes in HCM and detect more severe cases to improve the health management of HCM patients and may be used to non-invasively predicate elevated NT-proBNP and cTnT to avoid the risks caused by clinical operations. What's more, some studies have indicated that CMR-FT can be used to predict the adverse prognosis of HCM patients (6–8). Certainly, it warrants to be verified in future studies as to whether predicting the prognosis of HCM patients by using CMR-FT together with cardiac biomarkers simultaneously is better than such prediction by using them separately.

Limitation

First, as this is a single-centered retrospective study based upon a small sample focusing on inpatients with HCM, the applicable range of its conclusion cannot be extended to all HCM patients with preserved LVEF. Moreover, some multi-centered and extensive sample prospective studies are needed to validate the accuracy and significance of the views proposed by this study. Second, as a retrospective study, some data were missing, such as some values of NT-proBNP and height. Moreover, as this is a retrospective study, it is hardly possible to explore the relationship between the strain and other parameters based on CMR, such as T_1 mapping, extracellular volume, and T_2 mapping. Meanwhile, the comparison between CMR-FT and other imaging techniques that can assess cardiac strain, such as speckle tracking echocardiography, was also impossible. Finally, this study focused on the correlations between LV strain patterns and cardiac biomarkers in HCM patients. However, as mentioned in the discussion section, the ability to predict the prognosis of HCM patients by combining CMR-FT and cardiac biomarkers is worth further study.

Conclusion

LV strain patterns can be used to assess the subclinical cardiac function of HCM patients on the merit of being more sensitive than LVEF. In addition, LV strain patterns can detect serious HCM patients and may be helpful to non-invasively predict elevated NT-proBNP and cTnT.

Data availability statement

The original contributions presented in the study are included in the article/supplementary material, further inquiries can be directed to the corresponding author.

Ethics statement

The studies involving human participants were reviewed and approved by Ethics Committee of Sichuan University West China Hospital. Written informed consent for participation was not required for this study in accordance with the national legislation and the institutional requirements.

Author contributions

LZ and YW planned and wrote the manuscript. BH, LW, DZ, and FG edited the manuscript. All authors contributed to the article and approved the submitted version.

Funding

The project was supported by the National Natural Science Foundation of China (Nos. 81930046 and 81829003).

Conflict of interest

The authors declare that the research was conducted in the absence of any commercial or financial relationships that could be construed as a potential conflict of interest.

Publisher's note

References

1. Maron BJ, Maron MS. Hypertrophic cardiomyopathy. *Lancet.* (2013) 381:242–55. doi: 10.1016/S0140-6736(12)60397-3

2. Ommen SR. Hypertrophic cardiomyopathy. *Curr Probl Cardiol.* (2011) 36:409–53. doi: 10.1016/j.cpcardiol.2011.06.001

3. Shimada YJ, Hoeger CW, Latif F, Takayama H, Ginns J, Maurer MS. Myocardial contraction fraction predicts cardiovascular events in patients with hypertrophic cardiomyopathy and normal ejection fraction. *J Card Fail.* (2019) 25:450–6. doi: 10.1016/j.cardfail.2019.03.016

4. Ochs A, Riffel J, Ochs MM, Arenja N, Fritz T, Galuschky C, et al. Myocardial mechanics in dilated cardiomyopathy: prognostic value of left ventricular torsion and strain. *J Cardiovasc Magn Reson.* (2021) 23:136. doi: 10.1186/s12968-021-00829-x

5. Song Y, Li L, Chen X, Ji K, Lu M, Hauer R, et al. Left Ventricular longitudinal dyssynchrony by CMR feature tracking is related to adverse prognosis in advanced arrhythmogenic cardiomyopathy. *Front Cardiovasc Med.* (2021) 8:712832. doi: 10.3389/fcvm.2021.712832

6. Yang L, Zhang L, Cao S, Gao C, Xu H, Song T, et al. Advanced myocardial characterization in hypertrophic cardiomyopathy: feasibility of CMR-based feature tracking strain analysis in a case-control study. *Eur Radiol.* (2020) 30:6118–28. doi: 10.1007/s00330-020-06922-6

7. Hinojar R, Fernández-Golfín C, González-Gómez A, Rincón LM, Plaza-Martin M, Casas E, et al. Prognostic implications of global myocardial mechanics in hypertrophic cardiomyopathy by cardiovascular magnetic resonance feature tracking. Relations to left ventricular hypertrophy and fibrosis. *Int J Cardiol.* (2017) 249:467–72. doi: 10.1016/j.ijcard.2017.07.087

8. Negri F, Muser D, Driussi M, Sanna GD, Masè M, Cittar M, et al. Prognostic role of global longitudinal strain by feature tracking in patients with hypertrophic cardiomyopathy: the STRAIN-HCM study. *Int J Cardiol.* (2021) 345:61–7. doi: 10.1016/j.ijcard.2021.10.148

9. Bosello S, De Luca G, Berardi G, Canestrari G, de Waure C, Gabrielli FA, et al. Cardiac troponin T and NT-proBNP as diagnostic and prognostic biomarkers of primary cardiac involvement and disease severity in systemic sclerosis: a prospective study. *Eur J Intern Med.* (2019) 60:46–53. doi: 10.1016/j.ejim.2018.10.013

10. Chmielewski P, Truszkowska G, Kowalik I, Rydzanicz M, Michalak E, Sobieszczańska-Małek M, et al. Titin-related dilated cardiomyopathy: the clinical trajectory and the role of circulating biomarkers in the clinical assessment. *Diagnostics (Basel).* (2021) 12:692235. doi: 10.21203/rs.3.rs-692235/v1

11. deFilippi C, Wasserman S, Rosanio S, Tiblier E, Sperger H, Tocchi M, et al. Cardiac troponin T and C-reactive protein for predicting prognosis, coronary atherosclerosis, and cardiomyopathy in patients undergoing long-term hemodialysis. *JAMA.* (2003) 290:353–59. doi: 10.1001/jama.290.3.353

12. Elliott PM, Anastasakis A, Borger MA, Borggrefe M, Cecchi F, Charron P, et al. 2014 ESC guidelines on diagnosis and management of hypertrophic cardiomyopathy: the task force for the diagnosis and management of hypertrophic cardiomyopathy of the European Society of Cardiology (ESC). *Eur Heart J.* (2014) 35:2733–79. doi: 10.1093/eurheartj/ehu284

13. Saenger AK, Beyrau R, Braun S, Cooray R, Dolci A, Freidank H, et al. Multicenter analytical evaluation of a high-sensitivity troponin T assay. *Clin Chim Acta.* (2011) 412:748–54. doi: 10.1016/j.cca.2010.12.034

14. Yancy CW, Jessup M, Bozkurt B, Butler J, Casey DE, Jr., Colvin MM, et al. 2017 ACC/AHA/HFSA focused update of the 2013 ACCF/AHA guideline for the management of heart failure: a report of the American College of Cardiology/American Heart Association task force on clinical practice guidelines and the heart failure society of America. *Circulation.* (2017) 136:e137–161. doi: 10.1161/CIR.0000000000000509

15. Koo TK, Li MY. A guideline for selecting and reporting intraclass correlation coefficients for reliability research. *J Chiropr Med.* (2016) 15:155–63. doi: 10.1016/j.jcm.2016.02.012

16. Mahmod M, Raman B, Chan K, Sivalokanathan S, Smillie RW, Samat AHA, et al. Right ventricular function declines prior to left ventricular ejection fraction in hypertrophic cardiomyopathy. *J Cardiovasc Magn Reson.* (2022) 24:36. doi: 10.1186/s12968-022-00868-y

17. Knaapen P, Germans T, Camici PG, Rimoldi OE, ten Cate FJ, ten Berg JM, et al. Determinants of coronary microvascular dysfunction in symptomatic hypertrophic cardiomyopathy. *Am J Physiol Heart Circ Physiol.* (2008) 294:H986. doi: 10.1152/ajpheart.00233.2007

18. Kawasaki T, Sugihara H. Subendocardial ischemia in hypertrophic cardiomyopathy. *J Cardiol.* (2014) 63:89–94. doi: 10.1016/j.jjcc.2013.10.005

19. Raman B, Ariga R, Spartera M, Sivalokanathan S, Chan K, Dass S, et al. Progression of myocardial fibrosis in hypertrophic cardiomyopathy: mechanisms and clinical implications. *Eur Heart J Cardiovasc Imaging.* (2019) 20:157–67. doi: 10.1093/ehjci/jey135

20. Augustine D, Lewandowski AJ, Lazdam M, Rai A, Francis J, Myerson S, et al. Global and regional left ventricular myocardial deformation measures by magnetic resonance feature tracking in healthy volunteers: comparison with tagging and relevance of gender. *J Cardiovasc Magn Reson.* (2013) 15:8. doi: 10.1186/1532-429X-15-8

21. Taylor RJ, Umar F, Moody WE, Meyyappan C, Stegemann B, Townend JN, et al. Feature-tracking cardiovascular magnetic resonance as a novel technique for the assessment of mechanical dyssynchrony. *Int J Cardiol.* (2014) 175:120–5. doi: 10.1016/j.ijcard.2014.04.268

22. Hasegawa K, Fujiwara H, Doyama K, Miyamae M, Fujiwara T, Suga S, et al. Ventricular expression of brain natriuretic peptide in hypertrophic cardiomyopathy. *Circulation.* (1993) 88:372–80. doi: 10.1161/01.CIR.88.2.372

23. Cao Z, Jia Y and Zhu B. BNP and NT-proBNP as diagnostic biomarkers for cardiac dysfunction in both clinical and forensic medicine. *Int J Mol Sci.* (2019) 20:e1820. doi: 10.3390/ijms20081820

24. Malachias MVB, Jhund PS, Claggett BL, Wijkman MO, Bentley-Lewis R, Chaturvedi N, et al. NT-proBNP by itself predicts death and cardiovascular events in high-risk patients with type 2 diabetes mellitus. *J Am Heart Assoc.* (2020) 9:e017462. doi: 10.1161/JAHA.120.017462

25. Wu G, Liu J, Wang S, Yu S, Zhang C, Wang D, et al. N-terminal pro-brain natriuretic peptide and sudden cardiac death in hypertrophic cardiomyopathy. *Heart.* (2021) 107:1576–83. doi: 10.1136/heartjnl-2020-317701

26. Li Y, Liu J, Cao Y, Han X, Shao G, Zhou X, et al. Predictive values of multiple non-invasive markers for myocardial fibrosis in hypertrophic cardiomyopathy patients with preserved ejection fraction. *Sci Rep.* (2021) 11:4297. doi: 10.1038/s41598-021-83678-z

27. Hernández-Romero D, Jover E, Martínez CM, Andreu-Cayuelas JM, Orenes-Piñero E, Romero-Aniorte AI, et al. TWEAK and NT-proBNP levels predict exercise capacity in hypertrophic cardiomyopathy. *Eur J Clin Invest.* (2015) 45:179–86. doi: 10.1111/eci.12394

28. Coats CJ, Gallagher MJ, Foley M, O'Mahony C, Critoph C, Gimeno J, et al. Relation between serum N-terminal pro-brain natriuretic peptide and prognosis in patients with hypertrophic cardiomyopathy. *Eur Heart J.* (2013) 34:2529–37. doi: 10.1093/eurheartj/eht070

29. Bégué C, Mörner S, Brito D, Hengstenberg C, Cleland JGF, Arbustini E, et al. Mid-regional proatrial natriuretic peptide for predicting prognosis in hypertrophic cardiomyopathy. *Heart.* (2020) 106:196–202. doi: 10.1136/heartjnl-2019-314826

30. Ponikowski P, Voors AA, Anker SD, Bueno H, Cleland JGF, Coats AJS, et al. 2016 ESC guidelines for diagnosing and treating acute and chronic heart failure. *Rev Esp Cardiol (Engl Ed).* (2016) 69:81. doi: 10.15829/1560-4071-2017-1-7-81

31. Liu J, Wang D, Ruan J, Wu G, Xu L, Jiang W, et al. Identification of heart failure with preserved ejection fraction helps risk stratification for hypertrophic cardiomyopathy. *BMC Med.* (2022) 20:21. doi: 10.1186/s12916-021-02219-7

32. Sato Y, Yamada T, Taniguchi R, Nagai K, Makiyama T, Okada H, et al. Persistently increased serum concentrations of cardiac troponin t in patients with idiopathic dilated cardiomyopathy are predictive of adverse outcomes. *Circulation.* (2001) 103:369–74. doi: 10.1161/01.CIR.103.3.369

33. Kubo T, Kitaoka H, Yamanaka S, Hirota T, Baba Y, Hayashi K, et al. Significance of high-sensitivity cardiac troponin T in hypertrophic cardiomyopathy. *J Am Coll Cardiol.* (2013) 62:1252–9. doi: 10.1016/j.jacc.2013.03.055

34. Kubo T, Ochi Y, Baba Y, Sugiura K, Takahashi A, Hirota T, et al. Elevation of high-sensitivity cardiac troponin T and left ventricular remodelling in hypertrophic cardiomyopathy. *ESC Heart Fail.* (2020) 7:3593–600. doi: 10.1002/ehf2.12852

35. Kawahara C, Tsutamoto T, Nishiyama K, Yamaji M, Sakai H, Fujii M, et al. Prognostic role of high-sensitivity cardiac troponin T in patients with nonischemic dilated cardiomyopathy. *Circ J.* (2011) 75:656–61. doi: 10.1253/circj.CJ-10-0837

36. Chen S, Huang L, Zhang Q, Wang J, Chen Y. T2-weighted cardiac magnetic resonance image and myocardial biomarker in hypertrophic cardiomyopathy. *Medicine (Baltimore).* (2020) 99:e20134. doi: 10.1097/MD.0000000000020134

frontiers | Frontiers in Cardiovascular Medicine

TYPE Original Research
PUBLISHED 10 November 2022
DOI 10.3389/fcvm.2022.995366

EDITED BY
Giuseppe Pannarale,
Sapienza University of Rome, Italy

REVIEWED BY
Alberto Guido Pozzoli,
Istituto Cardiocentro Ticino,
Switzerland
Steffen Ringgaard,
Aarhus University Hospital, Denmark

*CORRESPONDENCE
Li Jiang
jianglifs@163.com
Zhi-Gang Yang
yangzg666@163.com;
yangzhigang@scu.edu.cn

†These authors have contributed equally to this work and share first authorship

SPECIALTY SECTION
This article was submitted to Cardiovascular Imaging,
a section of the journal
Frontiers in Cardiovascular Medicine

RECEIVED 15 July 2022
ACCEPTED 25 October 2022
PUBLISHED 10 November 2022

CITATION
Tang S-S, Shi R, Zhang Y, Li Y, Li X-M, Yan W-F, Jiang L and Yang Z-G (2022) Additive effects of mitral regurgitation on left ventricular strain in essential hypertensive patients as evaluated by cardiac magnetic resonance feature tracking.
Front. Cardiovasc. Med. 9:995366.
doi: 10.3389/fcvm.2022.995366

Additive effects of mitral regurgitation on left ventricular strain in essential hypertensive patients as evaluated by cardiac magnetic resonance feature tracking

Si-Shi Tang[1,2†], Rui Shi[1†], Yi Zhang[1,3], Yuan Li[1], Xue-Ming Li[1], Wei-Feng Yan[1], Li Jiang[1]* and Zhi-Gang Yang[1]*

[1]Department of Radiology, West China Hospital, Sichuan University, Chengdu, China, [2]Department of Radiology, Chengdu Fifth People's Hospital, Chengdu, China, [3]Department of Radiology, Sichuan Cancer Hospital and Institute, Sichuan Cancer Center, School of Medicine, University of Electronic Science and Technology of China, Chengdu, China

Objectives: Hypertension is one of the leading risk factors for cardiovascular disease. Mitral regurgitation (MR) is a heart valve disease commonly seen in hypertensive cases. This study aims to assess the effect of MR on left ventricle (LV) strain impairment among essential hypertensive cases and determine factors that independently impact the global peak strain of the LV.

Materials and methods: We enrolled 184 essential hypertensive patients, of which 53 were patients with MR [HTN (MR +) group] and 131 were without MR [HTN (MR−) group]. Another group of 61 age-and gender-matched controls was also included in the study. All participants had received cardiac magnetic resonance examination. The HTN (MR +) group was classified into three subsets based on regurgitation fraction, comprising mild MR (n = 22), moderate MR (n = 19), and severe MR (n = 12). We compared the LV function and strain parameters across different groups. Moreover, we performed multivariate linear regression to determine the independent factors affecting LV global radial peak strain (GRS), circumferential peak strain (GCS), and global longitudinal peak strain (GLS).

Results: HTN (MR−) cases exhibited markedly impaired GLS and peak diastolic strain rate (PDSR) but preserved LV ejection fraction (LVEF) compared to the controls. However, HTN (MR +) patients showed a decrease in LVEF and further deteriorated GRS, GCS, GLS, PDSR, and the peak systolic strain rate (PSSR) compared to the HTN (MR−) group and controls. With increasing degrees of regurgitation, the LV strain parameters were gradually reduced in HTN (MR +) patients. Even the mild MR group showed impaired GCS, GLS, PDSR, and PSSR compared to the HTN (MR−) group. Multiple regression analyses indicated that the degree of regurgitation was independently associated with GRS (β = -0.348), GCS (β = -0.339), and GLS (β = -0.344) in HTN (MR +) patients.

Conclusion: GLS was significantly impaired in HTN (MR−) patients. MR may further exacerbate the deterioration of LV strain among essential hypertensive cases. Besides, the degree of regurgitation was independently correlated with GRS, GCS, and GLS in HTN (MR +) patients.

KEYWORDS

magnetic resonance imaging, hypertension, mitral valve insufficiency, left ventricular function, peak strain (PS)

Introduction

Hypertension is one of the leading risk factors for cardiovascular disease (1). Hypertensive heart disease is characterized by complex and diverse alterations in cardiac structure and function caused by hypertension (2, 3). Mitral regurgitation (MR) is a common heart valve disease in hypertensive cases (4). A longitudinal cohort study demonstrated that a 20 mmHg elevation in systolic blood pressure (SBP) was linked to a 26% higher risk of MR, while a 10-mmHg elevation in the diastolic blood pressure (DBP) was associated with a 24% higher risk of MR (5). MR may enhance left ventricular (LV) preload and aggravate myocardial damage of the hypertensive heart. Therefore, early evaluation of cardiac dysfunction in hypertensive patients with MR is crucial, which may facilitate the timely application of interventional measures, thus preventing adverse cardiovascular events and improving the prognosis.

Myocardial strain is an earlier and more sensitive indicator for subclinical myocardial dysfunction than LV ejection fraction (LVEF) (6, 7). It can provide early information on the diagnosis and therapy of myocardial damage (8–10). Moreover, the myocardial strain has been shown to have prognostic value for adverse cardiac outcomes (11–13). Cardiac magnetic resonance examination is regarded as the gold standard for non-invasively evaluating cardiac structure and function due to its strengths, such as high spatial resolution, multi-parametric, and multiplanar imaging (14). Recently, the routinely acquired cine sequence-based cardiac magnetic resonance feature-tracking has been applied to identify myocardial strain impairment (10, 15–17). However, to the best of our knowledge, cardiac magnetic resonance feature tracking is rarely utilized to detect the cumulative impact of MR on myocardial strain among hypertensive cases (9, 12). Therefore, this work compared LV strain and function among essential hypertensive cases with/without MR by cardiac magnetic resonance to investigate the effect of MR on LV myocardial strain impairment among hypertensive patients and identified risk factors that independently affected the LV global peak strain (PS).

Materials and methods

This work was approved by the biomedical research ethics committee of our hospital. Informed consent was waived due to the retrospective nature of this investigation.

Study population

From July 2012 to October 2021, 476 patients who were diagnosed with essential hypertension and had undergone cardiac magnetic resonance examination at our institution were enrolled in our study. The exclusion criteria were: ischemic heart disease, rheumatic heart disease, congenital heart disease, primary myocardiopathy, other valvular heart diseases, documented surgical procedures for heart diseases, image with artifacts caused by arrhythmia and the inability of adequate breath hold, leading to poor image quality inadequate for analysis, and incomplete key clinical data. Finally, 184 essential hypertensive cases aged 57.67 ± 14.10 years, with a body mass index (BMI) of 24.38 ± 3.39 kg/m^2 were eligible and included

---

Abbreviations: MR, mitral regurgitation; LV, left ventricular; HTN (MR +), hypertensive patients with mitral regurgitation; HTN (MR−), hypertensive patients without mitral regurgitation; PS, peak strain; GRS, global radial peak strain; GCS, global circumferential peak strain; GLS, global longitudinal peak strain; PSSR, peak systolic strain rate; PDSR, peak diastolic strain rate; LVEF, left ventricular ejection fraction; BMI, body mass index; SBP, systolic blood pressure; DBP, diastolic blood pressure; LVSV, left ventricular stroke volume; RVSV, right ventricular stroke volume; LVEDV, left ventricular end-diastolic volume; LVESV, left ventricular end-systolic volume; BSA, body surface area; LVEDVI, left ventricular end-diastolic volume indexed to body surface area; LVESVI, left ventricular end-systolic volume indexed to body surface area; LVSVI, left ventricular stroke volume indexed to body surface area; LVMI, left ventricular mass indexed to body surface area; RF, regurgitation fraction; IPMD, interpapillary muscle distance; ICC, intraclass correlation coefficient.

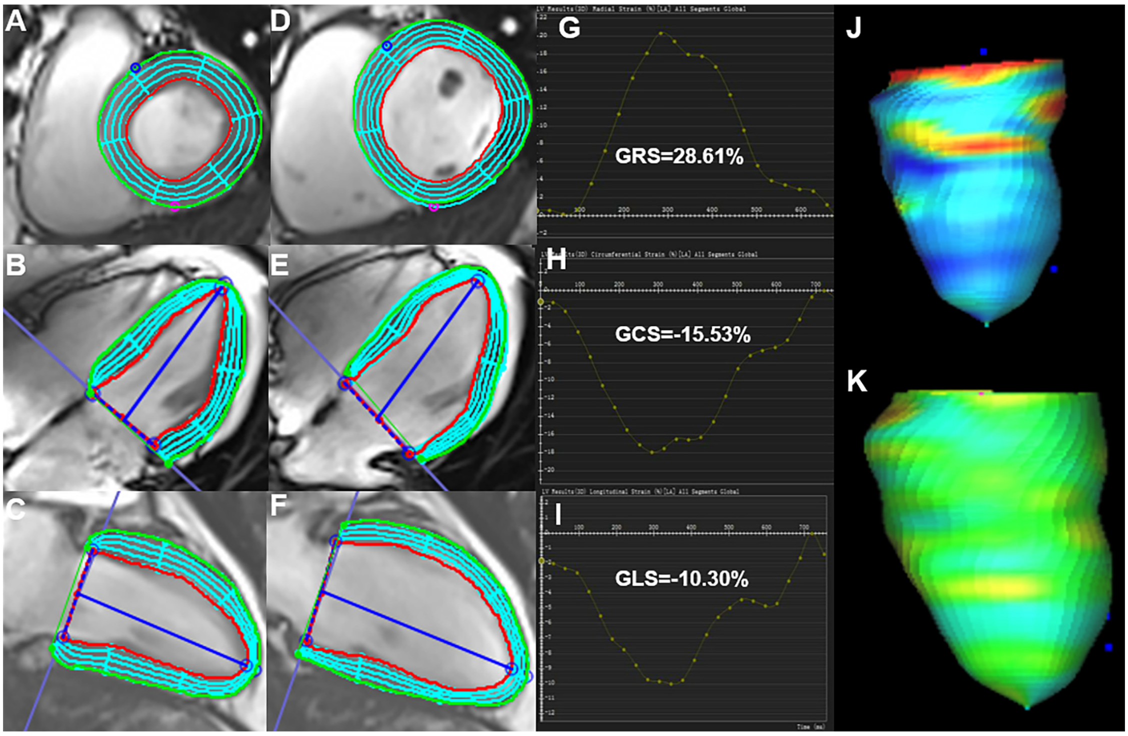

FIGURE 1
Cardiac magnetic resonance feature-tracking technology on cvi42 for the analysis of the LV strain. Manual drawing of the endocardium and epicardium of the LV at the end-systolic **(A–C)** and end-diastolic **(D–F)** phases. Then, the software automatically traced each voxel of the myocardium and calculated the LV strain parameters. **(G–I)** Measurement of the LV global peak strain parameters: GRS of 28.61%, GCS of −15.53%, and GLS of −10.31% were obtained. **(J,K)** 3D pseudo-color images for the LV end-systolic/end-diastolic GLS. LV, left ventricle; GRS, global radial peak strain; GLS, global longitudinal peak strain; GCS, global circumferential peak strain.

in the study. Depending on whether the hypertensive patients were combined with MR upon detection by cardiac magnetic resonance, they were divided into hypertensive patients without MR [HTN (MR−) group] (131/184, 71.20%) and hypertensive patients with MR [HTN (MR +) group] (53/184, 28.80%). The study further included 61 patients of matched age and sex (average age of 55.27 ± 9.76 years; BMI of 22.63 ± 2.47 kg/m^2) in the control group. The exclusion criteria for the control subjects were as follows: heart disease (coronary heart disease, valvular disease, etc.); chronic disease (hypertension, diabetes, hyperlipidemia, etc.); known systemic diseases; medication history. All the control subjects had also received cardiac magnetic resonance examination.

Cardiac magnetic resonance protocol

All patients were examined in a supine position with a whole-body 3.0 T Siemens MAGNETOM Skyra scanner or a MAGNETOM Trio Tim system (Siemens Medical Solutions, Erlangen, Germany). This study also used the breath-holding technique and the standard ECG-triggering device throughout the process. All image data were acquired at the end of expiration. Furthermore, we performed cine imaging with the balanced steady-state free-precession sequence to acquire images in 8–12 continuous slices from the mitral valve to the LV apex in the short-axis view, as well as two, three, and four-chamber pictures in the long-axis view. The imaging parameters for the MAGNETOM Skyra scanner were: field of view-360 mm × 300 mm; matrix size-256 × 166; slice thickness-8 mm; temporal resolution-39.34 ms; repetition time-2.69 ms; echo time-1.2 ms; flip angle-38°. The imaging parameters for the MAGNETOM Trio Tim scanner were as follows: field of view-250 mm × 300 mm; matrix size-208 × 139; slice thickness-8 mm; temporal resolution-40.35 ms; repetition time-3.4 ms; echo time-1.31 ms; flip angle-50°.

Cardiac magnetic resonance data analysis

Determination of cardiac volumetric and functional parameters

Two experienced cardiac radiologists with an experience of over 3 years analyzed the cardiac magnetic resonance images using commercially available offline software (cvi42, v. 5.11.2;

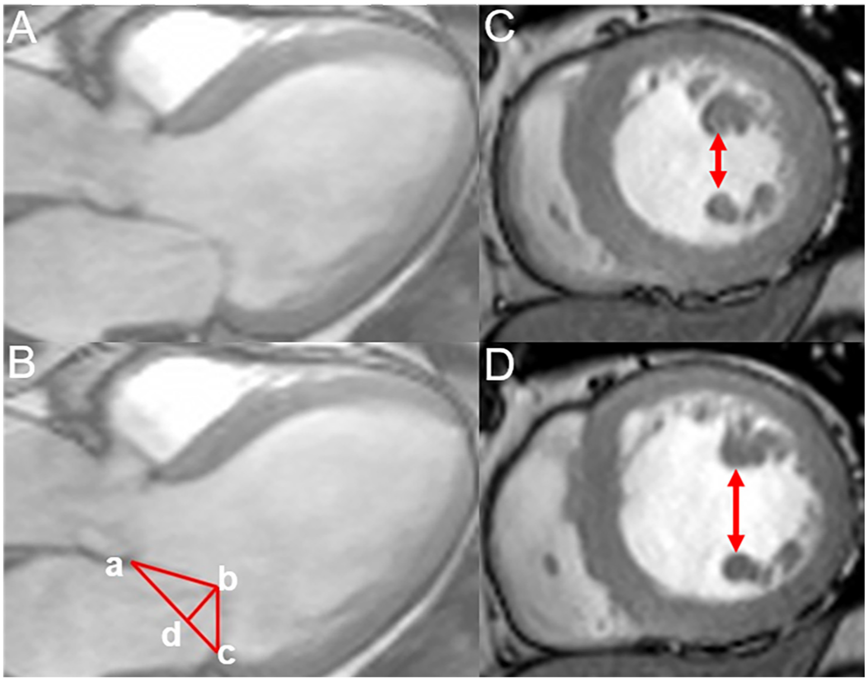

FIGURE 2
Measurement of the mitral annular geometric parameters and interpapillary muscle distance. **(A,B)** Measurement of the annular geometric parameters using cardiac magnetic resonance under a three-chamber view (mid-systolic); tethering height (b–d),mitral annular diameter (a–c), tethering area (enclosed by a–b–c), posterior tethering angle = ∠bca, and anterior tethering angle =∠bac. **(C,D)** Measurement of the interpapillary muscle distance during end-systolic and end-diastolic periods under the short axis.

Circle Cardiovascular Imaging Inc., Calgary, Alberta, Canada). They did not know the clinical information beforehand. This study manually outlined LV and the right ventricular (RV) endocardial/epicardial borders at the end-diastolic/end-systolic phases in each slice. The trabeculae and papillary muscles were eliminated. Then, the volumetric and functional parameters, including the LV/RV stroke volume (LVSV/RVSV), LV end-diastolic/end-systolic volume (LVEDV/LVESV), LV mass, and LVEF, were calculated automatically. Furthermore, we also indexed LVESV, LVEDV, LV mass, and LVSV for the body surface area (BSA) as LVESVI, LVEDVI, LVMI, and LVSVI, respectively, using the Mosteller formula (18).

Analysis of left ventricle strain

The LV short-axis, long-axis of horizontal four-chamber and vertical two-chamber cine images were loaded in the feature-tracking module of the cvi42 software. In addition, the epicardial/endocardial borders in all the above series were outlined at end-diastole and end-systole. Then, the LV global radial peak strain (GRS), global longitudinal peak strain (GLS), and global circumferential peak strain (GCS) (**Figure 1**), peak systolic strain rate (PSSR) in radial (PSSR-R), circumferential (PSSR-C), and longitudinal (PSSR-L) directions, and the peak diastolic strain rate (PDSR) in radial (PDSR-R), longitudinal (PDSR-L), circumferential (PDSR-C) directions were automatically acquired.

Evaluation of the mitral regurgitation fraction and mitral valve apparatus

MR was manifested as limited mitral valvular closure. An abnormal reversal of black blood flow was observed from LV to the left atrium *via* the mitral valve in the systolic stage in short-axis, two and three-chamber long-axis views. The regurgitation fraction (RF) was obtained using the formula RF = (LVSV-RVSV)/LVSV. Then, HTN (MR +) patients were classified into three subsets, mild ($RF < 30\%$), moderate ($30 \leq RF < 50\%$), and severe regurgitation ($RF \geq 50\%$)(19, 20).

We measured the geometric parameters for the mitral valve apparatus, including the mitral annular diameter (the linear distance between two ends of the mitral annulus), tethering height (the vertical distance between the coaptation of leaflets and the mitral annular plane), tethering area (the region surrounded *via* the annular plane and mitral leaflets), and the anterior and posterior tethering angles under the three-chamber view (mid-systolic). Besides, interpapillary muscle distance (IPMD), which was the distance between papillary muscle tips during the end-diastolic and end-systolic stages, was evaluated under the short-axis view (**Figure 2**) (21).

TABLE 1 Baseline features of the study cohort.

	Controls	HTN	
	(*n* = 61)	MR− (*n* = 131)	MR + (*n* = 53)
Sex, male (%)	36 (59.02%)	77 (58.78%)	28 (52.83%)
Age, years	55.27 ± 9.76	57.32 ± 14.27	58.52 ± 13.89
BMI, kg/m^2	22.63 ± 2.47	24.39 ± 3.42*	24.34 ± 3.37*
SBP, mmHg	116.0 ± 11.3	137.0 ± 19.4*	137.3 ± 19.2*
DBP, mmHg	73.6 ± 7.8	83.9 ± 13.9*	86.1 ± 14.7*
Resting heart rate, bpm	71.0 ± 12.4	74.7 ± 14.4	69.5 ± 13.9
Diabetic history	-	26 (19.85%)	12 (22.64%)
TG, mmol/L	-	1.33 (0.97, 1.86)	1.37 (0.96, 2.29)
TC, mmol/L	-	4.30 ± 0.98	4.24 ± 1.19
HDL, mmol/L	-	1.30 ± 0.39	1.27 ± 0.35
LDL, mmol/L	-	2.50 ± 0.82	2.37 ± 0.92
Uric acid	-	335.00 (292.50, 407.50)	341.00 (265.13, 576.60)
eGFR, mL/min/1.73 m^2	-	96.86 (83.06, 106.96)	84.34 (71.82, 107.93)
HTN with mild regurgitation, *n* (%)	-	-	22 (41.51%)
HTN with moderate regurgitation, *n* (%)	-	-	19 (35.85%)
HTN with severe regurgitation, *n* (%)	-	-	12 (22.64%)
ACEI/ARB, *n* (%)	-	55 (41.99%)	25 (47.17%)
Beta-blocker, *n* (%)	-	43 (32.82%)	11 (20.76%)
Calcium channel blocker, *n* (%)	-	74 (56.49%)	27 (50.94%)
Diuretics, *n* (%)	-	16 (12.21%)	12 (22.64%)

Data are presented as the number of patients (percentage) or as mean ± standard deviations.
HTN, hypertension; MR, mitral regurgitation; BMI, body mass index; SBP, systolic blood pressure; DBP, diastolic blood pressure; TG, triglycerides; TC, total cholesterol; HDL, high-density lipoprotein; LDL, low-density lipoprotein; eGFR, estimated glomerular filtration rate; ACEI, angiotensin-converting enzyme inhibitor; ARB, angiotensin II receptor blocker.
*Adjusted $P < 0.05$, HTN vs. control group.

Intra- and inter-observer reproducibility

The parameters of the LV strain and mitral valve apparatus of 80 randomized patients and the MR fraction of 30 randomized HTN (MR +) patients were evaluated by two independent observers blinded to clinical data to determine interobserver variability. One month later, one observer reanalyzed the parameters of the same subjects to determine the intra-observer variability.

Statistical analysis

The statistical software SPSS version 24.0 (IBM Corp., Armonk, NY, USA) was used for statistical analysis. Categorical data, including sex, diabetic history, and types of antihypertensive drugs in the hypertensive and control groups, were presented as percentages and frequencies, while the chi-square test was applied for comparison among groups. Continuous variables, including age, BMI, SBP, DBP, resting heart rate, serum indices, LV function, strain, and mitral apparatus parameters, were presented as mean ± standard deviations if normally distributed and as median (25–75%, interquartile range) if not normally distributed. We compared the continuous variables among different groups using the one-way ANOVA along with the Bonferroni *post hoc* correction or the Kruskal–Wallis tests. Serum indexes were compared between two hypertensive groups using the student's *t*-test. Spearman's or Pearson's correlation coefficient was calculated to examine the association of LV global PS with clinical indices and regurgitation degree. In the univariate analysis, variables with a *p*-value of < 0.1 and no collinearity in the sex, age, BMI, SBP, and history of diabetes were included in a multivariable backward linear regression analysis to evaluate the factors that independently predicted the LV strain among HTN (MR +) cases. Moreover, we determined the intraclass correlation coefficient (ICC) to evaluate the intra- and inter-observer variabilities. For all analyses, a *p*-value of < 0.05 (two-sided) indicated statistically significant differences between the groups.

Results

Baseline characteristics of the participants

No differences in sex, age, or resting heart rate were observed between the controls and hypertensive patients. There were also no differences in the history of diabetes, serum markers, and the use of antihypertensive drugs between HTN (MR−) and HTN (MR +) patients. However, HTN (MR−)

TABLE 2 Comparison of cardiac magnetic resonance findings among hypertensive and control groups.

	Controls	HTN	
	(*n* = 61)	MR− (*n* = 131)	MR + (*n* = 53)
LV function parameters			
LVEDVI, mL/m^2	71.61 (61.52, 77.43)	76.62 (61.53, 77.43)	114.66 (86.71, 145.81)*†
LVESVI, mL/m^2	24.47 (19.32, 29.48)	27.48 (20.00, 30.07)	57.91 (30.80, 96.51)*†
LVSVI, mL/m^2	46.38 (37.87, 52.10)	48.55 (39.89, 55.36)	53.84 (46.06, 60.77)
LVEF, %	63.52 ± 6.36	63.56 ± 7.20	48.88 ± 16.41*†
LVMI, g/m^2	38.80 ± 13.60	54.14 ± 14.78*	70.67 ± 22.05*†
LV strain parameters			
PS, %			
GRS	33.93 (31.29, 40.87)	30.76 (26.08, 36.25)	17.72 (11.37, 30.65) *†
GCS	−20.56 ± 2.60	−19.89 ± 3.60	−14.66 ± 5.50*†
GLS	−14.72 ± 2.42	−12.38 ± 2.74*	−8.96 ± 3.58*†
PSSR, 1/s			
Radial	2.07 (1.63, 2.36)	1.82 (1.43, 2.27)	0.99 (0.66, 1.57)*†
Circumferential	−1.03 (−0.88, −1.20)	−1.00 (−0.88, −1.16)	−0.73 (−0.57, −0.94)*†
Longitudinal	−0.80 (−0.72, −0.93)	−0.75 (−0.60, −0.90)	−0.51 (−0.39, −0.71) *†
PDSR, 1/s			
Radial	−2.36 (−2.00, −2.92)	−1.91 (−1.44, −2.55)*	−1.04 (−0.63, −1.70)*†
Circumferential	1.25 (1.04, 1.41)	1.06 (0.86, 1.32)*	0.74 (0.56, 0.99)*†
Longitudinal	0.93 ± 0.33	0.76 ± 0.29*	0.55 ± 0.23*†

Data are presented as mean ± standard deviations or median (25%–75%, interquartile range).

HTN, hypertension; MR, mitral regurgitation; LV, left ventricular; EDV, end diastolic volume; ESV, end systolic volume; SV, stroke volume; EF, ejection fraction; M, mass; I, indexed to BSA; GRS, global radial peak strain; PS, peak strain; GCS, global circumferential peak strain; GLS, global longitudinal peak strain; PSSR, peak systolic strain rate; PDSR, peak diastolic strain rate.

*Adjusted $P < 0.05$, HTN vs. Control.

†Adjusted $P < 0.05$, HTN (MR +) vs. HTN (MR−).

and HTN (MR +) patients had significantly higher BMI than the control patients. The SBP and DBP in the HTN (MR−) group (137.0 ± 19.4 mmHg, 83.9 ± 13.9 mmHg) and HTN (MR +) group (137.3 ± 19.2 mmHg, 86.1 ± 14.7 mmHg) were significantly higher than the control group (116.0 ± 11.3 mmHg, 73.6 ± 7.8 mmHg) (all adjusted $P < 0.05$). Table 1 presents the baseline characteristics of all participants.

Comparison of left ventricle function and strain among hypertensive and control groups

The HTN (MR−) patients demonstrated higher LVMI, lower GLS and PDSR (-R, -C, -L) compared to controls (adjusted $P < 0.05$). Compared to the control and HTN (MR−) groups, the HTN (MR +) group showed higher LVEDVI, LVESVI, LVMI, and lower LVEF (adjusted $P < 0.05$). Furthermore, the HTN (MR +) group showed decreased PS, PDSR, and PSSR in every direction compared to the HTN (MR−) group and controls (adjusted $P < 0.05$). The detailed LV function and strain parameters are presented in Table 2.

Comparison of left ventricle strain in hypertensive cases with different degrees of regurgitation

Among 53 HTN (MR +) patients, 22 (41.51%) showed mild regurgitation, 19 (35.85%) showed moderate regurgitation, and 12 (22.64%) showed severe regurgitation (Figure 3).

The GCS, GLS, PSSR-L, and PDSR-L in mild MR patients were decreased compared to HTN (MR−) patients (adjusted $P < 0.05$). The GRS, GCS, GLS, PSSR, and PDSR in all three directions in the moderate MR patients were lower than the HTN (MR−) patients. The moderate MR group showed lower GRS, GCS, GLS, PSSR-C, and PDSR-C than the mild MR group. The GRS, GCS, GLS, PDSR, and PSSR in all three directions were markedly reduced among the severe MR cases compared to the HTN (MR−) patients. Compared to the mild MR group, the GRS, GCS, GLS, PSSR-R, PDSR-R, PSSR-C, and PDSR-C of severe MR patients were markedly decreased (adjusted $P < 0.05$). The GRS, GCS, GLS, PSSR, and PDSR did not significantly differ between severe and moderate MR groups. More details of LV strain parameters among hypertensive patients are presented in Table 3.

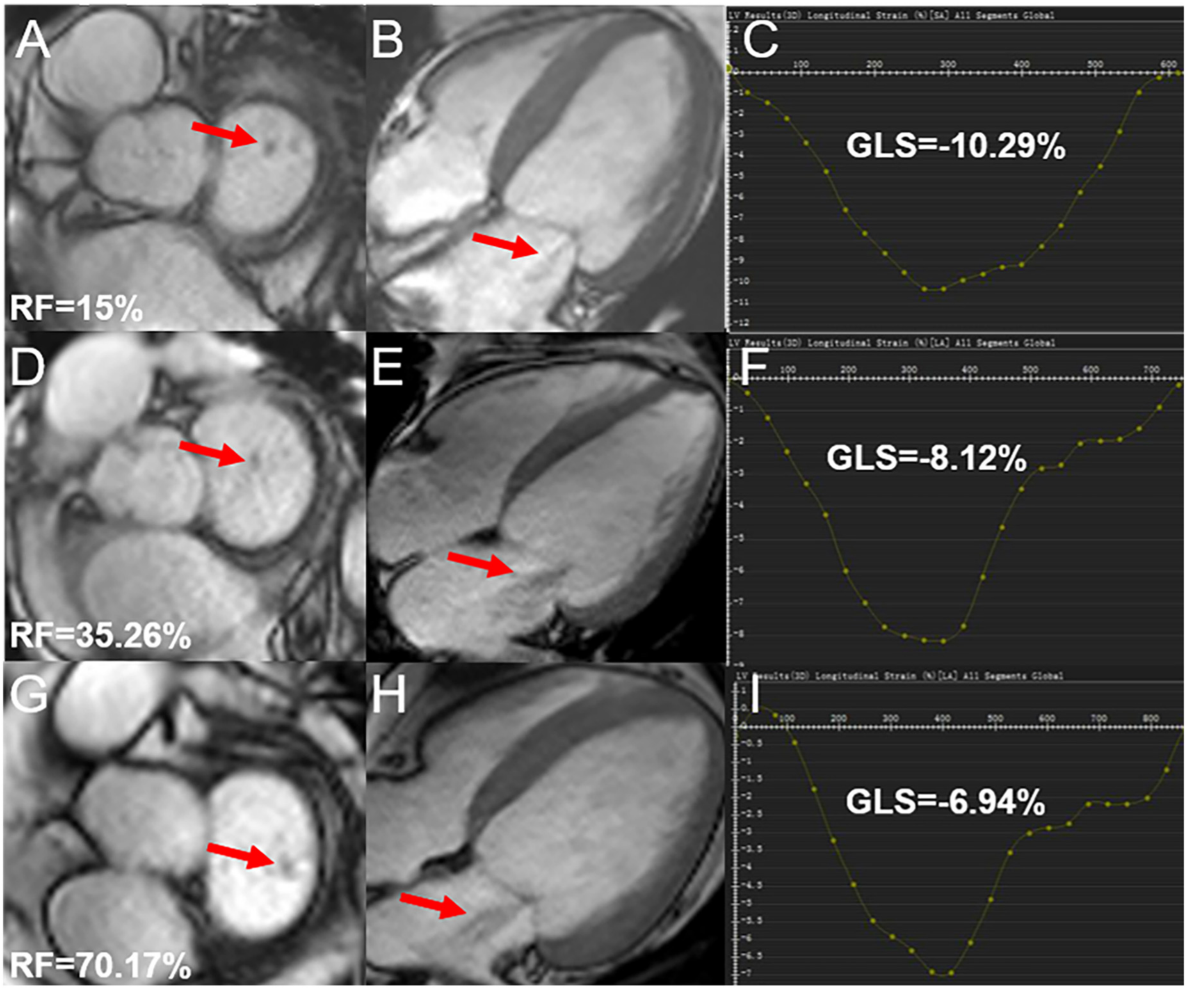

FIGURE 3
Cardiac magnetic resonance cine and GLS images in hypertensive cases showing mild, moderate, and severe degrees of regurgitation; **(A,B)** mild mitral regurgitation patient, male, 72-year-old, RF = 15%, LV short-axis **(A)**, 4-chamber **(B)** cine images demonstrating the regurgitation signal from the LV to LA (red arrow); **(D,E)** moderate mitral regurgitation patient, male, 52-year-old, RF = 35.26%, LV short-axis **(D)**, 4-chamber **(E)** cine images demonstrating the regurgitation signal from LV to LA (red arrow); **(G,H)** severe mitral regurgitation patient, male, 42 years old, RF = 70.17%, LV short-axis **(G)**, 4-chamber **(H)** cine images demonstrating abnormally reversed blood flow from LV to LA (red arrow); **(C,F,I)** the curves for LV GLS. RF, regurgitation fraction; GLS, global longitudinal peak strain; LV, left ventricle; LA, left atrium.

Comparison of mitral valve apparatus among different groups

All cases in the HTN (MR +) group showed higher mitral annular geometry parameters and IPMD (end-systolic/end-diastolic) compared to the patients of the HTN (MR−) and the control group. Differences between HTN (MR−) and control group were not significant. Moderate MR patients showed increased end-systolic/end-diastolic IPMD compared to mild MR patients. Severe MR patients showed higher mitral annular geometry parameters and IPMD than mild patients (adjusted $P < 0.05$). Differences between severe and moderate MR groups were not significant. The detailed mitral annular geometry parameters of hypertensive patients and controls are presented in Table 4.

Independent predictive factors of left ventricle global peak strain among hypertensive patients showing mitral regurgitation

Based on the univariate linear regression analysis, the regurgitation degree was negatively correlated with GRS ($R = -0.464$, $P = 0.001$), GLS ($R = -0.359$, $P = 0.008$), and GCS ($R = -0.437$, $P = 0.001$) (Figure 4). The smoking history was negative associated with GCS ($R = -0.291$, $P = 0.043$).

TABLE 3 Comparison of LV strain in hypertensive cases with different degrees of regurgitation.

	HTN patients			
	without MR ($n = 131$)	**mild MR ($n = 22$)**	**moderate MR ($n = 19$)**	**severe MR ($n = 12$)**
LVEF, %	63.56 ± 7.20	56.53 ± 15.80*	48.04 ± 14.57*†	35.08 ± 10.55*†
PS, %				
GRS	30.76 (26.08, 36.25)	26.39 (14.83, 38.27)	13.49 (11.17, 26.87)*†	11.96 (9.75, 14.20)*†
GCS	−19.89 ± 3.60	−17.27 ± 5.35*	−13.47 ± 4.61*†	−11.11 ± 4.15*†
GLS	−12.38 ± 2.74	−10.52 ± 3.84*	−8.13 ± 2.96*†	−7.06 ± 2.57*†
PSSR, 1/s				
Radial	1.82 (1.43, 2.27)	1.37 (0.99, 1.97)	0.95 (0.62, 1.33) *	0.62 (0.56, 1.56) *†
Circumferential	−1.00 (−0.88, −1.16)	−0.92 (−0.72, −1.09)	−0.67 (−0.53, −0.92) *†	−0.60 (−0.52, −0.94) *†
Longitudinal	−0.75 (−0.60, −0.90)	−0.64 (−0.39, −0.79)*	−0.47 (−0.34, −0.71)*	−0.42 (−0.32, −0.56)*
PDSR, 1/s				
Radial	−1.91 (−1.44, −2.55)	−1.45 (−0.81, −2.19)	−1.04 (−0.62, −1.90)*	−0.75 (−0.50, −0.96)*†
Circumferential	1.06 (0.86, 1.32)	0.96 (0.68, 1.12)	0.74 (0.44, 0.93)*†	0.57 (0.53, 1.04)*†
Longitudinal	0.76 ± 0.29	0.59 ± 0.23*	0.51 ± 0.25*	0.51 ± 0.20*

Data are presented as mean ± standard deviations or median (25%–75%, interquartile range).
LV, left ventricular; HTN, hypertension; MR, mitral regurgitation; EF, ejection fraction; PS, peak strain; GRS, global radial peak strain; GCS, global circumferential peak strain; GLS, global longitudinal peak strain; PSSR, peak systolic strain rate; PDSR peak diastolic strain rate.
*Adjusted $P < 0.05$, HTN (MR +) vs. HTN (MR−).
†Adjusted $P < 0.05$, HTN with severe/moderate MR vs. HTN with mild MR.

TABLE 4 Comparison of mitral annular geometry and interpapillary muscle distance among different groups.

	Controls	HTN patients			
	($n = 61$)	**without MR ($n = 131$)**	**mild MR ($n = 22$)**	**moderate MR ($n = 19$)**	**severe MR ($n = 12$)**
Mitral annular geometry					
Annulus diameter, mm	27.19 ± 2.28	27.72 ± 2.54	29.17 ± 1.58*	30.18 ± 2.81*	31.80 ± 2.16*†
Coaptation height, mm	7.15 (6.45, 7.80)	7.53 (6.86, 8.0)	8.44 (7.72, 9.05)*	8.79 (8.47, 9.58)*	9.34 (9.05, 9.73)*†
Tenting area, mm^2	99.34 (93.29, 110.92)	102.13 (93.42, 112.80)	123.18 (112.71, 133.61)*	133.19 (120.44,136.53)*	141.47 (138.22, 159.89)*†
Anterior tethering angle°	23.01 ± 3.27	23.87 ± 3.15	25.46 ± 2.48*	27.11 ± 3.95*	29.10 ± 1.71*†
Posterior tethering angle°	33.76 (31.06, 35.88)	35.00 (32.54, 37.18)	37.97 (33.51, 39.00)*	38.05 (35.50, 41.42)*	41.11 (39.17, 42.47)*†
IPMD					
End-systolic, mm	8.27 ± 3.21	8.61 ± 2.83	12.40 ± 5.44*	15.78 ± 5.44*†	19.68 ± 4.30*†
End-diastolic, mm	20.04 (16.86, 21.46)	20.00 (16.83, 21.98)	22.72 (18.91, 25.26)*	23.96 (22.63, 27.06)*†	27.48 (25.70, 30.46)*†

Data are presented as mean ± standard deviations or median (25%–75%, interquartile range).
HTN, hypertension; MR, mitral regurgitation; IPMD, Interpapillary muscle distance.
*Adjusted $P < 0.05$, HTN (MR +) vs. HTN (MR−) and HTN (MR +) vs. controls.
†Adjusted P < 0.05, HTN with severe/moderate MR vs. HTN with mild MR.

Moreover, the level of triglycerides was negatively related to GCS ($R = -0.357$, $P = 0.013$) and GRS ($R = -0.332$, $P = 0.023$). According to the multivariate regression, the regurgitation degree independently predicted GRS ($\beta = -0.348$), GCS ($\beta = -0.339$), and GLS ($\beta = -0.344$) after adjusting the gender, age, BMI, SBP, and history of diabetes (Table 5).

Inter-and intra-observer variabilities

Excellent agreement between and within the observer was observed in the measurement of LV PS (ICC = 0.920–0.947 and 0.913–0.975, respectively), PSSR (ICC = 0.837–0.876 and 0.922–0.962, respectively), PDSR (ICC = 0.825–0.974 and 0.902–0.977, respectively), mitral annular geometry (ICC = 0.850–0.884 and 0.851–0.890, respectively), IPMD (ICC = 0.894–0.967 and 0.928–0.969, respectively) and MR fraction (ICC = 0.859 and 0.887, respectively) (Table 6).

Discussion

In this study, we investigated the influence of MR on the function and strain in hypertension using cardiac

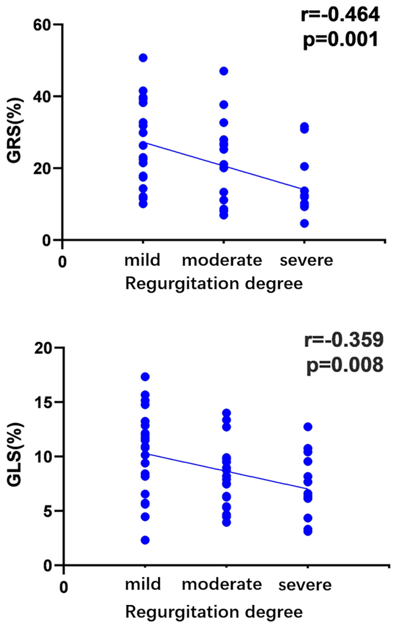

FIGURE 4
Correlation of regurgitation degree in hypertensive patients with left ventricular global peak strain. The absolute values of the circumferential and longitudinal-peak strain were analyzed to avoid the effect of the directional sign. r, correlation coefficient; GRS, global radial peak strain; GCS, global circumferential peak strain; GLS, global longitudinal peak strain.

TABLE 5 Univariate and multivariate analysis between clinical indexes and LV global PS among hypertensive patients showing MR.

	GRS			GCS			GLS		
	Univariate	**Multivariate**		**Univariate**	**Multivariate**		**Univariate**	**Multivariate**	
	R	**β (R2 = 0.338)**	***P***	***R***	**β (R2 = 0.426)**	***P***	***R***	**β (R2 = 0.475)**	***P***
MR degree	−0.464a	−0.348	0.029	−0.437a	−0.339	0.031	−0.359a	−0.344	0.018
SBP	0.136	0.068	0.671	0.107	0.117	0.479	−0.044	0.071	0.621
DBP	−0.076	–	–	−0.144	–	–	−0.236	–	–
Diabetes	0.095	0.272	0.108	−0.040	0.215	0.198	0.135	0.234	0.122
TG	−0.332*a*	−0.184	0.315	−0.357a	−0.071	0.726	−0.244b	−0.010	0.950
HR	−0.220	–	–	−0.245b	−0.123	0.506	−0.228	–	–
CH	−0.134	–	–	−0.144	–	–	−0.076	–	–
eGFR	0.274	–	–	0.233	–	–	0.044	–	–
Smoking	−0.175	–	–	−0.291a	−0.166	0.307	−0.271b	−0.015	0.923

a = $P < 0.05$; b = $P < 0.1$, factors with $P < 0.1$ and SBP, diabetic history were included in the multivariable backward linear regression after adjusting age, gender, body mass index.
LV, left ventricular; PS, peak strain; MR, mitral regurgitation; GRS, global radial peak strain; GCS, global circumferential peak strain; GLS, global longitudinal peak strain; SBP, systolic blood pressure; DBP, diastolic blood pressure; TG, triglycerides; HR, resting heart rate; CH, Coaptation height; eGFR, estimated glomerular filtration rate; R, correlation coefficient; β, regression coefficient; R2, coefficient of determination.

magnetic resonance feature tracking. The main results were: (1) impaired GLS and PDSR, but preserved LVEF was observed in hypertensive patients without MR; (2) when hypertensive patients were concomitant with MR, significantly decreased LVEF and further deteriorated LV strain were observed in the radial, longitudinal and circumferential directions; (3) with deterioration of the degrees of regurgitation, LV strain was progressively reduced in hypertensive patients with MR, while the parameters of the mitral valve apparatus increased significantly; (4) the degree of regurgitation was independently correlated with GRS, GCS, and GLS.

Chronic mechanical stress from elevated blood pressure in hypertension can lead to LV remodeling, which involves LV cardiomyocyte hypertrophy and myocardial fibrosis, causing myocardial stiffness, decreased myocardial compliance, and consequent LV diastolic and systolic dysfunction (2, 3, 22,

TABLE 6 Intra-and inter-observer variabilities of LV strain, mitral annular geometry and mitral regurgitation fraction.

	Intra-observer		**inter-observer**	
	ICC	**95% CI**	**ICC**	**95% CI**
PS				
GRS	0.931	0.895–0.955	0.925	0.886–0.925
GCS	0.975	0.961–0.984	0.947	0.919–0.966
GLS	0.913	0.867–0.943	0.920	0.873–0.951
PSSR				
Radial	0.932	0.897–0.956	0.837	0.756–0.892
Circumferential	0.962	0.942–0.976	0.944	0.913–0.963
Longitudinal	0.922	0.882–0.950	0.876	0.814–0.919
PDSR	0.902	0.851–0.936	0.825	0.739–0.884
Radial	0.977	0.964–0.985	0.974	0.960–0.983
Circumferential	0.952	0.923–0.970	0.904	0.854–0.937
Longitudinal	0.932	0.897–0.956	0.837	0.756–0.892
Mitral annular geometry				
Annulus diameter	0.890	0.741–0.956	0.867	0.688–0.947
Coaptation height	0.873	0.698–0.949	0.850	0.651–0.940
Tenting area	0.853	0.658–0.941	0.875	0.704–0.950
Anterior tethering angle	0.867	0.615–0.946	0.872	0.552–0.956
Posterior tethering angle	0.851	0.579—-0.945	0.884	0.696–0.955
Interpapillary muscle distance				
End-systolic	0.969	0.915–0.989	0.967	0.907–0.988
End-diastolic	0.928	0.812–0.972	0.894	0.739–0.959
Mitral regurgitation fraction	0.887	0.778–0.945	0.859	0.724–0.930

LV, left ventricular; ICC, The intraclass correlation coefficients; CI, confidence interval; PS, peak strain; GRS, global radial peak strain; GCS, global circumferential peak strain; GLS, global longitudinal peak strain. PSSR, peak systolic strain rate; PDSR, peak diastolic strain rate.

23). In our study, the HTN (MR−) patients showed markedly reduced GLS compared to control patients, but the GCS was not significantly decreased, which was similar to the results of previous echocardiographic studies (24, 25). We hypothesized that LV myocardial fibrosis predominantly involved the subendocardial fiber. Therefore, the GLS, which mainly reflected the shortening of the subendocardial longitudinally oriented fiber, could deteriorate even in the early stages of hypertension. However, the GCS, which mainly represented the contractility of circumferential muscle fibers in the middle layer, remained spared, which could compensate for the longitudinal contractile dysfunction (10, 26). Therefore, traditional systolic indices, including LVEF, LVEDVI, LVESVI, and LVSVI, were preserved in HTN (MR−) patients in this study. These data were consistent with the findings of previous research (26, 27).

Cardiac magnetic resonance feature tracking is used to detect the diastolic function in the form of PDSR (16, 28). The PDSR in the HTN (MR−) patients was significantly impaired in all three directions compared to the control, whereas the PSSR, which represented the systolic data, was not significantly reduced. These data indicate that the abnormalities of diastolic function might occur before the systolic abnormalities in hypertension, which was consistent with previous research (29). Thus, our study adds to this body of evidence. In general, our research demonstrated that feature tracking technology might reveal subclinical LV dysfunction before traditional LVEF in hypertensive patients.

Hypertension may cause LV remodeling, resulting in LV geometric changes, papillary muscle shift, mitral annular dilation, change in the natural vertical angulation of the chordae tendineae, and tethering of the mitral leaflets, ultimately causing MR (30, 31). We observed that HTN (MR +) patients showed remarkably increased LVEDI, LVESI, LVMI, and decreased LVEF, PS, PDSR, and PSSR compared to controls and HTN (MR−) patients. The results indicated that MR might have a superimposed influence on LV function and strain in hypertensive patients, which is similar to the findings of a previous study (32). The pathological model may be that regurgitated volume in MR can increase LV preload, leading to LV remodeling, LV dilation, and eccentric hypertrophy, resulting in LV dysfunction (33). Significantly impaired LV dysfunction may occur under the double effect of hypertension and MR. Therefore, hypertensive patients with MR should be paid closer attention, and intervention should be made to prevent long-term adverse cardiac events.

When comparing the parameters of different degrees of MR regurgitation in hypertensive patients, it was observed that LVPS, PDSR, and PSSR were gradually reduced with the aggravation of the degree of MR regurgitation. Even the mild MR group showed impaired systolic and diastolic function compared to hypertensive patients without MR. Multivariate linear regression analysis indicated that the MR regurgitation degree was independently related to GRS, GCS, and GLS in HTN (MR +) patients. Our study demonstrated that the impairment of global PS possibly progressed with an increase in the degree of regurgitation. Several studies have reported that reduced GLS in patients with MR was correlated with LV dysfunction after intervention and higher risk for all-cause mortality (12, 34). Furthermore, the presence of MR may result in aggravated MR, which may be explained by the fact that MR—induced overload of the LV volume could induce LV dilatation, which puts more pressure on the mitral valve apparatus, causing further damage to the valve apparatus and aggravation of MR. In this situation, a vicious cycle between the ever-increasing LV volume and MR could be initiated (35). Therefore, even mild MR in hypertensive patients should be taken seriously.

A previous study reported that the diameter of the mitral annulus and IPMD were strongly correlated with the degree of MR regurgitation (21). This study observed that the parameters of mitral annular geometry and IPMD in groups with different degrees of MR were higher than those without MR. Compared to the mild MR group, the moderate MR group had higher end-systolic and end-diastolic IPMD, whereas the severe MR group showed an increase in mitral annular geometry and IPMD. Our results further suggest that the mitral valve apparatus might participate in the formation and aggravation of MR in hypertensive patients.

Limitations

This study has certain limitations. First, this study was unicentric and cross-sectional, with a possible selection bias. Multi-center studies will be conducted in the future to validate the findings of this study further. Second, the lack of a follow-up in this study made the long-term impact of MR on the mortality of hypertensive patients unclear. This will be addressed in a future study. Third, no animal experiments were done in this study. Future research focusing on relevant pathological mechanisms will be carried out.

Conclusion

Significant impairment of GLS was observed in hypertensive cases, and MR possibly deteriorated LV strain damage and cardiac insufficiency. The regurgitation degree was independently correlated with GCS, GRS, and GLS in the HTN (MR +) patients. Evaluation of LV strain in cardiac magnetic resonance feature tracking possibly assists clinicians in monitoring the development of cardiac deformation and facilitates additional therapies to delay LV myocardial damage among hypertensive cases developing MR.

Data availability statement

The raw data supporting the conclusions of this article will be made available by the authors, without undue reservation.

Ethics statement

The studies involving human participants were reviewed and approved by West China Hospital of Sichuan University Biomedical Research Ethics Committee. Written informed consent from the participants' legal guardian/next of kin was not required to participate in this study in accordance with the national legislation and the institutional requirements. Written informed consent was not obtained from the minor(s)' legal guardian/next of kin for the publication of any potentially identifiable images or data included in this article.

Author contributions

S-ST, RS, LJ, and Z-GY designed the research and wrote and reviewed the manuscript. S-ST, RS, YZ, YL, Z-GY, and LJ performed the experiments. S-ST, RS, LJ, YZ, X-ML, and W-FY collected and sorted statistical data. W-FY, YL, X-ML, and Z-GY analyzed the data. All authors read and approved the final manuscript.

Funding

This work was supported by the 1.3.5 project for disciplines of excellence, West China Hospital, Sichuan University (ZYGD18013).

Acknowledgments

We thank all the subjects, research coordinators, and investigators who participated in the trials.

Conflict of interest

The authors declare that the research was conducted in the absence of any commercial or financial relationships that could be construed as a potential conflict of interest.

Publisher's note

References

1. Stanaway JD, Afshin A, Gakidou E, Lim SS, Abate D, Abate KH, et al. Global, regional, and national comparative risk assessment of 84 behavioural, environmental and occupational, and metabolic risks or clusters of risks for 195 countries and territories, 1990–2017: a systematic analysis for the Global Burden of Disease Study 2017. *Lancet.* (2018) 392:1923–94. doi: 10.1016/S0140-6736(18)32225-6

2. Drazner MH. The progression of hypertensive heart disease. *Circulation.* (2011) 123:327–34. doi: 10.1161/CIRCULATIONAHA.108.845792

3. Santos M, Shah AM. Alterations in cardiac structure and function in hypertension. *Curr Hypertens Rep.* (2014) 16:428. doi: 10.1007/s11906-014-0428-x

4. Imbalzano E, Vatrano M, Ghiadoni L, Mandraffino G, Dalbeni A, Khandheria BK, et al. Arterial stiffness and mitral regurgitation in arterial hypertension: an intriguing pathophysiological link. *Vascul Pharmacol.* (2018) 111:71–6. doi: 10.1016/j.vph.2018.10.007

5. Rahimi K, Mohseni H, Otto CM, Conrad N, Tran J, Nazarzadeh M, et al. Elevated blood pressure and risk of mitral regurgitation: a longitudinal cohort study of 5.5 million United Kingdom adults. *PLoS Med.* (2017) 14:e1002404. doi: 10.1371/journal.pmed.1002404

6. Yan WF, Gao Y, Zhang Y, Guo YK, Wang J, Jiang L, et al. Impact of type 2 diabetes mellitus on left ventricular diastolic function in patients with essential hypertension: evaluation by volume-time curve of cardiac magnetic resonance. *Cardiovasc Diabetol.* (2021) 20:73. doi: 10.1186/s12933-021-01262-1

7. Tadic M, Sala C, Carugo S, Mancia G, Grassi G, Cuspidi C. Myocardial strain and left ventricular geometry: a meta-analysis of echocardiographic studies in systemic hypertension. *J Hypertens.* (2021) 39:2297–306. doi: 10.1097/HJH.0000000000002911

8. Szymanski C, Lévy F, Tribouilloy C. Should LVEF be replaced by global longitudinal strain? *Heart.* (2014) 100:1655–6. doi: 10.1136/heartjnl-2014-306186

9. Niu J, Zeng M, Wang Y, Liu J, Li H, Wang S, et al. Sensitive marker for evaluation of hypertensive heart disease: extracellular volume and myocardial strain. *BMC Cardiovasc Disord.* (2020) 20:292. doi: 10.1186/s12872-020-01553-7

10. Claus P, Omar AMS, Pedrizzetti G, Sengupta PP, Nagel E. Tissue tracking technology for assessing cardiac mechanics: principles, normal values, and clinical applications. *JACC Cardiovasc Imaging.* (2015) 8:1444–60. doi: 10.1016/j.jcmg.2015.11.001

11. Romano S, Judd RM, Kim RJ, Heitner JF, Shah DJ, Shenoy C, et al. Feature-tracking global longitudinal strain predicts mortality in patients with preserved ejection fraction: a multicenter study. *JACC Cardiovasc Imaging.* (2020) 13:940–7. doi: 10.1016/j.jcmg.2019.10.004

12. Namazi F, van der Bijl P, Hirasawa K, Kamperidis V, van Wijngaarden SE, Mertens B, et al. Prognostic value of left ventricular global longitudinal strain in patients with secondary mitral regurgitation. *J Am Coll Cardiol.* (2020) 75:750–8. doi: 10.1016/j.jacc.2019.12.024

13. Schuster A, Hor KN, Kowallick JT, Beerbaum P, Kutty S. Cardiovascular magnetic resonance myocardial feature tracking: concepts and clinical applications. *Circ Cardiovasc Imaging.* (2016) 9:e004077. doi: 10.1161/CIRCIMAGING.115.004077

14. Xie LJ, Dong ZH, Yang ZG, Deng MY, Gao Y, Jiang L, et al. Assessment of left ventricular deformation in patients with type 2 diabetes mellitus by cardiac magnetic resonance tissue tracking. *Sci Rep.* (2020) 10:13126. doi: 10.1038/s41598-020-69977-x

15. Zhang Y, Wang J, Ren Y, Yan WF, Jiang L, Li Y, et al. The additive effects of kidney dysfunction on left ventricular function and strain in type 2 diabetes mellitus patients verified by cardiac magnetic resonance imaging. *Cardiovasc Diabetol.* (2021) 20:11. doi: 10.1186/s12933-020-01203-4

16. Shen LT, Jiang L, Zhu YW, Shen MT, Huang S, Shi R, et al. Additive effect of aortic regurgitation degree on left ventricular strain in patients with type 2 diabetes mellitus evaluated via cardiac magnetic resonance tissue tracking. *Cardiovasc Diabetol.* (2022) 21:37. doi: 10.1186/s12933-022-01471-2

17. Shi K, Yang MX, Huang S, Yan WF, Qian WL, Li Y, et al. Effect of diabetes mellitus on the development of left ventricular contractile dysfunction in women with heart failure and preserved ejection fraction. *Cardiovasc Diabetol.* (2021) 20:185. doi: 10.1186/s12933-021-01379-3

18. Mosteller RD. Simplifed calculation of body-surface area. *N Engl J Med.* (1987) 317:1098. doi: 10.1056/NEJM198710223171717

19. Garg P, Swift AJ, Zhong L, CarlhällC J, Ebbers T, Westenberg J, et al. Assessment of mitral valve regurgitation by cardiovascular magnetic resonance imaging. *Nat Rev Cardiol.* (2020) 17:298–312. doi: 10.1038/s41569-019-0305-z

20. Krieger EV, Lee J, Branch KR, Hamilton-Craig C. Quantitation of mitral regurgitation with cardiac magnetic resonance imaging: a systematic review. *Heart.* (2016) 102:1864–70. doi: 10.1136/heartjnl-2015-309054

21. Bouma W, Willemsen HM, Lexis CP, Prakken NH, Lipsic E, Van Veldhuisen DJ, et al. Chronic ischemic mitral regurgitation and papillary muscle infarction detected by late gadolinium-enhanced cardiac magnetic resonance imaging in patients with ST-segment elevation myocardial infarction. *Clin Res Cardiol.* (2016) 105:981–91. doi: 10.1007/s00392-016-1006-9

22. Nwabuo CC, Vasan RS. Pathophysiology of hypertensive heart disease: beyond left ventricular hypertrophy. *Curr Hypertens Rep.* (2020) 22:11. doi: 10.1007/s11906-020-1017-9

23. Diez J, Frohlich ED. A translational approach to hypertensive heart disease. *Hypertension.* (2010) 55:1–8. doi: 10.1161/HYPERTENSIONAHA.109.141887

24. Galderisi M, Lomoriello VS, Santoro A, Esposito R, Olibet M, Raia R, et al. Differences of myocardial systolic deformation and correlates of diastolic function in competitive rowers and young hypertensives: a speckle-tracking echocardiography study. *J Am Soc Echocardiogr.* (2010) 23:1190–8. doi: 10.1016/j.echo.2010.07.010

25. Tadic M, Sala C, Carugo S, Mancia G, Grassi G, Cuspidi C. Myocardial strain in hypertension: a meta-analysis of two-dimensional speckle tracking echocardiographic studies. *J Hypertens.* (2021) 39:2103–12. doi: 10.1097/HJH.0000000000002898

26. Shin SM, Shim WJ, Park SM. Early changes of left ventricular function in young adults with never-treated hypertension and no left ventricular hypertrophy: relationships to ambulatory blood pressure monitoring. *Clin Exp Hypertens.* (2014) 36:517–23. doi: 10.3109/10641963.2013.863326

27. Li XM, Peng LQ, Shi R, Han PL, Yan WF, Yang ZG. Impact of gender on left ventricular deformation in patients with essential hypertension assessed by cardiac magnetic resonance tissue tracking. *J Magn Reson Imaging.* (2021) 53:1710–20. doi: 10.1002/jmri.27500

28. Zhang Y, Yan WF, Jiang L, Shen MT, Li Y, Huang S, et al. Aggravation of functional mitral regurgitation on left ventricle stiffness in type 2 diabetes mellitus patients evaluated by CMR tissue tracking. *Cardiovasc Diabetol.* (2021) 20:158. doi: 10.1186/s12933-021-01354-y

29. de Simone G, Greco R, Mureddu G, Romano C, Guida R, Celentano A, et al. Relation of left ventricular diastolic properties to systolic function in arterial hypertension. *Circulation.* (2000) 101:152–7. doi: 10.1161/01.cir.101.2.152

30. Faggiano P, Ciliberto R. L'insufficienza mitralica funzionale [Functional mitral insufficiency]. *Ital Heart J.* (2000) 1:1298–303.

31. Athanasuleas CL, Stanley AWH, Buckberg GD. Mitral regurgitation: Anatomy is destiny. *Eur. J. Cardiothorac. Surg.* (2018) 54:627–34. doi: 10.1093/ejcts/ezy174

32. Kontos J, Papademetriou V, Wachtell K, Palmieri V, Liu JE, Gerdts E, et al. Impact of valvular regurgitation on left ventricular geometry and function in hypertensive patients with left ventricular hypertrophy: the LIFE study. *J Hum Hypertens.* (2004) 18:431–6. doi: 10.1038/sj.jhh.1001715

33. Perrucci GL, Zanobini M, Gripari P, Songia P, Alshaikh B, Tremoli E, et al. Pathophysiology of aortic stenosis and mitral regurgitation. *Compr Physiol.* (2011) 7:799–818. doi: 10.1002/cphy.c160020

34. Bijvoet GP, Teske AJ, Chamuleau SAJ, Hart EA, Jansen R, Schaap JR. Global longitudinal strain to predict left ventricular dysfunction in asymptomatic patients with severe mitral valve regurgitation: literature review. *Neth. Heart J.* (2020) 28:63–72. doi: 10.1007/s12471-019-01318-8

35. Nishimura RA, Otto CM, Bonow RO, Carabello BA, Erwin JP III, Fleisher LA, et al. 2017 AHA/ACC Focused Update of the 2014 AHA/ACC guideline for the management of patients with valvular heart disease: a report of the American College of Cardiology/American Heart Association Task Force on Clinical Practice Guidelines. *Circulation.* (2017) 70:252–89. doi: 10.1161/CIR.0000000000000503

frontiers | Frontiers in Cardiovascular Medicine

TYPE Original Research
PUBLISHED 15 December 2022
DOI 10.3389/fcvm.2022.1022987

OPEN ACCESS

EDITED BY
Giuseppe Pannarale,
Sapienza University of Rome, Italy

REVIEWED BY
Haoming Song,
Tongji University, China
Mengmeng Li,
Shandong University, China
Roberta Manganaro,
University Hospital of Policlinico
G. Martino, Italy
Xinhao Li,
Chinese Academy of Medical Sciences
and Peking Union Medical College,
China

*CORRESPONDENCE
Jieyan Shen
shenjieyan@renji.com

†These authors have contributed equally to this work

SPECIALTY SECTION
This article was submitted to
Cardiovascular Imaging,
a section of the journal
Frontiers in Cardiovascular Medicine

RECEIVED 19 August 2022
ACCEPTED 23 November 2022
PUBLISHED 15 December 2022

CITATION
Wang J, Ni C, Yang M, Zhang X,
Ruan B, Sun L, Shen X and Shen J
(2022) Apply pressure-strain loop
to quantify myocardial work
in pulmonary hypertension:
A prospective cohort study.
Front. Cardiovasc. Med. 9:1022987.
doi: 10.3389/fcvm.2022.1022987

Apply pressure-strain loop to quantify myocardial work in pulmonary hypertension: A prospective cohort study

Jian Wang[1,2†], Chao Ni[3†], Menghui Yang[1], Xueming Zhang[1], Binqian Ruan[1], Lingyue Sun[1], Xuedong Shen[1] and Jieyan Shen[1]*

[1]Department of Cardiology, Renji Hospital, Shanghai Jiao Tong University School of Medicine, Shanghai, China, [2]Department of Cardiology, Ningbo First Hospital, Ningbo Hospital of Zhejiang University, Ningbo, China, [3]Children's Heart Center, Institute of Cardiovascular Development and Translational Medicine, The Second Affiliated Hospital and Yuying Children's Hospital of Wenzhou Medical University, Wenzhou, China

Objectives: Pressure-strain loop (PSL) is a novel method to quantify myocardial work in many cardiovascular diseases. To investigate the value of myocardial work parameters derived from PSL for evaluating cardiac function and clinical prognosis in patients with pulmonary hypertension (PH).

Methods: A total of 52 patients with PH and 27 healthy controls were enrolled in this prospective study. PSLs determined by echocardiography were used to calculate global work index (GWI) of left ventricle (LV) and right ventricle (RV). Global constructive work (GCW) comprised the sum of myocardial work performed during shortening in systole and during lengthening in isovolumic relaxation. Global wasted work (GWW) comprised the sum of myocardial work performed during lengthening in systole and during shortening in isovolumic relaxation. Global work efficiency (GWE) was defined as GCW/(GCW + GWW).

Results: LVGWW, RVGWI, RVGCW and RVGWW were significantly higher in patients than controls (all $P < 0.001$). LVGWE, LVGWI, LVGCW, and RVGWE were lower in patients than controls (all $P < 0.01$). Myocardial work parameters correlated well with clinical and other conventional echocardiographic assessments (all $P < 0.05$). In binary logistic regression analysis, the combination of RVGWE and estimation of pulmonary arterial systolic pressure (ePASP) was the best model to predict clinical outcomes (OR = 0.803, $P = 0.002$ and OR = 1.052, $P = 0.015$, respectively). Receiver operating characteristic curv demonstrated the combination of RVGWE and ePASP was the best predictor of adverse events with 100% sensitivity and 76.3% specificity (AUC = 0.910, $P < 0.001$).

Conclusion: Myocardial work parameters derived from PSL are emerging markers of cardiac function. And the combination of RVGWE and ePASP is a useful predictor of clinical outcome in PH patients.

KEYWORDS

pressure-strain loop, pulmonary hypertension, myocardial work, cardiac function, prognosis

Introduction

Pulmonary hypertension (PH) is a pathological state or disease caused by abnormal increase of pulmonary circulation pressure due to various factors or diseases (1). According to the results from a National Prospective Registry, the median survival of PH patients is 2.8 years (95% CI 1.9–3.7 years) in the absence of effective treatment (2).

It is well acknowledged that cardiac function is directly related to the prognosis of patients. A great number of studies have shown that PH patients in World Health Organization functional class (WHO-FC) IIIWH have worse outcomes in the long-term prognosis (3, 4). Previous studies on PH have mostly focused on the right ventricular (RV) function, as long-term RV afterload will directly cause RV dysfunction which is the major determinant of survival in these patients (5, 6). However, recently, scholars find that left ventricle (LV) is also impaired in PH patients despite of normal LV ejection fraction (LVEF) and LV dysfunction is associated well with poor clinical outcomes (7, 8). Therefore, both RV and LV function should be concentrated on equally in PH patients.

Echocardiography is widely used to evaluate cardiac function in PH patients at the advantage of non-invasion (1). Global longitudinal strain (GLS) has proven benefit for assessing both LV function and RV function. Yet GLS is load dependency and is not adjusted for afterload, which may influence the accuracy of cardiac function evaluation (9), especially in PH patients at high level of afterload. Recently, Russell et al. (10) propose a novel non-invasive method by quantifying myocardial work to assess ventricular systolic function, which is termed as pressure-strain loop (PSL). It takes account of GLS data with non-invasive estimated ventricular pressure curves simultaneously and the area within PSL represents myocardial work. Study on hypertension has shown that LV myocardial work parameters are significantly higher in moderate to severe hypertension patients while LVGLS are preserved compared to controls (11).

No previous study has assessed myocardial work in PH patients. Thus, in this study, we aimed to quantify LV and RV myocardial work in PH patients by non-invasive PSL, and explore the value of myocardial work parameters of evaluating cardiac function and clinical prognosis.

Materials and methods

Study population

Fifty-two patients diagnosed with PH between January 2019 and June 2020 in Shanghai Renji Hospital were consecutively enrolled in this prospective study. Given PH prevalence and incidence were mostly in middle-aged women, we recruited twenty-seven age- and gender- matched healthy controls from medical center for further study. According to 2015 ESC/ERS Guidelines of PH (1), the diagnosis of all patients was mean pulmonary arterial pressure (mPAP) $\geq$ 25 mmHg, pulmonary artery wedge pressure (PAWP) $\leq$ 15 mmHg and pulmonary vascular resistance (PVR) >3 Wood unit at rest detected by right heart catheterization (RHC), including type I, type IV and type V pulmonary hypertension. Exclusion criteria were listed as the following: PH due to left heart disease; PH due to hypoxia; arrhythmia (atrial fibrillation or flutter, left or right bundle branch block, et al.); pregnancy; cancer; patients with obscure endocardium in echocardiography; lost to follow-up.

Clinical data collection

Clinical data of PH patients were acquired by reviewing electronic medical records. Age, gender, etiological classification, brain natriuretic peptide (BNP), RHC data including pulmonary arterial systolic pressure (PASP), pulmonary arterial diastolic pressure (PADP), mPAP, PAWP, cardiac output (CO), cardiac index (CI) and PVR, as well as the specific drug therapy were recorded from all patients. Patients underwent RHC and echocardiography within 3 days of each other. Before echocardiography, all patients' blood pressure (BP) by a brachial artery cuff were measured immediately. In order to evaluate the cardiac function, all patients underwent 6-minute walking distance (6MWD) to identify function capacity and functional class was determined by clinical investigator based on the WHO-FC (12).

Echocardiography

Standard transthoracic echocardiography connecting with electrocardiogram were performed in all of the 52 PH patients and 27 controls using a Vivid E95 ultrasound machine (GE Healthcare, Horten, Norway) equipped with an M5S probe by an experienced doctor. As recommended by the American Society of Echocardiography (13), images in parasternal long-axis, apical four-chamber, apical two-chamber and apical long-axis views were acquired. All the images were transferred from the machine at least three consecutive beats, and then offline measured using EchoPAC (version 203, GE Healthcare, Horten, Norway) by another independent echocardiographer who did not take part in the image acquisition and was blinded to clinical data. LVEF was measured by using Simpson's technique. Tricuspid annular plane systolic excursion (TAPSE) was obtained by an M-mode cursor oriented to the junction of the RV free wall and the tricuspid valve plane. RV fractional area change (FAC) was calculated as following formula: (RV end-diastolic area − RV end-systolic area)/RV end-diastolic area × 100%. Right atrial area (RAA) was measured in end-systole. Right ventricle and left ventricle basal diameter were measured to get right ventricle/left ventricle basal diameter ratio (RV/LV). In the absence of pulmonic valve or right ventricular outflow tract stenosis, the estimation of PASP (ePASP) was equal to right ventricular systolic pressure (RVSP), which was calculated by adding tricuspid regurgitation peak gradient to the right atrial pressure (RAP). RAP was estimated by observing inferior vena cave (IVC) diameter and its collapse during inspiration.

Ventricular global longitudinal strain and myocardial work analysis

Images from apical four-chamber, apical two-chamber and apical long axis views were put into offline workstation (EchoPAC version 203, GE Healthcare, Horten, Norway) to yield LV global longitudinal strain (LVGLS). RV global longitudinal strain (RVGLS) was assessed by using an apical four-chamber view focusing on the RV in offline workstation.

Ventricular myocardial work was quantified by a novel non-invasive PSL method which used GLS combined with estimated non-invasive pressure (10). The PW Doppler signal of the LV outflow tract was used to set marker of aortic valve closure time. As referenced to Russel et al. (10), the ventricular pressure was estimated using a standard pressure trace which was personalized by stretching it in time according to valvular event times (mitral valve open/close and aortic valve open/close) by echocardiography and in amplitude according to measured systolic artery pressure. Myocardial work or global work index (GWI) was calculated as the integral of power from mitral valve close to mitral valve open which was generated by differentiating the strain curve over time, giving the myocardial shortening rate, and then multiplying this with instantaneous ventricular pressure (**Figure 1**). Global constructive work (GCW) comprised the sum of myocardial work performed during shortening in systole and during lengthening in isovolumic relaxation, whereas global wasted work (GWW) comprised the sum of myocardial work performed during lengthening in systole and during shortening in isovolumic relaxation (14). Global work efficiency (GWE) was defined as GCW divided by the sum of GCW and GWW, expressed as a percentage.

LV pressure was replaced by the cuff systolic pressure. Because of the particularity of RV, in order to improve the accuracy of pulmonary arterial systolic pressure obtained by echocardiography, other right cardiac function parameters obtained from echocardiography, including ePASP, TAPSE, FAC, RAP, RAA, RV/LV, LVGLS and RVGLS, were used for adjusting, then the calculated pulmonary arterial systolic pressure (PASPcal) were obtained. In the absence of left/right bundle branch block, the left and right heart could be considered as synchronous contraction. Similarly, the estimation of real time RV pressure was acquired by using an empiric reference curve which was adjusted by stretching it in time according to valvular event times (mitral valve open/close and aortic valve open/close) by echocardiography and in amplitude according to PASPcal. LVGWE, LVGWI, LVGCW, LVGWW, RVGWE, RVGWI, RVGCW, and RVGWW were eventually obtained by the algorithm above-mentioned.

The interobserver reliability of GLS and myocardial work parameters was assessed using the measurements of 10 randomly chosen PH patients and 5 randomly chosen controls by two experienced cardiologists.

Follow-up

All patients with PH were followed up regularly at 3-month intervals by telephone calls to ascertain present symptom, therapy, and cardiac function. The deadline of the last visit of the last patient was May 2021. Major adverse events defined as all-cause of mortality, hospitalization and need of new specific drug therapy or enhancement on the original therapy basis were recorded.

Statistical analysis

Normally distributed continuous variables were presented as mean ± standard deviation, and non-normally distributed

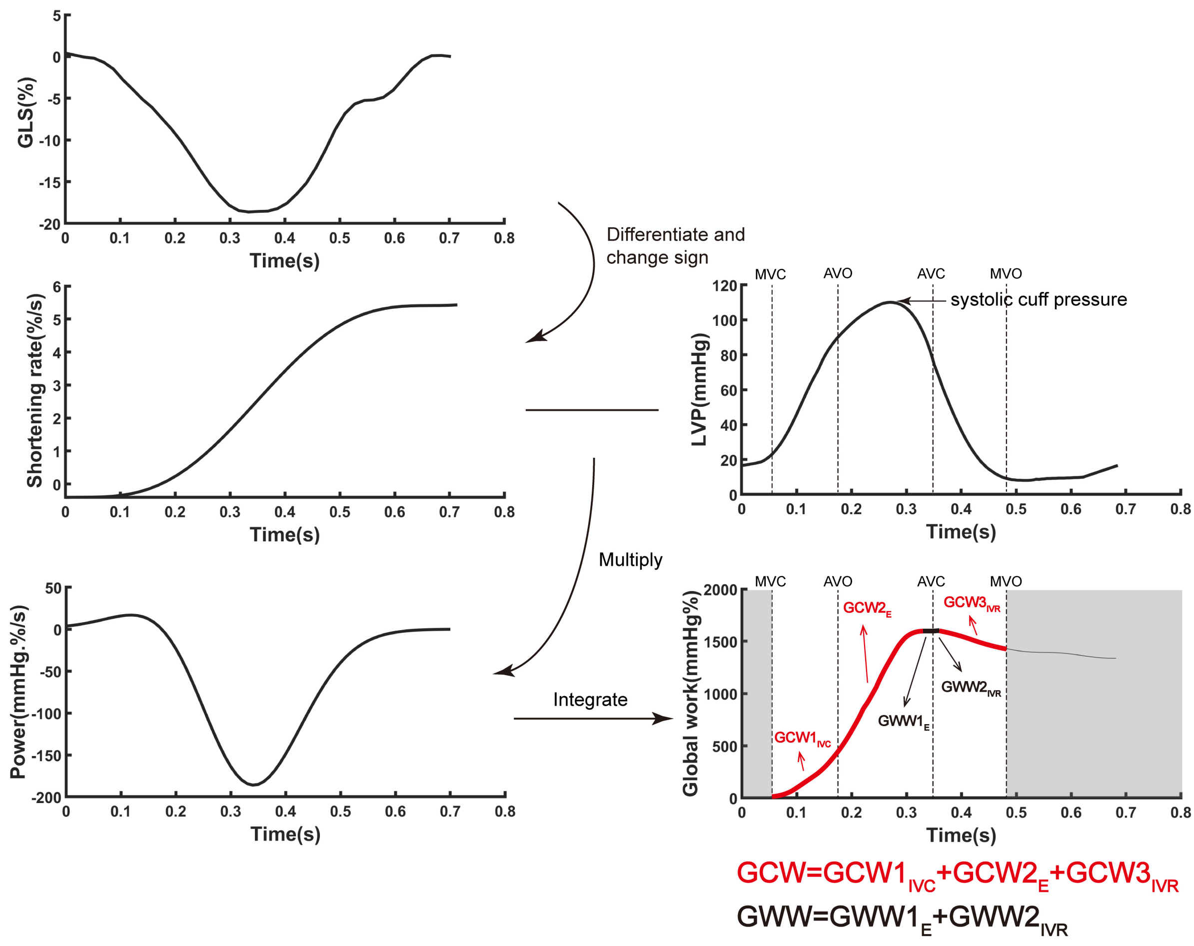

FIGURE 1
The algorithm of ventricular myocardial work by incorporating global longitudinal strain and ventricular pressure. Myocardial work was quantified by calculating the rate of segmental shortening by differentiating the strain curve and multiplying the resulting value by the instantaneous ventricular pressure. E, ejection period; IVC, isovolumic contraction period; IVR, isovolumic relaxation period; GCW, global constructive work; LVP, left ventricular pressure; GLS, global longitudinal strain; GWW, global wasted work.

continuous variables as median (first and third quartiles). Categorical variables were expressed as numbers (percentage). Independent sample *t*-test or Mann-Whitney *U* test was used to compare variables between PH patients with controls, while Pearson's Chi-Squared test or Fisher exact test to compare the categorical variables (15). PASPcal was adjusted for TAPSE, FAC, RAP, RAA, RV/LV, LVGLS and RVGLS by multiple linear regression, and Bland-Altman plot was used for agreement analysis. And the Spearmen correlation coefficients were tested to analyze the relationship between BNP, 6MWD, WHO-FC, TAPSE, FAC, RAA, RV/LV with myocardial work parameters in PH patients. At the end of follow-up, we performed binary logistic regression and receiver operating characteristic (ROC) curve to predict the risk factor of adverse events. Hosmer-Lemeshow test was used to test the fitting degree of logical regression. Statistical analysis was performed with SPSS 21.0 (IBM Corp., Armonk, NY, USA). Figures were performed with MATLAB (R2020, Mathworks, Nattick, USA) and GraphPad Prism 8 (GraphPad Software, La Jolla, CA). For all tests, a 2-tailed P value of < 0.05 was considered to be statistically significant.

Results

Main clinical characteristics of pulmonary hypertension patients and controls

A total of 52 PH patients and 27 controls (female 84.6 vs 85.2%, $P = 0.947$; age 44.1 ± 13.2 vs 43.0 ± 13.7 years, $P = 0.748$) were included in this clinical study. Main clinical characteristics of patients were shown in **Table 1**.

TABLE 1 Baseline clinical characteristics of pulmonary hypertension patients.

Characteristic	PH ($n = 52$)
Gender (% female)	44 (84.6)
Age (years)	44.1 ± 13.2
SBP (mmHg)	120.4 ± 18.1
DBP (mmHg)	75.7 ± 13.4
BNP (pg/ml)	188.0 (44.5,435.5)
6MWD (m)	430.6 ± 109.7
WHO-FC (%)	
I	15 (28.8)
II	16 (30.8)
III	18 (34.6)
IV	3 (5.8)
Etiology (%)	
Connective tissue disease associated with pulmonary arterial hypertension	33 (63.5)
Idiopathic pulmonary arterial hypertension	5 (9.6)
Congenital heart disease associated with pulmonary arterial hypertension	4 (7.7)
Portopulmonary hypertension	1 (1.9)
Chronic thromboembolic pulmonary hypertension	6 (11.5)
Pulmonary hypertension with unclear and/or multifactorial mechanisms	3 (5.8)
Specific drug therapy	
None (%)	5 (9.6)
Endothelin receptor antagonists (%)	35 (67.3)
Phosphodiesterase type 5 inhibitors (%)	35 (67.3)
Riociguat (%)	3 (5.8)
Prostacyclin analogues (%)	7 (13.5)
RHC data	
Pulmonary arterial systolic pressure (mmHg)	72.9 ± 18.0
Pulmonary arterial diastolic pressure (mmHg)	34.8 ± 8.3
Mean pulmonary arterial pressure (mmHg)	48.8 ± 10.5
Pulmonary artery wedge pressure (mmHg)	10.5 ± 3.8
Cardiac output (L/min)	4.6 ± 1.6
Cardiac index (L/min·m^2)	2.9 ± 0.9
Pulmonary vascular resistance (dyn·s·cm^{-5})	785.8 ± 403.9

Values are mean ± SD, *n* (%), or median (first and third quartiles).
6MWD, 6-minute walking distance; BNP, brain natriuretic peptide; DBP, diastolic blood pressure; PH, pulmonary hypertension; RHC, right heart catheterization; SBP, systolic blood pressure; WHO-FC, World Health Organization functional class.

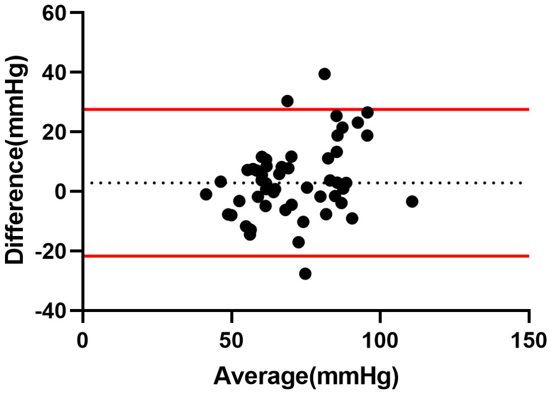

FIGURE 2
Agreement analysis between PASPcal and PASP from RHC. Bland-Altman plot showed great agreement between PASPcal and PASP (mean bias 3.554 mmHg, 95% limits of agreement −21.17 to 28.27 mmHg). LV-PSL, left ventricular pressure-strain loop; RV-PSL, right ventricular pressure-strain loop.

TABLE 2 Intra-class correlation coefficient of global longitudinal strain and myocardial work parameters.

	ICC	95%CI	*P*-value
LVGLS	0.961	0.883–0.987	< 0.001
RVGLS	0.981	0.944–0.994	< 0.001
LVGWE	0.897	0.694–0.966	< 0.001
LVGWI	0.939	0.818–0.979	< 0.001
LVGCW	0.923	0.770–0.974	< 0.001
LVGWW	0.889	0.669–0.963	< 0.001
RVGWE	0.804	0.416–0.934	0.002
RVGWI	0.982	0.945–0.994	< 0.001
RVGCW	0.990	0.969–0.997	< 0.001
RVGWW	0.815	0.449–0.938	0.002

CI, confidence interval; ICC, intra-class correlation coefficient; LVGCW, left ventricular global constructive work; LVGLS, left ventricular global longitudinal strain; LVGWE, left ventricular global work efficiency; LVGWI, left ventricular global work index; LVGWW, left ventricular global wasted work; RVGCW, right ventricular global constructive work; RVGLS, right ventricular global longitudinal strain; RVGWE, right ventricular global work efficiency; RVGWI, right ventricular global work index; RVGWW, right ventricular global wasted work.

Echocardiography and myocardial work parameters

Multiple linear regression showed that PASPcal had a good correlation with PASP from RHC ($R^2 = 0.560$, $P < 0.001$). The formula was as follows: PASPcal = 0.609∗ePASP + 0.187∗TAPSE − 0.182∗FAC + 0.153∗ RAP + 0.12∗RAA − 0.128∗RV/LV − 0.153∗LVGLS + 0.135∗ RVGLS. Bland-Altman plot also showed great agreement between PASPcal and PASP (Figure 2). Intra-class correlation coefficients of GLS and myocardial work parameters were shown in Table 2.

The representative PSL and global work curves of participants were presented in Figure 3. As summarized in Table 3, PH patients had higher ePASP (74.0 ± 27.4 vs 25.2 ± 2.6 mmHg, $P < 0.001$), RAA (18.2 ± 6.6 vs 10.7 ± 2.0 cm^2, $P < 0.001$), RV/LV (1.3 ± 0.4 vs 0.7 ± 0.1, $P < 0.001$), LVGLS (−15.3 ± 3.4 vs −19.3 ± 2.0%, $P < 0.001$), RVGLS (−13.5 ± 4.3 vs −21.8 ± 2.5%, $P < 0.001$) and lower TAPSE (16.5 ± 3.5 vs 24.0 ± 3.2 mm, $P < 0.001$), FAC (31.2 ± 12.2 vs 52.1 ± 6.7%, $P < 0.001$) than controls. However, there was no significant difference in LVEF (69.9 ± 5.7 vs 67.6 ± 3.9%, $P = 0.075$). Compared to the controls, LVGWW

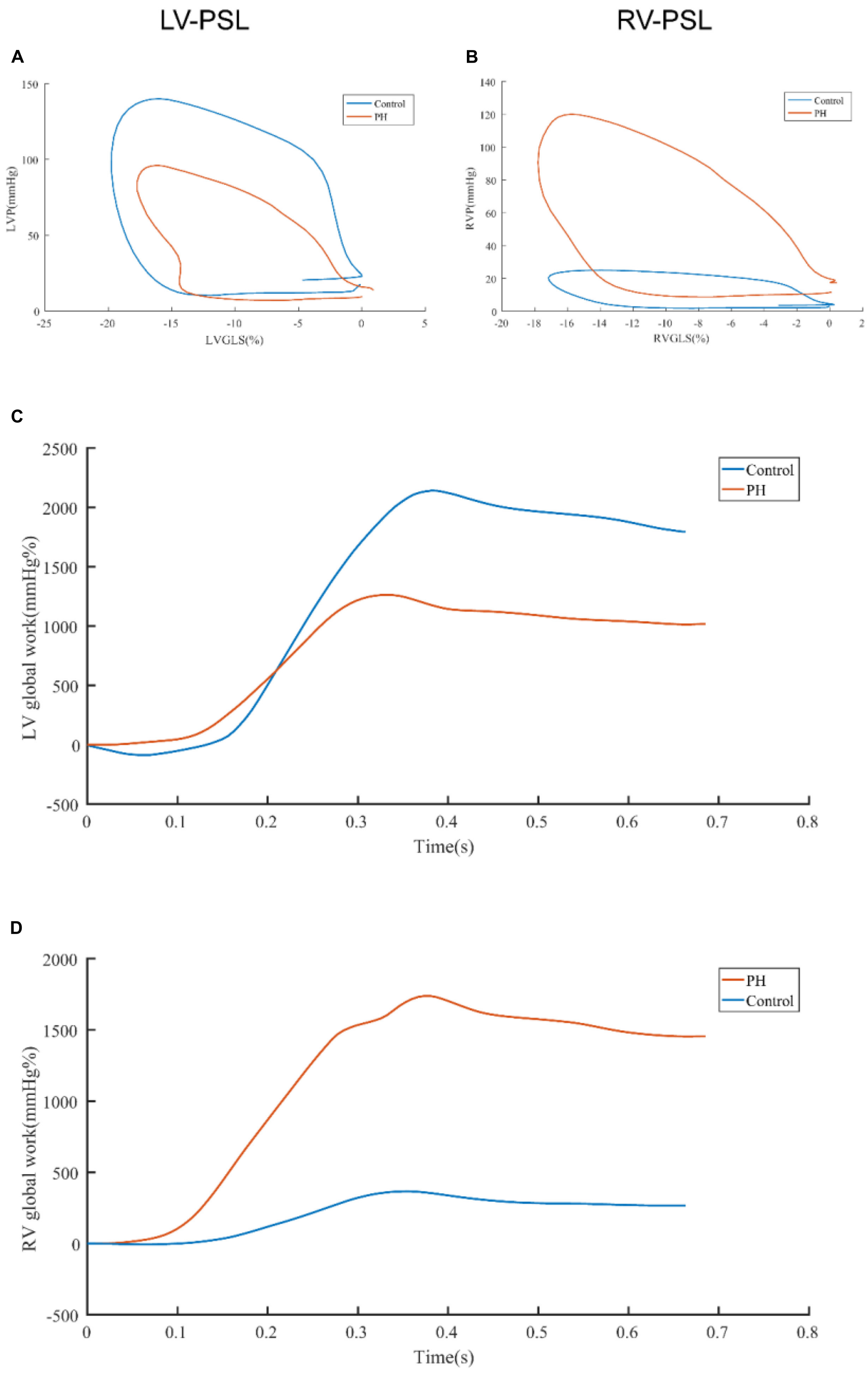

FIGURE 3

Representative pressure-strain loops and global work curves. The difference of LV-PSL **(A)** and RV-PSL **(B)** between PH patients and control was shown. The difference of LV global work curve **(C)** and RV global work curve **(D)** was shown. LV-PSL, left ventricular pressure-strain loop; RV-PSL, right ventricular pressure-strain loop.

TABLE 3 Comparison of myocardial work parameters between pulmonary hypertension patients and controls.

Characteristic	Controls ($n = 27$)	PH ($n = 52$)	P-value
Gender (% female)	23 (85.2)	44 (84.6)	0.947
Age (years)	43.1 ± 13.7	44.1 ± 13.2	0.748
SBP (mmHg)	118.4 ± 13.8	120.4 ± 18.1	0.627
DBP (mmHg)	75.7 ± 10.3	75.7 ± 13.4	0.997
Conventional echocardiography measurements			
ePASP (mmHg)	25.2 ± 2.6	74.0 ± 27.4	< 0.001
TAPSE (mm)	24.0 ± 3.2	16.5 ± 3.5	< 0.001
FAC (%)	52.1 ± 6.7	31.2 ± 12.2	< 0.001
RAA (cm^2)	10.7 ± 2.0	18.2 ± 6.6	< 0.001
RV/LV	0.7 ± 0.1	1.3 ± 0.4	< 0.001
LVEF (%)	67.6 ± 3.9	69.9 ± 5.7	0.075
LVGLS (%)	−19.3 ± 2.0	−15.3 ± 3.4	< 0.001
RVGLS (%)	−21.8 ± 2.5	−13.5 ± 4.3	< 0.001
Myocardial work parameters			
LVGWE (%)	94.0 (93.0, 95.0)	84.0 (80.0, 90.0)	< 0.001
LVGWI (mmHg%)	1,560 (1,364.0, 1,884.0)	1,330.0 (1,061.3, 1,467.5)	< 0.001
LVGCW (mmHg%)	1,989.0 (1,795.0, 2,323.0)	1,810.0 (1,494.8, 2,024.5)	0.004
LVGWW (mmHg%)	110.0 (83.0, 130.0)	296.5 (172.0, 461.5)	< 0.001
RVGWE (%)	92.0 (90.0, 95.0)	85.0 (76.3, 92.5)	0.001
RVGWI (mmHg%)	352.0 (314.0, 412.0)	571.5 (373.5, 796.0)	< 0.001
RVGCW (mmHg%)	474.0 (435.0, 526.0)	793.5 (624.5, 1,173.0)	< 0.001
RVGWW (mmHg%)	38.0 (23.0, 57.0)	151.5 (60.5, 223.0)	< 0.001

Values are mean ± SD, *n* (%), or median (first and third quartiles).
ePASP, estimation of pulmonary arterial systolic pressure; FAC, fractional area change; LVEF, left ventricular ejection fraction; RV/LV, right ventricle/left ventricle basal diameter ratio; TAPSE, tricuspid annular plane systolic excursion; other abbreviations as in Tables 1, 2.

[296.5 (172.0, 461.5) vs 110.0 (83.0, 130.0), $P < 0.001$], RVGWI [571.5 (373.5, 796.0) vs 352.0 (314.0 412.0), $P < 0.001$], RVGCW [793.5 (624.5, 1,173.0) vs 474.0 (435.0, 526.0), $P < 0.001$] and RVGWW [151.5 (60.5, 223.0) vs 38.0 (23.0, 57.0), $P < 0.001$] were significantly increased in PH patients. LVGWE [84.0 (80.0, 90.0) vs 94.0 (93.0, 95.0), $P < 0.001$], LVGWI [1,330.0 (1,061.3, 1,467.5) vs 1,560.0 (1,364.0, 1,884.0), $P < 0.001$], LVGCW [1,810.0 (1,494.8, 2,024.5) vs 1,989.0 (1,795.0, 2,323.0), $P = 0.004$], and RVGWE [85.0 (76.3, 92.5) vs 92.0 (90.0, 95.0), $P = 0.001$] were significantly lower in PH patients than controls.

Relationship of myocardial work parameters and other clinical data in pulmonary hypertension patients

We used linear correlation analysis to assess relationship between myocardial work parameters and other clinical data in PH patients, which were described in Figure 4. LVGWE presented a positive correlation with 6MWD ($r = 0.406$, $P = 0.003$), and FAC ($r = 0.457$, $P = 0.001$), but a negative correlation with WHO-FC ($r = -0.415$, $P = 0.002$), and RV/LV ($r = -0.280$, $P = 0.044$). LVGWI significantly correlated with 6MWD ($r = 0.466$, $P < 0.001$), WHO-FC ($r = -0.455$, $P = 0.001$), FAC ($r = 0.572$, $P < 0.001$), RV/LV (-0.351, $P = 0.011$). The correlations between LVGCW and 6MWD ($r = 0.344$, $P = 0.013$), WHO-FC ($r = -0.331$, $P = 0.016$), and FAC ($r = 0.396$, $P = 0.004$) were also significant. LVGWW was only correlated with 6MWD (-0.277, $P = 0.047$), WHO-FC ($r = 0.293$, $P = 0.035$) and FAC ($r = -0.305$, $P = 0.028$). As for RV function, RVGWE showed a negative correlation with BNP ($r = -0.314$, $P = 0.023$), WHO-FC ($r = -0.288$, $P = 0.039$), and RV/LV ($r = -0.352$, $P = 0.010$) and a positive correlation with 6MWD ($r = 0.288$, $P = 0.039$), and FAC ($r = 0.461$, $P = 0.001$). In addition, RVGWI correlated well with BNP ($r = -0.297$, $P = 0.032$), TAPSE ($r = 0.306$, $P = 0.028$), and FAC ($r = 0.373$, $P = 0.006$). The correlations of RVGWW with 6WMD ($r = -0.294$, $P = 0.034$), WHO-FC ($r = 0.319$, $P = 0.021$), FAC ($r = -0.332$, $P = 0.016$) and RV/LV ($r = 0.339$, $P = 0.014$) were significant as well.

Association of myocardial work parameters and clinical outcomes in pulmonary hypertension patients

PH patients were followed for a median of 515.0 days (386.5, 535.8) at termination. During the follow-up period, adverse events occurred in 14 patients (26.9%): 12 patients (23.1%)

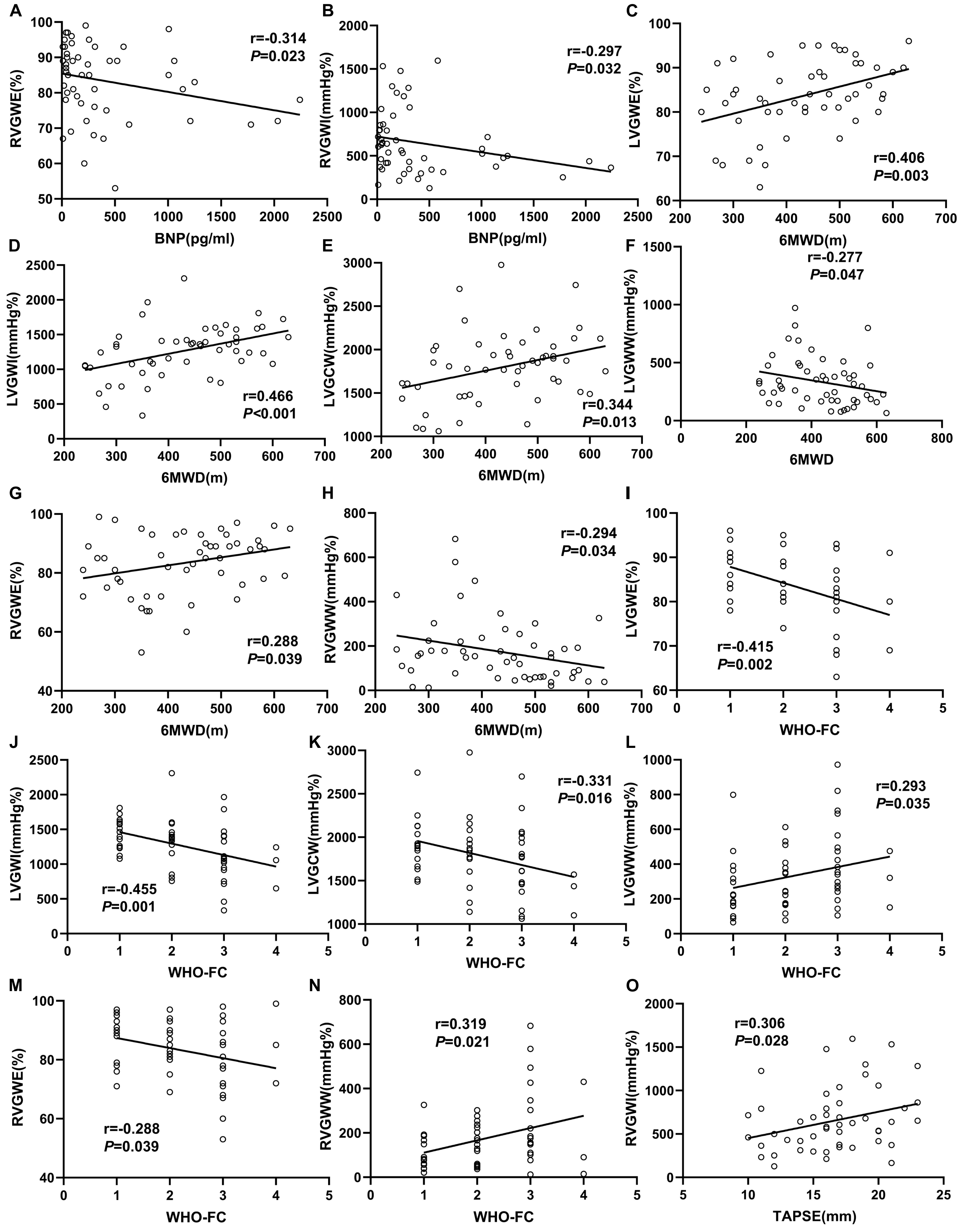

FIGURE 4
(Continued)

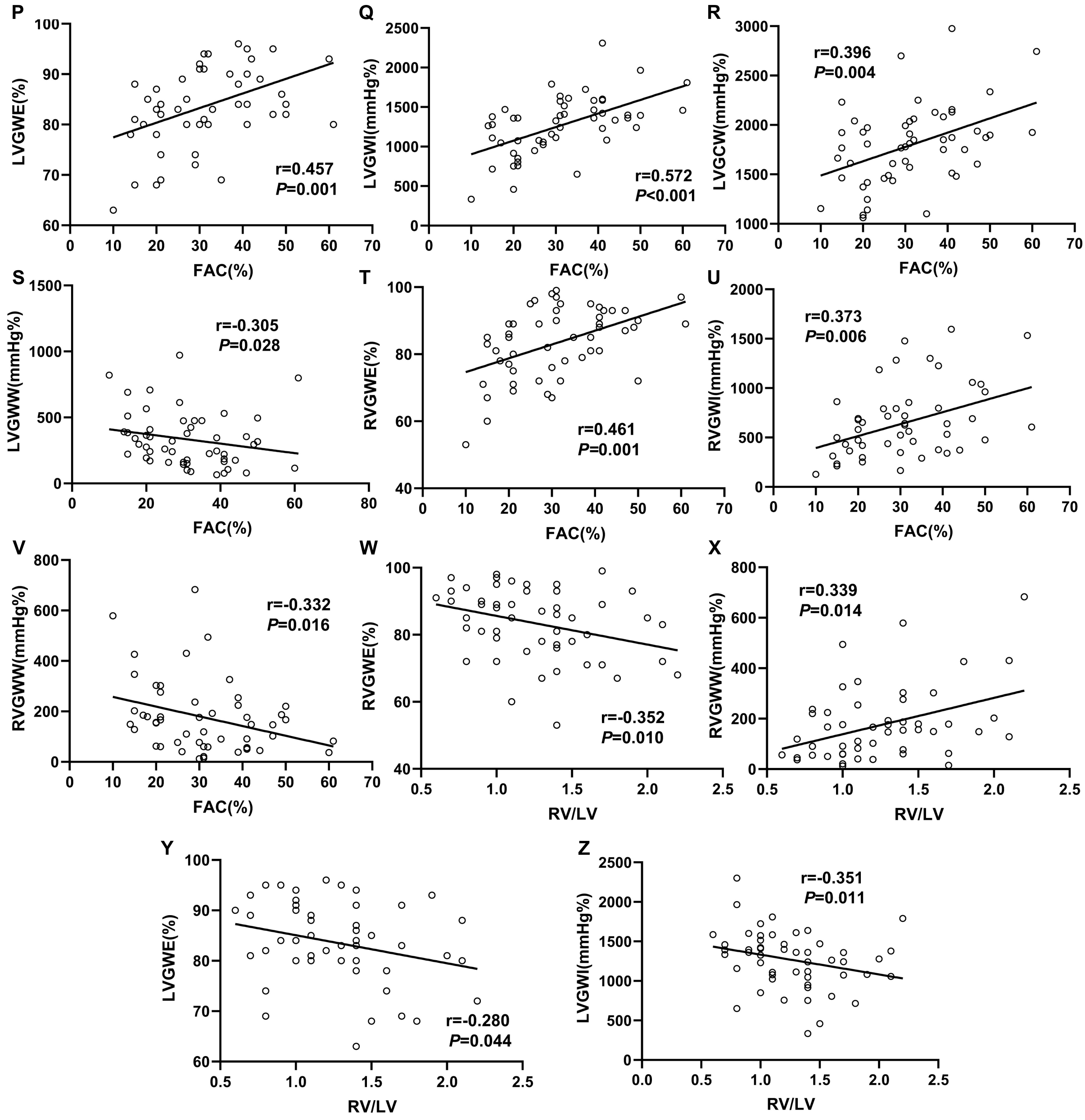

FIGURE 4
Correlation between clinical measurements and myocardial work parameters in the PH patients. The Spearmen correlation coefficients were tested to analyze the relationship between BNP **(A,B)**, 6MWD **(C–H)**, WHO-FC **(I–N)**, TAPSE **(O)**, FAC **(P–V)**, and RV/LV **(W–Z)** with myocardial work parameters. All abbreviations as in **Tables 1**, **2**.

had hospitalization and 2 patients (3.8%) needed enhancement on the basis of original therapy. Best binary logistic model for evaluating adverse events was shown in Table 4 (Hosmer-Lemeshow χ^2 = 4.84, P = 0.775). The formula was as follows: logit (P) = 12.586 – 0.22*RVGWE + 0.051*ePASP. In the model, RVGWE had an OR of 0.803 (95%CI 0.698–0.922, P = 0.002) and ePASP had an OR of 1.052 (95%CI 1.010–1.096, P = 0.015). Furthermore, based on the model, ROC curves showed the combination of RVGWE and ePASP had the biggest area under curve (AUC) with 0.910 (P < 0.0001), which were described in Table 5 and Figure 5.

Discussion

PSL was firstly proposed by Urheim et al. (16) to quantify regional myocardial function by combining LV pressure from micromanometer with myocardial longitudinal strains from

TABLE 4 Best binary logistic model for evaluating adverse events.

Variable	OR	95%CI	*P*-value
RVGWE (%)	0.803	0.698–0.922	0.002
ePASP (mmHg)	1.052	1.010–1.096	0.015

OR, odds ratio; other abbreviations as in Tables 2, 3.

TABLE 5 Receiver operating characteristic analysis for the prediction of adverse events.

Parameter	AUC	*P*-value	Sensitivity (%)	Specificity (%)
RVGWE + ePASP	0.910	< 0.0001	100.0	76.3
RVGWE (%)	0.861	< 0.0001	92.9	73.7
ePASP (mmHg)	0.719	0.016	92.9	44.7

AUC, area under curve; other abbreviations as in Tables 2, 3.

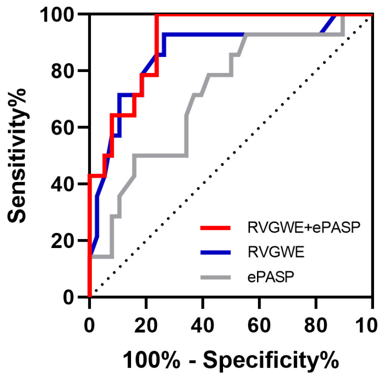

FIGURE 5
ROC curves for the prediction of adverse events. Major adverse events were defined as hospitalization and need of new specific drug therapy or enhancement on the original therapy basis. All abbreviations as in Tables 2, 3.

strain Doppler echocardiography or sonomicrometry. On the basis of this, Russell et al. (10) established an improved non-invasive pressure curve and applied this to measure PSL area which was approximately equivalent to GWI. Furthermore, GCW, GWW and GWE derived from myocardial work assessment were put forward and measured to understand cardiac function more easily (14). Recent studies had shown that LVGWE, LVGCW, and LVGWW exhibited favorable applicability to predict response to cardiac resynchronization therapy (CRT) and long-term cardiac outcome in CRT candidates (17–21). Besides, it has proven that myocardial work parameters were superior to GLS to detect significant coronary artery disease in patients with no regional wall motion abnormalities and normal LVEF by Edwards et al. (22). Butcher et al. (23) also applied RV-PSL to assess RV function in a cohort of patients with heart failure with reduced left ventricular ejection fraction and found that RVGCW could reflect RV systolic function well and it correlated closely with invasively measured stroke volume and stroke volume index. Recently, Butcher et al. reported that decreased values of RVGCW and RVGWI were associated with all-cause mortality in patients with PH (24). This is the first study that quantifies myocardial work through PSL method to evaluate cardiac function and predict clinical prognosis in patients with PH.

Non-invasive PSL refers to estimated ventricular pressure and strain derived from echocardiography. According to Russell et al. (10), LV peak ventricular pressure can be substituted by systolic cuff pressure. Analogously, RV peak ventricular pressure should be equal to PASP from RHC. Echocardiography is widely used to measure non-invasive ePASP, and there is a good correlation between the estimation and actual value (25). A meta-analysis including 29 studies showed that the correlation coefficient between ePASP and PASP was 0.70 (26). However, the accuracy of ePASP is still questioned due to the effect of tricuspid regurgitation. In order to improve the agreement between PASP estimated from echocardiography and measured by RHC, PASPcal is generated by adjusting for TAPSE, FAC, RAP, RAA, RV/LV, LVGLS and RVGLS. It will be more accurate to apply PASPcal instead of ePASP to non-invasive PSL method to calculate RV myocardial work.

In our study, RVGWI, RVGCW and RVGWW substantially increase in PH patients compared to healthy controls while RVGWE decrease to a certain extent. RV is not composed of a single layer of myocardium, but mainly composed of superficial myocardium from the basal part of interventricular septum (IVS) and deep longitudinal myocardium. Under normal conditions, the contraction patterns of RV are mainly as follows: contraction of LV and IVS pull the free wall of RV to move inward, resulting in passive contraction of RV myocardium; the deep longitudinal myocardium of RV free wall contract, causing the tricuspid annular plane to approach to the apex (27); IVS rotates and contracts, participating in the shortening of RV long axis (28). With compensatory hypertrophy of the longitudinal myocardium of inner layer of RV in patients with PH, myocardial work increases to maintain RV ejection volume.

LV and RV are closely related in structure and function, and there is an interaction between two ventricles (29). In Hardegree et al. study (30), despite normal LV size and normal conventional measures of LV systolic function, including end-diastolic dimension, LVEF, and CI, patients with PH had reduced LV free wall systolic strain. The phenomenon may be explained by the reason that chronic RV pressure overload enlarges RV volume and forces IVS to deviate to LV, which further causes LV geometric deformation and dysfunction (31). This is supported by the results of the present study, in which PH patients have poorer LVGWE, LVGWI and LVGCW than healthy controls, whereas LVGWW abnormally increases in PH patients. Meanwhile, we also find that LVEF of patients was not significantly different from that of the control group, which may be due to compensatory enhancement of RV contractility to support LV systolic function (32).

In this study, as an emerging quantitative marker of cardiac function, myocardial work parameter has potential value to definite present cardiac function in PH patients. In clinical practice, WHO-FC remains a determinant part for assessing cardiac function, as it provides cardiologists with valuable information for determining disease severity, improvement, deterioration or stability. A follow-up cohort study containing 982 PH patients with WHO-FC III at baseline in the REVEAL Registry have shown that patients who improve from WHO-FC III to I/II have better prognosis than those who remain III or worsen to IV by Kaplan-Meier estimates of 3-year survival (33). WHO-FC presents substantial utility of evaluation of patients with PH. However, there is certain subjectivity and interobserver variation in WHO-FC assessment which is dependent on the experience of cardiologists (34). As supplements, myocardial stress markers such as BNP (35), exercise capacity tests such as 6MWD (36) and other echocardiography characteristics such as TAPSE (37), FAC (38), RAA (39), and RV/LV (40) are referred to evaluate cardiac function in PH patients more accurately. The NORRE study had proven LV myocardial work parameters correlate well with traditional parameters of systolic function in healthy subjects (41, 42). In the present study, myocardial work parameters correlate significantly with other clinical assessments of cardiac function. Myocardial work parameters will provide quantifiable information for identification of cardiac function status as another supplement to aid in clinical decision making.

Management of cardiac function is critical to the prognosis of patients with PH. Guidelines put emphasis on the importance of RV function in PH patients (1), as RV function has proven been a major determinant of prognosis among PH patients irrespective of etiology (43). RV is sensitive to pressure overload. And analysis of RV function independent of the effect of pulmonary artery pressure, does not provide accurate clinical evidence. RV-pulmonary artery coupling explains RV function in the perspective of the pulmonary circulation as a whole (44). There is no conclusive evidence for non-invasive assessment of RV-pulmonary artery coupling (45). In our current study, combination of RVGWE and ePASP is a potential novel model for assessment of RV-pulmonary artery coupling. RVGWE is a form of RV intrinsic contractility derived from PSL which is less dependent on the load. In addition, ePASP can reflect the elasticity of the pulmonary artery indirectly. In the prognostic study, the value of combination of RVGWE and ePASP is superior to individual parameter with the biggest AUC of 0.910. It is worthwhile to highlight that combination of RVGWE and ePASP has potential prognostic value to assist physicians in deliberating on the therapeutic schedule for each patient during follow-up.

There are some limitations in the present study. First, this is a single-center and small population cohort study, which may produce a selection bias. Because of a relatively short follow-up period, the prognostic use of myocardial work by PSL method needs to be further demonstrated. Second, in the absence of myocardial work analysis before specific drug therapy, we have no chance to explore the short- and long-term effect of specific drug therapy on myocardial work parameters.

Conclusion

Non-invasive PSL is feasible for quantifying myocardial work in patients with PH. Myocardial work parameters derived from PSL method are the emerging markers of cardiac function and the combination RVGWE and ePASP is a useful predictor of the clinical outcome in patients with PH.

Data availability statement

The original contributions presented in this study are included in the article/supplementary material, further inquiries can be directed to the corresponding author.

Ethics statement

The studies involving human participants were reviewed and approved by Clinical Ethics Committee of Shanghai Renji Hospital. The patients/participants provided their written informed consent to participate in this study.

Author contributions

JW: original manuscript drafting and writing—review and editing. CN: statistical analysis and figures graphing. MY and XZ: data collection and literature research. BR and LS: clinical studies. XS and JS: conceptualization, supervision, project administration, and funding acquisition. All authors have studied concepts/study design or data acquisition or data analysis/interpretation, manuscript drafting or manuscript revision for important intellectual content, approval of final version of submitted manuscript, and agreed to ensure any questions related to the work are appropriately resolved.

Funding

This work was supported by National Natural Science Foundation of China (CN) (81970047 and 81800048) and Clinical Research Innovation and Incubation Foundation of

Renji Hospital, Shanghai Jiao Tong University School of Medicine (PYII20-13).

Conflict of interest

The authors declare that the research was conducted in the absence of any commercial or financial relationships that could be construed as a potential conflict of interest.

Publisher's note

References

1. Galie N, Humbert M, Vachiery J, Gibbs S, Lang I, Torbicki A, et al. 2015 ESC/ERS guidelines for the diagnosis and treatment of pulmonary hypertension: the joint task force for the diagnosis and treatment of pulmonary hypertension of the European society of cardiology (ESC) and the European respiratory society (ERS): endorsed by: association for european paediatric and congenital cardiology (AEPC), international society for heart and lung transplantation (ISHLT). *Eur Respir J.* (2015) 46:903–75. doi: 10.1183/13993003.01032-2015

2. D'Alonzo G, Barst R, Ayres S, Bergofsky E, Brundage B, Detre K, et al. Survival in patients with primary pulmonary hypertension. Results from a national prospective registry. *Ann Intern Med.* (1991) 115:343–9. doi: 10.7326/0003-4819-115-5-343

3. Nickel N, Golpon H, Greer M, Knudsen L, Olsson K, Westerkamp V, et al. The prognostic impact of follow-up assessments in patients with idiopathic pulmonary arterial hypertension. *Eur Respir J.* (2012) 39:589–96. doi: 10.1183/09031936.00092311

4. Lim Y, Low T, Chan S, Teo T, Jang J, Yip N, et al. Pulmonary arterial hypertension in a multi-ethnic Asian population: characteristics, survival and mortality predictors from a 14-year follow-up study. *Respirology.* (2019) 24:162–70. doi: 10.1111/resp.13392

5. van Wolferen S, Marcus J, Boonstra A, Marques K, Bronzwaer J, Spreeuwenberg M, et al. Prognostic value of right ventricular mass, volume, and function in idiopathic pulmonary arterial hypertension. *Eur Heart J.* (2007) 28:1250–7. doi: 10.1093/eurheartj/ehl477

6. van de Veerdonk M, Kind T, Marcus J, Mauritz G, Heymans M, Bogaard H, et al. Progressive right ventricular dysfunction in patients with pulmonary arterial hypertension responding to therapy. *J Am Coll Cardiol.* (2011) 58:2511–9. doi: 10.1016/j.jacc.2011.06.068

7. Kallianos K, Brooks G, Mukai K, Seguro de Carvalho F, Liu J, Naeger D, et al. Cardiac magnetic resonance evaluation of left ventricular myocardial strain in pulmonary hypertension. *Acad Radiol.* (2018) 25:129–35. doi: 10.1016/j.acra.2017.07.009

8. Padervinskienë L, Krivickienë A, Hoppenot D, Miliauskas S, Basevièius A, Nedzelskienë I, et al. Prognostic value of left ventricular function and mechanics in pulmonary hypertension: a pilot cardiovascular magnetic resonance feature tracking study. *Medicina.* (2019) 55:73. doi: 10.3390/medicina55030073

9. Hubert A, Le Rolle V, Leclercq C, Galli E, Samset E, Casset C, et al. Estimation of myocardial work from pressure-strain loops analysis: an experimental evaluation. *Eur Heart J Cardiovasc Imaging.* (2018) 19:1372–9. doi: 10.1093/ehjci/jey024

10. Russell K, Eriksen M, Aaberge L, Wilhelmsen N, Skulstad H, Remme E, et al. A novel clinical method for quantification of regional left ventricular pressure-strain loop area: a non-invasive index of myocardial work. *Eur Heart J.* (2012) 33:724–33. doi: 10.1093/eurheartj/ehs016

11. Chan J, Edwards N, Khandheria B, Shiino K, Sabapathy S, Anderson B, et al. A new approach to assess myocardial work by non-invasive left ventricular pressure-strain relations in hypertension and dilated cardiomyopathy. *Eur Heart J Cardiovasc Imaging.* (2019) 20:31–9. doi: 10.1093/ehjci/jey131

12. Rubin L. Diagnosis and management of pulmonary arterial hypertension: ACCP evidence-based clinical practice guidelines. *Chest.* (2004) 126(1 Suppl.):7S–10S. doi: 10.1378/chest.126.1_suppl.7S

13. Mitchell C, Rahko P, Blauwet L, Canaday B, Finstuen J, Foster M, et al. Guidelines for performing a comprehensive transthoracic echocardiographic examination in adults: recommendations from the American society of echocardiography. *J Am Soc Echocardiogr.* (2019) 32:1–64. doi: 10.1016/j.echo.2018.06.004

14. Russell K, Eriksen M, Aaberge L, Wilhelmsen N, Skulstad H, Gjesdal O, et al. Assessment of wasted myocardial work: a novel method to quantify energy loss due to uncoordinated left ventricular contractions. *Am J Physiol Heart Circ Physiol.* (2013) 305:H996–1003. doi: 10.1152/ajpheart.00191.2013

15. Sun L, Lyu Y, Zhang H, Shen Z, Lin G, Geng N, et al. Nuclear receptor NR1D1 regulates abdominal aortic aneurysm development by targeting the mitochondrial tricarboxylic acid cycle enzyme aconitase-2. *Circulation.* (2022) 146:1591–609. doi: 10.1161/CIRCULATIONAHA.121.057623

16. Urheim S, Rabben S, Skulstad H, Lyseggen E, Ihlen H, Smiseth O, et al. Regional myocardial work by strain Doppler echocardiography and LV pressure: a new method for quantifying myocardial function. *Am J Physiol Heart Circ Physiol.* (2005) 288:H2375–80. doi: 10.1152/ajpheart.00946.2004

17. van der Bijl P, Vo N, Kostyukevich M, Mertens B, Ajmone Marsan N, Delgado V, et al. Prognostic implications of global, left ventricular myocardial work efficiency before cardiac resynchronization therapy. *Eur Heart J Cardiovasc Imaging.* (2019) 20:1388–94. doi: 10.1093/ehjci/jez095

18. Galli E, Leclercq C, Hubert A, Bernard A, Smiseth O, Mabo P, et al. Role of myocardial constructive work in the identification of responders to CRT. *Eur Heart J Cardiovasc Imaging.* (2018) 19:1010–8. doi: 10.1093/ehjci/jex191

19. Galli E, Leclercq C, Fournet M, Hubert A, Bernard A, Smiseth O, et al. Value of myocardial work estimation in the prediction of response to cardiac resynchronization therapy. *J Am Soc Echocardiogr.* (2018) 31:220–30. doi: 10.1016/j.echo.2017.10.009

20. Galli E, Hubert A, Le Rolle V, Hernandez A, Smiseth O, Mabo P, et al. Myocardial constructive work and cardiac mortality in resynchronization therapy candidates. *Am Heart J.* (2019) 212:53–63. doi: 10.1016/j.ahj.2019.02.008

21. Vecera J, Penicka M, Eriksen M, Russell K, Bartunek J, Vanderheyden M, et al. Wasted septal work in left ventricular dyssynchrony: a novel principle to predict response to cardiac resynchronization therapy. *Eur Heart J Cardiovasc Imaging.* (2016) 17:624–32. doi: 10.1093/ehjci/jew019

22. Edwards N, Scalia G, Shiino K, Sabapathy S, Anderson B, Chamberlain R, et al. Global myocardial work is superior to global longitudinal strain to predict significant coronary artery disease in patients with normal left ventricular function and wall motion. *J Am Soc Echocardiogr.* (2019) 32:947–57. doi: 10.1016/j.echo.2019.02.014

23. Butcher S, Fortuni F, Montero-Cabezas J, Abou R, El Mahdiui M, van der Bijl P, et al. Right ventricular myocardial work: proof-of-concept for non-invasive assessment of right ventricular function. *Eur Heart J Cardiovasc Imaging.* (2021) 22:142–52. doi: 10.1093/ehjci/jeaa261

24. Butcher S, Feloukidis C, Kamperidis V, Yedidya I, Stassen J, Fortuni F, et al. Right ventricular myocardial work characterization in patients with pulmonary hypertension and relation to invasive hemodynamic parameters and outcomes. *Am J Cardiol.* (2022) 177:151–61. doi: 10.1016/j.amjcard.2022.04.058

25. Shen J, Chen S, Wu Y, Tao R, Gu Y, Bao C, et al. Pulmonary hypertension in systemic lupus erythematosus. *Rheumatol Int.* (1999) 18:147–51. doi: 10.1007/s002960050074

26. Janda S, Shahidi N, Gin K, Swiston J. Diagnostic accuracy of echocardiography for pulmonary hypertension: a systematic review and meta-analysis. *Heart.* (2011) 97:612–22. doi: 10.1136/hrt.2010.212084

27. Sallin E. Fiber orientation and ejection fraction in the human left ventricle. *Biophys J.* (1969) 9:954–64. doi: 10.1016/S0006-3495(69)86429-5

28. Buckberg G, Nanda N, Nguyen C, Kocica M. What is the heart? Anatomy, Function, Pathophysiology, and Misconceptions. *J Cardiovasc Dev Dis.* (2018) 5:33. doi: 10.3390/jcdd5020033

29. Naeije R, Badagliacca R. The overloaded right heart and ventricular interdependence. *Cardiovasc Res.* (2017) 113:1474–85. doi: 10.1093/cvr/cvx160

30. Hardegree E, Sachdev A, Fenstad E, Villarraga H, Frantz R, McGoon M, et al. Impaired left ventricular mechanics in pulmonary arterial hypertension: identification of a cohort at high risk. *Circ Heart Fail.* (2013) 6:748–55. doi: 10.1161/CIRCHEARTFAILURE.112.000098

31. Puwanant S, Park M, Popović Z, Tang W, Farha S, George D, et al. Ventricular geometry, strain, and rotational mechanics in pulmonary hypertension. *Circulation.* (2010) 121:259–66. doi: 10.1161/CIRCULATIONAHA.108.844340

32. Hardziyenka M, Campian M, Reesink H, Surie S, Bouma B, Groenink M, et al. Right ventricular failure following chronic pressure overload is associated with reduction in left ventricular mass: evidence for atrophic remodeling. *J Am Coll Cardiol.* (2011) 57:921–8. doi: 10.1016/j.jacc.2010.08.648

33. Barst R, Chung L, Zamanian R, Turner M, McGoon M. Functional class improvement and 3-year survival outcomes in patients with pulmonary arterial hypertension in the REVEAL Registry. *Chest.* (2013) 144:160–8. doi: 10.1378/chest.12-2417

34. Taichman D, McGoon M, Harhay M, Archer-Chicko C, Sager J, Murugappan M, et al. Wide variation in clinicians' assessment of New York heart association/World Health Organization functional class in patients with pulmonary arterial hypertension. *Mayo Clin Proc.* (2009) 84:586–92. doi: 10.4065/84.7.586

35. Warwick G, Thomas P, Yates D. Biomarkers in pulmonary hypertension. *Eur Respir J.* (2008) 32:503–12. doi: 10.1183/09031936.00160307

36. Fritz J, Blair C, Oudiz R, Dufton C, Olschewski H, Despain D, et al. Baseline and follow-up 6-min walk distance and brain natriuretic peptide predict 2-year mortality in pulmonary arterial hypertension. *Chest.* (2013) 143:315–23. doi: 10.1378/chest.12-0270

37. Forfia P, Fisher M, Mathai S, Housten-Harris T, Hemnes A, Borlaug B, et al. Tricuspid annular displacement predicts survival in pulmonary hypertension. *Am J Respir Crit Care Med.* (2006) 174:1034–41. doi: 10.1164/rccm.200604-547OC

38. Raymond R, Hinderliter A, Willis P, Ralph D, Caldwell E, Williams W, et al. Echocardiographic predictors of adverse outcomes in primary pulmonary hypertension. *J Am Coll Cardiol.* (2002) 39:1214–9.

39. Bustamante-Labarta M, Perrone S, De La Fuente R, Stutzbach P, De La Hoz R, Torino A, et al. Right atrial size and tricuspid regurgitation severity predict mortality or transplantation in primary pulmonary hypertension. *J Am Soc Echocardiogr.* (2002) 15(10 Pt. 2):1160–4. doi: 10.1067/mje.2002.123962

40. Forfia P, Vachiéry J. Echocardiography in pulmonary arterial hypertension. *Am J Cardiol.* (2012) 110(6 Suppl.):16S–24S. doi: 10.1016/j.amjcard.2012.06.012

41. Manganaro R, Marchetta S, Dulgheru R, Ilardi F, Sugimoto T, Robinet S, et al. Echocardiographic reference ranges for normal non-invasive myocardial work indices: results from the EACVI NORRE study. *Eur Heart J Cardiovasc Imaging.* (2019) 20:582–90. doi: 10.1093/ehjci/jey188

42. Manganaro R, Marchetta S, Dulgheru R, Sugimoto T, Tsugu T, Ilardi F, et al. Correlation between non-invasive myocardial work indices and main parameters of systolic and diastolic function: results from the EACVI NORRE study. *Eur Heart J Cardiovasc Imaging.* (2020) 21:533–41. doi: 10.1093/ehjci/jez203

43. McLaughlin V, Presberg K, Doyle R, Abman S, McCrory D, Fortin T, et al. Prognosis of pulmonary arterial hypertension: ACCP evidence-based clinical practice guidelines. *Chest.* (2004) 126(1 Suppl.):78S–92S. doi: 10.1378/chest.126.1_suppl.78S

44. Kubba S, Davila C, Forfia P. Methods for evaluating right ventricular function and ventricular-arterial coupling. *Prog Cardiovasc Dis.* (2016) 59:42–51. doi: 10.1016/j.pcad.2016.06.001

45. Tello K, Wan J, Dalmer A, Vanderpool R, Ghofrani H, Naeije R, et al. Validation of the tricuspid annular plane systolic excursion/systolic pulmonary artery pressure ratio for the assessment of right ventricular-arterial coupling in severe pulmonary hypertension. *Circ Cardiovasc Imaging.* (2019) 12:e009047. doi: 10.1161/CIRCIMAGING.119.009047

frontiers | Frontiers in Cardiovascular Medicine

TYPE Original Research
PUBLISHED 22 December 2022
DOI 10.3389/fcvm.2022.1065131

Check for updates

OPEN ACCESS

EDITED BY
Giuseppe Pannarale,
Sapienza University of Rome, Italy

REVIEWED BY
Ferdinando Loiacono,
Humanitas Research Hospital, Italy
Federico Fortuni,
Leiden University Medical Center
(LUMC), Netherlands

*CORRESPONDENCE
Luigi P. Badano
✉ l.badano@auxologico.it

SPECIALTY SECTION
This article was submitted to
Cardiovascular Imaging,
a section of the journal
Frontiers in Cardiovascular Medicine

RECEIVED 09 October 2022
ACCEPTED 09 December 2022
PUBLISHED 22 December 2022

CITATION
Muraru D, Baldea SM, Genovese D, Tomaselli M, Heilbron F, Gavazzoni M, Radu N, Sergio C, Baratto C, Perelli F, Curti E, Parati G and Badano LP (2022) Association of outcome with left ventricular volumes and ejection fraction measured with two- and three-dimensional echocardiography in patients referred for routine, clinically indicated studies.
Front. Cardiovasc. Med. 9:1065131.
doi: 10.3389/fcvm.2022.1065131

Association of outcome with left ventricular volumes and ejection fraction measured with two- and three-dimensional echocardiography in patients referred for routine, clinically indicated studies

Denisa Muraru[1,2], Sorina Mihaila Baldea[3], Davide Genovese[4], Michele Tomaselli[2], Francesca Heilbron[2], Mara Gavazzoni[2], Noela Radu[3], Caravita Sergio[2,5], Claudia Baratto[1,2], Francesco Perelli[1], Emanuele Curti[1], Gianfranco Parati[2] and Luigi P. Badano[1,2]*

[1]Department of Medicine and Surgery, University of Milano-Bicocca, Milan, Italy, [2]Department of Cardiology, Istituto Auxologico Italiano, IRCCS, Milan, Italy, [3]Department of Cardiology, University of Medicine and Pharmacy Carol Davila, Bucharest, Romania, [4]Cardiology Unit, Cardio-Neuro-Vascular Department, Ca' Foncello Hospital, Treviso, Italy, [5]Department of Management, Information and Production Engineering, University of Bergamo, Dalmine, Italy

Objectives: We sought to analyze if left ventricular (LV) volumes and ejection fraction (EF) measured by three-dimensional echocardiography (3DE) have incremental prognostic value over measurements obtained from two-dimensional echocardiography (2DE) in patients referred to a high-volume echocardiography laboratory for routine, clinically-indicated studies.

Methods: We measured LV volumes and EF using both 2DE and 3DE in 725 consecutive patients (67% men; 59 ± 18 years) with various clinical indications referred for a routine clinical study.

Results: LV volumes were significantly larger, and EF was lower when measured by 3DE than 2DE. During follow-up (3.6 ± 1.2 years), 111 (15.3%) all-cause deaths and 248 (34.2%) cardiac hospitalizations occurred. Larger LV volumes and lower EF were associated with worse outcome independent of age, creatinine, hemoglobin, atrial fibrillation, and ischemic heart diseases). In stepwise Cox regression analyses, the associations of both death and cardiac hospitalization with clinical data (CD: age, creatinine, hemoglobin, atrial fibrillation, and ischemic heart disease) whose Harrel's C-index (HC) was 0.775, were augmented more by the LV volumes and EF obtained by 3DE than by 2DE parameters. The association of CD with death was not affected by LV end-diastolic volume (EDV) either measured by 2DE or 3DE. Conversely, it was incremented by 3DE LVEF (HC = 0.84, $p < 0.001$) more than 2DE LVEF (HC = 0.814, $p < 0.001$). The association of CD with the composite endpoint (HC = 0.64, $p = 0.002$) was augmented more by 3DE LV EDV (HC = 0.786, $p < 0.001$), end-systolic volume (HC = 0.801, $p < 0.001$), and EF (HC = 0.84, $p < 0.001$) than by the correspondent 2DE parameters (HC = 0.786, HC = 0.796, and 0.84, all $p < 0.001$) In addition, partition values for mild, moderate and severe reduction of the LVEF measured by 3DE showed a higher discriminative power than those measured by 2DE for cardiac death (Log-Rank: $\chi^2 = 98.3$ vs. $\chi^2 = 77.1$; $p < 0.001$). Finally, LV dilation defined according to the 3DE threshold values showed higher discriminatory power and prognostic value for death than when using 2DE reference values (3DE LVEDV: $\chi^2 = 15.9$, $p < 0.001$ vs. $\chi^2 = 10.8$, $p = 0.001$; 3DE LVESV: $\chi^2 = 24.4$, $p < 0.001$ vs. $\chi^2 = 17.4$, $p = 0.001$).

Conclusion: In patients who underwent routine, clinically-indicated echocardiography, 3DE LVEF and ESV showed stronger association with outcome than the corresponding 2DE parameters.

KEYWORDS

three-dimensional echocardiography, two-dimensional echocardiography, left ventricular volumes, left ventricular ejection fraction, outcome

Introduction

Left ventricular (LV) volumes and ejection fraction (EF) are key parameters to establish a diagnosis and stratify the prognosis in patients with various cardiac conditions (1–5). Moreover, important treatment decisions and evaluation of therapeutic effects are based on these parameters (6–9). Although several imaging techniques can be used to measure LV geometry and function, two-dimensional echocardiography (2DE) represents by far the most frequent imaging modality to obtain LV volumes and EF for both clinical and research purposes. However, 2DE calculations are hampered by view acquisition errors (i.e., view foreshortening), taking into account the function of a limited amount of LV myocardium, and reliance on fixed geometrical assumptions about the geometry of the LV, all of them affecting both the accuracy and the reproducibility of volume calculations (10–13).

The introduction of three-dimensional echocardiography (3DE) in the clinical routine represented a change in paradigm in clinical echocardiography. 3DE overcomes the geometric assumptions about LV geometry, considers the contribution of the whole myocardial shell to LV EF, and enables an accurate and reproducible measurement of LV volumes and EF to be used to manage patient (14). Several studies have shown that 3DE measurements of LV volumes are significantly more accurate than 2DE calculations when compared with cardiac magnetic resonance as the reference imaging modality (10, 15). Accordingly, the American Society of Echocardiography and the European Association of Cardiovascular Imaging have published guidelines about the acquisition and postprocessing of 3DE datasets of the LV, and the recently published guidelines for the cardiac chamber quantification with echocardiography recommends, whenever feasible, the 3DE measurement of LV volumes and EF (16, 17).

Since then, several studies have reported the additive prognostic power of LV volumes and EF measured by 3DE over those calculated by 2DE (18–20). However, despite all these pieces of evidence, the use of 3DE for the assessment of LV volumes and LVEF is not widespread in the clinical arena, yet. Indeed, the added value of 3DE over 2DE parameters describing the LV geometry and function on the prediction of patients' outcome remains to be clarified in the clinical routine of the echocardiography laboratory.

Accordingly, the aim of our study was to test the hypothesis that LV volumes and EF measured with 3DE has an incremental value over 2DE in predicting outcome in routine patients referred for clinically indicated echocardiography studies.

Materials and methods

Study design

We performed a single center, prospective analysis of retrospectively acquired echocardiographic studies obtained

---

Abbreviations: 2DE, two-dimensional echocardiography; 3DE, three-dimensional echocardiography; CD, clinical data; EDV, end-diastolic volume; EF, ejection fraction; ESV, end-systolic volume; LV, left ventricular.

from both in- and out-patients performed from October 2018 to December 2021 at our laboratory. Exclusion criteria were age less than 18 years, lack of 3DE acquisitions or incomplete 2DE data for LV volume quantitation, poor quality of the either 2DE or 3DE acquisitions (defined as the impossibility to visualize the endocardium of two or more adjacent LV myocardial segments without the use of contrast agents), echocardiographic studies performed for non-clinical indications (e.g., driving license, sports activity screening, etc.), and lack of follow-up data.

Clinical information at the time of the echocardiographic study included patients risk factors such as hypertension (either blood pressure >140/90 mm Hg or active antihypertensive treatment), hypercholesterolemia (LDL cholesterol >130 mg/dl or active statin treatment), diabetes (fasting glucose > 126 mg/dl), serum levels of creatinine, hemoglobin, atrial fibrillation, and history of ischemic heart disease (previous myocardial infarction or documented coronary artery disease). Data were obtained from the clinical records of our hospital (**Table 1**). This retrospective analysis of prospectively acquired data was approved by the Ethics Committee of the Istituto Auxologico Italiano, IRCCS (record #2021_05_18_13, approved on May 18, 2021). The need for patient written informed consent was waived due to the retrospective nature of the acquisitions.

Echocardiography

All 2DE and 3DE acquisitions were obtained during the same echocardiographic study using a commercially available echocardiography system (Vivid E95, GE Healthcare, Horten, NO) equipped with both standard 2DE (M5S) and 3DE (4Vc) probes. All echocardiography studies were stored in a digital archive to be exported and analyzed offline using a commercially available software (Echopac BT204, GE Healthcare, Horten, NO).

From the apical four- and two-chamber views, the 2D LV volumes and EF were measured offline by a single experienced operator using the biplane method of disks' summation (modified Simpson's rule, **Figure 1**) (17). 3DE datasets of the LV were obtained from the apical approach using multi-beat full-volume acquisition during breath-holding and taking care to encompass the entire LV cavity in the dataset (16, 21). 3D LV volumes and EF (**Figure 1**) were measured offline by a single experienced operator using a dedicated software package for the LV analysis (4D AutoLVQ, GE Healthcare, Horten, NO). Measurement workflow started with the semi-automated detection of the LV endocardial borders. When needed, manual editing was used to optimize the endocardial contour identification (22). To trace the endocardial borders of both the 2DE and 3DE datasets, the end-diastolic frame was selected as the frame before the mitral valve closure, whereas the end-systolic frame was identified as the frame before mitral valve opening.

Follow-up and study endpoints

The primary clinical endpoint was the occurrence of death for any cause. The secondary endpoint was the composite of all-cause death and hospitalization for cardiac indication (either from heart failure, acute coronary syndromes, or arrhythmias). Information concerning both survival and hospitalization were obtained at regular intervals via: (*i*). review of electronic medical records of regular outpatient visits and hospital admission records; (*ii*). telephone interview with the patient, or if deceased, with family members; and (*iii*). contact with the patient's physicians. Mortality status was verified independently through the Social Security Death Index and death certificates. For patients without events, the date of the last contact was used for survival analysis. Assignment of clinical events was performed by physicians unaware of the patients' echocardiographic and clinical characteristics.

Statistical analysis

The normal distribution of continuous variables was tested with Kolmogorov–Smirnov test. Continuous variables were expressed as mean ± SD or as median (interquartile range). Categorical variables were expressed as absolute numbers (percentages). We compared the clinical and echocardiographic characteristics between patients who died and those who survived. Student's t test for independent samples was used to compare differences between two groups of normally distributed continuous variables, while Mann-Whitney's test was used to compare differences between two groups of non-normally distributed continuous variables. The chi-square test was used to assess differences between two groups of categorical variables. Pearson correlation coefficient was used to assess correlations between 2DE and 3DE parameters. Kaplan Meier curves were constructed to assess the prognostic stratification for the different 2DE and 3DE parameters. The log-rank test was used to assess the statistical significance between strata.

Since there was a high correlation between 2DE and 3DE LV volumes and EF, we built several pairs of models by separately adding the 2DE and 3DE parameters into the baseline clinical model. The first step used only the clinical variables available in our cohort (thus excluding the echocardiographic parameters), in a stepwise Cox proportional-hazard model, censoring data at first event. The clinical variables with significance level < 0.05 were included into the multivariate baseline clinical model (CM). Next, the 2DE parameters were added sequentially to the baseline CM, and then we built a third model by adding sequentially the 3DE

TABLE 1 Clinical and echocardiographic data of the whole study population and their comparison between patients who died and those who survived.

	Study cohort (n = 725)	All-cause deaths (n = 111)	Survivors (n = 614)	P-value
Age, years	59 ± 18	69 ± 16	57 ± 18	**0.025**
Male, n(%)	487 (67)	75 (68)	412 (67)	0.852
Heart rate, bpm	70 ± 15	74 ± 19	69 ± 15	**0.003**
Systolic blood pressure, mm Hg	125 ± 20	120 ± 20	125 ± 19	0.813
Diastolic blood pressure, mm Hg	74 ± 11	71 ± 2	75 ± 11	0.906
Body mass index > 25 Kg/m^2, n (%)	365 (50)	330 (51)	35 (42)	0.113
Hypertension, n (%)	401 (55)	356 (56)	45 (54)	0.831
Smoking, n (%)	259 (36)	234 (36)	25 (30)	0.258
Diabetes, n (%)	113 (16)	92 (14)	21 (25)	**0.010**
Dyslipidemia, n (%)	306 (42)	273 (43)	33 (40)	0.631
Chronic kidney disease, n (%)	363 (50)	296 (46)	67 (81)	**<0.001**
Anemia, n (%)	211 (29)	159 (25)	52 (63)	**<0.001**
Atrial fibrillation, n (%)	133 (18)	102 (16)	31 (37)	**<0.001**
Ischemic heart disease, n (%)	178 (25)	142 (22)	36 (43)	**<0.001**
2DLeft ventricular end-diastolic volume, ml/m^2	73 ± 28	85 ± 42	71 ± 24	**<0.001**
2DLeft ventricular end-systolic volume, ml/m^2	36 ± 24	50 ± 37	33 ± 20	**<0.001**
2DLeft ventricular stroke volume, ml/m^2	37 ± 10	35 ± 11	37 ± 10	0.499
2D Left ventricular ejection fraction,%	54 ± 12	46 ± 14	55 ± 11	**<0.001**
3DLeft ventricular end-diastolic volume, ml/m^2	81 ± 30	94 ± 43	78 ± 26	**<0.001**
3DLeft ventricular end-systolic volume, ml/m^2	42 ± 28	59 ± 42	38 ± 23	**<0.001**
3DLeft ventricular stroke volume, ml/m^2	39 ± 11	35 ± 10	40 ± 71	0.359
3D Left ventricular ejection fraction,%	52 ± 13	43 ± 16	54 ± 12	**<0.001**

Bold values represent the statistically significant.

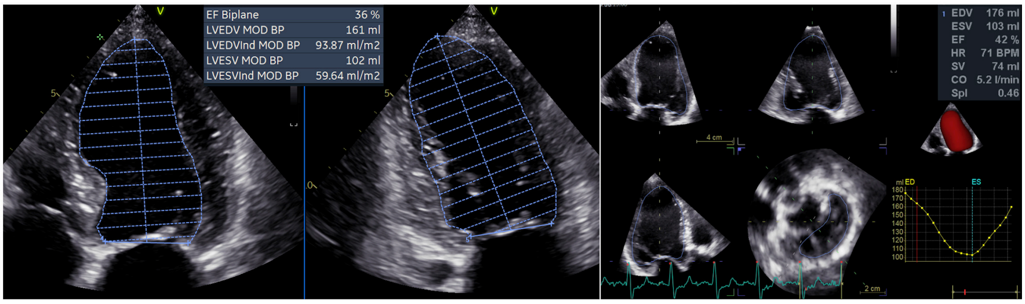

FIGURE 1
Left ventricular volumes and ejection fraction calculated by two-dimensional echocardiography **(left panel)** and measured by three-dimensional echocardiography **(right panel)**. CO, cardiac output; EDV, left ventricular end-diastolic volume; ESV, left ventricular end-systolic volume; EF, ejection fraction; HR, heart rate; LV, left ventricular; MOD BP, biplane mode; SV, stroke volume; SpI, sphericity index.

parameters to the baseline CM, resulting in pairs of models for the end-diastolic volume (EDV), the end-systolic volume (ESV), and EF. The proportional hazards assumption for the Cox regression models was verified by visual assessment of Kaplan-Meier curves. The whole process was repeated for both the all-cause death and the composite endpoint. The independent and incremental value of each model compared to the previous one was assessed by comparing model χ^2 statistics. Model discrimination was further assessed using Harrel's C-index. Comparison of the C statistics of the various multivariable models was performed using the method proposed by Newson RB (23).

Time-dependent Receiver Operating Characteristics (ROC) curve analyses for censored event times were used to compare the prognostic value of the LVEF severity grading threshold values obtained with 2DE and 3DE and Areas Under Curve (AUC) were derived. The De Long test was used to compare the AUCs of tested threshold values (24).

Data were analyzed using SPSS v.24.0 (SPSS Inc., Chicago, IL, USA) and MedCalc 20, (MedCalc Software Ltd., Ostend, Belgium). Statistical significance was defined as $p < 0.5$.

Results

Clinical data and outcome

The final study population included 725 patients with various cardiac conditions (**Table 1**) who underwent echocardiography for various clinical reasons (**Figure 2**).

During the follow-up period of (median 3.39 years, IQR = 2.6 years), 111 (15.3%) deaths (83 of them, 75% were cardiac deaths), and 248 (34.2%) cardiac hospitalizations occurred. The latter were distributed as follows: 151 (20.8%) for heart failure, 51 (7.0%) for acute coronary syndrome, and 46 (6.3%) for arrhythmias. Finally, 304 (41.9%) patients reached the composite endpoint of all-cause death or cardiac hospitalization.

Patients who died were older and had higher heart rate than survivors (**Table 1**). In addition, patients who died had a higher prevalence of diabetes, chronic kidney disease, anemia, permanent atrial fibrillation, and history of ischemic heart disease than the survivors (**Table 1**). Conversely, sex and body mass index distribution, as well as the prevalence of smoking, hypertension, and dyslipidemia were similar between the two groups.

Comparison between 2D and 3D echocardiography and association with outcomes

As expected, there was a close correlation between the 2DE and 3DE LV EDVs ($r = 0.964$; $p < 0.001$), ESVs ($r = 0.972$; $p < 0.001$), and EFs ($r = 0.925$; $p < 0.001$). However, 3DE LV volumes were larger than the 2DE LV volumes (bias = + 21 ml, LOI ± 18 ml for the EDV, and bias = + 19 ml, LOI ± 10 ml for the ESV, respectively), whereas the 3D LVEF was lower than the 2D LVEF (bias = −2%, LOI ± 10).

2DE and 3DE LV volumes were categorized into normal or dilated according to technique-specific threshold values. The incidence of LV dilatation was significantly higher when LV EDV and ESV were calculated by 2DE than when they were measured with 3DE (45% vs. 35%, $X^2 = 12.93$; $p = 0.0003$ and 56 vs. 51%, $X^2 = 4.237$; $p = 0.034$, respectively).

The patients who died had larger LV EDV and ESV, as well as lower EF, by both 2DE and 3DE than the survivors (**Table 1**). Although 2DE LV volumes were associated to worse all-cause death survival and event-free survival, 3DE LV volumes were stronger predictors of both. 3DE EDV $\leq$ 85 ml/m^2 in men and $\leq$ 78 ml/m^2 in women ($X^2 = 15.661$; $p < 0.001$) and 3DE ESV $\leq$ 34 ml/m^2 in men and $\leq$ 28 ml/m^2 in women ($X^2 = 20.173$; $p < 0.001$) were more strongly associated (all

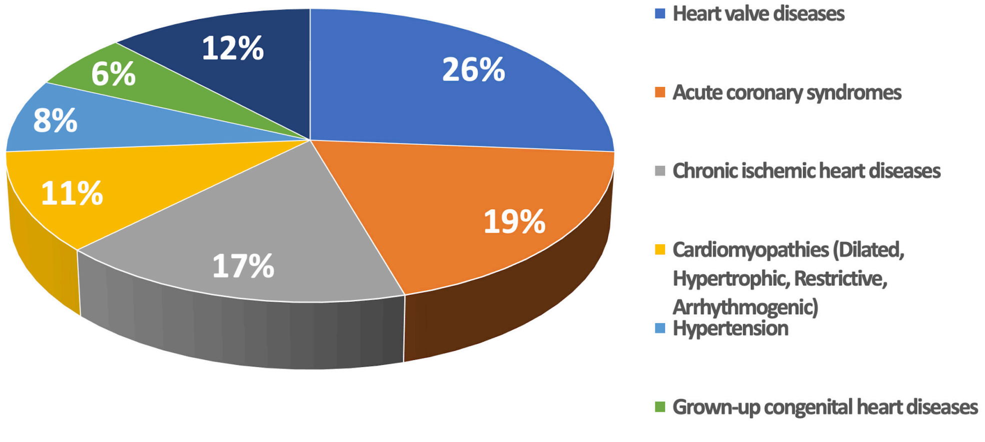

FIGURE 2
Frequency of the different clinical indications for the echocardiographic study.

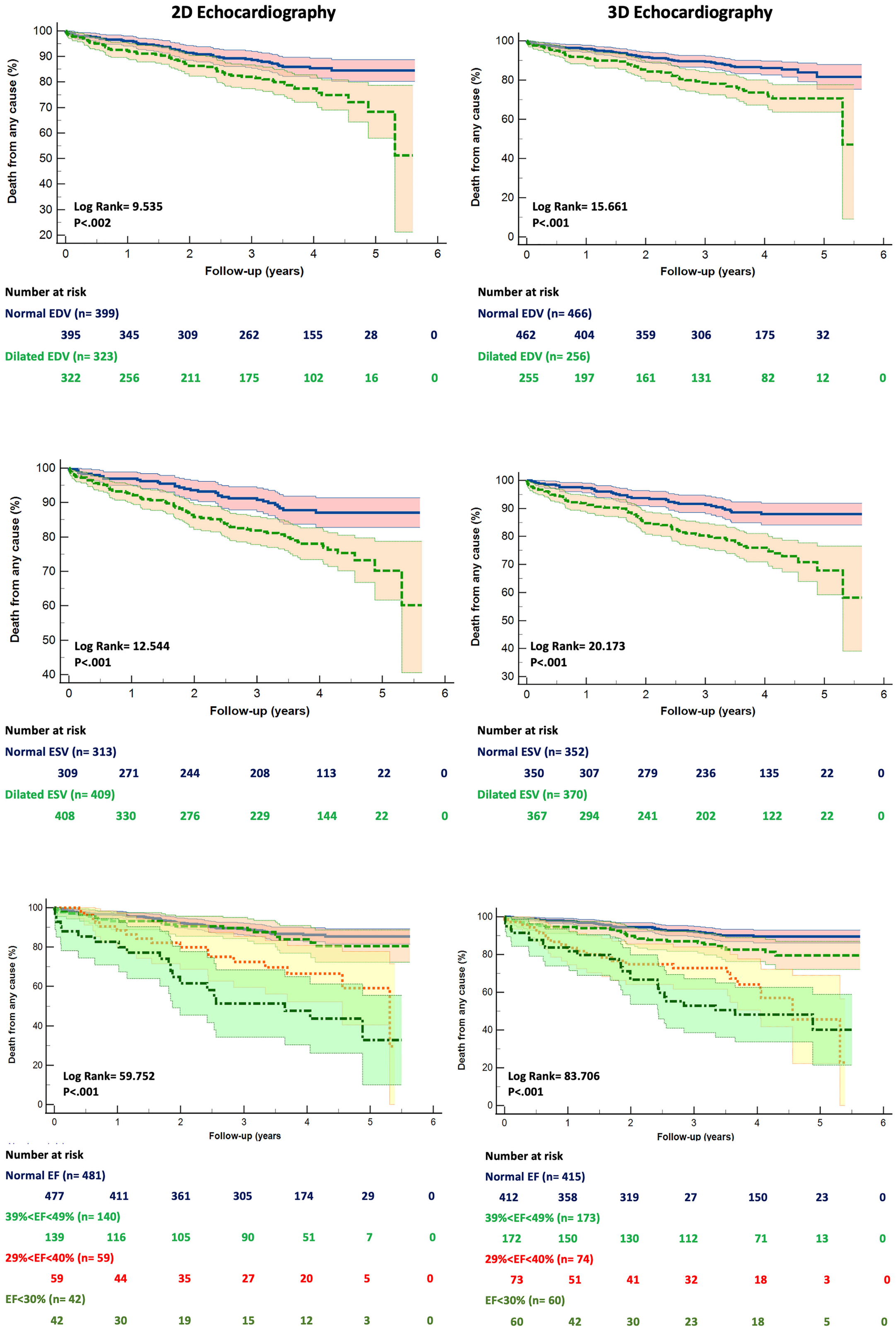

Number at risk (2D Echocardiography, upper panel)

Normal EDV (n= 399)	395	345	309	262	155	28	0
Dilated EDV (n= 323)	322	256	211	175	102	16	0

Number at risk

Normal EDV (n= 466)	462	404	359	306	175	32	
Dilated EDV (n= 256)	255	197	161	131	82	12	0

Number at risk

Normal ESV (n= 313)	309	271	244	208	113	22	0
Dilated ESV (n= 409)	408	330	276	229	144	22	0

Number at risk

Normal ESV (n= 352)	350	307	279	236	135	22	0
Dilated ESV (n= 370)	367	294	241	202	122	22	0

Number at risk

Normal EF (n= 481)	477	411	361	305	174	29	0
39%<EF<49% (n= 140)	139	116	105	90	51	7	0
29%<EF<40% (n= 59)	59	44	35	27	20	5	0
EF<30% (n= 42)	42	30	19	15	12	3	0

Number at risk

Normal EF (n= 415)	412	358	319	27	150	23	0
39%<EF<49% (n= 173)	172	150	130	112	71	13	0
29%<EF<40% (n= 74)	73	51	41	32	18	3	0
EF<30% (n= 60)	60	42	30	23	18	5	0

FIGURE 3

Kaplan Meyers survival curves for dilated left ventricular end-diastolic **(upper panels)**, end-systolic **(mid panels)** volumes and reduced ejection fraction **(bottom panels)** obtained by two- **(left panels)** and three-dimensional **(right panels)** echocardiography, respectively. Abbreviations as in **Figure 1**.

$p = 0.001$) with all-cause death than either 2DE EDV ≤ 74 ml/m^2 in men and ≤ 61 ml/m^2 in women ($X^2 = 9.595$; $p = 0.002$) or 2DE ESV ≤ 31 ml/m^2 in men and ≤ 24 ml/m^2 in women ($X^2 = 12.544$; $p < 0.001$) (**Figure 3**). Similarly, 3DE EDV ≤ 85 ml/m^2 in men and ≤ 78 ml/m^2 in women ($X^2 = 25.998$; $p < 0.001$) and 3DE ESV ≤ 34 ml/m^2 in men and ≤ 28 ml/m^2 in women ($X^2 = 19.491$; $p < 0.001$) were more strongly associated (all $p = 0.001$) with the composite endpoint of all-cause death or cardiac hospitalizations than either 2DE EDV ≤ 74 ml/m^2 in men and ≤ 61 ml/m^2 in women ($X^2 = 16.794$; $p = 0.002$) or 2DE ESV ≤ 31 ml/m^2 in men and ≤ 24 ml/m^2 in women ($X^2 = 12.092$; $p < 0.001$) (**Figure 4**).

Survival analysis based on LVEF ranges derived from 2DE and 3DE measurements

We divided our study population into four groups, according to the ranges of the LVEF recommended by current guidelines: normal LVEF (> 52% for men, > 54% for women), mildly reduced LVEF (51-41% for men, 53%-41% for women), moderately reduced LVEF (40-30% for men and women), and severely reduced LVEF (< 30% for men and women). The grading of LV EF was more severe when 3DE was used to measure LV volumes ($X^2 = 13.22$; p = 0.0042, **Figure 3**) than when LV volumes were calculated using 2DE.

Kaplan Meier survival curves were derived for the different ranges of the 2DE LVEF and 3DE LVEF, respectively (**Figures 3**, **4**).

Both 2DE and 3DE LVEF curves could significantly stratify the risk of death among the different ranges of the LVEF. However, the Kaplan Meier curves for the 3DE LVEF thresholds of LV dysfunction had a higher χ^2 at the log-rank discrimination analysis by comparison with the 2DE LVEF threshold values ($\chi^2 = 83.706$, $p < 0.001$ vs. $\chi^2 = 59.752$, $p < 0.001$). Moreover, the Receiver Operating Curves for both 2DE and 3DE LVEF threshold values showed a higher area under the curve (AUC) for the 3DE LVEF ranges than for the 2DE LVEF ranges in predicting death (0.76 ± 0.03 vs. 0.69 ± 0.04; $p < 0.001$).

Furthermore, only the 3DE LVEF was a significant predictor of time-to-event for each change in the LVEF category [2DE LVEF: HR 1.33 (0.88-2.01), $p = 0.169$; 3DE LVEF: HR 0.35 (0.24-0.52), $p < 0.001$]. Moreover, the HR increase for the three categories with reduced LVEF compared with the group with normal LVEF were higher when using the 3DE LVEF threshold values (mildly reduced LVEF: HR 2.40 (1.23-4.65), $p = 0.01$; moderately reduced LVEF: HR 7.68 (4.15-14.24), $p < 0.001$; severely reduced LVEF: HR 10.4 (5.67-19.09), $p < 0.001$; $\chi^2 = 98.26$, $p < 0.001$) than when using the 2DE LVEF ones (mildly reduced LVEF: HR 1.46 (0.77-2.77), $p < 0.25$; moderately reduced LVEF: HR 3.68 (2.03-6.7), $p < 0.001$; severely reduced LVEF: HR 7.66 (4.43-13.25), $p < 0.001$; $\chi^2 = 77.10$, $p < 0.001$).

Incremental value of left ventricular volumes and ejection fraction to predict outcome

The clinical parameters associated with all-cause death and the composite endpoint are listed in **Table 2**. Clinical parameters associated with all-cause death were age, dyslipidemia, permanent atrial fibrillation, ischemic heart disease, and serum levels of creatinine and hemoglobin (**Table 2**). Clinical parameters associated with the composite endpoint of all-cause death and cardiac hospitalization were permanent atrial fibrillation, ischemic heart disease, and serum levels of creatinine and hemoglobin (**Table 2**).

Clinical predictors identified at multivariable analysis as independently associated with outcome were placed in two separate stepwise regression models (CM_{death} and $CM_{composite}$) for all-cause death and the composite endpoint, respectively. For all-cause death, the Harrel's C-index (HC) of the CM_{death} was 0.78 (95%CI 0.72-0.84). The addition of the EDV to CM_{death} increased the HC at the same value using both 2DE (HC = 0.79, 95%CI 0.73-0.85) and 3DE (HC = 0.79, 95%CI 0.73-0.85). Conversely, the addition of ESV (HC = 0.83, 95%CI 0.74-0.91) and EF (HC = 0.84, 95%CI 0.78-0.9) by 3DE was associated with greater HC than the same parameters obtained with 2DE (HC = 0.80, 95%CI 0.75-0.85, and HC = 0.81, 95%CI 0.76-0.86) (**Figure 5**).

For the composite endpoint, the HC of the $CM_{composite}$ was 0.64 (95%IC 0.61-0.68). The addition of the EDV by 2DE increased the HC of the model (0.79, 95%CI 0.73-0.85), but the 3DE EDV was associated with a larger increase of the HC (0.81, 95%CI 0.75-0.88). Conversely the increase of the HC of the $CM_{composite}$ obtained by adding the ESV and EF was similar for the 2DE (HC = 0.80, 95%CI 0.74-0.85) and HC = 0.84, 95%CI 0.77-0.92, respectively for 2DE ESV and EF) and 3DE (HC = 0.80, 95%CI 0.75-0.86) and HC = 0.84, 95%CI 0.78-0.90, respectively for 3DE ESV and EF) (**Figure 6**).

Discussion

Our study shows that, in unselected patients undergoing clinically indicated routine echocardiography, the LV volumes and EF measured with 3DE were more strongly associated with outcome than the same parameters calculated by 2DE. The main findings of our study can be summarized as it follows: (1) As expected, in addition to the clinical predictors (age, anemia, chronic kidney disease, atrial fibrillation, and ischemic heart disease), both LV volumes and EF were associated with both all-cause mortality and the composite endpoint of death and cardiac hospitalization; (2) Survival analysis based on LV dilation according to 2DE and 3DE measurements showed that the 3DE threshold values for LV dilation had a higher discriminative power than the 2DE cutoff values in predicting both all-cause death and the cumulative endpoint of death and cardiac hospitalization; (3) Survival analysis based on LVEF

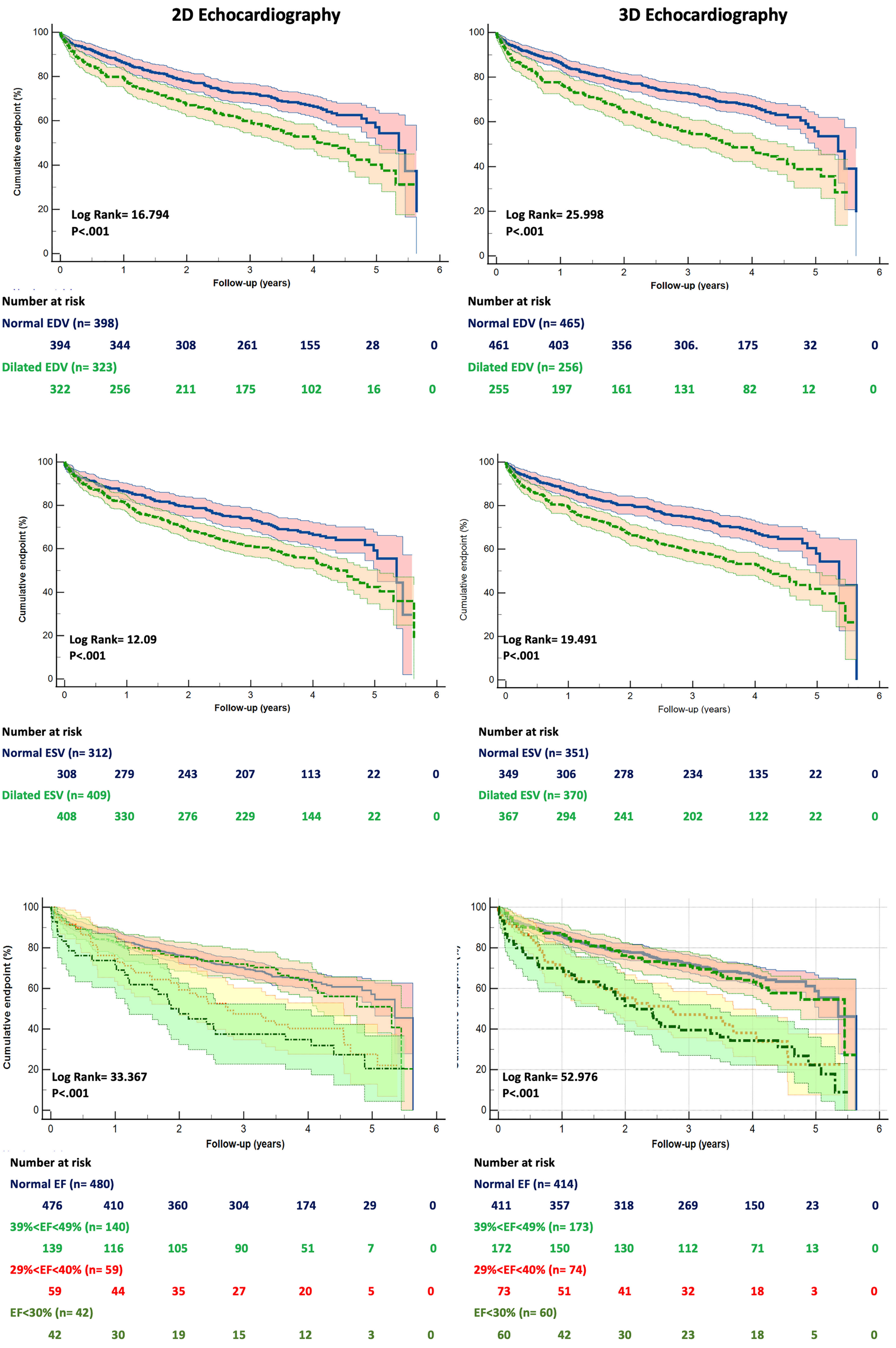

Number at risk (2D Echocardiography)

Normal EDV (n= 398)						
394	344	308	261	155	28	0
Dilated EDV (n= 323)						
322	256	211	175	102	16	0

Number at risk (3D Echocardiography)

Normal EDV (n= 465)						
461	403	356	306.	175	32	0
Dilated EDV (n= 256)						
255	197	161	131	82	12	0

Number at risk

Normal ESV (n= 312)						
308	279	243	207	113	22	0
Dilated ESV (n= 409)						
408	330	276	229	144	22	0

Number at risk

Normal ESV (n= 351)						
349	306	278	234	135	22	0
Dilated ESV (n= 370)						
367	294	241	202	122	22	0

Number at risk

Normal EF (n= 480)						
476	410	360	304	174	29	0
39%<EF<49% (n= 140)						
139	116	105	90	51	7	0
29%<EF<40% (n= 59)						
59	44	35	27	20	5	0
EF<30% (n= 42)						
42	30	19	15	12	3	0

Number at risk

Normal EF (n= 414)						
411	357	318	269	150	23	0
39%<EF<49% (n= 173)						
172	150	130	112	71	13	0
29%<EF<40% (n= 74)						
73	51	41	32	18	3	0
EF<30% (n= 60)						
60	42	30	23	18	5	0

FIGURE 4

Kaplan Meyers curves for freedom from the cumulative event of death and cardiac hospitalization for dilated left ventricular end-diastolic **(upper panels)**, end-systolic **(mid panels)** volumes and reduced ejection fraction **(bottom panels)** obtained by two- **(left panels)** and three-dimensional **(right panels)** echocardiography, respectively. Abbreviations as in Figure 1.

TABLE 2 Demographic and clinical parameters associated with both all-cause death and the composite endpoint of death and cardiac hospitalization.

	All-cause deathHR (95% CI)				Composite endpointHR (95% CI)			
	Univariate	*P*	Multivariate (X^2 = 242.56)	*P*	Univariate	*P*	Multivariate (X^2 = 131.57)	*P*
Age	1.031 (1.015-1.047)	**<0.001**	1.031 (1.015-1.047)	**< 0.001**	1.002 (0.993-1.01)	0.677	–	–
Gender	1.040 (0.68-1.59)	0.856	–	–	0.929 (0.718-1.204)	0.979	–	–
Body mass index	0.985 (0.931-1.043)	0.615	–	–	0.989 (0.753-1.286	0.907	–	–
Diabetes	1.029 (0.439-1.041)	0.905	–	–	0.915 (0.668-1.254)	0.581	–	–
Hypertension	0.676 (0.390-0.886)	0.076	–	–	0.984 (0.753-1.286)	0.907	–	–
Dyslipidemia	0.588 (0.387-1.013)	**0.011**	0.581 (0.387-0.873)	**0.009**	0.869 (0.676-1.118)	0.274	–	–
Atrial fibrillation	1.856 (1.202-2.867)	**0.005**	1.874 (1.215-2.889)	**0.004**	2.003 (1.529-2.623)	**< 0.001**	2.014 (1.552-2.614)	**<0.001**
Ischemic heart disease	2.253 (1.311-3.872)	**0.003**	2.247 (1.331-3.793)	**0.002**	1.776 (1.254-2.516)	**0.001**	1.659 (1.195-2.304)	**0.003**
Creatinine	1.003 (1.001-1.005)	**<0.001**	1.003 (1.001-1.005)	**<0.001**	1.003 (1.001-1.004)	**< 0.001**	1.003 (1.001-1.004)	**<0.001**
Hemoglobin	0.969 (0.958-0.980)	**<0.001**	0.968 (0.955-0.979)	**<0.001**	0.980 (0.983-0.997)	**0.004**	0.989 (0.982-0.995)	**<0.001**

CI, confidence interval; HR, hazard ratio. Bold values represent the statistically significant.

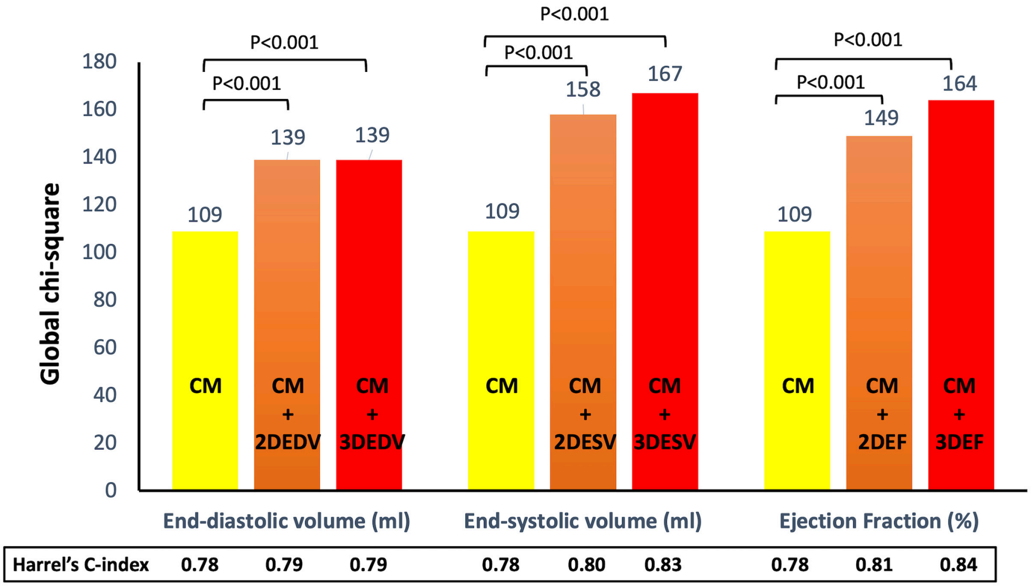

FIGURE 5
Addition of left ventricular volumes and ejection fraction obtained from both two- and three-dimensional echocardiography significantly increased the association with all-cause death of the clinical model based on permanent atrial fibrillation, ischemic heart disease, and serum levels of creatinine and hemoglobin. Both three-dimensional end-systolic volume and ejection fraction had stronger association with outcome than the corresponding two-dimensional parameters. CM, clinical model; EDV, end-diastolic volume; EF, ejection fraction; ESV, end-systolic volume.

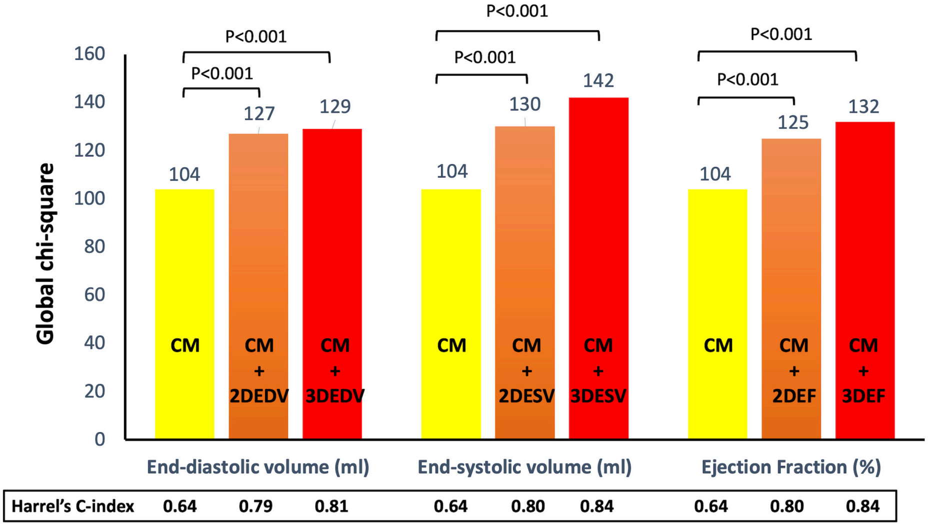

FIGURE 6
Addition of left ventricular volumes and ejection fraction obtained from both two- and three-dimensional echocardiography significantly increased the association with the composite endpoint of all-cause death and cardiac hospitalization of the clinical model based on age, dyslipidemia, permanent atrial fibrillation, ischemic heart disease, and serum levels of creatinine and hemoglobin. Both three-dimensional end-systolic volume and ejection fraction had stronger association with outcome than the corresponding two-dimensional parameters.

threshold values for defining LV dysfunction severity showed that the LVEFs measured by 3DE have higher discriminative power for all-cause mortality and the composite endpoint of death and cardiac hospitalization than the 2DE ones; (4) When added to the baseline clinical model developed for all-cause death (i.e., $\mathrm{CM}_{\mathrm{death}}$) both 3DE LVESV and EF were more strongly associated to the occurrence of all-cause mortality than the corresponding 2DE parameters.

Prognostic value of clinical and echocardiographic data

According to the reports of epidemiologic studies, cardiovascular diseases are the leading cause of death globally, and, particularly, in the most developed countries (25). In the European Union, cardiovascular diseases cause 35% of the deaths in women and men under the age of 75 years (26). In the next decade, the expected number of disability-adjusted-life-years that will be lost because of cardiovascular diseases will increase from 169 million in 2020 to 187 million in 2030[1].

Cardiovascular morbidity and mortality in the general population have been related to both non-modifiable (e.g., age, sex, genetics) (27) and potentially modifiable risk factors (28), and to the underlying cardiac condition[2]. Accordingly, in our study patients, age, chronic kidney disease, anemia, atrial fibrillation, and ischemic heart disease were significantly associated with clinical outcomes. In addition, also the LV volumes and EF measured by both 2DE and 3DE have been associated with clinical outcomes (19, 29, 30).

Non-invasive assessment of LV volumes and EF are critically important for clinical decision-making and represents the most frequent indication for an echocardiographic study. Eligibility to device implantation of patients with LV dysfunction, discontinuation of potentially cardiotoxic chemotherapy in cancer patients, indications to cardiac surgery or to treatment initiation in asymptomatic patients are among the most important clinical decisions that rely on an accurate measurement of LV EF. LV volume calculations by 2DE is highly operator dependent, uses only limited data contained in a few predetermined tomographic planes of the LV to assess global myocardial function, and relies on geometrical assumptions that may not be necessarily valid in every patient. The geometric assumptions about LV shape associated with the 2DE algorithms make the calculations of LV volumes and EF more inaccurate in patients in whom this information is more critical (i.e., patients in whom the LV geometry is distorted because of aneurysms, or in those with extensive wall motion abnormalities) (31, 32). With 3DE, LV volumes are actually measured (and not calculated anymore) without any assumption regarding LV shape (14). This technique has been extensively validated using the cardiac magnetic resonance as a reference modality (10, 15), and was demonstrated to be more timesaving, reproducible, repeatable and accurate than conventional 2DE for both LV volumes and EF measurements (11, 33–35).

---

[1] https://apps.who.int/iris/handle/10665/43007

[2] https://ec.europa.eu/eurostat/statistics-explained/index.php?title=Cardiovascular_diseases_statistics

Caselli et al. (36) showed that, in a limited cohort of 178 patients, 3DE LV volumes and EF had a significant association with the composite endpoint of death, myocardial infarction or stroke but not with the primary endpoint of cardiovascular death. Similarly, Mancuso et al. (37) showed that, in 89 patients with systolic heart failure, the LVEF measured by 3DE was an independent predictor for a composite endpoint of death, cardiac transplantation and hospitalization for HF, whereas LV volumes were not. However, in addition to the smaller number of patients and the specific clinical settings of this study, it should be noted that, in contrast with available data, the LV volumes measured by 3DE were smaller than those obtained with 2DE. In our study, the LV volumes measured by 3DE were significantly larger than those obtained by 2DE, in accordance to other studies that showed the higher accuracy of the 3DE for the measurement of the LV volumes in comparison to cardiac magnetic resonance (10). New 3DE technologies combined with an increased experience in 3DE of the cardiologists who perform echocardiography allow encompassing larger LVs into the 3DE dataset at a good volume rate, allowing good endocardial delineation and better measurements of the LV volumes. A previous study performed in unselected patients with a wide range of LV volumes showed that the 3DE LV volumes measured by different echocardiography systems were similar and had a better accuracy than 2DE when compared to cardiac magnetic resonance (38).

The present study adds to previous ones by showing that LV volumes and EF measured by 3DE provide incremental prognostic value over 2DE also in patients referred for a routine and clinically-indicated echocardiography study. Both LV volumes and EF calculated by 2DE were independently associated with either cardiac death or the composite of cardiac death and hospitalization for cardiac causes after adjusting for covariates. However, 3DE LV ESV and EF were able to significantly increase the power of the predictive model when added to a model including the clinical variables. These findings suggested that LV ESV and EF obtained from 3DE were superior to those derived from 2DE to predict cardiac death and the need of hospitalization for cardiac issues.

Survival analysis based on LVEF threshold values derived by 2DE and 3DE

When using LVEF values obtained from 3DE to grade the extent of LV dysfunction severity into normal function, and mild, moderate and severe LV dysfunction, LVEF measured by 3DE showed higher discriminant power for survival than LVEF measured by 2DE. These results are consistent with the findings by Stanton et al. (19) who compared the occurrence of the composite endpoint between patients with "normal" and "abnormal" LVEF measured by 2DE and 3DE. LVEF measured by 3DE was also an independent predictor of major arrhythmic events and improved the ability to predict the arrhythmic risk in 172 patients with LVEF below 50% (39). In that study, when compared with 2DE LVEF, 3DE-measured LVEF changed the indication to implantable cardioverter-defibrillator implant in 20% of the patients. Finally, in our patients, only the 3DE measurement of the LVEF was an independent predictor of time to event for each change in the LVEF.

Survival analysis based on LV dilation according to 2DE and 3DE

The 3D LVEDV threshold values used to identify patients with dilated LV provided better stratification of the risk of death compared to 2D LVEDV. Dilated LVESV according to the 3DE cut-offs proposed by Muraru et al. (21) in normal individuals showed to be a predictor for time to event, as well, while the 2D LVESV cut-offs offered by the current guidelines for LV dilation did not (17).

Clinical implications

Our findings showed that, although LV volumes obtained by 2DE and 3DE are significantly correlated, 3DE might be better than 2DE in assessing the severity of LV dysfunction and the prognosis of the patients referred to the echocardiography laboratory for routine, clinically indicated study, and physicians should use parameters measured by 3DE to better guide patients' management. Future research should focus on whether 3DE can improve the predictive value in larger and prospective cohorts of consecutive patients, and whether 3DE guided therapy can improve clinical outcomes.

Limitations

This study has several limitations. This study was single-center and retrospective, and no causal relationship can be established from our findings. Second, only patients with stable clinical conditions and good quality 2DE and 3DE datasets were enrolled in the study, and whether these findings can be extrapolated to the general population of consecutive patients that are examined in the echocardiography laboratory remain to be established. Finally, this study was carried on in tertiary center with a long-standing experience in transthoracic 3DE. Whether our results can be applied to the generality of the echocardiography laboratories require further prospective and multicenter studies.

Conclusion

In patients referred to the echocardiography laboratory for a clinically indicated, routine echocardiography study, 3DE was a better predictor than 2DE of both cardiac death and the composite of cardiac death and hospitalization for cardiac cause. Our findings support the recommendation made by the European Association of Cardiovascular imaging and American Society of Echocardiography that, in laboratories with experience and equipment, 3DE should be used for LV volume and EF measurements and implemented into the clinical routine of the echocardiography laboratory.

Data availability statement

The raw data supporting the conclusions of this article will be made available by the authors, without undue reservation.

Ethics statement

The studies involving human participants were reviewed and approved by Ethics Committee of the Istituto Auxologico Italiano, IRCCS. Written informed consent for participation was not required for this study in accordance with the national legislation and the institutional requirements.

Author contributions

DM and LB developed the concept, designed the study, drafted the first manuscript, and approved its final version. SB and DG prepared the database, made all the statistical analyses, and revised the manuscript critically. NR, MG, FP, MT, EC, and GP critically revised the manuscript draft for important intellectual content. CS and CB prepared the figures, drafted the tables, and revised the manuscript draft for important intellectual content. All authors have approved the final manuscript that has been submitted.

Funding

This study was partially supported by the Italian Ministry of Health. SB was supported by a Mobility Grant offered by the University of Medicine and Pharmacy Carol Davila Bucharest, PFE_23/2018.

Conflict of interest

The authors declare that the research was conducted in the absence of any commercial or financial relationships that could be construed as a potential conflict of interest.

Publisher's note

References

1. Marwick T. Ejection fraction pros and cons: JACC state-of-the-art review. *J Am Coll Cardiol.* (2018) 72:2360–79. doi: 10.1016/j.jacc.2018.08.2162

2. Lund L, Pitt B, Metra M. Left ventricular ejection fraction as the primary heart failure phenotyping parameter. *Eur J Heart Fail.* (2022) 24:1158–61.

3. Anand V, Yang L, Luis S, Padang R, Michelena H, Tsay J, et al. Association of left ventricular volume in predicting clinical outcomes in patients with aortic regurgitation. *J Am Soc Echocardiogr.* (2021) 34:352–9.

4. Yang L, Anand V, Zambito E, Pellikka P, Scott C, Thapa P, et al. Association of echocardiographic left ventricular end-systolic volume and volume-derived ejection fraction with outcome in asymptomatic chronic aortic regurgitation. *JAMA Cardiol.* (2021) 6:189–98. doi: 10.1001/jamacardio.2020.5268

5. Vejpongsa P, Xu J, Quinones M, Shah D, Zoghbi W. Differences in cardiac remodeling in left-sided valvular regurgitation: implications for optimal definition of significant aortic regurgitation. *JACC Cardiovasc Imaging.* (2022) 15:1730–41. doi: 10.1016/j.jcmg.2022.05.006

6. Priori S, Blomstrom-Lundqvist C. 2015 European society of cardiology guidelines for the management of patients with ventricular arrhythmias and the prevention of sudden cardiac death summarized by co-chairs. *European Heart J.* (2015) 36:2757–9. doi: 10.1093/eurheartj/ehv445

7. Aimo A, Vergaro G, Gonzalez A, Barison A, Lupón J, Delgado V, et al. Cardiac remodelling - Part 2: clinical, imaging and laboratory findings. A review from the study group on biomarkers of the heart failure association of the European society of cardiology. *Eur J Heart Fail.* (2022) 24:944–58. doi: 10.1002/ejhf.2522

8. McDonagh T, Metra M, Adamo M, Gardner R, Baumbach A, Böhm M, et al. 2021 ESC guidelines for the diagnosis and treatment of acute and chronic heart failure. *Eur Heart J.* (2021) 42:3599–726.

9. Vahanian A, Beyersdorf F, Praz F, Milojevic M, Baldus S, Bauersachs J, et al. 2021 ESC/EACTS guidelines for the management of valvular heart disease. *Eur Heart J.* (2021) 43:561–632.

10. Dorosz J, Lezotte D, Weitzenkamp D, Allen L, Salcedo E. Performance of 3-dimensional echocardiography in measuring left ventricular volumes and ejection fraction: a systematic review and meta-analysis. *J Am Coll Cardiol.* (2012) 59:1799–808. doi: 10.1016/j.jacc.2012.01.037

11. Jenkins C, Bricknell K, Chan J, Hanekom L, Marwick T. Comparison of two- and three-dimensional echocardiography with sequential magnetic resonance imaging for evaluating left ventricular volume and ejection fraction over time in patients with healed myocardial infarction. *Am J Cardiol.* (2007) 99:300–6. doi: 10.1016/j.amjcard.2006.08.026

12. Chukwu E, Barasch E, Mihalatos D, Katz A, Lachmann J, Han J, et al. Relative importance of errors in left ventricular quantitation by two-dimensional echocardiography: insights from three-dimensional echocardiography and cardiac magnetic resonance imaging. *J Am Soc Echocardiogr.* (2008) 21:990–7. doi: 10.1016/j.echo.2008.07.009

13. Gordon E, Schnittger I, Fitzgerald P, Williams P, Popp R. Reproducibility of left ventricular volumes by two-dimensional echocardiography. *J Am Col Cardiol.* (1983) 2:506–13.

14. Guta A, Badano L, Ochoa-Jimenez R, Genovese D, Previtero M, Civera S, et al. Three-dimensional echocardiography to assess left ventricular geometry and function. *Expert Rev Cardiovasc Ther.* (2019) 17:801–15.

15. Shimada Y, Shiota T. A meta-analysis and investigation for the source of bias of left ventricular volumes and function by three-dimensional echocardiography in comparison with magnetic resonance imaging. *Am J Cardiol.* (2011) 107:126–38. doi: 10.1016/j.amjcard.2010.08.058

16. Lang R, Badano L, Tsang W, Adams D, Agricola E, Buck T, et al. EAE/ASE recommendations for image acquisition and display using three-dimensional echocardiography. *Eur Heart J Cardiovasc Imaging.* (2012) 13:1–46.

17. Lang R, Badano L, Mor-Avi V, Afilalo J, Armstrong A, Ernande L, et al. Recommendations for cardiac chamber quantification by echocardiography in adults: an update from the American society of echocardiography and the European association of cardiovascular imaging. *Eur Heart J Cardiovasc Imaging.* (2015) 16:233–70.

18. Yingchoncharoen T, Negishi T, Stanton T, Marwick T. Incremental value of three-dimensional echocardiography in the evaluation of left ventricular size in mitral regurgitation: a follow-up study after mitral valve surgery. *J Am Soc Echocardiogr.* (2014) 27:608–15. doi: 10.1016/j.echo.2014.02.009

19. Stanton T, Jenkins C, Haluska B, Marwick T. Association of outcome with left ventricular parameters measured by two-dimensional and three-dimensional echocardiography in patients at high cardiovascular risk. *J Am Soc Echocardiogr.* (2014) 27:65–73. doi: 10.1016/j.echo.2013.09.012

20. Badano L, Hahn R, Rodriguez-Zanella H, Araiza Garaygordobil D, Ochoa-Jimenez R, Muraru D. Morphological assessment of the tricuspid apparatus and grading regurgitation severity in patients with functional tricuspid regurgitation: thinking outside the box. *JACC Cardiovasc Imaging.* (2019) 12:652–64. doi: 10.1016/j.jcmg.2018.09.029

21. Muraru D, Badano L, Peluso D, Dal Bianco L, Casablanca S, Kocabay G, et al. Comprehensive analysis of left ventricular geometry and function by three-dimensional echocardiography in healthy adults. *J Am Soc Echocardiogr.* (2013) 26:618–28.

22. Muraru D, Badano L, Piccoli G, Gianfagna P, Del Mestre L, Ermacora D, et al. Validation of a novel automated border-detection algorithm for rapid and accurate quantitation of left ventricular volumes based on three-dimensional echocardiography. *Eur J Echocardiogr.* (2010) 11:359–68. doi: 10.1093/ejechocard/jep217

23. Newson R. Comparing the predictive powers of survival models using Harrell's C or Somers' D. *Stata J.* (2010) 10:339–58.

24. DeLong E, DeLong D, Clarke-Pearson D. Comparing the areas under two or more correlated receiver operating characteristic curves: a nonparametric approach. *Biometrics.* (1988) 44:837–45.

25. Gbd 2017 Causes of Death Collaborators. Global, regional, and national age-sex-specific mortality for 282 causes of death in 195 countries and territories, 1980-2017: a systematic analysis for the global burden of disease study 2017. *Lancet.* (2018) 392:1736–88. doi: 10.1016/S0140-6736(18)32203-7

26. Ganczak M, Miazgowski T, Kozybska M, Kotwas A, Korzeń M, Rudnicki B, et al. Changes in disease burden in Poland between 1990-2017 in comparison with other Central European countries: a systematic analysis for the global burden of disease study 2017. *PLoS One.* (2020) 15:e0226766. doi: 10.1371/journal.pone.0226766

27. Jorstad H, Colkesen E, Boekholdt S, Tijssen J, Wareham N, Khaw K, et al. Estimated 10-year cardiovascular mortality seriously underestimates overall cardiovascular risk. *Heart.* (2016) 102:63–8.

28. Yusuf S, Joseph P, Rangarajan S, Islam S, Mente A, Hystad P, et al. Modifiable risk factors, cardiovascular disease, and mortality in 155 722 individuals from 21 high-income, middle-income, and low-income countries (PURE): a prospective cohort study. *Lancet.* (2020) 395:795–808. doi: 10.1016/S0140-6736(19)32008-2

29. Angaran P, Dorian P, Ha A, Thavendiranathan P, Tsang W, Leong-Poi H, et al. Association of left ventricular ejection fraction with mortality and hospitalizations. *J Am Soc Echocardiogr.* (2020) 33:802–811.e6.

30. Kato M, Kitada S, Kawada Y, Nakasuka K, Kikuchi S, Seo Y, et al. Left ventricular end-systolic volume is a reliable predictor of new-onset heart failure with preserved left ventricular ejection fraction. *Cardiol Res Pract.* (2020) 2020:3106012.

31. Qin J, Jones M, Shiota T, Greenberg N, Tsujino H, Firstenberg M, et al. Validation of real-time three-dimensional echocardiography for quantifying left ventricular volumes in the presence of a left ventricular aneurysm: in vitro and in vivo studies. *J Am Coll Cardiol.* (2000) 36:900–7. doi: 10.1016/s0735-1097(00)00793-2

32. Arai K, Hozumi T, Matsumura Y, Sugioka K, Takemoto Y, Yamagishi H, et al. Accuracy of measurement of left ventricular volume and ejection fraction by new real-time three-dimensional echocardiography in patients with wall motion abnormalities secondary to myocardial infarction. *Am J Cardiol.* (2004) 94:552–8. doi: 10.1016/j.amjcard.2004.05.015

33. Volpato V, Ciampi P, Johnson R, Hipke K, Tomaselli M, Oliverio G, et al. Feasibility and time analysis of three-dimensional and myocardial deformation versus conventional two-dimensional echocardiography to assess cardiac chambers. *J Am Soc Echocardiogr.* (2022) 35:1102–5. doi: 10.1016/j.echo.2022.05.017

34. Baldea S, Velcea A, Rimbas R, Andronic A, Matei L, Calin S, et al. 3-D echocardiography is feasible and more reproducible than 2-D echocardiography for in-training echocardiographers in follow-up of patients with heart failure with reduced ejection fraction. *Ultrasound Med Biol.* (2021) 47:499–510. doi: 10.1016/j.ultrasmedbio.2020.10.022

35. Thavendiranathan P, Liu S, Verhaert D, Calleja A, Nitinunu A, Van Houten T, et al. Feasibility, accuracy, and reproducibility of real-time full-volume 3D transthoracic echocardiography to measure LV volumes and systolic function: a fully automated endocardial contouring algorithm in sinus rhythm and atrial fibrillation. *JACC Cardiovasc Imaging.* (2012) 5:239–51. doi: 10.1016/j.jcmg.2011.12.012

36. Caselli S, Canali E, Foschi M, Santini D, Di Angelantonio E, Pandian N, et al. Long-term prognostic significance of three-dimensional echocardiographic parameters of the left ventricle and left atrium. *Eur J Echocardiogr.* (2010) 11:250–6. doi: 10.1093/ejechocard/jep198

37. Mancuso F, Moises V, Almeida D, Poyares D, Storti L, Brito F, et al. Prognostic value of real-time three-dimensional echocardiography compared to two-dimensional echocardiography in patients with systolic heart failure. *Int J Cardiovasc Imaging.* (2018) 34:553–60. doi: 10.1007/s10554-017-1266-0

38. Muraru D, Cecchetto A, Cucchini U, Zhou X, Lang R, Romeo G, et al. Intervendor consistency and accuracy of left ventricular volume measurements using three-dimensional echocardiography. *J Am Soc Echocardiogr.* (2018) 31:158–168.e1. doi: 10.1016/j.echo.2017.10.010

39. Rodriguez-Zanella, H, Muraru D, Secco E, Boccalini F, Azzolina D, Aruta P, et al. Added value of 3- versus 2-dimensional echocardiography left ventricular ejection fraction to predict arrhythmic risk in patients with left ventricular dysfunction. *JACC Cardiovasc Imaging.* (2019). 12:1917–26. doi: 10.1016/j.jcmg.2018.07.011

frontiers | Frontiers in Cardiovascular Medicine

TYPE Original Research
PUBLISHED 22 December 2022
DOI 10.3389/fcvm.2022.1023483

A tomographic microscopy-compatible Langendorff system for the dynamic structural characterization of the cardiac cycle

Hector Dejea[1,2]*, Christian M. Schlepütz[1], Natalia Méndez-Carmona[3,4], Maria Arnold[3,4], Patricia Garcia-Canadilla[5,6], Sarah L. Longnus[3,4], Marco Stampanoni[1,2], Bart Bijnens[7,8] and Anne Bonnin[1]

[1]Paul Scherrer Institute, Villigen, Switzerland, [2]Institute for Biomedical Engineering, University and ETH Zürich, Zurich, Switzerland, [3]Department of Cardiac Surgery, Inselspital, Bern University Hospital, Bern, Switzerland, [4]Department for BioMedical Research, University of Bern, Bern, Switzerland, [5]BCNatal-Barcelona Center for Maternal-Fetal and Neonatal Medicine, Hospital Sant Joan de Déu and Hospital Clínic, University of Barcelona, Barcelona, Spain, [6]Cardiovascular Diseases and Child Development, Institut de Recerca Sant Joan de Déu, Esplugues de Llobregat, Spain, [7]Institut d'Investigacions Biomèdiques August Pi i Sunyer (IDIBAPS), Barcelona, Spain, [8]Institution for Research and Advanced Studies (ICREA), Barcelona, Spain

Introduction: Cardiac architecture has been extensively investigated *ex vivo* using a broad spectrum of imaging techniques. Nevertheless, the heart is a dynamic system and the structural mechanisms governing the cardiac cycle can only be unveiled when investigating it as such.

Methods: This work presents the customization of an isolated, perfused heart system compatible with synchrotron-based X-ray phase contrast imaging (X-PCI).

Results: Thanks to the capabilities of the developed setup, it was possible to visualize a beating isolated, perfused rat heart for the very first time in 4D at an unprecedented 2.75 μm pixel size (10.6 μm spatial resolution), and 1 ms temporal resolution.

Discussion: The customized setup allows high-spatial resolution studies of heart architecture along the cardiac cycle and has thus the potential to serve as a tool for the characterization of the structural dynamics of the heart, including the effects of drugs and other substances able to modify the cardiac cycle.

KEYWORDS

synchrotron, tomographic microscopy, Langendorff, 4D imaging, cardiac cycle

OPEN ACCESS

EDITED BY
Carlo Gaudio,
Sapienza University of Rome, Italy

REVIEWED BY
Andrew Scott,
Royal Brompton Hospital,
United Kingdom
Jiaji Li,
Nanjing University of Science and Technology, China

*CORRESPONDENCE
Hector Dejea
✉ hector.dejea@bme.lth.se

SPECIALTY SECTION
This article was submitted to Cardiovascular Imaging, a section of the journal Frontiers in Cardiovascular Medicine

RECEIVED 19 August 2022
ACCEPTED 07 December 2022
PUBLISHED 22 December 2022

CITATION
Dejea H, Schlepütz CM, Méndez-Carmona N, Arnold M, Garcia-Canadilla P, Longnus SL, Stampanoni M, Bijnens B and Bonnin A (2022) A tomographic microscopy-compatible Langendorff system for the dynamic structural characterization of the cardiac cycle. *Front. Cardiovasc. Med.* 9:1023483. doi: 10.3389/fcvm.2022.1023483

1. Introduction

The cardiomyocytes are the contractile cellular units of the myocardium. Within a surrounding fibrous matrix, they aggregate into a complex three-dimensional (3D) mesh with predominant orientations. However, there is still controversy on the exact mode in which individual cardiomyocytes are arranged in 3D. The cardiomyocytes' aggregation and orientation within the ventricular walls determines the propagation of electrical excitation and the force generated by the heart. Therefore, a detailed description is required to achieve a complete understanding of the cardiac cycle and the alterations caused by cardiac remodeling (1, 2). In this context, high resolution four-dimensional (4D) imaging techniques are paramount to assess the structural dynamics of the heart and investigate how cardiomyocyte orientation evolves along the cardiac cycle.

Cardiac architecture has been investigated *ex vivo* using a wide range of imaging techniques, including ultrasound, several optical microscopy techniques, magnetic resonance (MRI) and X-ray imaging (i.e., micro-CT and synchrotron-based X-PCI) (3). However, to study the heart as a dynamic system, *in vitro* (based on isolated heart perfusion) and *in vivo* studies are necessary.

In vitro preparations are based on so-called isolated, perfused heart systems. These consist of a series of pumps, tubing and glassware that keep hearts beating outside the donor thanks to the use of specific perfusate, temperature, and oxygenation conditions. Within these systems, Langendorff preparations are based on aortic retrograde perfusion, in which the aortic valve is kept shut, directing the perfusate into the coronary vasculature (4–6).

Among the mentioned imaging techniques, ultrasound and MRI have already been used to investigate how the cardiomyocyte orientation changes along the cardiac cycle. Ultrasound-based techniques, such as shear wave and 3D back-scatter tensor imaging, have been applied in *in vitro* and *in vivo* adult mammals (7, 8). These techniques are cheap and have very high temporal resolution, but lack the spatial resolution to assess cardiomyocyte arrangement at cellular scale. MRI, and more specifically diffusion tensor imaging (DTI) and T_2^* imaging, has been also applied *in vitro* in isolated, perfused rat hearts (9–15), in rabbit hearts (16, 17) and *in vivo* in pig and human studies (18–31). While allowing whole heart field of views, both spatial and temporal resolution are insufficient to describe the cardiac cycle in detail at the cardiomyocyte-level. Additionally, these techniques often require heart fixation and/or the use of gadolinium-based contrast agents.

On the other hand, synchrotron-based X-PCI has been widely used in the last years for the *ex vivo* study of heart architecture. Grating interferometry (GI) and propagation-based (PB) have been the main X-PCI techniques used. GI has been applied to mice (32), fetal and neonatal human hearts (33–35), while PB X-PCI has been widely used in healthy and pathological cases of rodents (36–39), fetal human hearts (40) and pieces or whole adult human hearts (41–47). While GI allows to obtain three different types of images at once (absorption, differential phase contrast and dark-field), PB X-PCI can achieve higher resolution and faster scans without the use of gratings. These *ex vivo* studies, together with the combined ultra-fast and high resolution capabilities that this technique has shown in other fields (48–50), prove PB X-PCI to be a very powerful candidate for the time-resolved 3D investigation of heart architecture.

This manuscript presents a proof-of-concept of a novel methodology for the study of heart architecture dynamics in rat models by combining PB X-PCI and a customized Langendorff system. The presented developments allowed to dynamically image beating hearts in 4D at an unprecedented 2.75 μm pixel size (10.6 μm spatial resolution) and 1 ms temporal resolution. Therefore, the presented methodology is able to characterize the structural mechanisms responsible for the cardiac cycle, including the consequences of remodeling diseases and the effect of clinically-relevant drugs.

2. Materials and methods

2.1. X-ray tomographic microscopy-compatible Langendorff system

To achieve *in vitro* beating heart imaging, a Radnoti Rat Working Heart Apparatus was customized to fulfill the requirements of a synchrotron-based tomographic microscopy-compatible Langendorff setup. As illustrated in Figure 1 and listed in Table 1, the Langendorff system consists of a perfusate reservoir with an oxygenation line, a compliance chamber, connecting tubing and two pumps for the buffer solution and circulating water bath. The chambers and most tubing are double-walled, so that both the perfusate and the water bath can circulate. The difference in height between the compliance chamber and the aortic valve sets the pressure at which the perfusate will enter the coronary circulation (60 mmHg/∼90 cm water column). To make the system compatible with tomography, a dedicated sample stage and aquarium were designed.

The sample stage consists of a Micos UPR 160-AIR (PI miCos, Eschbach, Germany) rotation motor with two perpendicular linear motors, which are placed top-bottom, so that hearts can hang from them. In addition, a Moflon MQR4-S12(N2325) (Moflon Technology, Sha Jing, China) multi-channel rotary union for liquid and electricity allows continuous delivery of the buffer solution to the heart without entangling the tubing during rotation. Electrical feed-through is also necessary to connect electrodes for electrocardiogram (ECG) measurements. The rotary union has its own heating system to avoid temperature loss. From the stage, modular in-house 3D-printed sample holders keep the metallic cannulae in position to bring the perfusate to the heart and hold it stable. Custom aortic and left atrial cannulae were metal by design in order to optimize their shape and be able to transmit electrical signal to the ECG electrodes, without damaging the heart.

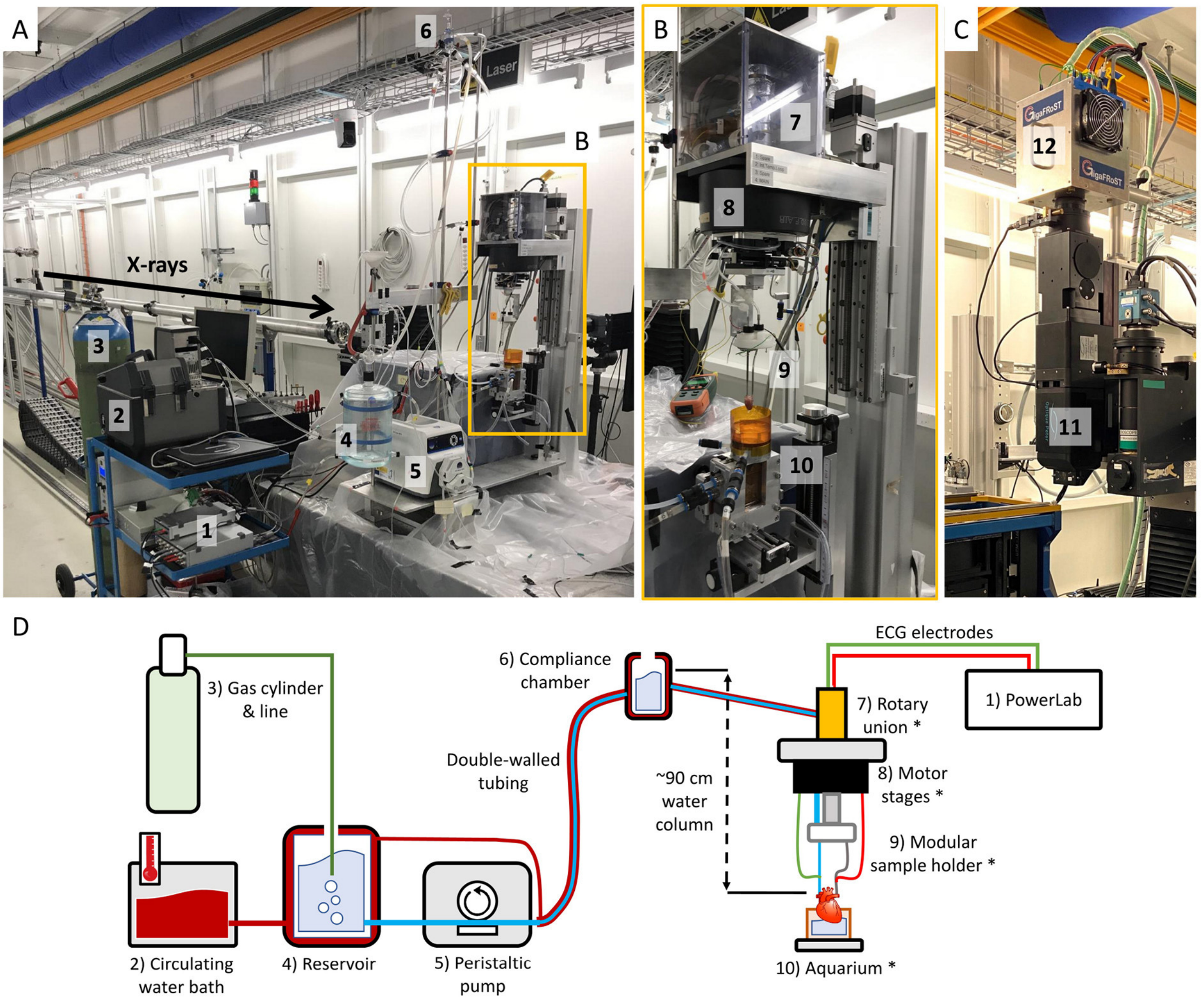

FIGURE 1
(A) X-ray tomographic microscopy-compatible Langendorff system at the TOMCAT beamline. (1) PowerLab data acquisition hardware. (2) Circulating water bath to keep the circuit at ∼ 37°C. (3) 95% O_2/5% CO_2 gas bottle for perfusate oxygenation. (4) Perfusate reservoir. (5) Peristaltic pump circulating the perfusate up to the compliance chamber. (6) Compliance chamber. The height difference with the aorta determines the perfusion pressure (60 mmHg/∼90 cm water column). **(B)** Close-up of the custom stage tower. (7) Rotary union system to ensure that the heart can be rotated without entangling tubes and wires. (8) Motor stage. (9) Modular sample holder, where the heart is attached at the ends of metallic aortic and left atrial cannulae. (10) Aquarium to keep the heart warm and collect the perfusate. **(C)** TOMCAT ultra-fast end-station. (11) High-numerical aperture 4x macroscope (53). (12) GigaFRoST detector (54). **(D)** Simplified sketch of the system components shown in **(A, B)**.

The customized aquarium is an aluminum structure with kapton foil walls, which have negligible X-ray absorption. The aquarium is then filled with perfusate right until the level of the apex. This helps to preserve the tissue temperature and absorb the perfusate drops falling from the heart, thus reducing related heart motion.

Finally, a PowerLab 8/35 (AD Instruments Ltd) equipped with LabChart Pro 8 was used to measure the ECG signal of the heart, the exposure signal of the detector and the angular feedback of the rotation motor. Angular feedback was obtained by recording the sin/cos signals from the motor controller, as described by for multiscale imaging of human pancreatic tissue by Frohn et al. (51).

2.2. Langendorff preparation and perfusion protocol

Animal care and experimentation followed the European Convention for Animal Care and was approved by the Swiss Animal Welfare Authorities (Authorization number 75737/32784).

Wistar rats (3 males and 3 females, 12 weeks old) were obtained from Janvier Labs (France). The rats were housed and maintained at 22°C with a 12-h day/night cycle. Food and water were administered ad libitum.

The animals were anesthetized *via* intraperitoneal injection with a mixture of 125 mg/kg ketamine and 12.5 mg/kg

TABLE 1 Description and function of the hardware components of the tomographic microscopy-compatible Langendorff system, labeled with respect to Figure 1.

Component and label	Description and function
PowerLab (1)	Data acquisition instrument to record ECG, detector exposure and motor angular readback signals.
Circulating water bath (2)	Warms up water to the desired temperature and pumps it through the heating circuit of the system.
Double-walled tubing	Allows simultaneous buffer and warm water circuits, so that the buffer can arrive to the heart at the target temperature ($\sim$ 37^{o}C).
Gas bottle and oxygenation line (3)	95% O_2/5% CO_2 gas mixture bottle and line to oxygenate the buffer solution and achieve appropriate pH values.
Reservoir (4)	Initial chamber, where the buffer solution is heated and oxygenated.
Peristaltic pump (5)	In charge of pumping the buffer from the reservoir to the compliance chamber.
Compliance chamber (6)	Highest chamber. The difference in height between the compliance chamber and the aorta sets the constant pressure at which the heart will be perfused (60 mmHg / $\sim$90 cm water column).
Rotary union* (7)	Both for liquid and electrical signal, ensures that tubes and cables do not entangle while tomographic rotation occurs. Includes heating patches and a power supply to ensure temperature control.
Motor stages* (8)	Allow sample alignment (translation) and rotation.
Modular sample holder* (9)	Easily-exchangeable 3D-printed cap with metallic cannulae made in-house, which will hold the heart in place. The custom metallic cannulae allow a compact design and conduct ECG signal without attaching the electrodes directly on the heart.
Aquarium* (10)	Aluminium frame with Kapton walls that keeps the heart environment at the desired temperature and collects the perfusate dripping from the apex.

Customized components are marked by *.

TABLE 2 Experimental dynamic acquisition parameters at the TOMCAT beamline.

Parameter	Value
Energy	21.9 keV
Propagation distance	220 cm
Pixel size	2.75 μm
Field of view	5.54 x 2.75 mm^2
Field of view (pixels)	2,016 x 1,000
Projections, flats and darks	160,000; 300; 50
Exposure time	1 ms
Angular range	720^o
Scintillator	LuAG:Ce 150 μm
Detector	GigaFRoST

xylazine, and provided with 100% medical oxygen *via* nose cone. Once loss of the pedal withdrawal reflex was verified, a rapid laparotomy and thoracotomy were performed. The heart was then removed from the chest cavity and placed in ice-cold physiologic buffer. The isolated, perfused preparation was then established by cannulating the aorta and left atrium. Even if the latter is not required for a Langendorff preparation, it was used for stabilization of the heart during tomographic measurements.

Perfusion was achieved with a modified Krebs-Henseleit solution (in [mM]: NaCl 118.0, KCl 4.7, KH_2PO_4 1.2, $CaCl_2{\cdot}2H_2O$ 1.5, $MgSO_4{\cdot}7H_2O$ 1.2, Glucose 11.0, and $NaHCO_3$ 25.0). The hearts started beating spontaneously. Their function was monitored until stabilization through ECG measurement, which was achieved by attaching one electrode to each cannula.

2.3. Image acquisition

The synchrotron-based X-ray tomography campaign was performed at the TOMCAT beamline of the Swiss Light Source (Paul Scherrer Institute, Villigen, Switzerland) (52). A PB X-PCI setup combined with the TOMCAT ultra-fast end-station was used to capture the dynamics of the cardiac architecture. As summarized in Table 2, a monochromatic X-ray beam at 21.9 keV energy and 220 cm propagation distance (sample-detector distance) were chosen. X-rays were converted to visible light by a LuAG:Ce 150 μm scintillator, magnified by a 4x high-numerical aperture macroscope (53) and recorded by the GigaFRoST detector (54). A total of 160,000 projections (1 ms exposure time, 2.75 μm voxel size, 5.54 x 2.75 mm^2 field of view) were thus continuously acquired in continuous rotation over 720^o. Assuming a constant cardiac cycle duration of 200 ms and considering the 1 ms exposure applied, 160,000 projections would then lead to a maximum of 800 projections per time-point within the heartbeat (a total of 800 heartbeats would occur during 160 s).

While conventional tomography is commonly achieved with 180^o of rotation, a wider angular range was included to ensure a uniform angular distribution and compensate for potential cardiac dysfunction over time. In other words, if hearts start to lose contractility due to ischemia or radiation damage during a 180^o measurement, only a fraction of the projections (concentrated in a fraction of 180^o) would be useful for reconstruction, thus leading to a very skewed angular distribution and the impossibility to achieve a successful tomogram.

2.4. Retrospective gating and image reconstruction

Retrospective gating (see sketch in Figure 2 was achieved by detecting the ECG feature corresponding to ventricular contraction and using it as a reference time-point to gate the time-series with a time resolution of 1 ms.

First, the detector exposure signal was used to select which exact ECG data points corresponded to each of the acquired projections. Then, by direct visual comparison of the ECG data points with their projections, the ECG feature indicating the start of ventricular contraction was found.

To detect this specific feature for every single heartbeat throughout the entire ECG, a single heartbeat signal was cross-correlated with the whole ECG. This allowed to detect the position of every heartbeat for independent processing. Then, within each heartbeat, the largest negative peak (corresponding to ventricular contraction) was detected.

Once this time-point was detected, it was used as the reference to calculate 190 additional time-points (1 ms each) by applying fixed time-offsets in each beat cycle. This was done under the assumption that ventricular contractions are reproducible in space and time. This is a demanding requirement at such high spatial and temporal resolutions and will affect the reconstruction quality when not holding true, as later discussed. In terms of heart physiology, this assumption should be correct unless contractility changes are induced by drugs or radiation damage.

Finally, all projection numbers with their corresponding time-bin number and acquisition angle were saved in a retrospective gating file, which was used as input to a script that generated every time-point dataset.

Due to the short exposure times and the use of a multilayer monochromator, the acquired projections were able to capture changes in beam uniformity, thus invalidating conventional flat-field correction based on the average of all flat-fields. To overcome this problem, a dynamic flat-field correction algorithm based on principal component analysis of the recorded flat-fields was applied to every dataset. In doing so, every individual projection was thus corrected with the most appropriate combination of eigen-flat-fields, as thoroughly detailed by Van Nieuwenhove et al. (55).

Phase information was retrieved applying the Paganin single-distance phase-retrieval algorithm (56). The δ/β ratio was finely tuned to a value of 200 from visual inspection of the reconstructions. Reconstructions were achieved by using the GridRec algorithm (57).

In order to investigate heartbeat reproducibility and the reduction on heart function over time, a window reconstruction method was applied. Reconstructions over 180^o were computed with 20^o steps from 0 to 360^o, thus allowing observation of structural changes happening already during the first half of the scan. As a result, it was decided to keep dynamic reconstructions to the first 180^o.

Spatial resolution was calculated using a Fourier analysis-based criterion (58) previously used in other phase contrast tomography studies (59, 60). Line profiles of all rows and columns for each image were obtained and their mean power spectral density was calculated. The power spectral density converges to the noise baseline, which can be converted to the corresponding spatial frequency, and thus to spatial resolution. These calculations lead to a spatial resolution of 3.86 pixels, or 10.6 μm. This is due to smoothing from optical components, low signal-to-noise ratio, image artifacts and phase reconstruction, among others (53, 58, 59).

Data visualization was achieved with the open-source software *ImageJ* (61), while retrospective gating and generation of time-series datasets was performed using in-house scripts in Python 3.4 and Matlab 2018a.

3. Results

In this proof-of-concept experiment, we used 6 rats with the goal to learn the possibilities offered by the setup and find potential technical challenges to be considered. Out of these, 1 female rat was successfully imaged, for which the corresponding results are presented in this section. The rest of rats allowed to improve the stability of the setup, optimize the acquisition scheme and understand the response of heart function to synchrotron radiation. A summary of technical recommendations can be found in Table 3.

An illustrative time-series of the successfully imaged female heart is shown in Figure 3, Supplementary Video 1, using as reference time-point the start of the contraction (0 ms). This specific slice shows the region where the left ventricle, the septum and the right ventricle meet together. By following the marked structure (*, right ventricular trabeculation) through time, it can be noted how the right ventricular cavity is in a relaxed position during the negative time points (–30 and –15 ms). Then, systole starts at time 0 ms and ventricular contraction can be observed by the collapse of the cavity and the displacement of the heart, which was freely hanging in the air. As time evolves, the heart returns to its initial position and the cavity slowly opens again until the initial relaxation state. Figure 4, Supplementary Video 2 show two different resliced versions of the same time-series. In addition,

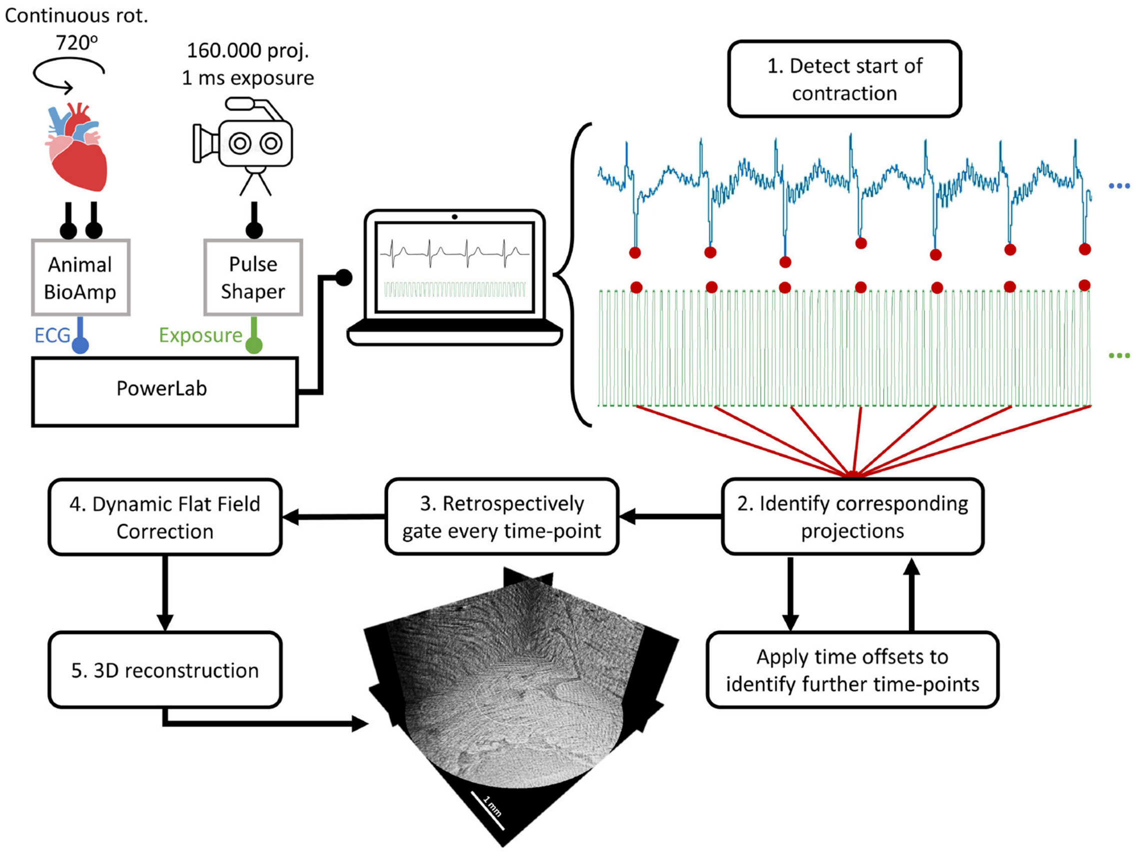

FIGURE 2
Sketch of the retrospective gating procedure. In dynamic scans, 160,000 projections (1 ms exposure) were acquired over 720° of continuous rotation. The ECG of the beating heart was recorded by the PowerLab through an Animal BioAmp. Simultaneously, the exposure signal from the detector was sent through a pulse shaper to the PowerLab. For the retrospective gating, (1) the feature corresponding to the start of the contraction was detected in the ECG. (2) Then, all the corresponding projections acquired at that specific time-point were identified. To identify the projections in the rest of time-points, 1 ms offsets were applied until the time-series were completed. (3) With all projections assigned to each time-point, the data was gated and all individual datasets for every time-point were created. (4) All datasets were corrected using dynamic flat-field correction and (5) reconstructed to obtain the 3D volumes for every time-point in the heartbeat.

Supplementary Video 3 presents sliding orthogonal views of a single time-point to demonstrate the 3D nature of the data.

The data presented in Figures 3, 4 was obtained using the projections acquired only during the first 180^o, which were a total of 199 angular projections per time-point. This number comes from the fact that 199 heartbeats occurred during the first 180^o. Such restriction was decided after observing data quality degradation over time as larger angular ranges were allowed. In this context, a window reconstruction method was applied to identify the sources of diminishing data quality.

Figure 5 shows the changes of a representative slice as the allowed reconstruction angles were varied. Each reconstruction corresponds to an angular range of 180^o but the starting angle is shifted by 20^o in every iteration. The arrows mark illustrative myocardial structures that change over time, thus indicating changes in cardiac function and/or structure over time. The largest changes can be observed during the last three reconstructions (marked by *). These are most probably caused by the sliding and dripping of perfusate over the heart surface or a change in heart motion due to degradation. Since the observed changes are mainly progressive and slow, they are indicative of either ischemia (tissue shrinkage) and/or progressive dysfunction. These are probably caused by a combination of radiation damage, which leads to ischemia due to DNA damage and formation of radicals, local temperature increase, and from the *in vitro* preparation itself, which is not completely physiological.

In Figures 3, 5, Supplementary Videos 1, 3 central ring artifacts can be observed. These are typical from micro-CT measurements and can arise during flat and dark field correction, commonly from dirt particles in the scintillator or malfunctioning pixels, among other reasons. While ring removal could help eliminate these artifacts, they often cause (over)smoothing of the data, especially when trying to

TABLE 3 Summary of experimental considerations and corresponding recommendations.

Topic	Description and recommendation
Temperature control	Temperature losses can occur in unexpected parts of the Langendorff system. Make sure to warm up as many components of the setup as possible, including the hearts' surrounding air, and install temperature probes at different locations to detect the temperature leakage zones and correct as required.
Buffer pressure	As in the temperature case, points of pressure loss can be present. Make sure to detect them in advance with a pressure transducer and correct the water column height as required.
Buffer solution refill	The buffer solution's reservoir needs to be refilled periodically. Make sure to pre-warm and pre-oxygenate the new batch before adding it into the system to avoid temperature fluctuations that might affect heart function.
Surgery and perfusion	A rapid perfusion of the isolated heart is key to achieve a fully functioning sample. Perform the surgery as close as possible to the Langendorff system to minimize ischemia. In the reported experiment, an operation table was installed at the beamline (2 m from the setup).
Bubbles in circulation	For diverse reasons, air bubbles might enter in the Langendorff system and get stuck on the aortic valve, compromising coronary perfusion. During set up, make sure to remove all air from the tubing and perform motor rotations to extract as much air from the system as possible. Additionally, install extra tubing to allow possible bubbles to scape by creating a tubing T-junction right before the cannullae.
ECG quality	Place ECG electrodes so that optimal signal can be measured. Before proceeding, perform motor translations and rotations to ensure that these do not cause the electrodes to move nor signal distortions.
Heart motion	Due to the hanging position of the hearts, these will swing while beating and thus create unwanted motion. Try to minimize the swing by using 2 cannullae going as deep as possible into the heart, wihout damaging the cardiac valves or chambers. Since hearts are mechano-sensitive, adding physical constraints (i.e., a weighted net) will affect their function.
Cardiac function degradation	Due to radiation damage, heart function will degrade over time. Before deciding your acquisition scheme, make sure to understand the exposure that hearts can tolerate before heavily degrading. The evolution of the ECG signal is a good indicator.

eliminate very sharp rings, which we wanted to avoid in the presented datasets.

4. Discussion

This manuscript presents the successful customization of an isolated, perfused heart system to allow *in vitro* synchrotron-based phase contrast tomographic experiments. The developed Langendorff setup has allowed dynamic imaging of a beating rat heart. This is a unique setup worldwide and, even if it has been specifically designed for the TOMCAT beamline, the same hardware customization principles and retrospective-gating technique could be applied at any other beamline or laboratory setup wishing to perform similar tomographic experiments.

Dynamic recordings of the beating heart were achieved at 2.75 μm pixel size (10.6 μm spatial resolution) and 1 ms temporal resolution, which is an unprecedented level of detail in this kind of heart measurements (3, 13–15). Reconstructions were obtained through retrospective gating using the ECG signal as reference. Illustrative time-series are presented in Figures 3, 4, Supplementary Videos 1, 2. While the motion observed is a combination of contraction and heart swinging from the cannulae, a clear wall thickening and contraction of the right ventricle can be observed in the data. The contraction process is observed to occur very rapidly within 20 ms after ventricular electrical activation, while full relaxation is slow and takes up to ~150 ms. All trials to reduce heart swinging were abandoned, since heart function was shown compromised due to the mechanosensitivity of the heart.

Due to the complexity of the experiment and the local field of view, dynamic data was currently limited to the qualitative observation of cardiomyocyte aggregates and larger cardiac structures, such as right ventricular trabeculation, cardiac wall and large vasculature. While the voxel size is 2.75 μm, the computed spatial resolution was 10.6 μm due to blurring and artifacts (e.g., low amount of projections). The challenge of the experiment lies in the efficient detection of X-rays while keeping the lowest exposure time possible, due to the rapid motion of the heart and cardiac function degradation over time. In this context, the developed setup included the available state-of-the-art equipment, such as the ultra-fast TOMCAT end-station (54) and high-numerical aperture 4x macroscope (53). This configuration allowed an exposure time as low as 1 ms. This means, therefore, that any movement larger than 1 pixel within 1 ms (2.75 μm/ms) will lead to motion artifacts in the reconstruction, as can be observed mostly during contraction (see Figures 3–5).

Similarly, function degradation leading to changes larger than a pixel will also introduce an artifact in the reconstruction. To tackle this issue, scans were recorded over several rotations with the goal to ensure enough angular sampling. After the experiment, 180^o window reconstructions with a step of 20^o were compared to assess how reproducible heartbeats were over time (see Figure 5). Seeing that after the first 180^o some changes observed in the reconstruction started to appear, it was decided to limit the retrospectively-gated

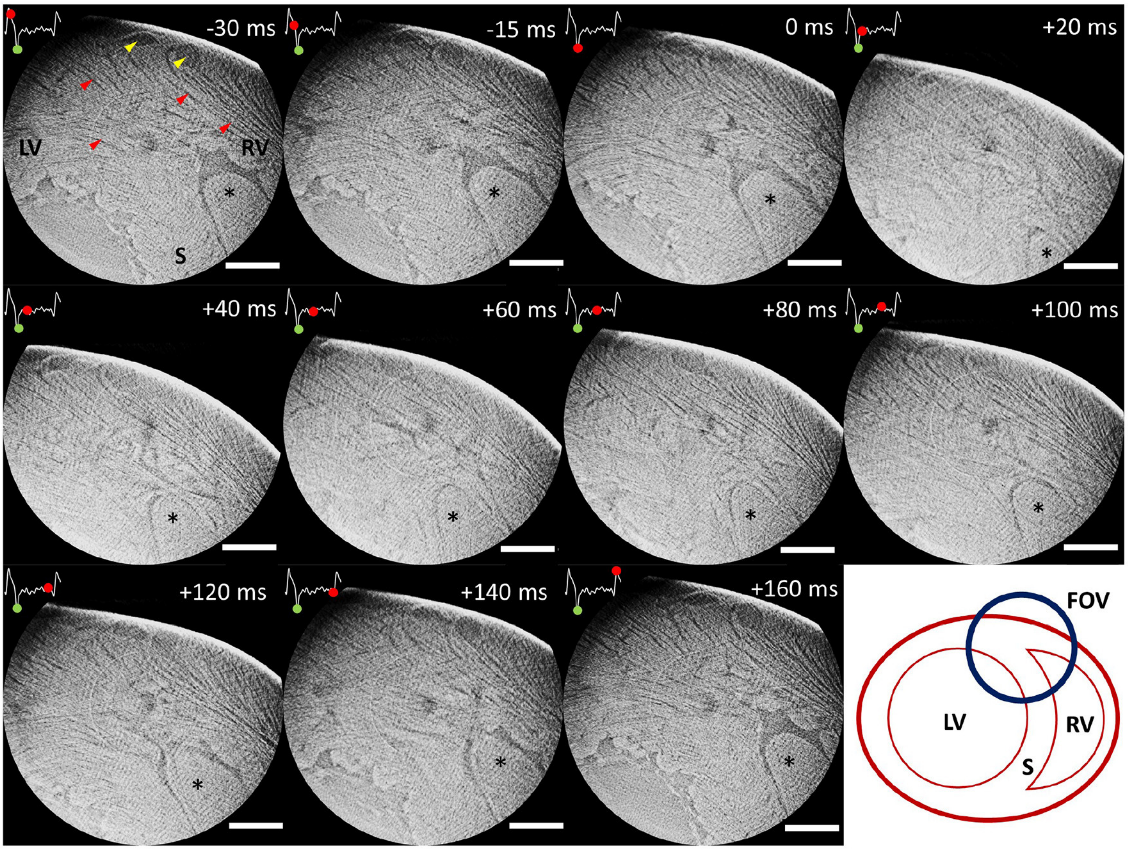

FIGURE 3
Time-series of an illustrative slice showing the region where left ventricular wall (LV), septum (S) and right ventricular wall (RV) join. Time is indicated using the start of the contraction as reference (0 ms). An ECG signal corresponding to a full heartbeat is included in every slice. The green dot on the ECG indicates the start of the contraction (reference time-point), while the advancing red dot corresponds to the exact reconstruction location. A right ventricular trabeculation has been marked (*) to clearly follow myocardial contraction and relaxation over time. Yellow arrows point at coronary vasculature, while red arrows point at cardiomyocyte aggregates. The bottom right image shows a sketch of the presented heart region. Scale bar is 1 mm.

reconstructions to the projections acquired in this initial 180^o. This decision dramatically reduced the number of projections available for reconstruction to 199 per tomogram, which in turn reduced image quality and introduced streak artifacts. To compensate for these artifacts, the use of iterative reconstruction algorithms or new acquisitions schemes should be investigated.

Given these physical and (current) technological limitations, a deep quantitative analysis, such as cardiomyocyte orientation, would possibly lead to misleading results. Nevertheless, the dynamically reconstructed data shown in this manuscript are still very promising. In the future, the use of efficient lower magnification microscopes and detectors with faster read-out speed would allow to increase the area of the heart imaged at one time. Even if at the expense of a larger pixel size, this would improve image quality and temporal resolution, while trying to keep dose deposition as low as possible. Moreover, the addition of heart function sensors for e.g., coronary flow or LV cavitiy volume, would allow for a deeper understanding of heart behavior during measurements.

By approximating rat hearts as cylinders of skeletal muscle with 15 mm diameter and following the dose calculations described in other biomedical applications of synchrotron radiation (59, 62, 63), the dynamic acquisitions presented in this manuscript have been estimated to lead to total absorbed dose of ~18 kGy per scan (for the first 180^o tomography, ~4.5 kGy), which are typical values in synchrotron-based X-PCI (59, 64). Dose distribution is specially important for tomographic scans with reduced field of view in comparison with the total volume of the sample.

With the mentioned improvements, the dynamic data could be used to determine whether cardiomyocytes are organized in so called sheets and whether these slide on each other during the cardiac cycle (65). This is nowadays one of the main hypothesis that could describe the mechanics of the heartbeat and partially explain how the myocardium is able to thicken

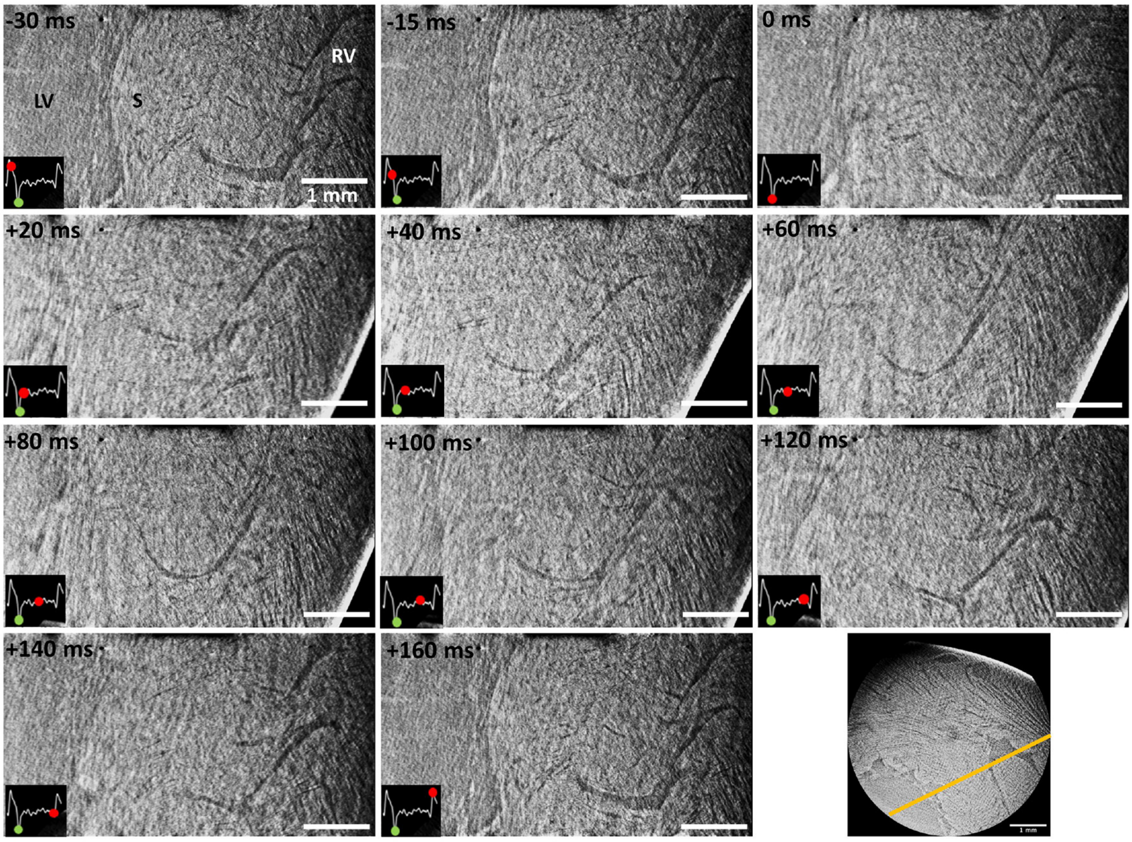

FIGURE 4
Time-series of an illustrative reslice (see bottom right, yellow line) from the scanned region including part of the left ventricular chamber (LV), septum (S) and right ventricular wall (RV). Time is indicated using the start of the contraction as reference (0 ms). An ECG signal corresponding to a full heartbeat is included in every slice. The green dot on the ECG indicates the start of the contraction (reference time-point), while the advancing red dot corresponds to the exact reconstruction location. Scale bar is 1 mm.

in a range of 28–50% during contraction, while individual cardiomyocytes can only thicken by ∼8% (12, 66–69). Therefore, further developments of this setup have the potential to answer one of the main current questions in the field of cardiac anatomy and biomechanics.

Furthermore, the implementation of this setup opens the possibility to use cardiac remodeling models or even create them *in situ*, so that their very acute responses could be assessed. For instance, an ischemic model could be easily achieved by ligating the left anterior descendant artery while the heart is mounted, which is a commonly investigated animal model of cardiac infarct (37, 39, 70).

On top of that, the versatility of the setup allows to modify the perfusion solution given to the heart to change its behavior in a controlled manner. In that sense, cardioplegic arrest studies would be possible by using elevated K^+ (diastolic arrest) or Na^+-free Li^+ Tyrode (systolic arrest) solutions (13, 14). In addition, iodine-based contrast agents could be added to the perfusate to investigate vascular behavior in real-time. Finally, specific drugs modifying heart contractility or causing vascular dilation-contraction could be easily investigated using this setup.

One of the main constraints of synchrotron experiments is the limited availability and duration of time slots. In the presented methodology, the bulk of the time is dedicated to the installation of the Langendorff system (∼6 h), its synchronization with the beamline (∼2 h) and stabilization of the perfusate temperature to the targeted ∼37^{o}C (∼1 h). The time required for eventual refilling of perfusate is minimized, since it can be pre-warmed and -oxygenated through a parallel circuit while the system runs normally. Once these steps are achieved, the time needed between the application of anesthesia and a stable isolated, perfused heart is around 30 min. Acquisition of projections, flats and darks as applied in this study is well below 10 min. However, future more complex protocols as discussed above could extend the preparation and acquisition times. Therefore, one can assume that 1–2 h of experiment per heart are required, which would potentially allow to perform statistically supported studies.

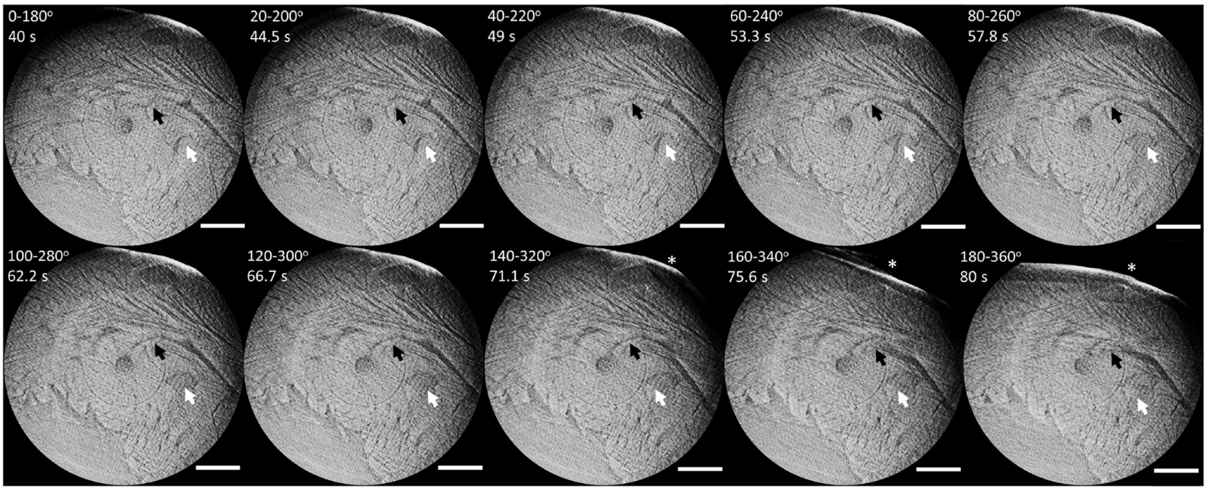

FIGURE 5
Series of representative window-reconstructed slices from 0–180° to 180–360° in 20° steps. **Black** and **white** arrows indicate example structures progressively changing over time, thus indicating function and/or tissue degradation. The star marks a large variation on the heart surface, probably due to sliding perfusate. Scale bar is 1 mm.

This manuscript presents the customization of an isolated, perfused heart system compatible with tomographic PB X-PCI experiments at the TOMCAT beamline. The development of this type of setup opens the door to the dynamic study of heart architecture at a quasi-single cardiomyocyte level. This includes not only the study of normal heart structural dynamics, but also the possibility to create ischemic models *in situ* or to investigate the heart function effects of the administration of certain drugs in the perfusion solution. In the future, further analysis of this type of data could lead to more realistic computational models (71, 72) and a better understanding of the effects of remodeling in cardiac tissue deformation and heart function.

Data availability statement

The raw data supporting the conclusions of this article will be made available by the authors, without undue reservation.

Ethics statement

The animal study was reviewed and approved by Swiss Animal Welfare Authorities.

Author contributions

HD, PG-C, SL, MS, BB, and AB designed the study. HD, CS, NM-C, MA, SL, and AB designed the experimental setup. HD, NM-C, MA, and SL handled the animals. HD and CS performed image and data processing. HD drafted the manuscript. All authors participated in the imaging experiments, revised, and contributed to the manuscript.

Funding

This project was supported by the Grant No. #2017-303 of the Strategic Focal Area Personalized Health and Related Technologies (PHRT) of the ETH Domain, the Spanish Ministry of Economy and Competitiveness (Grant No. TIN2014-52923-R) and FEDER. Open access funding provided by PSI (Paul Scherrer Institute).

Acknowledgments

The authors thank Rahel Wyss, Selianne Graf, and Manuel Egle for their support during operation of the Langendorff system, and Philipp Zuppiger for his technical support in customizing the presented setup. The authors acknowledge the Paul Scherrer Institute, Villigen, Switzerland for provision of synchrotron radiation beamtime at the TOMCAT beamline X02DA of the SLS.

Conflict of interest

The authors declare that the research was conducted in the absence of any commercial or financial relationships that could be construed as a potential conflict of interest.

Publisher's note

Supplementary material

The Supplementary Material for this article can be found online at: https://www.frontiersin.org/articles/10.3389/fcvm.2022.1023483/full#supplementary-material

References

1. Anderson RH, Smerup M, Sanchez-Quintana D, Loukas M, Lunkenheimer PP. The three-dimensional arrangement of the myocytes in the ventricular walls. *Clin Anatomy*. (2009) 22:64–76. doi: 10.1002/ca.20645

2. Anderson RH, Niederer PF, Sanchez-Quintana D, Stephenson RS, Agger P. How are the cardiomyocytes aggregated together within the walls of the left ventricular cone? *J Anat*. (2019) 235:697–705. doi: 10.1111/joa.13027

3. Dejea H, Bonnin A, Cook A, Garcia-Canadilla P. Cardiac multi-scale investigation of the right and left ventricle ex-vivo: a review. *Cardiovasc Diagn Ther*. (2020) 10:1701–17. doi: 10.21037/cdt-20-269

4. Sutherland FJ, Hearse DJ. The isolated blood and perfusion fluid perfused heart. *Pharmacol Res*. (2000) 41:613–27. doi: 10.1006/phrs.1999.0653

5. Skrzypiec-Spring M, Grotthus B, Szelag A, Schulz R. Isolated heart perfusion according to Langendorff–still viable in the new millennium. *J Pharmacol Toxicol Methods*. (2007) 55:113–26. doi: 10.1016/j.vascn.2006.05.006

6. Méndez-Carmona N, Wyss RK, Arnold M, Joachimbauer A, Segiser A, Fiedler GM, et al. Differential effects of ischemia/reperfusion on endothelial function and contractility in donation after circulatory death. *J Heart Lung Transplant*. (2019) 38:767–77. doi: 10.1016/j.healun.2019.03.004

7. Lee WN, Pernot M, Couade M, Messas E, Bruneval P, Bel A, et al. Mapping myocardial fiber orientation using echocardiography-based shear wave imaging. *IEEE Trans Med Imaging*. (2011) 31:554–62. doi: 10.1109/TMI.2011.2172690

8. Papadacci C, Finel V, Provost J, Villemain O, Bruneval P, Gennisson JL, et al. Imaging the dynamics of cardiac fiber orientation in vivo using 3D ultrasound backscatter tensor imaging. *Sci Rep*. (2017) 7:1–9. doi: 10.1038/s41598-017-00946-7

9. Hsu EW, Buckley DL, Bui JD, Blackband SJ, Forder JR. Two-component diffusion tensor MRI of isolated perfused hearts. *Magn Reson Med*. (2001) 45:1039–45. doi: 10.1002/mrm.1138

10. Köhler S, Hiller KH, Waller C, Bauer WR, Haase A, Jakob PM. Investigation of the microstructure of the isolated rat heart: A comparison between T* 2-and diffusion-weighted MRI. *Magn Reson Med*. (2003) 50:1144–50. doi: 10.1002/mrm.10636

11. Köhler S, Hiller KH, Waller C, Jakob PM, Bauer WR, Haase A. Visualization of myocardial microstructure using high-resolution T imaging at high magnetic field. *Magn Reson Med*. (2003) 49:371–5. doi: 10.1002/mrm.10346

12. Chen J, Liu W, Zhang H, Lacy L, Yang X, Song SK, et al. Regional ventricular wall thickening reflects changes in cardiac fiber and sheet structure during contraction: quantification with diffusion tensor MRI. *Am J Physiol Heart Circ Physiol*. (2005) 289:H1898–907. doi: 10.1152/ajpheart.00041.2005

13. Hales PW, Schneider JE, Burton RA, Wright BJ, Bollensdorff C, Kohl P. Histo-anatomical structure of the living isolated rat heart in two contraction states assessed by diffusion tensor MRI. *Prog Biophys Mol Biol*. (2012) 110:319–30. doi: 10.1016/j.pbiomolbio.2012.07.014

14. Gilbert SH, Benoist D, Benson AP, White E, Tanner SF, Holden AV, et al. Visualization and quantification of whole rat heart laminar structure using high-spatial resolution contrast-enhanced MRI. *Am J Physiol Heart Circ Physiol*. (2012) 302:H287–98. doi: 10.1152/ajpheart.00824.2011

15. Lohezic M, Teh I, Bollensdorff C, Peyronnet R, Hales PW, Grau V, et al. Interrogation of living myocardium in multiple static deformation states with diffusion tensor and diffusion spectrum imaging. *Prog Biophys Mol Biol*. (2014) 115:213–25. doi: 10.1016/j.pbiomolbio.2014.08.002

16. Burton RA, Plank G, Schneider JE, Grau V, Ahammer H, Keeling SL, et al. Three-dimensional models of individual cardiac histoanatomy: tools and challenges. *Ann N Y Acad Sci*. (2006) 1080:301–19. doi: 10.1196/annals.1380.023

17. Bishop MJ, Plank G, Burton RA, Schneider JE, Gavaghan DJ, Grau V, et al. Development of an anatomically detailed MRI-derived rabbit ventricular model and assessment of its impact on simulations of electrophysiological function. *Am J Physiol Heart Circ Physiol*. (2010) 298:H699-H718. doi: 10.1152/ajpheart.00606.2009

18. Nielles-Vallespin S, Mekkaoui C, Gatehouse P, Reese TG, Keegan J, Ferreira PF, et al. In vivo diffusion tensor MRI of the human heart: reproducibility of breath-hold and navigator-based approaches. *Magn Reson Med*. (2013) 70:454–65. doi: 10.1002/mrm.24488

19. Nielles-Vallespin S, Khalique Z, Ferreira PF, de Silva R, Scott AD, Kilner P, et al. Assessment of myocardial microstructural dynamics by in vivo diffusion tensor cardiac magnetic resonance. *J Am Coll Cardiol*. (2017) 69:661–76. doi: 10.1016/j.jacc.2016.11.051

20. Scott AD, Ferreira PF, Nielles-Vallespin S, Gatehouse P, McGill LA, Kilner P, et al. Optimal diffusion weighting for in vivo cardiac diffusion tensor imaging. *Magn Reson Med*. (2015) 74:420–30. doi: 10.1002/mrm.25418

21. Ferreira PF, Kilner PJ, McGill LA, Nielles-Vallespin S, Scott AD, Ho SY, et al. In vivo cardiovascular magnetic resonance diffusion tensor imaging shows evidence of abnormal myocardial laminar orientations and mobility in hypertrophic cardiomyopathy. *J Cardiovasc Magn Reson*. (2014) 16:87. doi: 10.1186/s12968-014-0087-8

22. Von Deuster C, Sammut E, Asner L, Nordsletten D, Lamata P, Stoeck CT, et al. Studying dynamic myofiber aggregate reorientation in dilated cardiomyopathy using in vivo magnetic resonance diffusion tensor imaging. *Circulation*. (2016) 9:e005018. doi: 10.1161/CIRCIMAGING.116.005018

23. Sharrack N, Das A, Kelly C, Teh I, Stoeck C, Kozerke S, et al. The relationship between myocardial microstructure and strain in chronic infarction using cardiovascular magnetic resonance diffusion tensor imaging and feature tracking. *J Cardiovasc Magn Reson*. (2022) 24:1–14. doi: 10.1186/s12968-022-00892-y

24. Stoeck CT, Scott AD, Ferreira PF, Tunnicliffe EM, Teh I, Nielles-Vallespin S, et al. Motion-induced signal loss in *in vivo* cardiac diffusion-weighted imaging. *J Magn Reson Imaging*. (2020) 51:319. doi: 10.1002/jmri.26767

25. Moulin K, Verzhbinsky IA, Maforo NG, Perotti LE, Ennis DB. Probing cardiomyocyte mobility with multi-phase cardiac diffusion tensor MRI. *PLoS ONE*. (2020) 15:e0241996. doi: 10.1371/journal.pone.0241996

26. Moulin K, Croisille P, Viallon M, Verzhbinsky IA, Perotti LE, Ennis DB. Myofiber strain in healthy humans using DENSE and cDTI. *Magn Reson Med*. (2021) 86:277–92. doi: 10.1002/mrm.28724

27. Lasič S, Szczepankiewicz F, Dall'Armellina E, Das A, Kelly C, Plein S, et al. Motion-compensated b-tensor encoding for in vivo cardiac diffusion-weighted imaging. *NMR Biomed*. (2020) 33:e4213. doi: 10.1002/nbm.4213

28. Sosnovik DE, Mekkaoui C, Huang S, Chen HH, Dai G, Stoeck CT, et al. Microstructural impact of ischemia and bone marrow-derived cell therapy revealed with diffusion tensor magnetic resonance imaging tractography of the heart in vivo. *Circulation*. (2014) 129:1731–41. doi: 10.1161/CIRCULATIONAHA.113.005841

29. Nguyen C, Fan Z, Sharif B, He Y, Dharmakumar R, Berman DS, et al. In vivo three-dimensional high resolution cardiac diffusion-weighted MRI: a motion compensated diffusion-prepared balanced steady-state free precession approach. *Magn Reson Med*. (2014) 72:1257–67. doi: 10.1002/mrm.25038

30. Nguyen CT, Buckberg G, Li D. Magnetic resonance diffusion tensor imaging provides new insights into the microstructural alterations in dilated cardiomyopathy. *Circulation*. (2016) 9:e005593. doi: 10.1161/CIRCIMAGING.116.005593

31. Nguyen CT, Christodoulou AG, Coll-Font J, Ma S, Xie Y, Reese TG, et al. Free-breathing diffusion tensor MRI of the whole left ventricle using second-order motion compensation and multitasking respiratory motion correction. *Magn Reson Med*. (2021) 85:2634–48. doi: 10.1002/mrm.28611

32. Weitkamp T, Diaz A, David C, Pfeiffer F, Stampanoni M, Cloetens P, et al. X-ray phase imaging with a grating interferometer. *Opt Express*. (2005) 13:6296–304. doi: 10.1364/OPEX.13.006296

33. Kaneko Y, Shinohara G, Hoshino M, Morishita H, Morita K, Oshima Y, et al. Intact imaging of human heart structure using x-ray phase-contrast tomography. *Pediatr Cardiol*. (2017) 38:390–3. doi: 10.1007/s00246-016-1527-z

34. Tsukube T, Yagi N, Hoshino M, Nakashima Y, Nakagawa K, Okita Y. Impact of synchrotron radiation-based X-ray phase-contrast tomography on understanding various cardiovascular surgical pathologies. *Gen Thorac Cardiovasc Surg*. (2015) 63:590–2. doi: 10.1007/s11748-015-0565-4

35. Shinohara G, Morita K, Hoshino M, Ko Y, Tsukube T, Kaneko Y, et al. Three Dimensional visualization of human cardiac conduction tissue in whole heart specimens by high-resolution phase-contrast CT imaging using synchrotron radiation. *World J Pediatr Congenital Heart Surgery*. (2016) 7:700–5. doi: 10.1177/2150135116675844

36. Gonzalez-Tendero A, Zhang C, Balicevic V, Cárdenes R, Loncaric S, Butakoff C, et al. Whole heart detailed and quantitative anatomy, myofibre structure and vasculature from X-ray phase-contrast synchrotron radiation-based micro computed tomography. *Eur Heart J Cardiovasc Imaging*. (2017) 18:732–41. doi: 10.1093/ehjci/jew314

37. Dejea H, Garcia-Canadilla P, Cook AC, Guasch E, Zamora M, Crispi F, et al. Comprehensive analysis of animal models of cardiovascular disease using multiscale x-ray phase contrast tomography. *Sci Rep*. (2019) 9:1–12. doi: 10.1038/s41598-019-43407-z

38. Reichardt M, Frohn J, Khan A, Alves F, Salditt T. Multi-scale X-ray phase-contrast tomography of murine heart tissue. *Biomed Opt Express*. (2020) 11:2633–51. doi: 10.1364/BOE.386576

39. Planinc I, Garcia-Canadilla P, Dejea H, Ilic I, Guasch E, Zamora M, et al. Comprehensive assessment of myocardial remodeling in ischemic heart disease by synchrotron propagation based X-ray phase contrast imaging. *Sci Rep*. (2021) 11:1–13. doi: 10.1038/s41598-021-93054-6

40. Garcia-Canadilla P, Dejea H, Bonnin A, Balicevic V, Loncaric S, Zhang C, et al. Complex congenital heart disease associated with disordered myocardial architecture in a midtrimester human fetus. *Circulation*. (2018) 11:e007753. doi: 10.1161/CIRCIMAGING.118.007753

41. Mirea I, Varray F, Zhu YM, Fanton L, Langer M, Jouk PS, et al. Very high-resolution imaging of post-mortem human cardiac tissue using X-ray phase contrast tomography. In: *International Conference on Functional Imaging and Modeling of the Heart*. Maastricht: Springer (2015). p. 172–9.

42. Varray F, Mirea I, Langer M, Peyrin F, Fanton L, Magnin IE. Extraction of the 3D local orientation of myocytes in human cardiac tissue using X-ray phase-contrast micro-tomography and multi-scale analysis. *Med Image Anal*. (2017) 38:117–32. doi: 10.1016/j.media.2017.02.006

43. Mirea I, Wang L, Varray F, Zhu YM, Serrano ED, Magnin IE. Statistical analysis of transmural laminar microarchitecture of the human left ventricle. In: *2016 IEEE 13th International Conference on Signal Processing (ICSP)*. Chengdu: IEEE (2016). p. 53–6.

44. Wang S, Mirea I, Varray F, Liu WY, Magnin IE. Investigating the 3D Local Myocytes Arrangement in the Human LV Mid-Wall with the transverse angle. In: *International Conference on Functional Imaging and Modeling of the Heart*. Bordeaux: Springer (2019). p. 208–16.

45. Loncaric F, Garcia-Canadilla P, Garcia-Alvarez A, Sanchis L, Prat S, Doltra A, et al. Etiology-discriminative multimodal imaging of left ventricular hypertrophy and synchrotron-based assessment of microstructural tissue remodeling. *Front Cardiovasc Med Cardiovasc Imaging*. (2021) 8:670734. doi: 10.3389/fcvm.2021.670734

46. Reichardt M, Jensen PM, Dahl VA, Dahl AB, Ackermann M, Shah H, et al. 3D virtual histopathology of cardiac tissue from COVID-19 patients based on phase-contrast X-ray tomography. *Elife*. (2021) 10:e71359. doi: 10.7554/eLife.71359

47. Walsh C, Tafforeau P, Wagner W, Jafree D, Bellier A, Werlein C, et al. Imaging intact human organs with local resolution of cellular structures using hierarchical phase-contrast tomography. *Nat Methods*. (2021) 18:1532–41. doi: 10.1038/s41592-021-01317-x

48. Lovric G, Mokso R, Schlepütz CM, Stampanoni M. A multi-purpose imaging endstation for high-resolution micrometer-scaled sub-second tomography. *Phys Med*. (2016) 32:1771–8. doi: 10.1016/j.ejmp.2016.08.012

49. García-Moreno F, Kamm PH, Neu TR, Bülk F, Mokso R, Schlepütz CM, et al. Using X-ray tomoscopy to explore the dynamics of foaming metal. *Nat Commun*. (2019) 10:1–9. doi: 10.1038/s41467-019-11521-1

50. Marone F, Schlepütz CM, Marti S, Fusseis F, Velásquez-Parra A, Griffa M, et al. Time resolved in situ X-ray tomographic microscopy unraveling dynamic processes in geologic systems. *Front Earth Sci*. (2020) 7:346. doi: 10.3389/feart.2019.00346

51. Frohn J, Pinkert-Leetsch D, Missbach-Güntner J, Reichardt M, Osterhoff M, Alves F, et al. 3D virtual histology of human pancreatic tissue by multiscale phase-contrast X-ray tomography. *J Synchrotron Radiat*. (2020) 27:1707–19. doi: 10.1107/S1600577520011327

52. Stampanoni M, Groso A, Isenegger A, Mikuljan G, Chen Q, Meister D, et al. TOMCAT: a beamline for TO mographic M icroscopy and C oherent r A diology experimen T s. In: *AIP Conference Proceedings, Vol. 879*. Daegu: American Institute of Physics (2007). p. 848–51.

53. Bührer M, Stampanoni M, Rochet X, Büchi F, Eller J, Marone F. High-numerical-aperture macroscope optics for time-resolved experiments. *J Synchrotron Radiat*. (2019) 26(Pt 4):1161–72. doi: 10.1107/S1600577519004119

54. Mokso R, Schlepütz CM, Theidel G, Billich H, Schmid E, Celcer T, et al. GigaFRoST: the gigabit fast readout system for tomography. *J Synchrotron Radiat*. (2017) 24:1250–9. doi: 10.1107/S1600577517013522

55. Van Nieuwenhove V, De Beenhouwer J, De Carlo F, Mancini L, Marone F, Sijbers J. Dynamic intensity normalization using eigen flat fields in X-ray imaging. *Opt Express*. (2015) 23:27975–89. doi: 10.1364/OE.23.027975

56. Paganin D, Mayo SC, Gureyev TE, Miller PR, Wilkins SW. Simultaneous phase and amplitude extraction from a single defocused image of a homogeneous object. *J Microsc*. (2002) 206:33–40. doi: 10.1046/j.1365-2818.2002.01010.x

57. Marone F, Stampanoni M. Regridding reconstruction algorithm for real-time tomographic imaging. *J Synchrotron Radiat*. (2012) 19:1029–37. doi: 10.1107/S0909049512032864

58. Modregger P, Lübbert D, Schäfer P, Köhler R. Spatial resolution in Bragg-magnified X-ray images as determined by Fourier analysis. *Physica Status Solidi*. (2007) 204:2746–52. doi: 10.1002/pssa.200675685

59. Lovric G, Barré SF, Schittny JC, Roth-Kleiner M, Stampanoni M, Mokso R. Dose optimization approach to fast X-ray microtomography of the lung alveoli. *J Appl Crystall*. (2013) 46:856–60. doi: 10.1107/S0021889813005591

60. Pierantoni M, Silva Barreto I, Hammerman M, Verhoeven L, Törnquist E, Novak V, et al. A quality optimization approach to image Achilles tendon microstructure by phase-contrast enhanced synchrotron micro-tomography. *Sci Rep*. (2021) 11:1–14. doi: 10.1038/s41598-021-96589-w

61. Schindelin J, Arganda-Carreras I, Frise E, Kaynig V, Longair M, Pietzsch T, et al. Fiji: an open-source platform for biological-image analysis. *Nat Methods*. (2012) 9:676–82. doi: 10.1038/nmeth.2019

62. Salditt T, Aspelmeier T, Aeffner S. *Biomedical Imaging: Principles of Radiography, Tomography and Medical Physics*. Berlin: Walter de Gruyter GmbH & Co KG (2017).

63. Hubbell J, Seltzer S. *X-Ray Mass Attenuation Coefficients: NIST Standard Reference Database 126*. Gaithersburg, MD: National Institute of Standards and Technology (2004).

64. Immel A, Le Cabec A, Bonazzi M, Herbig A, Temming H, Schuenemann VJ, et al. Effect of X-ray irradiation on ancient DNA in sub-fossil bones-guidelines for safe X-ray imaging. *Sci Rep*. (2016) 6:32969. doi: 10.1038/srep32969

65. LeGrice IJ, Smaill B, Chai L, Edgar S, Gavin J, Hunter PJ. Laminar structure of the heart: ventricular myocyte arrangement and connective tissue architecture in the dog. *Am J Physiol Heart Circ Physiol*. (1995) 269:H571–82. doi: 10.1152/ajpheart.1995.269.2.H571

66. Sonnenblick EH, Ross Jr J, Covell JW, Spotnitz HM, Spiro D. The ultrastructure of the heart in systole and diastole: > changes in sarcomere length. *Circ Res*. (1967) 21:423–31. doi: 10.1161/01.RES.21.4.423

67. Rodriguez EK, Hunter WC, Royce MJ, Leppo MK, Douglas AS, Weisman HF. A method to reconstruct myocardial sarcomere lengths and orientations at transmural sites in beating canine hearts. *Am J Physiol Heart Circ Physiol*. (1992) 263:H293-H306. doi: 10.1152/ajpheart.1992.263.1.H293

68. Ross Jr J, Sonnenblick EH, Covell JW, Kaiser GA, Spiro D. The architecture of the heart in systole and diastole: technique of rapid fixation and analysis of left ventricular geometry. *Circ Res*. (1967) 21:409–21. doi: 10.1161/01.RES.21.4.409

69. Bogaert J, Rademakers FE. Regional nonuniformity of normal adult human left ventricle. *Am J Physiol Heart Circ Physiol.* (2001) 280:H610–20. doi: 10.1152/ajpheart.2001.280.2.H610

70. Cooper CJ, Pfeffer JM, Finn P, Pfeffer MA. Characteristics of a model of myocardial infarction produced by coronary artery ligation in the rat. *Cardiovasc Pathol.* (1995) 4:189–94. doi: 10.1016/1054-8807(95)00021-V

71. Lamata P, Casero R, Carapella V, Niederer SA, Bishop MJ, Schneider JE, et al. Images as drivers of progress in cardiac computational modelling. *Prog Biophys Mol Biol.* (2014) 115:198–212. doi: 10.1016/j.pbiomolbio.2014.08.005

72. Walmsley J, van Everdingen W, Cramer MJ, Prinzen FW, Delhaas T, Lumens J. Combining computer modelling and cardiac imaging to understand right ventricular pump function. *Cardiovasc Res.* (2017) 113:1486–98. doi: 10.1093/cvr/cvx154

frontiers | Frontiers in Cardiovascular Medicine

TYPE Original Research
PUBLISHED 23 December 2022
DOI 10.3389/fcvm.2022.1074956

Check for updates

OPEN ACCESS

EDITED BY
Francesco Pelliccia,
Sapienza University of Rome, Italy

REVIEWED BY
Jian Wu,
Fudan University, China
Yosuke Nabeshima,
University of Occupational and
Environmental Health Japan, Japan

*CORRESPONDENCE
Christophe Beyls
✉ beyls.christophe59@gmail.com

SPECIALTY SECTION
This article was submitted to
Cardiovascular Imaging,
a section of the journal
Frontiers in Cardiovascular Medicine

RECEIVED 20 October 2022
ACCEPTED 05 December 2022
PUBLISHED 23 December 2022

CITATION
Beyls C, Huette P, Vangreveninge P, Leviel F, Daumin C, Ammar B, Touati G, Roger B, Caus T, Dupont H, Abou-Arab O, Momar D and Mahjoub Y (2022) Interchangeability of right ventricular longitudinal shortening fraction assessed by transthoracic and transoesophageal echocardiography in the perioperative setting: A prospective study. *Front. Cardiovasc. Med.* 9:1074956. doi: 10.3389/fcvm.2022.1074956

Interchangeability of right ventricular longitudinal shortening fraction assessed by transthoracic and transoesophageal echocardiography in the perioperative setting: A prospective study

Christophe Beyls[1,2]*, Pierre Huette[1,2], Paul Vangreveninge[1], Florent Leviel[1], Camille Daumin[1], BenAmmar Ammar[1], Gilles Touati[3], Bouzerar Roger[4], Thierry Caus[3], Hervé Dupont[1,2], Osama Abou-Arab[1], Diouf Momar[5] and Yazine Mahjoub[1,2]

[1]Department of Anesthesiology and Critical Care Medicine, Amiens University Hospital, Amiens, France, [2]UR UPJV 7518 SSPC (Simplification of Care of Complex Surgical Patients) Research Unit, University of Picardie Jules Verne, Amiens, France, [3]Department of Cardiac Surgery, Amiens University Hospital, Amiens, France, [4]Department of Biophysics and Image Processing, Amiens University Hospital, Amiens, France, [5]Department of Biostatistics, Amiens University Hospital, Amiens, France

Background: Conventional transthoracic (TTE) and transoesophageal echocardiography (TEE) parameters assessing right ventricle (RV) systolic function are daily used assuming their clinical interchangeability. RV longitudinal shortening fraction (RV-LSF) is a two-dimensional speckle tracking parameter used to assess RV systolic function. RV-LSF is based on tricuspid annular displacement analysis and could be measured with TTE or TEE.

Objective: The aim of the study was to determine if RV-LSF$_{TTE}$ and RV-LSF$_{TEE}$ measurements were interchangeable in the perioperative setting.

Methods: Prospective perioperative TTE and TEE echocardiography were performed under general anesthesia during scheduled cardiac surgery in 90 patients. RV-LSF was measured by semi-automatic software. Comparisons were performed using Pearson correlation and Bland-Altman plots. RV-LSF clinical agreement was determined as a range of −5 to 5%.

Results: Of the 114 patients who met the inclusion criteria, 90 were included. The mean preoperative RV-LSF$_{TTE}$ was 20.4 ± 4.3 and 21.1 ± 4.1% for RV-LSF$_{TEE.}$ The agreement between RV-LSF measurements was excellent, with a bias at −0.61 and limits of agreement of −4.18 to 2.97 %. All measurements fell within the determined clinical agreement interval in the Bland-Altman plot. Linear regression analysis showed a high correlation between RV-LSF$_{TTE}$ and

RV-LSF$_{TEE}$ measurement (r = 0.9; confidence interval [CI] 95%: [0.87–0.94], $p < 0.001$).

Conclusion: RV-LSF$_{TTE}$ and RV-LSF$_{TEE}$ measurements are interchangeable, allowing RV-LSF to be a helpful parameter for assessing perioperative changes in RV systolic function.

NCT: NCT05404737. https://www.clinicaltrials.gov/ct2/show/NCT05404737.

KEYWORDS

right ventricular shortening fraction, speckle tracking, interchangeability, right ventricle, tricuspid

Introduction

Echocardiography is a non-invasive, simple, and helpful technique in patients undergoing interventional cardiology procedures, cardiac surgery, high-risk non-cardiac surgery, and for diagnosing intra- or post-operative complications (1). Two-dimensional transthoracic echocardiography (TTE) and transoesophageal echocardiography (TEE) are routinely used to qualitatively and quantitatively evaluate the structure and function of the heart (2). TTE and TEE echocardiographic assessment of the right ventricular (RV) systolic function is challenging and requires a multiparametric approach that combines conventional parameters, such as tricuspid annular plane displacement (TAPSE), RV fractional area change (RV-FAC), and advanced speckle tracking parameters (3).

In interventional cardiology procedures, TEE is used to guide device placement and assess the periprocedural changes of RV systolic function (4). During cardiac surgery, intraoperative TEE is crucial in assisting surgical decision-making. It is also a helpful monitoring tool for providing an immediate point-of-care assessment of RV systolic function, especially with TAPSE and RV-FAC parameters (1, 3, 5). In the intensive care unit, RV systolic function is routinely assessed using conventional parameters measured by transthoracic echocardiography. This evaluation is crucial for RV failure diagnosis, global hemodynamic management, and ventilator parameters setting (5). In daily practice, RV systolic parameters measured by TTE and by TTE are often used interchangeably and assumed clinically equivalent, even if their measurement must be done with caution (6). Actually, the values of conventional RV-systolic function parameters obtained in TTE and TEE were not comparable due to a large variability, a poor correlation (8), and an underestimation with TEE (7). For some authors, RV strain parameters and 3D RV ejection fraction (3D-RVEF) should be used to avoid the variability and angle dependency of the conventional RV systolic parameters (6). However, the measurement of RV strain parameters and 3D-RVEF required high image quality and specific probes, thus limiting their use in clinical routine.

The right ventricle longitudinal shortening fraction (RV-LSF) is a two-dimensional speckle tracking echocardiography (2D-STE) parameter based on the longitudinal tricuspid annular displacement (TAD) that assesses the global RV systolic function (9). RV-LSF is a semi-automatic, angle-independent, and accurate 2D-STE parameter for assessing RV systolic dysfunction in several clinical settings (10, 11). Besides, RV-LSF is a fast and reproducible post-processing 2D-STE parameter less dependent on image quality (12) and loading conditions (13) than RV strain parameters. RV-LSF combines the longitudinal displacement of the lateral (TAD$_{lat}$) and septal (TAD$_{sep}$) portion of the tricuspid ring toward the RV apex. RV-LSF can be measured by TTE or TEE (14). In TTE, RV-LSF is more correlated to the RV ejection fraction, evaluated in magnetic resonance imaging (9) or three-dimensional echocardiography (12), than conventional and strain parameters. Besides, RV-LSF is more accurate for identifying patients with RV dysfunction (10).

However, to our knowledge, RV-LSF values measured by TTE and TEE have not been compared. Mainly, there are no data assessing the interchangeability of RV-LSF$_{TTE}$ and RV-LSF$_{TEE}$. In TEE, several factors could affect RV-LSF measurement and, therefore, its interchangeability: TEE view is foreshortened and does not fully display the apical portion of the RV, which is crucial for ROI placement. Besides, the dynamic and non-planarity of the tricuspid annulus could also affect the measurement of TAD$_{lat}$ and TAD$_{sep}$.

The first aim of the study was to determine whether RV-LSF$_{TTE}$ and RV-LSF$_{TEE}$ measurements could be considered interchangeable in the perioperative setting. The second aim was to study the interchangeability of the two components of RV-LSF (TAD$_{lat}$ and TAD$_{sep}$).

Abbreviations: 2D-STE, two-dimensional speckle tracking echocardiography; LOA, limits of agreements; RV, right ventricle; RV-LSF, right ventricle longitudinal shortening fraction; TAD, tricuspid annular displacement; TEE, transesophageal echocardiography; TTE, transthoracic echocardiography.

Methods

Study population

This prospective interventional study was conducted at Amiens university hospital (Amiens, France) between August 2021 and April 2022. We prospectively included all adult patients (>18 years old) hospitalized for a scheduled cardiac surgery under cardiopulmonary bypass that required intraoperative TEE. Exclusion criteria were patients with a contraindication to TEE performance (gastric or esophageal pathology), a poor echogenicity on TEE, a TTE not allowing evaluation of RV-LSF, and patients with a rapid supraventricular rhythm disorder at the time of TEE and TTE.

Ethics

This is a single-center, prospective and interventional study of patients hospitalized at Amiens University Hospital for scheduled cardiac surgery under cardiopulmonary bypass (CPB). The study was approved by the Amiens University Hospital IRB (CHU–Place V. Pauchet, 80054 AMIENS Cedex) and by an institutional ethics committee (Comité de Protection des Personnes Ile de France VIII, ID-RCB 2021_A000908-33). Oral and written information was provided to the patients.

Echocardiography procedure

Echocardiography images were obtained using high-quality commercially available probes (S5-1 for TTE, X7-2T for TEE, Philips Healthcare) and ultrasound systems (CX 50, Philips Healthcare). To assess the interchangeability of RV-LSF, TTE and TEE exams, respectively, were performed in patients under general anesthesia immediately after induction of anesthesia, oral intubation, and muscle blockade. The procedures for general anesthesia and mechanical ventilation were standardized for all patients. The TEE and TTE echocardiography protocols followed the American Society of Echocardiography and the European Society of Cardiology recommendations for assessing RV systolic function (3, 15).

RV-LSF measurement

RV-LSF was measured using dedicated software (Automated Cardiac Motion Quantification, QLAB version 15.0, Philips Medical Systems, Andover, MA, USA). For RV-LSF analysis, three regions of interest (ROI) were used to initialize the first diastolic frame in a mild-esophageal four-chamber (ME-4CH) view (Figure 1A, Supplementary Video 1) for the TEE procedure and in an RV-focused apical four-chamber view for the TTE procedure (Figure 1B, Supplementary Video 2). These ROI were placed 1) on the tricuspid annulus at the insertion of the anterior tricuspid valve leaflet (RV free wall), 2) on the tricuspid annulus at the insertion of the septal leaflet, and 3) on the RV apex. The software automatically tracked and calculated three parameters: (1) the displacement between the RV free wall and the RV apex (TAD_{lat}), (2) the displacement between the interventricular septum and the RV apex (TAD_{sep}), and (3) the RV-LSF. RV-LSF was calculated as the maximum end-systolic displacement (LES) of the mid-annular point from the measured annular motion and is expressed as a percentage of the end-diastolic RV longitudinal dimension (LED): 100 × (LED–LES)/LED. The software automatically selected the mid-annular point.

RV-LSF was analyzed in a single beat, and the reported value was the average of 3 measurements. All TTE and TEE RV-LSF measurements were analyzed offline (separately and randomly) by an expert sonographer 2 weeks after the inclusion period.

RV systolic conventional parameters

In TTE, conventional RV systolic parameters were measured according to international guidelines: tricuspid annular plane systolic excursion (TAPSE) was measured using M-mode with a cursor placed at the junction of the lateral tricuspid leaflet and the RV free wall. RV-S' wave was measured in the apical four-chamber view using Doppler tissue imaging mode. RV systolic and diastolic areas were measured in the apical four-chamber view in 2D mode. RV-fractional area change was calculated by subtracting the end-systolic area from the end-diastolic area and dividing this value by the end-diastolic area. The following variables were recorded: age, gender, body weight, personal medical history, logistic EuroSCORE II, type of cardiac surgery, preoperative plasmatic creatinine, and hemoglobin.

Statistical analysis

Continuous variables were expressed as mean and 95% confidence interval or standard deviation. Categorical variables are presented as absolute numbers and percentages. The correlation between TTE_{RV-LSF} and TEE_{RV-LSF} measurements was quantified using Pearson's coefficient. Bland-Altman (BA) analysis was performed to assess the level of agreement between $RV\text{-}LSF_{TTE}$ and $RV\text{-}LSF_{TEE.}$

Sample size calculation

Assuming a common standard deviation equal to 5 points for each of the RV-LSF values (TTE and TEE), the standard deviation of the difference between the two measures is estimated to be 3.87 if a correlation coefficient (ρ) of 0.7 is assumed between the two RV-LSF measures. Thus, according to Bland and Altman (16), at least 90 evaluable patients would be required to estimate the limits of agreement (LOA) with an

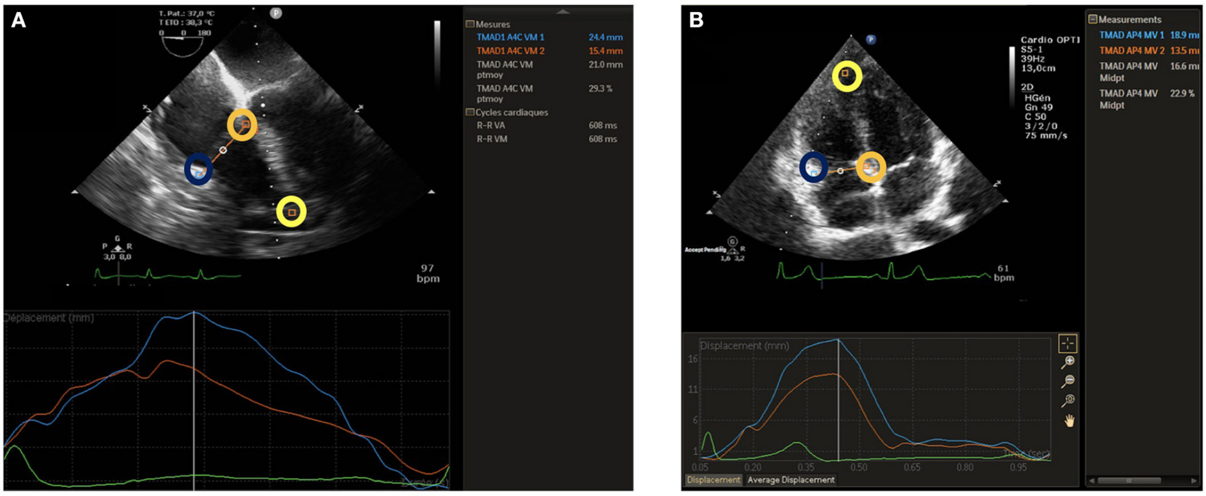

Mesures
TMAD1 A4C VM 1 24.4 mm
TMAD1 A4C VM 2 15.4 mm
TMAD A4C VM ptmoy 21.0 mm
TMAD A4C VM ptmoy 29.3 %
Cycles cardiaques
R-R VA 608 ms
R-R VM 608 ms

Measurements
TMAD AP4 MV 1 18.9 mı
TMAD AP4 MV 2 13.5 mı
TMAD AP4 MV Midpt 16.6 mı
TMAD AP4 MV Midpt 22.9 %

FIGURE 1
TEE RV-LSF measurement **(A)** and TTE RV-LSF measurement **(B)**. A lateral point (blue circle) and a septal point (orange circle) were placed at the bottom of the RV free wall and the bottom of the interventricular septum. A third point was placed at the apex (yellow circle). TAD lateral, septal, and RV longitudinal shortening fraction (RV-LSF) values were automatically displayed in percentage. The mid-annular point is automated and selected by the software.

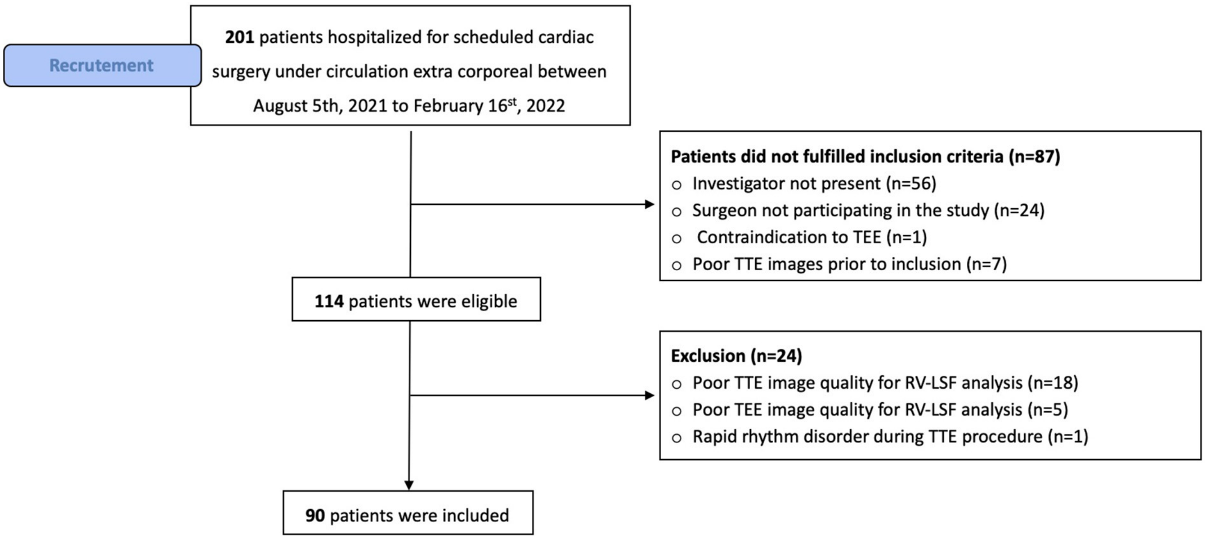

FIGURE 2
Flow chart of the study.

accuracy equal to 1 point in RV-LSF. We also performed Bland and Altman analysis to evaluate the levels of agreement between $\text{TAD}_{\text{lat}-\text{TTE}}$, $\text{TAD}_{\text{lat}-\text{TEE}}$, $\text{TAD}_{\text{sep}-\text{TTE}}$, and $\text{TAD}_{\text{sep}-\text{TEE}}$.

Limits of clinical relevance for RV-LSF: given that the mean $\text{RV-LSF}_{\text{TTE}}$ from healthy volunteers was 25.6 ± 4.8% (13), we expect a clinically insignificant difference between $\text{RV-LSF}_{\text{TTE}}$ and $\text{RV-LSF}_{\text{TEE}}$ to be 5 % (clinical LOA was −5 to 5%). The threshold for statistical significance was set to $p < 0.05$. To analyze the discrepancy between the different measures, we performed a Spearman correlation and a calculation of the intra-class coefficient (ICC). All statistical analyses were performed with R software (version 4.0.4).

Results

From August 2021 to February 2022, 201 consecutive patients were hospitalized for scheduled cardiac surgery under

TABLE 1 Demographics and echocardiographic data of the population.

Variables	Overall population ($n = 90$)
Age (years)	63 ± 11
BMI (kg.m^{-2})	27.3 ± 5.8
Male gender *(n %)*	74 (82)
Medical history, *n* (%)	
Angina severity according to CCS ($n = 32$)	
1	7 (22)
2	7 (22)
3	12 (37)
4	6 (18)
Myocardial infarction	5 (6)
Peripheral vascular disease	11 (12)
Hypertension	53 (59)
Smoking	21 (23)
Diabetes mellitus	19 (21)
Dyslipidemia	57 (63)
Chronic renal disease	6 (6)
Stroke	11 (12)
Atrial fibrillation	20 (22)
Chronic obstructive pulmonary disease	8 (9)
Logistic EuroSCORE (%)	4.3 ± 4
Hemoglobin (g/dl) Creatinine (µmol/l)	14.1 ± 4.7 95 ± 60.9
Preoperative TTE	
Left ventricular ejection fraction (%)	59.1 ± 11.2
TAPSE (mm)	21.2 ± 4.8
RV-S' (cm.s^{-1})	12.11 ± 5.6
RV-FAC (%)	47.1 ± 8.2
Cardiac surgery procedure, *n* (%)	
Valve repair/replacement	33 (37)
CABG	26 (29)
Combined	26 (29)
Others	5 (6)
RV 2D-STE parameter in TTE	
RV-LSF (%)	20.4 ± 4.3
TAD$_{lat}$ (mm)	20.3 ± 4.8
TAD$_{sep}$ (mm)	11.5 ± 3.1
RV 2D-STE parameter in TEE	
• RV-LSF (%)	21.1 ± 4.1
• TAD$_{lat}$ (mm)	17.8 ± 4.4
• TAD$_{sep}$ (mm)	9.4 ± 3.1

Data are expressed as mean (standard deviation) and count (%).2D-STE, bi-dimensional speckle tracking echocardiography; BMI, body mass index; CABG, coronary artery bypass graft; CCS, Canadian cardiovascular society; RV, right ventricle; RV-FAC, right ventricle fractional area change; RV-LSF, right ventricular longitudinal shortening fraction; TAPSE, tricuspid annular plane systolic excursion; TAD$_{lat}$, tricuspid annular displacement of the lateral portio; TAD$_{sep}$, tricuspid annular displacement of the septal portion; TEE, transoesophageal echocardiography; TTE, transthoracic echocardiography.

cardiopulmonary bypass. Among the 114 patients who met the inclusion criteria, 90 patients were included, and 24 patients were finally excluded: 18 patients for poor TTE image quality, five patients due to a failed ROI placement, and one for rapid rhythm disorder (see Figure 2, Flow chart). Demographic and preoperative data were summarized in Table 1. Among the 90 patients, 82% ($n = 74/90$) were men with an average age of 63 ± 11 years. The average logistic EuroSCORE II was 4.3 ± 4, and valve repair/replacement was the main cardiac surgical procedure ($n = 33/90$, 37%).

TTE and TEE RV-LSF measurement

The mean preoperative RV-LSF$_{TTE}$ was 20.4 ± 4.3% and 21.1 ± 4.1% for RV-LSF$_{TEE}$ measurements. Bland-Altman analysis showed an excellent agreement between RV-LSF$_{TTE}$ and RV-LSF$_{TEE}$ measurements. The bias between the two methods was −0.61%, with LOA ranging from −4.18 to 2.97% (Table 2). Figure 3A showed that 95% of RV-LSF measurements fell within the LOA (−4.18 to 2.97 %) and, therefore, within the clinical relevance limits (−5 to 5%) that we had initially determined. Linear regression analysis showed that there was a strong positive correlation between RV-LSF$_{TTE}$ and RV-LSF$_{TEE}$ with a Pearson linear correlation coefficient of 0.91 (CI95% = [0.87–0.94]; $P < 0.001$) and with an excellent model fit ($y = 0.36 + 0.95x$, $r = 0.82$, Figure 4A).

TTE and TEE for TAD$_{sep}$ and TAD$_{lat}$ measurement

The mean preoperative TAD$_{lat-TTE}$ was 20.3 ± 4.8 mm and 17.8±4.4 mm for TAD$_{lat-TEE}$ measurement. Figure 3B showed a reasonable agreement between the two echocardiographic methods for TAD$_{lat}$ measurement with a bias of 2.44 mm and

TABLE 2 Correlation coefficient and difference between RV-LSF, TADsep, and TADlat measurement in TTE and TTE.

	TTE $_{RV-LSF}$ vs. TEE $_{RV-LSF}$ (%)	TTE $_{TADsep}$ vs. TEE $_{TADsep}$ (mm)	TTE$_{TADlat}$ vs. TEE$_{TADla}$ (mm)
Difference between measurement	−0,61	1.42	2.44
Lower limit of agreement	−4.18	−4.91	−4.11
Upper limit of agreement	2.97	7.76	8.99
Pearson correlation coefficient [95% CI]	r = 0.91 [0.87–0.94]; $p < 0.001$	r = 0.56 [0.40–0.69]; $p < 0.001$	r = 0.74 [0.63–0.82]; $p < 0.001$
Regression line equation	y = 0.36+0.95x	y = 7,1+0.44x	y = 5.74+0,81x

Data are expressed as numbers. CI, confidence interval; RV-LSF, right ventricular longitudinal shortening fraction; TAD$_{lat}$, tricuspid annular displacement of the lateral portion; TAD$_{sep}$, tricuspid annular displacement of the septal portion; TEE, transoesophageal echocardiography; TTE, transthoracic echocardiography.

LOA ranging from −4.11 to 8.99 mm (outside the range for clinical agreement). The 2.44 mm bias corresponded to 12.8% relative bias compared to the overall TAD$_{lat}$ measurements with LOA from −21.6 to 47.3%. A good correlation was found between TAD$_{lat-TTE}$ and TAD$_{lat-TEE}$ (r = 0.74, CI95% = [0.63–0.82], $P < 0.001$, Figure 4B). For the TTE and TEE TAD$_{sep}$ measurements, Figure 3C showed that TEE underestimated the TAD$_{sep}$ measurement compared to the TAD$_{sep-TTE}$ measurement with a bias of 1.42 mm and LOA ranging from −4.9 to 7.7 mm. The corresponding relative bias of TAD$_{sep}$ was 13.1% with LOA from −45.2 to 71.0% and moderate correlation between two TAD$_{sep}$ measurements (r = 0.56, CI95% = [0.40–0.69], $P < 0.001$, Figure 4C). We found similar results after calculating the Spearman correlation and intra-class coefficients (Appendix Table 1).

Discussion

The main findings of the present study can be summarized as follows: (1) RV-LSF measurements using TTE and TEE techniques were interchangeable, (2) TAD$_{lat}$ exhibited a limited bias and good agreement between the two techniques but outside acceptable clinical agreement, and (3) TEE underestimated TAD$_{sep}$ measurement.

RV-LSF agreement between TTE and TTE

Clinicians need interchangeable RV parameters between TTE and TEE because an accurate assessment of RV systolic function is of utmost importance for perioperative RV monitoring and precise diagnosis of RV dysfunction during postoperative follow-up. The most used TTE RV systolic parameters were RV-FAC and TAPSE, which are assumed to apply to TEE. In TEE, TAPSE measurement is challenging due to a problematic M-mode alignment. Hence, modified methods were proposed for assessing tricuspid systolic excursion with controversial results (7). RV-FAC measurement is limited by the endocardial border definition and its poor reproducibility (8). Despite significant disagreement between TTE and TEE measures (7, 8), RV systolic parameters are often used interchangeably in daily practice.

In this study, we demonstrated that RV-LSF measurements were interchangeable between TTE and TEE. The graphical Bland-Altman analysis showed a limited bias and LOA between the two ultrasound techniques. This is the first study to report an excellent agreement between TTE and TEE techniques using a clinical significance agreement (−5 to 5%) for a 2D-RV global systolic function parameter (8). Several factors explain this result: first, RV-LSF is a highly reproducible, repeatable, and accurate 2D-STE parameter (10). Indeed, RV-LSF is measured semi-automatically by the software (10). Second, unlike RV-strain assessment, RV-LSF measurement does not require high-resolution images. Moreover, during the TEE procedure, tricuspid annulus tracking is less affected by acoustic shadowing than RV-free wall myocardium (needed for strain analysis) (7). Hence, RV-LSF might be helpful in clinical follow-up from admission to the post-operative setting.

TTE and TEE measurement of TAD lateral and TAD septal

This is the first study that reported data about TAD$_{lat}$ and TAD$_{sep}$ measurement interchangeability. We found that TTE and TEE TAD$_{sep}$ measurements were poorly correlated (r = 0.5) and not interchangeable. We observed a good correlation (r = 0.7) between TTE and TEE TAD$_{lat}$ measurements. However, the graphical Bland-Altman analysis showed that both TAD$_{lat}$ measurement were underestimated, and the LOA between the two methods were too broad for reasonable clinical interchangeability. The underestimation of the TEE measurement was probably because the TEE ME-4CH view may not represent the true long axis of the interventricular septum and causes a "foreshortening" view. Foreshortening view is a frequent problem in 2D echocardiography examinations. It occurs when the ultrasound beam does not cut through the true apex, leading to geometric distortion of the image. Therefore, the long axis of the ventricle appears shorter. Previous studies on

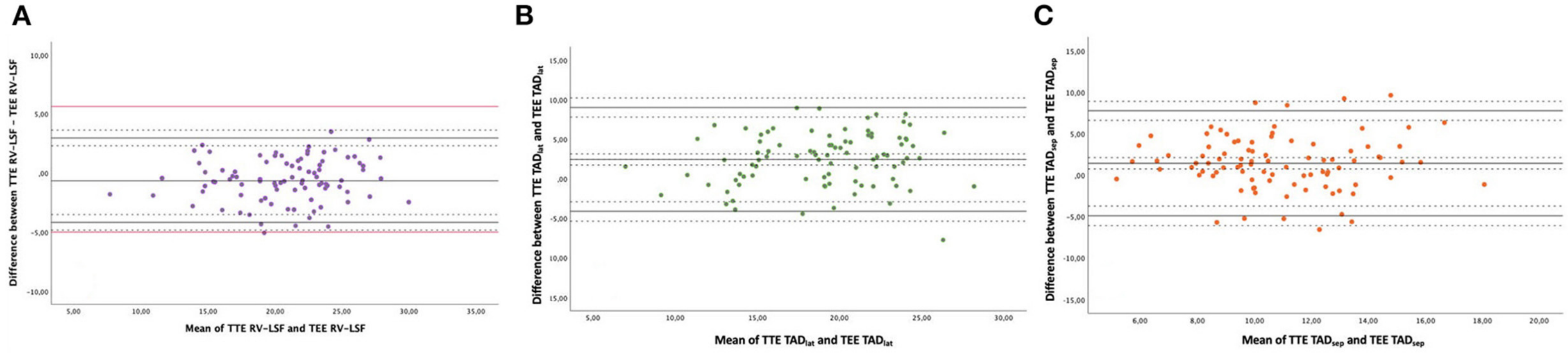

FIGURE 3

Bland-Altman plots between TTE and TEE measurements with **(A)** TTE RV-LSF vs. TEE RV-LSF. **(B)** TTE TADlat vs. TEE TADlat. **(C)** TTE TADsep vs. TEE TADsep**.** This plot displays a scatter diagram of the difference between the two techniques' measurements plotted against the average of the two technique's measurements. The black plain line represents the mean of the difference (= bias) between the two ultrasound methods. The other plain lines represent the upper and lower limits of agreement. Dotted black horizontal lines represent the 95% CI interval for the bias and the limits of agreement. The red line represents the determined pertinent clinical agreement (−5; +5%) of the RV-LSF measurement.

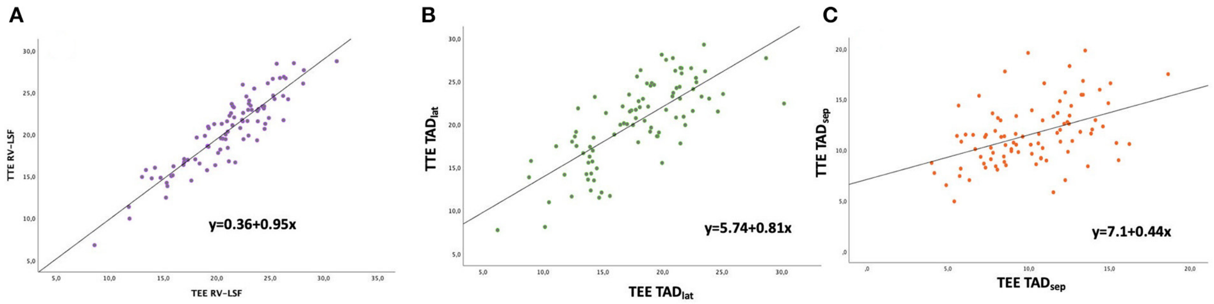

FIGURE 4
Scatter plots of TTE as a function of TEE measurements of **(A)** RV-LSF **(B)** TAD lateral, and **(C)** TAD septal.

LV function identified similar findings about underestimation of volumes due to foreshortening of the transesophageal imaging plane (17). The impact of the foreshortening view on RV-LSF measurement was probably limited because RV-LSF is a length ratio and because the underestimation of TAD_{sep} and $\text{TAD}_{\text{lateral}}$ values, on which RV-LSF value depends, is relatively homogeneous (close to 12% for both).

Besides, as in our study, these results are probably related to using the RV apex as the reference point. Selection of RV apex can be challenging because TEE only partially reveals the apical portion of the RV, which is truncated or shortened; this leads to underestimating the measured parameters. The use of 3D echocardiography for assessing the RV systolic function is the best approach to avoid a foreshortening view and an underestimation of ventricle size or volumes (18).

Our results were close to that of other studies which assess the interchangeability between the longitudinal displacement analysis of the lateral portion of the tricuspid annular and TAPSE. Markin et al. compared TTE TAPSE by M-mode and TEE TAPSE by speckle tracking in 84 patients. They found that TAPSE by M-mode was correlated with TAPSE by speckle tracking in the ME-4CH view (Pearson $r = 0.62$), but they did not analyze the agreement between the two methods. In the study by Mauermann et al., TAD lateral (named speckle tracking TAPSE) was assessed in TEE and compared to TTE TAPSE. The authors found a significant correlation ($r = 0.59$) but with large LOA (−9.4 to 8.4 mm) (7).

Strengths and limitations

This study had several strengths. First, this study prospectively acquired TTE and TEE images under identical clinical situations in mechanically ventilated patients under general anesthesia. Secondly, we performed a sample size calculation to assess clinical agreement between the two techniques to avoid underpowered analysis. Nevertheless, this study admits some limitations. First, $\text{RV-LSF}_{\text{TEE}}$ and $\text{RV-LSF}_{\text{TTE}}$ were calculated from loops recorded in a supine position, possibly resulting in a foreshortened apical view in TTE. To limit the impact of a foreshortening apical view on RV long-axis measurement due to supine position, we measured RV-LSF in an RV-focused apical four-chamber view as recommended (3). Second, we did not evaluate the inter-observer reproducibility for TTE and TEE for RV-LSF measurement. Indeed, because both ultrasound procedures were performed just before the surgical draping of the patient, we chose to shorten the duration of image acquisition to avoid any extensive delay before starting the surgical procedure. Third, TEE and TTE measurements were acquired by an echocardiography expert (level III competence according to the EACVI definition) (19) because the main issue is related to the imaging window. The ROI positioning on the lateral part of the tricuspid annular or the RV-apex may be limited because the sector window is too narrow and requires an optimal view. We believe that RV-LSF measurement should be performed by a physician with advanced training in TTE. Fourth, we failed to measure $\text{RV-LSF}_{\text{TEE}}$ in four patients with large aortic root. Hence, the use of RV-LSF appears to be limited for monitoring RV systolic function in aortic root surgery. Finally, as with many 2D-STE parameters, the software version is a potential limitation. It is possible that RV-LSF values measured by the Philips QLAB version 15.0 may not reflect results from another version of the same software (20, 21).

Conclusion

In this study, we showed that $\text{RV-LSF}_{\text{TTE}}$ and $\text{RV-LSF}_{\text{TEE}}$ measured in the operating room for patients undergoing cardiac surgery exhibited excellent clinical agreement, and thus were interchangeable. RV-LSF could be helpful in assessing RV systolic function during and after high-risk surgery.

Data availability statement

The raw data supporting the conclusions of this article will be made available by the authors, without undue reservation.

Ethics statement

The studies involving human participants were reviewed and approved by Comité de Protection des Personnes Ile de France VIII, ID-RCB 2021_A000908-33. The patients/participants provided their written informed consent to participate in this study.

Author contributions

Study conception and manuscript drafting: CB, OA-A, DM, and YM. Clinical data collection: PV, FL, CD, PH, BA, GT, and TC. Statistical analysis: BR and DM. Manuscript revision: CB, HD, and YM. All authors approved the final version of the manuscript.

Acknowledgments

We want to thank Mrs. Annabelle Boussault for his precious help in this work.

Conflict of interest

The authors declare that the research was conducted in the absence of any commercial or financial relationships that could be construed as a potential conflict of interest.

Publisher's note

Supplementary material

The Supplementary Material for this article can be found online at: https://www.frontiersin.org/articles/10.3389/fcvm.2022.1074956/full#supplementary-material

References

1. An Updated Report by the American Society of Anesthesiologists and the Society of Cardiovascular Anesthesiologists Task Force on Transesophageal Echocardiography. Practice Guidelines for Perioperative Transesophageal Echocardiography. *Anesthesiology.* (2010) 112:1084–96. doi: 10.1097/ALN.0b013e3181c51e90

2. Mahmood F, Shernan SK. Perioperative transoesophageal echocardiography: current status and future directions. *Heart.* (2016) 102:1159–67. doi: 10.1136/heartjnl-2015-307962

3. Lang RM, Badano LP, Mor-Avi V, Afilalo J, Armstrong A, Ernande L, et al. Recommendations for cardiac chamber quantification by echocardiography in adults: an update from the american society of echocardiography and the european association of cardiovascular imaging. *J Am Soc Echocardiogr.* (2015) 28:1–39.e14. doi: 10.1016/j.echo.2014.10.003

4. Labus J, Uhlig C. Role of echocardiography for the perioperative assessment of the right ventricle. *Curr Anesthesiol Rep.* (2021) 11:306–17. doi: 10.1007/s40140-021-00474-1

5. Vieillard-Baron A, Naeije R, Haddad F, Bogaard HJ, Bull TM, Fletcher N, et al. Diagnostic workup, etiologies and management of acute right ventricle failure: a state-of-the-art paper. *Intensive Care Med.* (2018) 44:774–90. doi: 10.1007/s00134-018-5172-2

6. Gebhardt BR, Asher S, Maslow A. the limitations of using transthoracic echocardiographic–derived normative values for grading intraoperative transesophageal echocardiography examinations of the right ventricle: are they really interchangeable? *J Cardiothorac Vasc Anesth.* (2020) 34:1260–2. doi: 10.1053/j.jvca.2020.02.024

7. Mauermann E, Vandenheuvel M, François K, Bouchez S, Wouters P. Right ventricular systolic assessment by transesophageal versus transthoracic echocardiography: displacement, velocity, and myocardial deformation. *J Cardiothorac Vasc Anesth.* (2020) 34:2152–61. doi: 10.1053/j.jvca.2020.03.009

8. Roberts SM, Klick J, Fischl A, King TS, Cios TJ. A comparison of transesophageal to transthoracic echocardiographic measures of right ventricular function. *J Cardiothorac Vasc Anesth.* (2020) 34:1252–9. doi: 10.1053/j.jvca.2019.11.039

9. Ahmad H, Mor-Avi V, Lang RM, Nesser H-J, Weinert L, Tsang W, et al. Assessment of right ventricular function using echocardiographic speckle tracking of the tricuspid annular motion: comparison with cardiac magnetic resonance: tricuspid annular displacement by speckle tracking. *Echocardiography.* (2012) 29:19–24. doi: 10.1111/j.1540-8175.2011.01519.x

10. Beyls C, Bohbot Y, Huette P, Booz T, Daumin C, Abou-Arab O, et al. Usefulness of right ventricular longitudinal shortening fraction to detect right ventricular dysfunction in acute cor pulmonale related to COVID-19. *J Cardiothorac Vasc Anesth.* (2021) 35:3594–03. doi: 10.1053/j.jvca.2021.01.025

11. Beyls C, Bohbot Y, Huette P, Abou-Arab O, Mahjoub Y. Tricuspid longitudinal annular displacement for the assessment of right ventricular systolic dysfunction during prone positioning in COVID-19 patients. *J Am Soc Echocardiogr.* (2020) 33:1055 doi: 10.1016/j.echo.2020.05.016

12. Maniwa N, Hozumi T, Takemoto K, Wada T, Kashiwagi M, Shimamura K, et al. Value of tissue-tracking tricuspid annular plane by speckle-tracking echocardiography for the assessment of right ventricular systolic dysfunction. *Echocardiography.* (2019) 36:110–8. doi: 10.1111/echo.14206

13. Beyls C, Bohbot Y, Caboche M, Huette P, Haye G, Dupont H, et al. Preload dependency of 2D right ventricle speckle tracking echocardiography parameters in healthy volunteers: a prospective pilot study. *JCM.* (2021) 11:19. doi: 10.3390/jcm11010019

14. Shen T, Picard MH, Hua L, Burns SM. Andrawes MN. Assessment of tricuspid annular motion by speckle tracking in anesthetized patients using transesophageal echocardiography. *Anesth Analg.* (2018) 126:62–7. doi: 10.1213/ANE.0000000000002614

15. Hahn RT, Abraham T, Adams MS, Bruce CJ, Glas KE, Lang RM, et al. Guidelines for performing a comprehensive transesophageal echocardiographic examination: recommendations from the American Society of Echocardiography and the Society of Cardiovascular Anesthesiologists. *J Am Soc Echocardiogr.* (2013) 26:921–64. doi: 10.1016/j.echo.2013.07.009

16. Bland JM, Altman DG. Statistical methods for assessing agreement between two methods of clinical measurement. *Lancet.* (1986) 1:307–10. doi: 10.1016/S0140-6736(86)90837-8

17. Chengode S. Left ventricular global systolic function assessment by echocardiography. *Ann Card Anaesth.* (2016) 19:26. doi: 10.4103/0971-9784.192617

18. Medvedofsky D, Mor-Avi V, Amzulescu M, Fernández-Golfín C, Hinojar R, Monaghan MJ, et al. Three-dimensional echocardiographic quantification of the left-heart chambers using an automated adaptive analytics algorithm: multicentre validation study. *Eur Heart J Cardiovasc Imaging.* (2018) 19:47–58. doi: 10.1093/ehjci/jew328

19. Popescu BA, Andrade MJ, Badano LP, Fox KF, Flachskampf FA, Lancellotti P, et al. European Association of Echocardiography recommendations for training, competence, and quality improvement in echocardiography. *Eur J Echocardiogr.* (2009) 10:893–905. doi: 10.1093/ejechocard/jep151

20. Il'Giovine ZJ, Mulder H, Chiswell K, Arges K, Tomfohr J, Hashmi A, et al. Right Ventricular Longitudinal Strain Reproducibility Using Vendor-Dependent and Vendor-Independent Software. *J Am Soc Echocardiogr.* (2018) 31:721–32.e5. doi: 10.1016/j.echo.2018.01.008

21. Silverton NA, Lee JP, Morrissey CK, Tanner C, Zimmerman J, A. Comparison of left- and right-sided strain software for the assessment of intraoperative right ventricular function. *J Cardiothorac Vasc Anesth.* (2019) 33:1507–15. doi: 10.1053/j.jvca.2018.10.038

Appendix

TABLE A1 Spearman correlation coefficient and ICC between RV-LSF, TAD_{sep}, and TAD_{lat} measurement in TTE and TTE.

	Spearman correlation coefficient	ICC
$RV\text{-}LSF_{TTE}$ vs. $RV\text{-}LSF_{TEE}$	0.89 [0.82–0.93]	0.91 [0.86–0.96]
$TAD_{lat\text{-}TTE}$ vs. $TAD_{lat\text{-}TEE}$	0.74 [0.63–0.82]	0.74 [0.63–0.82]
$TAD_{sep\text{-}TTE}$ vs. $TAD_{sep\text{-}TEE}$	0.46 [0.25–0.62]	0.44 [0.26–0.59]

Data are expressed in numbers and 95% confidence interval [-]. ICC, interclass coefficient; RV-LSF, right ventricular longitudinal shortening fraction; TAD_{lat}, tricuspid annular displacement of the lateral portion; TAD_{sep}, tricuspid annular displacement of the septal portion; TEE, transoesophageal echocardiography; TTE, transthoracic echocardiography.

frontiers | Frontiers in Cardiovascular Medicine

TYPE Original Research
PUBLISHED 04 January 2023
DOI 10.3389/fcvm.2022.1040647

OPEN ACCESS

EDITED BY
Francesco Pelliccia,
Sapienza University of Rome, Italy

REVIEWED BY
Sergio Sánchez-Martínez,
Institut de Recerca Biomèdica August Pi i Sunyer (IDIBAPS), Spain
Abdallah Fayssoil,
Hôpital Raymond-Poincaré, France

*CORRESPONDENCE
Joanna Nan Wang
✉ joanna.nan.wang@gmail.com

SPECIALTY SECTION
This article was submitted to Cardiovascular Imaging, a section of the journal Frontiers in Cardiovascular Medicine

RECEIVED 09 September 2022
ACCEPTED 09 December 2022
PUBLISHED 04 January 2023

CITATION
Wang JN, Olsen NT, Taraldsen IA and Mogelvang R (2023) Whole-cycle analysis of echocardiographic tissue Doppler velocities as a marker of biological age. *Front. Cardiovasc. Med.* 9:1040647. doi: 10.3389/fcvm.2022.1040647

Whole-cycle analysis of echocardiographic tissue Doppler velocities as a marker of biological age

Joanna Nan Wang[1,2]*, Niels Thue Olsen[3,4],
Ida Arentz Taraldsen[1] and Rasmus Mogelvang[1,2,4,5]

[1]Department of Cardiology, The Heart Centre, Copenhagen University Hospital – Rigshospitalet, Copenhagen, Denmark, [2]Copenhagen City Heart Study, Copenhagen University Hospital – Bispebjerg and Frederiksberg Hospital, Frederiksberg, Denmark, [3]Department of Cardiology, Copenhagen University Hospital – Herlev and Gentofte, Copenhagen, Denmark, [4]Faculty of Health and Medical Sciences, Institute of Clinical Medicine, University of Copenhagen, Copenhagen, Denmark, [5]Cardiovascular Research Unit, University of Southern Denmark, Svendborg, Denmark

Purpose: Tissue Doppler imaging (TDI) is a sensitive marker of impaired cardiac function and different phases of the TDI curve carry different prognostic information. It is not known how continuous TDI curves change with age in normal subjects, and whether these changes differ from changes seen in individuals at risk of future cardiac events.

Methods: A total of 1,763 individuals from the general population were examined with color TDI at the septal and lateral mitral sites. A low-risk group was defined as without cardiac risk factors (hypertension, diabetes or ischemic heart disease) at baseline and without any cardiac events (cardiovascular death or admission due to either heart failure or acute myocardial infarction) during 10-years follow-up. All TDI curves were corrected for heart rate, and whole-cycle analysis of age-related changes to TDI velocities was performed in both low-risk (n = 881) and high-risk individuals (n = 882).

Results: In the low-risk population, four phases where myocardial velocity differed most ($p < 10^{-10}$) according to age were identified [in a standardized cardiac cycle of 1 second (s)]: Systolic peak (0.09–0.13 s), systolic plateau (0.18–0.27 s), early diastole (0.43–0.54 s) and late diastole (0.88–0.95 s). With increasing age, systolic velocities decreased, early diastolic velocities decreased and had delayed peak, and late diastolic velocities increased until age 70 and then stopped increasing. In the high-risk population, comparison to corresponding age groups of the low-risk population showed: Lower early diastolic velocities in 20–40-year-olds; higher late diastolic velocities and lower peak systolic velocities in 40–60-year-olds; further decreased systolic velocities including the systolic plateau and decreased late diastolic velocities in 60-year-olds. The time segments around the systolic peak (p = 0.002) and early diastole ($p < 0.001$) differed significantly between the high-risk and low-risk population, thus making it possible to use the individual age gap between a TDI-derived biological age and the real chronological age as a tool to discriminate high-risk individuals from low-risk individuals.

Conclusion: We found that individuals with cardiac risk factors display findings compatible with an accelerated aging of the heart and thus propose TDI-derived biological age as a tool to identify high-risk patients.

KEYWORDS

tissue Doppler imaging, healthy aging, cardiac degeneration, accelerated aging, biological age

Introduction

Measurement of myocardial velocities with tissue Doppler imaging (TDI) has become an integrated part of the assessment of diastolic heart function in clinical echocardiography (1). Both systolic as well as diastolic TDI velocities have been demonstrated to be sensitive markers of impaired cardiac function (2–4) and prognosis (5–7), and there is a significant association between TDI peak values and age (8–10). While current recommendations and existing studies mainly focus on peak values of TDI velocities, it has been shown that different phases of the TDI curve carry different prognostic information (11). It is not known how continuous TDI curves change with increasing age in normal subjects, and whether these changes differ qualitatively from changes seen in individuals at risk of future adverse events. Computer-aided automated analysis of TDI curves could allow the integration of information from a large number of examinations to answer these questions.

Thus, we set out to achieve the following aims: (1) Perform whole-cycle analysis of TDI myocardial velocities in a low-risk population without cardiac risk factors to determine age-related changes. (2) Compare whole-cycle TDI velocities in high-risk individuals with cardiac risk factors to low-risk individuals at different age levels. (3) Relate the effect of cardiac risk factors on TDI velocities with changes during normal aging.

Materials and methods

Study population

This study is an echocardiographic sub-study of the 4th Copenhagen City Heart Study, a Danish cohort study of cardiovascular disease and risk factors (12, 13). The present study includes 1,763 randomly selected men and women (20–93 years old) from the general population who underwent an echocardiographic examination including color TDI. Whether a participant underwent echocardiography was independent of health status and other risk factors. Individuals with atrial fibrillation or significant valvular stenosis or regurgitation were excluded. All subjects gave informed consent to participate. The study was performed in accordance with the Helsinki Declaration and approved by the regional ethics committee.

Health examination

Systolic and diastolic blood pressures were measured on the left upper arm, in a sitting position after 5 min of rest. Hypertension was defined as systolic blood pressure $\geq$ 140 mmHg, diastolic blood pressure $\geq$ 90 mmHg or use of antihypertensive medication. Diabetes was defined as plasma glucose concentration $\geq$ 11.1 mmol/L, HbA_{1c} level > 7.0%, self-reported disease or use of insulin or another antidiabetic medication. Ischemic heart disease (IHD) was defined as ischemic alterations on the electrocardiogram (Minnesota codes 1.1–3) or a history of hospital admission due to acute coronary artery occlusion, percutaneous coronary intervention or coronary artery bypass grafting.

Tissue Doppler imaging

Three experienced echo technicians performed all echocardiograms. Color TDI loops were obtained in the apical four-chamber view at the highest possible frame rate, using GE Vingmed Ultrasound's Vivid Five with a 2.5 MHz probe (Horten, Norway). For each individual, one TDI loop and the corresponding electrocardiogram were saved and analyzed offline by investigators blinded to other information. TDI velocity curves were obtained by measuring within a 6 mm circular region of interest at the septal and lateral mitral annular positions. The data of the septal and lateral TDI velocity curves of one heart cycle and the concurrent electrocardiogram were saved in one CSV file for each individual.

Outcome and definitions

Participants were followed from the examination in 2001 through 2003 until April 2013 or time of event. The primary endpoint was a cardiac event within 10 years of follow-up, defined as the combined endpoint of cardiovascular death or admission due to either heart failure or acute myocardial infarction. Low-risk individuals were defined as being free of hypertension, diabetes and IHD at baseline and without any cardiac event at 10 years of follow-up. High-risk individuals were defined as having one or more of the following: Hypertension, diabetes or IHD at baseline, or cardiac event within 10 years of follow-up. Follow-up data on cardiovascular deaths were collected from the national Danish Causes of Death Registry. Follow-up data on admissions with heart failure and acute myocardial infarction were obtained from the Danish National Board of Health's National Patient Registry. Follow-up was 100% complete.

Data analysis

Importing data

In order to analyze the entire TDI curve of all individuals at once, all the CSV files were imported into a 3D array. Each 2D layer in the array was labeled with a unique study-ID and contained the values of the TDI curves and electrocardiogram of that individual. Baseline data and follow-up data were saved in separate data frames but labeled by the same unique ID, making all data easily accessible for analysis.

Standardizing heart cycles

In order to standardize the length of the TDI curves of individuals with different heart rate, heart cycles were standardized to a length of 1 s in the following way:

- **Defining starting point of heart cycle:** Time of R-peak in the electrocardiogram was defined as the starting point of time = 0 in the standardized heart cycle.
- **Identifying length of systole and diastole:** Start of systole was defined as time = 0. End of systole was defined as the time of the first negative TDI value (either septal or lateral) after 0.2 s. The limit of 0.2 s was set to avoid the initial negative TDI values at the beginning of systole (isovolumetric contraction). Diastole was defined as the rest of the heart cycle from end of systole.
- **Standardizing length of systole:** Fridericia's cube-root formula for QTc correction was used to correct the duration of systole to fit a heart cycle of 1 s (14). The values of the formula $QTc = QT/RR^{1/3}$ were: QT = length of systole; RR = length of heart cycle = maximum time value of the TDI curve. Application of this method meant that all the systolic time values of the TDI curve were divided by $RR^{1/3}$.
- **Standardizing length of diastole:** First, the time values of the diastole were parallel shifted to fit the new time position of the end of systole. Afterward, all the time values were equally distributed between the time of end of systole to time = 1 (end of heart cycle).
- **Standardizing amount and frequency of time observations:** Due to different cycle lengths and the standardization process, different individuals now had a different amount of time observations and time values. To make further analyses possible, we defined that all individuals should have TDI values each 0.01 s, making up 101 observations from $t = 0.00$ to $t = 1.00$. To impute TDI values at the exact 0.01 time-intervals, we made a linear fit through the TDI values of the two nearest available time data points to derive the TDI value that fitted the newly created 0.01 time-position.

Regression-based TDI velocities

To generate reference TDI velocities for any given age, we made a regression model based on all the TDI curves of the low-risk population. Septal and lateral TDI values for each individual were averaged before performing regression. Linear regression with a quadratic age-variable was performed in all 101 time-positions (from $t = 0.00$ to $t = 1.00$). A quadratic age-variable was chosen because of non-linearity in some time-positions. Normality was checked with QQ-plots. In **Figure 1**, the presented normal reference TDI velocities are generated from this regression model, and *p*-values were calculated for each 0.01 time-position. In **Figure 3**, regression curves for the high-risk population were generated from a similar regression model based on the data of the high-risk population. The *p*-values of the age-adjusted association between TDI values and risk group were calculated for each 0.01 time-position.

Biological age

Based on the data of the low-risk population, a regression model was made for the association between age and the mean TDI values of each of the two important phases of the heart cycle identified in **Figure 3** (systolic peak and early diastole), respectively. Then, for each individual, a biological age was calculated for each phase by inserting their mean TDI values of the phase into the corresponding regression model. Then we subtracted their real chronological age from their calculated biological age, yielding an individual age gap. These individual age gaps are presented in **Table 3** for each cardiac risk group, including an average age gap based on both phases.

Statistics

In **Table 1**, Welch two-sample *t*-test was used for continuous variables and Chi-square test for categorical variables. In **Table 2**, comparisons between groups were done by ANOVA. In **Table 3**, Welch two-sample *t*-test was used to compute *p*-values in comparison to the reference (low-risk) group of same TDI area.

All data analyses were performed in R statistical software version 4.0.5 (15).

TABLE 1 Population characteristics.

	Low-risk	High-risk	*p*-value
n	881	882	
Male sex, *n* (%)	372 (42)	389 (44)	0.45
Age, years (SD)	49.2 (±14.6)	66.3 (±12.0)	<0.001
BMI, kg/m^2 (SD)	24.4 (±3.3)	26.4 (±4.1)	<0.001
Heart rate, bpm (SD)	65 (±10)	69 (±11)	<0.001
Hypertension, *n* (%)	0	742 (84)	
Diabetes, *n* (%)	0	179 (20)	
IHD, *n* (%)	0	231 (26)	
BBB, *n* (%)	11 (1.3)	36 (4.1)	<0.001
LVEF,% (SD)	59.9 (±1.0)	59.6 (±2.5)	0.001
LAVI, mL/m2 (SD)	18.1 (±5.2)	20.0 (±7.0)	<0.001
E,m/s (SD)	0.75 (±0.16)	0.68 (±0.16)	<0.001
A,m/s (SD)	0.62 (±0.15)	0.77 (±0.18)	<0.001
DT, ms (SD)	160 (±40)	180 (±40)	<0.001
Creatinine, µmol/L (SD)	79.3 (±13.8)	81.6 (±18.8)	0.003
Cholesterol, mmol/L (SD)	5.3 (±1.1)	5.8 (±1.1)	<0.001
Cardiac event at 10-year follow-up, *n* (%)	0	202 (23)	
- AMI admission, *n* (%)	0	56 (6.3)	
- HF admission, *n* (%)	0	101 (11.5)	
- Cardiac death, *n* (%)	0	107 (12.1)	

Baseline characteristics and follow-up data. High-risk group defined as the presence of hypertension, diabetes or ischemic heart disease at baseline or the occurrence of a cardiac event at 10 years of follow-up. Continuous variables presented as mean (± SD). Categorical variables presented as *n* (%). BMI, body mass index; bpm, beats per minute; IHD, ischemic heart disease; BBB, bundle branch block; LVEF, left ventricle ejection fraction; LAVI, left atrial volume index; E, transmitral E-wave; A, transmitral A-wave; DT, deceleration time; AMI, acute myocardial infarction; HF, heart failure.

Results

The study population consisted of 1,763 persons of which 42% ($n = 742$) had hypertension, 10% ($n = 179$) had diabetes, and 13% ($n = 231$) were known with IHD. During 10-year follow-up (IQR 9.8–10 years), 11.5% ($n = 202$) had a cardiac event defined as cardiac death or admission due to myocardial infarction or heart failure.

The study population was divided into two groups: A low-risk group ($n = 881$) without cardiac risk factors at baseline (hypertension, diabetes, and/or IHD) and without any cardiac events during a 10-year period, and a high-risk group comprising the rest ($n = 882$) (see **Table 1**).

TDI curves in low-risk population

There was a significant association between age and peak TDI velocities in both risk groups, as presented in **Table 2**. In the low-risk population, automated whole-cycle analysis generated reference TDI velocities for any given age. In **Figure 1**, reference TDI curves are presented for ages of every 10 years.

As indicated by the background colors of **Figure 1**, there was a significant association between age and TDI-values throughout most of the heart cycle. Thus, **Figure 1** illustrates how TDI curves change according to chronological age in low-risk individuals. Four phases of the heart cycle where the velocity trace differed most according to age were identified ($p < 10^{-10}$; dark blue areas): Systolic peak (0.09–0.13 s), systolic plateau (0.18–0.27 s), early diastole (0.43–0.54 s) and late diastole (0.88–0.95 s). With increasing age, systolic velocities decreased, early diastolic velocities decreased and their peak was delayed, and late diastolic velocities increased until age 70 and then stopped increasing (absolute velocity values are considered when defining an increase/decrease here and in the following).

TDI curves in high-risk population

Figures 2A–C compare the median TDI curve for low-risk and high-risk populations within the same age groups. In the age group of 20–40-year-olds (**Figure 2A**), the high-risk population was very small ($n = 22$) and thus the signal of the TDI curve is less smooth. However, the high-risk group seems to have lower early diastolic velocity.

In the high-risk group of 40–60-year-olds (**Figure 2B**), early diastolic velocity is clearly lower and late diastolic velocity is slightly higher. Peak systolic velocity was also lower, while the systolic plateau remained the same compared to the low-risk group.

TABLE 2 Mean peak velocities by age group.

	Low-risk				High-risk			
	20–40 years	40–60 years	> 60 years	*p*	20–40 years	40–60 years	>60 years	*p*
s' (cm/s)	6.7 (± 1.3)	6.2 (± 1.3)	5.7 (± 1.5)	$p < 0.001$	6.9 (± 1.4)	5.8 (± 1.2)	5.2 (± 1.2)	$p < 0.001$
e' (cm/s)	10.8 (± 2.0)	8.5 (± 1.9)	6.2 (± 1.8)	$p < 0.001$	9.7 (± 1.7)	7.0 (± 1.9)	5.1 (± 1.6)	$p < 0.001$
a' (cm/s)	4.4 (± 1.5)	6.2 (± 1.7)	7.4 (± 1.8)	$p < 0.001$	5.6 (± 1.9)	6.8 (± 1.8)	7.0 (± 2.0)	$p = 0.005$

Presented as mean (± SD). s', peak systolic velocity; e', peak early diastolic velocity; a', peak late diastolic velocity.

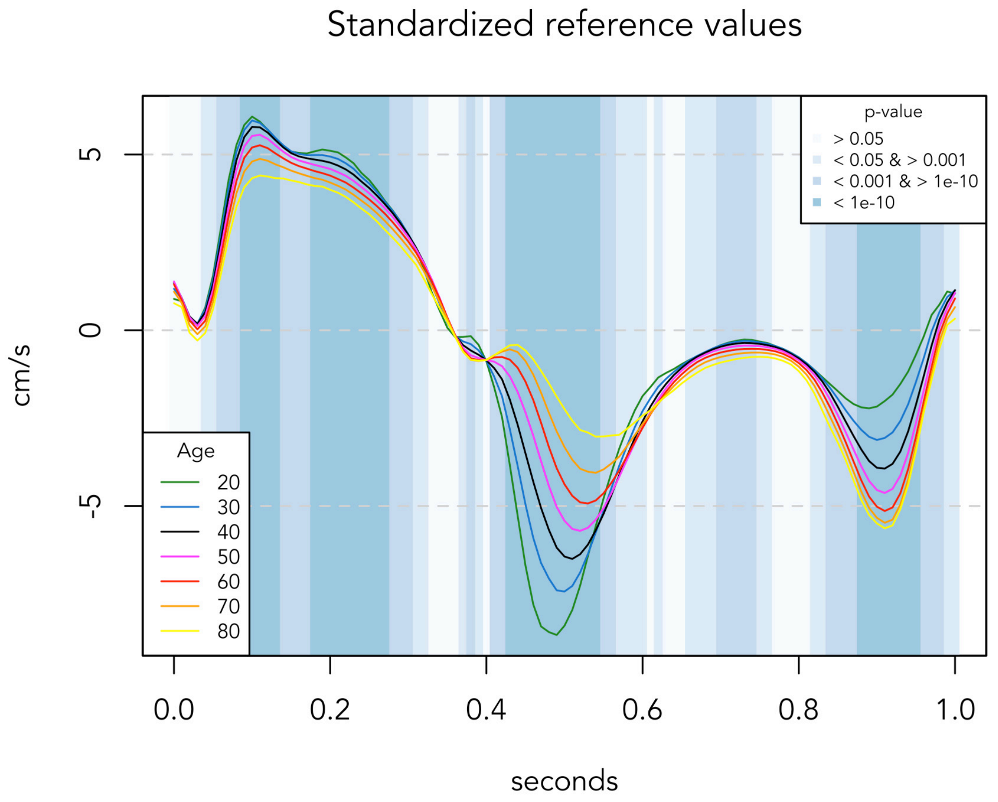

FIGURE 1
Regression-based reference TDI curves of the low-risk population (*n* = 881). Colored lines represent reference TDI curves for each age. Background colors indicate significance levels of the association between age and TDI values at each 0.01 s time-position. TDI values are averaged for septal and lateral mitral sites, presented for one standardized heart cycle of 1 s.

In the high-risk group older than 60 years (**Figure 2C**), the decrease of early diastolic and systolic velocities was further accentuated, now also involving the systolic plateau. However, the late diastolic velocity reached a turning point and now began to decrease compared to the low-risk group.

Distinction between TDI curves in high-risk and low-risk populations

Figure 3 presents automated whole-cycle analysis of the data presented in **Figure 2**. The regression-based reference velocities of the low-risk group (as presented in **Figure 1**) were compared to the regression-based velocities of the high-risk group for the corresponding age at each time point. To ease visual comparison to **Figure 2**, TDI curves of 30-, 50-, and 70-year-olds are illustrated. For the entire population, of the four important phases identified in **Figure 1**, only the systolic peak ($p = 0.002$) and early diastole ($p < 0.001$) differed significantly between the low-risk and high-risk population, as velocities during these periods were lower in high-risk individuals.

Biological age vs. chronological age

As a tool to discriminate high-risk individuals from low-risk individuals, we present a concept of assessing the individual age gap between the TDI-derived biological age and the real chronological age of each individual. For each individual, biological age was calculated based on their mean TDI values in the two important phases of the heart cycle significantly associated with risk group and age (systolic peak and early diastole), and the corresponding individual age gaps are presented in **Table 3** for each cardiac risk group and for the high-risk group as a whole.

Example for reading **Table 3**: An individual with a chronological age of e.g., 60 years and known hypertension, has systolic peak velocities like a 76-year-old low-risk individual (real age + 16 years) and early diastolic velocities like a 69-year-old (real age + 9 years). On an average, this 60-year-old individual with hypertension has a heart in the same condition as a 72-year-old low-risk individual (real age + 12 years).

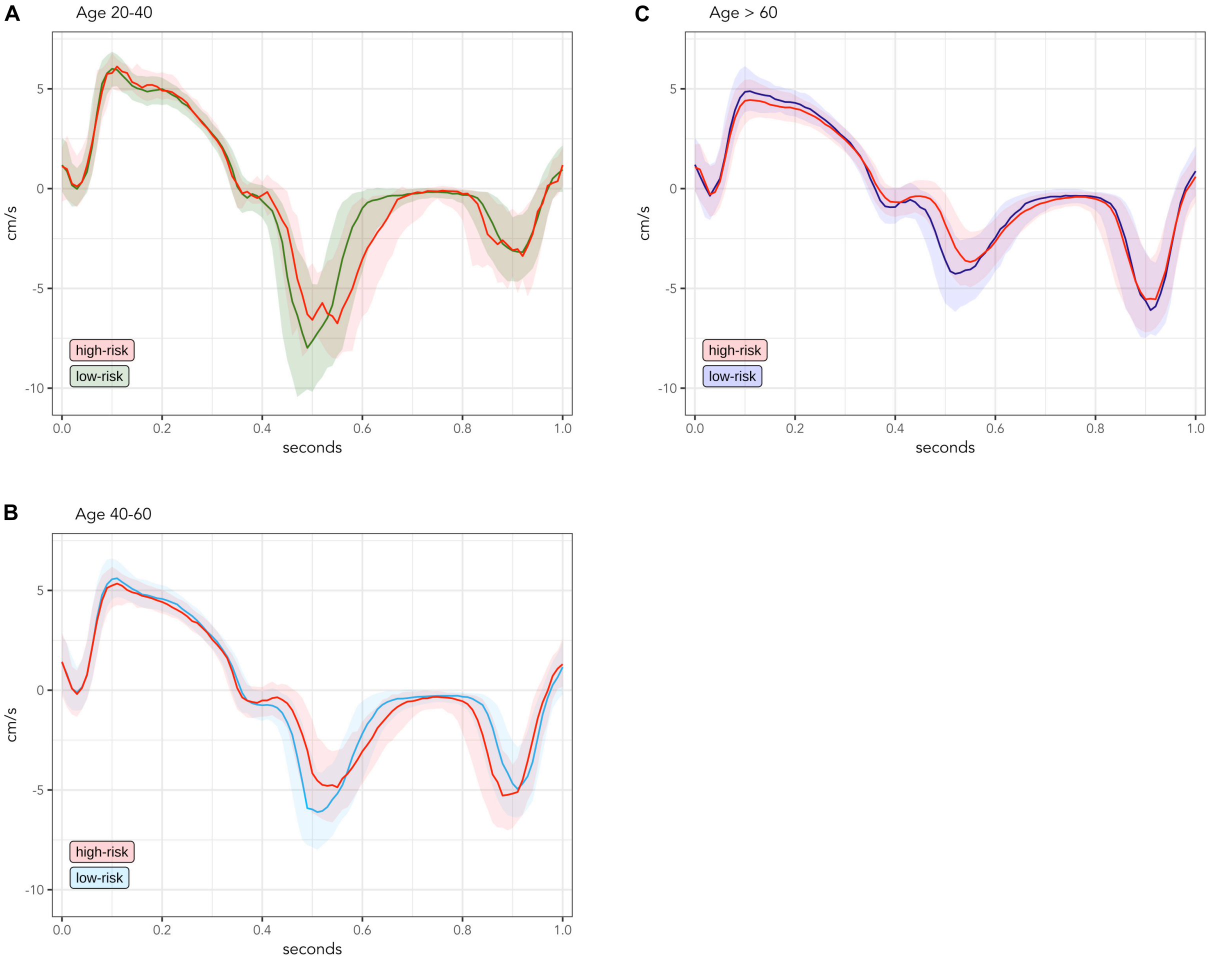

FIGURE 2
Comparison of median and interquartile range of measured TDI-values between low-risk and high-risk groups, divided into age groups of 20–40-year-olds [**(A)**; low-risk *n* = 226; high-risk *n* = 22], 40–60-year-olds [**(B)**; low-risk *n* = 432; high-risk *n* = 216] and > 60 year-olds [**(C)**; low-risk *n* = 223; high-risk *n* = 644]. TDI values are averaged for septal and lateral mitral sites, presented for one standardized heart cycle of 1 s. Solid lines are median values. Transparent colored areas represent interquartile range.

Table 3 shows that all cardiac risk populations had a higher biological age than their chronological age, when looking at the systolic as well as the early diastolic TDI values.

Discussion

In this study, we present a novel and automated whole-cycle approach to analyzing TDI velocity curves and apply this analysis to a large group of individuals from the general population. In this way, four highly significant phases of the cardiac cycle that differ the most with age were identified: The systolic peak, the systolic plateau, early diastole, and late diastole. Using the same type of analysis, we demonstrate significant differences between low-risk and high-risk individuals during two of these phases, as TDI velocities of high-risk and low-risk individuals differ significantly at the systolic peak and early diastolic part of the TDI curve. We found that individuals with cardiac risk factors display findings compatible with an accelerated aging of the heart, and we propose a way of quantifying the individual age gap between the TDI-derived biological age and the chronological age.

Myocardial velocities in healthy aging

In Figure 1, we show how whole-cycle TDI curves change in normal healthy aging of the heart. Using a regression model on standardized curves corrected for heart rate, we found that there was a significant association with age throughout most of the TDI curve, but with large differences in the strength of the association during different phases of the cardiac cycle. We identified four highly

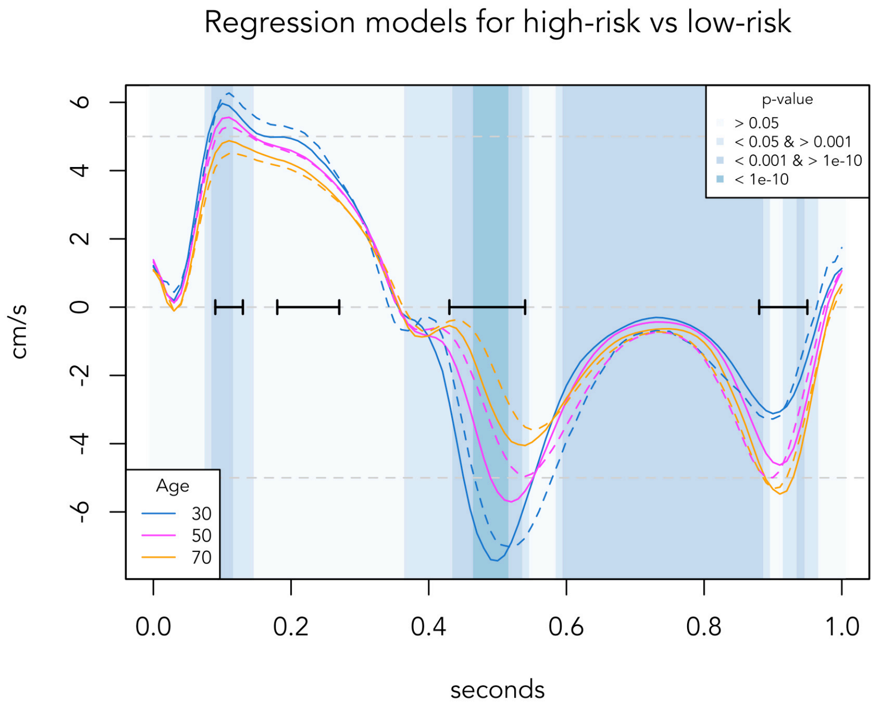

FIGURE 3
Regression-based TDI curves of selected age groups, comparing the low-risk population (solid lines) with the corresponding age group in the high-risk population (dashed lines). Background colors indicate significance levels of the age-adjusted association between risk group and TDI values at each 0.01 s time-position. Black horizontal bars indicate the four phases identified in **Figure 1**, where the TDI values differed most according to age. TDI values are averaged for septal and lateral mitral sites, presented for one standardized heart cycle of 1 s.

TABLE 3 **Individual age gap between biological and chronological age.**

	Low-risk	High-risk, total	Hypertension	Diabetes	IHD	Cardiac event
	(*n* = 881)	(*n* = 882)	(*n* = 742)	(*n* = 179)	(*n* = 231)	(*n* = 202)
Systolic peak	0 (ref.)	15 (10–20) years	16 (10–21) years	11 (1–20) years	16 (8–25) years	21 (12–30) years
		$p < 0.001$	$p < 0.001$	$p = 0.02$	$p < 0.001$	$p < 0.001$
Early diastole	0 (ref.)	8 (6–10) years	9 (7–11) years	7 (4–10) years	8 (6–11) years	8 (5–11) years
		$p < 0.001$	$p < 0.001$	$p < 0.001$	$p < 0.001$	$p < 0.001$
Average	0 (ref.)	12 (8–15) years	12 (9–15) years	9 (3–14) years	12 (7–17) years	15 (10–20) years
		$p < 0.001$	$p < 0.001$	$p = 0.002$	$p < 0.001$	$p < 0.001$

Individual age gap calculated as biological age subtracted by chronological age. Computed based on the two areas of the TDI curve significantly associated with risk group and age (systolic peak and early diastole). Presented as mean age gap in years (95% confidence intervals). *P*-value computed in comparison to low-risk group based on same TDI area.

significant phases: The systolic peak, the systolic plateau, early diastole and late diastole. The general pattern of age-related changes—an early shift of diastolic velocities while systolic velocities and thus the total heart movement remain preserved until older age—is similar to previous findings (8, 9).

This presentation of standardized reference values for the continuous TDI curve, and the identification of highly significant areas, made it possible to compare the changes in healthy aging in low-risk individuals with the differences in myocardial velocities seen in high-risk individuals.

Changes to myocardial velocities associated with cardiac risk factors

To evaluate the effects of cardiac risk factors separately from normal age-related changes, we compared whole-cycle TDI curves between low-risk and high-risk individuals within each age group (**Figure 2**). Even though our study is cross-sectional, the distinct TDI differences between low-risk and high-risk individuals in each age group could be seen as the chronological development of different TDI changes associated with duration of cardiac risk factors, since older individuals are likely to have longer-lasting contribution from risk-factors than younger individuals (16).

Our data suggest that the earliest degenerative change associated with cardiac risk factors is a decrease in early diastolic velocities. Later, there is an increase in late diastolic velocities and decrease in peak systolic velocities. With further duration, these changes are accentuated, and velocities of the systolic plateau also begin to decrease. However, the increase of late diastolic velocities will reach a turning point after which they will start to decrease, which makes the late diastolic phase less suited for discrimination between individuals at high and low risk.

These changes seen in **Figure 2** are also well illustrated in the regression-based curves of **Figure 3**. Surprisingly, in the regression curve of the youngest group, the whole systole seems to be higher in the high-risk group than the low-risk group. However, this deviation of the regression model is likely due to the small number of high-risk individuals aged 20–40 years (n = 22) and should be interpreted with caution. From the regression model, we identified two important phases of the heart cycle that were both strongly associated with age and also significantly differed between risk groups after adjusting for age. Thus, our data confirm that the systolic peak and the early diastole are the best phases of the TDI curve to distinguish high-risk individuals from low-risk individuals, as previously suggested by other studies (11, 17, 18).

Individuals at high risk of cardiac events show signs of accelerated aging of the heart

Held together, our whole-cycle analyses demonstrate that the changes in TDI velocities associated with cardiac risk factors in subjects within the same age group appeared to be similar to the changes of the TDI curve seen in healthy aging. Thus, it suggests that conditions associated with increased cardiac risk cause a general accelerated aging of the heart. In the literature, the idea of a disease-related acceleration of normal cardiac aging is also suggested in a study on hypertension (19).

Consequently, it might become possible to screen for high-risk patients by taking the TDI curve of any given patient and compare it to a set of normal reference TDI curves. If the patient's TDI curve corresponds to an older age than expected, then the patient is likely to have some accelerated cardiac deterioration and thus be at an increased risk of cardiac event.

To illustrate this potential application, we built a model to estimate biological heart age based on the two highly significant areas of the reference TDI curves (systolic peak and early diastole). Based on this, we present a quantification of the individual age gaps between biological age and chronological age for different risk groups (**Table 3**). With further studies and software development it might be possible to use this approach to identify high-risk patients during echocardiography by comparing the measured TDI curve with built-in reference TDI curves.

Compared with 2D strain deformation imaging, TDI offers a number of potential advantages. TDI directly measures motion, and the temporal resolution is high, which allows a reproducible determination of peak motion during individual phases of the cardiac cycle. Only measurements from the mitral sites are needed for TDI, and the examination is thus feasible in most patients even when image quality is suboptimal.

Study strengths

This study has certain strengths. 1) The unique extensive national Danish registries made it possible to have a 100% complete follow-up of our large study population of 1,763 individuals. 2) This study is the first study to analyze whole-cycle TDI velocity curves. Our method of correcting for heart rate made it possible to compare standardized whole-cycle curves for any individual in an automated manner and thus allowed the hypothesis-free identification of important phases of the heart cycle.

Study limitations

This study has certain limitations. 1) The inhabitants of Denmark and thus the study population are predominantly Caucasian, which may limit the generalizability of our findings. 2) Standardizing velocity curves of different heart rates is a theoretical approach that might not be an exact reflection of reality, thus risking a slight time-shift of individual peak values, resulting in lower mean peak values in the standardized reference values. An alternative to our approach would be to identify temporal valve events and use these to define periods of the cardiac cycle, which would also better allow analysis of the isovolumetric phases. This approach would require manual analysis and thus be less suited for the kind of automated analysis we have developed here. 3) Averaging the septal and lateral wall velocity curve serves to reduce variability but might hide differences between the two walls.

Conclusion

In the general population, TDI myocardial velocities are significantly associated with age throughout most of the cardiac cycle, and individuals with cardiac risk factors display TDI changes compatible with a general accelerated aging of the heart.

The systolic peak and early diastolic part of the TDI curve are best at distinguishing between low-risk individuals and high-risk individuals and may thus be used to calculate a TDI-derived biological age—a potential tool for identifying high-risk patients at risk of future cardiac events.

Data availability statement

The datasets presented in this article are not readily available because individual-level data are identifiable data and cannot be shared publicly. However, relevant intermediate-level data can be made available on request and following appropriate ethical review. Requests to access the datasets should be directed to corresponding author.

Ethics statement

The studies involving human participants were reviewed and approved by the regional ethics committee. The patients/participants provided their written informed consent to participate in this study.

Author contributions

All authors have contributed significantly to all parts of the submitted work (study concept and design, analysis and interpretation of data, and drafting and revision of the manuscript).

Conflict of interest

The authors declare that the research was conducted in the absence of any commercial or financial relationships that could be construed as a potential conflict of interest.

Publisher's note

References

1. Nagueh S, Smiseth O, Appleton C, Byrd B, Dokainish H, Edvardsen T, et al. Recommendations for the evaluation of left ventricular diastolic function by echocardiography: an update from the American Society of echocardiography and the european association of cardiovascular imaging. *Eur Heart J Cardiovasc Imaging.* (2016) 17:1321–60. doi: 10.1093/ehjci/jew082

2. Poulsen S, Andersen N, Ivarsen P, Mogensen C, Egeblad H. Doppler tissue imaging reveals systolic dysfunction in patients with hypertension and apparent "isolated" diastolic dysfunction. *J Am Soc Echocardiogr.* (2003) 16:724–31. doi: 10.1016/S0894-7317(03)00403-6

3. di Bonito P, Moio N, Cavuto L, Covino G, Murena E, Scilla C, et al. Early detection of diabetic cardiomyopathy: usefulness of tissue doppler imaging. *Diabet Med.* (2005) 22:1720–5. doi: 10.1111/j.1464-5491.2005.01685.x

4. Nagueh S, McFalls J, Meyer D, Hill R, Zoghbi William A, Tam J, et al. Tissue doppler imaging predicts the development of hypertrophic cardiomyopathy in subjects with subclinical disease. *Circulation.* (2003) 108:395–8. doi: 10.1161/01.CIR.0000084500.72232.8D

5. Wang M, Yip G, Wang A, Zhang Y, Ho P, Tse M, et al. Peak early diastolic mitral annulus velocity by tissue doppler imaging adds independent and incremental prognostic value. *J Am Coll Cardiol.* (2003) 41:820–6. doi: 10.1016/S0735-1097(02)02921-2

6. Ballo P, Guarini G, Simioniuc A, Gistri T, Fontanive P, Bello V, et al. Prognostic value of pulsed tissue doppler imaging for the assessment of left ventricular systolic function in patients with nonischemic dilated cardiomyopathy. *Echocardiography.* (2012) 29:291–7. doi: 10.1111/j.1540-8175.2011.01561.x

7. Nikitin N, Loh P, de Silva R, Ghosh J, Khaleva O, Goode K, et al. Prognostic value of systolic mitral annular velocity measured with doppler tissue imaging in patients with chronic heart failure caused by left ventricular systolic dysfunction. *Heart.* (2006) 92:775–9. doi: 10.1136/hrt.2005.067140

8. Innelli P, Sanchez R, Marra F, Esposito R, Galderisi M. The impact of aging on left ventricular longitudinal function in healthy subjects: a pulsed tissue doppler study. *Eur Heart J Cardiovasc Imaging.* (2008) 9:241–9. doi: 10.1016/j.euje.2007.03.044

9. Nikitin N, Witte K, Thackray S, de Silva R, Clark A, Cleland J. Longitudinal ventricular function: normal values of atrioventricular annular and myocardial velocities measured with quantitative two-dimensional color doppler tissue imaging. *J Am Soc Echocardiogr.* (2003) 16:906–21. doi: 10.1016/S0894-7317(03)00279-7

10. Grue J, Storve S, Støylen A, Torp H, Haugen B, Mølmen H, et al. Normal ranges for automatic measurements of tissue Doppler indices of mitral annular motion by echocardiography. Data from the HUNT3 Study. *Echocardiography.* (2019) 36:1646–55. doi: 10.1111/echo.14476

11. Mogelvang R, Biering-Sørensen T, Jensen J. Tissue doppler echocardiography predicts acute myocardial infarction, heart failure, and cardiovascular death in the general population. *Eur Heart J Cardiovasc Imaging.* (2015) 16:1331–7. doi: 10.1093/ehjci/jev180

12. Appleyard M, Hansen A, Schnohr P, Jensen G, Nyboe J. The copenhagen city heart study. osterbroundersogelsen. A book of tables with data from the first examination (1976-78) and a five year follow-up (1981-83). *Scand J Soc Med Suppl.* (1989) 41:1–160.

13. Mogelvang R, Sogaard P, Pedersen S, Olsen N, Schnohr P, Jensen J. Tissue doppler echocardiography in persons with hypertension, diabetes, or ischaemic heart disease: the Copenhagen City Heart Study. *Eur Heart J.* (2009) 30:731–9. doi: 10.1093/eurheartj/ehn596

14. Funck-Brentano C, Jaillon P. Rate-corrected QT interval: techniques and limitations. *Am J Cardiol.* (1993) 72:B17–22. doi: 10.1016/0002-9149(93)90035-B

15. R Core Team. *R: a language and environment for statistical computing.* Vienna: R Foundation for Statistical Computing (2021).

16. Shivalkar B, Dhondt D, Goovaerts I, Van Gaal L, Bartunek J, Van Crombrugge P, et al. Flow mediated dilatation and cardiac function in type 1 diabetes mellitus. *Am J Cardiol.* (2006) 97:77–82. doi: 10.1016/j.amjcard.2005.07.111

17. Bountioukos M, Schinkel A, Bax J, Lampropoulos S, Poldermans D. The impact of hypertension on systolic and diastolic left ventricular function. A tissue doppler echocardiographic study. *Am Heart J.* (2006) 151:1323.e7–12. doi: 10.1016/j.ahj.2006.02.031

18. Kosmala W, Kucharski W, Przewlocka-Kosmala M, Mazurek W. Comparison of left ventricular function by tissue doppler imaging in patients with diabetes mellitus without systemic hypertension versus diabetes mellitus with systemic hypertension. *Am J Cardiol.* (2004) 94:395–9. doi: 10.1016/j.amjcard.2004.04.048

19. Boyd A, Eshoo S, Richards D, Thomas L. Hypertension accelerates the ‘normal’ aging process with a premature increase in left atrial volume. *J Am Soc Hypertens.* (2013) 7:149–56. doi: 10.1016/j.jash.2012.12.008

frontiers | Frontiers in Cardiovascular Medicine

TYPE Original Research
PUBLISHED 11 January 2023
DOI 10.3389/fcvm.2022.1081664

OPEN ACCESS

EDITED BY
Giuseppe Pannarale,
Sapienza University of Rome, Italy

REVIEWED BY
Balint Karoly Lakatos,
Semmelweis University, Hungary
Vito Starc,
University of Ljubljana, Slovenia

*CORRESPONDENCE
Christine Bjørkvik Erevik
✉ cbjorkvik@hotmail.com

SPECIALTY SECTION
This article was submitted to Cardiovascular Imaging, a section of the journal Frontiers in Cardiovascular Medicine

RECEIVED 27 October 2022
ACCEPTED 22 December 2022
PUBLISHED 11 January 2023

CITATION
Erevik CB, Kleiven Ø, Frøysa V, Bjørkavoll-Bergseth M, Chivulescu M, Klæboe LG, Dejgaard L, Auestad B, Skadberg Ø, Melberg T, Urheim S, Haugaa K, Edvardsen T and Ørn S (2023) Myocardial inefficiency is an early indicator of exercise-induced myocardial fatigue.
Front. Cardiovasc. Med. 9:1081664.
doi: 10.3389/fcvm.2022.1081664

Myocardial inefficiency is an early indicator of exercise-induced myocardial fatigue

Christine Bjørkvik Erevik[1]*, Øyunn Kleiven[1], Vidar Frøysa[1], Magnus Bjørkavoll-Bergseth[1], Monica Chivulescu[2], Lars Gunnar Klæboe[2], Lars Dejgaard[2], Bjørn Auestad[3,4], Øyvind Skadberg[5], Tor Melberg[1], Stig Urheim[6], Kristina Haugaa[2], Thor Edvardsen[2] and Stein Ørn[1]

[1]Department of Cardiology, Stavanger University Hospital, Stavanger, Norway, [2]ProCardio Center for Innovation, Department of Cardiology, Oslo University Hospital, Rikshospitalet, Oslo, Norway, [3]Department of Mathematics and Physics, University of Stavanger, Stavanger, Norway, [4]Research Department, Stavanger University Hospital, Stavanger, Norway, [5]Department of Biochemistry, Stavanger University Hospital, Stavanger, Norway, [6]Department of Cardiology, Bergen University Hospital, Bergen, Norway

Background: The effect of prolonged, high-intensity endurance exercise on myocardial function is unclear. This study aimed to determine the left ventricular (LV) response to increased exercise duration and intensity using novel echocardiographic tools to assess myocardial work and fatigue.

Materials and methods: LV function was assessed by echocardiography before, immediately, and 24 h after a cardiopulmonary exercise test (CPET) and a 91-km mountain bike leisure race. Cardiac Troponin I (cTnI) was used to assess myocyte stress.

Results: 59 healthy recreational athletes, 52 (43–59) years of age, 73% males, were included. The race was longer and of higher intensity generating higher cTnI levels compared with the CPET ($p < 0.0001$): Race/CPET: exercise duration: 230 (210, 245)/43 (40, 45) minutes, mean heart rate: 154 ± 10/132 ± 12 bpm, max cTnI: 77 (37, 128)/12 (7, 23) ng/L. Stroke volume and cardiac output were higher after the race than CPET ($p < 0.005$). The two exercises did not differ in post-exercise changes in LV ejection fraction (LVEF) or global longitudinal strain (GLS). There was an increase in global wasted work ($p = 0.001$) following the race and a persistent reduction in global constructive work 24 h after exercise ($p = 0.003$).

Conclusion: Increased exercise intensity and duration were associated with increased myocardial wasted work post-exercise, without alterations in LVEF and GLS from baseline values. These findings suggest that markers of myocardial inefficiency may precede reduction in global LV function as markers of myocardial fatigue.

KEYWORDS

myocardial work, sports cardiology, exercise, left ventricular function, myocardial strain, exercise-induced cardiac fatigue, myocardial efficiency, athletes heart

Introduction

Increased physical activity increases health benefits (1–4). However, prolonged high-intensity endurance exercise may be associated with an increased risk of adverse clinical outcomes (5) and alterations in left and right ventricular (LV and RV) function (6, 7). These exercise-induced alterations in myocardial function are often called exercise-induced cardiac fatigue (8–10).

Numerous studies have reported on post-exercise LV function assessed by echocardiography (8). A large meta-analysis reported an overall reduction in LV global longitudinal strain (GLS), LV ejection fraction (EF), and diastolic function after bouts of prolonged, high-intensity exercise exceeding 2 h of duration (8). However, the studies included in the meta-analysis did not compare the response to different exercise intensities and durations within the same individuals. Furthermore, echocardiographic parameters, such as LV volumes and GLS, are influenced by pre- and afterload, potentially precluding the assessment of the myocardial response to exercise (11, 12).

A novel echocardiographic method has been developed to assess non-invasive parameters of myocardial work (MW) (13–16). MW uses a combination of LV GLS and systolic blood pressure (SBP) to obtain LV pressure-strain loops. These MW parameters offer new insights into alterations in LV function following exercise compared with traditional echocardiographic parameters. Moreover, since MW parameters can identify pathological alterations in myocardial function due to ischemia, these parameters may present new insights into exercise-induced cardiac fatigue (17, 18).

This study aimed to determine the LV response to increased exercise workload by comparing two exercises of different exercise intensity and duration, using both traditional and MW echocardiographic parameters before and after exercise.

Materials and methods

Study participants were recruited among healthy, prior participants in the NEEDED 2013 and 2014 studies (19, 20). Exclusion criteria were age below 18 years of age, any prior history, signs or symptoms of cardiac disease, pathological ECG or echocardiographic findings, and a normal CT coronary angiography, without obstructive CAD following exercise.

The present study was conducted in 2018. Echocardiography was acquired before exercise, immediately after, and at 24 h following two episodes of high-intensity endurance exercise in 2018 (**Figure 1**). The first exercise was a cardiopulmonary exercise test (CPET) (**Supplementary material 1**). The second exercise was participating in the 91-km North Sea Race Mountain bike leisure race in 2018. Cardiac Troponin I (cTnI) was used as a biomarker of myocardial stress (21). Blood samples were acquired before (baseline) and at 3-h (the expected maximum elevation) and 24 h (to assess recovery) following both exercises. During the race, power meters (Stages Power Meters, Boulder, CO, US) were used to assess the amount of work performed. Exercise intensity was assessed by continuous heart rate measurement using Garmin heart rate straps and Garmin Forerunner 935 Sport Watch (Garmin, Olathe, KS, USA). A CT coronary angiography was performed 2–3 weeks after the race in 2018 to ensure the absence of new coronary artery obstruction potentially influencing the echocardiographic assessments and cTnI response. Informed consent was obtained from all study participants prior to study inclusion. The Regional Ethics Committee approved the study (REK nr 2013/550).

Echocardiographic image acquisition

GE Vivid E 95 ultrasound systems and 4V probes (Vingmed Horten, Norway) were used for all echocardiographic assessments. Three medical doctors were responsible for acquiring images in relation to the CPET, and six medical doctors worked on parallel stations in relation to the cycle

---

Abbreviations: BMI, Body mass index; CPET, Cardiopulmonary exercise test; MET, Metabolic equivalent of task; cTnI, Cardiac Troponin I; SBP, Systolic blood pressure; DBP, Diastolic blood pressure; HR, Heart rate; CVD, Cardiovascular disease; Vo2 Max, Maximal oxygen consumption; AT, Anaerobic threshold; E/A, Ratio of early to late diastolic transmitral blood flow velocities; E`, Early diastolic myocardial tissue velocity; LV, Left ventricle; RV, Right ventricle; LAVi, Left atrial volume index; EDV, End diastolic volume; ESV, End systolic volume; GLS, Global longitudinal strain; EF, Ejection fraction; SVi, Stroke volume index; CO, Cardiac output; EDVi, End diastolic volume index; ESVi, End systolic volume index; GWI, Global work index; GCW, Global constructive work; GWW, Global wasted work; GWE, Global work efficiency; PSS, Post systolic shortening; PSI, Post systolic shortening index; ESL, Early systolic lengthening.

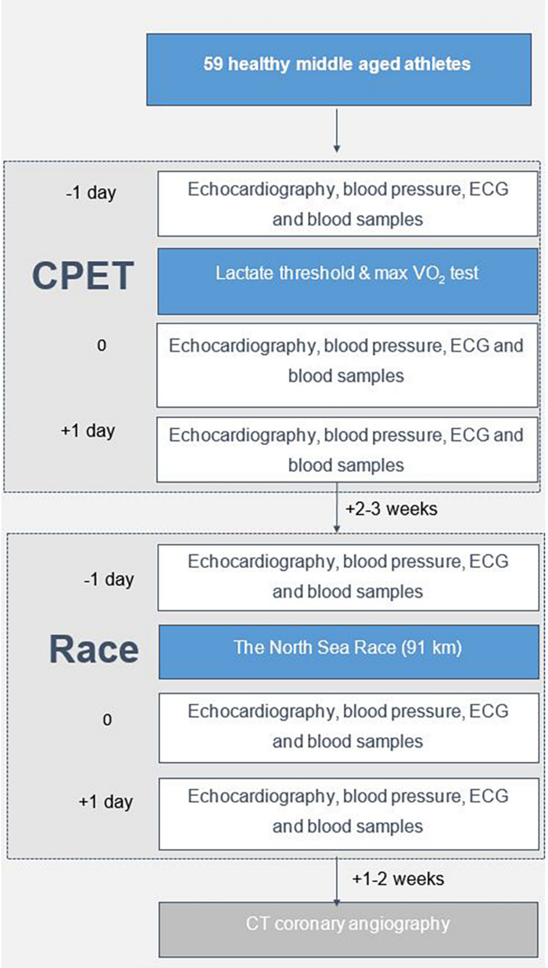

FIGURE 1
Flow chart of the study.

race to acquire images immediately after finishing the race. Comprehensive imaging protocols were applied. Appropriate frame rates were applied, to allow later high-quality post-processing, including speckle-tracking strain analysis.

Analysis of myocardial function and morphology

All echocardiographic analyses were performed offline on EchoPAC V202 (General Electric Vingmed Ultrasound AS) by a researcher blinded to clinical data and exercise information. All echocardiographic parameters were calculated according to the European Association of Cardiovascular Imaging (22, 23). The Devereux formula was used to determine LV mass. Mitral valve inflow was assessed using pulsed-wave Doppler at the mitral valve leaflets; pulsed-wave tissue Doppler imaging was performed to assess septal mitral annular velocity. LV volumes and EF were assessed using three-dimensional imaging. Two-dimensional speckle tracking imaging was used to study LV deformation. LV GLS was calculated as an average longitudinal strain value based on apical two-, three-, and four-chamber views at a 60–70 frames/second frame rate using the automated function imaging (AFI). Time to peak strain was defined as the time from onset Q/R wave on ECG to peak negative longitudinal strain during the entire cardiac cycle. Post-systolic strain was calculated as the absolute difference between peak global longitudinal strain (peak G) and peak longitudinal strain during systole (peak S). Post-systolic index (PSI) was defined as [(peak G–peak S)/peak G] × 100. Early systolic lengthening was determined in 18 left ventricular segments, and peak P represents the maximal positive strain value in early systole. Mechanical dispersion (MD) was defined as the standard deviation of time to peak negative strain in 18 left ventricular segments.

Myocardial work (MW) analysis

Myocardial work (MW) calculation was performed offline using EchoPAC software version 202 (General Electric Vingmed Ultrasound AS). A commercially available algorithm was used to calculate four MW parameters (see below). The LV pressure curve was estimated using an empiric reference pressure curve that was adjusted according to the duration of the isovolumic and ejection phases. SBP was measured with a brachial cuff with study subjects sitting. The opening and closure of the aortic and mitral valves were determined manually in the three- and four-chamber apical views based on Doppler signals and visualization of valve opening and closure.

Pressure strain was generated in each myocardial segment by the EchoPAC software, and global values were calculated as mean values of all segments. The global work index (GWI) parameter is the total work performed by the left ventricle, using the area of the pressure-strain loop between the mitral valve closure and opening. Global constructive work (GCW) is the sum of positive work due to myocardial shortening in systole and negative work due to myocardial lengthening during isovolumetric relaxation. Global wasted work (GWW) is the sum of myocardial lengthening in systole and shortening in isovolumetric relaxation, reflecting the work that does not contribute to LV ejection. Global work efficiency (GWE) is constructive work divided by the sum of constructive work and wasted work.

Cardiac Troponin I (cTnI) measurements

The High sensitivity cTnI assay (STAT) from Abbott Diagnostics was used for the measurement of cTnI, before exercise and at 3 and 24 h following exercise. The assay was analyzed on an Architect SR2000i (Abbott Diagnostics, Abbott Park, IL, USA). Overall 99th percentile is 26 ng/L (men: 34 ng/L and women: 16 ng/L) (IFCC Committee on Clinical Applications of Cardiac Bio-Markers).

Statistical analysis

Normally distributed continuous variables are reported as mean ± SD, while continuous variables with markedly skewed distributions are reported as the median and interquartile range (25th, 75th percentile). The Shapiro–Wilk test was used to test for normality. For continuous variables, The Mann–Whitney *U* test or a Student *T*-test was used to compare groups, as appropriate. Spearman analysis was used to calculate bivariate correlations. A two-tailed p-value < 0.05 was considered significant. SPSS version 26.0.0.1 was used for statistical analyses.

Results

A total of 59 healthy, well-trained, recreational athletes, 52 (43, 59) years of age, 73% males, without obstructive coronary artery disease (> 50% stenosis) verified by CT scans, were included in the study (**Table 1**). The study participants had a median training volume of 61 (47, 102) MET hours/week and a median training experience of 10 (7, 21) years.

Before CPET (baseline), the mean SBP (systolic blood pressure) was 136 ± 16 mmHg, and the heart rate (HR) was 59 ± 10 bpm. Echocardiographic recordings at baseline showed a mean LV mass index of 87.5 ± 14.5 g/m^2 and a mildly elevated median LV end-diastolic volume index of 82 (69, 97) mL/m^2 compared to reference values (22). All other baseline echocardiographic measurements were within normal ranges.

TABLE 1 Baseline characteristics (*n* = 59).

Characteristic	
Age, years	51.1 ± 9.7
Male sex, *n* (%)	43 (72.9)
BMI, kg/m^2	24.9 (23.3, 27.1)
Waist circumference, cm	85.0 (81.0, 93.0)
SBP, mmHg	135 ± 16
DBP, mmHg	82 ± 10
Former smoker, *n* (%)	27 (44.3)
Family history of CVD	4 (6.6)
Prior CVD, *n* (%)	0
Diabetes, *n* (%)	0
Training experience	
Years of endurance training	10.0 (7.0, 21.3)
Number of prior competitions	10.0 (5.0, 20.0)
Exercise volume (MET hours/week)	61.3 (47.1, 101.7)
Cardiopulmonary exercise test (CPET)	
Max VO2 (mL/min/kg)	41.2 ± 8.4
Power at max VO2 (watt/kg)	3.8 ± 0.8
HR at VO2 max (bpm)	177 ± 12
Power at AT (watt)	200 ± 47
HR at AT (bpm)	162 ± 13

Normally distributed values are reported as mean ± SD, and markedly skewed values are reported as median (25th, 75th percentile). BMI, body mass index; SBP, systolic blood pressure; DBP, diastolic blood pressure; CVD, cardiovascular disease; MET, metabolic equivalent; HR, heart rate; AT, anaerobic threshold.

The impact of exercise on physiological and echocardiographic parameters

Both CPET and the race exercises were of high physical intensity (**Table 2**). There was a highly significant increase in cTnI after both exercises, with the highest values at 3 h after exercise, with declining values at 24 h (**Table 2**).

Immediately after exercise, SBP and DBP (diastolic blood pressure) decreased, but HR increased, and so did cardiac output (CO) and mechanical dispersion (**Table 3**). Most echocardiographic parameters were lower than pre-exercise values immediately following exercise, including LV stroke volume (SV), left atrial volume index (LAVi), LV diastolic and systolic volumes (EDV and ESV), E/A ratio, E, E', E/E', LV GLS, GWI, and GCW (**Table 4**). There were no significant differences in LVEF following exercise.

Global wasted work (GWW) was significantly higher after the race (*p* 0.001) compared with the pre-exercise value and global work efficiency (GWE) was lower (*p* 0.006), this was not observed following the CPET. Twenty-four hours after the race GWW and GWE returned to baseline values.

Echocardiography at 24 h showed increased LV EDV and ESV, but a decreased CO compared with pre-exercise values.

The impact of increased exercise intensity and duration, comparison of race, and CPET results

The race was of higher workload and longer duration than the CPET, resulting in higher post-exercise cTnI values (**Table 2**). Immediately following exercise, there was a significant reduction in SBP and DBP for both exercises, and still significantly lower than pre-exercise values at 24 h (**Supplementary materials 2, 3**). The reduction in SBP from before to after exercise was significantly larger for the race than

TABLE 2 Physical measurements cardiopulmonary exercise test (CPET) and race ($n = 59$).

Exercise parameters	CPET	Race	*P*-value
Duration of exercise (min)	43 (40, 45)	230 (210, 245)	<0.001
ATHR (bpm)	162 ± 13		
AT (Watt)	200 ± 47		
HR peak (bpm)	177 ± 12	175 ± 12	0.08
HR mean (bpm)	132 ± 12	154 ± 10	<0.001
SBP peak (mmHg)	201 (181, 216)	230 (210, 245)	<0.001
SBP mean (mmHg)	183 ± 14	166 ± 15	<0.001
DBP peak (mmHg)	83 (68, 94)	100 (90, 110)	<0.001
DBP mean (mmHg)	83 ± 9	84 ± 8	0.54
Power (watt/kg), peak	3.8 ± 0.8	9.2 ± 6.8	0.001
Power (watt/kg), mean	2.9 ± 0.5	2.1 ± 0.5	<0.001
Work total (watt × min)	8650 ± 1778	40289 ± 7714	<0.001
Work/kg total (watt/kg × min)	107 ± 21	496 ± 65	<0.001
Weight reduction (kg)	0.4 (0.2, 0.6)	1.3 (0.8, 1.8)	<0.001
Delta creatinine 3 h (µmol/L)	2.7 ± 4.5	11.0 ± 12.7	<0.001
cTnI			
Pre-exercise (ng/L)	3.2 (2.0, 7.0)	4.0 (2.1, 7.5)	0.77
3-h post-exercise (ng/L)	11.6 (7.0, 23.2)	77.1 (37.1, 128)	<0.001
24-h post-exercise (ng/L)	5.0 (2.9, 9.5)	15.7 (7.7, 32.1)	<0.001

Normally distributed values are reported as mean ± SD, and skewed values are reported as median (25th, 75th percentile). AT, anaerobic threshold; HR, heart rate; bpm, beats per minute; SBP, systolic blood pressure; DBP, diastolic blood pressure; cTnI, Cardiac Troponin I.

the CPET ($p < 0.05$). Post-race HR was only higher than CPET immediately after the race returning to baseline values, equal to the CPET values, at 24 h following the race (Table 3). At all time-points following the race, there were smaller diastolic and systolic volumes compared with the CPET, but higher SV, larger cardiac output, and larger GWI compared with the CPET (Tables 3, 4). There was a lower E/A ratio and smaller LAVi immediately following the race that returned to baseline after 24 h with no difference compared with CPET. There was a significant reduction in LV GLS immediately after both the CPET and the race ($p < 0.05$), with a similar reduction after both exercises. LVEF did not change after the CPET nor after the race.

There were no significant correlations between echocardiographic parameters and cTnI after the CPET. There was a weak positive correlation between cTnI and end systolic- and diastolic volumes 24 h after the race (Spearman's ρ 0.26 and 0.29, $p = 0.05$ and $p = 0.03$). There was also a positive correlation between LV GLS immediately after the race and cTnI 3 h after the race (Spearman's ρ 0.275, $p = 0.044$) and 24 h after the Race (Spearman's ρ 0.298, $p = 0.028$). There were no significant correlations between cTnI, LVEF, diastolic parameters, and MW parameters.

Differences in pre-exercise measurements between the CPET and the race

Comparing the pre-exercise assessment before the CPET and the race revealed several significant differences (Tables 3, 4). Before the race, there was a significantly ($p < 0.001$) higher pre-exercise SBP than the CPET, but no difference in heart rate. A large portion of the echocardiographic findings before the race differed from pre-CPET findings (Tables 3, 4). The following echocardiographic values were higher before the race compared with the values before the CPET: CO ($p = 0.005$), LV SV ($p < 0.001$), E′($p < 0.001$), GWI ($p < 0.001$), GCW ($p = 0.006$), GWE ($p = 0.024$), and post systolic shortening index ($p = 0.015$). The following values were lower: ESV ($p = 0.018$), E/E′ ($p = 0.048$), and post-systolic shortening ($p = 0.009$).

Percentual changes from baseline to post-exercise

The difference in many pre-exercise parameters before the CPET and the race indicates the presence of significant confounders complicating a direct comparison between the race and the CPET. In order to reduce the impact of baseline confounders, the difference in post-exercise parameters between the race and the CPET was assessed by the percentual change from each pre-exercise value (Figure 2). When using this approach, there were no significant post-exercise differences regarding LV EF, LV GLS, GWI, and GWE. However, there was increased GWW immediately after the race compared with the CPET ($p = 0.025$), and there was a significant persisting reduction in GCW 24 h following the race ($p = 0.015$). Figure 3 illustrates representative pressure-strain loops from one of the study subjects after the CPET and the race with a significant reduction in GWI immediately post-exercise for both CPET and the race, with a reduction in the pressure-strain loop area. Twenty-four hours after the CPET the area under the pressure strain loop is back to baseline area but still reduced 24 h after the race, illustrating a reduced ability to recover after the race.

Reproducibility

Intra- and inter-observer variability analysis confirmed high reproducibility of the parameters LV GLS, four-chamber strain, three-chamber strain, and two-chamber strain analyses, and the myocardial work parameters GWI, GCW, GWW, and GWE (Supplementary material 4).

TABLE 3 Hemodynamic and echocardiographic parameters (n = 59).

		CPET	Race	*P*-value
Blood pressure				
SBP (mmHg)	Baseline	135 (122, 146)	143 (129, 156)	<0.001
	Post-exercise	128 (119, 136)	128 (122, 139)	0.037
	24 h	126 (119, 137)	135 (126, 151)	<0.001
DBP (mmHg)	Baseline	81 (74, 89)	78 (71, 87)	0.32
	Post-exercise	78 (70, 84)	72 (68, 81)	0.10
	24 h	78 (69, 86)	73 (69, 81)	0.08
Heart rate (bpm)	Baseline	58 (51, 65)	57 (50, 66)	0.78
	Post-exercise	79 (70, 90)	87 (83, 95)	<0.001
	24 h	56 (50, 63)	55 (50, 66)	0.74
LV volume 3D				
EDVi (mL/m^2)	Baseline	81.6 (69.1, 96.5)	81.4 (70.3, 90.3)	0.32
	Post-exercise	79.8 (72.0, 88.9)	73.8 (64.2, 82.1)	<0.001
	24 h	92.1 (85.4, 103.3)	88.1 (80.3, 100.0)	<0.001
ESVi (mL/m^2)	Baseline	33.8 (29.1, 39.4)	32.8 (28.0, 37.6)	0.018
	Post-exercise	34.2 (31.7, 39.8)	30.5 (26.3, 36.5)	<0.001
	24 h	39.4 (35.9, 42.9)	36.3 (32.9, 40.8)	0.002
LV function				
E/A ratio	Baseline	1.3 (1.1, 1.7)	1.2 (1.1, 1.6)	0.07
	Post-exercise	1.0 (0.9, 1.2)	0.9 (0.8, 1.1)	<0.001
	24 h	1.4 (1.1, 1.6)	1.3 (1.1, 1.7)	0.26
E' septal (m/sek)	Baseline	0.11 (0.09, 0.12)	0.12 (0.10, 0.14)	<0.001
	Post-exercise	0.10 (0.09, 0.12)	0.11 (0.08, 0.12)	0.29
	24 h	0.11 (0.09, 0.13)	0.11 (0.09, 0.14)	0.002
E/E' septal	Baseline	7.0 (6.0, 8.4)	6.9 (6.1, 7.9)	0.048
	Post-exercise	6.6 (5.5, 7.9)	6.6 (5.2, 8.3)	0.95
	24 h	7.2 (6.4, 8.9)	7.0 (6.0, 9.0)	0.38
EF (%)	Baseline	59.0 (55.0, 60.0)	58.0 (56.0, 63.0)	0.10
	Post-exercise	57.0 (55.0, 60.0)	58.0 (55.0, 61.5)	0.08
	24 h	58.0 (56.0, 60.0)	59.0 (56.0, 61.0)	0.28
SVi (mL/m^2)	Baseline	43.0 (38.9, 52.0)	47.6 (42.8, 57.4)	<0.001
	Post-exercise	39.7 (34.4, 46.6)	42.8 (38.0, 50.1)	0.014
	24 h	43.3 (37.3, 50.6)	46.0 (41.6, 51.6)	0.001
CO (mL/min/m^2)	Baseline	2610 (2151, 3055)	2907 (2446, 3268)	0.005
	Post-exercise	3328 (2724, 3831)	3772 (3311, 4379)	<0.001
	24 h	2388 (2178, 2814)	2575 (2260, 3053)	0.008
GLS (%)	Baseline	20.0 (18.0, 22.5)	20.8 (19.0, 22.4)	0.21
	Post-exercise	19.0 (17.0, 20.0)	19.5 (18.0, 22.0)	0.013
	24 h	20.0 (19.0, 22.0)	20.0 (18.0, 22.0)	0.54
Mechanical dispersion (msec)	Baseline	33.5 (29.0, 40.0)	31.5 (22.5, 40.8)	0.014
	Post-race	39.0 (28.0, 49.0)	36.0 (31.0, 43.0)	0.64
	24 h	35.0 (27.0, 41.5)	31.0 (24.5, 37.5)	0.025
Left atrial volume 3D				
EDVi (mL/m^2)	Baseline	31.7 (25.0, 38.6)	30.6 (23.0, 37.8)	0.17
	Post-exercise	26.2 (22.9, 33.3)	23.7 (19.9, 27.5)	<0.001
	24 h	30.8 (25.1, 35.8)	31.8 (27.5, 39.0)	0.24
RV				
RV base diameter, mm	Baseline	40.0 (36.8, 42.0)	41.0 (37.8, 44.0)	0.12
	Post-exercise	39.0 (36.0, 42.0)	39.0 (35.5, 42.0)	0.43
	24 h	39.0 (37.0, 41.8)	40.0 (38.0, 42.0)	0.019
RV GLS, 3 segments, %	Baseline	27.0 (24.7, 28.8)	26.6 (23.8, 29.6)	0.98
	Post-exercise	25.9 (21.3, 28.6)	25.6 (22.6, 30.0)	0.19
	24-h	27.0 (25.1, 29.1)	25.9 (21.3, 28.6)	0.64

Values are median (25th, 75th percentile). SBP, systolic blood pressure; DBP, diastolic blood pressure; LV, left ventricle; EDVi, end-diastolic volume index; ESVi, end-systolic volume index; EF, ejection fraction; SVi, stroke volume index; CO, cardiac output; GLS, global longitudinal strain; RV, right ventricle.

Discussion

This is the first study to provide evidence suggesting myocardial inefficiency as an early indicator of exercise-induced myocardial fatigue. The study is based upon multiple echocardiographic assessments before and after exercise comparing two different workloads, in well-trained middle-aged

TABLE 4 Myocardial work parameters (*n* = 59).

		CPET	Race	*P*-value
GWI (mmHg%)	Baseline	2156 (1899, 2399)	2493 (2192, 2638)	<0.001
	Post-exercise	1865 (1621, 2201)	2073 (1889, 2391)	<0.001
	24-h	2011 (1764, 2208)	2312 (2104, 2496)	<0.001
GCW (mmHg%)	Baseline	2383 (2152, 2668)	2601 (2360, 2811)	0.006
	Post-exercise	2096 (1972, 2434)	2252 (2036, 2580)	0.005
	24-h	2356 (2096, 2641)	2497 (2254, 2676)	0.43
GWW (mmHg%)	Baseline	66.0 (37.5, 128.0)	53.0 (36.0, 81.0)	0.06
	Post-exercise	58.0 (41.8, 104.3)	82.0 (41.5, 129.0)	0.21
	24-h	49.0 (33.5, 88.0)	49.0 (30.8, 66.8)	0.12
GWE (%)	Baseline	97.0 (95.0, 98.0)	98.0 (96.0, 98.0)	0.024
	Post-exercise	96.0 (95.0, 98.0)	96.0 (94.8, 98.0)	0.83
	24-h	97.0 (95.0, 98.0)	97.0 (97.0, 98.0)	0.012
PSS (%)	Baseline	−0.2 (−0.4, −0.1)	−0.4 (−0.9, 0.13)	0.009
	Post-exercise	−0.4 (−0.7, −0.2)	−0.6 (−2.1 to 0, 0.2)	0.005
	24-h	−0.1 (−0.3, −0.1)	−0.2 (−0.4, −0.1)	0.75
PSI (%)	Baseline	1.2 (0.6, 1.9)	2.0 (0.7, 5.0)	0.015
	Post-exercise	2.2 (1.1, 3.6)	2.7 (1.2, 11.5)	0.010
	24-h	0.7 (0.4, 1.6)	0.8 (0.4, 1.7)	0.98
ESL (%)	Baseline	1.7 (1.0, 2.8)	1.6 (0.9, 2.1)	0.28
	Post-exercise	2.7 (1.6, 3.8)	2.0 (1.2, 3.7)	0.07
	24-h	1.4 (0.8, 2.4)	1.8 (0.9, 3.0)	0.17

Values are median (25th, 75th percentile). GWI, global work index; GCW, global constructive work; GWW, global wasted work; GWE, global work efficiency; PSS, post systolic shortening; PSI, post systolic shortening index; ESL, early systolic lengthening.

athletes, without obstructive coronary artery disease verified by CT scans. The study found that increased exercise workload was associated with increased post-exercise wasted myocardial work without alterations in LVEF and GLS adjusting for baseline values. These findings suggest that markers of myocardial inefficiency may precede reduction in global LV function as markers of myocardial fatigue.

Exercise-induced cardiac fatigue is a reversible myocardial dysfunction caused by strenuous exercise (24, 25). A large range of parameters have been used to assess exercise-induced cardiac fatigue, the most common are LVEF and LV-GLS (8, 26, 27). Since echocardiographic parameters, such as LVEF and GLS are influenced by pre- and afterload, it is unknown whether post-exercise cardiac dysfunction represents a global vascular load-related mechanism or a more local intrinsic mechanism in the cardiomyocyte. The present study found exercise-induced changes in left ventricular function consistent with cardiac fatigue (8). LV GLS and GWI were reduced after both exercises. In contrast, there was a significant increase in wasted myocardial work (GWW) and mechanical dispersion after the highest workload (the race) compared with the CPET. The level of constructive myocardial work was reduced after both exercises and remained reduced at 24 h after the race but not after the CPET, suggesting that the increased workload during the race resulted in reduced LV recovery.

Myocardial work by echocardiography combines strain analysis with SBP providing a less load-dependent and more comprehensive assessment of LV systolic function (28). Myocardial work parameters may be used to evaluate athletes' hearts (29) and to distinguish pathology from athletic remodeling (28, 30). A recent study of marathon runners found a post-exercise increase in myocardial work (GWI) in a subgroup of athletes with higher BNP values and heart rates (31). However, no study has determined the role of myocardial inefficiency in exercise-induced myocardial fatigue.

Muscular inefficiency occurs in skeletal muscle when workloads exceed maximal oxygen consumption intensity (32). The prolonged duration of these high-intensity workloads is linked with a progressive reduction in muscular efficiency (33). Exercise-induced skeletal muscular inefficiency is associated with electromechanical delay, potentially leading to exercise intolerance (34, 35). Several potential mechanisms are suggested to be related to muscular inefficiency, including muscle metabolite accumulation, decreased free energy of adenosine triphosphate breakdown, increased muscle temperature, and reactive oxygen species production (32).

Our echocardiographic findings suggest that there may be a similar relation between workload and myocardial inefficiency, as previously described in skeletal muscle. In our study, the increased workload and the duration of work during the race (**Table 2**) were associated with a post-exercise reduction in myocardial efficiency, indicated by parameters such as global wasted work (GWW), global constructive work (GCW), post-systolic shortening, and mechanical dispersion. These parameters of myocardial inefficiency may add additional information to traditional parameters of exercise-induced myocardial fatigue. The underlying mechanisms responsible

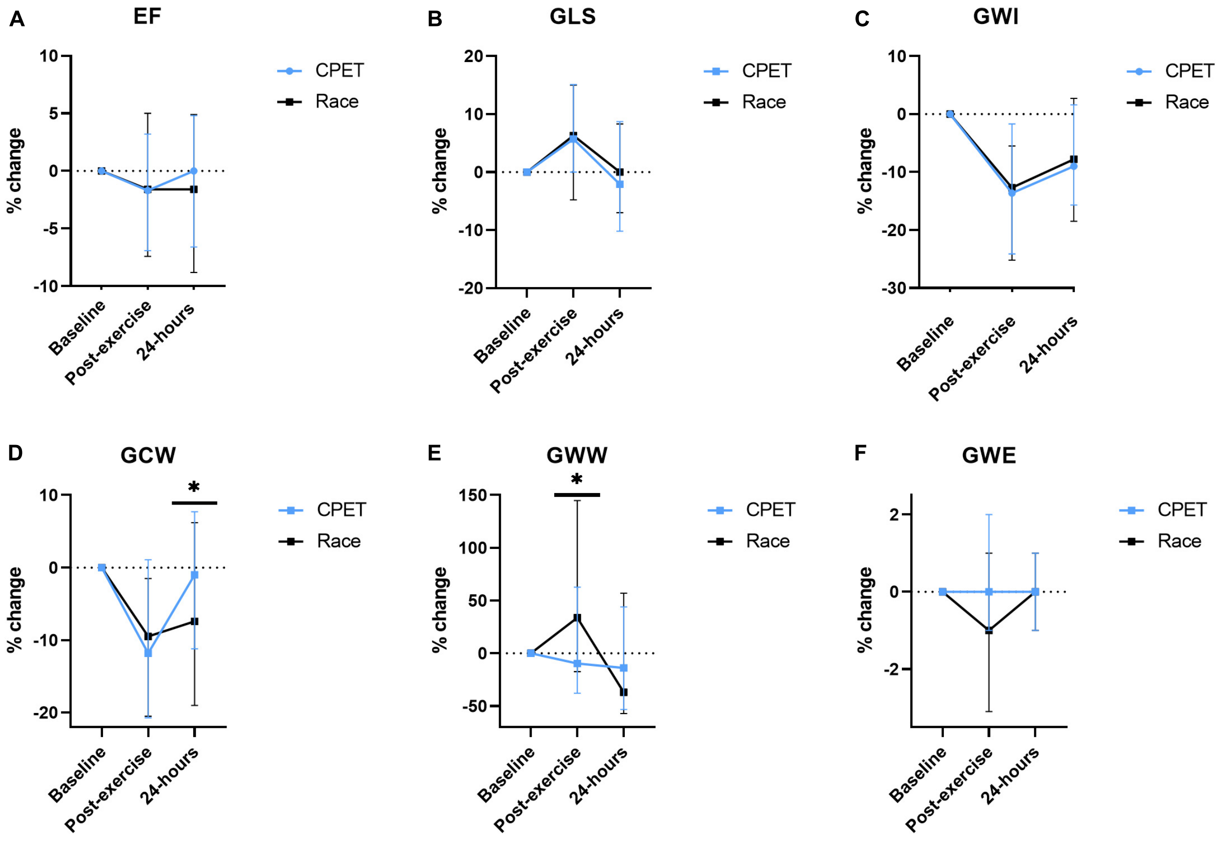

FIGURE 2
The percentual change of echocardiographic measurements from baseline (before exercise) and immediately and 24 h following a cardiopulmonary exercise test (CPET) and the North Sea Race in 2018 (Race). The following parameters were assessed **(A)** LVEF (left ventricular ejection fraction), **(B)** GLS (global longitudinal strain), **(C)** GWI (global work index), **(D)** GCW (global constructive work), **(E)** GWW (global wasted work), and **(F)** GWE (global work efficiency). *$p < 0.05$.

for the observed exercise-induced cardiac inefficiency are unknown. However, exercise-induced alterations in cardiac electromechanical delay may represent similar mechanisms to those described in skeletal muscle. Chan-Dewar et al. (36) reported an increase in post-exercise electromechanical delay without changes in QRS duration, suggesting an intrinsic myocyte mechanism responsible for exercise-induced cardiac fatigue. Sahlèn et al. (37) found exercise-induced cardiac fatigue associated with abnormalities in ventricular repolarization, suggesting a transient state of electrical instability following endurance exercise.

Our study also found increases in other parameters of myocardial inefficiencies, such as post-systolic shortening (PSS) and early systolic lengthening (ESL) immediately after both exercises. Post-systolic shortening relates directly to LV systolic function (38). Myocardial contraction after aortic valve closure and lengthening of myocardial fibers during systole reflect paradoxical deformation of the myocardial wall segments, attenuating LV ejection. Since GWW considers SBP, it is less load-dependent than PSS and ESL and, therefore, a more accurate measure of LV efficiency. Post-race increase in GWW and the persistent reduction in GCW following the race may indicate an exercise-induced reduction in myocardial efficiency caused by the prolonged myocardial work during the race. In contrast, neither LV GLS nor LVEF showed any difference between the two types of exercise, despite a large increase in cTnI following the race, indicating increased myocardial stress (21). Interestingly, in line with recent publications (25), there was a significant increase in mechanical dispersion following the race suggesting increased LV mechanical discoordination and reduced mechanical efficiency during cardiac ejection after prolonged high-intensity workload (39).

Left ventricular (LV) rotation and twist are important factors of LV systolic and diastolic performance. During diastole, the untwisting results in the abrupt release of the energy stored in elastic components, resulting in a negative intraventricular pressure gradient that facilitates LV filling at low filling pressure (40, 41). Park et al. (42) found that rotation and twist both showed higher values in the abnormal relaxation group than in the healthy group, paralleled by the reduced peak velocity of the

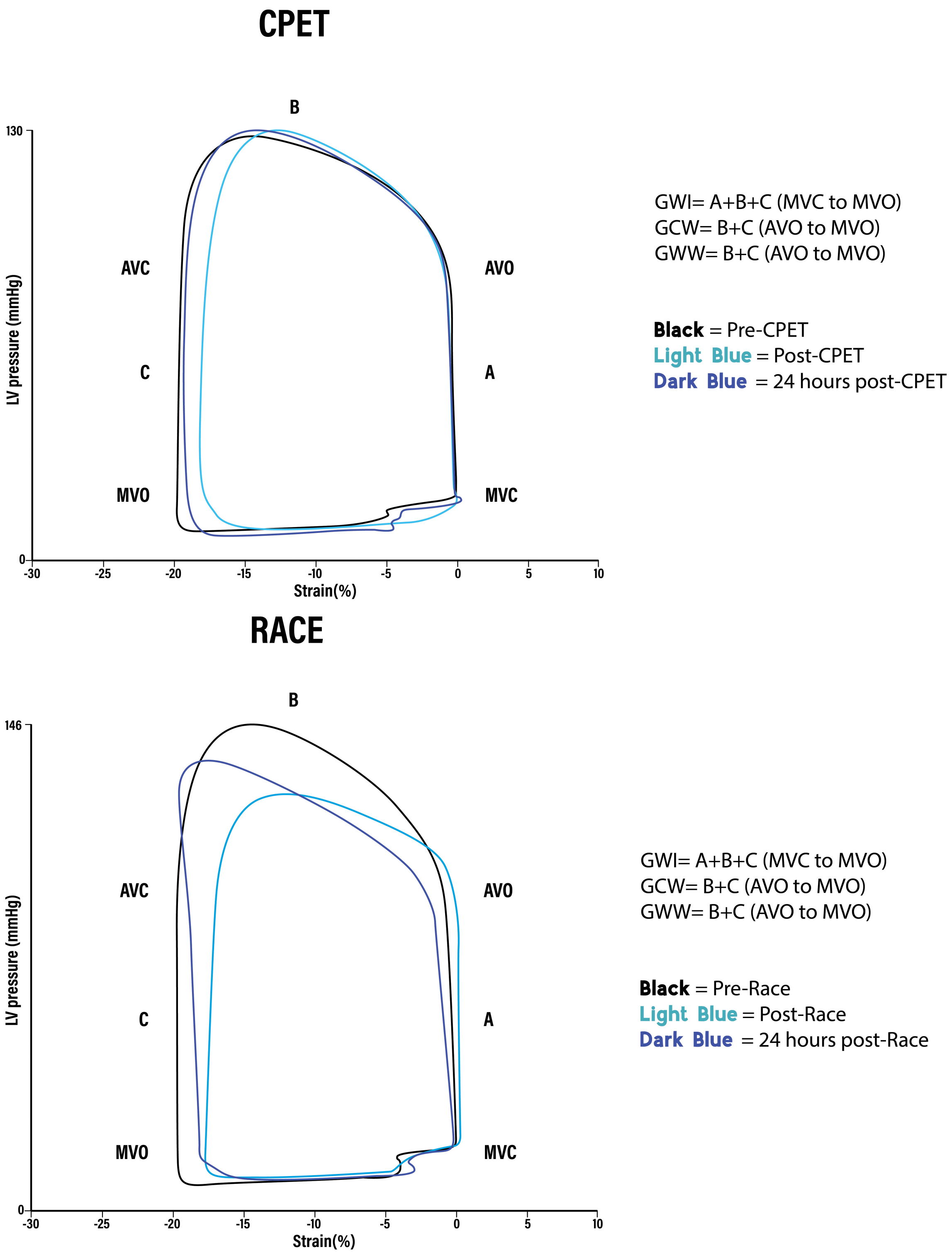

FIGURE 3

Representative global pressure-strain loops from the same person after (A) cardiopulmonary exercise test (CPET) and (B) Race. GWI, Global work index. Amount of myocardial work performed by the left ventricle during systole: Area of the pressure-strain loop from mitral valve closure to mitral valve opening (A + B + C). GCW, Global constructive work. Work that contributes to left ventricular ejection. Positive work performed in (B) systole (shortening) + negative work performed in (C) isovolumetric relaxation (lengthening). GWW, Global wasted work. Work that does not contribute to left ventricular ejection. Negative work performed in (B) systole (lengthening) + positive work performed in (C) isovolumetric relaxation (shortening).

early diastolic filling wave (E) and peak early diastolic annular velocity (E'), similar to the findings in the present study. At the end of systole and during isovolumic relaxation, myocytes are still active and exert the force to oppose the ventricular pressure and residual elastic forces due to the twist, which is the highest at the apex. One may speculate that the faster the untwisting, the more negative intraventricular pressure is generated, thus unloading the myocytes, which can eventually result in the myocyte shortening during isovolumic relaxation and increased global wasted work (GWW). However, the exact mechanisms and consequences for the observed reduced cardiac inefficiency are unknown, and further work regarding the mechanisms underpinning the reduced efficiency following intense exercise is required.

In line with previous exercise studies, there were significant post-exercise reductions in 3D-derived LV end-diastolic, left atrial volumes, and alterations in diastolic function (6, 8, 43). A significantly increased post-exercise heart rate, reduced LV filling time and left-sided volumes may explain some of the observed alterations of the echocardiographic assessments performed just after exercise. The interactions between the left and right atria and ventricles are central in the post-exercise alterations in cardiac function (44). Altered loading conditions cause alterations in RV volumes and function with a subsequent impact on left atrial preload, LV filling, and LV function (43). In contrast to La Gerche et al. (43), the present study did not find significant alterations in RV function. There may be several explanations for this discrepancy. The study by La Gerche et al. found a more significant reduction in RV functions in athletes competing for a longer duration (up to 11 h). In the present study, exercise duration was significantly shorter. We, therefore, cannot exclude that alterations in right heart volumes and functions had an impact on the present findings.

The present study used two different workloads to assess the post-exercise response. The CPET was used to define the reference LV response to standardized exercise intensity, ensuring that all study individuals were exposed to an exercise of similar duration with the same metabolic demands (lactate threshold and max V02). Furthermore, the CPET allowed interpretation of the implications of the work performed during the race using power meters. The power meters indicated a substantial increase in the exercise above max VO2 level during the race, increasing the likelihood of developing myocardial inefficiency.

Impact of pre-exercise stress on myocardial work parameters

As indicated by the significant increase in blood pressure the day before the race, the race and the preparation for the next day may have induced a stress response in the race contenders. To adjust for this increased stress, echocardiographic parameters were corrected by using the pre-exercise measurements as a baseline, and the percentual change from each pre-exercise value assessed the difference in post-exercise parameters.

The present study demonstrates pre-exercise stress's impact on assessing resting echocardiographic parameters. SBP was higher before the race compared with the CPET. This increase in SBP affects the MW parameters, causing increased GWI and GCW compared with the assessment before the CPET. The increased blood pressure is most likely due to the mental stress caused by the competitive event, resulting in increased myocardial work before the race. The present study's findings underscore the impact of emotional stress on myocardial work and the need to consider the influence of emotional stress when baseline MW parameters are interpreted.

Limitations

The study provides insights into the longitudinal cardiac morphology changes and measures after prolonged exercise in middle-aged recreational athletes. The present study addresses morphological and functional changes in a population different from younger athletes, and the current findings may not apply to a younger population with a higher functional capacity. When calculating MW, we used SBP as a substitute for force; therefore, the use of pressure and strain does not provide a direct measure of work (wall thickness and radius of curvature are not included). Calculation of work is underestimated in dilated ventricles because of higher wall stress at any given LV pressure, and this could also be the case in our study, where study subjects had mildly dilated ventricles. Calculating the myocardial work parameters relies on global longitudinal strain measurements, systolic blood pressure, and valvular events. Small changes in the timing of valvular events could potentially lead to significant differences in the work parameters, especially the global wasted work and global work efficiency parameters. When assessing and evaluating these parameters, it is essential to be aware of these challenges.

Conclusion

Changes in left ventricular function, consistent with exercise-induced fatigue, were seen after both exercises with the varying workload. However, increased endurance exercise duration and workload, as performed at the race, were associated with decreased myocardial efficiency following exercise. When correcting for alterations in baseline parameters, there was no difference in LVEF and GLS comparing the two exercise workloads and durations. These findings suggest that myocardial work parameters may be more sensitive measures of myocardial inefficiency than traditional markers of systolic myocardial dysfunction.

Data availability statement

The raw data supporting the conclusions of this article will be made available by the authors, without undue reservation.

Ethics statement

The studies involving human participants were reviewed and approved by the Regional Ethics Committee (REK nr 2013/550). The patients/participants provided their written informed consent to participate in this study. Written informed consent was obtained from the individual(s) for the publication of any potentially identifiable images or data included in this article.

Author contributions

CE and SØ drafted the manuscript. CE, ØK, MB-B, VF, MC, LK, LD, TM, ØS, and SØ contributed to the data collection. CE and BA performed the statistical analyses. All authors contributed to drafting and critically revising the manuscript and approved the submitted version.

Funding

Data collection in 2018 was funded by grants from ConocoPhillips, the Simon Fougner Hartmanns Family Trust, the Western Norway Regional Health Authority, and GE Healthcare.

Acknowledgments

The authors thank GE Healthcare for providing state-of-the-art echocardiography machines and post-processing software for the study, Abbott Norway for supplying ECG equipment, Garmin Norway for providing sports watches and Stages for Power Meters for the study. The authors also thank ConocoPhillips and the Simon Fougner Hartmanns Family Trust for funding the study.

Conflict of interest

The authors declare that the research was conducted in the absence of any commercial or financial relationships that could be construed as a potential conflict of interest.

Publisher's note

Supplementary material

The Supplementary Material for this article can be found online at: https://www.frontiersin.org/articles/10.3389/fcvm.2022.1081664/full#supplementary-material

References

1. Wen C, Wai J, Tsai M, Yang Y, Cheng T, Lee M, et al. Minimum amount of physical activity for reduced mortality and extended life expectancy: a prospective cohort study. *Lancet.* (2011) 378:1244–53. doi: 10.1016/S0140-6736(11)60749-6

2. Blond K, Brinklov C, Ried-Larsen M, Crippa A, Grontved A. Association of high amounts of physical activity with mortality risk: a systematic review and meta-analysis. *Br J Sports Med.* (2020) 54:1195–201. doi: 10.1136/bjsports-2018-100393

3. Arem H, Moore S, Patel A, Hartge P, Berrington de Gonzalez A, Visvanathan K. Leisure time physical activity and mortality: a detailed pooled analysis of the dose-response relationship. *JAMA Intern Med.* (2015) 175:959–67. doi: 10.1001/jamainternmed.2015.0533

4. Nystoriak M, Bhatnagar A. Cardiovascular effects and benefits of exercise. *Front Cardiovasc Med.* (2018) 5:135. doi: 10.3389/fcvm.2018.00135

5. Schnohr P, O'Keefe J, Lavie C, Holtermann A, Lange P, Jensen G, et al. U-shaped association between duration of sports activities and mortality: copenhagen city heart study. *Mayo Clin Proc.* (2021) 96:3012–20. doi: 10.1016/j.mayocp.2021.05.028

6. Donaldson J, Wiles J, Coleman D, Papadakis M, Sharma R, O'Driscoll J. Left ventricular function and cardiac biomarker release-the influence of exercise intensity, duration and mode: a systematic review and meta-analysis. *Sports Med.* (2019) 49:1275–89. doi: 10.1007/s40279-019-01142-5

7. Elliott A, La Gerche A. The right ventricle following prolonged endurance exercise: are we overlooking the more important side of the heart? A meta-analysis. *Br J Sports Med.* (2015) 49:724–9. doi: 10.1136/bjsports-2014-093895

8. Lord R, Utomi V, Oxborough D, Curry B, Brown M, George K. Left ventricular function and mechanics following prolonged endurance exercise: an update and meta-analysis with insights from novel techniques. *Eur J Appl Physiol.* (2018) 118:1291–9. doi: 10.1007/s00421-018-3906-z

9. Oxborough D, Birch K, Shave R, George K. "Exercise-induced cardiac fatigue"– a review of the echocardiographic literature. *Echocardiography.* (2010) 27:1130–40. doi: 10.1111/j.1540-8175.2010.01251.x

10. Middleton N, Shave R, George K, Whyte G, Simpson R, Florida-James G, et al. Impact of repeated prolonged exercise bouts on cardiac function and biomarkers. *Med Sci Sports Exerc.* (2007) 39:83–90. doi: 10.1249/01.mss.0000239395.93578.60

11. Klaeboe L, Edvardsen T. Echocardiographic assessment of left ventricular systolic function. *J Echocardiogr.* (2019) 17:10–6. doi: 10.1007/s12574-018-0405-5

12. Yingchoncharoen T, Agarwal S, Popovic Z, Marwick T. Normal ranges of left ventricular strain: a meta-analysis. *J Am Soc Echocardiogr.* (2013) 26:185–91. doi: 10.1016/j.echo.2012.10.008

13. Boe E, Skulstad H, Smiseth O. Myocardial work by echocardiography: a novel method ready for clinical testing. *Eur Heart J Cardiovasc Imaging.* (2019) 20:18–20. doi: 10.1093/ehjci/jey156

14. Manganaro R, Marchetta S, Dulgheru R, Ilardi F, Sugimoto T, Robinet S, et al. Echocardiographic reference ranges for normal non-invasive myocardial work indices: results from the eacvi norre study. *Eur Heart J Cardiovasc Imaging.* (2019) 20:582–90. doi: 10.1093/ehjci/jey188

15. Morbach C, Sahiti F, Tiffe T, Cejka V, Eichner F, Gelbrich G, et al. Myocardial work - correlation patterns and reference values from the population-based staab cohort study. *PLoS One.* (2020) 15:e0239684. doi: 10.1371/journal.pone.0239684

16. Papadopoulos K, Ozden Tok O, Mitrousi K, Ikonomidis I. Myocardial work: methodology and clinical applications. *Diagnostics.* (2021) 11:573. doi: 10.3390/diagnostics11030573

17. Borrie A, Goggin C, Ershad S, Robinson W, Sasse A. Noninvasive myocardial work index: characterizing the normal and ischemic response to exercise. *J Am Soc Echocardiogr.* (2020) 33:1191–200. doi: 10.1016/j.echo.2020.05.003

18. Edwards N, Scalia G, Putrino A, Appadurai V, Sabapathy S, Anderson B, et al. Myocardial work and left ventricular contractile reserve during stress echocardiography: an angiographic validation. *Echocardiography.* (2021) 38:1711–21. doi: 10.1111/echo.15194

19. Kleiven O, Omland T, Skadberg O, Melberg T, Bjorkavoll-Bergseth M, Auestad B, et al. Race duration and blood pressure are major predictors of exercise-induced cardiac troponin elevation. *Int J Cardiol.* (2019) 283:1–8. doi: 10.1016/j.ijcard.2019.02.044

20. Skadberg O, Kleiven O, Bjorkavoll-Bergseth M, Melberg T, Bergseth R, Selvag J, et al. Highly increased troponin I levels following high-intensity endurance cycling may detect subclinical coronary artery disease in presumably healthy leisure sport cyclists: the north sea race endurance exercise study (needed) 2013. *Eur J Prev Cardiol.* (2017) 24:885–94. doi: 10.1177/2047487317693130

21. Aengevaeren V, Baggish A, Chung E, George K, Kleiven O, Mingels A, et al. Exercise-induced cardiac troponin elevations: from underlying mechanisms to clinical relevance. *Circulation.* (2021) 144:1955–72. doi: 10.1161/CIRCULATIONAHA.121.056208

22. Lang R, Badano L, Mor-Avi V, Afilalo J, Armstrong A, Ernande L, et al. Recommendations for cardiac chamber quantification by echocardiography in adults: an update from the american society of echocardiography and the European association of cardiovascular imaging. *Eur Heart J Cardiovasc Imaging.* (2015) 16:233–70. doi: 10.1093/ehjci/jev014

23. Badano L, Kolias T, Muraru D, Abraham T, Aurigemma G, Edvardsen T, et al. Standardization of left atrial, right ventricular, and right atrial deformation imaging using two-dimensional speckle tracking echocardiography: a consensus document of the EACVI/ASE/industry task force to standardize deformation imaging. *Eur Heart J Cardiovasc Imaging.* (2018) 19:591–600. doi: 10.1093/ehjci/jey042

24. Tran P, Maddock H, Banerjee P. Myocardial fatigue: a mechano-energetic concept in heart failure. *Curr Cardiol Rep.* (2022) 24:711–30. doi: 10.1007/s11886-022-01689-2

25. Charton M, Kervio G, Matelot D, Lachard T, Galli E, Donal E, et al. Exercise-induced cardiac fatigue in soldiers assessed by echocardiography. *Front Cardiovasc Med.* (2021) 8:785869. doi: 10.3389/fcvm.2021.785869

26. Middleton N, Shave R, George K, Whyte G, Hart E, Atkinson G. Left ventricular function immediately following prolonged exercise: a meta-analysis. *Med Sci Sports Exerc.* (2006) 38:681–7. doi: 10.1249/01.mss.0000210203.10200.12

27. Shave R, Oxborough D. Exercise-induced cardiac injury: evidence from novel imaging techniques and highly sensitive cardiac troponin assays. *Prog Cardiovasc Dis.* (2012) 54:407–15. doi: 10.1016/j.pcad.2012.01.007

28. D'Andrea A, Radmilovic J, Carbone A, Mandoli G, Santoro C, Evola V, et al. Speckle tracking evaluation in endurance athletes: the "optimal" myocardial work. *Int J Cardiovasc Imaging.* (2020) 36:1679–88. doi: 10.1007/s10554-020-01871-z

29. Ilardi F, D'Andrea A, D'Ascenzi F, Bandera F, Benfari G, Esposito R, et al. Myocardial work by echocardiography: principles and applications in clinical practice. *J Clin Med.* (2021) 10:4521. doi: 10.3390/jcm10194521

30. Tokodi, M, Olah A, Fabian A, Lakatos B, Hizoh I, Ruppert M, et al. Novel insights into the athlete's heart: is myocardial work the new champion of systolic function? *Eur Heart J Cardiovasc Imaging.* (2021) 23:188–97. doi: 10.1093/ehjci/jeab162

31. Sengupta S, Jain R, Burkule N, Olet S, Khandheria B. Myocardial work index: a novel method for assessment of myocardial function in south asian recreational athletes. *J Patient Cent Res Rev.* (2020) 7:147–56. doi: 10.17294/2330-0698.1730

32. Grassi B, Rossiter H, Zoladz J. Skeletal muscle fatigue and decreased efficiency: two sides of the same coin? *Exerc Sport Sci Rev.* (2015) 43:75–83. doi: 10.1249/JES.0000000000000043

33. Jones A, Grassi B, Christensen P, Krustrup P, Bangsbo J, Poole D. Slow component of Vo2 kinetics: mechanistic bases and practical applications. *Med Sci Sports Exerc.* (2011) 43:2046–62. doi: 10.1249/MSS.0b013e31821fcfc1

34. Zhou S, McKenna M, Lawson D, Morrison W, Fairweather I. Effects of fatigue and sprint training on electromechanical delay of knee extensor muscles. *Eur J Appl Physiol Occup Physiol.* (1996) 72:410–6. doi: 10.1007/BF00242269

35. Zhou S. Acute effect of repeated maximal isometric contraction on electromechanical delay of knee extensor muscle. *J Electromyogr Kinesiol.* (1996) 6:117–27. doi: 10.1016/1050-6411(95)00024-0

36. Chan-Dewar F, Oxborough D, Shave R, Gregson W, Whyte G, Noakes T, et al. Evidence of increased electro-mechanical delay in the left and right ventricle after prolonged exercise. *Eur J Appl Physiol.* (2010) 108:581–7. doi: 10.1007/s00421-009-1264-6

37. Sahlen A, Rubulis A, Winter R, Jacobsen P, Stahlberg M, Tornvall P, et al. Cardiac fatigue in long-distance runners is associated with ventricular repolarization abnormalities. *Heart Rhythm.* (2009) 6:512–9. doi: 10.1016/j.hrthm.2008.12.020

38. Brainin P, Biering-Sorensen S, Mogelvang R, de Knegt M, Olsen F, Galatius S, et al. Post-systolic shortening: normal values and association with validated echocardiographic and invasive measures of cardiac function. *Int J Cardiovasc Imaging.* (2019) 35:327–37. doi: 10.1007/s10554-018-1474-2

39. Li P, Zhang Y, Li L, Chen Y, Li Z, Liu S, et al. Assessment of left ventricular systolic function by non-invasive pressure-strain loop area in young male strength athletes. *Cardiovasc Ultrasound.* (2020) 18:45. doi: 10.1186/s12947-020-00227-w

40. Sengupta P, Korinek J, Belohlavek M, Narula J, Vannan M, Jahangir A, et al. Left ventricular structure and function: basic science for cardiac imaging. *J Am Coll Cardiol.* (2006) 48:1988–2001. doi: 10.1016/j.jacc.2006.08.030

41. Bloechlinger S, Grander W, Bryner J, Dunser M. Left ventricular rotation: a neglected aspect of the cardiac cycle. *Intensive Care Med.* (2011) 37:156–63. doi: 10.1007/s00134-010-2053-8

42. Park S, Miyazaki C, Bruce C, Ommen S, Miller F, Oh J. Left ventricular torsion by two-dimensional speckle tracking echocardiography in patients with diastolic dysfunction and normal ejection fraction. *J Am Soc Echocardiogr.* (2008) 21:1129–37. doi: 10.1016/j.echo.2008.04.002

43. La Gerche A, Burns A, Mooney D, Inder W, Taylor A, Bogaert J, et al. Exercise-induced right ventricular dysfunction and structural remodelling in endurance athletes. *Eur Heart J.* (2012) 33:998–1006. doi: 10.1093/eurheartj/ehr397

44. La Gerche A, Rakhit D, Claessen G. Exercise and the right ventricle: a potential Achilles' heel. *Cardiovasc Res.* (2017) 113:1499–508. doi: 10.1093/cvr/cvx156

Frontiers in Cardiovascular Medicine

TYPE Original Research
PUBLISHED 13 January 2023
DOI 10.3389/fcvm.2022.1071249

Identification of early cardiac dysfunction and heterogeneity after pressure and volume overload in mice by high-frequency echocardiographic strain imaging

Ran Xu[1†], Zhiwen Ding[1†], Hao Li[2], Jing Shi[1,3], Leilei Cheng[1,3], Huixiong Xu[4], Jian Wu[1]* and Yunzeng Zou[1]*

[1]Shanghai Institute of Cardiovascular Diseases, Zhongshan Hospital and Institutes of Biomedical Sciences, Fudan University, Shanghai, China, [2]State Key Laboratory of Cardiovascular Disease, Fuwai Hospital, National Center for Cardiovascular Diseases, Chinese Academy of Medical Sciences and Peking Union Medical College, Beijing, China, [3]Department of Echocardiography, Zhongshan Hospital, Fudan University, Shanghai, China, [4]Department of Ultrasound, Zhongshan Hospital, Fudan University, Shanghai, China

Object: Aortic stenosis and regurgitation are clinically important conditions characterized with different hypertrophic types induced by pressure or volume overload, respectively, but with comparable cardiac function in compensated stage. Speckle-tracking based strain imaging has been applied to assess subtle alterations in cardiac abnormality, but its application in differentiating these two types of ventricular hypertrophy is still sparse. Here, we performed strain imaging analysis of cardiac remodeling in these two loading conditions.

Methods: C57BL/6J mice were subjected to transverse aortic constriction (TAC)-induced pressure overload or aortic regurgitation (AR)-induced volume overload. Conventional echocardiography and strain imaging were comprehensively assessed to detect stimulus-specific alterations in TAC and AR hearts.

Results: Conventional echocardiography did not detect significant changes in left ventricular systolic (ejection fraction and fractional shortening) and diastolic (E/E′) function in either TAC or AR mice. On the contrary, global strain analysis revealed global longitudinal strain and strain rate were remarkably impaired in TAC while preserved in AR mice, although global radial, and circumferential strain and strain rate were significantly reduced in both models. Regional strain analysis in the long axis demonstrated that longitudinal strain and strain rate in all or most segments were decreased in TAC but maintained or slightly dented in AR mice, while radial strain and strain rate indicated overt decline in both models. Moreover, decreased radial and circumferential strain and strain rate were observed in most segments of TAC and AR mice in the short axis.

Conclusion: Strain imaging is superior to conventional echocardiography to detect subtle changes in myocardial deformation, with longitudinal strain and strain rate indicating distinct functional changes in pressure versus volume overload myocardial hypertrophy, making it potentially an advanced approach for early detection and differential diagnosis of cardiac dysfunction.

KEYWORDS

strain imaging, transverse aortic constriction, aortic regurgitation, left ventricle, pressure overload, volume overload

EDITED BY
Artur Dziewierz,
Jagiellonian University Medical College, Poland

REVIEWED BY
Stefano Carugo,
IRCCS Ca' Granda Foundation Maggiore Policlinico Hospital, Italy
Diego Fanti,
Integrated University Hospital Verona, Italy

*CORRESPONDENCE
Jian Wu
✉ wu.jian@zs-hospital.sh.cn
Yunzeng Zou
✉ zou.yunzeng@zs-hospital.sh.cn

†These authors have contributed equally to this work

SPECIALTY SECTION
This article was submitted to Cardiovascular Imaging, a section of the journal Frontiers in Cardiovascular Medicine

RECEIVED 16 October 2022
ACCEPTED 30 December 2022
PUBLISHED 13 January 2023

CITATION
Xu R, Ding Z, Li H, Shi J, Cheng L, Xu H, Wu J and Zou Y (2023) Identification of early cardiac dysfunction and heterogeneity after pressure and volume overload in mice by high-frequency echocardiographic strain imaging.
Front. Cardiovasc. Med. 9:1071249.
doi: 10.3389/fcvm.2022.1071249

1. Introduction

Heart failure is a leading cause of morbidity and mortality worldwide, with cardiac hypertrophy as its independent risk factor (1, 2). Pressure overload induced by hypertension and aortic stenosis and volume overload induced by valve regurgitation are clinically important pathogenesis to induce cardiac hypertrophy that are increasingly common in the aging world population. Although both pressure overload and volume overload are characterized with increased mechanical overload, they present distinct hypertrophy types, in which pressure overload causes concentric hypertrophy while volume overload induces eccentric hypertrophy. It is recently found that regression of heart failure is associated with early normalization of ventricular hypertrophy that precedes restoration of cardiac function (2). It is therefore especially important to monitor left ventricular (LV) function to determine the efficacy of therapies.

Conventional echocardiography is widely used to evaluate cardiac function and the severity of heart damage due to its non-invasive and easily available feature. However, conventional LV function indexes such as ejection fraction (LVEF) and fractional shortening (LVFS) are not able to discriminate between the two types of LV hypertrophy (3, 4). Our recent study demonstrates that in compensated phase, LVEF and LVFS are preserved in mice with pressure overload and volume overload (4). Thus, there is an urgent need to identify early functional deficiency and further undertake comparative analysis in LV hypertrophy under pressure and volume overload.

Echocardiographic speckle-tracking based strain imaging, also known as deformation imaging, is a technological advancement that has been developed to objectively quantify global and regional myocardial function (5, 6). Strain imaging has emerged as a promising means for the evaluation of myocardial function both in humans and animal models, being superior to the conventional echocardiographic measurements (7–10). Previous studies have shown that the indexes derived from strain imaging are consistent with the parameters of cardiac magnetic resonance in assessing cardiac volume and ejection fraction (11, 12). In addition, there is a good correlation between strain imaging derived-metrics and invasive cardiac hemodynamic measurements in the evaluation of heart function (13, 14). With the advancement of high frequency ultrasound, the strain imaging has been applied to murine models of myocardial infarction (15), pressure overload (16), and aging (10). However, few studies have ever evaluated the strain imaging of ventricular hypertrophy under volume overload, in comparison with that under pressure overload. In this study, we aim to utilize the speckle-tracking based strain imaging to evaluate cardiac dysfunction in mouse models of pressure overload and volume overload, and to elaborate the differences in LV myocardial activities between these two pathophysiological conditions.

2. Materials and methods

2.1. Animal models

The animal study protocol was approved by Animal Care and Use Committee of Zhongshan Hospital, Fudan University and were in accordance with National Institutes of Health Guide for the Care and Use of Laboratory Animals (No. 85-23, revised 1996, Bethesda, MD, USA). Adult C57BL/6J male mice (10–12 weeks old) were obtained from the Shanghai Branch of the National Rodent Laboratory Animal Resources (Shanghai, China). Animals were fed at 24 ± 2°C with 12 h-light/12 h-dark cycles. We used transverse aortic constriction (TAC) model and aortic regurgitation (AR) model to induce pressure overload and volume overload, respectively, as we described previously (4). Mice were randomly assigned into four groups: Sham-T group (sham TAC operation, $n = 8$), TAC group ($n = 12$), Sham-A group (sham AR operation, $n = 8$), and AR group ($n = 12$). Briefly, surgeries were performed under mixed anesthesia (i.p. 150 mg/kg ketamine and 10 mg/kg xylazine). For TAC model, 27-gauge needle were placed on the aorta between the innominate artery and the left common carotid artery. After ligated with 6–0 silk, the needle was removed to generate aortic constriction. The Sham-T group underwent a similar surgical procedure but without the ligation. For AR model, a flexible catheter containing a metal wire was inserted into the right common carotid artery and advanced to the aortic orifice under the guidance of ultrasound imaging, and then the metal wire was pushed to puncture the aortic valvular cusp repeatedly. When Doppler ultrasound showed diastolic flow reversal [around 400 mm/sec, we chose this peak velocity to ensure the mean LV wall stress was similar in both TAC and AR mice (4, 17)] at the aortic arch, the catheter with wire were withdrawn. The Sham-A group was performed the same procedure but without puncturing the aortic valve. We chose two weeks post-surgery as the end point of the observation, because our preliminary study showed that the compensated cardiac hypertrophy was observed 2 weeks after surgeries of TAC and AR, with LVEF and LVFS comparable between the mice with pressure/volume overload and the sham-operated controls (4).

2.2. Conventional echocardiography

Transthoracic echocardiography was performed 2 weeks after surgery. Briefly, mice were placed on a heating pad to maintain temperature at 37°C and limb electrodes were used to record the electrocardiogram. Mice were anesthetized with 1.5% isoflurane to keep the heart rate (HR) above 450 beats per minute during the procedure. Echocardiographic parameters were acquired from the Vevo 2100 system (VisualSonics, Toronto, Canada) with a 30 MHz transducer. B-model and M-mode images were obtained in parasternal long-axis view and mid-papillary level short-axis view. Then conventional echocardiographic parameters were measured or calculated as follows: LVEF, LVFS, LV internal dimension in systole and diastole (LVIDs and LVIDd), LV posterior wall thickness in systole and diastole (LVPWs and LVPWd), LV end-systolic and end-diastolic volume (LVESV and LVEDV) (**Table 1**). Moreover, pulsed wave Doppler was performed at the tip of the mitral leaflet in the apical four-chamber view. By simultaneously recording the mitral inflow curves, peak velocity of the early ventricular filling wave (E wave) and tissue Doppler mitral annular velocity, ratio of E wave to E' wave (E/E'), isovolumic relaxation time (IVRT), isovolumic contraction time (IVCT), and ejection time (ET) were evaluated (**Figure 1**). Considering merged mitral E and A waves were found in most cases of AR mice, which has been similarly reported in mice with AR or other heart diseases (18, 19), we

TABLE 1 **Conventional echocardiographic characteristics of mice subjected to pressure or volume overload.**

Parameter	Sham-T (n = 8)	TAC (n = 7)	P-value	Sham-A (n = 8)	AR (n = 9)	P-value
HR (bpm)	542 ± 4	532 ± 6	0.07449	551 ± 13	547 ± 13	0.8057
PSVa (mm/s)	911.73 ± 67.99	3785.05 ± 227.84**	**1.098E-13	970.44 ± 91.54	1442.65 ± 103.46**	**0.000000126
PDVa (mm/s)	0.00 ± 0.00	0.00 ± 0.00	/	0.00 ± 0.00	427.88 ± 67.52	/
HW/BW	4.68 ± 0.15	6.19 ± 0.04*	*0.0219	4.37 ± 0.06	6.54 ± 0.15*	*0.012
EF (%)	60.05 ± 1.76	58.08 ± 1.77	0.371	61.99 ± 1.51	59.58 ± 1.02	0.0667
FS (%)	32.77 ± 2.64	31.68 ± 1.16	0.384	33.17 ± 1.03	31.79 ± 0.72	0.141
LVIDd (mm)	4.11 ± 0.12	4.17 ± 0.23	0.719	4.11 ± 0.15	4.99 ± 0.25**##	**0.000172 ##0.000418
LVIDs (mm)	2.81 ± 0.23	3.28 ± 0.28	0.078	2.81 ± 0.17	4.03 ± 0.17**##	**0.00000371 ##0.00158
LVPWd (mm)	0.71 ± 0.04	1.05 ± 0.12**	**0.0000571	0.74 ± 0.02	0.81 ± 0.08##	##0.00157
LVPWs (mm)	1.09 ± 0.13	1.31 ± 0.06*	*0.0495	1.14 ± 0.08	1.01 ± 0.05##	##0.00321
LVEDV (μl)	72.00 ± 2.38	76.66 ± 7.59	0.487	75.53 ± 1.67	111.25 ± 5.44**##	**0.00000786 ##0.000306
LVESV (μl)	23.60 ± 1.30	46.95 ± 3.30**	**0.00481	30.22 ± 1.05	75.00 ± 7.02**##	**0.00000913 ##0.000413
E/E’	26.66 ± 1.58	39.66 ± 2.76**	**0.000404	27.56 ± 1.47	35.34 ± 5.62**	**0.00471
IVRT (ms)	14.10 ± 0.78	13.26 ± 1.70*	*0.0206	14.37 ± 1.03	15.54 ± 1.48##	##0.00264
IVCT (ms)	10.00 ± 1.66	11.58 ± 0.54	0.0698	10.62 ± 1.23	15.58 ± 0.96**##	**0.0000590 ##0.00125
ET (ms)	49.72 ± 3.98	51.67 ± 4.41	0.826	51.66 ± 2.96	54.17 ± 2.57##	##0.0067
Tei index	0.50 ± 0.14	0.47 ± 0.01	0.681	0.56 ± 0.13	0.60 ± 0.04##	##0.000244

HR, heart rate; PSVa and PDVa, peak velocities of aortic arch flow in systole and diastole; HW/BW, heart weight/body rate; EF, ejection fraction; FS, fractional shortening; LVIDd and LVIDs, left ventricular internal dimension in diastole and systole; LVPWd and LVPWs, left ventricular posterior wall thickness in diastole and systole; LVEDV and LVESV, left ventricular end-diastolic and end-systolic volume; E/E’, ratio of mitral valve early diastolic maximum velocity to peak mitral annular velocity during early filling; IVRT, isovolumic relaxation time; IVCT, isovolumic contraction time; ET, ejection time. All values are represented as Mean ± SD.

$^{*}P < 0.05$ vs. corresponding Sham; $^{**}P < 0.01$ vs. corresponding Sham; $^{\#\#}P < 0.01$ vs. TAC. Italic values represent the statistical values.

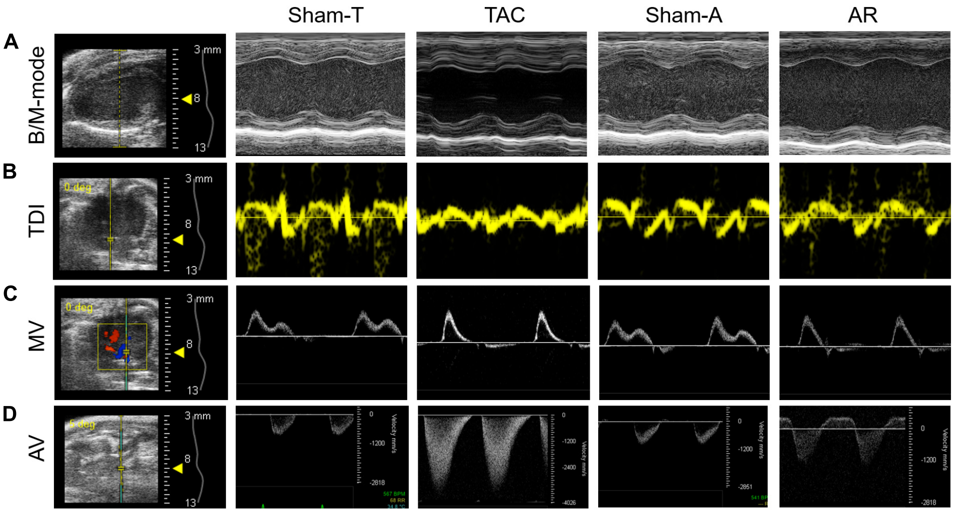

FIGURE 1

Representative images of conventional echocardiography. **(A)** Mouse B-mode and M-mode images of left ventricle in long-axis view. **(B,C)** Tissue Doppler imaging (TDI) and mitral valve (MV) Doppler was performed to record mitral annular velocity and mitral inflow curves. **(D)** Aortic valve (AV) Doppler was conducted to generate aortic arch flow in systole and diastole. Sham-T, sham TAC operation; TAC, transverse aortic constriction; Sham-A, sham AR operation; AR, aortic regurgitation.

used E/E’ to assess diastolic function as described previously (20). Meanwhile, Tei index was calculated by the following formula: Tei index = (IVRT + IVCT)/ET, as we previously reported (18). To confirm successful establishment of TAC and AR, the peak velocities of aortic arch flow in systole (PSVa) and diastole (PDVa) were recorded, respectively.

2.3. Speckle tracking based strain imaging

The strain imaging analysis was performed using VevoStrain software in an offline workstation (VisualSonics Inc., Toronto, Canada) on the aforementioned B-mode image cineloop acquired at a frame rate higher than 200 fps. Global and regional strain and strain rate were calculated by tracking the movement of endocardium and epicardium border in three consecutive cardiac cycles. Global longitudinal strain (GLS), radial strain (GRS), circumferential strain (GCS), longitudinal strain rate (GLSR), radial strain rate (GRSR), and circumferential strain rate (GCSR) were calculated (**Figure 2**). In addition to global measurements, regional myocardial strain was available for the six wall segments of the LV automatically assigned by the computer either in the long or short axis view (**Figure 3**). In the long axis, LV wall was divided into basal posterior (BP), mid posterior (MP), apical posterior (AP), apical anterior (AA), mid anterior (MA), and basal anterior (BA). In the short axis view at mid-papillary level, LV wall was divided into anterior free wall (AFW), lateral wall (LW), posterior wall (PW), inferior free wall (IFW), posterior septum (PS), and anterior septum (AS). All measurements were repeated three times and data processing was performed by a blinded investigator.

2.4. Intra and inter-observer variability

The original investigator re-analyzed the echocardiography data at an interval of two weeks to assess the intra-observer variability. Two different observers analyzed the same data to determine the inter-observer variability. Data are presented as means of the absolute differences between measurements and by the interclass correlation coefficient (ICC).

2.5. Statistics

All data are presented as means ± standard deviation. All statistical results were obtained using GraphPad Prism v6 (GraphPad Software, San Diego, CA, USA). The continuous variable between two groups were compared by Student's *t*-test. Multiple comparisons were conducted by one-way analysis of variance (ANOVA) with the Student-Newman-Keuls (S-N-K) test. The conventional echocardiographic assessment had good inter- and intraobserver agreement, as we reported previously (2, 4, 18). Inter- and intraobserver variability of strain related parameters was assessed by ICC using a two-way mixed model with absolute agreement. $P < 0.05$ was considered statistically significant.

3. Results

3.1. Conventional echocardiography demonstrates preserved systolic function but impaired diastolic function in pressure overload and volume overload mice

Conventional echocardiography was performed to recapitulate the structural and functional changes in TAC and AR murine hearts. Two weeks post-operation, PSVa or PDVa was satisfactorily elevated in TAC or AR mice, respectively (**Table 1**), indicating pressure overload or volume overload model was successfully established. The heart weight/body weight ratio (HW/BW) was comparably increased in TAC and AR mice. In TAC group, LVPW was remarkably increased compared to Sham-T animals, whereas LVID showed no significant changes, indicating concentric cardiac hypertrophy (**Table 1**). On the contrary, in AR group, LVPW was comparable to Sham-A counterparts, while LVID was robustly enlarged, suggesting eccentric cardiac hypertrophy (**Table 1**).

Compared with their corresponding sham mice, both TAC and AR mice showed preserved systolic function as evidenced by comparable LVEF and LVFS. As a sensitive marker for cardiac diastolic function, E/E' were prolonged in both TAC and AR mice compared to corresponding sham group. As for other parameters of diastolic function, IVRT was decreased in TAC group, whereas it showed a trend of increase but without statistical significance in AR mice. Intriguingly, IVCT was more increased than ET in AR versus TAC mice, leading to an increase in Tei index in AR mice.

3.2. Global strain analysis shows more compromised function in TAC mice compared with AR mice

To analyze both inter-observer and test–retest intra-observer reliability of strain related parameters, ICC were calculated and demonstrated in **Table 2**. All ICC coefficients were greater than 0.80, indicating a satisfactory inter- and intra-observer test–retest reliability.

The LV undergoes a complex pattern of deformation which can be examined in the longitudinal, radial, and circumferential directions in both systole and diastole (15). Strain imaging analyses trace the endocardium and epicardium frame-to-frame during the cine loop of cardiac cycles, providing assessment of the global and regional deformation reflected by strain and strain rate in each of these directions. Representative longitudinal, radial and circumferential curves from TAC and AR mice are shown in **Figures 2A–C**. Analysis was conducted to differentiate global myocardial deformation between TAC and AR mice. In TAC animals, strain measurements revealed that GRS and GLS obtained from parasternal long axis were significantly reduced relative to the corresponding parameters in Sham-T mice. However, in AR group, only GRS from parasternal long axis was decreased versus sham-A animals, while GLS showed no significant differences between AR and sham-operated animals (**Figures 2D, F**). In addition, GRS and GCS in short axis were significantly reduced in both TAC and AR group (**Figures 2H, J**). The GRSR, GLSR, and GCSR showed similar results corresponding to their specific global strain measures in the two models (**Figures 2E, G, I, K**).

3.3. Regional strain analysis unveils different pattern of myocardial dysfunction between pressure overload and volume overload models

Strain imaging allows the assessment of regional myocardial function by dividing the LV into six distinct segments in the short-

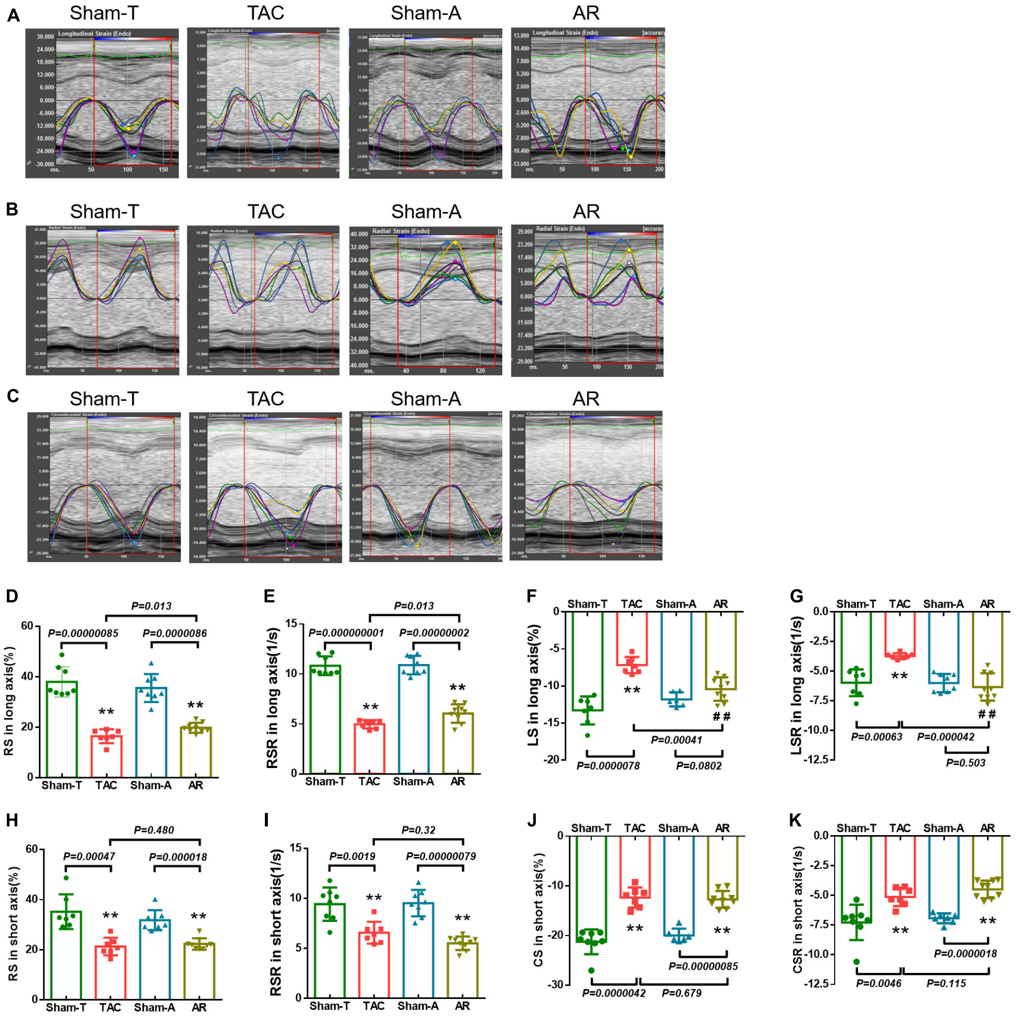

FIGURE 2
Strain and strain rate in pressure overload and volume overload models. **(A–C)** Representative longitudinal, radial and circumferential strain curves, and time-to-peak analysis in different models. **(D,E)** Global radial strain (GRS) and strain rate (GRSR) in long axis; **(F,G)** global longitudinal strain (GLS) and strain rate (GLSR) in long axis; **(H,I)** GRS and GRSR in short axis; **(J,K)** global circumferential strain (GCS) and strain rate (GCSR) in short axis. Data are shown as mean ± SD. $^{**}P < 0.01$, compared with corresponding sham-operated group. $^{\#\#}P < 0.01$, compared with TAC group.

and long-axis (Figure 3A). In order to further investigate the nuanced differences in LV dysfunction caused by TAC and AR, strain and strain rate of each segment were analyzed. Consistent with the results of global strain analysis, RS and RSR of all segments in the long axis were decreased in both TAC and AR groups, whereas the former owned more reduction in MP and AP (Figures 3B, D). Moreover, compared with corresponding sham-operated groups, decreased LS was observed in all segments except BA region in both TAC and AR mice, and the decrease was more pronounced in TAC mice. LSR decreased greatly in BP, MP, and BA region only in TAC group, while no significant alterations were detected in AR group, although LSR showed a declining trend with no statistical significance (Figures 3C, E).

Consistently, in both TAC and AR mice, regional strain analysis in short axis also revealed decreased RS and RSR in most segments, with the exception of AS segment, in which RS and RSR were comparable among all groups. (Figures 3F, H). CS and CSR of the two group were significantly decreased in PW, IFW, PS, and AS (Figures 3G, I). Specifically, CS and CSR changes in PW and IFW segments were slightly more dented in AR model than TAC model (Figures 3G, I). CS and CSR were largely preserved in AFW and LW in both murine models (Figures 3G, I).

3.4. Observer variability data

Intra- and interobserver variability of speckle tracing data are analyzed and shown in Table 2. In general, these results revealed acceptable intra- and interobserver variabilities.

4. Discussion

In this study, speckle tracking based strain imaging was employed to comparatively assess the cardiac function in mouse models of pressure overload and volume overload. Our results revealed that in compensated cardiac remodeling reflected by preserved LVEF and LVFS, strain imaging could detect early subtle changes in myocardial deformation and cardiac function, and LS and LSR could be used to distinguish functional changes in

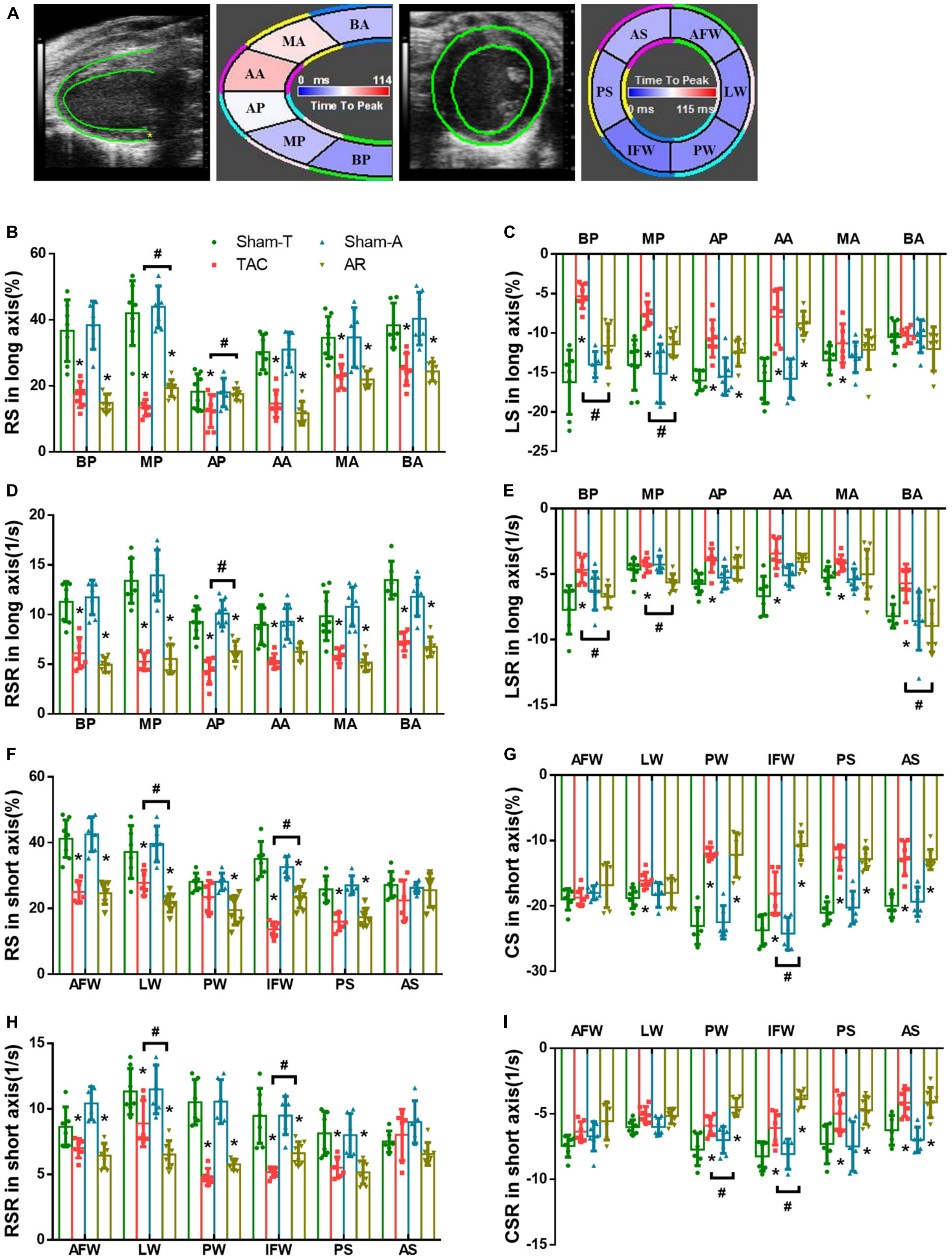

FIGURE 3

Comparison of changes in regional strain in pressure overload and volume overload mice. **(A)** Tracing the border of endocardium and epicardium and six segments of myocardium in both the long and short axis; BA, basal anterior; MA, mid anterior; AA, apical anterior; AP, apical posterior; MP, mid posterior; BP, basal posterior; AS, anterior septum; PS, posterior septum; IFW, inferior free wall; PW, posterior wall; LW, lateral wall; AFW, anterior free wall; **(B,C)** RS and LS in long axis; **(D,E)** RSR and LSR in long axis; **(F,G)** RS and CS in short axis; **(H,I)** RSR and CSR in short axis; BP, basal posterior; MP, mid posterior; AP, apical posterior; BA, basal anterior; MA, mid anterior; AA, apical anterior; AFW, anterior free wall; LW, lateral wall; PW, posterior wall; IFW, inferior free wall; PS, posterior septum; AS, anterior septum. Data are shown as Mean ± SD. $^{*}P < 0.05$, compared with corresponding sham group. $^{\#}P < 0.05$, compared with TAC group.

myocardial hypertrophy induced by different mechanical overload, being more sensitive than the conventional echocardiographic measurements.

Although conventional echocardiography parameters, such as LVEF, LVFS, and E/E', are widely used in assessing cardiac structure and function in clinical and basic studies, it reflects the overall

TABLE 2 Intra- and interobserver variability of strain parameters.

	Longitudinal strain	Radial strain	Circumferential strain
Mean	−15.86 ± 8.21	−33.45 ± 8.74	−20.55 ± 2.46
Intraobserver variability			
Mean absolute difference, %	5.93 ± 4.58	3.23 ± 2.21	2.25 ± 1.21
ICC	0.97	0.95	0.94
Interobserver variability			
Mean absolute difference, %	8.46 ± 3.66	5.52 ± 2.80	2.39 ± 2.28
ICC	0.88	0.93	0.97

Values are means ± SE. ICC, interclass correlation coefficient.

performance of heart and lacks sufficient sensitivity to reflect subtle cardiac function (10, 15, 21). Thus, changes detected by conventional echocardiography are often considered late manifestations of disease (15), making it difficult to identify early changes in cardiac function of the two types of hypertrophic hearts, for both pressure overload and volume overload induced cardiac remodeling characterized by myocyte enlargement and loss, fibrosis, metabolic abnormalities, and mitochondrial dysfunction, in "compensated" cardiac hypertrophy (22). Nevertheless, in clinical practice, subtle abnormalities in myocardial activity are typically uncovered by strain imaging even in the setting of normal cardiac function by conventional measures (21). Myocardial strain measurement was associated with subclinical ventricular dysfunction and the outcome in patients with aortic stenosis and preserved LVEF (22, 23). Moreover, strain analysis was applied to assess the left ventricular contraction patterns and the severity of cardiac remodeling in patients with chronic aortic regurgitation and preserved ejection fraction (24, 25). In basic studies, recently developed strain imaging designed specifically for rodents allows for early detection of intrinsic myocardial dysfunction in the setting of pressure overload, myocardial infarction, aging, and epirubicin treatment (6, 10, 15, 26). We in this study further found that when LVEF and LVFS remained normal, the strain and strain rate in radial and circumferential direction were decreased in both TAC and AR mice, suggestive of higher sensitivity and superiority of strain imaging over conventional echocardiography in murine models of mechanical stress.

Strain analysis is based on combined speckle tracking algorithms, thus strain and strain rate are supposed to reflect the global and regional myocardial function (14, 27). In this study, we found that LS and LSR were decreased evidently in TAC mice but largely unchanged in AR mice. Our findings suggest that LS and LSR could be used to distinguish the effects of different types of mechanical overload. It is documented that LS related parameters mainly depend on the condition of sub-endocardial myofibers and thus reflects the subendocardial status (6, 28). Recent studies further reported that LS is a particularly sensitive marker of the subendocardial myofiber dysfunction that occurs early during hypoperfusion or mechanical stress (15, 29). Coincidingly, previous studies from us and others indicate lateral hypertrophy in TAC cardiomyocytes while longitudinal hypertrophy in AR cardiomyocytes (3, 18). Thus, the stimulus-specific remodeling pattern of cardiomyocytes may contribute to the difference of LS related parameters in these two models.

Myocardial fibrosis defined as excessive deposition of extracellular matrix proteins, including collagens, is another conspicuous characteristic in the hearts of mechanical overload (30). Fibrosis increases ventricular stiffness and diffusion distance of oxygen to cardiomyocytes, leading to impaired cardiac function (3, 30). Previous comparative studies, including ours, demonstrate more prominent cardiac fibrosis is in TAC versus AR hearts (3, 4, 18). Based on these, we speculated that the distinguishing effect of LS and LSR may be closely associated with differential fibrosis between pressure and volume overload hearts. In addition, Bi and colleagues recently demonstrated in epirubicin treated mice that the collagen content in sub-endocardial layer was more prominent and LS was more reduced compared with that in sub-epicardial layer (6), strengthening the notion that LS and LSR served as the most specific indicator of all strain indexes.

Pressure overload and volume overload induce concentric and eccentric hypertrophy, respectively (4). The two types of cardiac hypertrophy also manifest different sensitivity and outcomes to similar therapeutics (3, 18). It is still controversial that which type is more maladaptive than the other. Several studies have suggested that volume overload is more harmful to the ventricle, because an augmentation of end-diastolic dimension and wall stress is already presented in the compensated phase of aortic regurgitation (21). On the other hand, other studies, including one from ours, have proposed that pressure overload is more detrimental, as pressure overload causes more fibrosis. The more prominent fibrosis in TAC mice is supposed to be associated with more activation of pro-hypertrophy effectors including Ca^{2+}/calmodulin-dependent protein kinase II (CaMKII) (4), which induces NLRP3 inflammasome activation in response to pressure overload (31). The novelty of this study is to investigate this issue by a direct comparison using state-of-the-art strain imaging, and unveil that LS and LSR are reduced in pressure rather than volume overload cardiac hypertrophy. Our findings thus support the notion that volume overload induces a more benign phenotype of cardiac hypertrophy.

4.1. Limitations

A comparative exploration in the association between cardiac fibrosis and strain alteration would more comprehensively elucidate the role of fibrosis in the discrepancy of strain changes between TAC and AR hearts. However, our previous study showed that cardiac fibrosis was more prominent in TAC heart and suggested that fibrosis contributed to the discrepancy. More in-depth analyses in different sections (such as sub-endocardial layer versus sub-epicardial layer) are warranted in future studies.

5. Conclusion

By using high frequency ultrasound, we successfully undertake global and regional strain analyses in mouse models of pressure overload and volume overload cardiac hypertrophy, and discover that reduction of strain and strain rate precedes changes of conventional echocardiographic parameters such as LVEF and LVFS. Pressure overload causes more reduction of strain and strain rate than volume overload, identifying LS and LSR as the most specific indicator of all strain indexes to differentiate left ventricular functional changes under distinct mechanical overload. The stimulus-specific heterogeneity in strain measurements makes it a sensitive approach for early detection of myocardial dysfunction in mechanistic and pharmacological studies.

Data availability statement

The original contributions presented in this study are included in this article/supplementary material, further inquiries can be directed to the corresponding authors.

Ethics statement

The animal study protocol was approved by Animal Care and Use Committee of Zhongshan Hospital, Fudan University and were in accordance with National Institutes of Health Guide for the Care and Use of Laboratory Animals (No. 85-23, revised 1996, Bethesda, MD, USA).

Author contributions

JW, YZ, and RX designed the study. RX, ZD, and JW predominantly performed echocardiography and data collection. RX, ZD, HL, JS, and LC analyzed the data. RX and ZD wrote the manuscript. HX, JW, and YZ revised the manuscript and provided critical advice. All authors read and approved the final version of the manuscript.

Funding

This work was supported by the National Natural Science Foundation of China (81730009, 81941002, 82170389, and 81900245) and Laboratory Animal Science Foundation of Science and Technology Commission of Shanghai Municipality (201409004300 and 21140904400).

Acknowledgments

We thank Yu-Qing Zhou (Translational Biology and Engineering Program, Ted Rogers Centre for Heart Research, Toronto, Canada) and Fan Su (Fujifilm VisualSonics Inc., Shanghai, China) for their excellent guidance on mouse model evaluation and strain analysis.

Conflict of interest

The authors declare that the research was conducted in the absence of any commercial or financial relationships that could be construed as a potential conflict of interest.

Publisher's note

References

1. Braunwald E. The war against heart failure: the lancet lecture. *Lancet.* (2015) 385:812–24. doi: 10.1016/S0140-6736(14)61889-4

2. Wu J, Dai F, Li C, Zou Y. Gender differences in cardiac hypertrophy. *J Cardiovasc Transl Res.* (2020) 13:73–84. doi: 10.1007/s12265-019-09907-z

3. Toischer K, Rokita A, Unsöld B, Zhu W, Kararigas G, Sossalla S, et al. Differential cardiac remodeling in preload versus afterload. *Circulation.* (2010) 122:993–1003. doi: 10.1161/CIRCULATIONAHA.110.943431

4. You J, Wu J, Zhang Q, Ye Y, Wang S, Huang J, et al. Differential cardiac hypertrophy and signaling pathways in pressure versus volume overload. *Am J Physiol Heart Circ Physiol.* (2018) 314:H552–62. doi: 10.1152/ajpheart.00212.2017

5. Tanaka H, Hara H, Saba S, Gorcsan J III. Usefulness of three-dimensional speckle tracking strain to quantify dyssynchrony and the site of latest mechanical activation. *Am J Cardiol.* (2010) 105:235–42. doi: 10.1016/j.amjcard.2009.09.010

6. Bi L, Zhang H, Han R, Chen W, Zhao N. Application of a combination of echocardiographic techniques in an experimental model of epirubicin-induced cardiotoxicity. *Int J Cardiovasc Imaging.* (2020) 36:841–54. doi: 10.1007/s10554-020-01777-w

7. Stoichescu-Hogea G, Buleu F, Christodorescu R, Sosdean R, Tudor A, Ember A, et al. Contribution of global and regional longitudinal strain for clinical assessment of HFpEF in coronary and hypertensive patients. *Medicina.* (2021) 57:1372.

8. Shehta M, Rayan M, Fahmy N, Onsy A, Bastawy I. Global longitudinal strain detects subtle left ventricular systolic dysfunction in duchenne muscular dystrophy patients and carriers. *Egypt Heart J.* (2021) 73:91. doi: 10.1186/s43044-021-00214-0

9. Earl C, Damen F, Yin M, Aasa K, Burris S, Goergen C. Strain estimation of the murine right ventricle using high-frequency speckle-tracking ultrasound. *Ultrasound Med Biol.* (2021) 47:3291–300. doi: 10.1016/j.ultrasmedbio.2021.07.001

10. de Lucia C, Wallner M, Eaton D, Zhao H, Houser S, Koch W. Echocardiographic strain analysis for the early detection of left ventricular systolic/diastolic dysfunction and dyssynchrony in a mouse model of physiological aging. *J Gerontol A Biol Sci Med Sci.* (2019) 74:455–61. doi: 10.1093/gerona/gly139

11. Chinali M, Franceschini A, Ciancarella P, Lisignoli V, Curione D, Ciliberti P, et al. Echocardiographic two-dimensional speckle tracking identifies acute regional myocardial edema and sub-acute fibrosis in pediatric focal myocarditis with normal ejection fraction: comparison with cardiac magnetic resonance. *Sci Rep.* (2020) 10:11321. doi: 10.1038/s41598-020-68048-5

12. Li Y, Zhang L, Gao Y, Wan X, Xiao Q, Zhang Y, et al. Comprehensive assessment of right ventricular function by three-dimensional speckle-tracking echocardiography: comparisons with cardiac magnetic resonance imaging. *J Am Soc Echocardiogr.* (2021) 34:472–82. doi: 10.1016/j.echo.2020.12.013

13. Ferferieva V, Van den Bergh A, Claus P, Jasaityte R, La Gerche A, Rademakers F, et al. Assessment of strain and strain rate by two-dimensional speckle tracking in mice: comparison with tissue doppler echocardiography and conductance catheter measurements. *Eur Heart J Cardiovasc Imaging.* (2013) 14:765–73. doi: 10.1093/ehjci/jes274

14. Mátyás C, Kovács A, Németh B, Oláh A, Braun S, Tokodi M, et al. Comparison of speckle-tracking echocardiography with invasive hemodynamics for the detection of characteristic cardiac dysfunction in type-1 and type-2 diabetic rat models. *Cardiovasc Diabetol.* (2018) 17:13. doi: 10.1186/s12933-017-0645-0

15. Bauer M, Cheng S, Jain M, Ngoy S, Theodoropoulos C, Trujillo A, et al. Echocardiographic speckle-tracking based strain imaging for rapid cardiovascular phenotyping in mice. *Circ Res.* (2011) 108:908–16.

16. Wang G, Zhang L, Ruan L, Quan X, Yang J, Lv C, et al. Speckle tracking echocardiography assessment of global and regional contraction dysfunction in the mice

model of pressure overload. *J Huazhong Univ Sci Technolog Med Sci.* (2015) 35:271–7. doi: 10.1007/s11596-015-1423-4

17. Zhou Y, Zhu S, Foster F, Cybulsky M, Henkelman R. Aortic regurgitation dramatically alters the distribution of atherosclerotic lesions and enhances atherogenesis in mice. *Arterioscler Thromb Vasc Biol.* (2010) 30:1181–8. doi: 10.1161/ATVBAHA.110.204198

18. Wu J, You J, Wang X, Wang S, Huang J, Xie Q, et al. Left ventricular response in the transition from hypertrophy to failure recapitulates distinct roles of Akt, β-arrestin-2, and CaMKII in mice with aortic regurgitation. *Ann Transl Med.* (2020) 8:219. doi: 10.21037/atm.2020.01.51

19. Schnelle M, Catibog N, Zhang M, Nabeebaccus A, Anderson G, Richards D, et al. Echocardiographic evaluation of diastolic function in mouse models of heart disease. *J Mol Cell Cardiol.* (2018) 114:20–8. doi: 10.1016/j.yjmcc.2017.10.006

20. Alemasi A, Cao N, An X, Wu J, Gu H, Yu H, et al. Exercise attenuates acute β-adrenergic overactivation-induced cardiac fibrosis by modulating cytokines. *J Cardiovasc Transl Res.* (2019) 12:528–38. doi: 10.1007/s12265-019-09894-1

21. Gorgulu S, Norgaz T, Nurkalem Z, Ergelen M, Eksik A, Genc A, et al. Comparison of left ventricular contractility in pressure and volume overload: a strain rate study in the clinical model of aortic stenosis and regurgitation. *Echocardiography.* (2010) 27:798–802. doi: 10.1111/j.1540-8175.2010.01149.x

22. Dahl J, Magne J, Pellikka P, Donal E, Marwick T. Assessment of subclinical left ventricular dysfunction in aortic stenosis. *JACC Cardiovasc Imaging.* (2019) 12:163–71. doi: 10.1016/j.jcmg.2018.08.040

23. Thellier N, Altes A, Appert L, Binda C, Leman B, Marsou W, et al. Prognostic importance of left ventricular global longitudinal strain in patients with severe aortic stenosis and preserved ejection fraction. *J Am Soc Echocardiogr.* (2020) 33:1454–64. doi: 10.1016/j.echo.2020.07.002

24. Broch K, de Marchi S, Massey R, Hisdal J, Aakhus S, Gullestad L, et al. Left ventricular contraction pattern in chronic aortic regurgitation and preserved ejection fraction: simultaneous stress-strain analysis by three-dimensional echocardiography. *J Am Soc Echocardiogr.* (2017) 30:422–30.e2. doi: 10.1016/j.echo.2016.11.01

25. Meucci M, Butcher S, Galloo X, van der Velde E, Marsan N, Bax J, et al. Noninvasive left ventricular myocardial work in patients with chronic aortic regurgitation and preserved left ventricular ejection fraction. *J Am Soc Echocardiogr.* (2022) 35:703–11.e3. doi: 10.1016/j.echo.2022.01.008

26. Ruppert M, Lakatos B, Braun S, Tokodi M, Karime C, Oláh A, et al. Longitudinal strain reflects ventriculoarterial coupling rather than mere contractility in rat models of hemodynamic overload-induced heart failure. *J Am Soc Echocardiogr.* (2020) 33:1264–75. doi: 10.1016/j.echo.2020.05.017

27. An X, Wang J, Li H, Lu Z, Bai Y, Xiao H, et al. Speckle tracking based strain analysis is sensitive for early detection of pathological cardiac hypertrophy. *PLoS One.* (2016) 11:e0149155. doi: 10.1371/journal.pone.0149155

28. Haland T, Almaas V, Hasselberg N, Saberniak J, Leren I, Hopp E, et al. Strain echocardiography is related to fibrosis and ventricular arrhythmias in hypertrophic cardiomyopathy. *Eur Heart J Cardiovasc Imaging.* (2016) 17:613–21. doi: 10.1093/ehjci/jew005

29. Wang J, Zhang Y, Zhang L, Tian F, Wang B, Xie Y, et al. Assessment of myocardial fibrosis using two-dimensional and three-dimensional speckle tracking echocardiography in dilated cardiomyopathy with advanced heart failure. *J Card Fail.* (2021) 27:651–61. doi: 10.1016/j.cardfail.2021.01.003

30. Travers J, Kamal F, Robbins J, Yutzey K, Blaxall B. Cardiac fibrosis: the fibroblast awakens. *Circ Res.* (2016) 118:1021–40. doi: 10.1161/CIRCRESAHA.115.306565

31. Suetomi T, Willeford A, Brand C, Cho Y, Ross R, Miyamoto S, et al. Inflammation and NLRP3 inflammasome activation initiated in response to pressure overload by Ca2+/Calmodulin-dependent protein kinase II δ signaling in cardiomyocytes are essential for adverse cardiac remodeling. *Circulation.* (2018) 138:2530–44. doi: 10.1161/CIRCULATIONAHA.118.034621

Frontiers in Cardiovascular Medicine

TYPE Case Report
PUBLISHED 24 January 2023
DOI 10.3389/fcvm.2022.1034703

OPEN ACCESS

EDITED BY
Artur Dziewierz,
Jagiellonian University Medical College, Poland

REVIEWED BY
Martin Manninger,
Medical University of Graz, Austria
Karolina Dorniak,
Medical University of Gdansk, Poland

*CORRESPONDENCE
Jiadong Lin
✉ jiadong_lin2022@163.com
Xinsheng Huang
✉ xinshenghuang586@163.com

SPECIALTY SECTION
This article was submitted to
Cardiovascular Imaging,
a section of the journal
Frontiers in Cardiovascular Medicine

RECEIVED 01 September 2022
ACCEPTED 30 December 2022
PUBLISHED 24 January 2023

CITATION
Lin J, Lu Z, Lin M, Wan Y, Li J and Huang X (2023) Case report: Multiple biventricular aneurysms in arrhythmogenic cardiomyopathy. *Front. Cardiovasc. Med.* 9:1034703.
doi: 10.3389/fcvm.2022.1034703

Case report: Multiple biventricular aneurysms in arrhythmogenic cardiomyopathy

Jiadong Lin[1]*, Zhijuang Lu[1], Mingqin Lin[1], Ying Wan[1], Jianfeng Li[1] and Xinsheng Huang[2]*

[1]Ultrasound Department, Dongguan Hospital of Guangzhou University of Chinese Medicine, Dongguan, China, [2]Cardiovascular Department, Jinshazhou Hospital of Guangzhou University of Chinese Medicine, Guangzhou, China

Arrhythmogenic cardiomyopathy (ACM) is a genetic disease characterized by fibro-fatty myocardial replacement and is clinically associated with malignant ventricular arrhythmias and sudden cardiac death. It presents a major diagnostic and therapeutic challenge due to its complex clinical presentation and multiparametric diagnostic scoring system that includes structural, histological, and electrocardiographic data. A 57-year-old man with a history of palpitation and premature ventricular contractions (PVC) experienced syncope and sustained ventricular tachycardia at a rate of 213 bpm, which was successfully rescued by synchronized cardioversion. Multiple ventricular aneurysms were found in the right ventricular free wall and the left ventricular apical regions, as well as mild biventricular systolic dysfunction, according to echocardiography and high-frequency ultrasound. The genetic analysis revealed the following desmoplakin genes, chr6-7585274-7585275, NM_004415, exon24, and c.7780delT (p.S2594Pfs*9), a heterozygous and likely pathogenic mutation, as the mutation sites in the patient and his 24-year-old daughter. During the 21-month follow-up, the patient did not experience syncope or pre-syncope symptoms while on β-blocker (bisoprolol) therapy. Among the multimodality imaging techniques of the ACM, late gadolinium enhancement on cardiac magnetic resonance (CMR) is accepted as a more objective indicator of myocardial fibrosis. Left ventricular systolic dysfunction, fibrosis on CMR, and frequent PVC are the primary and most sensitive clinical signs of desmoplakin cardiomyopathy. However, echocardiography continues to be the most commonly used imaging modality for assessing focal ventricular movement and structural abnormalities. The pathological characteristics of arrhythmogenic cardiomyopathy of the right ventricular anterior free wall and apical regions near the transducer can be better shown using high-frequency linear ultrasound with a higher resolution.

KEYWORDS

arrhythmogenic cardiomyopathy, echocardiography, desmoplakin, high-frequency ultrasound, sustained ventricular tachycardia, syncope

Introduction

An international task force proposed diagnostic criteria for arrhythmogenic right ventricular cardiomyopathy (ARVC) in 1994, based on identifying structural abnormalities, fatty or fibro-fatty replacement of the right ventricular myocardium, electrocardiographic changes, arrhythmias of right ventricular origin, and familial disease (1). In 2010, these criteria were revised to improve sensitivity for early diagnosis (2). A definite, borderline, or possible diagnosis of ARVC was established based on the fulfillment of major and/or minor criteria. Padua's diagnostic criteria for arrhythmogenic cardiomyopathy included dominant-right, biventricular, and dominant-left phenotypes (ACM) (3). The clinical profiles of asymptomatic family members with concealed structural abnormalities and no arrhythmias in symptomatic patients experiencing arrhythmic cardiac arrest or requiring a heart transplant because of refractory heart failure are only a few examples of how the phenotypic expression of ACM can differ (4). Diagnosis of ACM remains difficult due to the lack of a single gold standard diagnostic tool, poor specificity of ECG findings, multiple possible causes of right ventricular arrhythmias, difficulty evaluating the right ventricle using imaging, and occasional inconclusiveness of the pathogenicity of genetic variants detected (4). In this case report, we describe the case of a patient with ACM who had multiple ventricular aneurysms in both ventricles and mild biventricular systolic dysfunction. Although only 17% of probands had focal right ventricular sacculations (5), the sacculation may be a relatively specific echocardiographic phenotype of ACM.

Timeline

Date	Progress
2013	A history of palpitation with normal physical examination findings.
2019	Electrocardiographic frequent PVC.
November 2020	Sustained ventricular tachycardia with 213 bpm was immediately terminated by synchronized cardioversion. The coronary angiogram was normal. Holter monitoring showed 4,082 (4.4%) frequent different morphological PVC.
November 2020	Echocardiography showed multiple biventricular aneurysms with mild systolic dysfunction.
December 2020	The mutation site was the desmoplakin gene, likely a pathogenic mutation.
February 2021	Holter monitoring showed 4,065 (4.4%) frequent PVC.
May 2022	Echocardiographic findings were similar to November 2020. The patient did not experience syncope during the 21-month follow-up.

Case description

In 2013, a 57-year-old man had palpitation with normal physical examination findings. He was diagnosed with frequent premature ventricular contractions (PVCs) in 2019 despite not taking the antiarrhythmic medication regularly. He had palpitations, dyspnea, and sweating, followed by syncope during emotional disturbance, and regained consciousness ∼10 minutes later, in November 2020. He experienced another loss of consciousness and hemodynamic instability in the emergency department of an outside hospital, with a blood pressure of 84/50 mmHg. The 213 bpm electrocardiographically sustained ventricular tachycardia was quickly terminated by synchronized cardioversion (Figure 1A). Because of his normal coronary angiogram and echocardiographically normal systolic function without structural heart disease, he was diagnosed with idiopathic ventricular arrhythmias.

The patient was referred to our institute 20 days later. The 12-lead standard electrocardiogram revealed a single PVC with right bundle branch block (RBBB) morphology and a superior axis, indicating that the PVC originated in the left ventricle (Figure 1B). In November 2020, Holter monitoring revealed 4,082 (4.4%) frequent different morphological PVCs, including 165 couplets and 2 triplets. Different morphological PVCs have been identified, which may have originated in different regions (Figure 1C). Based on observational data and expert consensus, the patient was referred for appropriate radiofrequency ablation for PVC and/or implantable cardioverter defibrillator therapy for fast ventricular tachycardia. Despite informed consent, the patient refused radiofrequency ablation and/or an implantable cardioverter defibrillator. β-Blocker (bisoprolol) therapy was administered to the patient during the follow-up to alleviate symptoms.

Holter monitoring revealed 1,226 (1.5%) frequent PVCs in December 2020, including 30 couplets, and 4,065 (4.4%) frequent PVCs in February 2021, including 131 couplets and 1 triplet, with no non-sustained ventricular tachycardia over three consecutive PVCs.

Following the collection of clinical characteristics, electrocardiograms, echocardiograms, and laboratory examinations, a genetic analysis was performed. The peripheral venous blood samples of the patient and his 24-year-old daughter were sent to the medical laboratory of Beijing Mygenostics Co., Ltd. for relevant gene capture, gene enrichment, and Sanger sequencing. The desmoplakin genes, chr6-7585274-7585275, NM_004415, exon24, c.7780delT (p.S2594Pfs*9), a heterozygous and likely pathogenic mutation, were the sites of their mutation.

The first transthoracic echocardiographic examination of our institute was performed in November 2020, and subsequent echocardiography was performed in January 2021, July 2021, and May 2022, respectively. With mild biventricular systolic dysfunction (left ventricular ejection fraction of 47% and right ventricular ejection fraction of 40%), echocardiography revealed similar results with multiple ventricular aneurysms in the right ventricular free wall and left ventricular apical regions. The high-frequency ultrasound images were obtained using a commercial Philips EPIQ 7C ultrasound machine (Philips Medical Systems, Andover, MA, USA) equipped with a 3–12 MHz high-frequency linear transducer probe with a vascular carotid preset. The aneurysm measured by two-dimensional echocardiography was 13 (width) ×10 (depth) mm in the right ventricular apical free wall, 7 × 9 and 11 × 16 mm in the right ventricular anterior free wall, and 15 × 19 mm in the left ventricular apical region. High-frequency linear ultrasound with a higher resolution could better show and measure ventricular aneurysms near transducer regions (Figure 2). The patient was diagnosed with arrhythmogenic cardiomyopathy (ACM) after having echocardiographic multiple ventricular aneurysms and mild biventricular systolic dysfunction, after having sustained ventricular tachycardia, when diagnosed with >500 ventricular extrasystoles per 24 h (Holter), and upon the identification of a pathogenic mutation categorized as associated or probably associated with ACM (2, 3) or was diagnosed with arrhythmogenic cardiomyopathy (ACM) with a phenotype of multiple

---

Abbreviations: ACM, arrhythmogenic cardiomyopathy; ARVC, arrhythmogenic right ventricular cardiomyopathy; CMR, cardiac magnetic resonance; PVC, premature ventricular contractions.

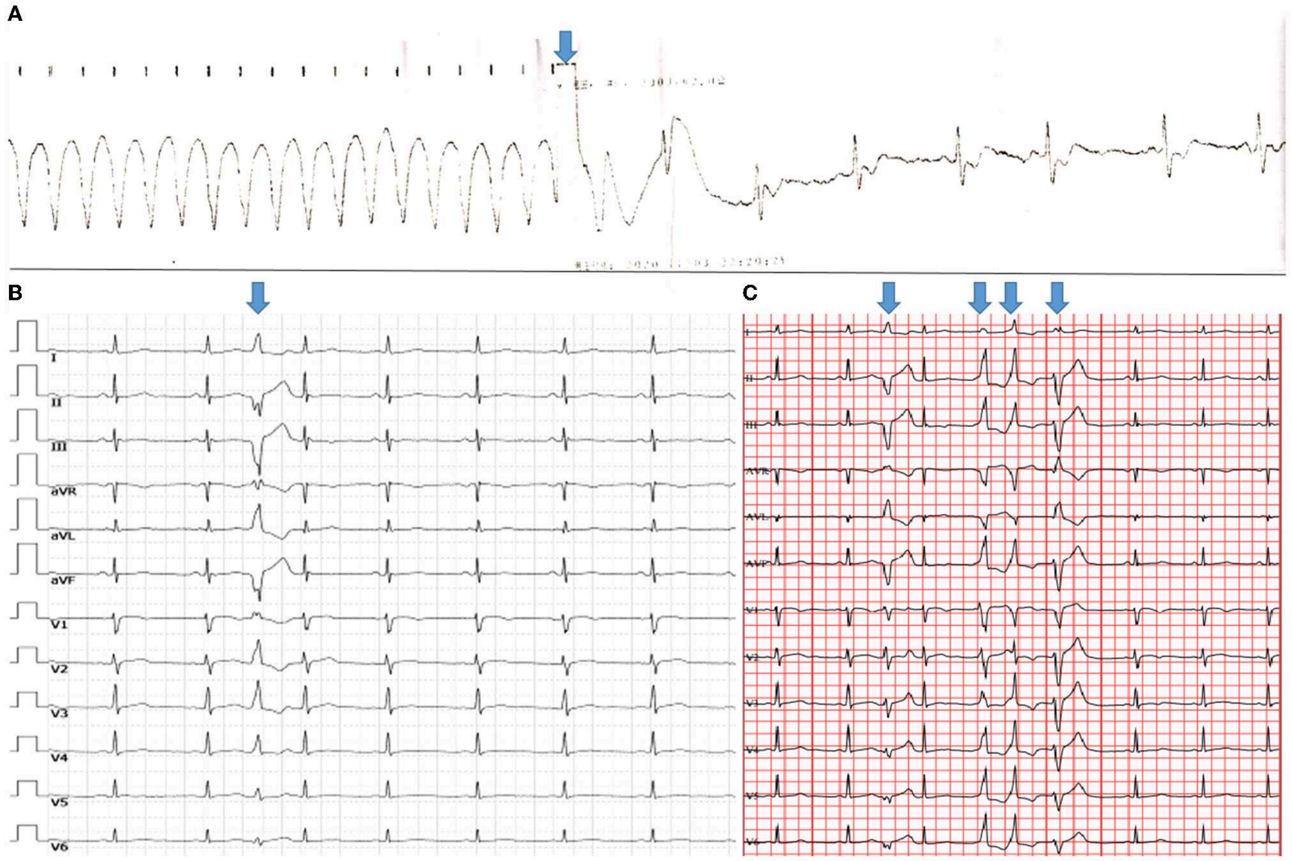

FIGURE 1
Ventricular arrhythmias. The height and weight of the patient were 170 cm and 55 kg, respectively. **(A)** Electrocardiography revealed that synchronized cardioversion restored ventricular tachycardia to sinus arrhythmia (arrow). **(B)** A 12-lead standard electrocardiogram revealed relatively low QRS-complex voltage at all leads, as well as a single PVC with RBBB morphology and a superior axis, indicating that the PVC originated in the left ventricle. **(C)** Holter demonstrated various morphological singles and triplets of PVC (arrows) that may have originated from different sites.

biventricular aneurysms. The echocardiography, 12-lead standard electrocardiogram, and Holter analysis of his daughter were all normal. During the 21-month follow-up, the patient did not present with syncope.

Discussion

Arrhythmogenic cardiomyopathy is believed to be a heredo-familial cardiac disease characterized by fibro-fatty myocardial replacement and an increased risk of sudden cardiac death. It is a heritable, progressive cardiac disease with a wide range of phenotypes. Although ARVC is the most common phenotype, several other ACM phenotypes have been recognized and described (1–3). Desmoplakin cardiomyopathy is increasingly being recognized in distinct arrhythmogenic cardiomyopathies with prominent involvement of the left ventricle, as opposed to the classical forms of ARVC (6). We present a patient with the phenotype of multiple biventricular aneurysms; it seems that the morphological abnormality of the right ventricle is more visible than that of the left ventricle. On the 12-lead standard electrocardiogram and Holter record, there were several morphological PVCs. The different morphological PVCs may have originated from different regions.

Although echocardiography is the most commonly used imaging technique, cardiac magnetic resonance (CMR) is the preferred initial test for patients with suspected ARVC due to its accuracy, availability, safety, and low cost (7). Among the multimodality imaging of the ACM, late gadolinium enhancement on CMR is accepted as a more objective indicator of myocardial fibrosis. Left ventricular systolic dysfunction, fibrosis on CMR, and frequent PVCs are the primary and most sensitive clinical signs of desmoplakin cardiomyopathy (6). CMR may increase the risk of ACM misdiagnosis due to the difficult and operator-dependent interpretation of RV wall motion abnormalities, which are the major diagnostic criteria (8).

When evaluating ventricular wall motion, echocardiography has a better temporal resolution than CMR. The high-frequency linear ultrasound with superior spatial and temporal resolution revealed a focal ventricular aneurysm and abnormal ventricular motion in the right ventricular anterior free wall and apical regions near the transducer. However, high-frequency ultrasound with higher attenuation has a limited penetration depth; the optimal exploration distance is <3–4 cm from the transducer to the region of interest.

To the best of our knowledge, this is the first case report that uses high-frequency ultrasound to assess a focal ventricular aneurysm associated with arrhythmogenic cardiomyopathy. It can better

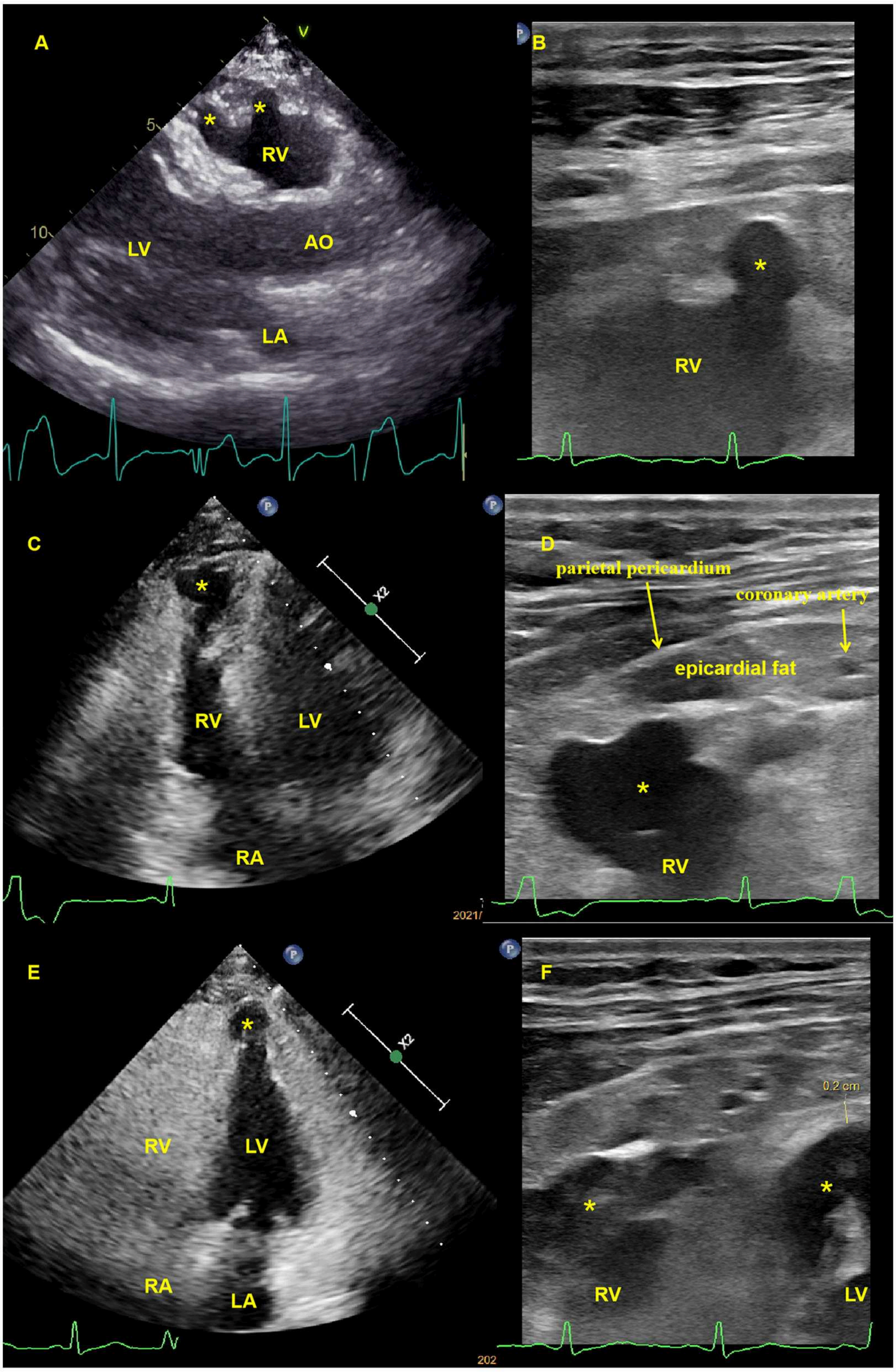

FIGURE 2
Transthoracic echocardiography and high-frequency linear ultrasound showed multiple biventricular aneurysms. **(A)**. Transthoracic echocardiography revealed an anterior right ventricular free wall aneurysm (asterisk) in the parasternal long axis view (see Supplementary Video 1), which had previously been identified using high-frequency linear ultrasound **(B, C)**. Transthoracic echocardiography revealed a right ventricular apical free wall aneurysm (asterisk) in the apical four-chamber view that was demonstrated by high-frequency linear ultrasound **(D)**, (see Supplementary Video 2), with a yellow arrow pointing to the apical epicardial coronary artery and a red arrow pointing to the parietal pericardium **(E)**. Transthoracic echocardiography revealed a left ventricular apical aneurysm (asterisk) in the apical four-chamber view, and high-frequency linear ultrasound revealed both ventricular apical aneurysms **(F)**, (asterisk) with an apical left ventricular thickness of 2 mm. High-frequency ultrasound can also reveal ventricular aneurysmal wall thickness, apical coronary artery, epicardial fat, and parietal pericardial thickness **(B, D, F)**. AO, aorta; LA, left atrium; LV, left ventricle; RA, right atrium; RV, right ventricle.

demonstrate the pathological characteristics of arrhythmogenic cardiomyopathy near the probe.

Data availability statement

The original contributions presented in the study are included in the article/Supplementary material, further inquiries can be directed to the corresponding authors.

Ethics statement

Ethical review and approval was not required for the study on human participants in accordance with the local legislation and institutional requirements. The patients/participants provided their written informed consent to participate in this study. Written informed consent was obtained from the individual for the publication of any potentially identifiable images or data included in this article.

Author contributions

The patient data were managed, analyzed, and interpreted by JLin and XH. JLin and XH made significant contributions to the composition of the manuscript. The manuscript was written by ZL and ML. The treatment and follow-up of the patient were handled by YW and JLi. The final written manuscript was reviewed and approved by all authors.

Acknowledgments

We appreciate the approval of the patient of this case report. We appreciate the assistance of our colleagues in the Ultrasound Laboratories and Cardiovascular Department in caring for this patient.

Conflict of interest

The authors declare that the research was conducted in the absence of any commercial or financial relationships that could be construed as a potential conflict of interest.

Publisher's note

Supplementary material

The Supplementary Material for this article can be found online at: https://www.frontiersin.org/articles/10.3389/fcvm.2022.1034703/full#supplementary-material

References

1. McKenna WJ, Thiene G, Nava A, Fontaliran F, Blomstrom-Lundqvist C, Fontaine G, et al. Diagnosis of arrhythmogenic right ventricular dysplasia/cardiomyopathy. Task force of the working group myocardial and pericardial disease of the European Society of Cardiology and the scientific council on cardiomyopathies of the international society and federation of cardiology. *Br Heart J.* (1994) 71:215–8. doi: 10.1136/hrt.71.3.215

2. Marcus FI, McKenna WJ, Sherrill D, Basso C, Bauce B, Bluemke DA, et al. Diagnosis of arrhythmogenic right ventricular cardiomyopathy/dysplasia: proposed modification of the task force criteria. *Circulation.* (2010) 121:1533–41. doi: 10.1161/CIRCULATIONAHA.108.840827

3. Corrado D, Perazzolo Marra M, Zorzi A, Beffagna G, Cipriani A, Lazzari M, et al. Diagnosis of arrhythmogenic cardiomyopathy: the Padua criteria. *Int J Cardiol.* (2020) 319:106–14. doi: 10.1016/j.ijcard.2020.06.005

4. Corrado D, Basso C, Judge DP. Arrhythmogenic cardiomyopathy. *Circ Res.* (2017) 121:784–802. doi: 10.1161/CIRCRESAHA.117.309345

5. Yoerger DM, Marcus F, Sherrill D, Calkins H, Towbin JA, Zareba W, et al. Multidisciplinary study of right ventricular dysplasia investigators. Echocardiographic findings in patients meeting task force criteria for arrhythmogenic right ventricular dysplasia: new insights from the multidisciplinary study of right ventricular dysplasia. *J Am Coll Cardiol.* (2005) 45:860–5. doi: 10.1016/j.jacc.2004.10.070

6. Smith ED, Lakdawala NK, Papoutsidakis N, et al. Desmoplakin cardiomyopathy, a fibrotic and inflammatory form of cardiomyopathy distinct from typical dilated or arrhythmogenic right ventricular cardiomyopathy. *Circulation.* (2020) 141:1872–84. doi: 10.1161/CIRCULATIONAHA.119.044934

7. Malik N, Mukherjee M, Wu KC, Zimmerman SL, Zhan J, Calkins H, et al. Multimodality imaging in arrhythmogenic right ventricular cardiomyopathy. *Circ Cardiovasc Imaging.* (2022) 15:e013725. doi: 10.1161/CIRCIMAGING.121.013725

8. Perazzolo Marra M, Rizzo S, Bauce B, De Lazzari M, Pilichou K, Corrado D, et al. Arrhythmogenic right ventricular cardiomyopathy. Contribution of cardiac magnetic resonance imaging to the diagnosis. *Herz.* (2015) 40:600–6. doi: 10.1007/s00059-015-4228-0

frontiers | Frontiers in Cardiovascular Medicine

TYPE Original Research
PUBLISHED 26 January 2023
DOI 10.3389/fcvm.2023.1018877

Diagnostic value of real-time four-dimensional transesophageal echocardiography on the implant-related thrombus

Yi Yu[1]*†, Rui Zhang[1]†, Yu-Han Chen[1]†, Ting Wang[1], Xiao-Li Tang[1], Chang-qi Gong[1], Yun Shao[1], Zheng Wang[2], Yue-Peng Wang[1]* and Yi-Gang Li[1]*

[1]Department of Cardiology, Xinhua Hospital Affiliated to School of Medicine, Shanghai Jiao Tong University, Shanghai, China, [2]Department of Rehabilitation Medicine, Shanghai Sixth People's Hospital, Shanghai, China

OPEN ACCESS

EDITED BY
Francesco Pelliccia,
Sapienza University of Rome, Italy

REVIEWED BY
Leilei Cheng,
Fudan University, China
Goverdhan Puri,
Post Graduate Institute of Medical Education and Research (PGIMER), India

*CORRESPONDENCE
Yi Yu
✉ yuyi01@xinhuamed.com.cn
Yue-Peng Wang
✉ ypwang555@aliyun.com
Yi-Gang Li
✉ liyigang@xinhuamed.com.cn

†These authors have contributed equally to this work

SPECIALTY SECTION
This article was submitted to Cardiovascular Imaging, a section of the journal Frontiers in Cardiovascular Medicine

RECEIVED 14 August 2022
ACCEPTED 10 January 2023
PUBLISHED 26 January 2023

CITATION
Yu Y, Zhang R, Chen Y-H, Wang T, Tang X-L, Gong C-q, Shao Y, Wang Z, Wang Y-P and Li Y-G (2023) Diagnostic value of real-time four-dimensional transesophageal echocardiography on the implant-related thrombus.
Front. Cardiovasc. Med. 10:1018877.
doi: 10.3389/fcvm.2023.1018877

Objectives: This study aims to evaluate the diagnostic value of real-time four-dimensional transesophageal echocardiography (RT4D-TEE) for implant-related thrombus (IRT).

Methods: We collected 1,125 patients with atrial fibrillation from May 2019 to February 2022 in our hospital. All patients accepted transesophageal echocardiography (TEE) examination to exclude any thrombi before the LAAC procedure.

Results: There were 760 patients with LAAC, 66 patients with CIED, and 299 patients without any implantations. A total of 40 patients with an established diagnosis of IRT were further analyzed. The accurate detection rate of IRT by RT4D-TEE was 4.8% (40/826), which was higher than 3.8% (31/826) by 2D-TEE ($P = 0.004$). No IRT was found on TEE in the rest of the 786 patients. These 40 patients were divided into LAAC ($n = 23$) and CIED ($n = 17$) groups according to the results of RT4D-TEE. In the LAAC group, IRT distributed on different parts of the LAA occluder surface, 91.3% (21/23) with clumps of thrombi, and 8.7% (2/23) with a thin layer of thrombi covering the surface of the occluder. In the CIED group, thrombi were seen attached to the leads in the right atrium and right ventricle. The thrombi were beaded in 17.6% (3/17), corded in 17.6% (3/17), and clotted in the remaining 64.7% (11/17) of cases. After adjusting the anticoagulant dosage and following up for 6 months, 20% (8/40) of cases were successfully resolved, 67.5% (27/40) became smaller, and 12.5% (5/40) showed no changes.

Conclusion: The accurate detection rate of IRT by RT4D-TEE was significantly higher than that by 2D-TEE. 2D-TEE has limitations, but RT4D-TEE can be used as an effective complementary method. Imaging and some clinical features differ significantly between IRT on occluder and IRT on CIED lead.

KEYWORDS

implant-related thrombus, real-time four-dimensional transesophageal echocardiography, left atrial appendage closure, cardiac implantable electronic device, imaging

1. Introduction

Transcatheter left atrial appendage closure (LAAC) devices and cardiac implantable electronic device (CIED) are both increasingly used in clinical practice. A potentially fatal complication following the device implantation is thrombus formation (1–4). The majority of patients with implant-related thrombus (IRT) are diagnosed by some imaging methods during early routine follow-up (1). Timely intervention by increasing the dosage of anticoagulants could usually result in excellent outcomes. Two-dimensional transesophageal echocardiography (2D-TEE) and computed tomography have been adopted for the diagnosis of IRT (4–8). Two-dimensional transesophageal echocardiography has been reported to be a common and useful tool for diagnosis (9–11). However, the incidence of IRT is underestimated by 2D-TEE due to some missed diagnoses (4, 5, 12, 13). Real-time four-dimensional transesophageal echocardiography (RT4D-TEE) is an appealing alternative because of its superior characteristics, such as high spatial resolution, multiplanar capabilities, four-dimensional viewing, and independent of the discrepancy among different operators. Nevertheless, there has been no study using RT4D-TEE for the diagnosis of IRT on occluder and CIED lead. Moreover, differences in their IRT features between 2D-TEE and 4D-TEE have not been systematically demonstrated. Our study aims to assess the value of RT4D-TEE in detecting IRT and to summarize the echocardiographic features of IRT.

2. Materials and methods

2.1. Patients

This was a retrospective single-center study of consecutive patients who underwent LAAC with either the Watchman nitinol cage device (Atritech, Boston Scientific, Natick, Massachusetts) or LACbes device (Pushi, Shanghai), and/or CIED, including pacemaker, implantable cardioverter defibrillator (ICD), and cardiac resynchronization therapy defibrillator (CRT-D) at Xinhua Hospital from May 2019 to February 2022. Recruited patients eligible for LAAC and CIED were selected according to appropriate local and European guidelines (7). The study was approved by the Ethics Committee of Xinhua Hospital affiliated with Shanghai Jiao Tong University School of Medicine (No. XHEC-D-2022-073) and complies with the Declaration of Helsinki.

The echocardiographic data were collected from records of follow-up during the same period. All patients underwent transthoracic echocardiography (TTE) and TEE examinations. Patients who received LAAC were scheduled for routine follow-ups with TEE after the procedures. TEE examinations were also performed for patients with CIED who had new-onset AF or recurrent AF to exclude the thrombi prior to the establishment of further therapy or to assess the suspected thrombus attached to the leads by TTE in detail as indicated. TTE and TEE were performed on a commercially available system (SC2000, Siemens Healthcare, Forchheim, Germany) equipped with broadband 4V1 and Z6Ms transducers. Imaging of 2D-TEE and 4D-TEE was collected from each patient during the course of the examination, especially for the LAAC device and/or CIED lead in the 4D mode in one to three cardiac cycles. Echocardiographic experts analyzed the 2D-TEE images first and then the 4D-TEE images to confirm the diagnosis. In case of disagreement in diagnosis occurred between the two echocardiographers, a third experienced cardiologist was invited to make diagnoses until reaching a consensus. IRT by TEE was defined as a homogenous echo-dense mass visible in multiple planes with independent motion and adherence to the atrial surface of the LAAC device (1, 14). Thrombus formation in patients with CIED was defined as the aforementioned description and adherence to the CIED lead (5). The therapeutic decision to initiate anticoagulation or adjust preexisting anticoagulation was predominantly based on findings from TEE.

Antithrombotic therapy following LAAC consisted of oral anticoagulation (OAC), single antiplatelet therapy (APT), dual antiplatelet therapy (DAPT), or OAC plus APT for 1–6 months. The team of physicians performing follow-up visits gave a general recommendation to patients after CIED. Other indications were necessitated (i.e., percutaneous coronary intervention, PCI). Decisions on the duration of therapy were made according to the physician’s judgment (15).

2.2. Statistical analysis

Statistical analysis was performed using SPSS 26.0 (v16.0, IBM Corp., Armonk, NY) software. Continuous data were described as mean ± standard deviation (SD) and as counts and percentages if categorical. Differences in continuous and categorical variables were assessed by the chi-square test or Fisher’s exact test (if the expected value in any cell was <5), respectively. Normally distributed continuous variables were assessed by independent samples *t*-test. A *P*-value of <0.05 was considered statistically significant.

3. Results

We collected 1,125 patients with AF from May 2019 to February 2022 in our hospital. All patients accepted the TEE examination to exclude any thrombi. There were 760 patients with LAAC, 66 patients with CIED, and 299 patients without any implantations. A total of 40 patients with an established diagnosis of IRT were further analyzed. The accurate detection rate of IRT by RT4D-TEE was 4.8% (40/826), which was higher than 3.8% (31/826) by 2D-TEE ($P = 0.004$). No IRT was found on TEE in the rest of the 786 patients. These 40 patients were divided into LAAC ($n = 23$) and CIED ($n = 17$) groups according to the results of RT4D-TEE (**Figure 1**).

(1) The characteristics of the patients with IRT

The general characteristics of the 40 patients identified with IRT are summarized in **Table 1**. There were no significant differences in age, gender distribution, or any other recorded clinical variable. The right atrium (RA) was dilated with different degrees of tricuspid regurgitation (TR) by echocardiography. Values of these parameters except the volume of RA were significantly higher in the CIED group compared with the LAAC group ($P < 0.05$). The time history of device implantation was in different patients. It was 97.12 ± 82.14 months from implantation to the end of data collection in the CIED group and 29.20 ± 20.46 months during the same period in the LAAC group.

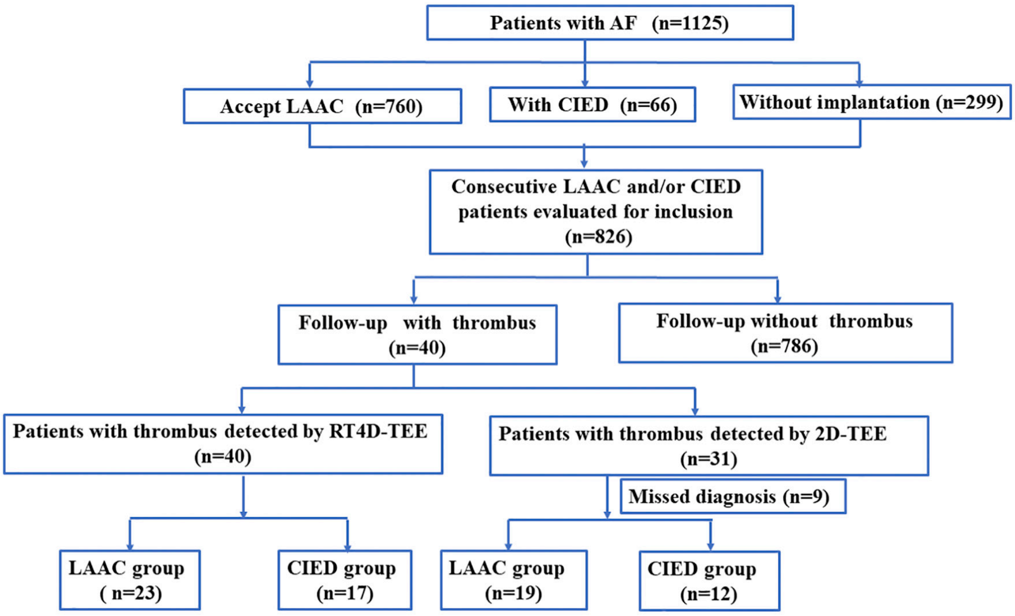

FIGURE 1
Flowchart of the study group.

TABLE 1 Clinical characteristics of the patients with implant-related thrombus.

Variables	LAAC group (*n* = 23)	CIED group (*n* = 17)	t/x^2	*P*-value
Age, $\bar{x} \pm$ s, y	70.96 ± 7.18	69.82 ± 10.60	−0.381	0.706
Sex, *n* (%)			1.153	0.284
Male, *n* (%)	16/23 (69.57)	9/17 (52.94)		
Female, *n* (%)	7/23 (30.43)	8/17 (47.06)		
Comorbidities and medical history				
History of LAA thrombus, *n* (%)	2/23 (8.70)	2/17 (11.77)		
Prior PCI, *n* (%)	1/23 (4.38)	3/17 (17.65)		
Prior stroke, *n* (%)	1/23 (4.38)	2/17 (11.77)		
systemic embolism, *n* (%)	2/23 (8.70)	0		
2D-TTE				
LAV, ml	66.83 ± 21.29	75.61 ± 45.96	0.809	0.423
RAV, ml	42.94 ± 12.36	65.82 ± 30.36	3.277	0.002
LVEF, $\bar{x} \pm s$,%	59.78 ± 6.29	57.12 ± 10.03	−0.961	0.346
CHA_2DS_2-VASc Score, $\bar{x} \pm$ s	3.35 ± 1.19	3.47 ± 1.97	0.228	0.822
HAS-BLED score, $\bar{x} \pm$ s	3.17 ± 1.11	3.82 ± 2.19	1.122	0.274
Anticoagulant therapy				0.001
No OAC, no APT, *n* (%)	–	8/17 (47.06)		0.001
Single APT, *n* (%)	1/23 (4.38)	–		1.000
Dual APT, *n* (%)	–	2/17 (11.77)		0.340
OAC, no APT, *n* (%)	21/23 (91.30)	6/17 (35.29)		0.001
OAC plus APT, *n* (%)	1/23 (4.38)	1/17 (5.88)		1.000
INR, $\bar{x} \pm$ s	1.12 ± 0.26	1.05 ± 0.13	−1.029	0.311

LAAC, left atrial appendage closure; CIEDs, cardiac implantable electronic devices; MI, myocardial infarction; PCI, percutaneous coronary intervention; 2D-TTE, two-dimensional transthoracic echocardiography; LAV, left atrial volume; RAV, right atrium volume; LVEF, left ventricular ejection fraction; OAC, oral anticoagulation; APT, antiplatelet therapy; INR, international normalized ratio.

TABLE 2 Thrombus diagnosed by real time four-dimensional Transoesophageal echocardiography.

Variables	LAAC group (n = 23)	CIED group (n = 17)	P-value
Optimal implantation placement, n (%)			0.248
Yes	20/23 (86.96)	17/17 (100.00)	
No	3/23 (13.04)		
LAA device-related thrombus, n (%)	23/23 (100.00)	–	
Position of thrombus			
Center, n (%)	3/23 (13.04)	–	
Periphery, n (%)	16/23 (69.57)	–	
Edge, n (%)	2/23 (8.70)	–	
Thin layer covering the surface, n (%)	2/23 (8.70)	–	
Peri-device leakage			
<5 mm, n (%)	7/23 (30.44)	–	
>5 mm, n (%)	1/23 (4.35)	–	
Residual leakage through the fabric, n (%)	3/23 (13.04)	–	
Incomplete endothelization, n (%)	10/23 (43.48)	–	
CIEDs-related thrombosis, n (%)	–	17/17 (100.00)	
Position of thrombus			
RA and RV lead, n (%)	–	5/17 (29.41)	
RA and RAA leads, n (%)	–	2/17 (11.77)	
RA lead, n (%)	–	7/17 (41.18)	
RV lead, n (%)	–	1/17 (5.88)	
RA lead and in LCS, n (%)	–	1/17 (5.88)	
RA lead and in LAA, n (%)	–	1/17 (5.88)	
Atrial septal puncture closed, n (%)	19/23 (82.61)	–	
6-month follow-up			0.002
Thrombus resolved, n (%)	7/23 (30.44)	1/17 (5.88)	
Thrombus become small, n (%)	16/23 (69.57)	11/17 (64.71)	
Thrombus without change, n (%)	0	5/17 (29.41)	

LAA, left atrial appendage; RA, right atrium; RV, right ventricular; RAA, right atrial appendage; LCS:, left coronary sinus.

(2) The characteristics of IRT in patients detected by RT4D-TEE, compared with that of 2D-TEE

In total 40 patients were precisely diagnosed with IRT by RT4D-TEE, while 77.5% (31/40) of patients were directly diagnosed with 2D-TEE. The characteristics of IRT in patients detected by RT4D-TEE are revealed in Table 2. A total of 18 out of 23 (78.26%) patients with IRT were diagnosed by 2D-TEE in the LAAC group and 5 out of 23 (21.74%) patients missed diagnosis. In addition, 13 out of 17 (76.47%) patients with IRT were diagnosed by 2D-TEE in the CIED group and 4 out of 17 (23.53%) patients missed diagnosis. Two patients with thrombosis attached to the leads were confirmed by RT4D-TEE, which were suspected of thrombus by TTE. There were no significant differences in the rate of IRT missed diagnosing by 2D-TEE between the two groups ($P = 0.893$).

In the LAAC group, we found that most of the IRT originated from the periphery. IRT was evaluated with RT4D-TEE in 13.0% (3/23) of cases at the top of the center, 69.6% (16/23) at the periphery, 8.7% (2/23) at the edge, and 8.7% (2/23) with a thin layer of thrombi covering the surface of LAA occluder (Figure 2 and Supplementary Video 1). IRT was described as laminar in 8.7% (2/23), pedunculated in 8.7% (2/23), and massed in 82.6% (19/23) of cases. Compared with 2D-TEE, four patients missed the diagnosis. RT4D-TEE found more scattered IRT on the surface of the occluder in three patients and showed more clearly than that of 2D-TEE. One patient with moderate mitral regurgitation was detected by 2D-TEE, the beam rushed to the surface of the occluder, which masked the thrombus. Here, only three patients had failed to cover the rim of the left atrial appendage (LAA) with significant thrombi on the edge of the device because the occlusive device selected was too small. The mobile thrombus was seen only in two patients who pedunculated and had a neck attached to the fabric (Supplementary Video 2), and a sessile thrombus was seen in the other 19 patients. Residual leakage into the LAA was observed in five patients at the time of thrombus detection. A major peri-device leak (>5 mm) was detected in 4.4% (1/23) of patients during TEE follow-up, and a small peri-device leak (flow <5 mm) was revealed in 30.4% (7/23) of patients. Residual leakage into the LAA through the fabric was found in 13.0% (3/23) of patients. Ten patients with incomplete endothelialization have been observed.

In the CIED group, the thrombi attached to the leads of the right chambers were detected by RT4D-TEE in all 17 patients (Figure 3 and Supplementary Video 3). Their thrombi were beaded in three cases (Supplementary Video 4), corded in three cases, and the other 11 cases were clots (Figure 4). In addition, thrombi were found simultaneously in LAA and the left aortic sinus attached to the aortic valve in one case (Supplementary Video 5), whereas four of the lead-attached thrombi detected by RT4D-TEE could not be visualized by 2D-TEE.

(3) Clinical Events and Follow-Up

A total of 40 patients with thrombus were regularly followed up under standardized medical treatment. At the time of finding implant-associated thrombus, the antithrombotic medication regimen consisted of oral anticoagulation in 67.5% (27/40) of patients, OAC plus APT in 5% (2/40) of patients, dual APT in 5% (2/40) of patients, single APT in 2.5% (1/40) of patients, and no antithrombotic therapy in 20% (8/40) of patients. Among those, antithrombotic therapy was mandated in 10% (4/40) of patients due to the need for prolonged triple therapy following percutaneous coronary intervention. Anticoagulants consisting of OAC or single APT were routinely administered to patients following LAAC. 2D-TEE results showed that the change of thrombi after adjusting anticoagulant in 31 patients coincided with that of 4D-TEE. The remaining nine cases of missed diagnosis by 2D-TEE were still unclear.

The incidence of IRT after LAAC was 3.0% (23/760) and clinical outcomes of thrombi were as follows: At 6-month follow-up after adjusting anticoagulant, 4D-TEE results showed that the thrombi were either completely resolved in 30.4% (7/23) of patients and became smaller in 69.6% (16/23) of patients. In the CIED group, the thrombi of three patients attached to the leads illustrated unchanged, which were detected by RT4D-TEE. Of note, their implanted pacemakers had been more than 10 years. The organized thrombi on the pacing lead did not dissolve during our follow-up.

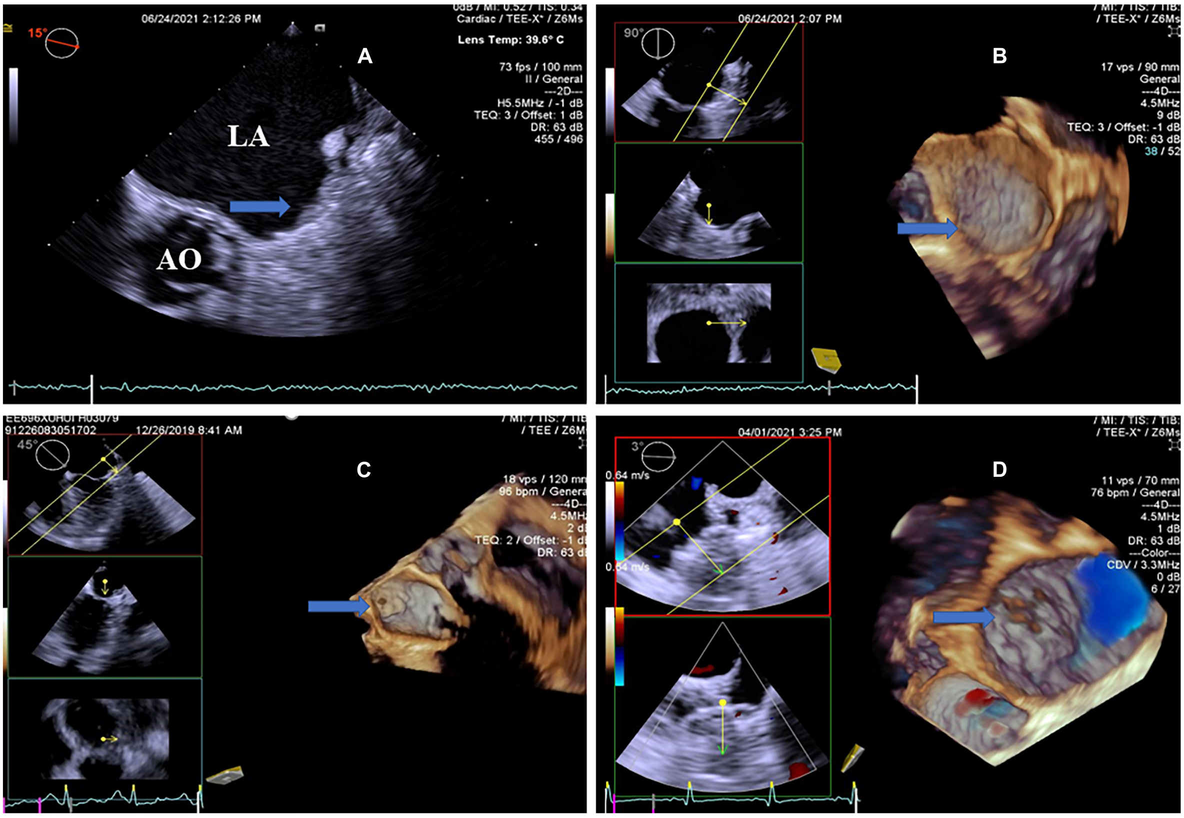

FIGURE 2
Transesophageal echocardiography follow-up images after LAAC showing optimal device placement and device-related thrombus. **(A)** 2D-TEE showed an echo-dense mass attached to the LACbes device, occupying most area of the occluder (arrow). Note severe spontaneous echo contrast throughout the left atrium. **(B)** RT4D-TEE demonstrated a thin layer of thrombi covering the whole surface of the well-seated LACbes device (arrow) after LAAC, as compared with 2D-TEE. **(C)** RT4D-TEE indicated complete LAA closure with the Watchman device, meanwhile demonstrating a mobile thrombus pedunculated with a neck attached to the occluder (arrow). **(D)** RT4D-TEE detected optimal device placement and a couple of scattered clots on the surface of the Watchman occluder (arrow). There was no residual peri-device leak at the LAA ostium detected by color Doppler. RT4D-TEE: Real-time four-dimensional echocardiography. LAAC, left atrial appendage closure; 2D-TEE, two-dimensional transesophageal echocardiography.

The incidence of IRT after CIED was 25% (17/66) and the clinical outcomes of thrombi were as follows: At 6-month follow-up after adjusting anticoagulant, their thrombi were completely resolved in 5.9% (1/17) of cases, became smaller in 64.7% (11/17), and remained unchanged in 29.4% (5/17) of patients as shown by 4D-TEE.

4. Discussion

The novel findings of our prospective study were as follows: First, IRT was an overall relatively infrequent event. Second, the detection rate of IRT by RT4D-TEE was 4.8%, significantly higher than that of 3.8% by 2D-TEE. Third, during a 6-month follow-up after adjusting the anticoagulant dosage, RT4D-TEE showed IRT completely dissolved in 20% of patients, became smaller in 67.5% of patients, and showed no change in 12.5% of patients. Compared with 2D-TEE, nine patients still missed the diagnosis. Therefore, RT4D-TEE was superior to 2D-TEE in the accurate diagnosis of IRT.

(1) Implant-related thrombus on occluder detected by RT4D-TEE

In the current study, RT4D-TEE found more scattered IRT on the surface of the occluder and was capable to detect some thrombus masked by mitral regurgitation with more clear imaging than that of 2D-TEE. IRT typically appeared morphologically different, with a large laminar base centering on the atrial facing surface of the device, which limited thrombosis mobility (16–18), and our results were in agreement with the aforementioned reports. The difference in the location where the thrombus stuck between our study and that of Sedaghat et al. (19), following LAAC may be related to a different type of LAA device, device malpositioning, or displacement after the procedure. Bai et al. (17) thought optimal implantation without peri-device gap, individual antithrombotic regimens, and careful monitoring with TEE follow-up could be conducive to the prevention of IRT. In most of the patients, they did not achieve optimal device placement, which was likely to be responsible for thrombus formation (18). In this study, the position of the thrombus stuck to the Watchman device was observed by RT4D-TEE on the central portion, periphery, or edge of the device, respectively. While a thin layer of thrombus was observed covering the surface of the LACbes occluder in two patients. To the best of our knowledge, the Watchman occluder is a plug blocking device, it is implanted slightly deeper into the appendage, leaving a volume of uncovered appendage, which may cause a potential space for the formation of thrombus. Nevertheless, the LACbes occluder is a type of disc blocker device with a slightly larger surface area, which may partly explain the thin layer of thrombus formation. Two patients with AF performed RFCA

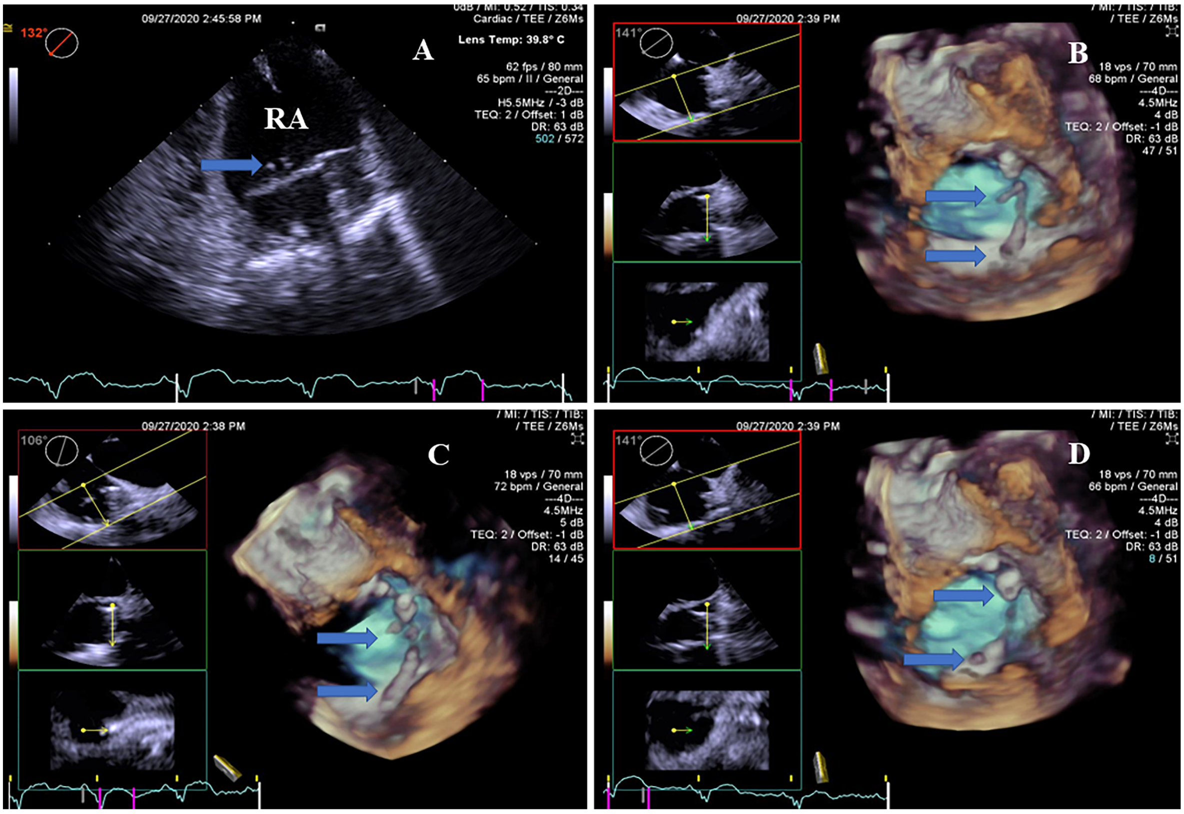

FIGURE 3
Real-time four-dimensional-TEE evaluating the pacemaker lead-related thrombus, as compared with 2D-TEE. **(A)** 2D-TEE showed two clots stuck to the lead of the pacemaker in the right atrium (arrow). Note severe spontaneous echo contrast throughout the right atrium. **(B)** RT4D-TEE demonstrated more clots attached to the lead of the pacemaker in the right atrium and more clearly than 2D-TEE (arrow). **(C)** RT4D-TEE showed more scatter clots on the lead of the pacemaker in the right atrium from a different angle (arrow). **(D)** RT4D-TEE revealed more lead-related thrombi throughout the lead of the pacemaker in the right atrium.

and LAAC of one stop operation after implanting CIED, and RT4D-TEE detected thrombi on the LAAC device. Nonetheless, OAC or OAC plus APT had been recommended in our present data. In this study, a patient with thrombi on both the occluder and the CIED lead did not appear at the same time.

Another finding from our study was residual shunt after LAAC was detected. Peri-device leak due to incomplete occlusion of the LAA can connect the residual LAA pouch to the systemic circulation (20). The degree of "acceptable" residual peri-device leak (jet of <5 mm in width) was not associated with an increased risk of thromboembolism in a *post hoc* analysis of the Watchman implantation cohort in the PROTECT-AF study (21). In contrast, the presence of a residual shunt of >5 mm typically leads to the continuation of anticoagulation treatment, which may mask the contribution to IRT formation from the residual leak (22, 23). Moreover, the time node of LAA device endothelialization was also an important factor, and it was difficult to form a thrombus after full device endothelialization (21, 24). Pracon et al. (25) demonstrated that IRT was observed early, late, and very late after LAAC in their real-world series, and it was related to patient and procedural characteristics but not to post-implantation DAPT duration. In the LAAC group, at 6-month follow-up after adjusting anticoagulant, 4D-TEE results showed that thrombi were completely resolved in 30.4% (7/23) of cases and the others became smaller. Compared with 2D-TEE, four of them still missed diagnoses. This may be associated with the 2D-TEE can see only a limited angle. Two-dimensional transesophageal echocardiography sections from 0 to 180 degrees do not show the full view of the occluder. Only analyzed by 3D-TEE and 4D-TEE using the software, the entire surface of the occluder can be fully displayed. Thus, it can be seen, thrombus formation on LAA occluder remains a clinical challenge, the evidence regarding the optimal antithrombotic strategy is still under debate as some studies support short-term OAC, whereas others favor single or DAPT only (26, 27).

(2) Implant-related thrombus on CIED lead detected by RT4D-TEE

In our study, RT4D-TEE revealed thrombi throughout the right atrial and ventricular leads and/or right auricula dextra pacing lead by multiple sectional views. The thrombi were non-occlusive, mobile, and either lead attached or in their immediate vicinity among which beaded thrombi were easily missed diagnosis by 2D-TEE. RT4D-TEE demonstrated thrombi on the leads and the other parts of the heart in several patients with an implanted pacemaker for more than 10 years. Even after adjusting the anticoagulant dosage, these thrombi were still difficult to resolve because they had been organized for a long time. Two patients with implanted CIED after RFCA and LAAC of one stop operation. The most frequent indications for CIED were systemic sinus arrest, sick sinus syndrome, or bradycardia. Conversely, Dukkipati et al. (12) demonstrated that after LAAC, most

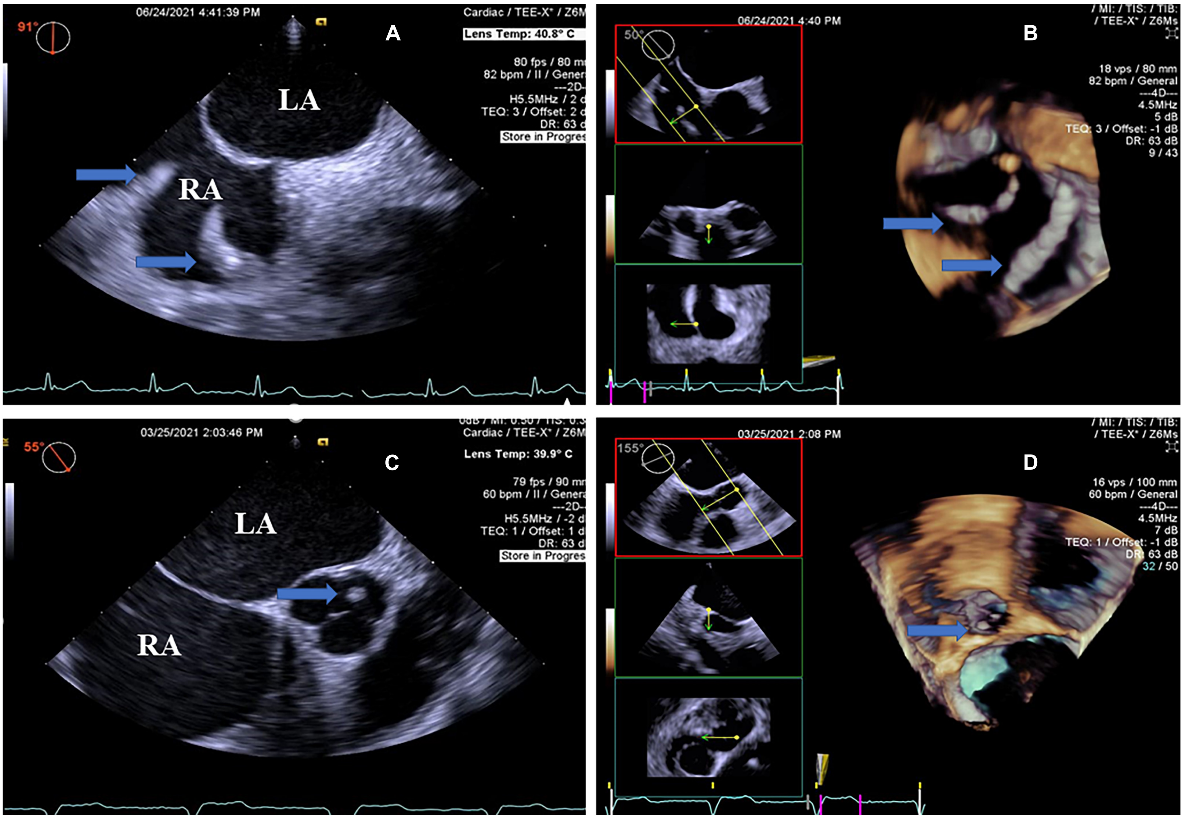

FIGURE 4

Real-time four-dimensional-TEE evaluating the pacemaker lead-related thrombus and additional thrombus, as compared with 2D-TEE. **(A)** 2D-TEE showing local thickening of the two leads of the pacemaker in the right atrium (arrow) from the double atrial section view and the beaded thrombi (arrow). Note severe spontaneous echo contrast in the left atrium and right atrium. **(B)** RT4D-TEE visualizing the beaded thrombi fused to the pacemaker wire in the right atrium (arrow). **(C)** On the aortic root short axis view, 2D-TEE shows a round mass thrombus in the left aortic sinus attached to the aortic valve (arrow). Note severe spontaneous echo contrast throughout the left atrium and right atrium. **(D)** RT4D-TEE demonstrating an echogenic mass, looks like a round clot thrombus in the left aortic sinus attached to the aortic valve and more clearly than 2D-TEE (arrow) (Movie I–V). Movie I. At a 6-month follow-up, a 64-year-old man revealed a thin layer of thrombus covering the whole surface of the LACbes occluder by RT4D-TEE. Movie II. RT4D-TEE detected a mobile thrombus pedunculated on the face of the Watchman device. Thrombus adhered to the periphery of the occluder. Movie III. RT4D-TEE showed a lead-related floating thrombus in the right atrium. Movie Iv. RT4D-TEE evaluating the beaded thrombi fused to the pacemaker wires in the right atrium. Movie V. RT4D-TEE demonstrating the round mass thrombus in the left aortic sinus from the aortic root short axis view.

systemic embolism occurred in patients without IRT. At that point, the post-implantation antithrombotic regimen was highly variable with patients receiving OAC. In this situation, the implantation may become a marker rather than the cause, and these patients may be suitable candidates for longer durations of anticoagulation therapy to treat what could be more systemic emboli issues.

The evolving indications and uses for CIEDs have led to a significant increase in the number of implanted devices each year (28). CIED lead-related thrombus may involve only the leads or the whole CIED system, even the extracardiac organs. Although numerous studies have documented an association of systemic embolism (such as cerebral embolism or massive pulmonary embolism) of a patient with a pacemaker (29–31), there are limited data for CIED subjects that our study provides. Generally, TEE is the first convenient tool in visualizing the intra-cardiac portion of the CIED lead. The finding of a free-floating thrombus attached to a pacing lead is much more uncommon. Moreover, it can be more life-threatening due to the high risk of pulmonary embolism. Furthermore, it has been described that the presence of right heart thrombi in acute pulmonary embolism is associated with hemodynamic compromise, right ventricular (RV) hypokinesis, congestive heart failure, poor prognosis, and a higher mortality rate (32). It is evident that massive pulmonary embolism or paradoxical embolism is the cause of the fatal outcome if the thrombus is mobile or free-floating. TEE plays an integral role in evaluating these pacemaker-related complications (33), but the diagnosis of thrombi by 2D-TEE may be technically challenging in patients with small or scattered thrombi. 2D-TEE can only detect parts of the lead from different views, while the whole lead cannot be shown simultaneously in the same section. Ho et al. (4) reported a part of mobile thrombi on transvenous leads was not detected until patients underwent lead extraction, and we think some small clots on the leads are not found by 2D-TEE. Thus, it is crucial to recognize that RT4D-TEE is a novel technique, it can further enhance the detection of lead-related thrombus in one cardiac cycle, and it has the advantage of imaging the lead in multiple views. The detection of thrombi by RT4D-TEE is invaluable by providing direct visualization, measurements of mass, and the ability to assess for associated cardiac involvement. By imaging in more than one RT4D-TEE plane, thrombus can be seen and confirmed, as oscillating intra-cardiac masses on the device lead. In addition, RT4D-TEE has a powerful ability to visualize the entire intra-cardiac route of the leads from the upper vena cava to the RV apex, even the lead in the right auricle, resulting in much higher sensitivity and specificity for this technique. On the other side, the clots on the pacing lead were difficult to resolve in case of longstanding thrombi. In general, anticoagulant drugs were not routinely used after pacemaker implantation, and it took a long time to find out thrombus or detect it by chance during an examination, as we have studied. But in that analysis, the number of patients included was relatively small, the thrombus attached to the lead was found at the time of TEE examination, limited imaging was available, and most importantly.

Notably, the volume of RA in the CIED group was much larger than in the LAAC group. Herein, we hypothesize that the risk of thrombus formation may be increased because the volume of RA has progressed to blood stasis in these patients. In reviewing the development of significant tricuspid regurgitation (TR) following the CIED placement, a number of different mechanisms of RV intra-cardiac lead-related TR should be considered, which might explain the RA dilation and AF occurrence. The aforementioned predisposing factor, combined with chambers dilated and evidence of hemodynamic impairment with signs of congestive heart failure, might have contributed to the CIED lead thrombus.

5. Limitations

First, this was not a randomized study, the sample size was relatively small, and the follow-up was not long enough to predict long-term improvement. Second, it could not further divide the patients into subgroups by different types of LAAC occluders and/or electronic devices. Third, we did not compare RT4D-TEE for the detection of IRT with other modalities such as cardiac computed tomography angiography and nuclear studies. However, these limitations may not affect echocardiographic findings. A multicenter study should be scheduled in the future to address these issues.

6. Conclusion

In summary, the accurate detection rate of IRT by RT4D-TEE was 4.8%, higher than that of 3.8% by 2D-TEE. The limitations of 2D-TEE include that cannot show the full view of the occluder and that reveals the whole lead simultaneously in one section. Thus, RT4D-TEE is a sensitive method. Imaging and some clinical features are also quite different between IRT on occluder and CIED lead.

Data availability statement

The original contributions presented in this study are included in the article/**Supplementary material**, further inquiries can be directed to the corresponding authors.

Ethics statement

The studies involving human participants were reviewed and approved by the Ethics Committee of Xinhua Hospital Affiliated to Shanghai Jiao Tong University School of Medicine. The patients/participants provided their written informed consent to participate in this study.

Author contributions

YY participated in conception and design. Y-GL and Y-PW provided the administrative support. Y-HC and RZ provided the materials or patients. YS, TW, and ZW performed the collection and assembly of data. X-LT and C-QG performed the data analysis and interpretation. All authors performed the article writing and final approval of article.

Funding

Funding for this study was provided in part by grant 17411954800 from the Shanghai Science and Technology Committee Clinical Field Project Fund (YY), by grant 202240110 from the Shanghai Health and Family Planning Commission (YY), and by grant XHKC2021-07 from the Xinhua Hospital affiliated with the School of Medicine (YY).

Acknowledgments

We appreciate the doctors in the Department of Cardiology, Xinhua Hospital of Jiaotong University who treated these patients.

Conflict of interest

The authors declare that the research was conducted in the absence of any commercial or financial relationships that could be construed as a potential conflict of interest.

Publisher's note

Supplementary material

The Supplementary Material for this article can be found online at: https://www.frontiersin.org/articles/10.3389/fcvm.2023.1018877/full#supplementary-material

References

1. Wazni O, Saliba W, Hussein A. Device-related thrombus after left atrial appendage occlusion. *JACC.* (2021) 78:314–6. doi: 10.1016/j.jacc.2021.05.028

2. Saw J, Tzikas A, Shakir S, Gafoor S, Omran H, Nielsen-Kudsk J, et al. Incidence and clinical impact of device-associate thrombus and peri-device leak following left atrial appendage closure with the amplatzer cardiac plug. *JACC Cardiovasc Interv.* (2017) 10:391–9. doi: 10.1016/j.jcin.2016.11.029

3. Alkhouli M, Busu T, Shah K, Osman M, Alqahtani F, Raybuck B. Incidence and clinical impact of device-related thrombus following percutaneous left atrial appendage occlusion: a meta-analysis. *JACC Clin Electrophysiol.* (2018) 4:1629–37. doi: 10.1016/j.jacep.2018.09.007

4. Ho G, Bhatia P, Mehta I, Maus T, Khoche S, Pollema T, et al. Prevalence and short-term clinical outcome of mobile thrombi detected on transvenous leads in patients undergoing lead extraction. *JACC Clin Electrophysiol.* (2019) 5:657–64. doi: 10.1016/j.jacep.2019.01.007

5. Korkeila P, Saraste M, Nyman K, Koistinen J, Lund J, Airaksinen K. Transesophageal echocardiography in the diagnosis of thrombosis associated with permanent transvenous pacemaker electrodes. *Pacing Clin Electrophysiol.* (2006) 29:1245–50. doi: 10.1111/j.1540-8159.2006.00519.x

6. Cochet H, Iriart X, Sridi S, Camaioni C, Corneloup O, Montaudon M, et al. Left atrial appendage patency and device-related thrombus after percutaneous left atrial appendage occlusion: a computed tomography study. *Eur Heart J Cardiovasc Imag.* (2018) 19:1351–61. doi: 10.1093/ehjci/jey010

7. Hindricks G, Potpara T, Dagres N, Arbelo E, Bax J, Blomström-Lundqvist C, et al. 2020 ESC guidelines for the diagnosis and management of atrial fibrillation developed in collaboration with the European Association for Cardio-Thoracic Surgery (EACTS): the task force for the diagnosis and management of atrial fibrillation of the European Society of Cardiology (ESC) developed with the special contribution of the European Heart Rhythm Association (EHRA) of the ESC. *Eur Heart J.* (2021) 42:373–98. doi: 10.1093/eurheartj/ehab648

8. Munawar D, Chan J, Emami M, Kadhim K, Khokhar K, O'Shea C, et al. Magnetic resonance imaging in non-conditional pacemakers and implantable cardioverter-defibrillators: a systematic review and meta-analysis. *Europace.* (2020) 22:288–98. doi: 10.1093/europace/euz343

9. Meier B, Blaauw Y, Khattab A, Lewalter T, Sievert H, Tondo C, et al. EHRA/EAPCI expert consensus statement on catheter-based left atrial appendage occlusion. *Euro Interv.* (2015) 10:1109–25. doi: 10.4244/EIJY14M09_18

10. Korsholm K, Jensen J, Nørgaard B, Nielsen-Kudsk J. Detection of device-related thrombosis following left atrial appendage occlusion: a comparison between cardiac computed tomography and transesophageal echocardiography. *Circ Cardiovasc Interv.* (2019) 12:e008112. doi: 10.1161/CIRCINTERVENTIONS.119.008112

11. Di Vincenzo A, Rizzo A, Russo L, Mioni R. Pacemaker-associated thrombosis in ongoing therapy with edoxaban tosylate. *J Thromb Thrombolysis.* (2018) 46:549–50. doi: 10.1007/s11239-018-1733-z

12. Dukkipati S, Kar S, Holmes D, Doshi S, Swarup V, Gibson D, et al. Device-related thrombus after left atrial appendage closure. *Circulation.* (2018) 138:874–85. doi: 10.1161/CIRCULATIONAHA.118.035090

13. Kar S, Doshi S, Sadhu A, Horton R, Osorio J, Ellis C, et al. Primary outcome evaluation of a next-generation left atrial appendage closure device: results from the PINNACLE FLX trial. *Circulation.* (2021) 143:1754–62. doi: 10.1161/CIRCULATIONAHA.120.050117

14. Main M, Fan D, Reddy V, Holmes D, Gordon N, Coggins T, et al. Assessment of device-related thrombus and associated clinical outcomes with the WATCHMAN left atrial appendage closure device for embolic protection in patients with atrial fibrillation (from the PROTECT-AF trial). *Am J Cardiol.* (2016) 117:1127–34. doi: 10.1016/j.amjcard.2016.01.039

15. Korsholm K, Nielsen K, Jensen J, Jensen H, Andersen G, Nielsen-Kudsk J. Transcatheter left atrial appendage occlusion in patients with atrial fibrillation and a high bleeding risk using aspirin alone for postimplant antithrombotic therapy. *EuroIntervention.* (2017) 12:2075–82. doi: 10.4244/EIJ-D-16-00726

16. Saw J, Nielsen-Kudsk J, Bergmann M, Daniels M, Tzikas A, Reisman M, et al. Antithrombotic therapy and device-related thrombosis following endovascular left atrial appendage closure. *JACC Cardiovasc Interv.* (2019) 12:1067–76. doi: 10.1016/j.jcin.2018.11.001

17. Bai Y, Xue X, Duenninger E, Muenzel M, Jiang L, Keil T, et al. Real-world survival data of device-related thrombus following left atrial appendage closure: 4-year experience from a single center. *Heart Vessel.* (2019) 34:1360–9. doi: 10.1007/s00380-019-01364-7

18. Aminian A, Schmidt B, Mazzone P, Berti S, Fischer S, Montorfano M, et al. Incidence, characterization and clinical impact of device-related thrombus following left atrial appendage occlusion in the prospective global AMPLATZER Amulet observational study. *JACC Cardiovasc Interv.* (2019) 12:1003–14. doi: 10.1016/j.jcin.2019.02.003

19. Sedaghat A, Schrickel J, Andrie R, Schueler R, Nickenig G, Hammerstingl C. Thrombus formation after left atrial appendage occlusion with the Amplatzer Amulet device. *JACC Clin Electrophysiol.* (2017) 3:71–5. doi: 10.1016/j.jacep.2016.05.006

20. Kanderian A, Gillinov A, Pettersson G, Blackstone E, Klein A. Success of surgical left atrial appendage closure: assessment by trans esophageal echocardiography. *J Am Coll Cardiol.* (2008) 52:924–9. doi: 10.1016/j.jacc.2008.03.067

21. Sivasambu B, Arbab-Zadeh A, Hays A, Calkins H, Berger R. Delayed endothelialization of watchman device identified with cardiac CT. *J Cardiovasc Electrophysiol.* (2019) 30:1319–24. doi: 10.1111/jce.14053

22. Staubach S, Schlatterbeck L, Mörtl M, Strohm H, Hoppmann P, Laugwitz K, et al. Long-term transesophageal echocardiography follow-up after percutaneous left atrial appendage closure. *Heart Rhythm.* (2020) 17:728–33. doi: 10.1016/j.hrthm.2019.12.004

23. Nguyen A, Gallet R, Riant E, Deux J, Boukantar M, Mouillet G, et al. Peridevice leak after left atrial appendage closure: incidence, risk factors, and clinical impact. *Can J Cardiol.* (2019) 35:405–12. doi: 10.1016/j.cjca.2018.12.022

24. Simrad T, Jung R, Lehenbauer K, Piayda K, Pracoń R, Jackson G, et al. Predictors of device-related thrombus following percutaneous left atrial appendage occlusion. *J Am Coll Cardiol.* (2021) 78:297–313. doi: <doi>

25. Cruz-González I, Korsholm K, Trejo-Velasco B, Thambo J, Mazzone P, Rioufol G, et al. Procedural and short-term results with the new Watchman FLX left atrial appendage occlusion device. *JACC Cardiovasc Interv.* (2020) 13:2732–41. doi: 10.1016/j.jcin.2020.06.056

26. Patti G, Sticchi A, Verolino G, Pasceri V, Vizzi V, Elvis B, et al. Safety and efficacy of single versus dual antiplatelet therapy after left atrial appendage occlusion. *Am J Cardiol.* (2020) 134:83–90. doi: 10.1016/j.amjcard.2020.08.013

27. Asmarats L, O'Hara G, Champagne J, Paradis J, Bernier M, O'Connor K, et al. Short-term oral anticoagulation versus antiplatelet therapy following transcatheter left atrial appendage closure. *Circ Cardiovasc Interv.* (2020) 13:e009039. doi: 10.1161/CIRCINTERVENTIONS.120.009039

28. Karavidas A, Lazaros G, Matsakas E, Kouvousis N, Samara C, Christoforatou E, et al. Early pacemaker lead thrombosis leading to massive pulmonary embolism. *Echocardiography.* (2004) 21:429–32. doi: 10.1111/j.0742-2822.2004.03078.x

29. Böhm A, Bányai F, Komáromy K, Pintér A, Préda I. Cerebral embolism due to a retained pacemaker lead: a case report. *PACE.* (1998) 21:629–30. doi: 10.1111/j.1540-8159.1998.tb00111.x

30. Arslan S, Gundogdu F, Bozkurt E. Permanent pacemaker lead thrombosis leading to recurrent pulmonary embolism. *Heart.* (2006) 92:597. doi: 10.1136/hrt.2005.075192

31. Buttigieg J, Asciak R, Mallia Azzopardi C. Pacemaker lead-associated thrombosis in cardiac resynchronisation therapy. *BMJ Case Rep.* (2015) 7:bcr2015210314. doi: 10.1136/bcr-2015-210314

32. Torbicki A, Galié N, Covezzoli A, Rossi E, Rosa M, Goldhaber S. ICOPER study group. right heart thrombi in pulmonary embolism: results from the International cooperative pulmonary embolism registry. *J Am Coll Cardiol.* (2003) 41:2245–51. doi: 10.1016/S0735-1097(03)00479-0

33. Almomani A, Siddiqui K, Ahmad M. Echocardiography in patients with complications related to pacemakers and cardiac defibrillators. *Echocardiography.* (2014) 31:388–99. doi: 10.1111/echo.12483

Frontiers in Cardiovascular Medicine

TYPE Original Research
PUBLISHED 17 March 2023
DOI 10.3389/fcvm.2023.1052178

Check for updates

OPEN ACCESS

EDITED BY
Artur Dziewierz,
Jagiellonian University Medical College, Poland

REVIEWED BY
James Cnota,
Cincinnati Children's Research Foundation, United States
Jiancheng Han,
Beijing Anzhen Hospital, Capital Medical University, China

*CORRESPONDENCE
Yun-Yun Ren
✉ renyunyun@hotmail.com

[†]These authors have contributed equally to this work and share first authorship

SPECIALTY SECTION
This article was submitted to Cardiovascular Imaging, a section of the journal Frontiers in Cardiovascular Medicine

RECEIVED 23 September 2022
ACCEPTED 27 February 2023
PUBLISHED 17 March 2023

CITATION
Zhu C, Li M, Xu C-J, Ding M-J, Xiong Y, Liu R and Ren Y-Y (2023) Comparison of the left and right ventricular size and systolic function of low-risk fetuses in the third trimester: Which is more dominant?
Front. Cardiovasc. Med. 10:1052178.
doi: 10.3389/fcvm.2023.1052178

Comparison of the left and right ventricular size and systolic function of low-risk fetuses in the third trimester: Which is more dominant?

Chen Zhu[1†], Man Li[1†], Cheng-Jie Xu[2], Meng-Juan Ding[1], Yu Xiong[3], Rui Liu[1] and Yun-Yun Ren[1*]

[1]Department of Ultrasound, Obstetrics and Gynecology Hospital of Fudan University, Shanghai, China, [2]Department of Information Technology, Obstetrics and Gynecology Hospital of Fudan University, Shanghai, China, [3]Department of Obstetrics, Obstetrics and Gynecology Hospital of Fudan University, Shanghai, China

Objective: To quantify fetal cardiovascular parameters utilizing fetal-specific 2D speckle tracking technique and to explore the differences in size and systolic function of the left and right ventricles in low-risk pregnancy.
Methods: A prospective cohort study was performed in 453 low-risk single fetuses (28^{+0}–39^{+6} weeks) to evaluate ventricular size [i.e., end-diastolic length (EDL), end-systolic length (ESL), end-diastolic diameter (ED), end-systolic diameter (ES), end-diastolic area, end-systolic area, end-diastolic volume (EDV), and end-systolic volume (ESV)] and systolic function [i.e., ejection fraction (EF), stroke volume (SV), cardiac output (CO), cardiac output per kilogram (CO/KG), and stroke volume per kilogram (SV/KG)].
Results: This study showed that (1) the reproducibility of the interobserver and intraobserver measurements was good to excellent (ICC 0.626–0.936); (2) with advancing gestation, fetal ventricular size and systolic function increased, whereas right ventricular (RV) EF decreased and left ventricular (LV) EF was not significantly changed; (3) LV length was longer than RV length in diastole (2.24 vs. 1.96 cm, $P < 0.001$) and systole (1.72 vs. 1.52 cm, $P < 0.001$); (4) LV ED-S1 and ES-S1 were shorter than the RV ED-S1 and ES-S1 (12.87 vs. 13.43 mm, $P < 0.001$; 5.09 vs. 5.61 mm, $P < 0.001$); (5) there were no differences between the LV and RV in EDA or EDV; (6) the mean EDV ratio of right-to-left ventricle was 1.076 (95% CI, 1.038–1.114), and the mean ESV ratio was 1.628 (95% CI, 1.555–1.701); (7) the EF, CO and SV of the LV were greater than the RV (EF: 62.69% vs. 46.09%, $P < 0.001$; CO: 167.85 vs. 128.69 ml, $P < 0.001$; SV: 1.18 vs. 0.88 ml, $P < 0.001$); (8) SV and CO increased with ED-S1 and EDL, but EF was not significantly changed.
Conclusion: Low-risk fetal cardiovascular physiology is characterized by a larger RV volume (especially after 32 weeks) and greater LV outputs (EF, CO, SV, SV/KG and CO/KG).

KEYWORDS

fetal echocardiography, fetal heart, ultrasound, speckle tracking, fetalHQ, ventricular size, systolic function

Introduction

The size and function of the left and right ventricles in normal fetuses are an important basis and reference for cardiac remodeling studies. Nonetheless, the fetal heart cannot be measured directly *in utero*. Thus, echocardiography is crucial for indirectly obtaining fetal ventricular size and function parameters and includes three general methods. (1) For conventional Doppler and tissue Doppler, the assessment of the fetal ventricular diastolic function of the cardiac cycle is performed with conventional Doppler through the flow velocity of atrioventricular valves (1) and with tissue Doppler through the displacement velocity of the atrioventricular annulus (2). (2) For 2D image and speckle tracking, the length and width of the ventricles are measured first, then the Simpson method is used to calculate the ventricular area and volume (3, 4), and finally the systolic and diastolic volumes are calculated to obtain the parameters of vetricular systolic function. (3) For 3D and 4D sonography the STIC and VOCAL techniques was used to obtain ventricular volume data without assuming geometric shapes (5, 6), then the systolic function parameters are further obtained.

However, these methods have limitations. Doppler velocity is angle-dependent and can make it more difficult to obtain correct images and good measurement reproducibility due to the influence of fetal position (1). It is also more difficult to successfully acquire good images using the 3D/4D method; it takes longer to analyze the images to obtain the data; and the results obtained are only close to (3), or possibly better than (5, 6) 2D measurements. In contrast, the use of 2D speckle tracking is more "cost effective". Previously, analysis of the rapidly beating fetal heart often resulted in biased measurements of fetal cardiac function parameters due to the low frame rate of ultrasound video and the limitations of the 2D speckle tracking software for adults (7).

The novel fetal-specific speckle tracking software (fetalHQ) solves this problem. The fetalHQ is a specialized software for the quantitative analysis of fetal heart. This software tracks myocardial speckle motion, identifies the endocardial boundaries sensitively and accurately, divides the ventricle into 24 segments, and calculates ventricular volumes using the Simpson method, then further obtain ventricular function parameters (3).

The objectives of this study were (1) to describe a reproducible approach to quantify ventricular volume calculations utilizing fetalHQ and (2) to explore the differences in the size and systolic function of the left and right ventricles in low-risk pregnancy at 28–39 weeks.

Methods

Study design and participants

We conducted a prospective study of singleton pregnant women who received prenatal examinations at the Obstetrics and Gynecology Hospital of Fudan University between April 2020 and July 2021 in Shanghai, China. The flowchart for the selection of the study population is shown in **Figure 1**. All participants signed a written informed consent form. The study was approved by the Ethics Committee of the Obstetrics and Gynecology Hospital of Fudan University (No. 2020-52).

The inclusion criteria for the study were as follows: (1) singleton pregnancy; (2) gestational age from 28^{+0} to 39^{+6} weeks; (3) complete prenatal ultrasound measurements (including growth ultrasound measurements and fetal echocardiography); and (4) delivery in our hospital with a complete medical history. The exclusion criteria were (1) irregular menstrual cycle, unclear last menstruation, or no crown-lump length record; (2) fetal malformation chromosomal abnormality or structural abnormalities identified by prenatal ultrasound; or (3) any clinical condition potentially associated with cardiovascular remodeling, such as conception by assisted reproductive technology (ART), maternal pregestational diabetes, hypertensive disorder complicating pregnancy (gestational hypertension, chronic hypertension, preeclampsia or eclampsia) or small for gestational age (EFW <10th centile) at the time of the scan.

EFW was calculated with the Hadlock-4 formula (8). According to the updated ISUOG guidelines (9), the EFW percentile standard recommends selecting criteria based on data from prospective low-risk population studies. The INTERGROWTH-21st standard meets this requirement, and the study data included Chinese low-risk fetuses. Therefore, we selected the INTERGROWTH-21st standard (10) as the EFW percentile standard for this study. The neonatal birth weight percentile evaluation criteria used the latest criteria for low-risk neonatal weight in China published in 2021 (11).

Fetal echocardiography

Two cardiac sonologists with more than 5 years of experience (CZ and ML) performed the ultrasound assessments following a strict protocol (12). All echocardiogram videos were reviewed and approved by the chief sonologist with more than 20 years of experience (Y-YR). All examinations were performed using a Voluson E10 BT19 and BT20 ultrasound device (GE Healthcare, Zipf, Autria) with a transabdominal transducer (GE C2–9, 2–9 MHz, C1–6, 1–6 MHz). All videos were obtained in the absence of fetal body motion and respiratory-like movements, and the pregnant women were asked to hold their breath. Three-second four-chamber loops of the fetal heart were acquired and saved, and during the acquisition time, the heart rate needed to remain stable.

The fetalHQ speckle tracking software (build-in the Voluson E10 ultrasound system) measures ventricular parameters as follows: (1) the M-Mode line is drawn from the apex through the lateral base of the left ventricle (mitral valve lateral anulus), and one cardiac cycle is selected (**Figure 2A**); (2) left ventricular end-systolic endocardial tracing is defined, and the three red anchor points and blue dots can be adjusted (**Figure 2B**); (3) left ventricular end-diastolic endocardial tracing is defined, and the red dots can be adjusted (**Figure 2C**); (4) the endocardial border of the right ventricle at end-systole and end-diastole is traced sequentially (**Figures 2D,E**); and (5) measurements are completed, with the results exported and reported (**Figure 2F**).

The parameters of the left and right ventricular size [24-segment end-diastolic transverse diameter (ED), 24-segment end-systolic transverse diameter (ES), end-diastolic length (EDL), end-systolic length (ESL), end-diastolic area (EDA), end-systolic area (ESA), end-diastolic volume (EDV), end-systolic volume (ESV)] and systolic function (EF, SV and CO) were measured and calculated on a four-chamber view by fetalHQ software.

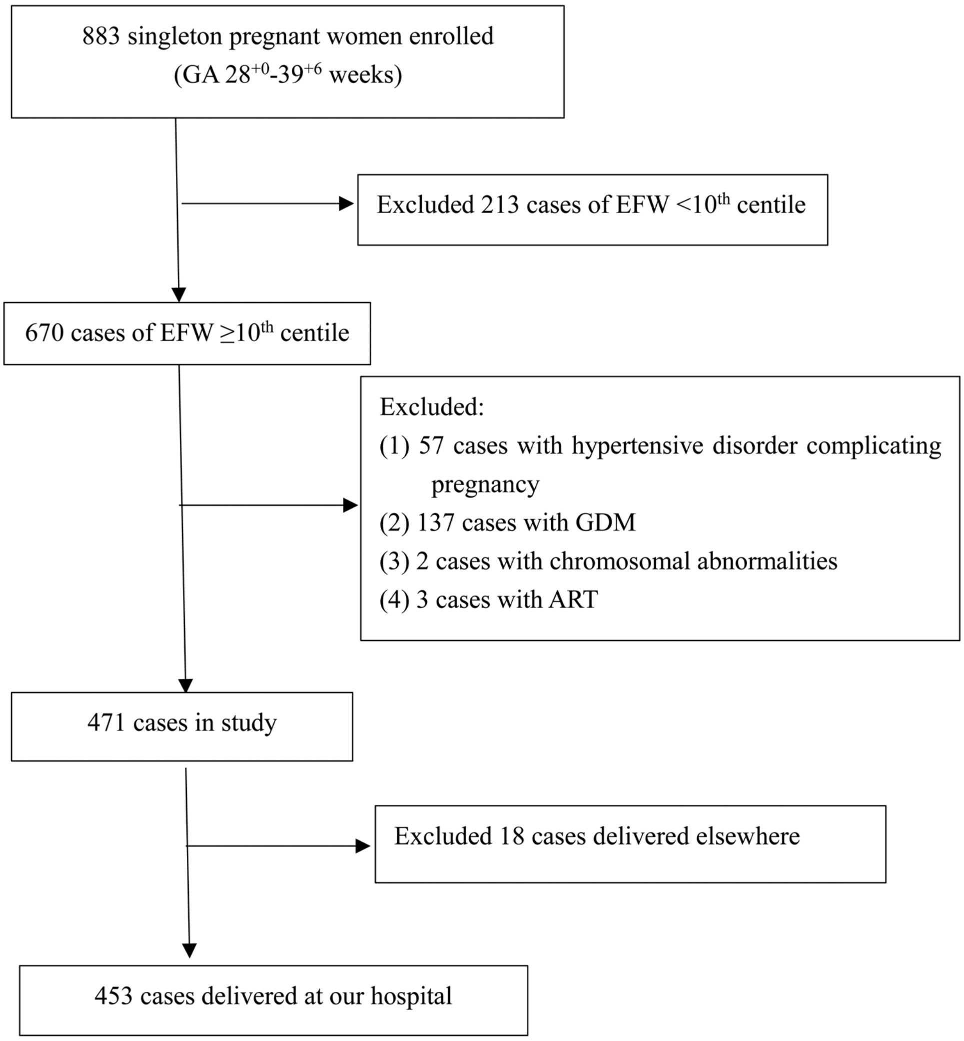

FIGURE 1
Study flowchart. ART, assisted reproductive technology; GDM, gestational diabetes mellitus.

Reproducibility

The interobserver reproducibility was estimated by comparing the measurements of two ultrasound sonologists (CZ and ML). Both repeatedly practiced tracing data from 30 pregnancies (10 patients per one of the following gestational ages: 28–31, 32–36 or 37–39 weeks) using fetalHQ software, with repeatability tests performed after 1 month. The first test measured the same 30 videos and was completed within 2 days. To assess intraobserver reproducibility, repeated measurements of the stored images of the same 30 videos were taken by the two researchers 1 week later.

Statistical analysis

Statistical analysis was performed using IBM SPSS Statistics for Windows, Version 25.0 (SPSS Inc., Chicago, IL, United States). Intraclass correlation coefficient (ICC) and 95% confidence interval (CI) were used to determine the interobserver and intraobserver variability of the fetal cardiac measurements. Continuous data that were normally or approximately normally distributed are expressed as the means ± standard deviations (SD), categorical data are expressed as n (%), and nonnormal variables are presented as the medians (25th and 75th). Student's t-test was used to compare the means, the Mann–Whitney U test was used to compare the medians, and the chi-square test or Fisher's exact test was used in the analysis of proportions between the two groups. $P < 0.05$ was considered statistically significant for all comparisons.

Results

Population characteristics

Of the 883 singleton pregnancies that were initially eligible for inclusion, 430 were excluded due to FGR noted on fetal ultrasound ($n = 213$), fetal chromosome abnormality ($n = 2$), ART ($n = 3$), maternal hypertension and preeclampsia ($n = 57$), maternal diabetes ($n = 137$) or loss to follow-up ($n = 18$). Therefore, a total of 453 low-

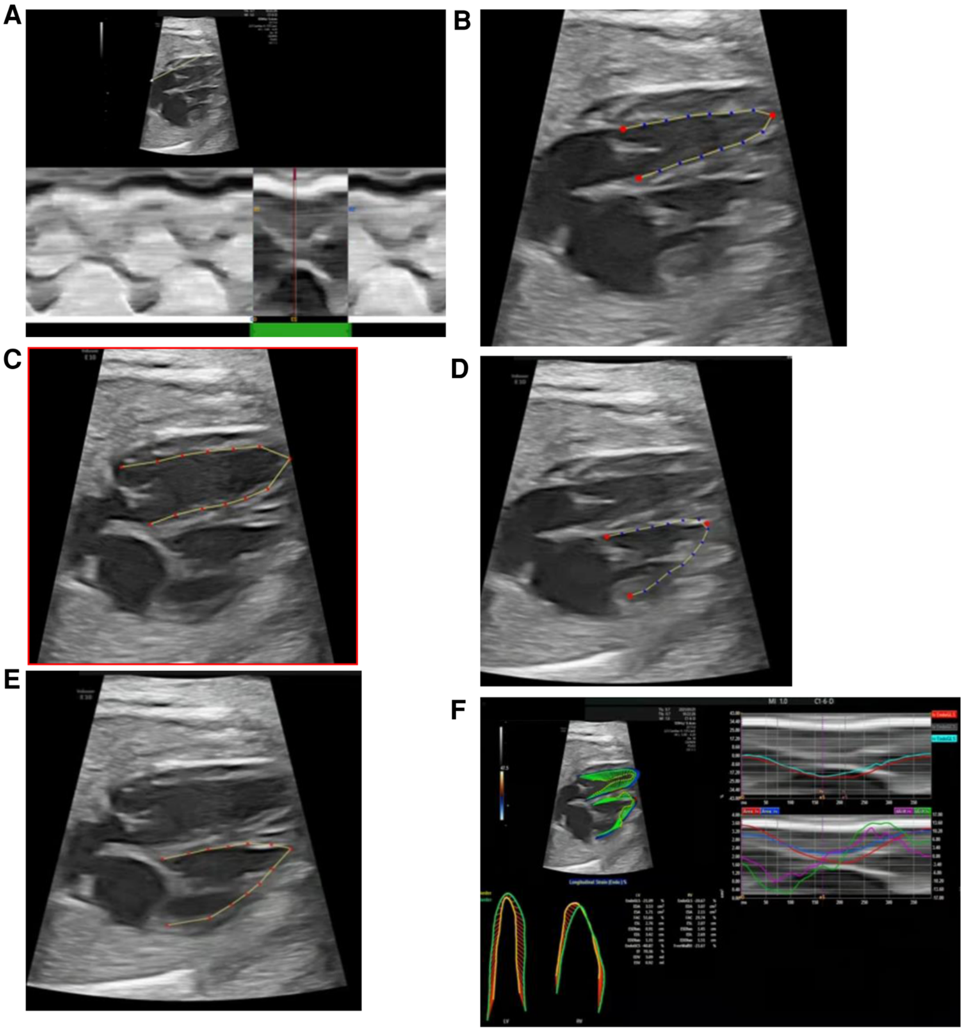

FIGURE 2
fetalHQ speckle tracking software measures left and right ventricular parameters. (A) Selection of one cardiac cycle (M-Mode); (B) defining of left ventricular end-systolic endocardial tracing; (C) defining of left ventricular end-diastolic tracing; (D) defining of right ventricular end-systolic endocardial tracing; (E) defining of right ventricular end-diastolic tracing; (F) obtaining of results and report.

risk singleton pregnancies were finally included in the data analysis (**Figure 1**). Fetal echocardiography data were collected once in each case, and the data from the first scan were selected for those pregnancies with more than two scans. A statistical summary of the characteristics of the research subjects is shown in **Table 1**. The median maternal age was 30 (28–33) years. Most women (77.9%) were nulliparous. The median gestational age at ultrasound scan was 32.5 (31.2–36.1) weeks, the median gestational age of delivery was 39 (38–40) weeks, the mean birth weight was 3228.5 ± 414.6 g, and the median birth weight percentile was 46.7%, interquartile range (24.0%–75.1%).

Reproducibility

The reproducibility analysis showed that after 1 month of training, the interobserver reproducibility was good-to-excellent (ICC 0.626–0.907), and the intraobserver reproducibility was also good-to-excellent (ICC 0.654–0.936) for all of the cardiac parameters evaluated (**Table 2**).

Comparison of left and right ventricular size

Fetal heart rate did not change with gestational age ($R = 0.019$, $P = 0.679$) from 28 to 39 weeks of gestation, median 142 bpm, range (116–177 bpm) (**Figure 3**).

The left and right ventricular ESL, EDL, ES-S1 and ED-S1 increased with gestational age (left: $R = 0.420–0.494$, $P < 0.001$; right: $R = 0.0.471–0.581$, $P < 0.001$). The EDL and ESL of the left ventricle were longer than those of the right ventricle (EDL: 2.24 ± 0.36 cm vs. 1.96 ± 0.34 cm, $P < 0.001$; ESL: 1.72 ± 0.29 cm vs. 1.52 ± 0.28 cm, $P < 0.001$). The left ventricular ED-S1 and ES-S1 were shorter than the right ventricular ED-S1 and ES-S1 (ED-S1: 12.87 ± 1.78 mm vs. 13.43 ± 2.18 mm, $P < 0.001$; ES-S1: 5.09 ± 0.75 mm vs. 5.61 ± 0.94 mm, $P < 0.001$) (**Table 3**).

TABLE 1 Maternal and pregnancy characteristics of the study population of 453 low-risk singleton pregnancies.

Parameters	Value
Maternal age (years)	30 (28–33)
Pregestational BMI (kg/m^2)	20.5 (19–22.3)
Prenatal BMI (kg/m^2)	25.6 (23.7–27.9)
Parity	
Nulliparous	353 (77.9)
Parous	100 (22.1)
GA at time of the scan (weeks)	32.5 (31.2–36.1)
EFW	2,028 (1,684–2,518)
EFW centile	52.4 (29.8–75.0)
Mode of delivery	
Vaginal	297 (65.6)
Cesarean	156 (34.4)
GA at delivery (weeks)	39 (38–40)
Preterm delivery	15 (3.3)
Birth weight (g)	3226.9 ± 415.2
Birth-weight centile	46.7 (24.0–75.1)
Neonatal gender	
Male	217 (47.9)
Female	236 (52.1)
5-min Apgar score*	9 (8–9)*
SGA	38 (8.4)
Adverse perinatal outcome	0
NICU admission	0

*Median (minimum−maximum).
Data are given as the mean ± SD, *n* (%), median (interquartile range) GA, gestational age; BMI, body mass index; EFW, estimated fetal weight; NICU, neonatal intensive care unit; SGA, small for gestational age (defined as birth weight <10th centile).

The left and right ventricular ESA and EDA increased with advancing gestational age (left: $R = 0.412–0.504$, $P < 0.001$; right: $R = 0.665–0.710$, $P < 0.001$). The left ventricular EDA was not significantly larger than that of the right (2.18 ± 0.54 cm^2 vs. 2.11 ± 0.54 cm^2, $P = 0.050$), and the ESA was shorter than that of the right (1.16 ± 0.34 cm^2 vs. 1.38 ± 0.41 cm^2, $P < 0.001$) (**Table 3**).

The left and right ventricular ESV and EDV increased with gestational age (left: $R = 0.386–0.486$, $P < 0.001$; right: $R = 0.640–0.678$, $P < 0.001$). The right-to-left ventricular volume ratios increased with advancing gestational age (EDV ratio: $R = 0.248$, $P < 0.001$; ESV ratio: $R = 0.252$, $P < 0.001$), the mean EDV ratio was 0.987 (95% CI, 0.940–1.034) at 28–32 weeks, 1.170 (95% CI, 1.112–1.229) at 33–39 weeks, and 1.076 (95% CI, 1.038–1.114) at 28–39 weeks (**Figure 4A**), and the mean ESV ratio was 1.628 (95% CI, 1.555–1.701) at 28–39 weeks (**Figure 4B**). The left ventricular EDV was not significantly different from the right, whereas the left ventricular ESV was significantly smaller than that of the right (EDV: 1.89 ± 0.71 ml vs. 1.92 ± 0.75 ml, $P = 0.565$; ESV:0.71 ± 0.33 ml vs. 1.04 ± 0.47 ml, $P < 0.001$) (**Table 3**).

Comparison of left and right ventricular function

The left ventricular EF showed no significant change with gestational age ($R = 0.021$, $P = 0.655$) (**Figure 5A**), and the right ventricular EF decreased with gestational age ($R = −0.131$,

TABLE 2 Intraclass correlation coefficients and interobserver and intraobserver variability for fetal cardiac measurements.

Parameters	ICC (95% confidence interval)			
	Interobserver		Intraobserver	
	LV	RV	LV	RV
Ventricular size				
ED-S1	0.699 (0.458–0.844)	0.691 (0.446–0.84)	0.762 (0.559–0.879)	0.767 (0.566–0.882)
ED-S12	0.704 (0.465–0.847)	0.727 (0.501–0.86)	0.742 (0.526–0.869)	0.792 (0.607–0.895)
ED-S24	0.646 (0.377–0.814)	0.626 (0.348–0.802)	0.871 (0.747–0.937)	0.766 (0.565–0.881)
ES-S1	0.706 (0.469–0.849)	0.759 (0.552–0.877)	0.800 (0.621–0.899)	0.752 (0.542–0.874)
ES-S12	0.695 (0.451–0.842)	0.761 (0.556–0.879)	0.733 (−0.51 to 0.863)	0.776 (0.582–0.887)
ES-S24	0.651 (0.385–0.817)	0.686 (0.438–0.837)	0.736 (0.516–0.865)	0.695 (0.452–0.842)
EDL	0.824 (0.632–0.916)	0.888 (0.740–0.949)	0.824 (0.632–0.916)	0.870 (0.726–0.938)
ESL	0.764 (0.565–0.880)	0.854 (0.638–0.936)	0.846 (0.679–0.926)	0.902 (0.777–0.955)
EDA	0.888 (0.731–0.950)	0.907 (0.803–0.956)	0.918 (0.808–0.963)	0.923 (0.838–0.963)
ESA	0.817 (0.648–0.907)	0.877 (0.683–0.947)	0.857 (0.701–0.932)	0.936 (0.866–0.970)
EDV	0.881 (0.707–0.948)	0.798 (0.619–0.899)	0.926 (0.825–0.967)	0.804 (0.628–0.902)
ESV	0.748 (0.538–0.871)	0.802 (0.624–0.9)	0.842 (0.667–0.925)	0.854 (0.716–0.928)
Ventricular function				
EF	0.740 (0.459–0.876)	0.681 (0.429–0.834)	0.712 (0.449–0.856)	0.704 (0.465–0.847)
SV	0.782 (0.541–0.896)	0.668 (0.411–0.827)	0.822 (0.575–0.920)	0.710 (0.475–0.851)
CO	0.803 (0.489–0.915)	0.713 (0.480–0.852)	0.832 (0.620–0.923)	0.742 (0.525–0.868)
SV/KG	0.692 (0.447–0.84)	0.663 (0.402–0.824)	0.732 (0.510–0.863)	0.660 (0.398–0.822)
CO/KG	0.641 (0.370–0.811)	0.626 (0.348–0.802)	0.680 (0.428–0.834)	0.654 (0.390–0.819)

ICC, intraclass correlation coefficient; LV, left ventricle; RV, right ventricle; ED, end-diastolic diameter; ES, end-systolic diameter; S1, segment 1; S12, segment 12; S24, segment 24; EDL, end-diastolic length; ESL, end-systolic length; EDA, end-diastolic area; ESA, end-systolic area; EDV, end-diastolic volume; ESV, end-systolic volume; EF, ejection fraction; SV, stroke volume; CO, cardiac output; KG, kilogram.

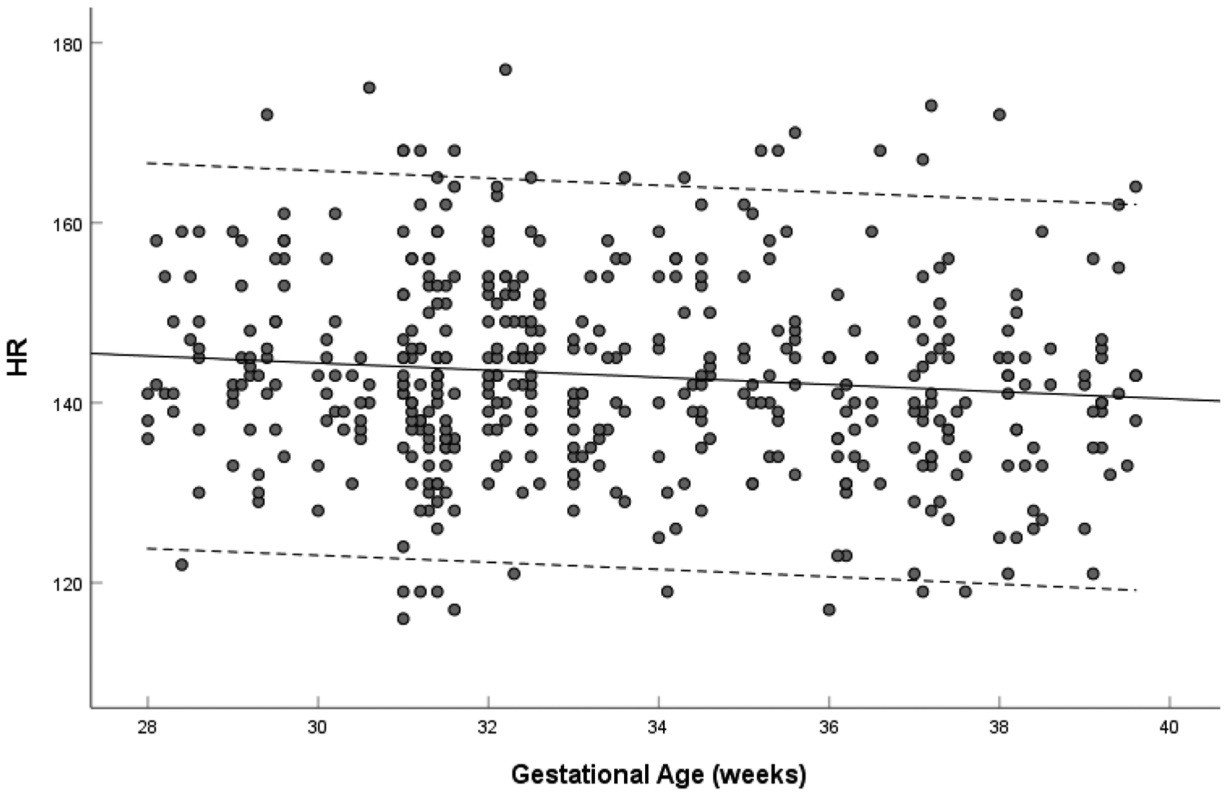

FIGURE 3
Scatterplots of heart rate, according to gestational age (weeks), in 453 low-risk singleton pregnancies from 28 to 39 weeks gestation. Regression lines with the 5% and 95% confidence intervals are plotted with the regression equation. HR, heart rate.

$P = 0.005$) (**Figure 5B**). The ratio of right-to-left ventricular EF decreased with gestational age ($R = -0.123$, $P = 0.009$), the mean EF ratio was 0.745 (95% CI, 0.730–0.760) at 28–39 weeks (**Figure 5C**). The EF of the left ventricle was larger than that of the right ventricle (62.69 ± 8.20% vs. 46.09 ± 9.06%, $P < 0.001$) (**Table 3**).

The left and right ventricular SV increased with gestational age (left: $R = 0.477$, $P < 0.001$; right: $R = 0.559$, $P < 0.001$) (**Figures 6A,B**). The ratio of right-to-left ventricular SV decreased with gestational age ($R = 0.156$, $P = 0.001$), the mean SV ratio was 0.802 (95% CI, 0.769–0.835) at 28–39 weeks (**Figure 6C**). The SV of the left ventricle was larger than that of the right ventricle (1.18 ± 0.46 vs. 0.88 ± 0.37, $P < 0.001$) (**Table 3**).

The left and right ventricular CO increased with gestational age (left: $R = 0.458$, $P < 0.001$; right: $R = 0.552$, $P < 0.001$) (**Figures 7A,B**). The ratio of right-to-left ventricular CO decreased with gestational age ($R = 0.165$, $P < 0.001$), the mean CO ratio was 0.828 (95% CI, 0.793–0.863) at 28–39 weeks (**Figure 7C**). The CO of the left ventricle was larger than that of the right ventricle (167.85 ± 64.30 vs. 128.69 ± 54.37, $P < 0.001$) (**Table 3**).

The left and right ventricular SV/KG and CO/KG increased with gestational age (left: $R = 0.209–0.236$, $P < 0.001$; right: $R = 0.011–$

TABLE 3 Comparison of the left and right ventricular size of low-risk fetuses in the third trimester.

Parameters	Left ventricle	Right ventricle	*P* value
Ventricular size			
ED Segment 1 (mm)	12.87 ± 1.78	13.43 ± 2.18	<0.001
Segment 12 (mm)	10.82 ± 1.66	11.85 ± 2.05	<0.001
Segment 24 (mm)	2.09 ± 0.44	1.74 ± 0.43	<0.001
ES Segment 1 (mm)	5.09 ± 0.75	5.61 ± 0.94	<0.001
Segment 12 (mm)	3.51 ± 0.76	4.89 ± 0.96	<0.001
Segment 24 (mm)	0.65 ± 0.13	0.73 ± 0.13	<0.001
EDL (cm)	2.24 ± 0.36	1.96 ± 0.34	<0.001
ESL (cm)	1.72 ± 0.29	1.52 ± 0.28	<0.001
EDA (cm^2)	2.18 ± 0.54	2.11 ± 0.54	0.050
ESA (cm^2)	1.16 ± 0.34	1.38 ± 0.41	<0.001
EDV (ml)	1.89 ± 0.71	1.92 ± 0.75	0.565
ESV (ml)	0.71 ± 0.33	1.04 ± 0.47	<0.001
Ventricular function			
EF (%)	62.69 ± 8.20	46.09 ± 9.06	<0.001
SV (ml)	1.18 ± 0.46	0.88 ± 0.37	<0.001
CO (ml/min)	167.85 ± 64.30	128.69 ± 54.37	<0.001
SV/KG (ml/kg)	0.57 ± 0.18	0.42 ± 0.14	<0.001
CO/KG (ml/min/kg)	81.27 ± 26.38	61.36 ± 21.13	<0.001

Data are given as the mean ± SD. ED, end-diastolic diameter; ES, end-systolic diameter; EDL, end-diastolic length; ESL, end-systolic length; EDA, end-diastolic area; ESA, end-systolic area; EDV, end-diastolic volume; ESV, end-systolic volume; EF, ejection fraction; FS, fractional shortening; SV, stroke volume; CO, cardiac output; KG, kilogram.

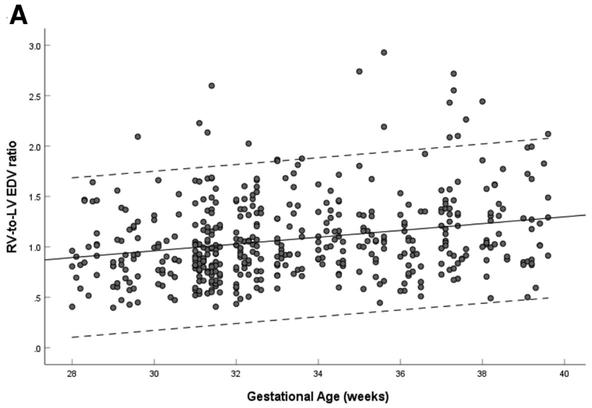

FIGURE 4
Scatterplots of right-to-left ventricular EDV ratio (A) and ESV ratio (B), according to gestational age (weeks), in 453 low-risk singleton pregnancies from 28 to 39 weeks gestation. Regression lines with the 5% and 95% confidence intervals are plotted with the regression equation. LV, left ventricle; RV, right ventricle; EDV, end-diastolic volume; ESV, end-systolic volume.

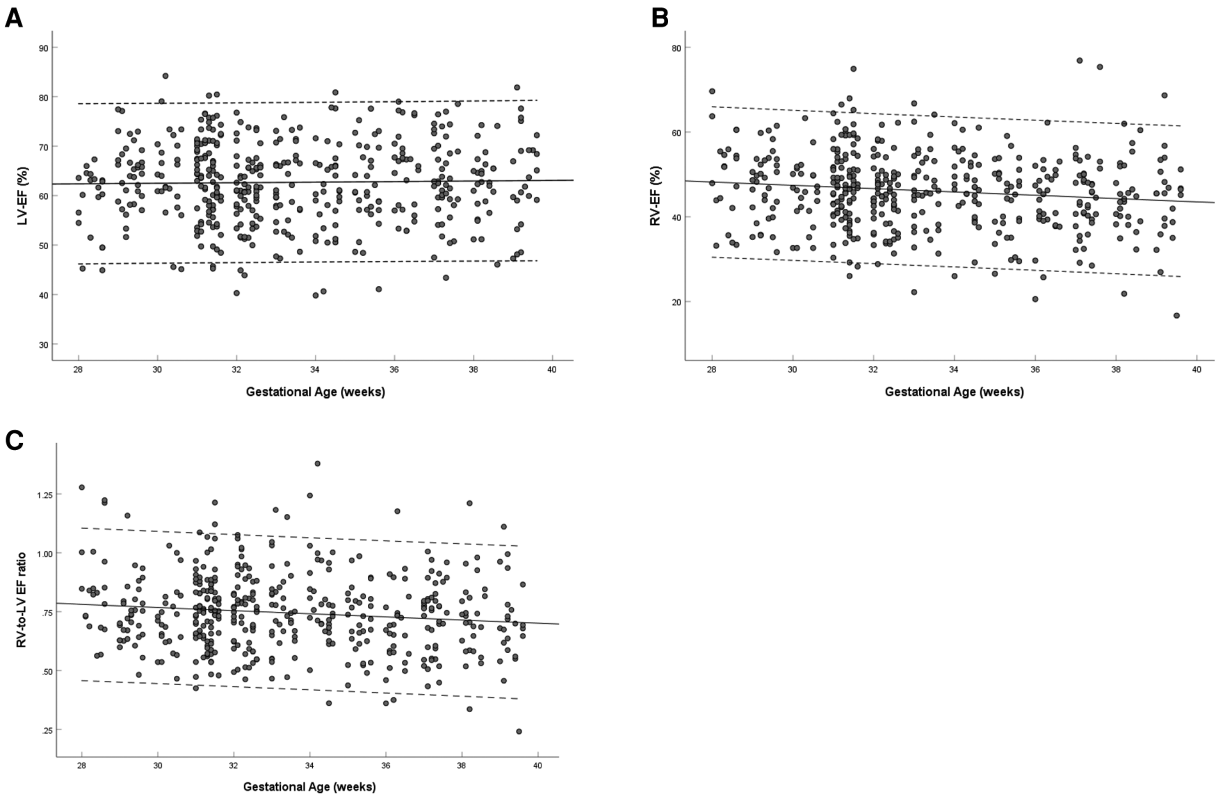

FIGURE 5
Scatterplots of left ventricular EF (A), right ventricular EF (B) and right-to-left ventricular EF ratio (C), according to gestational age (weeks), in 453 low-risk singleton pregnancies from 28 to 39 weeks gestation. Regression lines with the 5% and 95% confidence intervals are plotted with the regression equation. LV, left ventricle; RV, right ventricle; EF, ejection fraction.

0.018, $P = 0.706–0.820$). The SV/KG of the left ventricle was larger than that of the right ventricle (0.57 ± 0.18 vs. 0.42 ± 0.14, $P < 0.001$). The CO/KG of the left ventricle was larger than that of the right ventricle (81.27 ± 26.38 vs. 61.36 ± 21.13, $P < 0.001$) (**Table 3**).

Relationship between ventricular end-diastolic size and systolic function

The EF of the left and right ventricles did not significantly change with increasing ED-S1 (left: $R = 0.002$, $P = 0.958$; right:

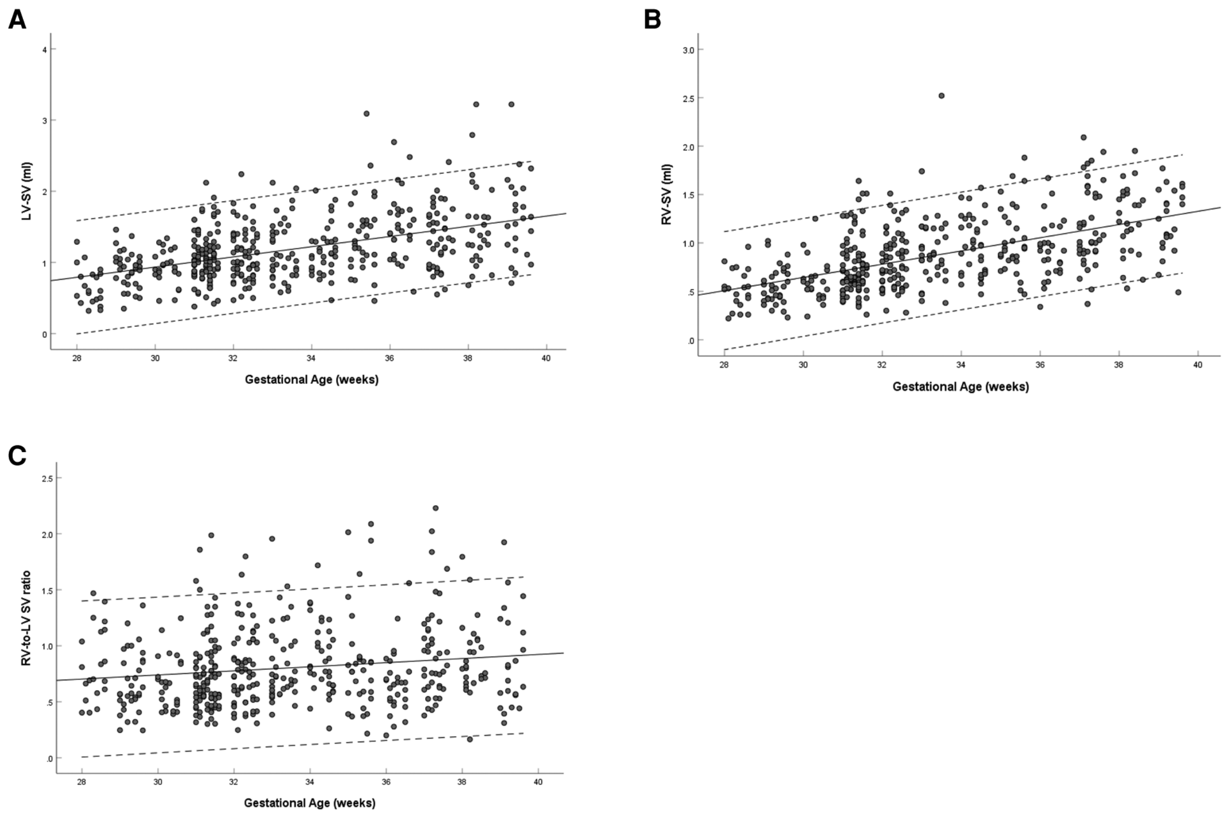

FIGURE 6
Scatterplots of left ventricular SV (A), right ventricular SV (B), and right-to-left ventricular SV ratio (C), according to gestational age (weeks), in 453 low-risk singleton pregnancies from 28 to 39 weeks gestation. Regression lines with the 5% and 95% confidence intervals are plotted with the regression equation. LV, left ventricle; RV, right ventricle; SV, stroke volume.

$R = 0.063$, $P = 0.180$) or EDL (left: $R = 0.018$, $P = 0.702$; right: $R = 0.004$, $P = 0.943$).

The SV of the left and right ventricles increased with ED-S1 (left: $R = 0.705$, $P < 0.001$; right: $R = 0.727$, $P < 0.001$) and EDL (left: $R = 0.644$, $P < 0.001$; right: $R = 0.565$, $P < 0.001$).

The CO of the left and right ventricles increased with ED-S1 (left: $R = 0.694$, $P < 0.001$; right: $R = 0.710$, $P < 0.001$) and EDL (left: $R = 0.630$, $P < 0.001$; right: $R = 0.554$, $P < 0.001$) (left: **Figure 8A**; right: **Figure 8B**).

Discussion

The main findings of this study were as follows: (1) the reproducibility of the interobserver and intraobserver measurements was good to excellent after full training; (2) fetal ventricular size and systolic function increased with advancing gestation, whereas right ventricular EF decreased and left ventricular EF was not significantly changed; (3) left ventricular length was longer than the right; (4) left ventricular ED-S1 and ES-S1 were shorter than the right; (5) there were no differences between the left and right ventricles for EDA or EDV; (6) the ratio of right-to-left ventricular volume increased with gestational age, and the right ventricle was found to be volumetrically greater in both EDV and ESV, especially after 32 weeks; (7) The mean EF, CO and SV ratio of right-to-left ventricle were less than 1 at 28–39 weeks, and the left ventricular EF, CO and SV were greater than the right; and (8) SV and CO increased with ED-S1 and EDL, whereas EF was not significantly changed.

Ventricular dominance in low-risk fetuses in terms of size

In this study, the two ventricular sizes increased with gestational age, whereas the right ventricle size was more associated with gestational age than the left ventricle size. The EDL and ESL of the left ventricle were significantly larger than those of the right ventricle ($P < 0.001$), which is consistent with the findings of DeVore et al. (13) (20–40 weeks). Meanwhile, in our study, the ED-S1 and ED-S12 of the left ventricle were significantly shorter than those of the right ventricle, but the ED-S24 was larger than that of the right ventricle ($P < 0.001$). The left ventricular EDA was not significantly larger than the right ventricular ESA ($P = 0.05$), but the ESA was shorter than the right ventricular EDA ($P < 0.001$). These results indicate that the left ventricle is longer than the right ventricle, that the right

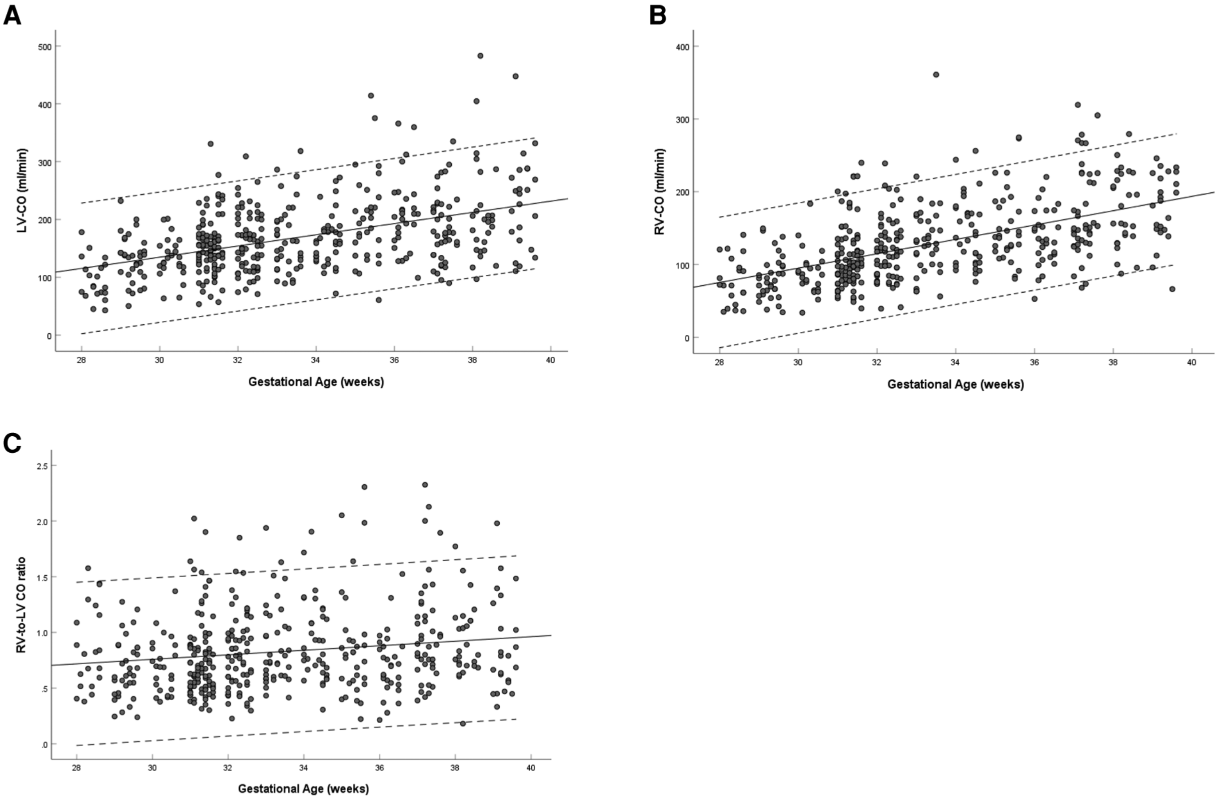

FIGURE 7
Scatterplots of left ventricular CO (**A**), right ventricular CO (**B**), and right-to-left ventricular CO ratio (**C**), according to gestational age (weeks), in 453 low-risk singleton pregnancies from 28 to 39 weeks gestation. Regression lines with the 5% and 95% confidence intervals are plotted with the regression equation. LV, left ventricle; RV, right ventricle; CO, cardiac output.

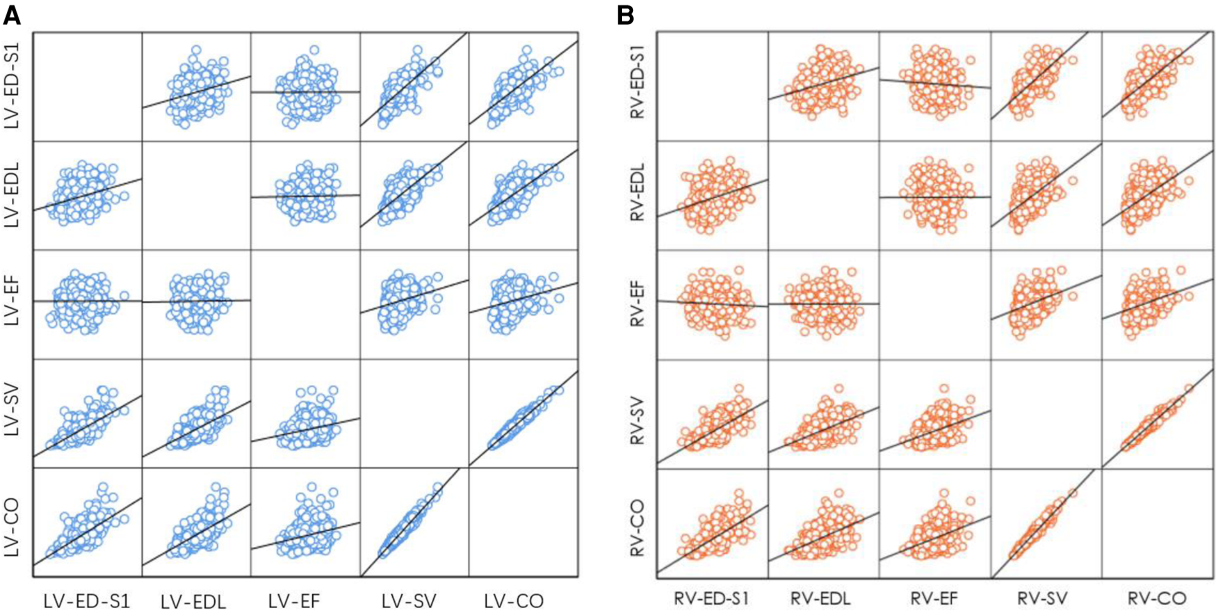

FIGURE 8
Correlation between end-diastolic ventricular size (ED-S1, EDL) and ventricular systolic function parameters (EF, SV, CO). (**A**) Left ventricle; (**B**) right ventricle. LV, left ventricle; RV, right ventricle; ED-S1, end-diastolic diameter segment 1; EDL, end-diastolic length; EF, ejection fraction; SV, stroke volume; CO, cardiac output.

ventricle is wider than the left ventricle and that the apical portion of the left ventricle is more rounded than the right ventricle, which is consistent with the anatomy of the right and left ventricles.

Previous studies have reported inconsistent results regarding the comparison of the area and diameter of the two ventricles. For example, DeVore et al. (13) (20–40 weeks) suggested that the EDA and ED-S1 of the left ventricle were significantly larger than those of the right ventricle. Schneider et al. (14) (15–39 weeks) suggested that the EDA of the left ventricle was significantly smaller than that of the right ventricle, and Gabbay-Benziv et al. (15) (16–38 weeks) and Sharland et al. (16) (17–41 weeks) suggested that the left ventricular ED-S1 was significantly smaller than that of the right ventricle.

Ventricular volume changes are most closely related to systolic function. This study analyzed the ratio of right-to-left ventricular volume and found the right ventricle was volumetrically greater in both EDV and ESV, especially after 32 weeks. When we compared ventricular volumes in end-systole, the right ventricle remained greater than the left ventricle, but in end-diastole, there was no difference between right and left ventricles. Many previous studies (5, 17–19) have shown that the EDV of the right ventricle was significantly greater than that of the left ventricle. However, the guidelines for performing the “basic” and “extended basic” cardiac scans (20, 21) and the study by Sutton (22) (20 weeks to term) reported that both ventricles of normal fetal hearts appear similar in size, consistent with the results of our study. Meanwhile, our study demonstrated the right ventricular dominance in the larger volume measurements, especially after 32 weeks.

Changes in ventricular size and morphology, particularly ventricular enlargement, are one of the manifestations of cardiac remodeling (23) and are important in the evaluation of intrauterine growth restriction (24). In contrast, fetal anomalies such as Ebstein’s malformation, pulmonary valve stenosis and cardiomyopathy (25) can also present with abnormalities in the left or right ventricular area.

Ventricular dominance in low-risk fetuses in terms of systolic function

The theory of normal fetal right ventricular dominance that most researchers currently accept was first derived from the results of left and right ventricular output in animal studies (26, 27). However, some researchers have challenged this theory with the equal weight of the right and left ventricles in cadaveric fetal specimens (28). Other researchers have argued that it is unreasonable to use the weight of the heart of a stillborn fetus to infer the predominance of the heart of a living fetus (19). However, the debate on the issue of fetal ventricular dominance is ongoing. There has been debate as to whether the right ventricular output is actually greater, the same as (5, 22, 28) (19–38 weeks), or less than that of the left ventricle (29, 30) (fetal lamb).

The EF, CO and SV can reflect ventricular volume changes. In our study, the mean EF, CO and SV ratio of right-to-left ventricle were less than 1 at 28–39 weeks, and the EF, CO, SV, CO/KG and SV/KG of the left ventricle were greater than those of the right ventricle. Although most studies consider right ventricular dominance in the fetal period, there are authoritative studies that have reported the same results as ours. Hamill et al. (5) (19–38 weeks) suggested that the left ventricular EF was significantly higher than the right ventricular EF, but there was no difference in the CO between the two ventricles using 4D-STIC and VOCAL. Meanwhile, early results from some animal tests support the notion that the output of the left ventricle is greater than that of the right ventricle (29, 30). There is support for the idea that humans have a much larger brain size and metabolic requirements than small animals (31). Under this reasoning, it is also reasonable that the left ventricle needs to contract more than the right ventricle to pump more blood to distribute to the developing brain (5). Anatomically, the right ventricular myofibers are thin, the epi-myocardial circumferential fibers are contiguous with the epi-myocardial oblique fibers of the left ventricle, and the subendomyocardial longitudinal fibers of the right ventricle are contiguous with the fibers of the interventricular septum. The myofibers of the left ventricle are thicker and composed of 3 layers of fibers. In addition to having the same subendomyocardial longitudinal fibers as the right ventricle, the left ventricle has an additional layer of circumferentially oriented fibers in the middle, which play a role in determining the range and extent of myocardial deformation (32).

Therefore, it is reasonable that the contractile force of the left ventricle is higher than that of the right ventricle. On the other hand, umbilical artery resistance decreases with gestational age, and fetal pulmonary vascular resistance is higher than systemic vascular resistance before birth (33). This makes the ESV of the left ventricle smaller than that of the right ventricle, and the EF, SV, and CO, among others, are greater for the left ventricle.

However, it is important to be reminded that many studies, as mentioned above, suggested that the volume of the right ventricle in the fetal period was larger than that of the left ventricle, especially in late pregnancy, which was contrary to the results of this study. The main reasons may be as follows. The structure of the right ventricle is relatively complex, including the right ventricular inflow tract, trabecular part and outflow tract. Because the measurements obtained in this study were based on the four-chamber view, the outflow tract would not be included in the right ventricle, so the EDV, ESV and CO parameters of the right ventricle would be underestimated, which may affect the results of this study.

Abnormal changes in fetal heart function, as well as disproportionate left and right ventricular ratios (34), suggest an abnormal fetal status. Devore et al. showed that (3) EF, SV, SV/KG, CO and CO/kg were significantly reduced in fetuses with severe aortic stenosis and severe anemia; SV, SV/KG, CO and CO/KG were significantly increased in fetuses with cardiomyopathy; and SV and SV/KG were not significantly increased in fetuses with growth restriction.

Relationship between ventricular end-diastolic size and systolic function

The results of our study showed that the ventricular size (end-diastolic length and diameter) was highly correlated with the output parameters (SV and CO) in low-risk fetuses but had a low correlation with EF. The correlation between ED-S1 and ventricular SV and CO was higher than that of EDL. Therefore, the effect of the changes in ED-S1 on systolic function was greater than that of EDL. Recent literature has reported that fetuses with an EFW <10th centile had an increased area of the 4-chamber view and an abnormal size of the ventricles. The proportion of global transverse width increase was the highest (24). In addition, FGR fetuses have wider left and right ventricles than normal fetuses (35).

Strengths and limitations

The greatest strength of our study is the finding of higher left ventricular systolic function (including EF, SV, CO, SV/KG and CO/KG) than right ventricle in low-risk fetuses using novel fetal-specific 2D speckle tracking software, followed by the right ventricle was found to be volumetrically greater in both EDV and ESV (especially after 32 weeks), then the finding that ED-S1 has a greater impact on systolic function than EDL.

The limitations are that (1) there remains a lack of a gold standard for validation of ventricular size and systolic function calculation methods, but previous study showed that the method of using volumetric measurements to calculate SV and CO is accurate and reliable (36); and (2) although the combined time for a four-chamber view video acquisition and 2D speckle tracking analysis is 4 min at most, it takes time to learn the professional knowledge that is needed and that a certain sample size for operation training is required to skillfully use the fetalHQ software.

Conclusion

In summary, the findings of this study suggest that right ventricular dominance was demonstrated by volume measurements, especially after 32 weeks, but that left ventricular dominance was observed in systolic function parameters (EF, CO, SV, SV/KG and CO/KG). ED-S1 has a greater impact on systolic function than EDL. These findings can provide some insights for further research demonstration in the field.

Data availability statement

The raw data supporting the conclusions of this article will be made available by the authors, without undue reservation.

Ethics statement

The study was approved by the Ethics Committee of the Obstetrics and Gynecology Hospital of Fudan University (No. 2020-52). The patients/participants provided their written informed consent to participate in this study.

Author contributions

CZ conceived and designed the analysis, collected the data, contributed data or analysis tools, performed the analysis, wrote the paper, and approved the final draft. Y-YR conceived and designed the analysis, collected the data, reviewed drafts of the paper, and approved the final draft. ML: collected the data, follow-up medical history, reviewed drafts of the paper. C-JX: provided follow-up medical history, contributed data or analysis tools, and reviewed drafts of the paper. M-JD: provided follow-up medical history, reviewed drafts of the paper. YX: collected the data, reviewed drafts of the paper. RL: provided follow-up medical history, reviewed drafts of the paper. All authors contributed to the article and approved the submitted version.

Funding

This work was supported by the special project of clinical research of the health industry of Shanghai Municipal Health Commission (No. 202140217) and the Ultrasound Branch of China Medical Doctor Association, China Ultrasound Physician "Science and Technology Rising Star" Project (No. KJXX2020004).

Conflict of interest

The authors declare that the research was conducted in the absence of any commercial or financial relationships that could be construed as a potential conflict of interest.

Publisher's note

References

1. Hernandez-Andrade E, Benavides-Serralde JA, Cruz-Martinez R, Welsh A, Mancilla-Ramirez J. Evaluation of conventional Doppler fetal cardiac function parameters: E/A ratios, outflow tracts, and myocardial performance index. *Fetal Diagn Ther*. (2012) 32(1–2):22–9. doi: 10.1159/000330792

2. Comas M, Crispi F. Assessment of fetal cardiac function using tissue Doppler techniques. *Fetal Diagn Ther*. (2012) 32(1–2):30–8. doi: 10.1159/000335028

3. DeVore GR, Klas B, Satou G, Sklansky M. Evaluation of fetal left ventricular size and function using speckle-tracking and the simpson rule. *J Ultrasound Med*. (2019) 38(5):1209–21. doi: 10.1002/jum.14799

4. Schmidt KG, Silverman NH, Hoffman JIE. Determination of ventricular volumes in human fetal hearts by 2-dimensional echocardiography. *Am J Cardiol*. (1995) 76 (17):1313–6. doi: 10.1016/S0002-9149(99)80365-8

5. Hamill N, Yeo L, Romero R, Hassan SS, Myers SA, Mittal P, et al. Fetal cardiac ventricular volume, cardiac output, and ejection fraction determined with 4-dimensional ultrasound using spatiotemporal image correlation and virtual organ computer-aided analysis. *Am J Obstet Gynecol*. (2011) 205(1):76.e1–e10. doi: 10.1016/j.ajog.2011.02.028

6. Luewan S, Yanase Y, Tongprasert F, Srisupundit K, Tongsong T. Fetal cardiac dimensions at 14-40 weeks' gestation obtained using cardio-STIC-M. *Ultrasound Obstet Gynecol*. (2011) 37(4):416–22. doi: 10.1002/uog.8961

7. Germanakis I, Gardiner H. Assessment of fetal myocardial deformation using speckle tracking techniques. *Fetal Diagn Ther*. (2012) 32(1-2):39–46. doi: 10.1159/000330378

8. Hadlock FP, Harrist RB, Sharman RS, Deter RL, Park SK. Estimation of fetal weight with the use of head, body, and femur measurements - a prospective-study. *Am J Obstet Gynecol*. (1985) 151(3):333–7. doi: 10.1016/0002-9378(85)90298-4

9. Comm CS. ISUOG practice guidelines: ultrasound assessment of fetal biometry and growth. *Ultrasound Obstet Gynecol*. (2019) 53(6):715–23. doi: 10.1002/uog.20272

10. Stirnemann J, Villar J, Salomon LJ, Ohuma E, Ruyan P, Altman DG, et al. International estimated fetal weight standards of the INTERGROWTH-21(st) project. *Ultrasound Obstet Gynecol*. (2017) 49(4):478–86. doi: 10.1002/uog.17347

11. Zong XN, Li H, Zhang YQ, Wu HH, Zhao GL, Feng Q, et al. Working committee of the China national newborn growth standards project. Construction of China national newborn growth standards based on a large low-risk sample. *Sci Rep*. (2021) 11(1):16093. doi: 10.1038/s41598-021-94606-6

12. DeVore GR, Polanco B, Satou G, Sklansky M. Two-dimensional speckle tracking of the fetal heart A practical step-by-step approach for the fetal sonologist. *J Ultrasound Med*. (2016) 35(8):1765–81. doi: 10.7863/ultra.15.08060

13. DeVore GR, Klas B, Satou G, Sklansky M. Evaluation of the right and left ventricles: an integrated approach measuring the area, length, and width of the chambers in normal fetuses. *Prenat Diagn*. (2017) 37(12):1203–12. doi: 10.1002/pd.5166

14. Schneider C, McCrindle BW, Carvalho JS, Hornberger LK, McCarthy KP, Daubeney PE. Development of Z-scores for fetal cardiac dimensions from echocardiography. *Ultrasound Obstet Gynecol*. (2005) 26(6):599–605. doi: 10.1002/uog.2597

15. Gabbay-Benziv R, Turan OM, Harman C, Turan S. Nomograms for fetal cardiac ventricular width and right-to-left ventricular ratio. *J Ultrasound Med*. (2015) 34 (11):2049–55. doi: 10.7863/ultra.14.10022

16. Sharland GK, Allan LD. Normal fetal cardiac measurements derived by cross-sectional echocardiography. *Ultrasound Obstet Gynecol*. (1992) 2(3):175–81. doi: 10.1046/j.1469-0705.1992.02030175.x

17. Messing B, Cohen SM, Valsky DV, Rosenak D, Hochner-Celnikier D, Savchev S, et al. Fetal cardiac ventricle volumetry in the second half of gestation assessed by 4D ultrasound using STIC combined with inversion mode. *Ultrasound Obstet Gynecol*. (2007) 30(2):142–51. doi: 10.1002/uog.4036

18. Zheng MJ, Schaal M, Chen Y, Li XK, Shentu WH, Zhang PY, et al. Real-time 3-dimensional echocardiographic assessment of ventricular volume, mass, and function in human fetuses. *Plos One*. (2013) 8(3):e58494. doi: 10.1371/journal.pone.0058494

19. Veille JC, Sivakoff M, Nemeth M. Evaluation of the human fetal cardiac size and function. *Am J Perinatol*. (1990) 7(1):54–9. doi: 10.1055/s-2007-999447

20. International Society of Ultrasound in Obstetrics and Gynecology, Carvalho JS, Allan LD, Chaoui R, Copel JA, DeVore GR, et al. ISUOG practice guidelines (updated): sonographic screening examination of the fetal heart. *Ultrasound Obstet Gynecol*. (2013) 41(3):348–59. doi: 10.1002/uog.12403

21. Cardiac screening examination of the fetus: guidelines for performing the 'basic' and 'extended basic' cardiac scan. *Ultrasound Obstet Gynecol*. (2006) 27(1):107–13. doi: 10.1002/uog.2677

22. Sutton MGT, Gewitz MH, Shah B, Cohen A, Reichek N, Gabbe S, et al. Quantitative assessment of growth and function of the cardiac chambers in the normal human-fetus: a prospective longitudinal echocardiographic study. *Circulation*. (1984) 69(4):645–54. doi: 10.1161/01.CIR.69.4.645

23. Rodriguez-Lopez M, Cruz-Lemini M, Valenzuela-Alcaraz B, Garcia-Otero L, Sitges M, Bijnens B, et al. Descriptive analysis of different phenotypes of cardiac remodeling in fetal growth restriction. *Ultrasound Obstet Gynecol*. (2017) 50 (2):207–14. doi: 10.1002/uog.17365

24. Hobbins JC, Gumina DL, Zaretsky MV, Driver C, Wilcox A, DeVore GR. Size and shape of the four-chamber view of the fetal heart in fetuses with an estimated fetal weight less than the tenth centile. *Am J Obstet Gynecol*. (2019) 221(5):495.e1–e9. doi: 10.1016/j.ajog.2019.06.008

25. Donofrio MT, Moon-Grady AJ, Hornberger LK, Copel JA, Sklansky MS, Abuhamad A, et al. Diagnosis and treatment of fetal cardiac disease: a scientific statement from the American heart association. *Circulation*. (2014) 129 (21):2183–242. doi: 10.1161/01.cir.0000437597.44550.5d

26. Acharya G, Erkinaro T, Makikallio K, Lappalainen T, Rasanen J. Relationships among Doppler-derived umbilical artery absolute velocities, cardiac function, and placental volume blood flow and resistance in fetal sheep. *Am J Physiol Heart Circ Physiol*. (2004) 286(4):H1266–72. doi: 10.1152/ajpheart.00523.2003

27. Anderson DF, Bissonnette JM, Faber JJ, Thornburg KL. Central shunt flows and pressures in the mature fetal lamb. *Am J Physiol*. (1981) 241(1):H60–6. doi: 10.1152/ajpheart.1981.241.1.H60

28. St John Sutton MG, Raichlen JS, Reichek N, Huff DS. Quantitative assessment of right and left ventricular growth in the human fetal heart: a pathoanatomic study. *Circulation*. (1984) 70(6):935–41. doi: 10.1161/01.CIR.70.6.935

29. Mahon WA, Goodwin JW, Paul WM. Measurement of individual ventricular outputs in the fetal lamb by a dye dilution technique. *Circ Res*. (1966) 19:191–8. doi: 10.1161/01.RES.19.1.191

30. Dawes GS, Mott JC, Widdicombe JG. The foetal circulation in the lamb. *J Physiol*. (1954) 126(3):563–87. doi: 10.1113/jphysiol.1954.sp005227

31. Garcia-Otero L, Soveral I, Sepulveda-Martinez A, Rodriguez-Lopez M, Torres X, Guirado L, et al. Reference ranges for fetal cardiac, ventricular and atrial relative size, sphericity, ventricular dominance, wall asymmetry and relative wall thickness from 18 to 41 gestational weeks. *Ultrasound Obstet Gynecol*. (2021) 58(3):388–97. doi: 10.1002/uog.23127

32. Ho SY, Nihoyannopoulos P. Anatomy, echocardiography, and normal right ventricular dimensions. *Heart*. (2006) 92:I2–I13. doi: 10.1136/hrt.2005.064378

33. Lakshminrusimha S. The pulmonary circulation in neonatal respiratory failure. *Clin Perinatol*. (2012) 39(3):655–83. doi: 10.1016/j.clp.2012.06.006

34. Quartermain MD, Cohen MS, Dominguez TE, Tian ZY, Donaghue DD, Rychik J. Left ventricle to right ventricle size discrepancy in the fetus: the presence of critical congenital heart disease can be reliably predicted. *J Am Soc Echocardiogr*. (2009) 22 (11):1296–301. doi: 10.1016/j.echo.2009.08.008

35. Patey O, Carvalho JS, Thilaganathan B. Perinatal changes in cardiac geometry and function in growth-restricted fetuses at term. *Ultrasound Obstet Gynecol*. (2019) 53(5):655–62. doi: 10.1002/uog.19193

36. Rizzo G, Capponi A, Cavicchioni O, Vendola M, Arduini D. Fetal cardiac stroke volume determination by four-dimensional ultrasound with spatio-temporal image correlation compared with two-dimensional and Doppler ultrasonography. *Prenat Diagn*. (2007) 27(12):1147–50. doi: 10.1002/pd.1870

frontiers | Frontiers in Cardiovascular Medicine

TYPE Systematic Review
PUBLISHED 27 March 2023
DOI 10.3389/fcvm.2023.980626

The clinical application of longitudinal layer specific strain as a diagnostic and prognostic instrument in ischemic heart diseases: A systematic review and meta-analysis

Shreeya Sharma[1]*, Mats Christian Højbjerg Lassen[1,2,3], Anne Bjerg Nielsen[1], Kristoffer Grundtvig Skaarup[1,2,3] and Tor Biering-Sørensen[1,2,3]

[1]Department of Cardiology, Copenhagen University Hospital – Herlev and Gentofte, Copenhagen, Denmark, [2]Center for Translational Cardiology and Pragmatic Randomized Trials, Department of Biomedical Sciences, Faculty of Health and Medical Sciences, University of Copenhagen, Copenhagen, Denmark, [3]The Copenhagen City Heart Study, Copenhagen University Hospital – Bispebjerg and Frederiksberg, Copenhagen, Denmark

Background: 2-dimensional Speckle-Tracking Echocardiography, to obtain longitudinal layer specific strain (LSS), has recently emerged as a novel and accurate non-invasive imaging technique for diagnosis as well as for prediction of adverse cardiac events. This systematic review and meta-analysis aimed to give an overview of the possible clinical implication and significance of longitudinal LSS.

Methods: We conducted a systematic review and meta-analysis with all the studies involving layer specific strain in patients with ischemic heart disease (IHD). Of 40 eligible studies, 9 met our inclusion criteria. Studies that were included either investigated the prognostic value ($n = 3$) or the diagnostic value ($n = 6$) of longitudinal LSS.

Results: The pooled meta-analysis showed that longitudinal LSS is a significant diagnostic marker for coronary artery disease (CAD) in patients with IHD. Endocardial LSS was found to be a good diagnostic marker for CAD in IHD patients (OR: 1.28, CI95% [1.11–1.48], $p < 0.001$, per 1% decrease). Epicardial (OR: 1.34, CI95% [1.14–1.56], $p < 0.001$, per 1% decrease), Mid-Myocardial (OR: 1.24, CI95% [1.12–1.38], $p < 0.001$, per 1% decrease) and endocardial (OR: 1.21, CI95% [1.09–1.35], $p < 0.001$, per 1% decrease) LSS all entailed diagnostic information regarding CAD, with epicardial LSS emerging as the superior diagnostic marker for CAD in patients with SAP. Endocardial LSS proved to be the better diagnostic marker of CAD in patients with non-ST elevation acute coronary syndrome (NSTE-ACS). LSS was shown to be a good prognostic maker of adverse cardiac events in IHD patients. Two studies found endocardial circumferential strain to be the good predictor of outcome in CAD patients and when added to baseline characteristics. Epicardial LSS emerged as best predictor in acute coronary syndrome (ACS) patients.

EDITED BY
Artur Dziewierz,
Jagiellonian University Medical College, Poland

REVIEWED BY
Natallia Maroz-Vadalazhskaya,
Belarusian State Medical University, Belarus
Tetsuji Kitano,
University of Occupational and Environmental Health Japan, Japan

*CORRESPONDENCE
Shreeya Sharma
✉ sharmashreeya@hotmail.com

SPECIALTY SECTION
This article was submitted to Cardiovascular Imaging, a section of the journal Frontiers in Cardiovascular Medicine

RECEIVED 28 June 2022
ACCEPTED 20 February 2023
PUBLISHED 27 March 2023

CITATION
Sharma S, Lassen MCH, Nielsen AB, Skaarup KG and Biering-Sørensen T (2023) The clinical application of longitudinal layer specific strain as a diagnostic and prognostic instrument in ischemic heart diseases: A systematic review and meta-analysis.
Front. Cardiovasc. Med. 10:980626.
doi: 10.3389/fcvm.2023.980626

Conclusion: In patients with SAP, epicardial LSS was the stronger diagnostic marker while in NSTE-ACS patients, endocardial LSS was the stronger diagnostic marker. In addition, endocardial circumferential strain is the better predictor of adverse outcome in CAD patients whilst in ACS patients, epicardial LSS was found to be a better predictor of outcome.

KEYWORDS

longitudinal layer specific strain, ischemic heart disease, coronary artery disease, acute coronary syndome, 2 dimensional speckle tracking echocardiography

Introduction

Despite the extensive and commendable advances in therapeutic treatments, cardiovascular diseases (CVDs) continue to be a leading cause of death worldwide (1), affecting 85.6 million American adults while accounting for approximately one of every three deaths in the United States as of 2016 (2).

Conventionally, cardiac function and contractility is assessed using non-invasive imaging techniques such as echocardiography (1). However, conventional echocardiography is not without limitations, as some CVDs (coronary artery disease) do not necessarily display wall abnormalities detectable by conventional echocardiographic methods (3). Additionally, the conventional methods fail to distinguish the non-homogenous nature of the myocardium with its three layers ranging from endo- to epicardium (4).

With ongoing technological advancements, studies performed during the last decade provide evidence for global longitudinal strain (GLS) obtained from 2-dimensional speckle-tracking echocardiography (2DSTE), as being a robust technique in evaluating left ventricular (LV) systolic function along with being an objective diagnostic marker (5–8). Strain, obtained by 2DSTE is a measure of deformation (5), defined as the percentage change in myocardial segmental length (6).

Novel echocardiographic software can now be used to sectionalize the myocardium in its individual layers allowing for obtainment of the layer specific strain (LSS). This distinction is relevant, especially in ischemic heart disease (IHD), since longitudinally oriented myocardial fibers located in the endocardium region are more susceptible to ischemia (7), as they are located furthest from supplying arteries (8). Longitudinal strain is also impaired amongst patients with subtle cardiac impairment and a preserved left ventricular ejection fraction (LVEF) (9). At the same time, longitudinal layer specific strain (LSS) emerges as a more powerful predictor of outcome than LVEF, as it may reflect even more subclinical LV systolic function (10, 11).

Thus, 2DSTE is likely to contribute further to the pathophysiological and morphological understanding of cardiac diseases (6).

Therefore, the aim of this systematic review and meta-analysis was to evaluate the diagnostic and prognostic value as well as clinical relevance of using 2DSTE measured LSS in patients with suspected or prevalent IHD.

Methods

Search process

A trained investigator searched the following databases: PubMed, Embase and Cochrane Library on January 27th 2019. The search strategy included terms and phrases relevant for the subject of the review. The search utilized MeSH terms and free text terms, such as “Layer Specific Strain”, “Speckle Tracking Echocardiography”, “2DSTE”, “Myocardial Strain”, “Global Longitudinal Strain”, “GLS” and “Left ventricular GLS”. Additional search strategies involved reviewing references in the search result to identify further relevant studies to be included. Two investigators (SS and MHL) independently reviewed the results of the searches to determine whether the articles qualified for inclusion in this review.

The search strategy of PubMed is displayed in (**Supplementary Table S1**).

Eligibility criteria and study selection

All full text articles describing the prognostic and diagnostic value of 2DSTE measured LSS, in patients with ischemic heart diseases were included in this review. Abstracts, other literature and systematic reviews, conference abstracts, poster presentations, editorials as well as studies reporting results obtained from 3D tracking techniques were excluded from this study.

Search results were primarily screened based on title and abstract as depicted in the Preferred Reporting Items for Systematic Reviews and Meta-Analyses PRISMA diagram (**Figure 1**).

From 40 full text articles, 23 were eliminated as the articles were not related to ischemic heart diseases, were reviews, were not LSS or used strain gradient instead of reporting absolute strain values. Furthermore, eight other articles were excluded as they did not use odds ratio (OR) hazard ratio (HR) or area under the curve (AUC) to report their findings.

The qualified studies were divided into two groups; Group 1: studies assessing the diagnostic value (6 studies/**Table 1**) and Group 2: studies assessing the prognostic value of longitudinal LSS (3 studies/**Table 2**).

From Group 1, studies reporting their results as OR were included in this meta-analysis. Three studies (4, 12, 13) reported

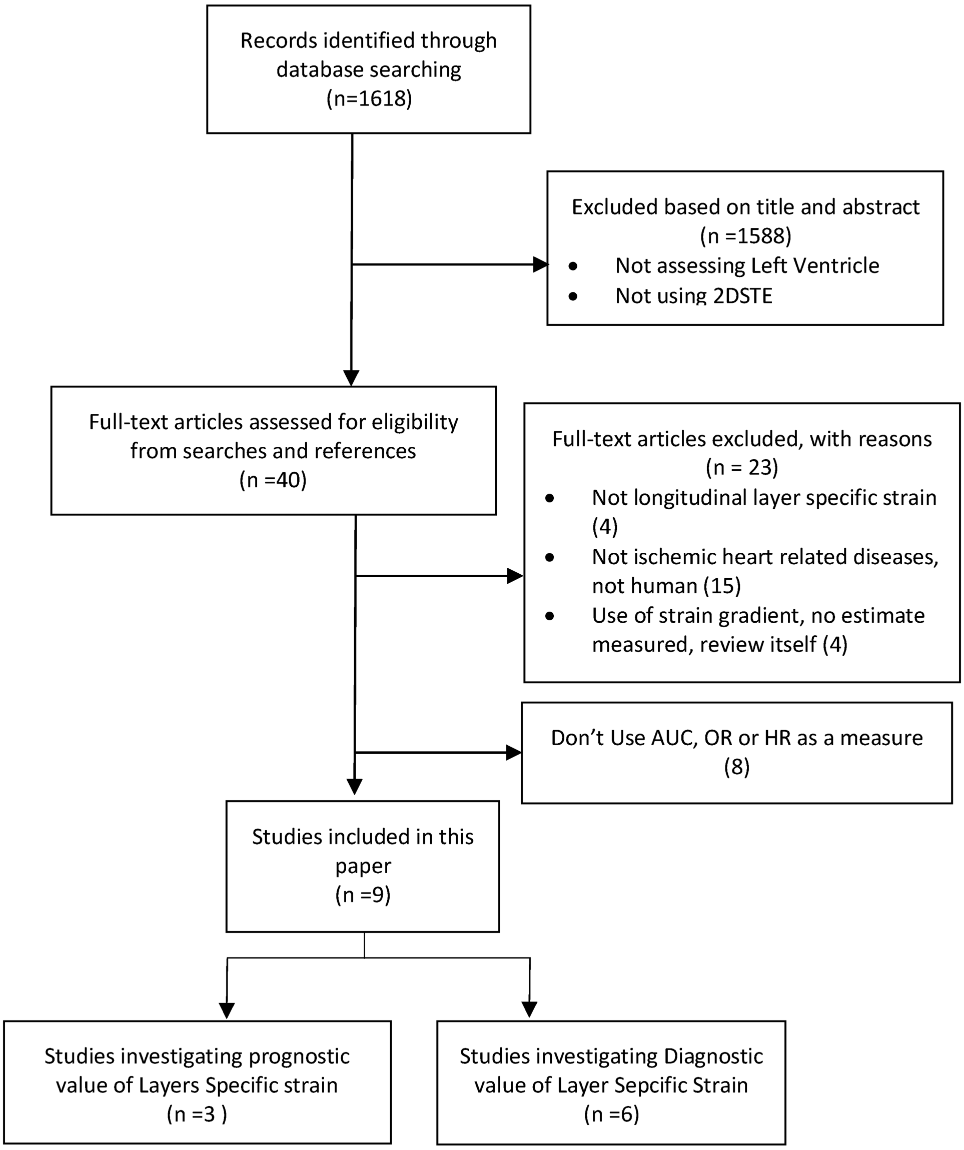

FIGURE 1
PRISMA flow diagram. PRISMA flow diagram displaying process of finding eligible studies for this review. Abbreviations: PRISMA, preferred reporting items for systematic review and meta-analysis.

OR with 95% confidence intervals (CI) for endo-, myo- and epicardium after multivariable adjustments whilst only one of the three studies also reported univariable OR with CI for all three layers. A fourth (5) study also reported OR with CI with both uni- and multivariable adjustments for the endocardial layer only. However, while the first three studies investigated the diagnostic value of LSS in diagnosing CAD in patients with SAP, the fourth study investigated LSS in diagnosing of CAD in NSTE-ACS patients. Pathophysiologically two different conditions are seen and hence the studies were not pooled together. Therefore, three studies were included in this meta-analysis. Because of the heterogeneity amongst the patients in the included studies, a random effect model was utilized. The remaining two studies could not be included in the meta-analysis since they did not report their results with OR. The findings are discussed in the discussion section.

Of the total six studies in the group, five studies (3, 5, 12) provided AUC values for multivariable adjustments whilst only two (3, 5) of the five studies reported the AUCs with 95% CI. Hence, due to lack of sufficient studies reporting AUCs with confidence intervals, AUCs were not included in this meta-analysis.

Group 2 constituted of three studies assessing the prognostic value of LSS in patients with IHD. Out of three studies included in the assessment of prognostic usefulness, one study (14) reported their results as HR whilst the other two studies (15, 16) used AUC. However, the two latter could not be pooled for meta-analysis as the studies used different multivariable adjustment models that could not be pooled together. Due to

TABLE 1 Studies evaluating the diagnostic significance of LSS.

Author Year	Country	Measurements investigated	Sample size (*n*)	Mean age of CAD pt	EF(%) of CAD pt	Population characteristics	LSS significant as a diagnostic marker for CAD?
Hagemann 2018*	Denmark	Longitudinal LSS (Endo, Epi, Myocardial), CAG	80 (control = 40 with stenosis = 28 without stenosis = 12)	63 ± 11	56 ± 4	Patients with reversible ischemia (SAP)	Yes (Epi-GLS)
Hagemann 2019*	Denmark	Longitudinal LSS (Endo, Epi, Myocardial), CAG, Global Circumferential strain (Endo, epi, myocardial)	285	63.8 ± 10.0	58 ± 4	Patients with SAP	Yes (Epi-GLS)
Yilmaztepe 2018	Turkey	Longitudinal LSS (Endo, Epi, Myocardial), regional longitudinal strains	79	60 ± 9.8	65.4 ± 5.3	Patients with SAP	Yes
Ejlersen, 2017*	Denmark	WM, Longitudinal LSS (Endo, Epi, Myocardial), CAG	132	65.7 Sd (7.2)	63 Sd (10)	Patients with chest pain referred for an invasive coronary angiography	Yes (Epi- GLS)
Sarvari, 2013*	Norway	Territorial longitudinal strain, Longitudinal LSS and Circumferential LSS (for all the cardiac layers)	77 (Coronary occlusion: 28 Stenosis: 21 No stenosis:28)	63.3 ± 9.3	59.0 ± 6	Patients with NSTE-ACS referred to hospital for coronary angiography	Yes (Endo-GLS)
Zhang, 2016	China	Territorial longitudinal strain, Territorial circumferential strain, Longitudinal LSS and Circumferential LSS (for all the cardiac layers)	139	55.4 ± 6.0	61.5 ± 2.0	Patients with NSTE-ACS recommended for undergoing coronary angiography	Yes (Endo-GLS)

*Studies that were included in the meta-analysis.

TABLE 2 LSS as a predictor for adverse cardiac events in IDH patients.

Author Year	Country	Sample size (*n*)	Population characteristics	Length of follow-up	Outcome/Event(s)	Number of events	LSS prognostic value?
Scharrenb-roich 2018	Germany	CAD: 137 AMI: 94	CAD and AMI patients	Mean: 3.6 ± 1.2 years	Cardiac death, Hospitalization due to MI, Unstable Angina Pectoris, heart insufficiency	AMI: 22 CAD: 47	Yes (Endo-LSS and Endo-GCS)
Skaarup 2018	Denmark	465	ACS patients	Median: 4.6 (IQR: 0.2–6.3) years	Heart failure or cardiovascular death	199	Yes (epi-LSS)
Hamada 2016	Germany	390	Patients with chronic ischemic cardiomyopathy (defined as known CAD and LVEF ≤50%	Mean: 4.9 ± 2.2 years	Readmission/worsenin-g of heart failure, ventricular arrhythmias, death of any cause.	133	Yes (Endo-GCS)

this, the studies could not be included in the meta-analysis, but their finding were explored in the results and discussions section. While all the studies included in the discussion of prognostic value of LSS focus on longitudinal LSS, two studies (15, 16) also included results of the value of circumferential strain which was also included in this review. Circumferential strain differs from longitudinal strain as it measures the systolic shortening of the short axis of the ventricles while longitudinal strain measures myocardial shortening from base to apex (17).

Quality assessment

Quality assessment for the risk of bias and the applicability of the included diagnostic studies was evaluated using the Quality Assessment of Diagnostic Accuracy Studies questionnaire (QUADAS-2) (18) (**Supplementary Tables S2 and S3**). The QUADAS-2 addresses domains regarding the applicability and risk of bias in the studies investigating diagnostic ability. The four domains for risk of bias assessment include patient selection, index test, reference test and flow and timing whilst three domains for applicability include: patient selection, index and reference test. The domains are designated a rating as high, low or moderate risk of bias.

Quality assessment of the studies investigating the prognostic value of LSS were evaluated using the Newcastle–Ottawa Quality Assessment Scale for cohort studies (**Supplementary Table S4**). This questionnaire consists of three categories: selection, comparability and outcome.

Statistics

The meta-analysis was conducted using STATA statistics/data analysis, SE 15.0 (StataCorp, College Station, TX, United States).

The pooled analyses were performed by using OR extracted from the included studies.

The results are presented as forest plots. A two-tailed *p*-value of < 0.05 was defined as statistical significance. The I^2 index was used to assess heterogeneity between studies. All pooled analyses were performed using a fixed effects model and, if heterogeneity was observed (defined as $I^2 > 50\%$ or Chi^2 *p*-value < 0.10), a random effects model was deployed instead. The possibility of publication bias was assessed using the Egger's test and by visual inspection of funnel plots (**Figure 2**).

Results

Patient characteristics and study design for the studies assessing usefulness of LSS for diagnosing CAD in patients suspected of IHD and predicting outcome in IHD

A total of four studies were included in group 1 of the meta-analysis (*n* = 574). The patient population used in the study is displayed in **Table 1**. All the patients included underwent echocardiography and CAG in order to diagnose for CAD and confirm the diagnosis of IHD. Some patients (13) also underwent exercise test (*n* = 80) and some underwent SPECT (*n* = 285). Baseline clinical and echocardiographic characteristics of the patients with and without CAD are displayed in **Table 3**. There were no significant differences between patients with and without CAD in clinical characteristics and comorbidities (all *p*-values > 0.05). There was no significant difference in the LVEF of patients with and without CAD (*p*-value: 0.365). However, GLS endo-, GLS epi-, and GLS mid-myocardium were significantly lower in patients with CAD.

TABLE 3 Baseline characteristics of patients included in the diagnostic studies (group 1).

	Patients without CAD (*n* = 400)	Patients with CAD (*n* = 360)	*P*-value
General characteristics			
Age	59.1 (53.6–63)	61.9 (55.4–65.7)	0.29
Gender (% male)	52.4 (33.3–79)	76.4 (55–89)	0.12
Smoking (%)	26.3 (19–34)	25.5 (20–36)	0.22
BMI (kg/m^2)	23 (26–29.7)	27.9 (26.9–29)	0.66
Comorbidities			
Hypertension (%)	60.3 (52–88.9)	69.9 (46–88.4)	0.42
Diabetes (%)	22.8 (10–27.8)	29.7 (15–62)	0.27
Hypercholestrolemia/ Dyslipidemia (%)	46.9 (29–69)	57.5 (37–83)	0.34
Family History (%)	34 (21–49)	38.5 (22–60)	0.66
Echocardiographic Characteristics			
LVEF (%)	62.2 (57–66.4)	60 (56–65.4)	0.37
GLS endo (%)	22.9 (19.2–28.5)	19.6 (15.4–23.7)	0.0006
GLS epi (%)	17.6 (13.9–21.9)	15.2 (12–16.7)	0.003
GLS mid (%)	19.5 (15.9–18.6)	17.3 (14.9–20.8)	0.0005

Data are expressed as means of the characterisitcs as reported in the studies. The range of means across the studies is reported in (). *P*-value is expressed as the mean *p*-values for studies reporting this value. Abbreviations: LVEF, left ventricular ejection fraction.

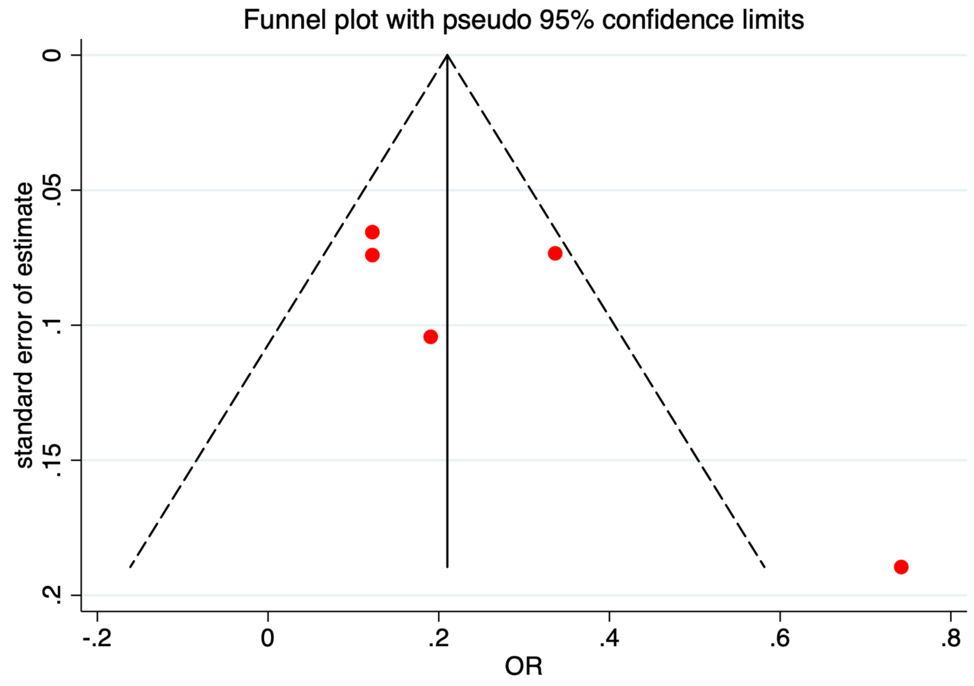

FIGURE 2
Funnel plot for odds ratio. Funnel plot assessing the possibility of publication bias with pseudo 95% confidence intervals. Abbreviations: SE, standard error; OR, odds ratio.

The total amount of patients included in group 2 of the meta-analysis included 1,086 patients for who the studies investigated the prognostic value of LSS, and amongst these 401 patients had a cardiac event during the follow-up period. The average follow-up period was 4.3 (0.2–7.1) years. The follow up period along with study characteristics for each study can be seen in Table 2. All the patients involved in the prognostic studies underwent echocardiography. Out of these, some also underwent CAG (*n* = 696) while others were additionally examined using cardiac magnetic resonance imaging (*n* = 390). Baseline clinical and echocardiographic characteristics of: the entire patient population, patients that experienced cardiac event and patients without and cardiac event were compared as displayed in Table 4. All the clinical and echocardiographic characteristics were without any significant difference within the patient groups across the different studies.

Three studies investigated the diagnostic usability of epi-, mid-myo- and endocardial LSS for coronary artery disease (CAD) in patients suspected of stable angina pectoris (SAP). Hence, three forest plots (one for each myocardial layer) were produced displaying the OR obtained from multivariable logistic regression models in these studies (Figures 3A–C).

TABLE 4 Baseline characteristics of patients included in the prognostic studies (group 2).

	All patients (*n* = 1086)	Cardiac event (*n* = 401)	No Cardiac event (*n* = 685)
General characteristics			
Age	64 (63–66) [0.035]	68 (67–69) [0.010]	62 (60–64) [0.010]
Gender (% male)	76 (69–85) [0.691]	75.3 (74–84) [0.573]	76.3 (69–86) [0.800]
Smoking (%)	43.5 (39–46) [0.387]	40.4 (37–47.2) [0.453]	44.4 (40–48) [0.430]
SBP (mmHg)	129 (118–137) [0.227]	132.5 (131–134) [0.130]	134.5 (138–131) [0.130]
DBP (mmHg)	76 (72–81) [0.215]	76.5 (73–80) [0.215]	77 (72–82) [0.215]
Heart rate (beats/min)	72 (68–75) [0.562]	73.5 (68–79) [0.446]	69 (67–71) [0.450]
Comorbidities			
Hypertension (%)	44.2 (41–48.5) [0.282]	43.3 (40–47.5) [0.423]	44.9 (42–49) [0.233]
Diabetes (%)	18.7 (9.7–25) [0.051]	29 (12.1–46) [0.062]	14.1 (7.9–23) [0.050]
Hypercholestrolemia/ Dyslipidemia (%)	31.7 (24–39) [0.492]	33.7 (25.1–28) [0.553]	30.6 (23.7–39) [0.494]
Family History (%)	27.8 (25.5–29.9) [0.251]	28.2 (23.6–33) [0.400]	28 (21.5–34.6) [0.367]
Echocardiographic Characteristics			
LVEF (%)	43.6 (40.8–49) [0.110]	59.9 (35.2–46.5) [0.046]	46.5 (43–51.5) [0.046]
GLS endo (%)	16.1 (14.8–17.5) [0.048]	13.7 (12.5–15) [0.018]	17.9 (16.6–19) [0.018]
GLS epi (%)	11.5 (11–12.5) [0.336]	9.8 (9.3–10) [0.280]	12.7 (12–13.5) [0.280]
GLS total (%)	14.4 (12.8–16) [0.027]	11.4 (10.7–12) [0.033]	15.8 (14.4–17) [0.033]

Data are expressed as means of the characterisitcs as reported in the studies. The range of means across the studies is reported in (). *P*-values expressed as the mean *p*-values for studies reporting this value and reported in []. Abbreviations: SBP, systolic blood pressure; DBP, diastolic blood pressure; LVEF, left ventricular ejection fraction.

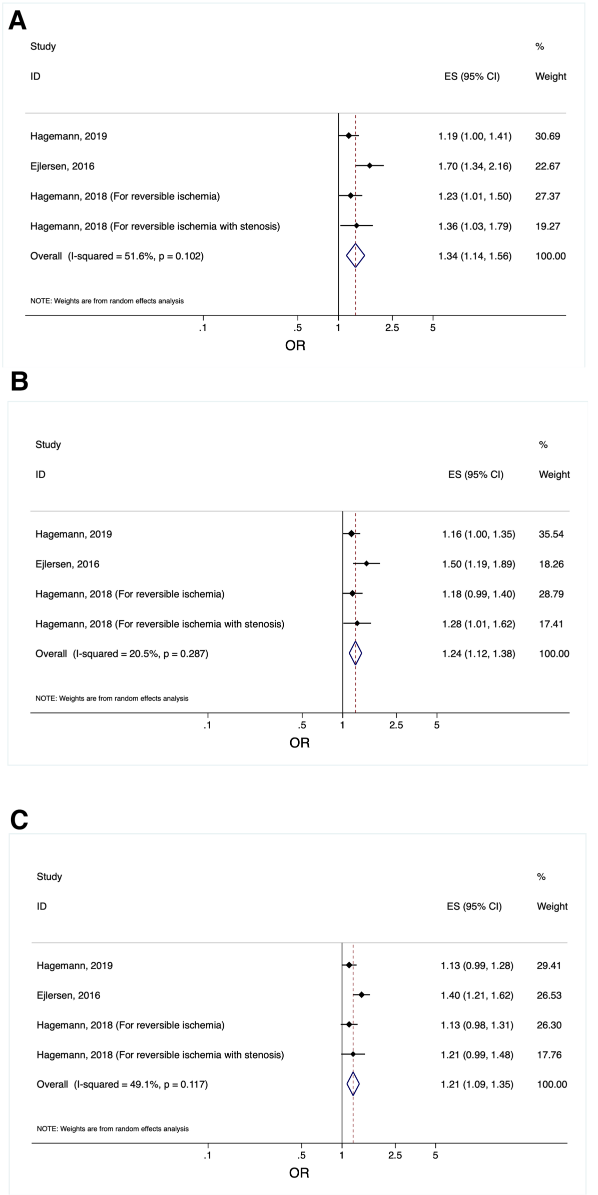

FIGURE 3
(A) Forest plot displaying the odds ratios obtained from multivariable logistic regression models in the included studies investigating the diagnostic value of epicardial longitudinal layer-specific strain in patients suspected of SAP. Odds ratios from the studies investigating the diagnostic value of measuring epicardial longitudinal layer-specific strain in patients suspected of SAP. Abbreviations: OR, odds ratio; CI, confidence interval. (B) Forest plot displaying the odds ratios obtained from multivariable logistic regression models in the included studies investigating the diagnostic value of mid-myocardial longitudinal layer-specific strain in patients suspected of SAP. Odds ratios from the studies investigating the diagnostic value of measuring mid-myocardial longitudinal layer-specific strain in patients suspected of SAP. Abbreviations: OR, odds ratio; CI, confidence interval. (C) forest plot displaying the odds ratios obtained from multivariable logistic regression models in the included studies investigating the diagnostic value of endocardial longitudinal layer-specific strain in patients suspected of SAP. Odds ratios from the studies investigating the diagnostic value of measuring endocardial longitudinal layer-specific strain in patients suspected of SAP. Abbreviations: OR, odds ratio; CI, confidence interval.

Usefulness of layer specific strain to diagnose coronary artery disease in SAP patients

Three studies investigated the diagnostic value of layer specific strain using OR with a total of 497 patients. From the pooled analysis, it was found that LSS, for all the myocardial layers, were significantly impaired in patients with SAP (**Figure 3**).

The strongest diagnostic association between LSS and CAD was for epicardial LSS after multivariable adjustment (OR: 1.34, CI95% [1.14–1.56], $p < 0.001$, per 1% decrease) (**Figure 3A**). Mid-myocardial LSS after multivariable adjustment (OR: 1.24, CI95% [1.12–1.38], $p < 0.001$, per 1% decrease) (**Figure 3B**) emerged to be the second-best diagnostic marker of CAD in all the myocardial layers. The performance of endocardial LSS as a diagnostic marker for CAD, after multivariable adjustment (OR: 1.21, CI95% [1.09–1.35], $p < 0.001$, per 1% decrease) (**Figure 3C**), was the weakest of all of the myocardial layers.

Usefulness of layer specific strain to predict outcome in IHD

Endocardial LSS (HR: 1.19 [1.10–1.28], $p < 0.001$, per 1% decrease) and epicardial LSS (HR: 1.26 [1.15–1.39], $p < 0.001$, per 1% decrease) both prove to provide the most prognostic information about cardiac outcome, with epicardial LSS being the better predictor in ACS patients. In chronic CAD patients, endocardial circumferential strain improves prediction of cardiac event. However, endocardial circumferential strain did not improve prediction of cardiac events in AMI patients (15). In patients with chronic ischemic cardiomyopathy (CAD patients with ejection fraction ≤50%), endocardial circumferential strain (AUC: 0.798, CI95% [0.737–0.833], p-value < 0.001) was the strongest prognostic measure followed by endocardial LSS (AUC: 0.780, CI95% [0.706–0.824], p-value < 0.001).

There was no evidence of publication bias as evaluated by the Egger's test and from visual inspection of the funnel plot (**Figure 2**) for the studies assessing LSS as a diagnostic measure for IHDs.

Qualitative assessment of the included studies in the meta-analysis as per QUADAS-2 assessment showed an overall low risk of bias (**Supplementary Tables S2 and S3**).

Discussion

The present meta-analysis demonstrates that LSS has significant value as a diagnostic marker for IHD. In patients with SAP, epicardial LSS seems to be the better diagnostic marker for CAD whilst endocardial LSS seems to be the weakest diagnostic marker for CAD. In NSTE-ACS patients, endocardial LSS was the better diagnostic marker for CAD.

In terms of the usefulness of LSS in predicting adverse outcome in IHD, endocardial circumferential strain appears to be a good predictor of adverse outcomes in chronic CAD patients while in ACS patients, epicardial LSS has been found to be a better predictor of outcome.

Layer-specific strain as a diagnostic marker of CAD

LSS as a new diagnostic tool for IHD has been investigated in a range of patient populations with different cardiac morbidities relating to IHD. Two studies focused on patients with ACS. Sarvari et al. (5) conducted a study aiming to evaluate the use of LSS as a diagnostic marker for CAD, in patients with NSTE-ACS ($n = 77$). Coronary angiography (CAG) was used to confirm CAD in NSTE-ACS patients and found coronary occlusion ($n = 28$), significant stenosis ($n = 21$) and no stenosis ($n = 28$) in patients. Multivariable regression analysis showed that reduced myocardial function as quantified by endocardial LSS was the only significant marker for the presence of significant CAD (OR: 2.10 CI95% [1.47–3.09], p-value < 0.001, per 1% change).

Zhang (19) and colleagues carried out a study similar to the study by Sarvari et al., as both studies looked at the usefulness of LSS in diagnosing CAD in patients with NSTE-ACS ($n = 139$). However, Zhang et al. not only looked at the LSS, but also compared its usefulness to the Syntax scoring method. The Syntax scoring method is used to assess the severity of coronary lesions (19). The group of patients with identified CAD were divided into three subgroups (according to the Syntax score). The results were, however, not reported in the form of OR for the LSS for the cardiac layers. Despite not being included in the pooled analysis, the findings of the study mirrored that of Sarvari's study, as endocardial LSS had the best diagnostic value in diagnosing CAD as compared to the other layers. Zhang used coronary angiography to confirm CAD diagnosis in patients.

Four studies focused on evaluating the diagnostic power of LSS in patients with stable angina pectoris (SAP). Two of these studies were published by Hagemann et al. The first study (Hagemann et al., 2018 (13)) was a retrospective study ($n = 80$) in which the objective was to determine whether LSS was affected at rest in patients with reversible ischemia as assessed by single photon emission computed tomography (SPECT) in SAP patients. The control group consisted of 40 patients whilst the study group ($n = 40$) compromised of patients demonstrating stress induced (bicycling or pharmacology stress) reversible ischemia as measured by SPECT. This group was further divided into patients with ($n = 28$) and without ($n = 12$) CAD as defined by a significant stenosis as assessed by CAG (true positive and false positive SPECT). After multivariable logistic regression, the LLS and the severity of reversible ischemia were found to be correlated such that, progressively impaired LSS was observed with no affected major coronary arteries to multivessel ischemia. This association was observed in both true positive and false positive SPECT. The study found that epicardial LSS had the strongest association with ischemia (OR: 1.23, CI95% [1.01–1.50],

p-value = 0.044). However, the results failed to show a significant association between LSS and the SPECT-measured severity of stenosis.

The works of Ejlersen et al. (12) mirrored the study mentioned above. Ejlersen also evaluated whether LSS under adenosine stress echocardiography provided incremental diagnostic information as compared to traditional echocardiographic measurements with regards to CAD in patients with suspected SAP ($n = 132$). The findings Ejlersen et al. put forward demonstrated that although all three layers were significantly associated with presence of CAD, the epicardium had the highest OR in logistic regressions in multivariable models (OR:1.7 CI95% [1.3–2.1], p-value < 0.0001) compared to mid-myocardial LSS (OR:1.5 CI95% [1.3–1.8], p-value <0.0001) and endocardial LSS (OR:1.4 CI95% [1.2–1.6], p-value < 0.0001).

The second study included by Hagemann et al. (2019) (4) was a prospective study evaluating the potential of LSS for diagnosing CAD in a population of patients with suspected SAP ($n = 285$). All the patients included in the study were examined by echocardiography and an exercise test followed by coronary angiography (CAG). Out of the 285 patients suspected of SAP, 104 had significant CAD whilst 181 had non-significant or no CAD. The study concluded that epi-, mid-myo-, and endocardial LSS were significantly impaired in CAD patients but only epi- and mid-myocardial LSS were independently associated with the presence of significant CAD (epi: OR:1.19, CI95% [1.00–1.41], p-value = 0.048 and mid-myocardial: OR: 1.16, CI95% [1.00–1.35], p-value = 0.047). After multivariable adjustment, endocardial LSS did not remain independently associated with CAD, and epicardial LSS emerged as being the strongest diagnostic marker.

Both of the studies by Hagemann and colleagues together with the study by Ejlersen and colleagues concluded that epicardial LSS had superior diagnostic accuracy for CAD detection as compared to the mid-myocardial and endocardial LSS in patients suspected of SAP. When considering the cardiac vascular distribution, endocardial layer is considered to be most prone to ischemia is IHD (8) and hence endocardial contractility and in turn endocardial longitudinal strain would be more likely reduced and hence a better diagnostic predictor. However, a possible reason for why epicardial LSS emerged as a superior diagnostic parameter in some studies may be due to technical aspects as the epicardial layer may have more accurate tracing compared to the endocardial region (4). Hagemann et al. And Ejlersen et el. results are in contrast with the findings of Sarvari et al. and Zhang et al. as they found endocardial LSS to have the better diagnostic accuracy in NSTE-ACS patients. The discrepancy in these results can be attributed to the fact that Hagemann et al.'s patient population (suspected SAP) was different from the population used in the two aforementioned studies (NSTEMI).

An additional retrospective study by Yilmaztepe et al. (3) also sought to investigate the diagnostic accuracy of LSS detecting CAD in patients ($n = 79$) with suspected SAP who had previously undergone diagnostic CAG for SAP. The patients were divided into control group ($n = 36$, no significant CAD) whilst 43 patients constituted the CAD group. Since no OR was reported as part of their results, this study was not included in the pooled analysis. However, in a multivariable adjusted model, GLS (AUC: 0.891, CI95% [0.823–0.954], p-value < 0.001) along with endocardial LSS (AUC: 0.881, CI95% [0.808–0.905], p-value < 0.001) remained independently associated with CAD. These results are different from Hagemann's studies of epicardial GLS being a superior diagnostic marker.

A meta-analysis and systematic review conducted by Liou et al. (20) (10 studies included in analysis) investigated if GLS could be used to improve diagnosis of CAD in patients with SAP or NSTE-ACS. It did, however, not include layer specific GLS. The study found GLS to be a good diagnostic marker for moderate to severe CAD in these patient groups. However, it should be noted that patient groups in these studies show heterogeneity and more studies in the field are needed to subgroup patients in more homogenous groups based on similar pathologies.

Prognostic value of LSS

In a retrospective study, Skaarup et al. (14), assessed the prognostic value of LSS in predicting heart failure (HF) and cardiovascular death (CD) following ACS in 465 patients. The primary endpoint was the occurrence of HF and/or CD with a median follow up time of 4.6 years (0.2–6.3). Of the patients included 42.7% suffered HF and/or CD (HF = 176 patients and CAD = 38 patients). It was shown that endo- and epicardial LSS were independently associated with the composite outcome (endocardial LSS: HR: 1.19 [1.10–1.28], and epicardial LSS HR: 1.26 [1.15–1.39], $p < 0.001$, per 1% decrease) whilst no other echocardiographic measure remained independently associated with the outcome. In addition to this Skaarup concluded that epicardial LSS, when added to other clinical and echocardiographic measures (such as LVEF and E/e'), provided incremental prognostic information on the risk of developing the endpoint.

Similarly, a prospective study by Scharrenbroich et al. (15) assessed the prognostic value of LSS, in relation to a composite outcome consisting of cardiac death and hospitalization due to MI, in patients previously diagnosed with AMI ($n = 94$) and CAD ($n = 137$). During the follow up time (mean: 3.6 ± 1.2 years) out of the AMI patient group, 22 experienced a cardiac event. At the same time, 47 patients with CAD experienced a cardiac event. While 2DSTE measured strains proved to be a sensitive tool for predicting events in CAD patients, it failed to provide independent prognostic information on adverse events in AMI patients. At the same time the study found endocardial circumferential strain (GCS) to be the measure that, when added to baseline characteristics and ejection fraction, improved the prediction of cardiac events.

Hamada et al. (16) evaluated the prognostic value of LSS, for readmission of heart failure, ventricular arrhythmias or all-cause mortality in patients with known chronic ischemic cardiomyopathy ($n = 399$) (defined as known CAD and LVEF ≤50%). Over the course of the follow up period (mean: 4.9 ± 2.2 years), 133 cardiac events occurred. Endocardial LSS (AUC: 0.780, CI95% [0.706–0.824], p-value < 0.001) was found to be a good predictor of the composite outcome while endocardial circumferential strain (AUC: 0.798, CI95% [0.737–0.833], p-value < 0.001) emerged to have the strongest prognostic value. However, it should be noted that patients in this study had chronic ischemic cardiomyopathy and therefore a large amount of these patients had a presence of post-infarction scars that can lead to depressed myocardial contractility and deformation. This was one of the reasons why a pooled analysis in the prognostic group was not performed as this would lead to incorrect prognostic results.

Limitations

There are several limitations to this study. Not all the included studies provided extractable data required for the pooled analysis, thereby limiting the extend of data available for the meta-analysis. In addition to this, patient populations with varying characteristics were included in the studies since the same inclusion and exclusion criteria were not followed across all studies. We cannot differentiate between patients with ischemic heart disease, coronary heart disease and significant coronary stenosis. However, heterogeneity, if present, was analyzed with random effect models to limit this bias. Patients baseline characteristics across studies were also assessed and no significant differences were seen. Diverse variables were included in the multivariable adjustments conducted across the studies resulting in uncertainty in comparison of the effect sizes. Since not many studies included univariable OR, a pooled analysis of the unadjusted effect sizes could not be conducted, for all the layers, in order to overcome this limitation. Results were reported differently across some of the included studies and hence could not be included in our pooled analysis. Furthermore, the study investigating the diagnostic power of LSS in NSTE-ACS patients only reported OR for endocardial layer. Hence, epi- and mid-myocardial layers could not be looked at while investigating the diagnostic significance of these layers in NSTE-ACS patients.

Clinical implications

With increasing understanding of 2DSTE and its implementation in the field of cardiology globally, longitudinal LSS is likely to prove itself as an accurate non-invasive technique to diagnose and predict conditions in IHD patients. This is due to the increased sensitivity of 2DSTE as compared to other conventional measures allowing for an early diagnosis. Earlier diagnosis by 2DSTE opens up possibilities for early medical intervention in high-risk patients, which may later aid in avoiding adverse outcomes. At the same time, since much of the cost related to cardiovascular diseases is spent on hospitalization due to cardiovascular events (21), early diagnosis and using 2DSTE as a predictive tool could potentially help lower the healthcare costs within the cardiovascular area. Since using 2DSTE to produce longitudinal LSS is mostly automated, it requires minimal training and increases reproducibility.

Conclusion

We found that 2DSTE measured LSS of the LV has significant diagnostic and prognostic value in patients with suspected and prevalent IHD. Through the studies included in this meta-analysis, it can be concluded that epicardial LSS seem to be the better diagnostic marker for CAD in patients suspected of SAP. Furthermore, it seems that endocardial LSS is a better diagnostic marker for CAD in NSTE-ACS patients. These finding suggests that the usability of LSS for each layer depends on the specific type of IHD. The prognostic value of longitudinal epicardial LSS was found to be predictive of outcome in ACS patients whereas in chronic CAD patients, it was endocardial circumferential strain that proved to be of better prognostic value.

Data availability statement

The original contributions presented in the study are included in the article/**Supplementary Material**, further inquiries can be directed to the corresponding author.

Author contributions

SS, ML and TS contributed to the conception and design of the study. SS and MHL independently reviewed the results of searching databases for relevant articles, to determine whether the articles qualified for inclusion in this review. SS wrote the first draft of the manuscript and the statistical analyses were performed by SS, ML and AN. KGS helped in the reviewing and finalizing process. All authors contributed to the article and approved the submitted version.

Conflict of interest

The authors declare that the research was conducted in the absence of any commercial or financial relationships that could be construed as a potential conflict of interest.

Publisher's note

Supplementary material

The Supplementary Material for this article can be found online at: https://www.frontiersin.org/articles/10.3389/fcvm.2023.980626/full#supplementary-material.

References

1. Sanz J, Fayad ZA. Progress article imaging of atherosclerotic cardiovascular disease. *Nature*. (2008) 451:953–7. doi: 10.1038/nature06803

2. Writing Group Members; Mozaffarian D, Benjamin EJ, Go AS, Arnett DK, Blaha MJ. Heart disease and stroke statistics—2016 update. *Circulation*. (2016) 133:447–54. doi: 10.1161/CIR.0000000000000350

3. Yılmaztepe MA, Uçar FM. Layer-specific strain analysis in patients with suspected stable angina pectoris and apparently normal left ventricular wall motion. *Cardiovasc Ultrasound*. (2018) 16:16–25. doi: 10.1186/s12947-018-0144-9

4. Hagemann CA, Hoffmann S, Hagemann RA, Fritz-Hansen T, Olsen FJ, Jørgensen PG. Usefulness of layer-specific strain in diagnosis of coronary artery disease in patients with stable angina pectoris. *Int J Cardiovasc Imaging*. (2019) 35:1989–199. doi: 10.1007/s10554-019-01652-3

5. Sarvari SI, Haugaa KH, Zahid W, Bendz B, Aakhus S, Aaberge L, et al. Layer-specific quantification of myocardial deformation by strain echocardiography may reveal significant CAD in patients with non-ST-segment elevation acute coronary syndrome. *JACC Cardiovasc Imaging*. (2013) 6:535–44. doi: 10.1016/j.jcmg.2013.01.009

6. Tarascio M, Leo LA, Klersy C, Murzilli R, Moccetti T, Faletra FF. Speckle-Tracking layer-specific analysis of myocardial deformation and evaluation of scar transmurality in chronic ischemic heart disease. *J Am Soc Echocardiogr*. (2017) 30:667–75. doi: 10.1016/j.echo.2017.03.015

7. Reimer KA, Lowe JE, Rasmussen MM, Jennings RB. The wavefront phenomenon of ischemic cell death. 1. Myocardial infarct size vs duration of coronary occlusion in dogs. *Circulation*. (1977) 56:786–94. doi: 10.1161/01.CIR.56.5.786

8. Algranati D, Kassab GS, Lanir Y. Why is the subendocardium more vulnerable to ischemia? A new paradigm. *Am J Physiol - Hear Circ Physiol*. (2011) 300:H1090–1100. doi: 10.1152/ajpheart.00473.2010

9. Kraigher-Krainer E, Shah AM, Gupta DK, Santos A, Claggett B, Pieske B. Impaired systolic function by strain imaging in heart failure with preserved ejection fraction. *J Am Coll Cardiol*. (2014) 11:447–56. doi: 10.1016/j.jacc.2013.09.052

10. Russo C, Jin Z, Elkind MSV, Rundek T, Homma S, Sacco RL, et al. Prevalence and prognostic value of subclinical left ventricular systolic dysfunction by global longitudinal strain in a community-based cohort. *Eur J Heart Fail*. (2014) 16:1301–9. doi: 10.1002/ejhf.154

11. Biering-Sørensen T, Solomon SD. Assessing Contractile function when ejection fraction is normal: a case for strain imaging. *Circ: Cardiovasc Imaging*. (2015) 8:8(11) editorial. doi: 10.1161/CIRCIMAGING.115.004181

12. Ejlersen JA, Poulsen SH, Mortensen J, May O. Diagnostic value of layer-specific global longitudinal strain during adenosine stress in patients suspected of coronary artery disease. *Int J Cardiovasc Imaging*. (2017) 33:473–80. doi: 10.1007/s10554-016-1022-x

13. Hagemann CE, Hoffmann S, Olsen FJ, Jørgensen PG, Fritz-Hansen T, Jensen JS. Layer-specific global longitudinal strain reveals impaired cardiac function in patients with reversible ischemia. *Echocardiography*. (2018) 35:632–42. doi: 10.1111/echo.13830

14. Skaarup KG, Iversen A, Jørgensen PG, Olsen FJ, Grove GL, Jensen JS. Association between layer-specific global longitudinal strain and adverse outcomes following acute coronary syndrome. *Eur Heart J Cardiovasc Imaging*. (2018) 19:1334–42. doi: 10.1093/ehjci/jey004

15. Scharrenbroich J, Hamada S, Keszei A, Schröder J, Napp A, Almalla M. Use of two-dimensional speckle tracking echocardiography to predict cardiac events: comparison of patients with acute myocardial infarction and chronic coronary artery disease. *Clin Cardiol*. (2018) 41:111–8. doi: 10.1002/clc.22860

16. Hamada S, Schroeder J, Hoffmann R, Altiok E, Keszei A, Almalla M. Prediction of outcomes in patients with chronic ischemic cardiomyopathy by layer-specific strain echocardiography: a proof of concept. *J Am Soc Echocardiogr*. (2016) 29:412–20. doi: 10.1016/j.echo.2016.02.001

17. Zhang K, Sheu R, Zimmerman NM, Alfirevic A, Sale S, Gillinov AM. A comparison of global longitudinal, circumferential, and radial strain to predict outcomes after cardiac surgery. *J Cardiothorac Vasc Anesth*. (2018) 33:1315–22. doi: 10.1053/j.jvca.2018.10.031

18. Whiting PF, Rutjes AWS, Westwood ME, Mallett S, Deeks JJ, Reitsma JB. Quadas-2: a revised tool for the quality assessment of diagnostic accuracy studies. *Ann Intern Med*. (2011) 155:529–36. doi: 10.7326/0003-4819-155-8-201110180-00009

19. Zhang L, Wu WC, Ma H, Wang H. Usefulness of layer-specific strain for identifying complex CAD and predicting the severity of coronary lesions in patients with non-ST-segment elevation acute coronary syndrome: compared with syntax score. *Int J Cardiol*. (2016) 223:1045–52. doi: 10.1016/j.ijcard.2016.08.277

20. Liou K, Negishi K, Ho S, Russell EA, Cranney G, Ooi SY. Detection of obstructive coronary artery disease using peak systolic global longitudinal strain dervied by two-dimensional speckle-tracking: a systematic review and meta-analysis. *J Am Soc Echocardiogr*. (2016) 29:724–35. doi: 10.1016/j.echo.2016.03.002

21. Weintraub WS. Reduce acute care costs, and all other healthcare costs too. *J Am Heart Assoc*. (2019) 8:1–3. doi: 10.1161/JAHA.119.012604

frontiers | Frontiers in Cardiovascular Medicine

TYPE Original Research
PUBLISHED 19 May 2023
DOI 10.3389/fcvm.2023.1081628

Deep learning approach for analyzing chest x-rays to predict cardiac events in heart failure

Kenya Kusunose[1*†], Yukina Hirata[2†], Natsumi Yamaguchi[2], Yoshitaka Kosaka[1], Takumasa Tsuji[3], Jun'ichi Kotoku[3] and Masataka Sata[1]

[1]Department of Cardiovascular Medicine, Tokushima University Hospital, Tokushima, Japan, [2]Ultrasound Examination Center, Tokushima University Hospital, Tokushima, Japan, [3]Department of Radiological Technology, Graduate School of Medical Care and Technology, Teikyo University, Tokyo, Japan

OPEN ACCESS

EDITED BY
Sebastian Kelle,
German Heart Center Berlin, Germany

REVIEWED BY
Satoshi Kodera,
The University of Tokyo, Japan
Zartasha Mustansar,
National University of Science and Technology, Pakistan

*CORRESPONDENCE
Kenya Kusunose
✉ echo.cardio@gmail.com
@Ken_Cardiology

[†]These authors have contributed equally to this work

RECEIVED 27 October 2022
ACCEPTED 24 April 2023
PUBLISHED 19 May 2023

CITATION
Kusunose K, Hirata Y, Yamaguchi N, Kosaka Y, Tsuji T, Kotoku J and Sata M (2023) Deep learning approach for analyzing chest x-rays to predict cardiac events in heart failure.
Front. Cardiovasc. Med. 10:1081628.
doi: 10.3389/fcvm.2023.1081628

Background: A deep learning (DL) model based on a chest x-ray was reported to predict elevated pulmonary artery wedge pressure (PAWP) as heart failure (HF).
Objectives: The aim of this study was to (1) investigate the role of probability of elevated PAWP for the prediction of clinical outcomes in association with other parameters, and (2) to evaluate whether probability of elevated PAWP based on DL added prognostic information to other conventional clinical prognostic factors in HF.
Methods: We evaluated 192 patients hospitalized with HF. We used a previously developed AI model to predict HF and calculated probability of elevated PAWP. Readmission following HF and cardiac mortality were the primary endpoints.
Results: Probability of elevated PAWP was associated with diastolic function by echocardiography. During a median follow-up period of 58 months, 57 individuals either died or were readmitted. Probability of elevated PAWP appeared to be associated with worse clinical outcomes. After adjustment for readmission score and laboratory data in a Cox proportional-hazards model, probability of elevated PAWP at pre-discharge was associated with event free survival, independent of elevated left atrial pressure (LAP) based on echocardiographic guidelines ($p < 0.001$). In sequential Cox models, a model based on clinical data was improved by elevated LAP ($p = 0.005$), and increased further by probability of elevated PAWP ($p < 0.001$). In contrast, the addition of pulmonary congestion interpreted by a doctor did not statistically improve the ability of a model containing clinical variables (compared $p = 0.086$).
Conclusions: This study showed the potential of using a DL model on a chest x-ray to predict PAWP and its ability to add prognostic information to other conventional clinical prognostic factors in HF. The results may help to enhance the accuracy of prediction models used to evaluate the risk of clinical outcomes in HF, potentially resulting in more informed clinical decision-making and better care for patients.

KEYWORDS
heart failure with reduced ejection fraction, heart failure with preserved ejection fraction, artificial intelligence, deep learning, chest x-ray

Introduction

Heart failure (HF) continues to be a significant socioeconomic issue and is one of the top causes of death from cardiovascular disease (CV) (1). Despite the development of current therapy, readmission rates for HF have remained high (2). The identification of hospitalized patients with a high risk of HF readmission is important for providing timely interventions. Understanding the underlying etiology, severity, and prognosis of HF requires evaluation of CV imaging (3, 4). A standard chest x-ray (CXR) in patients with suspected HF has a certain clinical value in the diagnosis and management of HF (5, 6). However, the sensitivity and specificity of this imaging modality is relatively low (7, 8).

Recently, artificial intelligence (AI) including deep learning (DL) has been used to provide precise recognition of understated patterns in medical images (9, 10). We reported that a DL model based on CXR analysis predicted elevated pulmonary artery wedge pressure (PAWP) in patients who had undergone right heart catheterization (11). The probability of elevated PAWP may therefore be a potential tool for managing HF in the clinical setting. We hypothesize that a previously developed application of a CXR-based DL algorithm could also be used to predict re-hospitalized HF in patients with HF. The aims of the current study were (1) to investigate the potential of probability of elevated PAWP for the prediction of clinical outcomes in association with other parameters, and (2) to evaluate whether probability of elevated PAWP based on AI added prognostic information to other clinical prognostic factors in patients with HF.

Methods

Study population

A single-center, retrospective study was designed (**Figure 1**). Two hundred seventy-two patients who were first HF hospitalized were enrolled initially. The study's time frame was from January 2013 to December 2017. Patients with HF were defined as having a clear history of HF with typical symptoms that were accompanied by signs including pulmonary congestion and BNP elevation (12). Exclusion criteria were post valve replacement, pacemaker implantation, active cancer, severe valvular disease and severe chronic obstructive pulmonary disease. Patients without clinical data at discharge were excluded. After these exclusions, 192 HF hospitalized patients were included in the final analysis. We divided this cohort into two groups: HF with reduced ejection fraction (HFrEF, $n = 99$) and HF with preserved EF (HFpEF, $n = 93$). Left ventricular ejection fraction (LVEF) less than 50% was designated as HFrEF, whereas LVEF greater than 50% was designated as HFpEF (13, 14). Patients collected to build the AI model were not included in this study.

Chest x-ray

The Radiology Department performed all chest radiographs. One attending cardiologist who had no prior knowledge of the patients' clinical information or hemodynamic status assessed the CXR images. A typical posteroanterior chest radiograph was used to measure the cardiothoracic ratio (CTR), which measures the size of the cardiac chambers. Consensus of two expert agreement of lung congestions on CXR images was used.

AI model for detection of PH

We used a previously developed AI model based on CXR analysis to predict elevated PAWP and then the continuous output of a classification network as a probability of elevated PAWP in the study cohort (11). The study involved examining

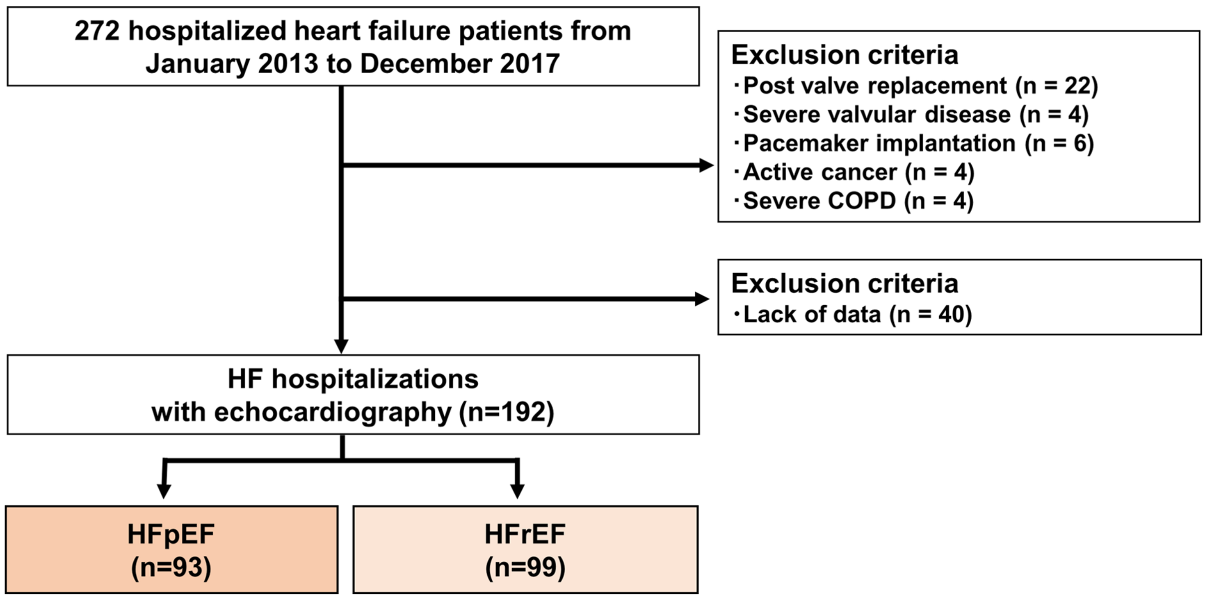

FIGURE 1
Flow chart showing recruitment of the patients. COPD, chronic obstructive pulmonary disease; HFpEF, heart failure with preserved ejection fraction; HFrEF, heart failure with reduced ejection fraction.

CXR data at admission and discharge. All patients underwent CXR within 24 h of admission and 48 h before discharge. The AUC of ResNet 50 for predicting elevated PAWP (mean PAWP >18 mmHg) was 0.77 in the study cohort (11). The batch size was set at 16, with the Adam optimizer used for training (15). The whole learning process was calculated by a graphics processing unit (Geforce RTX 2080 Ti 11 Gb, NVIDIA) using Ubuntu 18.04 and Chainer version 5.1.0. We performed gradient-weighted class activation mapping (Grad-CAM) to visualize how our model detected a PAWP >18 mmHg from a CXR of each patient (16).

Echocardiographic assessment

Echocardiography was performed using commercially available ultrasound machines. The echocardiographic data were obtained during the hospitalization according to the recommendations of the American Society of Echocardiography (17). Apical two- and four-chamber images were included. The biplane method of disks in two dimensions was used to calculate the volumes of the left atrium (LA) and LV. The LA volume index (LAVi) and LVEF were determined using these volumes. Based on 2016 recommendations, we implemented a decision tree using the mean E/e' ratio, tricuspid regurgitant: TR velocity, and LAVi to identify the existence of elevated LA pressure (LAP) (18). Three criteria are required to decide if there is raised LAP: E/e' ratio >14, LAVI > 34 ml/m², TR velocity >2.8 m/s.

Calculation of readmission risk scores

The Yale–CORE HF application [developed by Yale New Haven Health Services Corporation/Center for Outcomes Research and Evaluation (YNHHSC/CORE)] was used to determine the readmission risk for each patient (19). Readmission risk was calculated using 20 variables per patient, including demographic and historical variables abstracted from the medical record, admission physical examination variables, and laboratory and clinical variables (age, sex, in-hospital cardiac arrest, history of diabetes, previous HF, coronary artery disease, previous percutaneous coronary intervention, aortic stenosis, stroke, chronic obstructive pulmonary disease, prior diagnosis of dementia, systolic blood pressure, heart rate, respiratory rate, plasma sodium, creatinine, and glucose levels, blood urea nitrogen level, hematocrit, and LVEF). The risk scores could be calculated without any missing data.

Clinical outcomes

At Tokushima University Hospital, all patients received follow-up care, with clinical follow-up visits occurring at least every three months. After the follow-up echocardiography, the follow-up period began and terminated in May 2021. At Tokushima University Hospital or one of its affiliated hospitals, all the patients received follow-up care. There was no patient lost to follow-up. The AI data had little influence on clinical management. The primary endpoint was cardiac death or readmission due to HF using predetermined criteria. HF readmission was defined as admission for a primary diagnosis of HF and CV death as passing away from a CV cause, such as a myocardial infarction, a cerebrovascular accident, or sudden cardiac death. Based on previously published reports (20, 21), we mainly used variables measured at pre-discharge to assess the prognostic values in the study.

Statistical analysis

Categorical data were expressed as an absolute number and percentages, whereas continuous data were expressed as mean standard deviation. Based on the likelihood of an elevated PAWP (>50%) being normal or abnormal, the patients were split into two groups. The Mann-Whitney U test or the unpaired Student's t test, as applicable, was used to compare continuous variables. Depending on the situation, the Fisher's exact test or the 2 test were used to compare categorical variables. The probability of elevated PAWP was used to divide the patients into two groups for Kaplan–Meier analysis, with survival compared using the log-rank test. A median value of Δprobability of elevated PAWP was used as the definition of improved probability of elevated PAWP. We used a Cox proportional-hazard model to determine the factors associated with survival. The variables selected were based on previous knowledge for the assessment of prognosis in patients with HF. To ascertain the incremental value of the probability of elevated PAWP over clinical data in relation to the main endpoint, sequential Cox models were built. The incremental prognostic value was defined as an increase in the global log-likelihood χ^2 of the model that was statistically significant. The assumption of proportional hazards was assessed by plotting the scaled Schoenfeld residuals for each independent variable against time to determine whether these correlations were nonsignificant. Time-dependent receiver operating characteristic (ROC) curves were used to calculate the C-statistic analyzed by the R package survival ROC. The DeLong method was used to compare the C-statistic. All statistical analyses were performed using SPSS 21.0 (SPSS, Chicago, IL, USA), MedCalc 19.5.6 (Mariakerke, Belgium), and R 3.3.3 (R Foundation for Statistical Computing, Vienna, Austria). A P value < 0.05 was considered statistically significant.

Results

Clinical backgrounds

Table 1 shows the baseline characteristics of the patients at discharge. A total of 192 hospitalized patients with HF (mean age 69 ± 14 years; 61% male) were divided into two groups: those with HFrEF and those with HFpEF. The patients were treated with an ACEi/ACE (65%), β-blocker (79%), or diuretics (73%). No significant difference was observed between the two groups

TABLE 1 Clinical characteristics.

	All ($n = 192$)	HFpEF ($n = 93$)	HFrEF ($n = 99$)	p value
Age (years)	69 ± 14	71 ± 14	68 ± 14	0.07
Male, n (%)	117 (61%)	46 (49%)	71 (72%)	0.002
BSA (m^2)	1.62 ± 0.23	1.58 ± 0.22	1.66 ± 0.22	0.02
Heart rate (beats/min)	86 ± 20	82 ± 20	89 ± 20	0.01
Systolic BP (mmHg)	126 ± 24	129 ± 26	122 ± 23	0.05
Diastolic BP (mmHg)	74 ± 17	72 ± 18	75 ± 16	0.16
Readmission for HF, n (%)	57 (30%)	30 (32%)	27 (27%)	0.45
Backgrounds				
Hypertension, n (%)	131 (68%)	69 (74%)	62 (63%)	0.09
Diabetes, n (%)	80 (42%)	37 (40%)	43 (43%)	0.61
Chronic atrial fibrillation, n (%)	35 (18%)	20 (22%)	15 (15%)	0.26
Ischemic cardiomyopathy, n (%)	43 (22%)	11 (12%)	32 (32%)	<0.001
Laboratory data				
Hb (g/dl)	12.1 ± 2.3	11.9 ± 2.4	12.2 ± 2.2	0.25
eGFR (ml/min/1.73 m^2)	50 ± 25	50 ± 26	50 ± 24	0.94
BNP (pg/ml)	228 (92, 471)	192 (62, 350)	291 (127, 531)	0.002
Chest x-ray on pre-discharge				
CTR	56 ± 7	55 ± 8	56 ± 7	0.17
Lung congestion, n (%)	53 (28%)	26 (26%)	27 (27%)	0.88
Echocardiographic parameters				
LVEF (%)	45 ± 15	59 ± 7	32 ± 7	–
LVEDVi (ml/m^2)	83 ± 32	64 ± 26	101 ± 25	<0.001
LAVi (ml/m^2)	51 ± 19	50 ± 19	52 ± 19	0.57
E/e' ratio	13.8 ± 8.3	13.4 ± 8.2	14.2 ± 8.4	0.49
TR-V (m/s)	2.48 ± 0.46	2.55 ± 0.44	2.40 ± 0.47	0.02
Elevated LAP (%)	102 (53%)	50 (54%)	52 (53%)	0.86
AI parameters				
Probability of elevated PAWP on admission (%)	76 (23, 95)	70 (10, 95)	84 (26, 96)	0.16
Probability of elevated PAWP on pre-discharge (%)	11 (2, 62)	7 (2, 64)	13 (2, 55)	0.91
ΔProbability of elevated PAWP (%)	26 (2, 68)	12 (1, 61)	36 (3, 77)	0.17

Data are presented as number of patients (percentage), mean ± SD or median (interquartile range).

BSA, body surface area; BP, blood pressure; HF, heart failure; ACEi/ARB, angiotensin-converting-enzyme inhibitor/angiotensin II receptor blocker; HB, hemoglobin; eGFR, estimated glomerular filtration rate; BNP, brain natriuretic peptide; LVEF, left ventricular ejection fraction; LVEDVi, left ventricular end-diastolic volume index; LAVi, left atrial volume index; E, early diastolic transmitral flow velocity; e', early diastolic mitral annular motion; TR-V, tricuspid regurgitant velocity; LAP, left atrial pressure.

for age, blood pressure, and comorbidities except for ischemic cardiomyopathy. The patients with HFrEF included a higher number of males, a higher use of β-blockers, increased brain natriuretic peptide (BNP) levels, and a larger LV size. Interestingly, there was no difference in CXR profiles including CTR, lung congestion, probability of elevated PAWP on admission and pre-discharge between the two groups.

The characteristics and echocardiographic parameters of the two groups with and without an abnormal elevated PAWP at pre-discharge are shown in Table 2. In this analysis, LAVi ($p = 0.03$), TR velocity ($p = 0.01$), and the presence of elevated LAP ($p = 0.008$) were associated with an abnormal probability of elevated PAWP. This result indicated probability of elevated PAWP was linked to left ventricular diastolic function. In patients with a normal probability of elevated PAWP on pre-discharge, the median probability of elevated PAWP on admission was 69%, while change in probability of elevated PAWP from admission to pre-discharge (Δprobability of elevated PAWP) was 53%. On the other hand, in patients with an abnormal probability of elevated PAWP on pre-discharge, the median probability of elevated PAWP on admission was high (94%). The status of lung congestion in patients with a higher probability of elevated PAWP may not have been reduced at pre-discharge. Based on expert CXR assessments, lung congestion is more frequent in patients with an abnormal probability of elevated PAWP.

Cardiac mortality and readmission to HF

During a median follow-up period of 58 months (range, 11–80 months), 57 patients (30%) reached the primary endpoint (CV death, $n = 13$, or readmission due to HF, $n = 44$). During the follow-up period, no patient passed away from anything other than CV disease. Figure 2A shows the time to the primary endpoint. Probability of elevated PAWP appeared to be associated with worse clinical outcomes in both the HFpEF ($p < 0.001$) and HFrEF ($p = 0.003$) cohorts. Figure 2B shows the event-free survival of patients stratified according to the presence of an elevated LAP and abnormal probability of elevated PAWP (probability of elevated PAWP >50%). Patients with an elevated LAP and abnormal probability of elevated PAWP had significantly shorter event-free survival than those without these abnormalities ($p < 0.001$). In addition, Figure 2C shows the event-free survival of patients stratified according to improved or not improved probability of elevated PAWP (Δprobability of elevated PAWP, cut-off value: 26%). Patients without an improved probability of elevated PAWP had significantly shorter event-free survival than those with an improved probability of elevated PAWP ($p = 0.03$).

We used univariate and multivariate Cox proportional-hazard regression analysis to identify the variables connected to the main outcome. In the univariate model, the Yale-CPRE HF score, estimated glomerular filtration rate (eGFR), log BNP, LAVi, E/e' ratio, TR-V, and elevated LAP as defined by the 2016 recommendations were linked to the primary endpoint (Table 3). The probability of elevated PAWP at admission was not related to the primary endpoint. Importantly, probability of elevated PAWP at pre-discharge (per 1SD) was related significantly with the primary outcomes (hazard ratio: 1.46, 95% CI: 1.23–1.72, $p < 0.001$). In addition, Δprobability of elevated PAWP from admission to pre-discharge was also associated with clinical outcomes. Pulmonary congestion by expert assessment was weakly associated with clinical outcomes ($p = 0.049$).

TABLE 2 Clinical and echocardiographic parameters between normal and abnormal probability of elevated PAWP on pre-discharge.

x-ray group	Normal probability of elevated PAWP on pre-discharge	Abnormal probability of elevated PAWP on pre-discharge	p value
Number	134	58	
AI parameters			
Probability of elevated PAWP on pre-discharge (%)	3 (1, 13)	81 (65, 95)	–
Probability of elevated PAWP on admission (%)	69 (14, 92)	94 (67, 99)	<0.001
ΔProbability of elevated PAWP (%)	53 (6, 87)	9 (0, 44)	<0.001
Characteristics			
Age (years)	70 ± 14	69 ± 14	0.79
Male, %	38 (66)	82 (59)	0.39
Heart rate (beats/min)	86 ± 21	86 ± 19	0.89
Systolic BP (mmHg)	125 ± 22	128 ± 29	0.54
Yale-CORE HF score	22 ± 4	23 ± 4	0.26
Medications			
ACEi or ARB, n (%)	87 (65)	37 (64)	0.88
β-blocker, n (%)	107 (80)	45 (78)	0.73
Diuretics, n (%)	96 (72)	44 (76)	0.54
Laboratory data			
eGFR (ml/min/1.73 m^2)	52 ± 26	46 ± 22	0.12
BNP (pg/ml)	236 (91, 471)	210 (107, 464)	0.55
Chest x-ray on pre-discharge			
CTR	55 ± 8	58 ± 7	0.02
Lung congestion, n (%)	25 (19)	28 (48)	0.001
Echocardiographic parameters			
LVEF (%)	45 ± 15	46 ± 16	0.76
LVEDVi (ml/m^2)	84 ± 32	83 ± 30	0.84
LAVi (ml/m^2)	49 ± 18	56 ± 21	0.03
E/e' ratio	13.1 ± 7.4	15.3 ± 9.9	0.13
TR-V (m/s)	2.41 ± 0.41	2.61 ± 0.54	0.01
Elevated LAP (%)	63 (47%)	39 (67%)	0.008

See abbreviations as in Table 1.

In the multivariate analysis (**Table 4**), both elevated LAP and probability of elevated PAWP based on the AI algorithm were significant predictors for the primary outcomes after adjustment for the Yale-CORE HF score, log BNP, and eGFR. Furthermore, the Δprobability of elevated PAWP was also a predictor for the primary endpoint after adjustment for these variables.

Figure 3 shows the added benefit of AI parameters for predicting the primary outcomes. The addition of echocardiographic assessment (elevated LAP) and probability of elevated PAWP significantly improved the ability of a model containing the Yale-CORE HF score, eGFR, and log BNP (model 1), Yale-CORE HF score, $\chi^2 = 4.4$ (model 2), plus eGFR and log BNP, $\chi^2 = 16.8$, $p = 0.001$ (model 3), plus elevated LAP, $\chi^2 = 24.4$, $p = 0.005$, plus probability of elevated PAWP on pre-discharge, $\chi^2 = 41.1$, $p < 0.001$). In contrast, the addition of pulmonary congestion interpreted by a doctor did not statistically improve the ability of a model containing the Yale-CORE HF score, eGFR, log BNP, and elevated LAP (model 3 plus pulmonary congestion, from $\chi^2 = 24.4$ to $\chi^2 = 27.5$, compared $p = 0.086$).

For the Cox model based on lung congestion by expert assessment, the Harrell C concordance statistic was calculated as 0.55 (95% CI: 0.49–0.61). The Harrell C concordance statistic was calculated as 0.72 (95% CI: 0.65–0.78) for the Cox model based on the Yale-CORE HF score, eGFR, pro BNP, and elevated LAP. When probability of elevated PAWP was added to the model, the C-statistic improved significantly to 0.78 (95% CI: 0.71–0.84, $p = 0.039$ for the comparison).

Assessment of Grad-CAM

We analyzed the images to determine where AI was focused to help explain the AI assessment (**Figure 4**). Grad-CAM demonstrated that in our situations, whether a patient had primary events or not, our model focused on the heart region. The proposed AI model may thus offer fresh perspectives to accurately identify differences in CXR images in the future large dataset.

Discussion

The objective of this study was to assess the clinical meanings of probability of elevated PAWP based on an AI algorithm, as an association between probability of elevated PAWP and CV events. The study provided several insights into the interpretation of probability of elevated PAWP: (1) probability of elevated

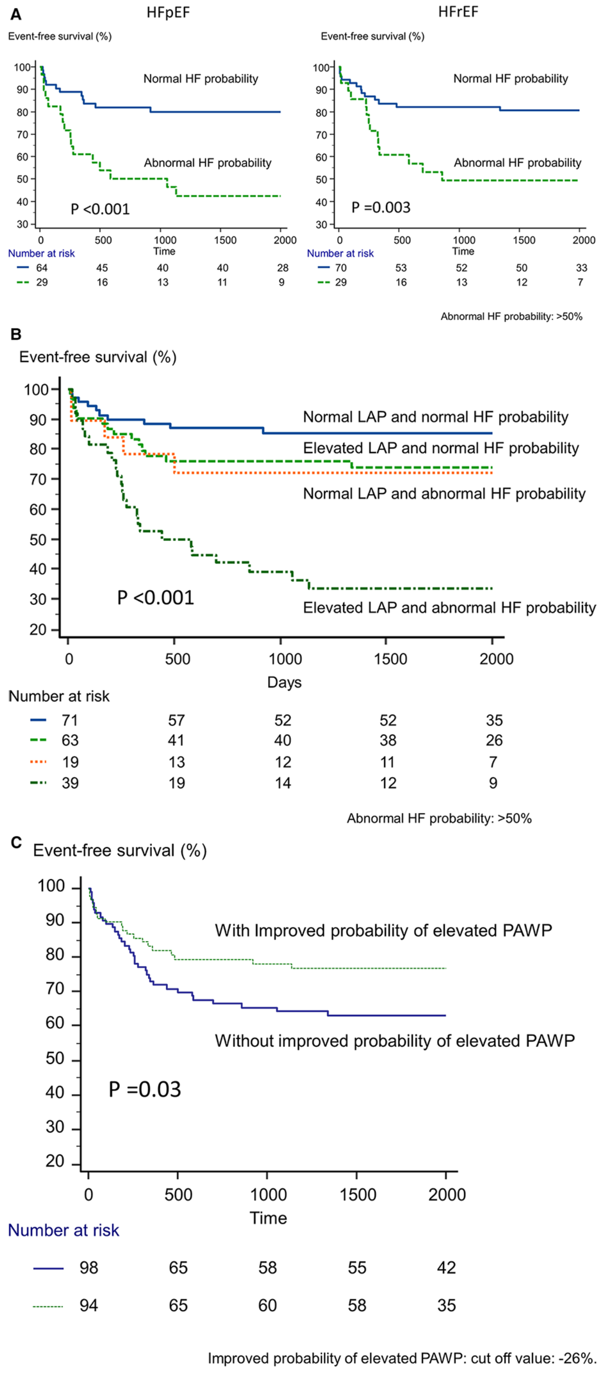

FIGURE 2
Kaplan-Meier analysis of event-free survival. (A) According to the presence or absence of abnormal probability of elevated PAWP in HFpEF and HFrEF, we divided patients into 2 groups. (B) According to the presence of an elevated left atrial pressure based on echocardiography and probability of elevated PAWP based on artificial intelligence, we divided patients into 4 groups. (C) According to the presence or absence of abnormal probability of elevated PAWP for improved and not-improved probability of elevated PAWP.

PAWP was related to left ventricular diastolic function; (2) patients with an abnormal probability of elevated PAWP had a significantly higher event rate compared to patients with a normal probability of elevated PAWP; (3) the association between probability of elevated PAWP and the primary endpoints remained significant after adjustment for HF risk score, laboratory data, and echocardiographic data. Interestingly, Lung congestion assessed by one attending cardiologist was only weakly associated with outcomes. This information might provide insights into the clinical utility of medical imaging based on an AI algorithm in patients with HF beyond assessments by experts. Our findings suggest that the likelihood of elevated PAWP may be helpful for clinical evaluation and follow-up during the ideal period of medical treatment.

Findings on probability of elevated PAWP in chest x-rays

The association between classical radiographic features of HF in CXR images and physiological hemodynamic parameters has been described previously (22, 23). Cephalization of pulmonary venous blood flow occurs with redistribution of pulmonary blood flow and typically when the PAWP is >10–15 mmHg. Interstitial edema characterized by Kerley B lines is thought to result when the PAWP is >20 mmHg due to thickening of the interlobular septa. Alveolar edema is present when the PAWP exceeds 25 mmHg. However, these radiographic changes are not always present and sometimes may only be partially present, or indeed absent, even in cases of clinically significant HF. An increased cardiothoracic ratio is more common and more sensitive; however, it is less specific (24). Although these important findings may be present in CXR images, diagnostic limitations of the clinical and simple radiographic parameters are also observed in the clinical setting. In this study, the assessment of CXR by experts was not so strongly associated with outcomes.

Previously, we trained the AI model to detect an elevated PAWP >18 mmHg (11). Theoretically, an elevated probability of elevated PAWP based on AI can be associated with residual pulmonary congestion and cardiac enlargement. Based on our results, abnormal probability of elevated PAWP is associated with larger LA volumes, relatively higher E/e' as a marker of LV filling pressure, higher tricuspid valve regurgitant velocity, and the proportion of elevated LAP (**Table 2**). Interestingly, the LV systolic function was not significantly associated with probability of elevated PAWP. Therefore, this index appears to be a sensitive marker of LV diastolic parameters in the clinical setting. Further studies are designed to clarify the detail of the hemodynamic mechanism for probability of elevated PAWP using simultaneous recordings of cardiac pressures measured using invasive catheters.

Probability of elevated PAWP and outcomes

In univariate analysis, the Yale-CORE HF score, BNP level, renal function, and elevated LAP measured by echocardiography were associated with clinical events. The parameters are used to predict CV events, including HF rehospitalization. After adjustment for these known factors, the probability of elevated PAWP based on an AI algorithm was associated with the primary outcome. There is a possible explanation for the association between probability of elevated PAWP and worse clinical outcomes. Based on our results of congestive CXR images, probability of elevated PAWP appears to reflect elevated LA pressures. Several studies have shown that an elevated PAWP was associated significantly with CV events (25, 26). These associations possibly explain the association between probability of elevated PAWP and clinical events. More importantly, the changes in probability of elevated PAWP between admission and pre-discharge were also associated with clinical events. A recent publication from PARADIGM-HF showed that signs of persistent congestion observed in physical examinations provided significant independent prognostic value even beyond symptoms and the levels of natriuretic peptides (27). When patients who do not respond satisfactorily to HF therapy are confirmed by a pre-discharge CXR, further administration of diuretics or other intensive treatment for HF may be considered in the clinical setting. We found that probability of elevated PAWP at admission was not associated with subsequent clinical events and therefore concluded that pre-discharge assessment should be recommended for hospitalized HF patients in order to provide more information about their status.

TABLE 3 Univariate associations of primary outcomes in hospitalized heart failure.

	HR (95%CI)	*p* value
Characteristics		
Age (years)	1.01 (0.99–1.03)	0.30
Male	0.97 (0.57–1.66)	0.92
Heart rate	0.99 (0.98–1.01)	0.25
Systolic BP	1.00 (0.99–1.01)	0.60
Yale-CORE HF score	1.08 (1.01–1.15)	0.03
Medications		
ACEi or ARB	0.86 (0.50–1.48)	0.59
β-blocker	0.80 (0.43–1.49)	0.48
Diuretics	1.55 (0.80–2.99)	0.19
Laboratory data		
eGFR (ml/min/1.73 m^2)	0.98 (0.97–0.99)	0.003
Log BNP	2.66 (1.53–4.65)	0.001
Chest x-ray on pre-discharge		
CTR	0.37 (0.01–13.08)	0.58
Lung congestion	1.73 (1.00–2.98)	0.049
Echocardiographic parameters		
LVEF (%)	0.99 (0.98–1.01)	0.41
LVEDVi (ml/m^2)	1.00 (0.99–1.01)	0.57
LAVi (ml/m^2)	1.02 (1.00–1.03)	0.02
E/e' ratio	1.04 (1.02–1.07)	0.001
TR-V (m/s)	1.85 (1.09–3.13)	0.02
Elevated LAP (%)	2.87 (1.59–5.18)	<0.001
AI parameters		
Probability of elevated PAWP on admission (per 1SD)	1.15 (0.94–1.41)	0.17
Probability of elevated PAWP on pre-discharge (per 1SD)	1.46 (1.23–1.72)	<0.001
ΔProbability of elevated PAWP (per 1SD)	0.71 (0.55–0.92)	0.01

HR, hazard ratio; CI, confidence interval; other abbreviations as in Table 1.

Artificial intelligence in the clinical setting

At present, many AI imaging studies estimate diagnostic accuracy using sensitivity and specificity (28), while there is limited data available to assess clinical outcomes. To help progress the study of AI in medical images it is necessary to assess the effects on clinically meaningful endpoints to improve applicability and allow effective deployment into clinical practice (29). In addition, it is essential to AI research to consistently use out-of-sample external validation and well-defined patient cohorts to augment the quality and interpretability of AI. In the present study we investigated an independent cohort with a previously published application of an AI model for probability of elevated PAWP used to provide prognostic value in patients with HF. We hope that AI imaging may be used in the near future not only for diagnostic accuracy but also for clinical utility (e.g., prediction of prognosis).

Clinical utility of probability of elevated PAWP

The results of this study suggest that the probability of elevated PAWP based on AI algorithm provides incremental value to known parameters including clinical data, laboratory data and echocardiography. To our knowledge, this study is the first to examine the clinical efficacy of AI algorithms in HF patients and their relationship to cardiac events during follow-up. The probability of elevated PAWP will be significant in that it is simple, reproducible, measurable at almost all institutes and

TABLE 4 Multivariate associations of primary outcomes in hospitalized heart failure.

	Model 1 (χ^2: 24.4)			Model 2 (χ^2: 31.4)			Model 3 (χ^2: 41.1)		
	HR	95%CI	*p* value	HR	95%CI	*p* value	HR	95%CI	*p* value
Clinical parameters									
Yale-CORE HF score	1.01	0.93–1.09	0.86	1.02	0.94–1.10	0.70	1.01	0.93–1.09	0.86
Log BNP	1.90	1.03–3.52	0.04	1.99	1.07–3.70	0.03	1.97	1.11–3.50	0.02
eGFR	0.99	0.97–1.00	0.08	0.99	0.98–1.00	0.16	0.99	0.98–1.01	0.23
Echocardiography									
Elevated LAP	2.29	1.24–4.21	0.008	2.19	1.19–4.03	0.012	1.97	1.07–3.62	0.03
ΔProbability of elevated PAWP (per 1SD)				0.73	0.57–0.95	0.017			
Probability of elevated PAWP on pre-discharge (Per 1SD)							1.39	1.17–1.65	<0.001

HR, hazard ratio; CI, confidence interval; other abbreviations as in Table 1.

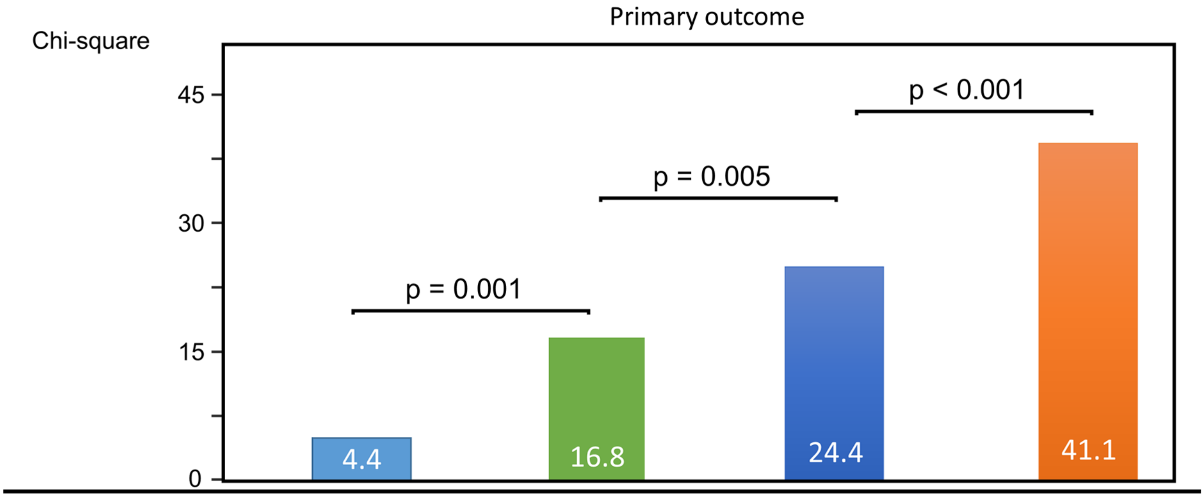

	Yale-CORE HF score	+eGFR and logBNP	+ Elevated LAP	+ HF probability
Yale-CORE HF score	HR: 1.07 (1.00-1.15), p=0.037	HR: 1.00 (0.92-1.08), p=0.91	HR: 1.01 (0.93-1.09), p=0.86	HR: 1.01 (0.93-1.09), p=0.86
eGFR		HR: 0.99 (0.97-1.00), p=0.050	HR: 0.99 (0.97-1.00), p=0.078	HR: 0.99 (0.98-1.01), p=0.23
Log BNP		HR: 2.35 (1.31-4.22), p=0.004	HR: 1.90 (1.03-3.52), p=0.040	HR: 1.97 (1.11-3.50), p=0.021
Elevated LAP			HR: 2.29 (1.24-4.21), p=0.008	HR: 1.96 (1.07-3.62), p=0.004
HF probability (per 1SD)				HR: 1.39 (1.17-1.65), p<0.001

FIGURE 3
Incremental value of echocardiographic parameters. These figures illustrate the global χ^2 of sequential Cox models that incorporated several clinical parameters. eGFR, estimate glomerular filtration rate; BNP, brain natriuretic peptide; LAP, left atrial pressure; HF, heart failure; HR, hazard ratio.

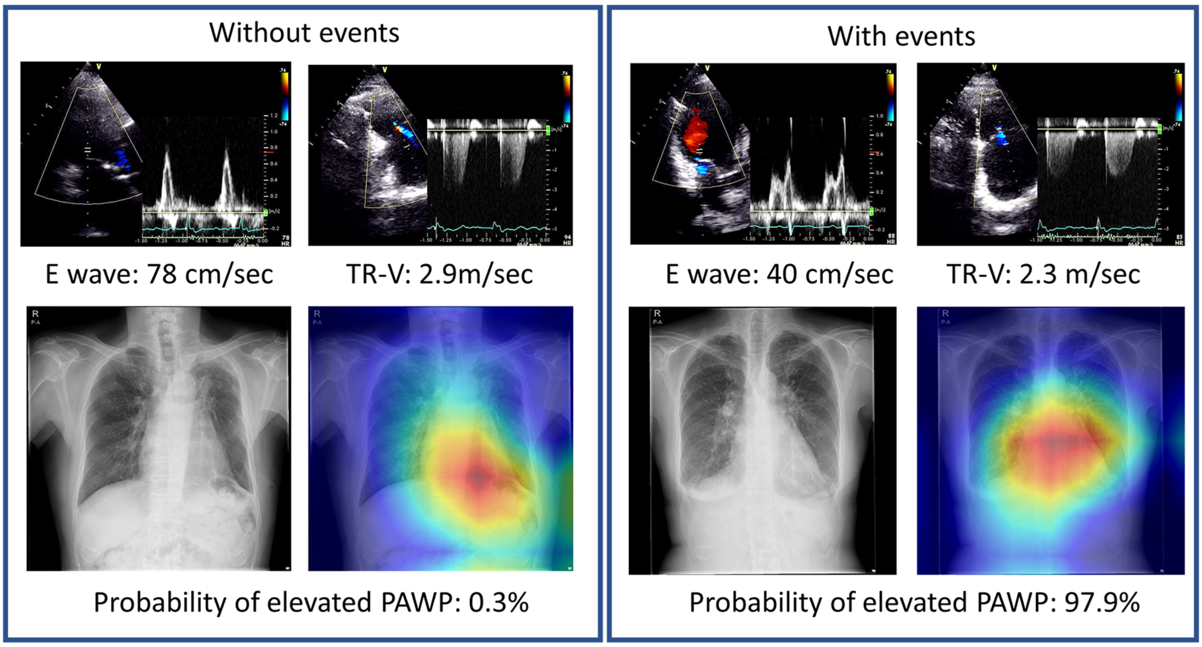

FIGURE 4
Representative cases with Grad-CAM images. Chest x-rays were visualized using Grad-CAM, with the yellow and red areas showing regions that the deep learning model considered important for probability of elevated PAWP.

reflects prognostic power in heart failure. Model performance on prediction is significant at pre-discharge and poor at admission. The results are consistent with the finding that rehospitalization is less likely if congestion is well controlled (30). This model may play an important role as a guide for treatment of residual congestion in HF. Our data suggested that the changes in probability of elevated PAWP on x-rays during hospitalization may reflect the course of treatment for heart failure. We expect that it can be modeled and validated with multicenter data and used in clinical settings in the future.

Limitations

The present study has several limitations. First, this was a single tertiary heart centers study with a small sample size in Japan. Therefore, the generalizability of the study findings was limited. On the other hand, we believed that the single-center study would have less biases than a study with a larger sample size, such as those caused by disparities in treatment effectiveness or a wide range of etiologies. Because there were so few events in the sample, there is a chance that the model will be overfit. Second, the cut-off value for abnormal probability of elevated PAWP (50%) was determined by our previous paper, thus, the accurate cut-off values may not be well organized in the different cohort. The validity and reliability of AI algorithms should improve in the near future with advances in machine learning and augmented data set. The study period was from 2013 to 2017. Some HF pharmacotherapies such as SGLT-2 inhibitors were not available routinely. Because this study was designed to evaluate the performance of AI for risk stratification of HF, it was not possible to assess this AI model in patients without HF. These limitations suggest that the current study should be considered as hypothesis-generating. Additional research is required to quantify the likelihood of elevated PAWP more fully in a multi-center large cohort that includes healthy populations.

Conclusions

CXR assessment using the AI model may provide important incremental prognostic value for predicting readmission and cardiac mortality risk assessment in patients with HF compared with doctor-interpreted pulmonary congestion. The results may help to enhance the accuracy of prediction models used to evaluate the risk of clinical outcomes in HF, potentially resulting in more informed clinical decision-making and better care for patients.

Data availability statement

The raw data supporting the conclusions of this article will be made available by the authors, without undue reservation.

Ethics statement

The present study was approved by the Institutional Review Board of the Tokushima University Hospital. Reference number: 3217-4. The ethics committee waived the requirement of written informed consent for participation.

Author contributions

Design of the work: KK; conduct of the work and data acquisition: YH, NY, and YK; data analysis and interpretation: TT and JK; drafting the work: KK and YH; reviewing the work and providing input: all authors. All authors contributed to the article and approved the submitted version.

Funding

This work was partially supported by JSPS KAKENHI grants (number 23K07509 to KK and 21K12706 to YH) and a grant from the Japan Agency for Medical Research and Development (AMED, JP22uk1024007 to KK).

Acknowledgments

The funding source had no role in the design and conduct of the study; collection, management, analysis, and interpretation of the data; preparation, review, or approval of the manuscript; and decision to submit the manuscript for publication.

Conflict of interest

The authors declare that the research was conducted in the absence of any commercial or financial relationships that could be construed as a potential conflict of interest.

Publisher's note

References

1. Tsao CW, Aday AW, Almarzooq ZI, Alonso A, Beaton AZ, Bittencourt MS, et al. Heart disease and stroke statistics—2022 update: a report from the American heart association. *Circulation*. (2022) 145(8):e153–639. doi: 10.1161/CIR.0000000000001052

2. Khera R, Wang Y, Nasir K, Lin Z, Krumholz HM. Evaluation of 30-day hospital readmission and mortality rates using regression-discontinuity framework. *J Am Coll Cardiol*. (2019) 74(2):219–34. doi: 10.1016/j.jacc.2019.04.060

3. Lassen MCH, Olsen FJ, Skaarup KG, Tolstrup K, Qasim AN, Gislason G, et al. The clinical application of the ratio of transmitral early filling velocity to early diastolic strain rate: a systematic review and meta-analysis. *J Echocardiogr*. (2020) 18(2):94–104. doi: 10.1007/s12574-020-00466-w

4. Tanaka H. Utility of strain imaging in conjunction with heart failure stage classification for heart failure patient management. *J Echocardiogr*. (2019) 17 (1):17–24. doi: 10.1007/s12574-018-0408-2

5. McMurray JJ, Adamopoulos S, Anker SD, Auricchio A, Bohm M, Dickstein K, et al. ESC Guidelines for the diagnosis and treatment of acute and chronic heart failure 2012: the task force for the diagnosis and treatment of acute and chronic heart failure 2012 of the European society of cardiology. Developed in collaboration with the heart failure association (HFA) of the ESC. *Eur Heart J*. (2012) 33 (14):1787–847. doi: 10.1093/eurheartj/ehs104

6. Ponikowski P, Voors AA, Anker SD, Bueno H, Cleland JG, Coats AJ, et al. 2016 ESC guidelines for the diagnosis and treatment of acute and chronic heart failure: the task force for the diagnosis and treatment of acute and chronic heart failure of the European society of cardiology (ESC). developed with the special contribution of the heart failure association (HFA) of the ESC. *Eur J Heart Fail*. (2016) 18 (8):891–975. doi: 10.1002/ejhf.592

7. Costanzo WE, Fein SA. The role of the chest x-ray in the evaluation of chronic severe heart failure: things are not always as they appear. *Clin Cardiol*. (1988) 11 (7):486–8. doi: 10.1002/clc.4960110710

8. Jogi J, Al-Mashat M, Radegran G, Bajc M, Arheden H. Diagnosing and grading heart failure with tomographic perfusion lung scintigraphy: validation with right heart catheterization. *ESC Heart Fail*. (2018) 5(5):902–10. doi: 10.1002/ehf2.12317

9. Kusunose K, Abe T, Haga A, Fukuda D, Yamada H, Harada M, et al. A deep learning approach for assessment of regional wall motion abnormality from echocardiographic images. *JACC Cardiovasc Imaging*. (2020) 13:374–81. doi: 10.1016/j.jcmg.2019.02.024

10. Kusunose K, Haga A, Abe T, Sata M. Utilization of artificial intelligence in echocardiography. *Circ J*. (2019) 83(8):1623–9. doi: 10.1253/circj.CJ-19-0420

11. Hirata Y, Kusunose K, Tsuji T, Fujimori K, Kotoku JI, Sata M. Deep learning for detection of elevated pulmonary artery wedge pressure using standard chest x-ray. *Can J Cardiol*. (2021) 37:1198–206. doi: 10.1016/j.cjca.2021.02.007

12. Ponikowski P, Voors AA, Anker SD, Bueno H, Cleland JG, Coats AJ, et al. 2016 ESC guidelines for the diagnosis and treatment of acute and chronic heart failure. *Eur Heart J*. (2016) 37:2129–200. doi: 10.1093/eurheartj/ehw128

13. Tsutsui H, Isobe M, Ito H, Ito H, Okumura K, Ono M, et al. JCS 2017/JHFS 2017 guideline on diagnosis and treatment of acute and chronic heart failure- digest version. *Circ J*. (2019) 83(10):2084–184. doi: 10.1253/circj.CJ-19-0342

14. Bozkurt B, Coats A, Tsutsui H. A report of the heart failure society of America, heart failure association of the European society of cardiology, Japanese heart failure society and writing committee of the universal definition of heart failure consensus conference. *Eur J Heart Fail*. (2021) 23:352–80. doi: 10.1002/ejhf.2115

15. Kingma DP, Ba J. *Adam: A method for stochastic opoimization*. arXiv preprint arXiv:14126980. (2014).

16. Selvaraju RR, Cogswell M, Das A, Vedantam R, Parikh D, Batra D. *Grad-CAM: visual explanations from deep networks via gradient-based localization. Proceedings of the IEEE international conference on computer vision*. (2017). p. 618–26. doi: 10.1109/ICCV.2017.74

17. Mitchell C, Rahko PS, Blauwet LA, Canaday B, Finstuen JA, Foster MC, et al. Guidelines for performing a comprehensive transthoracic echocardiographic examination in adults: recommendations from the American society of echocardiography. *J Am Soc Echocardiogr*. (2019) 32(1):1–64. doi: 10.1016/j.echo.2018.06.004

18. Nagueh SF, Smiseth OA, Appleton CP, Byrd BF 3rd, Dokainish H, Edvardsen T, et al. Recommendations for the evaluation of left ventricular diastolic function by echocardiography: an update from the American society of echocardiography and the European association of cardiovascular imaging. *J Am Soc Echocardiogr*. (2016) 29(4):277–314. doi: 10.1016/j.echo.2016.01.011

19. Keenan PS, Normand SL, Lin Z, Drye EE, Bhat KR, Ross JS, et al. An administrative claims measure suitable for profiling hospital performance on the basis of 30-day all-cause readmission rates among patients with heart failure. *Circ Cardiovasc Qual Outcomes*. (2008) 1(1):29–37. doi: 10.1161/CIRCOUTCOMES.108.802686

20. De Sousa Bispo J, Azevedo P, Freitas P, Marques N, Reis C, Horta E, et al. Mechanical dispersion as a powerful echocardiographic predictor of outcomes after myocardial infarction. *Eur Heart J*. (2020) 41(Supplement_2):ehaa946.0126. doi: 10.1093/ehjci/ehaa946.0126

21. Kokalj N, Kozak M, Jug B. Post-acute pre-discharge echocardiography in the long-term prognostic assessment of pulmonary thrombembolism. *Sci Rep*. (2021) 11 (1):1–7. doi: 10.1038/s41598-021-82038-1

22. Hublitz UF, Shapiro JH. The radiology of pulmonary edema: four decades of observations, clinical correlation, and studies of the underlying pathophysiology. *CRC Crit Rev Clin Radiol Nucl Med.*. (1974) 5:389–422. doi: 10.1161/CIRCOUTCOMES.108.802686

23. Mahdyoon H, Klein R, Eyler W, Lakier JB, Chakko S, Gheorghiade M. Radiographic pulmonary congestion in end-stage congestive heart failure. *Am J Cardiol*. (1989) 63(9):625–7. doi: 10.1016/0002-9149(89)90912-0

24. Collins SP, Pang PS, Lindsell CJ, Kyriacou DN, Storrow AB, Hollander JE, et al. International variations in the clinical, diagnostic, and treatment characteristics of emergency department patients with acute heart failure syndromes. *Eur J Heart Fail*. (2010) 12(11):1253–60. doi: 10.1093/eurjhf/hfq133

25. Eisman AS, Shah RV, Dhakal BP, Pappagianopoulos PP, Wooster L, Bailey C, et al. Pulmonary capillary wedge pressure patterns during exercise predict exercise capacity and incident heart failure. *Circ Heart Fail*. (2018) 11(5):e004750. doi: 10.1161/CIRCHEARTFAILURE.117.004750

26. Arase M, Kusunose K, Morita S, Yamaguchi N, Hirata Y, Nishio S, et al. Cardiac reserve by 6-minute walk stress echocardiography in systemic sclerosis. *Open Heart*. (2021) 8(1):e001559. doi: 10.1136/openhrt-2020-001559

27. Selvaraj S, Claggett B, Pozzi A, McMurray JJ, Jhund PS, Packer M, et al. Prognostic implications of congestion on physical examination among contemporary patients with heart failure and reduced ejection fraction: PARADIGM-HF. *Circulation*. (2019) 140 (17):1369–79. doi: 10.1161/CIRCULATIONAHA.119.039920

28. Liu X, Faes L, Kale AU, Wagner SK, Fu DJ, Bruynseels A, et al. A comparison of deep learning performance against health-care professionals in detecting diseases from medical imaging: a systematic review and meta-analysis. *Lancet Digit Health*. (2019) 1 (6):e271–297. doi: 10.1016/S2589-7500(19)30123-2

29. Oren O, Gersh BJ, Bhatt DL. Artificial intelligence in medical imaging: switching from radiographic pathological data to clinically meaningful endpoints. *Lancet Digit Health*. (2020) 2(9):e486–488. doi: 10.1016/S2589-7500(20)30160-6

30. Kobayashi M, Watanabe M, Coiro S, Bercker M, Paku Y, Iwasaki Y, et al. Mid-term prognostic impact of residual pulmonary congestion assessed by radiographic scoring in patients admitted for worsening heart failure. *Int J Cardiol*. (2019) 289:91–8. doi: 10.1016/j.ijcard.2019.01.091

frontiers | Frontiers in Cardiovascular Medicine

TYPE Review
PUBLISHED 24 May 2023
DOI 10.3389/fcvm.2023.1069745

Check for updates

OPEN ACCESS

EDITED BY
Guillaume Goudot,
Institut National de la Santé et de la Recherche Médicale (INSERM), France

REVIEWED BY
Georgios Benetos,
National and Kapodistrian University of Athens, Greece
Xiaoning Jiang,
North Carolina State University, United States

*CORRESPONDENCE
Pingyang Zhang
✉ zhpy28@126.com

[†]These authors have contributed equally to this work

RECEIVED 14 October 2022
ACCEPTED 08 May 2023
PUBLISHED 24 May 2023

CITATION
Yao Y and Zhang P (2023) Novel ultrasound techniques in the identification of vulnerable plaques—an updated review of the literature.
Front. Cardiovasc. Med. 10:1069745.
doi: 10.3389/fcvm.2023.1069745

Novel ultrasound techniques in the identification of vulnerable plaques—an updated review of the literature

Yujuan Yao[†] and Pingyang Zhang[*†]

Department of Cardiovascular Ultrasound, Nanjing First Hospital, Nanjing Medical University, Nanjing, China

Atherosclerosis is an inflammatory disease partly mediated by lipoproteins. The rupture of vulnerable atherosclerotic plaques and thrombosis are major contributors to the development of acute cardiovascular events. Despite various advances in the treatment of atherosclerosis, there has been no satisfaction in the prevention and assessment of atherosclerotic vascular disease. The identification and classification of vulnerable plaques at an early stage as well as research of new treatments remain a challenge and the ultimate goal in the management of atherosclerosis and cardiovascular disease. The specific morphological features of vulnerable plaques, including intraplaque hemorrhage, large lipid necrotic cores, thin fibrous caps, inflammation, and neovascularisation, make it possible to identify and characterize plaques with a variety of invasive and non-invasive imaging techniques. Notably, the development of novel ultrasound techniques has introduced the traditional assessment of plaque echogenicity and luminal stenosis to a deeper assessment of plaque composition and the molecular field. This review will discuss the advantages and limitations of five currently available ultrasound imaging modalities for assessing plaque vulnerability, based on the biological characteristics of the vulnerable plaque, and their value in terms of clinical diagnosis, prognosis, and treatment efficacy assessment.

KEYWORDS

contrast-enhanced ultrasound (CEUS), ultrasound molecular imaging (UMI), elastography, intravascular ultrasound imaging (IVUS), diagnosis, vulnerable plaque

1. Introduction

Atherosclerosis, characterized by the formation of lipid-rich plaques in the arterial wall, is the pathological basis of cardiovascular disease, which remains the major underlying factor of morbidity and mortality worldwide (1). Atherosclerotic plaques tend to develop quietly and are essentially asymptomatic when they remain intact. However, once progress, the ruptured plaques can lead to atherosclerotic thrombosis and a host of attendant complications. Therefore, early diagnosis as well as risk stratification -separating rupture-prone unstable plaques from relative stable plaque- is vitally important (2, 3).

Due to technical and cognitive limitations, previous studies on atherosclerotic plaque have largely been hampered. The size of atherosclerotic plaque and the accompanying luminal narrowing were previously thought to be closely related to acute ischemic cardiovascular events. However, increasing evidence shows that the composition of atherosclerotic plaques is more relevant to acute ischemic cardiovascular events (4). Certain structures and components of atherosclerotic plaques, including intraplaque

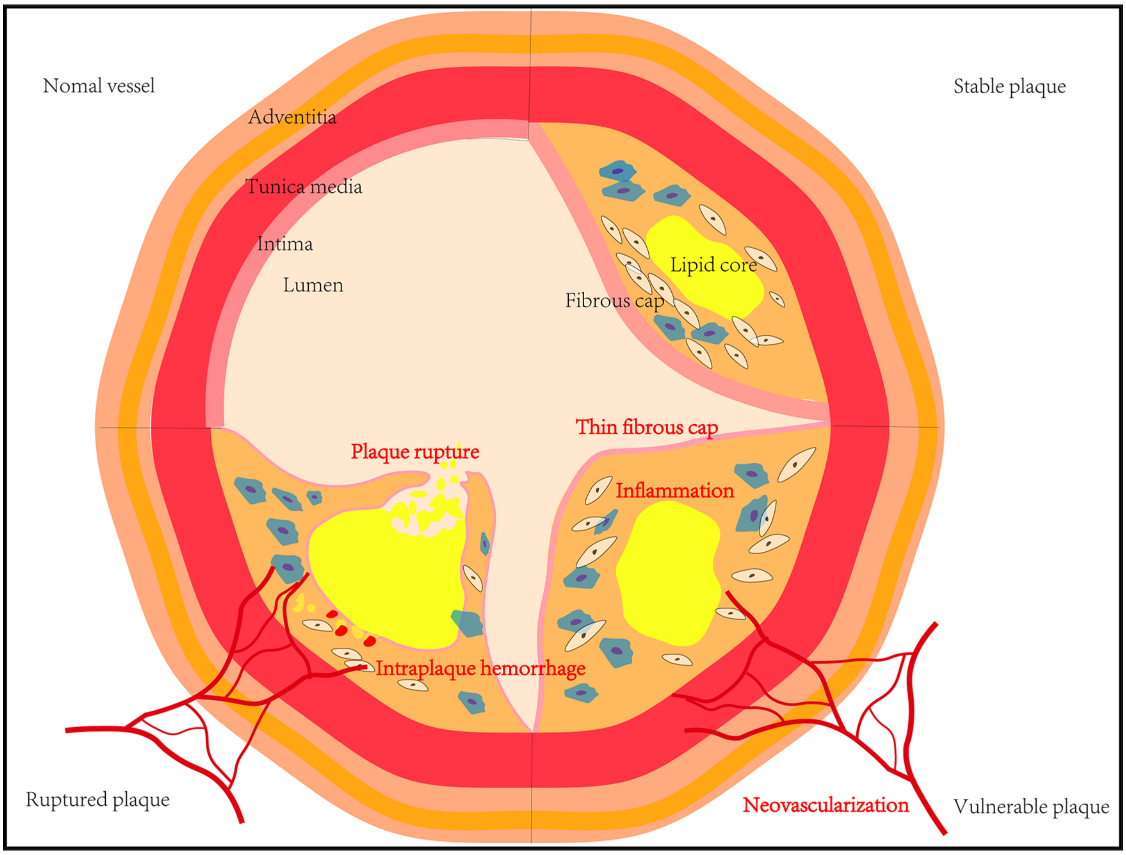

FIGURE 1
The development and main features of atherosclerotic plaques.

hemorrhage, large lipid necrotic core, thin fibrous caps, inflammation, and neovascularization, are all been considered promising rupture-prone (5, 6) (**Figure 1**). In addition, understanding the molecular and cellular mechanisms of atherosclerotic plaque development as well as researching new treatments to prevent or treat acute cardiovascular events are of great significance for both basic research and clinical practice (7).

Several imaging technologies have been developed to assess atherosclerotic disease, among which ultrasound has obvious advantages over other imaging modalities in terms of wide availability and low cost (8). In recent years, with the rapid development of technology, emerging ultrasound techniques including contrast-enhanced ultrasound (CEUS), Doppler ultrasound, ultrasound molecular imaging (UMI), ultrasound elastography and intravascular ultrasound imaging (IVUS) can not only screen and diagnose vulnerable plaques, but also propose the risk classification of vulnerable plaques through different ways, which will be greatly meaningful for the clinical management of patients with atherosclerosis.

Based on the latest literature data, we aim to provide an updated, objective, and comprehensive summary of the current progression of novel ultrasound techniques including the imaging principle, the application and development prospects as well as their limitations.

2. Contrast-enhanced ultrasound

CEUS generally makes up for the deficiency of conventional B-mode and color Doppler ultrasound which have long been challenged by their insufficient value to identify components and neovascularization within the plaque (9). It is a rather novel technique with the application of contrast agents in the form of microbubbles (10). In order to circulate freely in the bloodstream like red blood cells through capillaries, these microbubbles are designed into core-shell inflatable microspheres typically smaller than 7 μm in diameter. The shell is usually composed of proteins, lipids, polymers, surfactants, or a mixture, and thus constitutes a barrier between the surrounding environment and the encapsulated gas inside (11). The composition of the shell also determines the hardness of microbubbles, their susceptibility to recognition by the reticuloendothelial system, and their vandalism resistance in high-intensity ultrasonic fields. In addition, the air core encased inside the microbubble considerably enhances the backward scattered acoustic signal (12) (**Table 1**). Several types of microbubbles such as the Sonovue series are the main ultrasound contrast agents currently approved and recommended for clinical use (13). On the other hand, the conventional diagnostic ultrasound imaging frequency is usually less than 7.5 MHz in clinical practice. However, higher spatial

TABLE 1 The main composition of the microbubble and the function of each part.

Component items	Composition	Function
Shell	Proteins, lipids, polymers, surfactants or a mixture of them	◆ Constitute a barrier ◆ Determine the hardness ◆ Affect the susceptibility of recognition by the reticuloendothelial system ◆ Vandalism resistance
Core	Gas	Enhance the backward scattered acoustic signal
Diameter	1–10 µm	/

and temporal resolution is needed for the detection of fine vascular structures in preclinical applications, with 15–55 MHZ generally recommended (14). Besides, the penetration depth of CEUS is relatively poor compared with standard B-mode imaging. Although lower imaging frequencies improve penetration, spatial resolution will be negatively impacted. It may be useful for CEUS to use higher-frequency curvilinear transducers and high-frequency linear transducers to improve spatial resolution; however, the microbubble signal may not be as strong, resulting in an overall darker image (15). In theory, these gas-filled microbubbles can stay at the site of the capillary bed, and oscillate upon interacting with the ultrasound wave thus enhancing the reflected ultrasound signal, and improving the visualization of small vascular beds (16).

As is strongly recommended by the European Federation of Societies for Ultrasound in Medicine and Biology, CEUS has opened a new field of vision for the study of arterial pathology for it can not only quantitatively assess the degree of atherosclerosis stenosis, but also qualitatively assess the vulnerability of plaque based on the presence of ulceration, neovascularization, and inflammatory infiltration (17, 18). It is proved that the extent of intra-plaque neovascularization (IPN) displayed on CEUS has a good correlation with histology. In areas where plaques presented a larger degree of contrast enhancement, the corresponding region on histology also had increased density (19).

The utility of CEUS in the evaluation of carotid IPN to reclassify patients into more accurate risk categories has been confirmed by several studies. Based on the existence and location of ultrasound microbubbles within each plaque, IPN is typically graded into three levels in CEUS: grade0-no visible microbubbles in the plaque; grade1-minimal microbubbles confined to the shoulder or adventitial side of the plaque; grade2-plentiful microbubbles throughout the plaque (16, 20, 21) (**Figure 2**). Although mean carotid intima-media thickness (CIMT), maximum plaque height (MPH) and total plaque area (TPA) are typical indicators often used to measure the severity of atherosclerosis in patients, Mantella et al. proved that the carotid IPN score derived from CEUS was even more sensitive than CIMT, MPH or TPA for predicting participants who suffered from serious coronary artery disease (CAD). Furthermore, the study took an IPN score ≥1.25 as a proper cut-off value to predict significant CAD (20), yet Song et al. regarded the IPN score of 2 as the suitable predictor to predict the high rate of stroke recurrence (22). So to date, no consensus on the best predictive IPN score detected by CEUS capable of predicting significant CAD has been reached when taking IPN as an independent predictor of CAD.

As mentioned above, IPN was usually graded by a semiquantitative image analysis relying on the visual assessment which lacks internal standards, nor do IPN suitable for assessing highly calcified plaques, so divergence about the objectivity of CEUS simply employing IPN to evaluate vulnerable plaque still exists (23). Notably, Boswell-Patterson et al. employed a new measurement parameter- neovascularized enhancement ratio (NER) -to analyze complex atherosclerotic plaque models, which allows highly calcified plaques to be analyzed. The formula of NER is $(AP \times PER) - (AC \times CER)/(AP - AC)$, where Ap equals plaque area, AC equals calcified area, PER equals plaque enhancement rate and CER equals calcified area enhancement rate. NER in this study also shows a positive relationship with IPN volume (24). Recently, Lyu et al. proposed that the direction of contrast agent diffusion may severe as another complementary method for the prediction of unstable atherosclerotic plaques. Apart from the characteristic contrast filling of the depressions at the plaque-lumen boundary, microbubbles spreading from the arterial lumen and into the plaque in the form of rotating moving bright spots or lines can also be a complementary method of detecting plaque rupture (25). Another study reported that incorporating the analysis of stress and strain distribution apart from IPN can also improve the accuracy in the assessment of plaque rupture with neovascularization and IPH (26). Furthermore, the current CEUS-assessed plaque is mainly based on 2-D imaging which is prone to be interfered with by acoustic shadowing (23). The newer three-dimensional CEUS requires more validation studies on its function of further improving visualization and grading the unstable plaques (27). All of these studies pave the way for a more objective measurement of vulnerable plaque and clinical identification of the plaque progression.

To sum up, although it remains challenging to reach a consensus on the diagnostic standards and limited by some intrinsic factors such as artifacts and rather short enhancement time, contrast-enhanced ultrasound has obvious advantages over conventional US in providing quantifiable data and better image quality for identifying Intraplaque neovascularization in rupture-prone vulnerable plaques and formulating a more accurate risk stratification strategy.

3. Doppler ultrasound

Doppler ultrasound is a rapidly developing technology to evaluate vulnerable plaques from the perspective of blood flow visualization, among which ultrasonic microflow imaging (SMI) and ultrafast ultrasound imaging (UF) are the typical representatives.

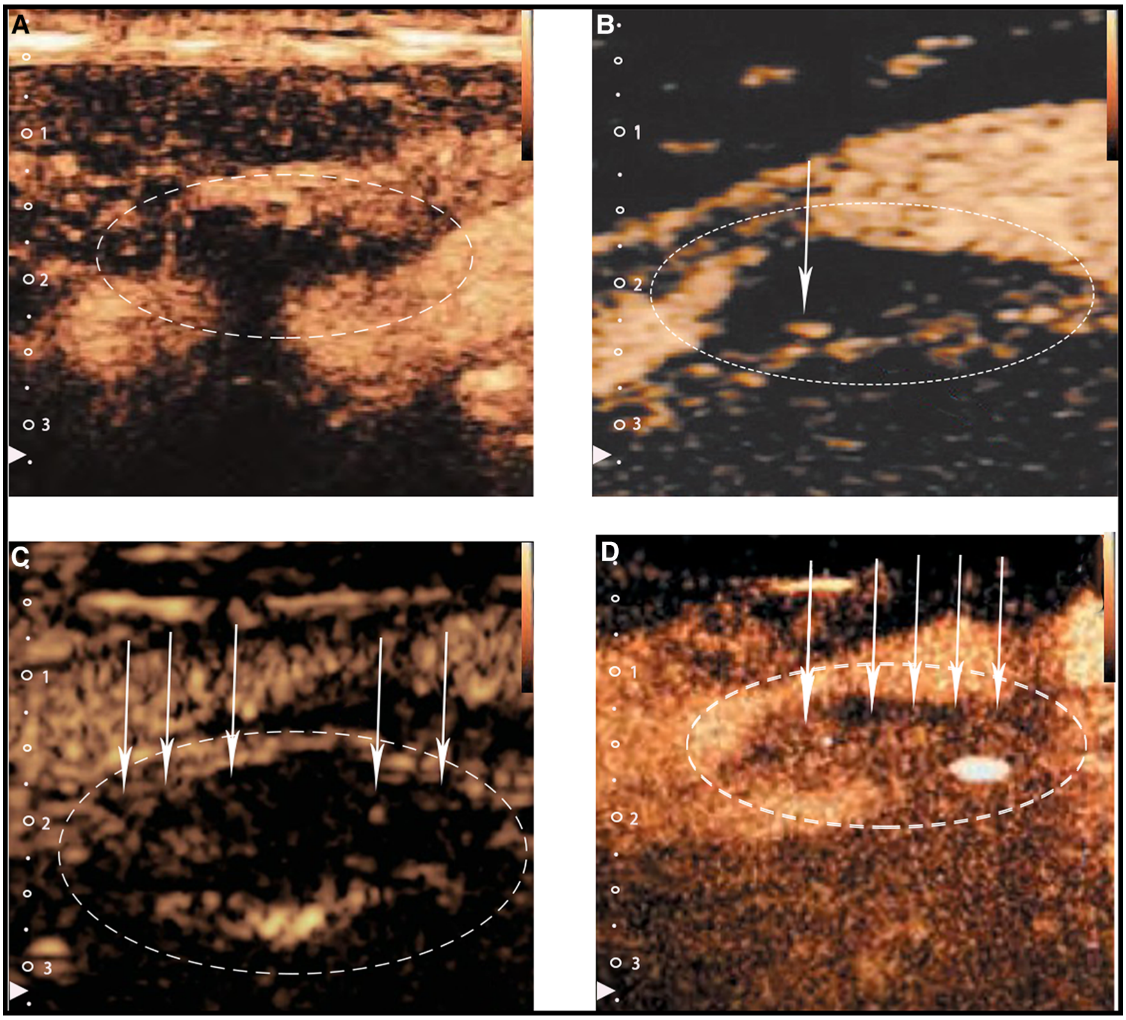

FIGURE 2
Typical CEUS images of carotid plaques. (Panel **A**) Shows no visible microbubbles in the plaque (grade 0). (Panels **B,C**) Show minimal microbubbles confined to the shoulder or the adventitial side of the plaque (grade 1). (Panel **D**) Shows plentiful microbubbles throughout the plaque (grade 2). The white arrows and dotted lines depict intraplaque contrast microbubbles.

SMI separates the blood flow signal and the overlapping tissue movement artifact by adaptive calculation method to accurately detect the low-velocity blood flow signal, which is useful for detecting neovascularization (28). Grading criteria of SMI for plaque neovascularization (29): Grade 0, no blood flow signal in plaques; Grade I, blood flow signal in the shoulder or base part of plaques; Grade II, diffuse blood flow signals in the plaques.

As we discussed in Part I, contrast-enhanced ultrasound is also valuable for detecting neovascularization, but it is susceptible to interference from intrinsic factors such as artifacts, and its enhancement duration is short. Most worryingly, CEUS requires intravenous contrast, which can cause pain and anxiety in patients (30). By contrast, SMI uses a new adaptive algorithm to identify and eliminate motion artifacts and preserve the smallest low-velocity blood flow signals, thus showing plaque neovascularization in high-resolution detail (31). In addition, there is no need to wait for the contrast agent to be distributed to blood vessels. The time required to observe new blood vessels is much shorter than that of CEUS by just changing the inspection mode to SMI mode by pressing the switch on the ultrasound system (32).

Zhang, H. et al. (33) and Oura, K. et al. (34) both compared the value of ultrasound microflow imaging (SMI) and contrast-enhanced ultrasound (CEUS) in the diagnosis of carotid plaque neovascularization. The results showed that patients with blood flow detected by SMI tended to also show plaque enhancement signals in CEUS with good consistency. Guo, Y. et al. (35) also studied the CEUS and SMI enhancement grade in different thicknesses of plaque plaques that thicker plaques showed a higher density of neovascularization and were more vulnerable. Moreover, studies have shown that SMI can detect more neovessels than contrast-enhanced ultrasound, especially when there is less neovascularization. This may be because SMI allows repeated scanning in many different parts and directions of the plaque (36). The correlation between SMI and histology has also been verified in corresponding studies (36, 37). Therefore, as a simpler and safer technique, SMI provides a new evaluation method for classifying plaques with different echo types. However, at present, SMI technology still has some difficulties in capturing neovascularization with blood flow velocity less than 0.4 cm/s, and there is still a lack of objective quantitative criteria for SMI, which may be the direction of future research.

Ultrafast ultrasound imaging (UF) is capable of capturing images at a frame rate 100 times faster than traditional imaging by using vector Doppler imaging to assess the flow velocities at each point on the image (38, 39). Goudot, G. et al. (40, 41) validated the feasibility of UF in measuring wall shear stress in carotid plaques and established wall shear stress values for different vulnerable carotid plaques. In the course of atherosclerotic plaque development, the advanced plaques begin to invade the lumen, and the endothelial cells begin to experience high shear stress (42). High maximum shear stress is associated with hemorrhage and calcification within the plaque (43). Therefore, accurate measurement of wall shear stress by UF lays a foundation for better characterization of plaques.

In conclusion, from the assessment of plaque microvascularization to calculation of the wall shear stress, the development of new Doppler techniques provide more dimensions and powerful tools for the assessment of atherosclerosis.

4. Ultrasound molecular imaging

Molecular imaging is an evolving discipline that enables noninvasive visualization, assessment, and quantification of specific biological processes at the cellular level in living subjects (44). These microbubbles possessing specific affinity towards vascular biomarkers of disease can not only improve their accumulation in tissues but also reduce off-target effects, improve safety, and is a promising approach for clinical applications (45) (**Figure 3**). The functionalization of microbubbles with different targeting ligands to assess atherosclerotic plaques in the early stage and the use of microbubbles for drug and gene delivery has been a hot topic of research in recent years (46, 47).

The development of atherosclerosis is often accompanied by significant changes in inflammatory biomarkers, such as TNF-α, and CRP (48). However, these factors can be elevated in a wide range of pathophysiological activities and are not specific enough to be used in the specific diagnosis of atherosclerosis. Therefore, there is an urgent need to test for biomarkers that are prominent in the atherosclerotic process (**Table 2**).

First of all, the initial hallmark of atherosclerotic lesion development is endothelial dysfunction and concomitant inflammatory activation, which promote the recruitment of monocytes to the arterial wall, precede the development of plaque and play a role in the occurrence and progression of plaque (65, 66). VCAM-1 and VEGF are classic inflammatory markers when vascular endothelial dysfunction occurs (67, 68). In the past, many studies have taken VCAM-1 and VEGF as targets to develop targeted microbubbles, which have initially realized the detection of early atherosclerosis (56, 57). Further research revealed that one of the main triggers for endothelial dysfunction is altered luminal blood flow, particularly at bifurcations and vessel bends where molecular changes in the endothelium may become apparent (69). Many studies have shown that junctional adhesion molecule A (JAM-A) is one of the most sensitive biomarkers for acute changes in local blood flow and is specifically upregulated on endothelial cells at sites of atherosclerosis predilection (70). As

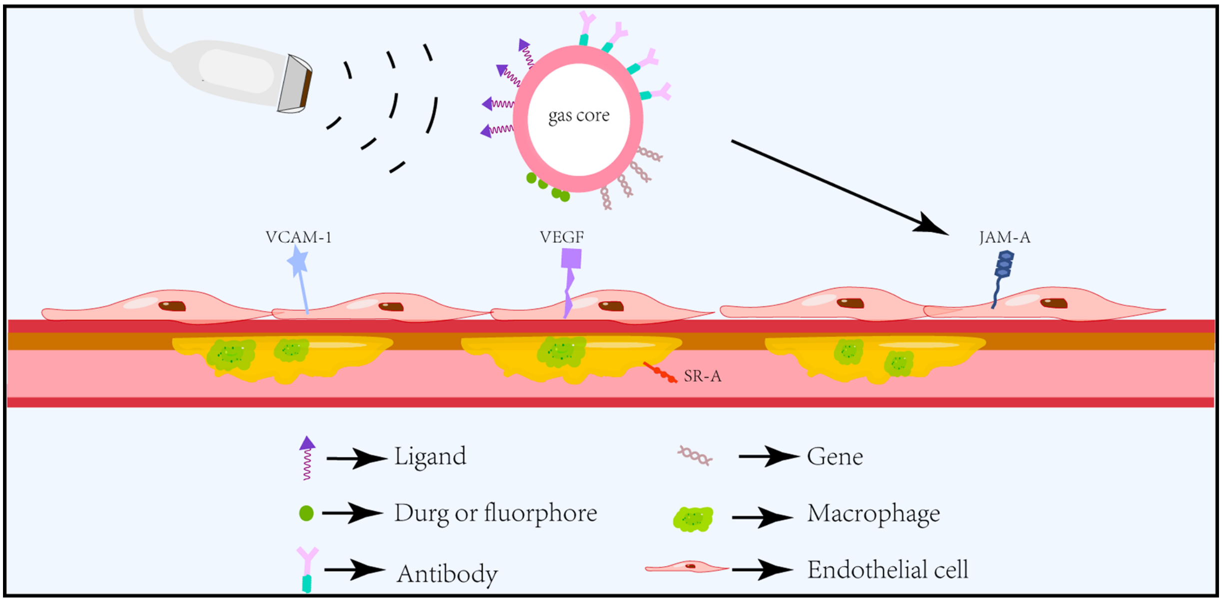

FIGURE 3
Schematic diagram of ultrasound molecular imaging. Functionalized microbubbles carrying different ligands can specifically and actively target different atherosclerotic endothelial or intraplaque biomarkers under the action of ultrasound and deliver drugs or genes for targeted therapy.

TABLE 2 Examples of targeted ultrasound molecular imaging in the identification and treatment of vulnerable plaque (2017–2022).

Shell	Core	Molecular process	Molecular target	Species	Main result	References
Phospholipid	Perfluorinated	Activated platelets	GP Ib and GP IIb/IIIa receptor	Mice	The reactiveness of ultrasound molecular imaging was different within the models according to the type of plaque.	(49)
Phospholipid	Decafluorobutane	Vascular endothelium	VCAM-1	Mice	Signals increased from 8 weeks to 32 weeks age in ApoE-/-mice in different stages.	(50)
Phospholipid	Decafourobutane	Activated platelets	GPIIb/IIIa receptor, selectin ligand	Mice	Dual targeting of microbubbles led to greater capture efficiency, especially at low to intermediate shear stress.	(51)
Phospholipid	Decafluorobutane	Vascular endothelium	P-selectin, VCAM-1, VWF and LOX-1	Mice	The signal for all four targeted microbubbles was significantly higher than that for control microbubbles in DKO mice, and was three to sevenfold higher than in wild-type mice, with the highest signal achieved for VCAM-1 and VWF.	(52)
SonoVue	Sulfur hexafluoride	Smooth muscle cell	miR-21	Mice	Local delivery of a miR-21 mimic rescued the vulnerable plaque rupture phenotype.	(53)
PBCA		Endothelial Dysfunction	JAM-A	Mice	The increment in JAM-A expression and JAM-A-targeted microbubble echogenicity was higher than in controls, peaking after 2 weeks.	(54)
Phospholipid	Perfluoropropane	Leucocytes	VCAM-1, ICAM-1, P-selectin	Mice	The microbubbles had a high affinity to inflammation in both static and dynamic flow conditions. Significantly enhanced ultrasound imaging signals were achieved in detecting the atherosclerosis progress when compared with the single- or dual-targeted microbubbles. Revealing a potential therapeutic efficacy of atorvastatin for early-stage atherosclerosis.	(55)
USphere$^{\text{TM}}$Labeler	/	Inflammatory response	IL-8	Rabbits	The peak intensity (PI), microvessel density (MVD), and macrophage count of the pretreatment group were significantly higher than those of both the control and IL-8 groups. Ultrasound-delivered IL-8 monoclonal antibodies alleviate inflammation within atherosclerotic plaques.	(47)
/	Decaflurobutane	Endothelial	VCAM	Mice	Microbubble showed increased attachment under continuous flow with increasing shear stress. UMI in double-knockout mice showed signal enhancement in early and late atherosclerosis in wild-type mice. UMI in human endarterectomy specimens showed a 100% increase in signal.	(56)
Biocompatible lipid	Sulfur hexafluoride	Endothelial	VEGFR-2	Rabbits	Targeted microbubbles exhibit high stability, can effectively identify atherosclerotic plaques, and show outstanding capability for ultrasound molecular imaging.	(57)
SonoVue	Sulfur hexafluoride	Inflammatory responses in macrophage	Glycogen synthase kinase (GSK)-3b	Rabbit	Vulnerable plaque factors and inflammation were suppressed *in vitro* and *in vivo* and changed the cytoskeleton of the foam cells *in vitro*.	(58)
Phospholipid	Decafluorobutane	Anti-inflammatory and anti-thrombotic	VCAM-1, *P*-selectin, VWF, GPIbα	Mice	All the remote plaque adverse changes were inhibited by anti-IL-1β therapy.	(59)
/	Perfluoropentane/ Fe3O4	Macrophages/ Activated platelets	SR-A/ (GP) IIb/IIIa	Mice	A high binding Affinity both for activated macrophages and blood clots. Effectively induce macrophage apoptosis, and destroy the thrombus.	(60)
Phospholipid	Perfluoropropane	Activated platelets	GPIIb/IIIa receptors	Mice	Advanced atherosclerotic plaques were rapidly detected and simultaneously giving targeted therapy by dissolving activated and aggregated platelets.	(61)
Phospholipid	Sulfur hexachloride	Endothelial cells	VEGFR-2	Mice	The acquisition of ultrasound information on atherosclerotic plaque neovascularization were enhanced.	(62)
PLT vesicles/ Sono Vue$^{\text{TM}}$	RAP@NPs	mTOR signaling pathway	mTOR	Mice	The targeting ability of nanoparticles to atherosclerotic plaques were increased by improving the efficiency of RAP release and the destruction of neovascularization in the plaques.	(63)
Phospholipid	C3F8	Apoptosis of macrophage	Annexin V	Mice	Strong and sustained echo enhancement were shown in plaque area of aortic arch *in vivo*. Imaging sensitive plaques presented more significant pathological changes with several vulnerable plaque features and abundant TUNEL-positive areas.	(64)

demonstrated by Curaj et al. using antibody-targeted poly microbubbles, transient blood flow changes cause JAM-A rearrangement in the endothelium, and JAM-A-targeted microbubbles can facilitate the early detection of cardiovascular risk areas and play an important role in preventing their progression to irreversible pathology (54).

Besides, macrophages, which account for more than 80% of all cellular components, are extremely abundant in vulnerable plaques and play vital immune and inflammatory roles in both the initiation and progression of vulnerable plaque pathology (71). Macrophages are an important target for diagnostic imaging and new therapies for atherosclerosis. Depending on their polarization status, macrophages function to promote or inhibit atherosclerotic inflammation (72). For instance, researchers have targeted SR-A, which is usually overexpressed on activated macrophages but not unactivated macrophages or other normal vascular wall cells, to distinguish vulnerable plaques (60). This provides a reliable and more specific means of diagnosing vulnerable phenotypes before they are visible morphologically, which substantially facilitates clinicians to set risk evaluation and secondary prevention strategies for the patients at an early stage.

Nonetheless, several existing bottlenecks for ultrasound molecular imaging need to be tackled. The first is its security in clinical applications. Traditionally, the conjunction of targeted ligands to the shell of microbubbles was characterized by a multistep, biotin-avidin-biotin bridging process, which could probably lead to the binding of endogenous biotin (73). Innovatively, Punjabi et al. recently combined microbubble with a nanobody, the smallest possible (10–15 kDa) antibody-derived polypeptide which did not induce complement-triggered cytotoxicity nor bind to Fc receptors on immune and other types of cells. The result indicated a totally increased signal in human endarterectomy specimens compared with the control group (56). So, the use of nanobodies or single-domain antibodies instead of full-size antibody ligands may pave the way for a more secure clinical translation of UMI to detect early atherosclerotic changes.

Secondly, the task to increase the affinity adhesion of targeted microbubbles remains challenging. Microbubbles have the probability to detach from the endothelial target spot, resulting in short contact time and insufficient cell adhesion, particularly in areas where exist high blood shear stresses such as vessel bifurcation (74). Some scholars attempted to utilize external forces such as acoustic radiation force and magnetic field force (75), while other researchers explored multi-targeted microbubbles to promote MB adhesion. Yan et al. developed triple-targeted microbubbles carrying VCAM-1, anti-ICAM-1, and synthetic polymeric sialyl Lewis X (sex) on the surface. Unlike single- or dual-targeted microbubbles, significantly enhancing ultrasound imaging signals were observed in triple-targeted microbubbles even under high shear stress (55).

Furthermore, the usual size of microbubbles of 1–5 µm limits their ability to effectively aggregate in tissue (76). Studies have demonstrated that nano-ultrasound bubbles under 780 nm in size can easily pass through fine capillaries and lymphatic endothelium, thus targeting plaque sites with nano-scale ultrasound contrast agents is expected to better enable early diagnosis of atherosclerosis. As shown in the study of Zhang et al. who designed a nanosized ultrasound contrast agent carrying anti-VEGFR-2 to image the vulnerable plaque in rabbit abdominal aorta, these nano-ultrasound bubbles smaller than the size of the open pores of atherosclerotic plaques significantly extravasate and remain at the plaque site, showing stronger echogenic signal within atherosclerotic plaque and lasted for 1–2 min (57).

Last but not least, more attention should be put on the optimization of the microbubble surface composition and setting a standardization of measurement protocols and quantification methods (10). Still, ultrasound molecular imaging and diagnostics are mostly limited to pre-clinical models and have not been tested in primates or humans up to now, so studies in large models are needed.

5. Elastography

Ultrasound elastography can quantify the mechanical characteristics of plaques, and reveal their composition and vulnerability by analyzing tissue displacement in response to either external (focused acoustic radiation) or internal (variation in blood pressure) mechanical excitations (77, 78). Depending on different motivation methods, ultrasound elastography can be classified into two imaging modes: strain elastography (SE) which utilize internal or external stress excitation, and shear-wave elastography (SWE) which utilizes shear wave excited by ultrasound.

5.1. Strain elastography

SE measures the plaque displacement gradient under different levels of stress induced by an external force and calculates semi-quantitative parameters such as strain, strain velocities, or strain rate (78). Since fatty elements are much softer than fibrous tissue, plaques with larger local deformations and more complex distribution of strain are more likely to be vulnerable (79). Besides, Liu et al. validated the *in vivo* inter-observer repeatability of ultrasound elastography in identifying vulnerable plaques with an intraclass correlation coefficient of 0.66 between the two operators (80).

Nevertheless, there is no consensus on the optimal imaging parameters up to now. The magnitude of plaque strain such as local maximum, mean, and minimum values or the whole spatially averaged strain are typically been considered suitable quantitative indices for plaque elastic assessment (81). Moreover, Huang et al. put forward that the vulnerability of the carotid atherosclerotic plaques can be better quantified by textural features -contrast, homogeneity, correlation, and angular second moment. In his study, the textural feature achieved 83.8% accuracy in plaque classification while the contrast was 81.3% (82). Another study conducted by Roy Cardinal et al. demonstrated that the ratio of cumulated axial strain to cumulated axial translation could serve as a novel parameter for detecting the vulnerability of plaque (83).

5.2. Shear-wave elastography

SWE estimates tissue elasticity by tracking the transverse velocity of the tissue after it has been subjected to an external force. The transducer emits a transverse wave through an acoustic radiation force pulse (ARFI) and measures the speed of the transverse wave propagation through the tissue, expressed as Young's modulus (YM), which reflects the tissue's resistance to elastic deformation and is largely depended on the composition of the tissue. Soft tissues such as lipid cores in plaques tend to show obvious elastic deformation, lower YM and lower transverse wave velocity; whereas harder tissues and lesions show less elastic deformation (77, 84) (**Figure 4**).

The potential clinical value of SWE in assessing the elasticity of carotid atherosclerotic plaques has been demonstrated in both vitro and vivo studies, and is demonstrated particularly useful in

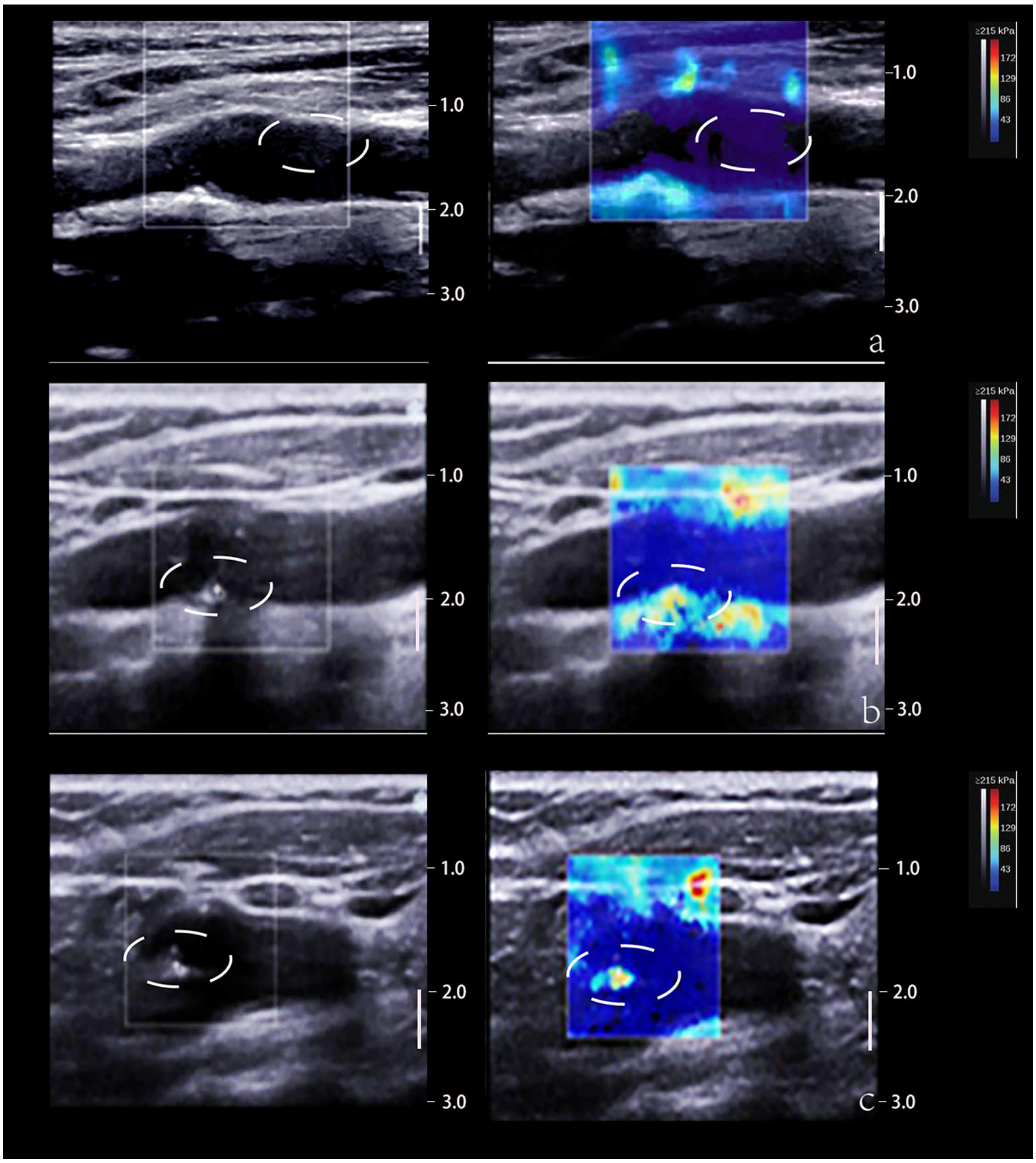

FIGURE 4
2D and SWE imaging of plaques with different hardness. (Panel A) The 2D image displays a predominantly hypoechoic plaque and the SWE image displays a blue color at the plaque, suggesting a soft texture. (Panel B) The 2D image shows a predominantly mixed echogenicity of the plaque and the SWE image shows a red-blue mix at the plaque, suggesting that the texture of the plaque is between soft and hard. (Panel C) The 2D image demonstrates that the plaque is predominantly strong echogenic and the SWE image demonstrates a red color at the plaque, suggesting a hard texture. The white dotted lines depict the plaque area.

distinguishing asymptomatic plaques from symptomatic plaques (85). In the study of Skoloudik et al., they divided asymptomatic plaques into stable and progressive groups (86). The results of this study clearly showed that there were significant differences between stable and progressive plaques in terms of measured mean, minimum, and maximum Young's modulus. Young's modulus measured in asymptomatic progressive plaques was even lower compared to symptomatic plaques, although there was no significant difference. Therefore, SWE measurements of plaque elasticity can be used as an adjunct parameter for the indication of carotid endarterectomy or angioplasty and stenting when asymptomatic carotid stenosis of >50% is first detected.

However, the complex composition of atherosclerotic plaques strongly requires a combination of other parameters to distinguish. In vitro studies have shown that a combination of spatio-temporal and frequency-dependent shear wave analysis can be used to non-invasively assess the characteristics of atherosclerotic plaques *in vivo* (87). Recently, Marlevi et al. further showed in an *in vivo* study that vulnerable plaques have significant group velocities and frequency-dependent phase velocities compared to other types of plaques. More interestingly, this parameter was also used in the study to classify specific components within the plaque, including thin fibrous caps, lipid-rich necrotic cores, and intraplaque hemorrhages (88). In addition, Torres et al. combine signal correlation and signal-to-noise ratio (SNR), expressed as a decimal logarithm of the acceleration variance, either directly or through displacement variance, called "log(Vo A)" to successfully describe the composition and structure of human carotid atherosclerotic plaque (89). Overall, these results are all clinically useful for predicting stroke risk and facilitating medical management.

As such, elastography provides a more in-depth assessment of plaques by bringing a novel dimension-analyzing tissue displacement- to clinical use. Still, it remains a challenge to reach intra/inter-observer reproducibility and agreement on standardized cutoff value (**Table 3**).

TABLE 3 Applications of ultrasound elastography in the identification of vulnerable plaque (2017–2022).

Patients involved	Plaques	Method	Measurement parameters	Reference standard	Main conclusion	References
52	80	ARFI	Texture analysis(strain rate images contrast, homogeneity, correlation and angular second moment)	MRI	Plaque classification using texture analysis is feasible. Larger local deformations and higher complexity of deformation patterns are more suggestive of plaque vulnerability.	(82)
25	26	ARFI	Peak displacement	Histology	ARFI can distinguish soft from stiff atherosclerotic plaque components and delineating fibrous cap thickness.	(90)
31	31	SWE	Maximum axial strain, cumulated axial strain, mean shear strain, cumulated shear Strain, cumulated axial translation, cumulated lateral translations, the ratio of cumulated axial strain	MRI	Cumulative axial translation and the ratio of cumulative axial strain to cumulative axial Translation are sensitive parameters for distinguishing between vulnerable and non-vulnerable carotid plaques.	(83)
61	271	SWE	Young's modulus	Neurological symptoms	Young's modulus can be used as an additional method to detect symptomatic carotid plaque.	(85)
/	24	SWE	Plaque geometry, push location, imaging plane, and wave speed metric	Vitro setup	Differentiation of simulated plaques with different mechanical stiffness can be achieved using SWE.	(87)
66	132	SWE	Plaque translation and elastography and echogenicity features	Neurological symptoms	The combination of elastography and echo analysis helps to differentiate plaque in symptomatic patients from asymptomatic ones.	(91)
142	129	SWE	Maximum, minimum, and mean values of shear wave velocity	Neurological symptoms	Echogenic plaques had higher shear wave velocity than echolucent ones.	(92)
25	25	ARFI	Decadic logarithm of the variance of acceleration [log(VoA)]	Histology	Log(VoA) is able to characterize the composition and structure of human carotid atherosclerotic plaques *in vivo* better than PD.	(89)
32	53	ARFI	The maximum 99th percentile of absolute axial strain rate	MRI	Ultrasound-based carotid elastography is reproducible and reliable in differentiating between vulnerable and stable plaques between two operators.	(80)
20	27	SWE	Group velocity and frequency-dependent phase velocities	MRI	The combined group velocity and frequency-dependent phase velocity can improve the ability of SWE to detect vulnerable carotid plaques, providing additional information for assessing plaque characteristics.	(88)
97	97	SWE	Mean, maximal and minimal elasticity	Neurological symptoms	SWE is a promising way to differentiate symptomatic, asymptomatic progressive, and asymptomatic stable carotid plaques.	(86)
46	46	SWE	Stiffness distribution	Histology	In vulnerable plaques, there was a significantly increased percentage of stiffness range of 3–5 m/s.	(41)

6. Intravascular ultrasound imaging

Using a miniature ultrasound probe guided to the target site via a trans-vascular guide wire, Intravascular ultrasound imaging contributes to a direct way to visualize the nature of selected atherosclerotic lesions (93). Although Coronary angiography (CAG) has long been recognized as the gold reference standard for the evaluation of coronary artery disease, it is incapable to evaluate the structural composition of unstable plaque and lacks objectivity since it relies heavily on contrast agent-filled vascular contour to assess the diameter of the lumen. IVUS is complementary to CAG in that it visualizes features of atherosclerotic plaques qualitatively within the vessel either from a longitudinal plane or an axial plane (94, 95).

6.1. Grayscale IVUS

Conventional grayscale IVUS offers grayscale cross-sections of coronary arteries with an axial resolution of approximately 100–250 μm (96). It determines the characteristics of plaques through the echo intensity of plaques into the following four types: (1) soft plaques: echo lower than the surrounding outer membrane; (2) calcified plaque: echo higher than the surrounding outer membrane; (3) fibrous plaques: moderate echo; (4) mixed plaques: two or more echo signals (97). The attenuated plaques (AP), characterized by hypoechoic areas of deep echogenic attenuation and echogenic hyaline plaques despite the absence of bright calcium and echolucent plaque (ELP), characterized by areas of non-echoic or hypoechoic plaques displayed on the IVUS were demonstrated to be linked with vulnerable plaque phenotype (98). This is mainly due to the fact that plaque hypoechoic areas usually represent plaques that are high in lipids and poor in collagen. Echo attenuation in ultrasound plaques is closely associated with microcalcifications and cholesterol crystals within the lipid-rich necrotic core, which promotes signal reflection and dispersion (99) (**Figure 5**).

An obvious drawback of greyscale IVUS is its low resolution, which limits detailed visualization of the plaque phenotype. Besides, caused by the strong reflection of intracavitary calcium to ultrasound, it has limited value to assess the calcification (97, 100).

FIGURE 5
Typical grayscale display of arterial cross-section image obtained by conventional grayscale IVUS.

6.2. Contrast-enhanced IVUS

As previously mentioned, new microvessels form within the outer membrane of the arterial wall, and the atherosclerotic plaque (i.e., vasa vasorum, VV) is an important marker of plaque inflammation (5, 6), which is a precursor or concomitant factor related to plaque rupture and plaque instability (101). The combination of conventional IVUS with contrast agents, e.g., microbubbles (contrast-enhanced IVUS, CE-IVUS) has proven useful for coronary plaque perfusion imaging and assessment of the amount and distribution of new vessels in atherosclerotic lesions, providing a step forward in the identification of vulnerable plaques (102, 103). An earlier study conducted by Carlier S showed the feasibility of contrast-enhanced IVUS plaque imaging with intracoronary microbubbles (104). But due to limitations at the time, they did not correlate their study with histopathological evidence of vasa vasorum. This was confirmed in a subsequent study by Vavuranakis M et al., who used CE-IVUS to detect and quantify rabbit aortic wall neovascularization (105). The density of VV also shows a positive correlation with plaque progression, inhibiting VV may be a promising approach to delay or even reverse the progression of atherosclerosis (101).

However, detecting VV is challenging because of the low acoustic scattering of blood compared to tissue, making it cumbersome to differentiate between contrast and tissue (usually called contrast-to-tissue ratio, CTR) (106). A new contrast imaging method based on the detection of higher harmonics named Super harmonic (SH) has been proposed, which performed with a low frequency transmitter and high frequency receiver. By increasing the contrast agent signal and suppressing the signal from the tissue, the technique has shown even higher CTR than second harmonic (107, 108). Ma, J. et al. designed a small aperture (0.6 × 3 mm) IVUS probe with dual frequency (6.5 MHz/30 MHz) transducer for high frequency contrast imaging. The microbubble is excited at low frequencies (near resonance) and its wideband harmonics are detected at high frequencies, minimizing the detected tissue backscattering (109). More recently, Lee, J. et al. reported a dual-element focused IVUS transducer, consisting of a 35 MHz ultrasonic transmission element and a 105 MHz third harmonic receiving element, which produces third harmonic images with higher spatial resolution and deeper imaging depth than fundamental wave images (110). In the future, we look forward to additional *in vitro* and *in vivo* trials of atherosclerotic plaque lesions to further validate the clinical value of these IVUS sensors.

6.3. Post-processing IVUS

Virtual histology (VH-IVUS), integrated backscatter (IB-IVUS), and IMAP-IVUS are all examples of the products of the evolution of post-processing algorithms. Based on different post-processing algorithms, a comparison of color coding methods of them is presented in **Figure 6** (111–113).

Despite different plaque characterization algorithms, the utility of post-processing IVUS in elucidating factors associated with compositional changes suggestive of increased plaque vulnerability is gaining more and more attention. Since current research on premature coronary artery disease is usually focused on genetics and epidemiology, and studies related to coronary plaque characteristics are still scarce, Xie J et al. analyzed the morphological, histological, and phenotypic characteristics of atherosclerotic plaques in 47 patients with premature CAD by iMap-IVUS and compared the differences with 155 patients with later CAD. The results revealed more fibrosis and less necrotic and calcified components within the plaques of patients with premature CAD compared with later CAD (114). This may provide important information for subsequent insights into the development of premature coronary artery disease.

In addition, studies have shown that acute cardiovascular events are usually caused by a vulnerable coronary plaque containing a large lipid-rich necrotic core covered by a thin inflamed fibrous cap, defined as thin-cap fibroatheroma (TCFA) (115). The advent of IVUS holds promise for the study of the impact of tissue characteristics of culprit lesions on myocardial tissue perfusion levels. Several clinical trials have already validated its usefulness in identifying clinical and lesion-related factors that put patients at risk of adverse cardiac events, as well as predicting future acute cardiovascular events.

PROSPECT is one of the most classic and largest of these observational studies. It is a prospective study with a median follow-up of up to 3.4 years and included a total of 697 patients with acute coronary syndromes, each of whom underwent coronary angiography, Grayscale IVUS, and VH-IVUS following percutaneous coronary intervention. Results showed that recurrent major adverse cardiovascular events were associated with both initially treated (culprit) lesions and untreated (non-culprit) lesions. Of the 157 recurrent events where the lesion could be located, 74 (47%) were associated with the original nonculprit lesion. And of the 51 recurrent events associated with non-culprit lesions, 26 (51%) occurred at sites of thin fibrous cap fibroatheroma (TCFA) detected on the basis of VH-IVUS, most of which showed no evidence of severe stenosis on conventional angiography. It is concluded that small lumen area, large plaque burden, and the presence of thin cap fibrous atherosclerosis were three important predictive features of recurrent events (116). This study provides prospective, systematic data on the origin of recurrent ischaemic events by using VH-IVUS to characterize the morphological features of plaques, enabling the prospective identification of thin-cap fibrous atherosclerosis. This also further demonstrates that the development of acute coronary syndromes is not necessarily dependent on the degree of angiographic stenosis at the site and that the development of VH-IVUS has made it possible to characterize the vessel wall using imaging techniques that can be comparable to histological findings.

An EARLY-MYO-ACS prospective observational study conducted on 408 patients investigated the relationship between culprit plaque characteristics before percutaneous coronary intervention (PCI) and myocardial tissue level perfusion after PCI in patients with non-ST-segment elevation acute coronary syndrome (NSTE-ACS) by IMAP-IVUS. The results showed that

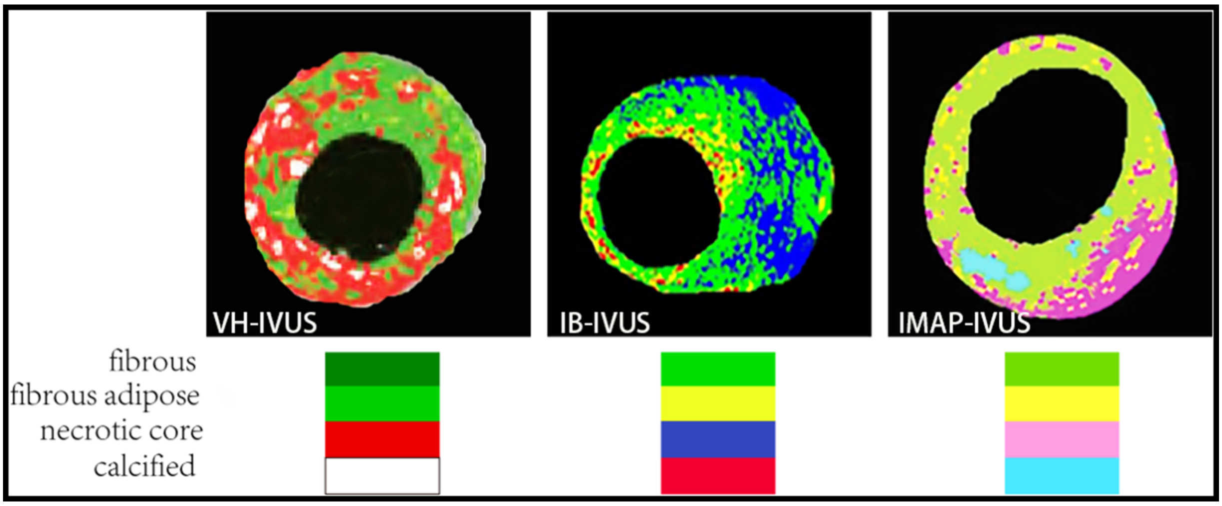

FIGURE 6
An illustration of color coding methods of VH-IVUS, IB-IVUS, and IMAP-IVUS.

TABLE 4 An overview of the mechanism, advantages, limitations and recent progression of novel ultrasound methods in the identification of vulnerable plaques.

Novel ultrasound method	Mechanism	Advantages	Limitations	Recent progressions
CEUS	Inject contrast agent microbubbles intravenously to enhance blood flow signals	◆ improve the visualization of small vascular beds ◆ have a good correlation with histolog ◆ promote cardiovascular risk stratification	◆ lack internal standards ◆ be interfered by artifact ◆ limited enhancement time ◆ requires rich experiences in operation	◆ predict significant coronary artery disease and future adverse cardiovascular events (16, 20, 22). ◆ early identification of carotid atherosclerosis (23) ◆ NER, the direction of contrast agent diffusion and analysis of stress and strain distribution may severe as complementary methods for the prediction (24–26)
Doppler Ultrasound	Visualize blood flow and assess the flow velocities	◆ detecting neovascularization ◆ high-resolution ◆ time-saving and safe	◆ can not detect blood flow velocity less than 0.4 cm/s ◆ lack of objective quantitative criteria ◆ low reproducibility	◆ show great consistency with CEUS and histology (33, 34, 36, 37) ◆ measuring wall shear stress (40, 41)
UMI	Gather microbubbles bounded with targeting ligands or antibodies in targeted tissue or organ	◆ targeted imaging at the cellular or molecular level ◆ diagnose vulnerable atherogenic phenotypes before they are morphologically visible ◆ improve transfection efficiency	◆ controversy over its safety ◆ poor affinity adhesion ◆ no standardization of measurement protocols	◆ visualize acute endothelial activation and dysfunction (54) ◆ detect vascular inflammation (56, 57). ◆ alleviate inflammation progression by delivering miRNA or antibodies (47, 53, 58) ◆ multi-targeted MBs (55)
Elastography	Analyze tissue displacement in response to either external or internal mechanical excitations	◆ assess mechanical characteristics and stiffness distribution of plaques ◆ classify fibrous cap, necrotic core, intraplaque hemorrhage	◆ no consensus on theoptimal imaging parameters ◆ Inter-observer and intra-observer variation	◆ validate the *in vivo* inter-obseXSSWrver repeatability (80) ◆ quantify vulnerable plaques by textural features (82) ◆ add the ratio of cumulated axial strain to cumulated axial translation as the novel parameter (83) ◆ VOA may be more consistent with histological thickness than PD (89)
IVUS	Employ a miniature ultrasound probe guided to the target site	◆ visualize the nature of selected atherosclerotic lesions directly ◆ complementary to CAG ◆ multiple planes imaging ◆ evaluate the mechanism underlying certain therapies	◆ invasive ◆ low resolution ◆ imited value to assess the calcification	◆ attenuated plaque (AP) and echolucent plaque (ELP) are highly associated with the prevalence of major cardiovascular events (98) ◆ premature CAD had more fibrotic with less necrotic and calcified components within the plaque than later CAD (114) ◆ increased percentage of necrotic plaque fraction is independently associated with impaired myocardial perfusion (117) ◆ explore several indicators of future severity cardiovascular events (127, 128) ◆ (PSS) and (WSS) may influence plaque development (129) ◆ the efficacy of treatment suppression on atherosclerotic plaques (122, 130, 131)

in these NSTE-ACS patients, an increase in the necrotic portion of the culprit lesion was independently associated with myocardial tissue level perfusion impairment (117). This reveals a valuable application of plaque composition assessment by pre-PCI IMAP-IVUS to predict myocardial tissue level perfusion injury after PCI in patients with NSTE-ACS.

IVUS also gains well recognization and validation for its ability to study mechanisms underlying certain therapies with its high imaging resolution (118). The SATURN trial and IBIS-4 study are classic studies that investigated the effect of atorvastatin and rosuvastatin in CAD and STEMI patients respectively by VH-IVUS-derived plaque components (119, 120). In a vivo study conducted by Andrews J et al., they measured plaque calcification and atheroma volume with IVUS and found that warfarin was independently associated with intravascular calcification in patients with coronary atherosclerosis, but not with atherosclerotic volume, statin therapy, or renal function (121). More recently, in a study combined with 9 randomized clinical trials, the authors first demonstrated a statistically significant independent association between oral calcium and progressive coronary calcification, as assessed by IVUS in terms of plaque calcification and atherosclerotic volume (122). Thus, imaging identification of high-risk patients using IVUS may one day help to justify the focal treatment of vulnerable plaques, and its safety and efficacy will need to be demonstrated in additional randomized trials.

However, in a 4.7-year study of AtheroRemo-IVUS, researchers reported that the small luminal area (minimal luminal area ≤4.0 mm^2) and large plaque burden (≥70% burden) measured by conventional IVUS, rather than the post-processing-IVUS-derived plaque composition characteristics (e.g., TCFA) by themselves, could predict adverse cardiovascular outcomes. However, no increased risk associated with minimal lumen area was observed in this study group during the previous 1-year follow-up. But the prognostic value of a plaque burden ≥70% was similarly confirmed, although there was inconsistent statistical significance across all the different cardiovascular event endpoints. More interestingly, the independent association between TCFA lesions as a feature of independent vulnerable plaques and 1-year adverse cardiovascular events did not persist at subsequent long-term follow-up. The study suggests possible reasons for this, one important being the dynamic development of TCFA lesions over time, particularly at the proximal end where the plaque burden is greater, where lesions heal more slowly and have a greater propensity to rupture, and therefore this should be taken into account as an important guideline for future clinical trials (123). In addition, as Stone, Get al. noted, these studies only imaged a single segment, and even in the PROSPECT study, only 3 epicardial coronary arteries proximal to 6 cm–8 cm were imaged, so the relationship between the imaged lesion and subsequent acute cardiovascular events using IVUS appears to require further investigation, as most events will originate from non-imaged lesions (124). Moreover, the GLAGOV study also challenged the use of VH-IVUS to assess plaque morphology, as they argued that in the evolocumab trial, VH imaging did not provide any incremental information other than the assessment of changes in plaque burden (125). Thus, it appears that the role of IVUS in quantitatively assessing the relationship between the vulnerable components and the pathogenesis of ischaemic events and the efficacy of various treatments requires further investigation.

7. Conclusion and prospect

Vulnerable plaques account largely for the occurrence of serious acute clinical complications. In this review, we made a comprehensive overview of recent updates concerning novel ultrasound techniques including CEUS, UMI, Doppler ultrasound, elastography and IVUS in the identification of vulnerable plaques, with the expectation to offer a more reliable classification of the vulnerable plaque and facilitate clinical risk stratification of the individuals.

Each ultrasound imaging method has its irreplaceable advantages. Contrast-enhanced ultrasound and Doppler ultrasound provide significantly detailed information on intra-plaque neovascularization in plaques which are highly associated with serious coronary artery disease. Ultrasound molecular imaging also gains increasing recognition for its ability to image the target plaque at the cellular or molecular level as well as enhance transfection efficiency to stabilize the plaque. Furthermore, elastography allows for better measurement of vulnerable plaque through analyzing tissue displacement in response to either external or internal mechanical excitations. Last but not least, rising evidence suggests that IVUS is a promising invasive tool for plaque vulnerability assessment which visualizes the nature of selected atherosclerotic lesions directly.

With the progress of various ultrasound imaging techniques, the image quality and measurement dimensions have been greatly improving, but the major challenge remains to reach a consensus on accurate diagnosis and stabilizing the vulnerable plaque. At the same time, the composition of plaques is so complex that evaluating just one plaque component may not be sufficient for risk stratification. As such, a multimodal image that combines the advantage of each imaging mode is a promising development direction, such as CE-IVUS, or IVUS-SE. Vavuranakis, M. et al. used computational analysis of CE-IVUS images to detect and quantify VV in rabbits, which is consistent with histological data (105). PROSPECT II is one of the prime examples and is the first multimodal multicentre study to combine near-infrared spectroscopy and intravascular ultrasound (126). This study greatly extends the value of imaging in the detection of vulnerable plaques before they cause acute cardiovascular events, laying the groundwork for future randomized trials of systemic and focal treatments.

Although is still in the early stage of research, we believe that through the joint efforts of researchers, novel ultrasound techniques will provide patients with more accurate and effective identification of vulnerable plaques. Overall, we provide an overview of the mechanism, advantages, limitations and recent progression of new ultrasound methods in the identification of vulnerable plaques in **Table 4**.

Author contributions

All authors contributed to the article and approved the submitted version.

Conflict of interest

The authors declare that the research was conducted in the absence of any commercial or financial relationships that could be construed as a potential conflict of interest.

Publisher's note

All claims expressed in this article are solely those of the authors and do not necessarily represent those of their affiliated

References

1. Criqui MH, Matsushita K, Aboyans V, Hess CN, Hicks CW, Kwan TW, et al. Lower extremity peripheral artery disease: contemporary epidemiology, management gaps, and future directions: a scientific statement from the American heart association. *Circulation*. (2021) 144:e171–91. doi: 10.1161/CIR.0000000000001005

2. Hafiane A. Vulnerable plaque, characteristics, detection, and potential therapies. *J Cardiovasc Dev Dis*. (2019) 6(3):26. doi: 10.3390/jcdd6030026

3. Song P, Fang Z, Wang H, Cai Y, Rahimi K, Zhu Y, et al. Global and regional prevalence, burden, and risk factors for carotid atherosclerosis: a systematic review, meta-analysis, and modelling study. *Lancet Glob Health*. (2020) 8:e721–9. doi: 10.1016/S2214-109X(20)30117-0

4. Bos D, Arshi B, van den Bouwhuijsen QJA, Ikram MK, Selwaness M, Vernooij MW, et al. Atherosclerotic carotid plaque composition and incident stroke and coronary events. *J Am Coll Cardiol*. (2021) 77:1426–35. doi: 10.1016/j.jacc.2021.01.038

5. Saba L, Saam T, Jäger HR, Yuan C, Hatsukami TS, Saloner D, et al. Imaging biomarkers of vulnerable carotid plaques for stroke risk prediction and their potential clinical implications. *Lancet Neurol*. (2019) 18:559–72. doi: 10.1016/S1474-4422(19)30035-3

6. Ouweneel AB, Verwilligen RAF, Van Eck M. Vulnerable plaque and vulnerable blood: two critical factors for spontaneous atherothrombosis in mouse models. *Atherosclerosis*. (2019) 284:160–4. doi: 10.1016/j.atherosclerosis.2019.03.006

7. Bäck M, Yurdagul A, Tabas I, Öörni K, Kovanen PT. Inflammation and its resolution in atherosclerosis: mediators and therapeutic opportunities. *Nat Rev Cardiol*. (2019) 16:389–406. doi: 10.1038/s41569-019-0169-2

8. Johri AM, Herr JE, Li TY, Yau O, Nambi V. Novel ultrasound methods to investigate carotid artery plaque vulnerability. *J Am Soc Echocardiogr*. (2017) 30:139–48. doi: 10.1016/j.echo.2016.11.003

9. Rafailidis V, Chryssogonidis I, Xerras C, Nikolaou I, Tegos T, Kouskouras K, et al. A comparative study of color Doppler imaging and contrast-enhanced ultrasound for the detection of ulceration in patients with carotid atherosclerotic disease. *Eur Radiol*. (2019) 29:2137–45. doi: 10.1007/s00330-018-5773-8

10. Rix A, Curaj A, Liehn E, Kiessling F. Ultrasound microbubbles for diagnosis and treatment of cardiovascular diseases. *Semin Thromb Hemost*. (2020) 46:545–52. doi: 10.1055/s-0039-1688492

11. Upadhyay A, Dalvi SV. Microbubble formulations: synthesis, stability, modeling and biomedical applications. *Ultrasound Med Biol*. (2019) 45:301–43. doi: 10.1016/j.ultrasmedbio.2018.09.022

12. Hameed S, Zhang M, Bhattarai P, Mustafa G, Dai Z. Enhancing cancer therapeutic efficacy through ultrasound-mediated micro-to-nano conversion. *Wiley Interdiscip Rev Nanomed Nanobiotechnol*. (2020) 12:e1604. doi: 10.1002/wnan.1604

13. Zlitni A, Gambhir SS. Molecular imaging agents for ultrasound. *Curr Opin Chem Biol*. (2018) 45:113–20. doi: 10.1016/j.cbpa.2018.03.017

14. Bruce M, Hannah A, Hammond R, Khaing ZZ, Tremblay-Darveau C, Burns PN, et al. High-frequency nonlinear Doppler contrast-enhanced ultrasound imaging of blood flow. *IEEE Trans Ultrason Ferroelectr Freq Control*. (2020) 67:1776–84. doi: 10.1109/TUFFC.2020.2986486

15. Fetzer DT, Vijay K, Caserta MP, Patterson-Lachowicz A, Dahiya N, Rodgers SK. Artifacts and technical considerations at contrast-enhanced US. *Radiographics*. (2023) 43:e220093. doi: 10.1148/rg.220093

16. Camps-Renom P, Prats-Sánchez L, Casoni F, González-de-Echávarri JM, Marrero-González P, Castrillón I, et al. Plaque neovascularization detected with contrast-enhanced ultrasound predicts ischaemic stroke recurrence in patients with carotid atherosclerosis. *Eur J Neurol*. (2020) 27:809–16. doi: 10.1111/ene.14157

17. Cantisani V, Di Leo N, David E, Clevert D-A. Role of CEUS in vascular pathology. *Ultraschall Med*. (2021) 42:348–66. doi: 10.1055/a-1403-2400

18. Sidhu PS, Cantisani V, Dietrich CF, Gilja OH, Saftoiu A, Bartels E, et al. The EFSUMB guidelines and recommendations for the clinical practice of contrast-enhanced ultrasound (CEUS) in non-hepatic applications: update 2017 (long version). *Ultraschall Med*. (2018) 3939(2):e2–e44. English. doi: 10.1055/a-0586-1107

19. Evdokimenko AN, Gulevskaya TS, Druina LD, Chechetkin AO, Shabalina AA, Kostyreva MV, et al. Neovascularization of carotid atherosclerotic plaque and quantitative methods of its dynamic assessment in vivo. *Bull Exp Biol Med*. (2018) 165:521–5. doi: 10.1007/s10517-018-4208-5

20. Mantella LE, Colledanchise KN, Hétu M-F, Feinstein SB, Abunassar J, Johri AM. Carotid intraplaque neovascularization predicts coronary artery disease and cardiovascular events. *Eur Heart J Cardiovasc Imaging*. (2019) 20:1239–47. doi: 10.1093/ehjci/jez070

21. Coli S, Magnoni M, Sangiorgi G, Marrocco-Trischitta MM, Melisurgo G, Mauriello A, et al. Contrast-enhanced ultrasound imaging of intraplaque neovascularization in carotid arteries: correlation with histology and plaque echogenicity. *J Am Coll Cardiol*. (2008) 52:223–30. doi: 10.1016/j.jacc.2008.02.082

22. Song Y, Dang Y, Wang J, Cai H, Feng J, Zhang H, et al. Carotid intraplaque neovascularization predicts ischemic stroke recurrence in patients with carotid atherosclerosis. *Gerontology*. (2021) 67:144–51. doi: 10.1159/000511360

23. Schinkel AFL, Bosch JG, Staub D, Adam D, Feinstein SB. Contrast-enhanced ultrasound to assess carotid intraplaque neovascularization. *Ultrasound Med Biol*. (2020) 46:466–78. doi: 10.1016/j.ultrasmedbio.2019.10.020

24. Boswell-Patterson CA, Hétu M-F, Kearney A, Pang SC, Tse MY, Herr JE, et al. Vascularized carotid atherosclerotic plaque models for the validation of novel methods of quantifying intraplaque neovascularization. *J Am Soc Echocardiogr*. (2021) 34:1184–94. doi: 10.1016/j.echo.2021.06.003

25. Lyu Q, Tian X, Ding Y, Yan Y, Huang Y, Zhou P, et al. Evaluation of carotid plaque rupture and neovascularization by contrast-enhanced ultrasound imaging: an exploratory study based on histopathology. *Transl Stroke Res*. (2021) 12:49–56. doi: 10.1007/s12975-020-00825-w

26. Li Z, Wang Y, Wu X, Liu X, Huang S, He Y, et al. Studying the factors of human carotid atherosclerotic plaque rupture, by calculating stress/strain in the plaque, based on CEUS images: a numerical study. *Front Neuroinform*. (2020) 14:596340. doi: 10.3389/fninf.2020.596340

27. Fresilli D, Di Leo N, Martinelli O, Di Marzo L, Pacini P, Dolcetti V, et al. 3D-Arterial Analysis software and CEUS in the assessment of severity and vulnerability of carotid atherosclerotic plaque: a comparison with CTA and histopathology. *Radiol Med*. (2022) 127:1254–69. doi: 10.1007/s11547-022-01551-z

28. Sztajzel R, Momjian S, Momjian-Mayor I, Murith N, Djebaili K, Boissard G, et al. Stratified gray-scale median analysis and color mapping of the carotid plaque: correlation with endarterectomy specimen histology of 28 patients. *Stroke*. (2005) 36:741–5. doi: 10.1161/01.STR.0000157599.10026.ad

29. Fleiner M, Kummer M, Mirlacher M, Sauter G, Cathomas G, Krapf R, et al. Arterial neovascularization and inflammation in vulnerable patients: early and late signs of symptomatic atherosclerosis. *Circulation*. (2004) 110:2843–50. doi: 10.1161/01.CIR.0000146787.16297.E8

30. Miyamoto Y, Ito T, Takada E, Omoto K, Hirai T, Moriyasu F. Efficacy of sonazoid (perflubutane) for contrast-enhanced ultrasound in the differentiation of focal breast lesions: phase 3 multicenter clinical trial. *AJR Am J Roentgenol*. (2014) 202:W400–7. doi: 10.2214/AJR.12.10518

31. Daly SM, Leahy MJ. 'Go with the flow': a review of methods and advancements in blood flow imaging. *J Biophotonics*. (2013) 6:217–55. doi: 10.1002/jbio.201200071

32. Gabriel M, Tomczak J, Snoch-Ziółkiewicz M, Dzieciuchowicz Ł, Strauss E, Oszkinis G. Comparison of superb micro-vascular ultrasound imaging (SMI) and contrast-enhanced ultrasound (CEUS) for detection of endoleaks after endovascular aneurysm repair (EVAR). *Am J Case Rep*. (2016) 17:43–6. doi: 10.12659/AJCR.895415

33. Zhang H, Du J, Wang H, Wang H, Jiang J, Zhao J, et al. Comparison of diagnostic values of ultrasound micro-flow imaging and contrast-enhanced ultrasound for neovascularization in carotid plaques. *Exp Ther Med*. (2017) 14:680–8. doi: 10.3892/etm.2017.4525

34. Oura K, Kato T, Ohba H, Terayama Y. Evaluation of intraplaque neovascularization using superb microvascular imaging and contrast-enhanced ultrasonography. *J Stroke Cerebrovasc Dis*. (2018) 27:2348–53. doi: 10.1016/j.jstrokecerebrovasdis.2018.04.023

35. Guo Y, Wang X, Wang L, Wei X, Duan Y, Yang X, et al. The value of superb microvascular imaging and contrast-enhanced ultrasound for the evaluation of neovascularization in carotid artery plaques. *Acad Radiol*. (2023) 30:403–11. doi: 10.1016/j.acra.2022.08.001

36. Meng Q, Xie X, Li L, Jiang C, Zhao K, Bai Z, et al. Assessment of neovascularization of carotid artery atherosclerotic plaques using superb microvascular imaging: a comparison with contrast-enhanced ultrasound imaging and histology. *Quant Imaging Med Surg*. (2021) 11:1958–69. doi: 10.21037/qims-20-933

37. Chen X, Wang H, Jiang Y, Li J, Li N, Kong J, et al. Neovascularization in carotid atherosclerotic plaques can be effectively evaluated by superb microvascular imaging (SMI): initial experience. *Vasc Med*. (2020) 25:328–33. doi: 10.1177/1358863X20909992

38. Yiu BYS, Lai SSM, Yu ACH. Vector projectile imaging: time-resolved dynamic visualization of complex flow patterns. *Ultrasound Med Biol.* (2014) 40:2295–309. doi: 10.1016/j.ultrasmedbio.2014.03.014

39. Villemain O, Baranger J, Friedberg MK, Papadacci C, Dizeux A, Messas E, et al. Ultrafast ultrasound imaging in pediatric and adult cardiology: techniques, applications, and perspectives. *JACC Cardiovasc Imaging.* (2020) 13:1771–91. doi: 10.1016/j.jcmg.2019.09.019

40. Goudot G, Poree J, Pedreira O, Khider L, Julia P, Alsac J-M, et al. Wall shear stress measurement by ultrafast vector flow imaging for atherosclerotic carotid stenosis. *Ultraschall Med.* (2021) 42:297–305. doi: 10.1055/a-1060-0529

41. Goudot G, Sitruk J, Jimenez A, Julia P, Khider L, Alsac J-M, et al. Carotid plaque vulnerability assessed by combined shear wave elastography and ultrafast Doppler compared to histology. *Transl Stroke Res.* (2022) 13:100–11. doi: 10.1007/s12975-021-00920-6

42. Tuenter A, Selwaness M, Arias Lorza A, Schuurbiers JCH, Speelman L, Cibis M, et al. High shear stress relates to intraplaque haemorrhage in asymptomatic carotid plaques. *Atherosclerosis.* (2016) 251:348–54. doi: 10.1016/j.atherosclerosis.2016.05.018

43. Hariri N, Russell T, Kasper G, Lurie F. Shear rate is a better marker of symptomatic ischemic cerebrovascular events than velocity or diameter in severe carotid artery stenosis. *J Vasc Surg.* (2019) 69:448–52. doi: 10.1016/j.jvs.2018.04.036

44. Li J, Wang K, Pan W, Li N, Tang B. Targeted imaging in atherosclerosis. *Anal Chem.* (2022) 94:12263–73. doi: 10.1021/acs.analchem.2c02644

45. Wang S, Hossack JA, Klibanov AL. Targeting of microbubbles: contrast agents for ultrasound molecular imaging. *J Drug Target.* (2018) 26:420–34. doi: 10.1080/1061186X.2017.1419362

46. Versluis M, Stride E, Lajoinie G, Dollet B, Segers T. Ultrasound contrast agent modeling: a review. *Ultrasound Med Biol.* (2020) 46:2117–44. doi: 10.1016/j.ultrasmedbio.2020.04.014

47. Yang H, Sun Y, Wei J, Xu L, Tang Y, Yang L, et al. The effects of ultrasound-targeted microbubble destruction (UTMD) carrying IL-8 monoclonal antibody on the inflammatory responses and stability of atherosclerotic plaques. *Biomed Pharmacother.* (2019) 118:109161. doi: 10.1016/j.biopha.2019.109161

48. Libby P. Inflammation in atherosclerosis-No Longer a theory. *Clin Chem.* (2021) 67:131–42. doi: 10.1093/clinchem/hvaa275

49. Zhou J, Tang YL, Sun YB, Song S, Yao LH. Targeted ultrasound molecular imaging in mouse atherosclerotic plaque model. *J Biol Regul Homeost Agents.* (2017) 31:697–703.

50. Sun R, Tian J, Zhang J, Wang L, Guo J, Liu Y. Monitoring inflammation injuries in the progression of atherosclerosis with contrast enhanced ultrasound molecular imaging. *PLoS One.* (2017) 12:e0186155. doi: 10.1371/journal.pone.0186155

51. Günther F, Heidt T, Kramer M, Khanicheh E, Klibanov AL, Geibel-Zehender A, et al. Dual targeting improves capture of ultrasound microbubbles towards activated platelets but yields no additional benefit for imaging of arterial thrombosis. *Sci Rep.* (2017) 7:14898. doi: 10.1038/s41598-017-15080-7

52. Moccetti F, Weinkauf CC, Davidson BP, Belcik JT, Marinelli ER, Unger E, et al. Ultrasound molecular imaging of atherosclerosis using small-peptide targeting ligands against endothelial markers of inflammation and oxidative stress. *Ultrasound Med Biol.* (2018) 44:1155–63. doi: 10.1016/j.ultrasmedbio.2018.01.001

53. Jin H, Li DY, Chernogubova E, Sun C, Busch A, Eken SM, et al. Local delivery of miR-21 stabilizes fibrous caps in vulnerable atherosclerotic lesions. *Mol Ther.* (2018) 26:1040–55. doi: 10.1016/j.ymthe.2018.01.011

54. Curaj A, Wu Z, Rix A, Gresch O, Sternkopf M, Alampour-Rajabi S, et al. Molecular ultrasound imaging of junctional adhesion molecule a depicts acute alterations in blood flow and early endothelial dysregulation. *Arterioscler Thromb Vasc Biol.* (2018) 38:40–8. doi: 10.1161/ATVBAHA.117.309503

55. Yan F, Sun Y, Mao Y, Wu M, Deng Z, Li S, et al. Ultrasound molecular imaging of atherosclerosis for early diagnosis and therapeutic evaluation through leucocyte-like multiple targeted microbubbles. *Theranostics.* (2018) 8:1879–91. doi: 10.7150/thno.22070

56. Punjabi M, Xu L, Ochoa-Espinosa A, Kosareva A, Wolff T, Murtaja A, et al. Ultrasound molecular imaging of atherosclerosis with nanobodies: translatable microbubble targeting murine and human VCAM (vascular cell adhesion molecule) 1. *Arterioscler Thromb Vasc Biol.* (2019) 39:2520–30. doi: 10.1161/ATVBAHA.119.313088

57. Zhang X, Wu M, Zhang Y, Zhang J, Su J, Yang C. Molecular imaging of atherosclerotic plaque with lipid nanobubbles as targeted ultrasound contrast agents. *Colloids Surf B Biointerfaces.* (2020) 189:110861. doi: 10.1016/j.colsurfb.2020.110861

58. Yang L, Chen L, Fang Y, Ma S. Downregulation of GSK-3β expression via ultrasound-targeted microbubble destruction enhances atherosclerotic plaque stability in New Zealand rabbits. *Ultrasound Med Biol.* (2021) 47:710–22. doi: 10.1016/j.ultrasmedbio.2020.11.002

59. Shentu W, Ozawa K, Nguyen TA, Wu MD, Packwood W, Xie A, et al. Echocardiographic molecular imaging of the effect of anticytokine therapy for atherosclerosis. *J Am Soc Echocardiogr.* (2021) 34(4):433–42.e3. doi: 10.1016/j.echo.2020.11.012

60. Gao B, Xu J, Zhou J, Zhang H, Yang R, Wang H, et al. Multifunctional pathology-mapping theranostic nanoplatforms for US/MR imaging and ultrasound therapy of atherosclerosis. *Nanoscale.* (2021) 13:8623–38. doi: 10.1039/d1nr01096d

61. Guo S, Zhang S, Chen K, Chen X, Hu F. Effects of diagnostic ultrasound with cRGD-microbubbles on simultaneous detection and treatment of atherosclerotic plaque in ApoE mice. *Front Cardiovasc Med.* (2022) 9:946557. doi: 10.3389/fcvm.2022.946557

62. Wang Y, Feng Y, Yang X, Wang W, Wang Y. Diagnosis of atherosclerotic plaques using vascular endothelial growth factor receptor-2 targeting antibody nano-microbubble as ultrasound contrast agent. *Comput Math Methods Med.* (2022):6524592. doi: 10.1155/2022/6524592

63. Zhou J, Niu C, Huang B, Chen S, Yu C, Cao S, et al. Platelet membrane biomimetic nanoparticles combined with UTMD to improve the stability of atherosclerotic plaques. *Front Chem.* (2022) 10:868063. doi: 10.3389/fchem.2022.868063

64. Ma X, Wang J, Li Z, Zhou X, Liang X, Wang J, et al. Early assessment of atherosclerotic lesions and vulnerable plaques in vivo by targeting apoptotic macrophages with AV nanobubbles. *Int J Nanomedicine.* (2022) 17:4933–46. doi: 10.2147/IJN.S382738

65. Xu S, Ilyas I, Little PJ, Li H, Kamato D, Zheng X, et al. Endothelial dysfunction in atherosclerotic cardiovascular diseases and beyond: from mechanism to pharmacotherapies. *Pharmacol Rev.* (2021) 73:924–67. doi: 10.1124/pharmrev.120.000096

66. Groh L, Keating ST, Joosten LAB, Netea MG, Riksen NP. Monocyte and macrophage immunometabolism in atherosclerosis. *Semin Immunopathol.* (2018) 40:203–14. doi: 10.1007/s00281-017-0656-7

67. Medina-Leyte DJ, Zepeda-García O, Domínguez-Pérez M, González-Garrido A, Villarreal-Molina T, Jacobo-Albavera L Endothelial dysfunction, inflammation and coronary artery disease: potential biomarkers and promising therapeutical approaches. *Int J Mol Sci.* (2021) 22(8):3850. doi: 10.3390/ijms22083850

68. Jain T, Nikolopoulou EA, Xu Q, Qu A. Hypoxia inducible factor as a therapeutic target for atherosclerosis. *Pharmacol Ther.* (2018) 183:22–33. doi: 10.1016/j.pharmthera.2017.09.003

69. Avgerinos NA, Neofytou P. Mathematical modelling and simulation of atherosclerosis formation and progress: a review. *Ann Biomed Eng.* (2019) 47:1764–85. doi: 10.1007/s10439-019-02268-3

70. Schmitt MMN, Megens RTA, Zernecke A, Bidzhekov K, van den Akker NM, Rademakers T, et al. Endothelial junctional adhesion molecule-a guides monocytes into flow-dependent predilection sites of atherosclerosis. *Circulation.* (2014) 129:66–76. doi: 10.1161/CIRCULATIONAHA.113.004149

71. Soehnlein O, Libby P. Targeting inflammation in atherosclerosis—from experimental insights to the clinic. *Nat Rev Drug Discov.* (2021) 20:589–610. doi: 10.1038/s41573-021-00198-1

72. Depuydt MAC, Prange KHM, Slenders L, Örd T, Elbersen D, Boltjes A, et al. Microanatomy of the human atherosclerotic plaque by single-cell transcriptomics. *Circ Res.* (2020) 127:1437–55. doi: 10.1161/CIRCRESAHA.120.316770

73. Kaul S. Myocardial contrast echocardiography: a 25-year retrospective. *Circulation.* (2008) 118:291–308. doi: 10.1161/CIRCULATIONAHA.107.747303

74. Wang S, Unnikrishnan S, Herbst EB, Klibanov AL, Mauldin FW, Hossack JA. Ultrasound molecular imaging of inflammation in mouse abdominal aorta. *Invest Radiol.* (2017) 52:499–506. doi: 10.1097/RLI.0000000000000373

75. Wu J, Leong-Poi H, Bin J, Yang L, Liao Y, Liu Y, et al. Efficacy of contrast-enhanced US and magnetic microbubbles targeted to vascular cell adhesion molecule-1 for molecular imaging of atherosclerosis. *Radiology.* (2011) 260:463–71. doi: 10.1148/radiol.11102251

76. Díaz-López R, Tsapis N, Santin M, Bridal SL, Nicolas V, Jaillard D, et al. The performance of PEGylated nanocapsules of perfluorooctyl bromide as an ultrasound contrast agent. *Biomaterials.* (2010) 31:1723–31. doi: 10.1016/j.biomaterials.2009.11.044

77. Davidhi A, Rafailidis V, Destanis E, Prassopoulos P, Foinitsis S. Ultrasound elastography: another piece in the puzzle of carotid plaque vulnerability? *Med Ultrason.* (2022) 24:356–63. doi: 10.11152/mu-3190

78. Sigrist RMS, Liau J, Kaffas AE, Chammas MC, Willmann JK. Ultrasound elastography: review of techniques and clinical applications. *Theranostics.* (2017) 7:1303–29. doi: 10.7150/thno.18650

79. Zhang Q, Li C, Zhou M, Liao Y, Huang C, Shi J, et al. Quantification of carotid plaque elasticity and intraplaque neovascularization using contrast-enhanced ultrasound and image registration-based elastography. *Ultrasonics.* (2015) 62:253–62. doi: 10.1016/j.ultras.2015.05.025

80. Liu Z, Bai Z, Huang C, Huang M, Huang L, Xu D, et al. Interoperator reproducibility of carotid elastography for identification of vulnerable atherosclerotic plaques. *IEEE Trans Ultrason Ferroelectr Freq Control.* (2019) 66:505–16. doi: 10.1109/TUFFC.2018.2888479

81. Huang C, Pan X, He Q, Huang M, Huang L, Zhao X, et al. Ultrasound-based carotid elastography for detection of vulnerable atherosclerotic plaques validated by magnetic resonance imaging. *Ultrasound Med Biol*. (2016) 42:365–77. doi: 10.1016/j.ultrasmedbio.2015.09.023

82. Huang C, He Q, Huang M, Huang L, Zhao X, Yuan C, et al. Non-invasive identification of vulnerable atherosclerotic plaques using texture analysis in ultrasound carotid elastography: an in vivo feasibility study validated by magnetic resonance imaging. *Ultrasound Med Biol*. (2017) 43:817–30. doi: 10.1016/j.ultrasmedbio.2016.12.003

83. Roy Cardinal M-H, Heusinkveld MHG, Qin Z, Lopata RGP, Naim C, Soulez G, et al. Carotid artery plaque vulnerability assessment using noninvasive ultrasound elastography: validation with MRI. *AJR Am J Roentgenol*. (2017) 209:142–51. doi: 10.2214/AJR.16.17176

84. Shiina T, Nightingale KR, Palmeri ML, Hall TJ, Bamber JC, Barr RG, et al. WFUMB Guidelines and recommendations for clinical use of ultrasound elastography: part 1: basic principles and terminology. *Ultrasound Med Biol*. (2015) 41:1126–47. doi: 10.1016/j.ultrasmedbio.2015.03.009

85. Lou Z, Yang J, Tang L, Jin Y, Zhang J, Liu C, et al. Shear wave elastography imaging for the features of symptomatic carotid plaques: a feasibility study. *J Ultrasound Med*. (2017) 36:1213–23. doi: 10.7863/ultra.16.04073

86. Školoudík D, Kešnerová P, Vomáčka J, Hrbáč T, Netuka D, Forostyak S, et al. Shear-wave elastography enables identification of unstable carotid plaque. *Ultrasound Med Biol*. (2021) 47:1704–10. doi: 10.1016/j.ultrasmedbio.2021.03.026

87. Marlevi D, Maksuti E, Urban MW, Winter R, Larsson M. Plaque characterization using shear wave elastography-evaluation of differentiability and accuracy using a combined ex vivo and in vitro setup. *Phys Med Biol*. (2018) 63:235008. doi: 10.1088/1361-6560/aaec2b

88. Marlevi D, Mulvagh SL, Huang R, DeMarco JK, Ota H, Huston J, et al. Combined spatiotemporal and frequency-dependent shear wave elastography enables detection of vulnerable carotid plaques as validated by MRI. *Sci Rep*. (2020) 10:403. doi: 10.1038/s41598-019-57317-7

89. Torres G, Czernuszewicz TJ, Homeister JW, Caughey MC, Huang BY, Lee ER, et al. Delineation of human carotid plaque features in vivo by exploiting displacement variance. *IEEE Trans Ultrason Ferroelectr Freq Control*. (2019) 66:481–92. doi: 10.1109/TUFFC.2019.2898628

90. Czernuszewicz TJ, Homeister JW, Caughey MC, Wang Y, Zhu H, Huang BY, et al. Performance of acoustic radiation force impulse ultrasound imaging for carotid plaque characterization with histologic validation. *J Vasc Surg*. (2017) 66(6):1749–57.e3. doi: 10.1016/j.jvs.2017.04.043

91. Cloutier G, Cardinal M-HR, Ju Y, Giroux M-F, Lanthier S, Soulez G. Carotid plaque vulnerability assessment using ultrasound elastography and echogenicity analysis. *AJR Am J Roentgenol*. (2018) 211:847–55. doi: 10.2214/AJR.17.19211

92. Shang J, Wang W, Feng J, Luo G-G, Dang Y, Sun J, et al. Carotid plaque stiffness measured with supersonic shear imaging and its correlation with Serum homocysteine level in ischemic stroke patients. *Korean J Radiol*. (2018) 19:15–22. doi: 10.3348/kjr.2018.19.1.15

93. Garcia-Garcia HM, Costa MA, Serruys PW. Imaging of coronary atherosclerosis: intravascular ultrasound. *Eur Heart J*. (2010) 31:2456–69. doi: 10.1093/eurheartj/ehq280

94. Mehanna E, Abbott JD. Vulnerable plaques, more than meets the i. *Catheter Cardiovasc Interv*. (2017) 90:1115–6. doi: 10.1002/ccd.27426

95. Zhang J, Gao X, Kan J, Ge Z, Han L, Lu S, et al. Intravascular ultrasound versus angiography-guided drug-eluting stent implantation: the ULTIMATE trial. *J Am Coll Cardiol*. (2018) 72:3126–37. doi: 10.1016/j.jacc.2018.09.013

96. Yonetsu T, Jang IK. Advances in intravascular imaging: new insights into the vulnerable plaque from imaging studies. *Korean Circ J*. (2018) 48(1):1–15. doi: 10.4070/kcj.2017.0182

97. Mintz GS, Nissen SE, Anderson WD, Bailey SR, Erbel R, Fitzgerald PJ, et al. American College of cardiology clinical expert consensus document on standards for acquisition, measurement and reporting of intravascular ultrasound studies (IVUS). A report of the American college of cardiology task force on clinical expert consensus documents. *J Am Coll Cardiol*. (2001) 37:1478–92. doi: 10.1016/S0735-1097(01)01175-5

98. Shishikura D, Kataoka Y, Di Giovanni G, Takata K, Scherer DJ, Andrews J, et al. Progression of ultrasound plaque attenuation and low echogenicity associates with major adverse cardiovascular events. *Eur Heart J*. (2020) 41:2965–73. doi: 10.1093/eurheartj/ehaa173

99. Pu J, Mintz GS, Biro S, Lee J-B, Sum ST, Madden SP, et al. Insights into echo-attenuated plaques, echolucent plaques, and plaques with spotty calcification: novel findings from comparisons among intravascular ultrasound, near-infrared spectroscopy, and pathological histology in 2,294 human coronary artery segments. *J Am Coll Cardiol*. (2014) 63:2220–33. doi: 10.1016/j.jacc.2014.02.576

100. Banchhor SK, Londhe ND, Araki T, Saba L, Radeva P, Laird JR, et al. Well-balanced system for coronary calcium detection and volume measurement in a low resolution intravascular ultrasound videos. *Comput Biol Med*. (2017) 84:168–81. doi: 10.1016/j.compbiomed.2017.03.026

101. Tian J, Hou J, Xing L, Kim S-J, Yonetsu T, Kato K, et al. Significance of intraplaque neovascularisation for vulnerability: optical coherence tomography study. *Heart*. (2012) 98:1504–9. doi: 10.1136/heartjnl-2012-302445

102. Ruiz EMG, Papaioannou TG, Vavuranakis M, Stefanadis C, Naghavi M, Kakadiaris IA. Analysis of contrast-enhanced intravascular ultrasound images for the assessment of coronary plaque neoangiogenesis: another step closer to the identification of the vulnerable plaque. *Curr Pharm Des*. (2012) 18:2207–13. doi: 10.2174/138161212800099919

103. Goertz DE, Frijlink ME, Tempel D, van Damme LCA, Krams R, Schaar JA, et al. Contrast harmonic intravascular ultrasound: a feasibility study for vasa vasorum imaging. *Invest Radiol*. (2006) 41:631–8. doi: 10.1097/01.rli.0000229773.11715.da

104. Carlier S, Kakadiaris IA, Dib N, Vavuranakis M, O'Malley SM, Gul K, et al. Vasa vasorum imaging: a new window to the clinical detection of vulnerable atherosclerotic plaques. *Curr Atheroscler Rep*. (2005) 7:164–9. doi: 10.1007/s11883-005-0040-2

105. Vavuranakis M, Papaioannou TG, Vrachatis D, Katsimboulas M, Sanidas EA, Vaina S, et al. Computational imaging of aortic vasa vasorum and neovascularization in rabbits using contrast-enhanced intravascular ultrasound: association with histological analysis. *Anatol J Cardiol*. (2018) 20:117–24. doi: 10.14744/AnatolJCardiol.2018.35761

106. Ma J, Martin KH, Li Y, Dayton PA, Shung KK, Zhou Q, et al. Design factors of intravascular dual frequency transducers for super-harmonic contrast imaging and acoustic angiography. *Phys Med Biol*. (2015) 60:3441–57. doi: 10.1088/0031-9155/60/9/3441

107. Bouakaz A, Krenning BJ, Vletter WB, ten Cate FJ, De Jong N. Contrast superharmonic imaging: a feasibility study. *Ultrasound Med Biol*. (2003) 29:547–53. doi: 10.1016/S0301-5629(03)00012-7

108. Gessner RC, Aylward SR, Dayton PA. Mapping microvasculature with acoustic angiography yields quantifiable differences between healthy and tumor-bearing tissue volumes in a rodent model. *Radiology*. (2012) 264:733–40. doi: 10.1148/radiol.12112000

109. Ma J, Martin K, Dayton PA, Jiang X. A preliminary engineering design of intravascular dual-frequency transducers for contrast-enhanced acoustic angiography and molecular imaging. *IEEE Trans Ultrason Ferroelectr Freq Control*. (2014) 61:870–80. doi: 10.1109/TUFFC.2014.6805699

110. Lee J, Moon J-Y, Chang JH. A 35 MHz/105 MHz dual-element focused transducer for intravascular ultrasound tissue imaging using the third harmonic. *Sensors (Basel)*. (2018) 18(7):2290. doi: 10.3390/s18072290

111. Garcìa-Garcìa HM, Gogas BD, Serruys PW, Bruining N. IVUS-based imaging modalities for tissue characterization: similarities and differences. *Int J Cardiovasc Imaging*. (2011) 27:215–24. doi: 10.1007/s10554-010-9789-7

112. Kitahara S, Kataoka Y, Sugane H, Otsuka F, Asaumi Y, Noguchi T, et al. Imaging of vulnerable plaque with intravascular modalities: its advantages and limitations. *Cardiovasc Diagn Ther*. (2020) 10:1461–79. doi: 10.21037/cdt-20-238

113. Calvert PA, Obaid DR, O'Sullivan M, Shapiro LM, McNab D, Densem CG, et al. Association between IVUS findings and adverse outcomes in patients with coronary artery disease: the VIVA (VH-IVUS in vulnerable atherosclerosis) study. *JACC Cardiovasc Imaging*. (2011) 4:894–901. doi: 10.1016/j.jcmg.2011.05.005

114. Xie J, Qi J, Mao H, Wang N, Ye X, Zhou L, et al. Coronary plaque tissue characterization in patients with premature coronary artery disease. *Int J Cardiovasc Imaging*. (2020) 36:1003–11. doi: 10.1007/s10554-020-01794-9

115. Mushenkova NV, Summerhill VI, Zhang D, Romanenko EB, Grechko AV, Orekhov AN. Current advances in the diagnostic imaging of atherosclerosis: insights into the pathophysiology of vulnerable plaque. *Int J Mol Sci*. (2020) 21(8):2992. doi: 10.3390/ijms21082992

116. Stone GW, Maehara A, Lansky AJ, de Bruyne B, Cristea E, Mintz GS, et al. A prospective natural-history study of coronary atherosclerosis. *N Engl J Med*. (2011) 364:226–35. doi: 10.1056/NEJMoa1002358

117. Yang G, Wang W, Sheng X, Yang F, Kong L, He J, et al. Tissue characteristics of culprit lesion and myocardial tissue-level perfusion in non-ST-segment elevation acute coronary syndromes: the EARLY-MYO-ACS study. *Int J Cardiol*. (2019) 287:32–8. doi: 10.1016/j.ijcard.2019.02.010

118. Daida H, Dohi T, Fukushima Y, Ohmura H, Miyauchi K. The goal of achieving atherosclerotic plaque regression with lipid-lowering therapy: insights from IVUS trials. *J Atheroscler Thromb*. (2019) 26:592–600. doi: 10.5551/jat.48603

119. Puri R, Libby P, Nissen SE, Wolski K, Ballantyne CM, Barter PJ, et al. Long-term effects of maximally intensive statin therapy on changes in coronary atheroma composition: insights from SATURN. *Eur Heart J Cardiovasc Imaging*. (2014) 15:380–8. doi: 10.1093/ehjci/jet251

120. Räber L, Taniwaki M, Zaugg S, Kelbæk H, Roffi M, Holmvang L, et al. Effect of high-intensity statin therapy on atherosclerosis in non-infarct-related coronary arteries (IBIS-4): a serial intravascular ultrasonography study. *Eur Heart J*. (2015) 36:490–500. doi: 10.1093/eurheartj/ehu373

121. Andrews J, Psaltis PJ, Bayturan O, Shao M, Stegman B, Elshazly M, et al. Warfarin use is associated with progressive coronary arterial calcification: insights from serial intravascular ultrasound. *JACC Cardiovasc Imaging*. (2018) 11:1315–23. doi: 10.1016/j.jcmg.2017.04.010

122. Bazarbashi N, Kapadia SR, Nicholls SJ, Carlo J, Gad MM, Kaur M, et al. Oral calcium supplements associate with serial coronary calcification: insights from intravascular ultrasound. *JACC Cardiovasc Imaging*. (2021) 14:259–68. doi: 10.1016/j.jcmg.2020.06.030

123. Schuurman A-S, Vroegindewey MM, Kardys I, Oemrawsingh RM, Garcia-Garcia HM, van Geuns R-J, et al. Prognostic value of intravascular ultrasound in patients with coronary artery disease. *J Am Coll Cardiol*. (2018) 72:2003–11. doi: 10.1016/j.jacc.2018.08.2140

124. Stone GW, Mintz GS, Virmani R. Vulnerable plaques, vulnerable patients, and intravascular imaging. *J Am Coll Cardiol*. (2018) 72:2022–6. doi: 10.1016/j.jacc.2018.09.010

125. Nicholls SJ, Puri R, Anderson T, Ballantyne CM, Cho L, Kastelein JJP, et al. Effect of evolocumab on coronary plaque composition. *J Am Coll Cardiol*. (2018) 72:2012–21. doi: 10.1016/j.jacc.2018.06.078

126. Erlinge D, Maehara A, Ben-Yehuda O, Bøtker HE, Maeng M, Kjøller-Hansen L, et al. Identification of vulnerable plaques and patients by intracoronary near-infrared spectroscopy and ultrasound (PROSPECT II): a prospective natural history study. *Lancet*. (2021) 397:985–95. doi: 10.1016/S0140-6736(21)00249-X

127. Imai M, Kawamura M, Kochi I, Matsuoka T, Kihara S, Yamamoto H. Anti-Apo B-100 autoantibody is a marker of unstable coronary plaque. *J Atheroscler Thromb*. (2021) 28:1025–34. doi: 10.5551/jat.58784

128. Akashi R, Koga S, Yonekura T, Ikeda S, Kawano H, Maemura K. Cardio-ankle vascular index is associated with coronary plaque composition assessed with iMAP-intravascular ultrasound in patients with coronary artery disease. *J Cardiol*. (2021) 78:502–8. doi: 10.1016/j.jjcc.2021.05.015

129. Costopoulos C, Maehara A, Huang Y, Brown AJ, Gillard JH, Teng Z, et al. Heterogeneity of plaque structural stress is increased in plaques leading to MACE: insights from the PROSPECT study. *JACC Cardiovasc Imaging*. (2020) 13:1206–18. doi: 10.1016/j.jcmg.2019.05.024

130. Kong Q, Liu M, Li Y, Zhu Q, Su G. Effect of evolocumab on the progression and stability of atherosclerotic plaques as evaluated by grayscale and iMAP-IVUS. *Ann Palliat Med*. (2020) 9:3078–88. doi: 10.21037/apm-20-690

131. Kurosawa T, Li Y, Sudo M, Haruta H, Hagikura K, Takayama T, et al. Effect of the dipeptidyl peptidase-4 inhibitor linagliptin on atherosclerotic lesions in watanabe heritable hyperlipidemic rabbits: iMap-IVUS and pathological analysis. *Heart Vessels*. (2021) 36:127–35. doi: 10.1007/s00380-020-01689-8

Frontiers in
Cardiovascular Medicine

Innovations and improvements in cardiovascular treatment and practice

Focuses on research that challenges the status quo of cardiovascular care, or facilitates the translation of advances into new therapies and diagnostic tools.

Discover the latest Research Topics

See more →

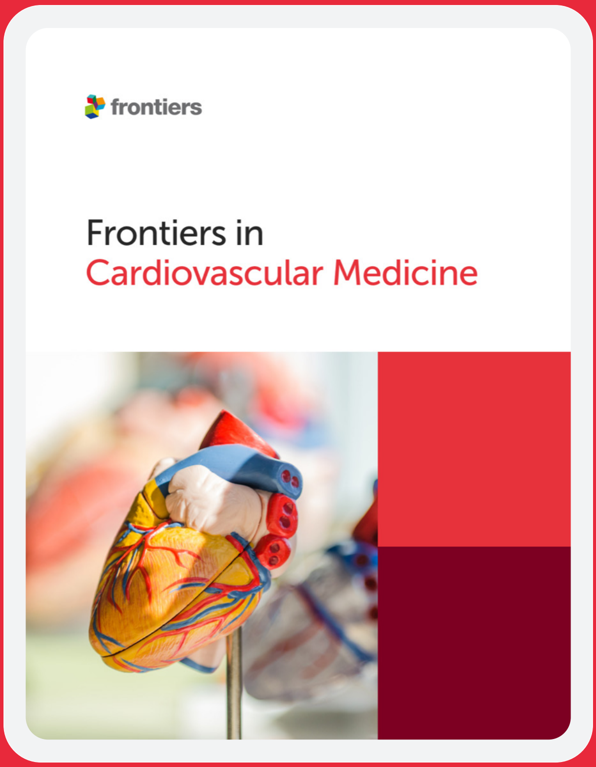

frontiers

Frontiers in
Cardiovascular Medicine

Frontiers
Avenue du Tribunal-Fédéral 34
1005 Lausanne, Switzerland
frontiersin.org

Contact us
+41 (0)21 510 17 00
frontiersin.org/about/contact